Comparative Studies of Strong Gravitational Lens Models

PhD Thesis

Comparative Studies of Strong Gravitational Lens Models

(強い重力レンズモデルの比較研究)

Alan T. Lefor

Department of Physics

Graduate School of Science

Tohoku University

March, 2015

This Dissertation is dedicated

To Chieko, who stood by me in my darkest hours, is always at my side, and supports me in pursuing my dreams, and

To Maarten who makes me incredibly proud, as I have watched him become a happy and fulfilled adult, finding his way toward the promise of a bright future, and

To my parents, may they rest in peace, who started me on this incredible journey

Therefore, there is no great chance of observing this phenomenon...

—Albert Einstein (in reference to gravitational lensing, 1936)

Acknowledgements

Lev Landau said "The way to identify theoretical physicists is to see how excited they are when they learn about relativity". My excitement to study relativity was prompted by R. Scott Dunbar many years ago in a University far far away, but this journey has not yet taken me far enough.

I gratefully acknowledge the unflagging support of my mentor, Professor Toshifumi Futamase, a brilliant theoretician who has always been the right mix of mentor and colleague. From the first time I contacted him prior to applying to Tohoku University, he has been consistently interested and helpful. He has given me the optimal balance of academic freedom and helpful guidance.

I gratefully acknowledge the help of Mohammad Akhlaghi, who dragged me kicking and screaming onto the Linux platform, and especially for the Journal Club.

I gratefully acknowledge the support of my colleagues at Jichi Medical University who allowed me to pursue this dream, and especially the friendship of Professor Yoshikazu Yasuda.

I acknowledge the contributions of many investigators worldwide, notably Adi Zitrin who is both brilliant and a real "mensch", and especially to Cristian E. Rusu who has always been willing to help.

Abstract

Data from strong gravitational lensing is critically important in this era of precision cosmology. Analysis of strong gravitational lensing depends on software analysis of observational data. This dissertation includes six studies that serve to compare the results of models using strong gravitational lens model software.

In order to identify the software available, we performed a systematic review of 26 lens model software packages. Lens models are classified as parametric models or non-parametric models, and are further divided into research and educational software. Fourteen of the 26 software packages are thoroughly reviewed with regard to software features (installation, documentation, files provided, etc.) and lensing features (type of model, input data, output data, etc.) as well as a brief review of studies where they have been used. The remaining 12 packages are reviewed in an abbreviated manner because either the software was not functional after download, or the software is not available for download and could only be reviewed from existing published reports. This is the first systematic review of strong gravitational lens modeling software, and includes most of the software being used today for studies of strong gravitational lensing as well as software available for demonstration and educational purposes. This review became the core of a similar review in an online resource for strong gravitational lens data.

The next study evaluates the behavior of strong gravitational lens modeling software with changes in redshift. Four different strong gravitational lens codes are directly compared (Lenstool, glafic, GRALE and PixeLens) in the analysis of a mock model and SDSSJ1004+4112. The percent change in time delays calculated at each redshift tested are compared with percent change in $D_{\rm d}D_{\rm s}/D_{\rm ds}$. A mock model with a singular isothermal ellipsoid and four images is tested with each code. Five models are used with a constant z_{lens} and a varying z_{source}, and five models with a constant z_{source} and a varying z_{lens}. In general, the changes in time delay are of a similar magnitude and direction, although some calculated time delays did not follow changes in $D_{\rm d}D_{\rm s}/D_{\rm ds}$. This variation is explained by changes in image position calculated by glafic and GRALE, which varied according to $D_{\rm ds}/D_{\rm s}$. Small changes in redshift affect the calculated time delay and mass, and that the effect on the calculations is dependent on the particular software used.

The use of multiple lens models may enhance the understanding of a system being studied. HydraLens, consisting of about 10,000 lines of Visual Basic code simplifies creation of model files for Lenstool, Gravlens/Lensmodel, glafic and PixeLens, using a custom designed GUI for each of the four codes that simplifies the entry of the model for each of these codes, obviating the need for user manuals to set the values of the many flags and in each data field. HydraLens can also translate a model generated for any of these four software packages into any of the other three. This software is available for download from the Astrophysics Source Code Library.

The objective of the next study is to directly compare the analysis of four lens systems using four lens model software codes to understand the differences and

limitations of the models. The software lens model translation tool, HydraLens, was used to generate multiple models for four strong lens systems including COSMOS J095930+023427, SDSS J1320+1644, SDSSJ1430+4105 and J1000+0021. All four systems were modeled with four different lens model programs including PixeLens, Lenstool, glafic, and Lensmodel. The calculation of the Einstein radius and enclosed mass for each lens model was comparable. The results were more dissimilar if the masses of more than one lens potential were free-parameters. The image tracing algorithms of the software are different, resulting in different output image positions and differences in time delay and magnification calculations, as well as ellipticity and position angle. Differences in optimization resulted in different results for ellipticity and position angle. In a comparison of different software versions using identical model input files, results differed significantly when using two versions of the same software.

The next study is a comparative study of time delays calculated by four lens model codes for two string gravitational lens systems which have been extensively studied in the past, including B1608+656 and RXJ1131−1231. This was performed as a follow-up to the study above where two systems were compared using four software codes and gave very disparate results. In this study, both systems have been extremely well studied by numerous investigators. For B1608+656 we used two models, one with a single SIE potential and one with two SIE potentials which closely resembles observational data. In the single SIE model, the results are somewhat variable but on the same order of magnitude as observational data, and close agreement for the velocity dispersion calculations. For the two SIE models, there is also some variation, but the results are somewhat similar to those with the single SIE model. The velocity dispersions calculated by the three codes are similar, but the mass of the G2 lens is greater than that from previous studies. The models of RXJ1131−1231 all use a single SIE potential, and the results are close to that calculated in previous studies. There is fairly close agreement with previous calculations of lens mass. Overall, the studies of these two systems showed less variation than that in our previous study of the mock model and SDSSJ1004+4112. Further studies will determine the value of H_0 using these models, and further refinement of the models.

The next study is a detailed study of MACSJ1149.5+2223, which includes the first observation of a GRAvitationally lensed yet MOrphologically Regular image (GRAMOR). The initial part of this study is development of the lens models using Lenstool and glafic. The Lenstool model used is based on that used in the Hubble Frontier Fields project. The initial phase of the project was designed to evaluate the ability of this model to constrain the cosmological parameters by evaluating the w_X vs. Ω_m plane. This study showed that the Lenstool model constrains the dark energy equation of state parameter in a manner similar to that observed with Abell1689. The Lenstool model uses five lens potentials which are PIEMDs. The first glafic model tested was not able to constrain the dark energy equation of state parameter. This model uses an NFW potential model. Further studies are pending including refinement of the glafic model, representing the GRAMOR image, and then determining whether or not the GRAMOR will further constrain the cosmological parameters.

Taken together, the results of these six studies further support the need for future lensing studies to include multiple lens models, use of open software, availability of lens model files use in studies, and computer challenges to develop new approaches.

Future studies need a standard nomenclature and specification of software used to allow improved interpretation, reproducibility and transparency of results.

Contents

Contents vii

List of Figures x

1 The Equivalence Principle 1
- 1.1 The Equivalence Principle . . . 1
- 1.2 The Bending of Light . . . 2
- 1.3 Organization of this Dissertation . . . 2

References 4

2 Special Relativity, General Relativity and Cosmology 5
- 2.1 Purpose and Organization of this Chapter . . . 5
- 2.2 Special Relativity . . . 5
- 2.3 General Relativity . . . 20
- 2.4 Fundamentals of Cosmology . . . 37
- 2.5 Chapter Summary . . . 74

References 75

3 Gravitational Lensing: Models and Applications in Cosmology 77
- 3.1 Purpose and Organization of this Chapter . . . 77
- 3.2 Distance Measurements in Cosmology . . . 78
- 3.3 Gravitational Lensing: Basic Principles . . . 79
- 3.4 Strong Gravitational Lensing . . . 106
- 3.5 Weak Gravitational Lensing . . . 113
- 3.6 Gravitational Lensing in Cosmology . . . 129
- 3.7 Gravitational Lens Models . . . 147

References 156

4 A Systematic Review of Strong Gravitational Lens Model Software 161
- 4.1 Purpose and Organization of this Chapter . . . 161
- 4.2 Introduction . . . 161
- 4.3 Classification and Review Methodology . . . 162
- 4.4 Research Software . . . 166
- 4.5 Educational Software . . . 182
- 4.6 Discussion . . . 189
- 4.7 Conclusions . . . 190

References **192**

5 Time delay and mass calculations are sensitive to changes in redshift and are model dependent **197**
5.1 Purpose and Organization of this Chapter . . . 197
5.2 Introduction . . . 197
5.3 Methods . . . 199
5.4 Results . . . 202
5.5 Discussion . . . 216
5.6 Conclusions . . . 221

References **223**

6 HydraLens: Computer-Assisted Strong Gravitational Lens Model Generation and Translation **229**
6.1 Purpose and Organization of this Chapter . . . 229
6.2 Introduction . . . 229
6.3 Methods . . . 231
6.4 Implementation . . . 237
6.5 Discussion . . . 240
6.6 Future Development and Conclusions . . . 241

References **242**

7 A direct, semi-independent comparative study of four strong gravitational lenses: SDSS J1320+1644, COSMOS J095930+023427, SDSSJ1430, and J1000+0021 **244**
7.1 Purpose and Organization of this Chapter . . . 244
7.2 Introduction . . . 245
7.3 Methods . . . 246
7.4 Results . . . 250
7.5 Discussion . . . 265
7.6 Conclusions . . . 266

References **268**

8 RXJ1131 and B1608: Comparative Studies of Time Delays for Two Well-Characterized Strong Gravitational Lenses **271**
8.1 Purpose and Organization of this Chapter . . . 271
8.2 Introduction . . . 272
8.3 Methods . . . 279
8.4 Results . . . 279
8.5 Discussion . . . 288
8.6 Conclusions and Future Plans . . . 291

References **292**

9 Cosmological Parameters from Strong Gravitational Lens Models: Studies of GRAMORs **295**
9.1 Purpose and Organization of this Chapter . . . 295
9.2 Introduction . . . 295
9.3 Methods . . . 307
9.4 Results . . . 309
9.5 Discussion . . . 312
9.6 Conclusions and Future Work . . . 316

References **317**

10 Conclusions and Outlook **319**
10.1 Gravitational Lens Model Software . . . 319
10.2 Comparative Studies: Strong Gravitational Lens Models . . . 319
10.3 Gravitational Lens Model Translation . . . 320
10.4 Comparative Studies: Time Delay Calculations . . . 320
10.5 Comparative Studies: Constraining Cosmological Parameters . . . 320
10.6 Outlook and Challenges for the Future of Lens Model Studies . . . 321

Appendix A HydraLens User Manual **322**
.1 Introduction . . . 323
.2 Generate a Lens Model . . . 323
.3 Read an Existing Lens Model . . . 325
.4 Translate a Lens Model . . . 326

List of Figures

1.1 The Equivalence Principle predicts that gravity will bend light. [3] 1

2.1 The Michaelson-Morley experiment [11] 9
2.2 Relationship of v and γ 13
2.3 Relativistic Addition of Velocities [19] 14
2.4 Spherical coordinate system. Figure shows r = constant surface, hence, $dr = 0$ on the surface [20]. 24
2.5 The geometry of space-time is changed by the presence of mass 36
2.6 Hubble diagrams showing the relationship between recessional velocities of distant galaxies and their distances. The left plot shows the original data of Hubble. The right plot shows more recent data, using significantly more distant galaxies (note difference in scale) from [28] 38
2.7 Homogeneity and the Hubble Law: A string of equally spaced galaxies Z, A, B, C, ... are shown with velocities as measured from A or B or C indicated by the lengths and directions of the attached arrows. The principle of homogeneity requires that the velocity of C as seen by B is equal to the velocity of B as seen by A, adding these two velocities gives the velocity of C as seen by A, indicated by an arrow twice as long. Proceeding in this way we can fill out the whole pattern of velocities shown in the figure. As can be seen the velocities obey the Hubble law: the velocity of any galaxy, as seen by others is proportional to the distance between them. This is the only pattern of velocities consistent with the principle of homogeneity. from [1] 39
2.8 The two dimensional analogues of the Friedmann models. A spherical surface, a plane, and a pseudo-sphere. Note that the global geometry of the universe affects the sum of angles of a triangle. From [1] 44
2.9 Hubble diagram from the Supernova Cosmology Project, from [28]. 52
2.10 Constraints on the dark-energy equation-of-state parameter, as a function of Ω_{M}, assuming a flat universe. These limits are derived from studies of supernovae, CMB anisotropies, measurements of the Hubble constant, large-scale structure, and primordial nucleosynthesis. From [28]. 55
2.11 Constraint on the baryon density from Big Bang Nucleosynthesis. Predictions are shown for four light elements. The solid vertical band is fixed by measurements of primordial deuterium. The boxes are the observations; there is only an upper limit on the primordial abundance of ^3He. From [10] 56

2.12 The CMB over the entire sky, color-coded to represent differences in temperature from the average 2.725 K: the color scale ranges from +300 μK (red) to −200 μK (dark blue), representing slightly hotter and colder spots (and also variations in density.) Results are from the WMAP satellite. The angular resolution is 0.2°. From [1]. 59
2.13 The Cosmic Energy Inventory, part of Table 1 in [15] 61
2.14 The Cosmic Energy Inventory, based on data from [15], as published by Pössel . 64
2.15 Cosmological Parameters, from [16]. 67

3.1 Angular deflection of a ray of light passing close to the limb of the Sun. Since the light ray is bent toward the Sun, the apparent positions of stars move away from the Sun. This is a schematic of what Eddington observed in 1919, which verified a prediction of General Relativity. [39] 81
3.2 Schematic diagram of Gravitational Lensing [61] 82
3.3 Illustration of the effects of convergence and shear on a circular source. Convergence magnifies the image isotropically, and shear deforms it to an ellipse. (From [39]). 84
3.4 Illustration of the geometrical meaning of the shear γ_i and of the ellipticity ϵ_i. A positive (negative) shear component γ_1 corresponds to an elongation (compression) along the x-axis. A positive (negative) value of the shear component γ_2 corresponds to an elongation (compression) along the $x = y$ axis. The ellipticity of an object is defined to vanish if the object is circular (*center*). The ellipticity components ϵ_1 and ϵ_2 correspond to compression and elongations similar to those for the shear components. From [50] 85
3.5 Examples of the most common configurations of galaxy-scale gravitational lens systems. A background source (top left) can produce four visible images (a "quad"; top right), an (incomplete) Einstein ring (bottom left), or two visible images (a "double"; bottom right), depending on the ellipticity of the projected mass distribution of the deflector and on the relative alignment between source and deflector [61] 86
3.6 Optical analogy to illustrate the gravitational lensing phenomenon. The optical properties of the stem of a wineglass are similar to those of a typical galaxy scale lens. Viewed through a wineglass, a background compact source such as distant candle (top left), can reproduce the quad (top right), Einstein ring (bottom left), and double (bottom rights) configurations observed in gravitational lensing and shown in Figure 3.5. [61]. 87
3.7 Compact source moving away from the center of an elliptical lens. Left panel: source crossing a fold caustic; right panel: source crossing a cusp caustic. Within each panel, the diagram on the left shows critical lines and image positions and the diagram on the right shows caustics and source positions. From [39] 90
3.8 This figure illustrates possible multiple-image configurations in a typical lens. An isothermal sphere with additional external shear was assumed. The core radius varies in the four panels. Caustics are solid, critical curves dashed. Filled symbols represent the source position while the corresponding images are indicated by the open symbols. If the core radius is large $x_c = 2.0$, then only one tangential critical curve appears, the second (radial) critical curve gives rise to radial arcs or four or five, respectively, images. From [57] 91

3.9 Five snapshots of a gravitational lens situation: From left to right the alignment between lens and source gets better and better, until it is perfect in the rightmost panel. This results in the image of an "Einstein ring". [63] 92
3.10 A source S on the optic axis of a circularly symmetric lens is imaged as a ring with an angular radius given by the Einstein radius $\theta_{\rm E}$. [39] 93
3.11 Mass density profiles of lens galaxies inferred from a strong lensing and dynamical analysis. In addition to the mass associated with the stars (red line), the data require a more extended mass component, identified as the dark matter halo (blue line). Although neither component is a simple power-law, the total mas profile is close to isothermal, i.e. $\gamma' = 2$. The vertical dashed line identifies the location of the Einstein radius. [61] 95
3.12 Sketch of a double source plane lens system. The cosmological scaling factor β is the product of $D_{\rm ls1}$ and $D_{\rm s2}$ (both in red) divided by the product of $D_{\rm ls2}$ and $D_{\rm s1}$ (both in blue). For a singular isothermal sphere, where the first source has no mass, β is the ratio of Einstein radii. Figure from [9]. 96
3.13 Double Einstein ring compound lens SDSSJ0946+1006. **Left:** color composite HST image. Note the foreground main deflector in the center, the bright ring formed by the images of the intermediate galaxy, and the fainter ring formed by the images of the background galaxy lensed by the two intervening objects. **Right:** Enclosed mass profile as inferred from the Einstein radii of the two rings (red solid points - the error bars are smaller than the points). The enclosed mass increases more steeply with radius than the enclosed light (solid blue line; rescaled by the best fit stellar mass-to-light ratio), indicating the presence of a more extended dark matter component. Even a "maximum bulge" solution (dotted blue line) cannot account for the mass at the outer Einstein radius. [61] 97
3.14 The galaxy-subtracted *HST* F814W image of SDSSJ0946+1006. The first source is modeled as only contributing to the flux observed within the green mask, and the second source is assumed to only have non-zero flux within the blue mask. The red crosses mark the 4 pixels which we map back on to the first lens plane and use to determine the centroid of the first source's mass. Figure from [9]. . . . 98
3.15 The w and $\Omega_{\rm M}$ plane. Red shows the 68, 95 and 99.7 per cent confidence constraints derived from our measurement of the cosmological scale factor in J0946. In the left, panel grey shows the WMAP9 constraints whilst the Planck 2013 constraints are shown on the right. In both panels, black shows the combined constraint from J0946 and the CMB prior. Figure from [9]. 99
3.16 Image configurations in quadruply lensed events. For the double quasars, there are two possible configurations not shown here. [60] 100
3.17 Imaging of a point source by a non-singular, circularly-symmetric lens. Left: image positions and critical lines; right: source position and corresponding caustics. [39] 101
3.18 Imaging of an extended source by a non-singular circularly-symmetric lens. A source close to the point caustic at the lens center produces two tangentially oriented arc-like images close to the outer critical curve, and a faint image at the lens center. A source on the outer caustic produces a radially elongated image on the inner critical curve, and a tangentially oriented image outside the outer critical curve. Because of these image properties, the outer and inner critical curves are called *tangential* and *radial*, respectively. 102

3.19 The caustic and critical lines of an elliptical lens. The left and right panels describe the caustic and the critical curves respectively. The upper panels show the relationship between source positions and the shapes of images around the cusp. Lower panels are the same but around the fold. [19] and [17]. 104
3.20 Sketch of the dependence of the overall scale of a lens system on the value of the Hubble constant [39]. 111
3.21 A circular source, shown at the left, is mapped by the inverse Jacobian $\mathcal{A}^{-1}$ onto an ellipse. In the absence of shear, the resulting image is a circle with modified radius, depending on κ. Shear causes an axis ratio different from unity, and the orientation of the resulting ellipse depends on the phase of the shear. From [55] . 116
3.22 The shape of image ellipses for a circular source, in dependence on their two ellipticity components χ_1 and χ_2; a corresponding plot in term of the ellipticity components ϵ_i would look quite similar. Note that the ellipticities are rotated by 90° when $\chi \rightarrow -\chi$ From [55] 116
3.23 Illustration of the tangential and cross-components of the shear, for an image with $\epsilon_1 = 0.3$, $\epsilon_2 = 0$, and three different directions ϕ with respect to a reference point. From [55] 118
3.24 We need to infer accurate information about the shape of the true surface brightness distribution (left) from images that have been corrupted by various sources of bias, such as pixellation, seeing and noise. Given a good description of the instrumental effects it is possible to simulate their effects and thus examine the performance of shape measurement algorithms. [21] 122
3.25 *Left panel:* Plot of the apparent magnitude versus half-light radius for RCS data. The rectangle indicates the sample of stars that can be used to model the PSF variation. Brighter stars saturate and their observed sizes increase as can be seen as well. *Right panel:* An example of the pattern of PSF anisotropy for MegaCam on CFHT. The sticks indicate the direction of the major axis of the PSF and the length is proportional to the PSF ellipticity. A coherent pattern across the field-of-view is clearly visible. [21] 124
3.26 X-ray emission from the 'Bullet' cluster of galaxies as observed by Chandra. The eponymous bullet is a small galaxy cluster which has passed through the larger cluster and whose hot gas is seen in X-rays as the triangular shape on the right. The contours correspond to the previous mass reconstruction. The dark matter distribution is clearly offset from the gas, which contains the majority of baryonic matter, but agrees well with the distribution of galaxies – as expected if both the dark matter and stars in galaxies are effectively collisionless. From [22] 127
3.27 Two ways of obtaining a given image configuration. The left panel displays a system with four images, with an elliptical lens that introduces convergence and shear at the position of the images. On the right panel, is shown the same image geometry and flux ratios, but the lens is now circular. One would in principle only obtain two images with such a lens. The shear required to obtain four images is introduced by the nearby cluster. The mass density of the cluster is represented through its convergence . The mass of the main lens is scaled accordingly by $1/(1-\kappa)$ so that the image configuration remains the same as in the left panel: the mass in the main lens and in the cluster are degenerate. If no independent measurement is available for at least one of the components (main lens or cluster), it is often difficult to know, from the modeling alone, what exactly are their respective contributions.[10]. 131

3.28 Rotation curve for a typical galaxy from [16]. The lower panel hows the H1 rotation curve (points). The curve labelled disk shows the expected rotation curve if the surface density distribution followed the surface brightness distribution in the upper panel. The curve labelled gas is the contribution to the rotation curve from the observed gas. The curve labelled halo is the rotation curve of the adopted dark halo model: the three labelled rotation curves, when added in quadrature, produce the total rotation curve that passes through the observed points. 139
3.29 Gravitational time-delay functions for the four circularly symmetric effective potentials listed in Tab. 3.2. (a) point mass; (b) singular isothermal sphere; (c) softened isothermal sphere with core radius θ_c; (d) constant density sheet. 153

4.1 Sample output from LensPerfect using a supplied test dataset 172
4.2 FITS image output by glafic for a sample model with a single point source, two lenses and two extended sources 174
4.3 Sample output from PixeLens 176
4.4 Sample data entry and output from SimpLens 177
4.5 Output from GRALE for one of the supplied sample data files 179
4.6 Sample output from Gravitational Lensing 185
4.7 Sample output from Lens showing the image plane (left) and the generated source plane (right) 186

5.1 The effect of changes in redshift on percent change in time delay for the mock model with z_{lens}=0.30 and varying z_{source}. Expected shows changes in the value of $D_{\rm d}D_{\rm s}/D_{\rm ds}$ with the changes in redshift. 203
5.2 The effect of changes in redshift on percent change in time delay for the mock model with z_{source}=2.50 and varying z_{lens}. Expected shows changes in the value of $D_{\rm d}D_{\rm s}/D_{\rm ds}$ with the changes in redshift. 204
5.3 The effect of changes in redshift on percent change in calculated mass inside the Einstein radius (M($<R_E$)) for the mock model with z_{lens}=0.30 and varying z_{source}. Expected shows changes in the value of $D_{\rm d}D_{\rm s}/D_{\rm ds}$ with the changes in redshift. 205
5.4 The effect of changes in redshift on percent change in calculated mass inside the Einstein radius (M($<R_E$)) for the mock model with z_{source}=2.50 and varying z_{lens}. Expected shows changes in the value of $D_{\rm d}D_{\rm s}/D_{\rm ds}$ with the changes in redshift. 206
5.5 The effect of changes in redshift on calculated time delays for SDSSJ1004 with z_{lens}=0.68 and varying z_{source}. Expected shows changes in the value of $D_{\rm d}D_{\rm s}/D_{\rm ds}$ with the changes in redshift. 210
5.6 The effect of changes in redshift on calculated time delays for SDSSJ1004 with z_{source}=1.734 and varying z_{lens}. Expected shows changes in the value of $D_{\rm d}D_{\rm s}/D_{\rm ds}$ with the changes in redshift. 211
5.7 The effect of changes in redshift on percent change in calculated mass inside the Einstein radius (M($<R_E$)) for SDSSJ1004 with z_{lens}=0.68 and varying z_{source}. Expected shows changes in the value of $D_{\rm d}D_{\rm s}/D_{\rm ds}$ with the changes in redshift. . 212
5.8 The effect of changes in redshift on percent change in calculated mass inside the Einstein radius (M($<R_E$)) for SDSSJ1004 with z_{source}=1.734 and varying z_{lens}. Expected shows changes in the value of $D_{\rm d}D_{\rm s}/D_{\rm ds}$ with the changes in redshift. . 213

6.1 Basic data structure of HydraLens showing the interactions of the four modules with the data arrays . . . 232
6.2 Parameter entry is greatly facilitated using a common parameter window, obviating the need to count columns as parameters are entered into labeled text boxes . . . 232
6.3 The opening screen allows the user to choose to generate a new model, read in an existing model, and translate a model . . . 238
6.4 The PixeLens model generation entry screen . . . 239

7.1 Table 1 . . . 252
7.2 Table 2 . . . 253
7.3 Image planes for COSMOS J095930+023427 calculated by (a)PixeLens, (b)Lenstool, (c)Lensmodel and (d)glafic. Red triangles show image positions. Axes are labeled in arc seconds. . . . 254
7.4 Table 3 . . . 256
7.5 Image planes for SDSS J1320+1644 calculated by (a)PixeLens, (b)Lenstool, (c)Lensmodel and (d)glafic. Red triangles show image positions. Axes are labeled in arc seconds. . . . 257
7.6 Table 4 . . . 259
7.7 Table 5 . . . 260
7.8 Image planes for SDSS J1430+4105 calculated by (a)PixeLens, (b)Lenstool, (c)Lensmodel and (d)glafic. Red triangles show image positions. Axes are labeled in arc seconds. . . . 261
7.9 Table 6 . . . 262
7.10 Image planes for J1000+0021 calculated by (a)PixeLens, (b)Lenstool, (c)Lensmodel and (d)glafic. Red triangles show image positions. Axes are labeled in arc seconds. . . . 263

8.1 Schematic diagram of a two-image time delay lens. The lens lies at the origin, with two images A and B at radii R_A and R_B from the lens center. The images define an annulus of average radius $\langle R\rangle = (R_A + R_B)/2$ and width $\Delta R = R_A - R_B$, and the images subtend an angle $\Delta\theta_{AB}$ relative to the lens center. For a circular lens $\Delta\theta_{AB} = 180°$ by symmetry. From [10] . . . 274
8.2 The original reduced *HST*/F814W image of B1608+656. The four images are labelled A, B, C, and D; the two lens galaxies are G1 and G2. From [24] . . . 276
8.3 Left: Critical (thick) and caustic curves (thin) of the SPLE1+D model. The galaxy positions are indicated by stars, the images positions by open squares and the source by a closed square. Right: The contours indicate constant time delays starting at Δt=0 at image B and increasing in steps of 10 h^{-1} days. From [11] . . . 277
8.4 *HST* ACS image of RXJ1131−1231 in F814W filter. The background AGN is lensed into four images (A, B, C and D) by the primary lens galaxy G and its satellite S. Left: observed image. Right: reconstructed image based on the most probable composite model. From [27] . . . 278
8.5 B1608 model made with Pixelens using geometry from [11]. . . . 282
8.6 B1608 model made with glafic using geometry from [11] and a single lens potential. The image plane is shown in the upper panel and the source plane is in the lower panel. . . . 283

8.7 B1608 model made with glafic using geometry from [11] with two lens potentials, G1 and G2. The image plane is shown in the upper panel and the source plane is in the lower panel. . . . 285
8.8 RXJ11311 model made with Pixelens . . . 287
8.9 RXJ1131 model made with glafic using a single lens potential. The image plane is shown in the upper panel and the source plane is in the lower panel. . . . 288

9.1 Lensing Geometry . . . 298
9.2 Model of MACSJ1149 by [18]. Large scale view of the multiply lensed galaxies identified by the model. In addition to the large spiral galaxy system 1, many other fainter sets of multiply lensed galaxies are uncovered by our model. The white curve overlaid shows the tangential critical curve corresponding to the distance of system 1. The larger critical curve overlaid in blue corresponds to the average distance of the fainter systems, passing through close pairs of lensed images in systems 2 and 3. This large scale elongated "Einstein ring" encloses a very large critically lensed region equivalent to 170 *kpc* in radius. For this cluster one arcsecond corresponds to 6.4 kpc/h_{70}, with the standard cosmology. . . . 299
9.3 Model of MACSJ1149 by [15]. The central $\sim 80'' \times 80''$ of the cluster showing the multiple image systems discussed in the text. The cyan (outer), magenta and yellow curves show the $z = 1.491$, $z = 1.894$ and $z = 2.497$ tangential critical curves respectively. The inner cyan curve shows the radial critical curve for $z = 1.491$. . . . 301
9.4 Model of MACSJ1149 by [13]. HST F814W/F606W/F555W RGB colour image from the Cluster Lensing And Supernova survey with Hubble (CLASH) observations of MACSJ1149 (north is up and east is left). Overlaid in white is the critical curve from the best model, for a source redshift of $z_s = 1.49$ and a cluster redshift of $z_l = 0.544$. The center of the reconstructed DM halo A is $\sim 1.5 arcsec$ left of the BCG. There are three separate main images labelled 1. The detailed morphology of the central image, 1.3, is more complicated, parts have a seven fold image configuration. . . . 302
9.5 MACSJ1149 image constraints and critical curves . . . 304
9.6 An illustration that similar dark energy constraints may be obtained from clusters with very different mass profiles. The solid and dashed contours correspond to PIEMD and NFW lenses respectively. For both cases the authors use mock catalogs of 21 images and assume only observational errors of $0.1''$ for each image. From [2] . . . 307
9.7 The Lenstool model of MACSJ1149.5+2223 with source plane optimization . . . 310
9.8 The glafic model of MACSJ1149.5+2223 with source plane optimization . . . 311
9.9 Lenstool: w_X varies with Ω_m . . . 312
9.10 Constraint of w_X and Ω_m in A1689 in the study of [9] . . . 313
9.11 Original Lenstool model of MACSJ1149.5+2223 with image plane optimization . 314

1 Initial window on program load allows generating a new model or reading an existing model. One of the two "action" buttons (enabled, in dark blue) is pressed after selecting the target software with the radio buttons. . . . 324
2 After selecting glafic as the output target, the user selects which of the glafic files will be generated. Usually, one starts with the 'Main Model File' . . . 324
3 After selecting the Main Model File generation, the user is presented with this window to enter all of the data for a glafic model . . . 325

Chapter 1

The Equivalence Principle

1.1 The Equivalence Principle

Perhaps the most beautiful and most important foundation of general relativity is the equivalence principle, which Einstein dubbed "My Happiest Thought" when he realized in about 1907, that a person in free-fall to the earth (i.e. in earth's gravitational field) does not sense gravity. From this thought, he deduced the equivalence principle, which in simple terms states that an accelerated reference frame in the absence of gravity (e.g. in deep space away from any gravitational fields) is the same as a reference frame at rest in a gravitational field (e.g. on the surface of the earth). Given an equivalent force, the mass in an accelerated reference frame equals the mass in a gravitational field. At the time, this was a revolutionary thought in physics, that most physicists at the time would have attributed to mere happenstance.

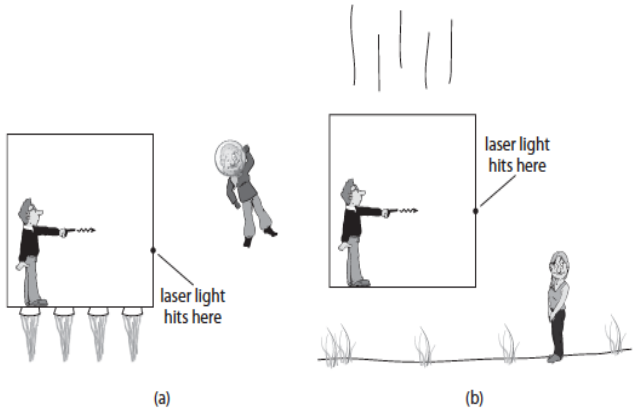

Figure 1.1: The Equivalence Principle predicts that gravity will bend light. [3]

From this simple idea, we can predict the bending of a beam of light in a gravitational field (aka, Gravitational Lensing) in a simple "gedanken" experiment. In the left-sided panel of Figure 1.1, we can see a man inside a box that is accelerating upward with an acceleration equal to g. He is unaware that he is in deep space, with no gravitational forces around him, but due to acceleration, he imagines he is on earth (the Equivalence Principle). He fires a laser

pistol at the wall opposite him, but because of the continued acceleration of the box, the laser beam will hit the wall slightly below where he aims (the opposite wall has moved up slightly in the time it took the light to travel across the box). He sees bending of the beam of light, due to acceleration of the box. If we accept the Equivalence Principle, then the same will happen in a gravitational field. Outside the box, an astronaut is floating and watches the whole thing. To this astronaut, everything (the box, the light, the target) is accelerating upward, and the light goes straight across. In the absence of gravity (i.e. in deep space away from any gravitational fields), light is not bent.

In the right-sided panel of Figure 1.1, a man is in a box that is falling toward earth in free fall (i.e. in a gravitational field). He fires the laser pistol again, and he, the light and the wall are all falling together so he sees the light hit exactly at the spot aimed for. In free-fall, there is no effect of gravity (as is well-known by real astronauts), and light is not bent. The observer outside the box sees that the light hits the wall at a slightly lower spot since the wall is falling and the target has dropped in the time it took the laser light to reach the opposite wall. To the outside observer, the beam of light is bent in the gravitational field of earth.

The Equivalence Principle predicts simply and elegantly that light is bent in a gravitational field, or in an accelerated reference frame which is in a place without gravity. Both "gedanken" experiments reach the same conclusion about the bending of light. This, simply put, is the core concept of everything to follow in this dissertation.

1.2 The Bending of Light

The main subject of this dissertation is Gravitational Lensing, which is the bending of light by gravity. This effect has been observed experimentally, but a little over 100 years ago would not have been believed by top physicists of the day.

Strong gravitational lensing, the ability of gravity to bend light, has been considered by scientists for over 200 years, perhaps longer. The amount of bending of light by gravity was predicted by the General Theory of Relativity, which was published in its complete form in 1915, and then demonstrated in a dramatic observational experiment by Eddington in 1919. The possibility of observing light from distant galaxies which has been affected by the gravitational effect of massive intervening galaxies was considered by Einstein in 1936 [1], but never thought to be observable. In the concluding paragraph of this short paper, Einstein concluded "Therefore, there is no great chance of observing this phenomenon, even if dazzling by the light of the much nearer star B is disregarded."

In 1937, Zwicky postulated that such observations may yield important information about the intervening galaxies [4]. The first gravitational lens was observed in 1979 by Walsh and colleagues and since then gravitational lensing has provided, with great promise for the future, some of the most important information in modern cosmology [2].

Gravitational lensing is evaluated by analysis of computer models based on the observed images. From these models, characteristics of the intervening galaxy, or cluster, (the lens, or deflector) including mass, dynamic motion, shape and substructure, can be deduced. The overarching goal of this dissertation is to deepen the understanding of the computer models that are used to obtain data from gravitational lens observations.

1.3 Organization of this Dissertation

Chapters 1, 2, and 3 constitute a general introduction to Special Relativity, General Relativity, Cosmology, Gravitational Lensing and Gravitational lens models. In Chapter 2, we develop the

fundamental physics and mathematics of special relativity, general relativity and cosmology. In Chapter 3, we develop the fundamentals of gravitational lensing and gravitational lens models as well as discussing their applications in cosmology.

Chapters 4, 5, 6, 7, 8 and 9 constitute the core of this dissertation with detailed discussions of the investigations of strong gravitational lens models that were undertaken. In Chapter 4, we review 26 software packages that are available to study strong gravitational lensing. In Chapter 5, we demonstrate that the results from different gravitational lens software models are not necessarily the same, suggesting the importance of using several techniques to analyze available data. In Chapter 6, we describe HydraLens, a software package written to facilitate the writing of model files for several of the available strong gravitational lens model software packages. In Chapter 7, using models generated by HydraLens, we perform direct, semi-independent comparisons of models for SDSS J1320+1644, COSMOS J095930+023427, SDSSJ1430, and J1000+0021 using Lenstool, Lensmodel, glafic and PixeLens. In Chapter 8, we compare results of time delay calculations from models in a study of two well-characterized lens systems. In Chapter 9, we use compare two gravitational lens models of MACS J1149.5+2223 to constrain cosmological parameters.

Finally, Chapter 10 is the Conclusion, with a discussion of possible future directions in strong gravitational lens models and applications of comparative lens model studies.

References

[1] A. Einstein. Lens-like action of a star by the deviation of light in a gravitational field. *Science*, **84**:506, 1936. 2

[2] D. Walsh, R. F. Carswell, and R. J. Weymann. 0957 + 561 A, B - Twin quasistellar objects or gravitational lens. *Nature*, **279**:381–384, May 1979. 2

[3] A Zee. *Einstein Gravity in a Nutshell*. Princeton University Press, 2013. x, 1

[4] F. Zwicky. On the masses of nebulae and of clusters of nebulae. *The Astrophysical Journal*, **86**:217, 1937. 2

Chapter 2

Special Relativity, General Relativity and Cosmology

2.1 Purpose and Organization of this Chapter

This chapter serves as a general introduction to the scientific foundations of gravitational lensing, including the Special Theory of Relativity, General Relativity, and Cosmology. The information in this chapter can be found in any number of textbooks, and serves as an introductory summary to these fascinating topics. It is generally presented in an historical context, as this is the best way to understand the development of this incredible field. This chapter is presented as background for what follows and the level of material presented is similar to contemporary textbooks. There is no attempt to develop new aspects of science in this chapter.

This chapter is organized as follows. We begin with a thorough discussion of Special Relativity including its historical background and mathematical formulation in Section 2.2. This includes a discussion of Galilean relativity, the difficulties Einstein saw with Maxwell's Equations and their incongruities with Galilean relativity, the Lorentz Transforms and then Special Relativity itself. We then go into the development of General Relativity, also with historical background and the reasons Einstein saw the need for a new explanation of gravity in Section 2.3. This section also includes a discussion of tensor analysis, the Einstein Field Equations, and tests of General Relativity. The chapter concludes with a discussion of the fundamentals of Cosmology as a prelude to the remainder of the dissertation in Section 2.4. This includes a number of fundamental topics such as the Cosmological Principle, the Cosmological Constant, the Hubble Parameter, the Standard Model, Cosmological Parameters and Large Scale Structure.

2.2 Special Relativity

Galilean Relativity

Einstein described relativity as a two-story building, the foundation being special relativity and the second floor being general relativity. It is important to begin with a brief discussion of special relativity. Perhaps the best way to discuss this important topic is to view it in an historical context. The idea of relativity did not originate with Einstein, and probably was first enunciated by Galileo. In its simplest form, the principle of relativity states "The laws of

physics take the same form in all frames of reference moving with constant velocity with respect to one another."

Galilean relativity was the product of this beautiful argument that later became the foundation of the principle of the relativity of motion, which Galileo presented as an imaginary ("gedanken") experiment, although clearly based in part on actual experience. Think of yourself in a cabin below deck in a ship, with water dripping from a container hanging from the ceiling, butterflies flitting about, and some fish swimming in a bowl. When the ship is at rest in dock, the water drips vertically to the floor, the butterflies fly anywhere with equal ease, and the fish swim likewise in all directions. Next consider the ship moving at any speed but always at a constant rate; according to Galileo, the experience is the same as when the ship is at rest. There is no preferred direction for the fish or butter flies, nor do they move with different speeds or different degrees of difficultly in specific directions. As well, the water drips vertically downward. The behavior is the same as whenever the ship is at rest. Drawing on personal experience, Galileo wrote: In confirmation of this I remember having often found myself in my cabin wondering whether the ship was moving or standing still; and sometimes at a whim I have supposed it going one way when its motion was the opposite [27].

The key idea of Galilean relativity is that time is a constant in all reference frames and the Galilean transformation, in the case of Newtonian relativity, is written as:

$$t' = t \tag{2.1}$$

$$x' = x + vt \tag{2.2}$$

Newtonian Assumptions about Space and Time

One of the greatest scientists of all times, Sir Isaac Newton, made innumerable contributions to science, mathematics and other fields of endeavour. Newton constructed dynamics on the basis of three laws:

First law (Principle of inertia) Free particles move with constant velocity (in a relativistic sense, they describe straight world-lines in spacetime).

Second law A particle acted upon by a force acquires an acceleration that is proportional to the force:

$$F = ma \tag{2.3}$$

The proportionality constant m is a property of the particle known as the mass. In terms of momentum, the law reads

$$F = dp/dt \tag{2.4}$$

Third law (action-reaction principle) Two particles interact by simultaneously exerting on each other, both equal and opposite forces

The first law is a special case of the second law (where F = 0). The first law establishes the tendency to perdurability as the main feature of motion (as it was imagined by Galileo and others, in contradistinction to the Aristotelian view).

The second law becomes the particle equation of motion, once the force is given as a function of r, u, t, etc. Then, a law for the involved interaction is also required (which can be gravitational, electromagnetic, etc.).

The third law implies the conservation of the total momentum of an isolated system of interacting particles. In fact, the sum of the reciprocal forces between the two particles must equal zero, since they are equal and opposite. If these are the only forces on each particle, we can use the second law to obtain $d(p1+p2)/dt = 0$. Thus $p1+p2$ is a conserved quantity. This argument can be extended to prove the conservation of the total momentum of any isolated system of particles [11].

Classical Mechanics allows for interacting forces at a distance. They are derived from potential energies depending on the distances between particles, which automatically provide interaction forces accomplishing Newton's third law.

Newton's fundamental laws of dynamics are not formulated to be used in any reference frame. In fact, it is evident that the first law cannot be valid in any frame, since a constant velocity u in a frame S does not imply a constant velocity u' in another frame S'. This can be easily understood by considering cases where S' rotates or accelerates with respect to S. However if S' translates uniformly with respect to S, either the particle has constant velocities u, u' in both frames or in none of them. Galilean addition of velocities is a particular example of this general statement. In fact, Galilean transformations were obtained for two equally oriented moving frames. These moving are in relative translation (absence of relative rotation).The translation is uniform, since the velocity V is constant. Thus u' is constant if and only if u is constant.

Although the principle of inertia cannot be valid in just any frame, at least it is true that if it is valid in a frame S, then it will be valid in any other frame S' uniformly translating with respect to S. Can we extent this statement to the second law? Newton's second law involves particle acceleration. In Galilean transformations, acceleration is invariant. The forces in Classical Mechanics depend on distances (like gravitational and elastic forces) or relative velocities (like the viscous force on a particle moving in a fluid, which depends on the velocity of the particle relative to the fluid). Both the distances and the relative velocities are invariant under Galilean transformations. In this way, each side of second law is invariant under changes of frames in relative uniform translation. Therefore, the invariance of distances and time intervals, which leads to Galilean transformations, is a key element of Newtonian dynamics because it allows the second law to be valid in a family of reference frames in relative uniform translation. This is the family of inertial frames, and an essential component of the principle of relativity [11]:

Principle of relativity The laws of physics have the same form in any inertial frame.

For instance, the same physical laws describe a free falling body both in a plane and at the earth surface. The principle of relativity in classical mechanics tells us that the state of motion of the frame cannot be revealed by a mechanical experiment: the result of the experiment will not depend on the motion of the frame because it is ruled by the same laws in all the inertial frames.

But how can we recognize whether a frame is inertial or not? We could effectively recognize a particle in rectilinear uniform motion; if we were sure that the particle is free of forces, then we would conclude that the frame is inertial. However, mechanics allows not only for contact forces but for forces at a distance. So how can we be sure that a particle is free of forces? Newton was aware of this annoying weakness of its formulation; he then considered that the laws of mechanics described the particle motion in the absolute space. Thus, the inertial frames are those fixed or uniformly translating with respect to Newton's absolute space.

While the inertial frames are defined by their states of motion with respect to Newton's absolute space, this (absolute) motion is not detectable, since the principle of relativity puts on an equal footing all the inertial frames; actually, only relative motions are detectable. Absolute space in classical mechanics plays the essential role of selecting the privileged family of inertial frames where the fundamental laws of physics are valid; but, surprisingly, it is not detectable. In some sense absolute space acts, because it determines the inertial trajectories of particles, but it does not receive any reaction because it is immutable. Leibniz criticized this feature of the Newtonian construction, by demanding that mechanics aimed to describe the relationships among particles instead of particle motions in absolute space. In practice, however, Newton's mechanics is successful because we can choose reference frames where the non-inertial effects are weak or can be understood in terms of inertial forces that result from referring the frame motion to another more inertial frame [11].

Special Relativity abandons the invariance of distances and time intervals (see below). This means that Galilean transformations are also abandoned. Newton's second law and the character of fundamental forces are reformulated by Einsteinian relativity. The inertial frames maintain their privileged status without a sound physical basis.

Maxwell's Equations and Physics in the Late 19th Century

The fundamental problem that physicists in the late 19th century had with Maxwell's equations is that they appeared to violate the Galilean principle of relativity which states that the laws of physics are the same in all inertial frames. This suggests that the laws of electromagnetism would hold in all inertial reference frames, which implies that the speed of light is always c. However, this violates the law of addition of velocities. In order to reconcile this, it was said that Maxwell's equations can only hold in a certain frame of reference. So, clearly, c should be just the speed of light as measured in the reference frame of the vacuum. Note that there is some tension here with the concept that all inertial frames are fundamentally equivalent. If this is so, one would not expect empty space itself to pick out one as special. To reconcile this in their minds, physicists decided that 'empty space' should not really be completely empty. Their thinking was that if it were completely empty, how could it support electromagnetic waves? So, they imagined that all of space was filled with a fluid-like substance which was referred to as the luminiferous ether. They supposed that electromagnetic waves were nothing other than wiggles of this fluid itself [17]. A great deal of physics was developed at that time to accommodate the concept of 'the ether' although no one was quite sure what the ether actually was.

Galilean Relativity and the Michaelson-Morley Experiment

Galilean relativity predicts that an observer moving with respect to the ether measures a different speed of propagation for electromagnetic waves. This prediction was dramatically contradicted by the Michelson-Morley result. The figure below illustrates the interferometer used in the Michaelson-Morley experiment. If the light waves traveled at different speeds (perpendicular light beams were used) relative to the ether, then it was expected that fringes would be observed.

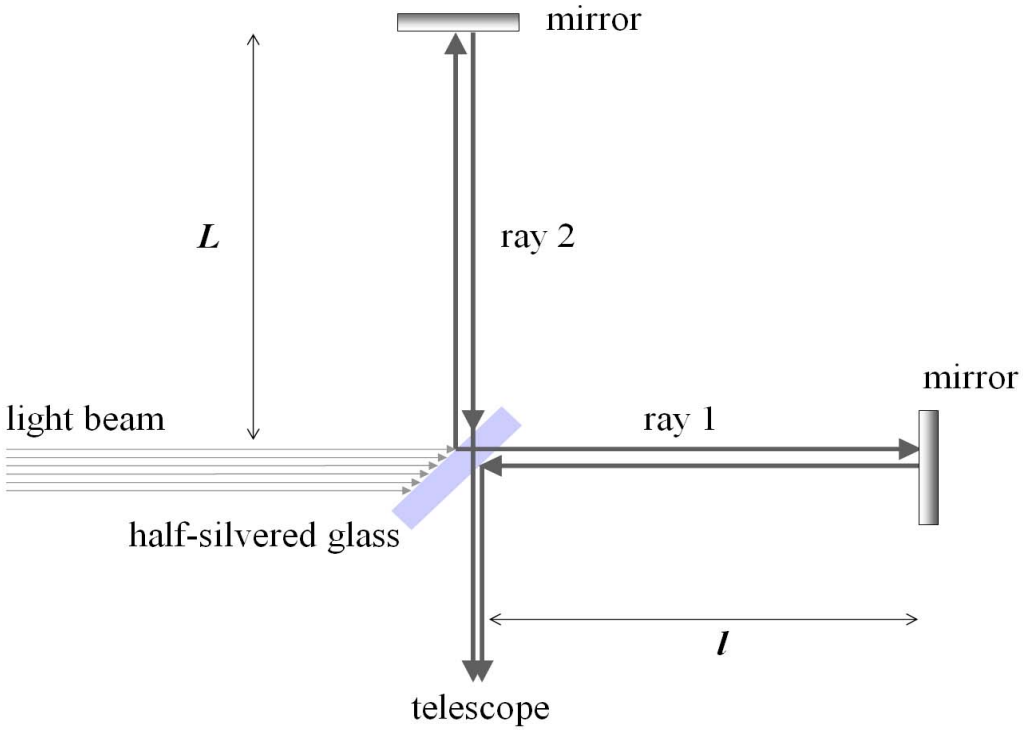

Figure 2.1: The Michaelson-Morley experiment [11]

After a failed attempt in 1881, Michelson joined Morley to improve the experimental sensitivity. In 1887 they used an interferometer whose arms were 11 m long. However, they still observed no displacement of fringes. Michelson was convinced that the null result meant that the Earth carried a layer of ether stuck to its surface.

The Lorentz Transforms

A new (Lorentzian) kind of invariance had to be introduced and was only later interpreted by Einstein in terms of new physics. While they are not invariant under the Galilean transforms, Maxwell's laws are invariant under Lorentz transforms.

Lorentz thought that Michelson-Morley's null result could be understood in a very different way, than they concluded. He considered that a body moving in the ether suffered a length contraction due to its interaction with the ether. The interaction would contract the body along the direction of its absolute motion V, but the transversal dimensions would not undergo any change. This proposal in 1892 had been independently advanced by FitzGerald three years before. This proposal did not mean abandonment of belief in the invariance of lengths, or the existence of the ether. The contraction was a dynamical effect and depended on an objective phenomena: the interaction between two material substances. The contraction should be observed in any frame, and all the frames should agree about the value of the contracted length [11].

The idea that light was a material wave (i.e., the idea that Maxwells laws were written to be used only in the ether frame) and the belief in the invariance of distances and time

intervals led physics down a blind alley. While complicated explanations were described to interpret experimental results, like Fresnels partial dragging of ether and FitzGerald-Lorentz length contraction caused by the ether, the experimental results were not so complicated. The experiments concluded that absolute motion cannot be detected [11].

It is partially for these reasons that Lorentz is not credited with developing Special Relativity. While he formulated the mathematical foundation, he did not enunciate the new physics that was implied, that is, abandonment of the idea of the ether and abandonment of the idea of length invariance.

Maxwell's Equations are not Galilean Transform Invariant

We are told early in our physics education, that classical electromagnetism is not Galilean invariant, that is, that the relationships between fields are not preserved under Galilean transformations. Maxwell's theory predicts the existence of electromagnetic waves traveling *in vacuo* at speed c and the Galilean non-invariance of velocities any velocity implies that Maxwell's equations in their simple form are valid only in a well-defined reference frame, which was referred to as the luminiferous ether, a space-filling medium supporting wave propagation. Thus, Galilean relativity predicts that an observer not at rest with respect to the ether measures a different speed of propagation for the electromagnetic waves [22].

A cursory approach may leave the wrong impression that the reason why classical electromagnetism is not Galilean invariant rests ultimately in the presence of the parameter c in Maxwell's equations. The parameter c in Maxwell's equations is actually a property of Newtonian free space itself, due to its very definition:

$$c = \frac{1}{\sqrt{\epsilon_0 \mu_0}} \tag{2.5}$$

in terms of two free space quantities, namely the vacuum permittivity ϵ_0 and the vacuum permeability μ_0, which can be separately determined. Since the vacuum in Newtonian physics is observer-invariant, both quantities can be regarded as observer independent scalars, i.e., universal constants characterizing the vacuum in any reference frame. Hence, resting on the definition above, it follows that this same observer independence characterizes Maxwell's parameter c as well, which therefore behaves as a scalar invariant under frame transformations [22].

The Origins of Special Relativity

While special relativity is founded on the work of several people, including Lorentz, Minkowski and Poincaré, it was clearly the genius of Einstein alone who saw the implications of this previous work to describe physics in a new way. Despite the fact that several of these people were close to the theory, it was only Einstein who saw the physical implications in their entirety.

In the "miracle year" of 1905, while employed as a patent clerk in Bern, Switzerland, Einstein wrote five papers that shook the very foundation of physics. It has been said by some that any one of these would have qualified to be the basis for a Nobel Prize, but it was the paper about the photoelectric effect that won the Nobel Prize for Einstein, although not until 1921, well after the description of General Relativity in 1915 and its verification by Eddington with the observation of gravitational lensing by the sun in 1919. The Nobel Committee cited Einstein "for his services to Theoretical Physics, and especially for his discovery of the law of the photoelectric effect". There was no mention of relativity at all.

At the time, most physicists believed that waves propagated in the ether, and that everything was relative to the ether frame of reference. The Michelson-Morley experiment disproved the

existence of the ether in 1896, but according to Einstein's own statements, he was not influenced at all by these results. Whether Einstein knew about the experiment or not is a matter of some historical controversy, but most authors take Einstein at his word on this matter [11].

The Contribution of Einstein

Einstein's 1905 paper about the special theory of relativity, in fact, was titled "On the Electrodynamics of Moving Bodies" which highlights the fact that special relativity has its roots in electrodynamics and not kinematics. For it was the incongruities of Maxwell's Equations with the physics of the day, as we described above, that led Einstein to develop the special theory of relativity.

The first sentence of Einstein's paper set-up the conceptual framework: It is well known that Maxwell's electrodynamics as usually understood when applied to moving bodies, leads to asymmetries that are not inherent in the phenomena. What were these well-known asymmetries, and what were the phenomena he was speaking of? Einstein went back to Faraday's experiment of a magnet moving through a conductor (or a loop of wire). With the conductor at rest, the moving magnet generated an electric field and this produced a current in the wire. If, on the other hand, the magnet were set at rest and the conductor moved over the magnet, even though (according to theory) there was no electric field around a stationery magnet, a current of the same strength as the former case was still produced in the wire. Einstein saw this as an asymmetry in interpretation in the two cases; one with, and one without, an electric field. Despite this apparent conceptual problem, the observable phenomenon here depends only on the relative motion of conductor and magnet, since in both cases electricity was produced in the wire. Undoubtedly, the asymmetry was not inherent in the phenomenon, as he said. From the viewpoint of the phenomenon, a current was produced by any relative motion between the magnet and the conductor, whereas the theory of electromagnetism affirmed that an electric field was produced only by a moving magnet, not one at rest [27].

In 1905, Einstein deduced the relativity principle from his interpretation of Faraday's experiment, coming from electrodynamics. We stated earlier that Galileo arrived at his relativity principle from the mechanics of motion. Putting the two together Einstein felt that examples of this sort lead to the conjecture that not only the phenomena of mechanics but also those of electrodynamics have no properties that correspond to the concept of absolute rest. This was a generalization of the relativity principle that encompassed both mechanics and electromagnetism. It was, partially, Einstein's attempt to unify the physics of motion with electromagnetism.

This is the problem which Einstein saw so clearly. The incongruity between Maxwell's equations and Galilean relativity had to be resolved, which meant choosing one of three alternatives:

1 The Galilean transformation was correct and something was wrong with Maxwell's equations.

2 The Galilean transformation applied to Newtonian mechanics only.

3 The Galilean transformation, and the Newtonian principle of relativity based on this transformation were wrong and that there existed a new relativity principle valid for both mechanics and electromagnetism that was not based on Galilean transformations.

The first possibility was eliminated since Maxwell's equations proved to be totally successful in their application. The second was unacceptable as it seemed something as fundamental as the transformation between inertial frames could not be restricted to only one set of natural phenomena. It seemed preferable to believe that physics was a unified subject. The third was all that was left, so Einstein set about trying to describe a new principle of relativity [9].

Principles of Special Relativity

The two fundamental principles of special relativity are:

Physics is the same in all inertial reference frames : All the laws of Newtonian mechanics are equally valid in all inertial reference frames, or, roughly speaking, in all non-rotating and non-accelerating laboratories, no matter how fast they move, which is referred to as Newtonian relativity. Any mechanical experiment will proceed identically in every such reference frame. For example, no one could tell the difference between a game of billiards played on earth and one played in a smoothly flying very fast jet airplane. It was indeed this property of Newtonian mechanics that allowed Galileo and Newton to champion Copernicus's idea of an earth flying around the sun, since terrestrial laboratories would even under these circumstances be considered good approximations to inertial frames [24]

Einstein, postulated in 1905 that not only the laws of mechanics, but all the laws of physics (including, for example, electromagnetism, optics, thermodynamics, etc.) are similarly valid in all inertial frames.This was a way to express the symmetry which Einstein found so beautiful in physics, and which he infused into his theories. In particular, he saw special relativity as a consequence of the symmetry in Maxwell's equations. The Lorentz transforms maintain the symmetry in Maxwell's equations.

The speed of light is constant : The origin of this concept is a product of Einstein's genius, which was totally counter to the ideas of contemporary physics at that time, and totally counterintuitive to our everyday experience where Galilean relativity makes sense. Einstein realized that Maxwell's equations demand a constant speed of light, no matter what the reference frame. Maxwell's laws are frame invariant. The speed of light depends only on μ and ϵ, not on any other physical quantities.

The beauty of special relativity is rooted in its simplicity, that it is mathematically based on the Pythagorean theorem. The first principle above, states that there are no preferred frames of reference and simply states that all laws of physics are the same in all reference frames. While Galileo and Newton saw this principle as applied to mechanics, Einstein simply extended it to all laws of physics. Simple, but powerful with far-reaching consequences [32].

The second principle, that the speed of light is a constant, seems radical at first glance, but after considering its origins, in Maxwell's equations, is easier to follow. It does, however, have great implications for all of physics.

Special relativity is in principle a theory of all physics, which aims to make all physical laws invariant from one inertial frame to another under Lorentz transformations. It required a review of the existing laws of physics, and a modification of any law that failed the test of 'Lorentz-invariance'. According to this criterion, Maxwell's theory was found to be already 'relativistic' and needed no revision (in vacuum). Newton's theory, as already noted, was not. Its relativistic modifications led to astonishing predictions, in one of the most striking instances of theory far outpacing observation [24]

Special Relativity- Mathematical Formulation

We will start with the Lorentz transforms, which were developed to replace the Galilean transformations, discussed above, as his way of explaining the fact that Maxwell's equations were not invariant under the Galilean transforms. Maxwell's equations are invariant under the Lorentz transforms. While the Lorentz transforms are an essential part of the mathematical description of special relativity, Lorentz saw them as a way to reconcile the results of the Michaelson-Morley

experiment with the existence of the ether. Einstein saw them as a way to redefine the physics of motion in mathematical terms. The Lorentz factor γ is usually written as:

$$\gamma = \frac{1}{\sqrt{1 - (v^2/c^2)}}$$

The figure below (from [24]) shows the Lorentz factor γ as a function of v as it approaches c. Note that γ stays very close to 1, until v becomes quite close to c. This figure illustrates in part, why c is an absolute 'speed limit'.

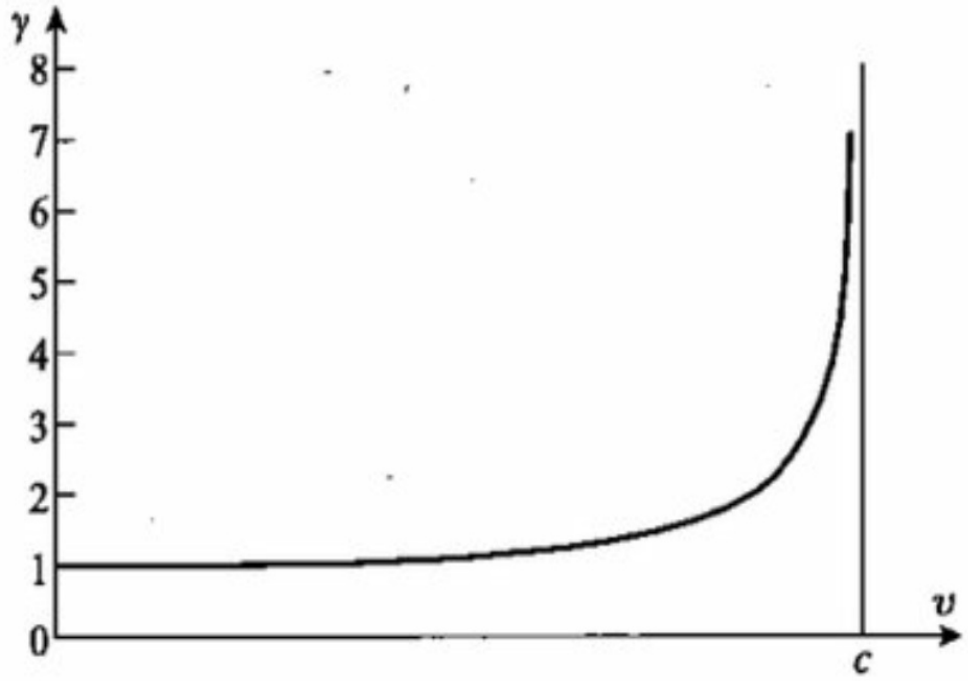

Figure 2.2: Relationship of v and γ

We can then write the Lorentz transforms as a function of γ:

$$x' = \gamma(x - v_x t) \tag{2.6}$$

$$y' = y \tag{2.7}$$

$$z' = z \tag{2.8}$$

$$t' = \gamma(t - vx/c^2) \tag{2.9}$$

These four equations explain the concept of time dilation and the Lorentz length contraction. Furthermore, the Lorentz transforms can be derived from the principles of Special Relativity. In summary, the Lorentz transforms lead to a description of spacetime in which the notions of simultaneity, time duration, and spatial distance are well-defined in each inertial reference frame, but their values, for a given pair of events, can vary from one reference frame to another. Objects evolve more slowly and are contracted along their direction of motion when observed in a reference frame relative to which they are in motion [26].

Special Relativity- Kinematics

In addition to the Lorentz transforms, special relativity also requires new ways of thinking about kinematics and the addition of velocities. This problem can be illustrated as follows. An object moves at speed v_1 with respect to reference frame S'. The frame S' is moving at speed v_2 with respect to frame S, in the same direction as the motion of the object.

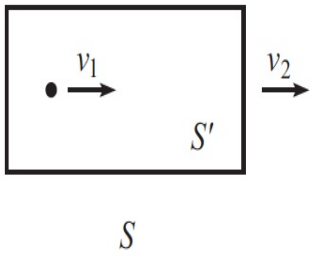

Figure 2.3: Relativistic Addition of Velocities [19]

What is the speed, u, of the object with respect to frame S? We know that, *without* relativistic considerations, $u = v_1 + v_2$. However, we know that special relativity makes this seemingly everyday situation more complicated because time is no longer absolute. The relative speed of the two frames is v_2. We also know that $v_1 = \Delta x'/\Delta t'$ from basic kinematics. Our goal is to determine $u \equiv \Delta x/\Delta t$.

The Lorentz transformations from S' to S are:

$$\Delta x = \gamma_2(\Delta x' + v_2 \Delta t') \tag{2.10}$$

and

$$\Delta t = \gamma_2(\Delta t' + v_2 \Delta x'/c^2 \tag{2.11}$$

where

$$\gamma_2 \equiv 1/\sqrt{1 - v_2^2/c^2} \tag{2.12}$$

and therefore

$$u \equiv \frac{\Delta x}{\Delta t} = \frac{\Delta x' + v_2 \Delta t'}{\Delta t' + v_2 \Delta x'/c^2} \tag{2.13}$$

$$= \frac{\Delta x'/\Delta t' + v_2}{1 + v_2(\Delta x'/\Delta t')/c^2} \tag{2.14}$$

$$= \frac{v_1 + v_2}{1 + v_1 v_2/c^2} \tag{2.15}$$

This last equation shows the velocity-addition formula, for adding velocities along the same line, with the correction required by special relativity [19].

Lorentz Invariance and 4-vectors

By using 4-vectors to describe the physical world, we bring together the concepts of space and time, which is essential for a complete understanding of both special and general relativity.

We can define X to be the vector (space-time displacement vector)

$$X = \begin{pmatrix} ct \\ x \\ y \\ z \end{pmatrix} \tag{2.16}$$

The Lorentz transforms can now be written in compact form by

$$\Lambda = \begin{pmatrix} \gamma & -\gamma\beta & 0 & 0 \\ -\gamma\beta & \gamma & 0 & 0 \\ 0 & 0 & 1 & 0 \\ 0 & 0 & 0 & 1 \end{pmatrix} \tag{2.17}$$

where

$$\beta = \frac{v}{c} \tag{2.18}$$

The entire Lorentz transform is then written as

$$X' = \Lambda X \tag{2.19}$$

It follows then that the inverse Lorentz transform is written as

$$X = \Lambda^{-1} X' \tag{2.20}$$

Under a Lorentz transformation, a 4-vector changes, but its length remains the same. When we make a change in coordinates for a line in space, we know that the length of the line is unchanged, and is still

$$r = \sqrt{x^2 + y^2 + z^2} \tag{2.21}$$

no matter what the coordinate change entails. The length of a 4-vector is calculated similarly, but with a crucial sign that enters in because time and space are not exactly the same as each other. The length of a 4-vector in space-time is calculated by

$$-(X^0)^2 + (X^1)^2 + (X^2)^2 + (X^3)^2 \tag{2.22}$$

This combination is Lorentz invariant, because of the crucial negative sign in front of the time term in this equation. Thus,

$$-c^2t'^2 + x'^2 + y'^2 + z'^2 = -c^2t^2 + x^2 + y^2 + z^2 \tag{2.23}$$

For a 4-vector X^T, we can write this quality in matrix notation as

$$-c^2t^2 + x^2 + y^2 + z^2 = X^T g X \tag{2.24}$$

where

$$g = \begin{pmatrix} -1 & 0 & 0 & 0 \\ 0 & 1 & 0 & 0 \\ 0 & 0 & 1 & 0 \\ 0 & 0 & 0 & 1 \end{pmatrix} \tag{2.25}$$

where g is called the 'metric' or the 'metric tensor'. For any quantity A that transforms in the same way as X, the scalar quantity A^TgA is Lorentz invariant', which means that the value will not change no matter what reference frame is used to calculate it. A generalized form of the metric tensor plays a central role in General Relativity, and will be used extensively in the following discussion of General Relativity. In order to consider Lorentz transformations of all kinds (for relative motion in any direction, with or without rotation and inversion) we regard g as the prior, given quantity, and then

$$\Lambda^T g \Lambda = g \tag{2.26}$$

is the defining property of Lorentz transformations Λ in general. For the sake of definitions, invariant, or Lorentz-invariant, means that a quantity is the same in all reference frames. Conserved means that a quantity is not changing over time. Covariant is a technical term applied to some 4-vector quantities, and is used to mean invariant when it is the mathematical form of an equation that is invariant. Rest mass is Lorentz-invariant but not conserved. Energy is conserved but not Lorentz-invariant [26]

The role of proper time, τ, in special relativity is central, and crucial to its understanding. If we consider a worldline, we would like to describe events along this line, and if possible we would like a description that does not depend on a choice of frame of reference. This is just like the desire to do classical (Newtonian) mechanics without picking any particular coordinate system: in Newtonian mechanics it is achieved by using 3-vectors. In Special Relativity, we use 4-vectors. We also need a parameter to indicate how far along the worldline it is. In Newtonian mechanics this is accomplished by time, because it is universal among reference frames connected by a Galilean transformation. In Special Relativity we use the proper time τ. Proper time is defined as the integral of the infinitesimal bits of proper time experienced by the particle along its history. This is a suitable choice because this proper time is Lorentz-invariant, agreed among all reference frames [26]. Proper time is shown mathematically by:

$$\tau = \int \sqrt{1 - \frac{v^2}{c^2}} dt \tag{2.27}$$

Special Relativity- Dynamics

We have discussed above the ways in which the principles of relativity as stated by Einstein affect our ideas about space and time. Given that, special relativity also has profound effects on our ideas about force, momentum and energy. We begin our exploration of relativistic dynamics by seeking the most useful denition of momentum in relativity, and we do this by investigating a simple collision in one dimension. Two bodies (A, B) approach each other and interact, then two bodies draw away from each other (C,D). In the absence of external forces, momentum is conserved. The classical definition of momentum is

Relativistic Considerations of Momentum

$$\vec{p} = m\vec{v} = m\frac{d\vec{x}}{dt} \tag{2.28}$$

This can be extended to a relativistic four vector by

$$p^{\mu} = mU^{\mu} = (\gamma mc, \gamma mv) \tag{2.29}$$

which has the appropriate non relativistic limit $\vec{p} = m\vec{v}$.

In a two body collision, the total momentum for the system is conserved, giving

$$m_A v_A + m_B v_B = m_C v_C + m_D v_D \tag{2.30}$$

as a frame-independent result. If momentum is conserved in all inertial reference frames, then mass must also be conserved. The conservation of mass is not an independent principle: it follows from the conservation of momentum plus the idea that any inertial reference frame is as good as any other inertial reference frame (from the principle of relativity).

If we use the particle's own time, τ, which is the proper time, then

$$\vec{p} = m\frac{d\vec{x}}{d\tau} \tag{2.31}$$

We know that the proper time τ is related to a change in the time t in the frame through time dilation

$$dt = \frac{d\tau}{\sqrt{1 - (v^2/c^2)}} \tag{2.32}$$

where v is the velocity of the particle in the frame. This means that momentum is now defined with relativistic considerations as

$$\vec{p} = \frac{m\vec{v}}{\sqrt{1 - (v^2/c^2)}} \tag{2.33}$$

Relativistic Considerations of Energy

The Taylor expansion shows that

$$\frac{1}{\sqrt{1-x}} = 1 + \frac{x}{2} + \frac{3x^2}{8} + ... \tag{2.34}$$

Applying this expansion, and multiplying by c^2 shows that

$$\frac{mc^2}{\sqrt{1-(v^2/c^2)}} = mc^2(1+\frac{1}{2}\frac{v^2}{c^2}) \tag{2.35}$$

Which reduces to

$$\frac{mc^2}{\sqrt{1-(v^2/c^2)}} = mc^2 + \frac{1}{2}mv^2 \tag{2.36}$$

combining this with the relativistic definition of energy, and noticing that the second term above is just kinetic energy,

$$E = \frac{mc^2}{\sqrt{1-(v^2/c^2)}} \tag{2.37}$$

results in perhaps the most famous equation of all time

$$\Delta E = \Delta mc^2 \tag{2.38}$$

This is sometimes considered as the equivalence of mass and energy, but it is not exactly a true equivalence. The energy is the timelike component of the momentum four-vector, while the mass is the invariant length of the four-vector. The energy in the rest system indeed equals mc^2, but while in motion, the energy varies with velocity, as shown above. Thus

$$E = mc^2 \tag{2.39}$$

holds only in the rest system.

Some treatments of relativity refer to the mass of a motionless particle as the rest mass m_0, and the mass of moving particle as the relativistic mass with $m_{rel} = \gamma m_0$. This terminology is misleading and should be avoided. There is no such thing as relativistic mass. There is only one mass associated with an object. This mass is what the above treatments would call the rest mass. Since there is only one type of mass, there is no need to use the qualifier rest. We therefore simply use the notation m [19].

Special Relativity and Accelerated Frames of Reference

It is essential here to dispel one of the commonly held misbeliefs about special relativity, namely that accelerated frames of reference cannot fall under the descriptions afforded by special relativity. In fact, special relativity can handle the physics of accelerated frames of reference [18]. Special relativity cannot handle the physics of reference frames in a gravitational field. Gravity is not invariant under the Lorentz transforms. Special relativity postulates that all laws of physics are invariant under Lorentz transformations, which include ordinary rotations and changes in the velocity of a reference frame.

Physical Consequences of Special Relativity

We can summarize some of the fundamental physical effects which are a direct result of the Lorentz transform and the two postulates of special relativity:

Classical Limit If $v << c$, then the Lorentz transforms reduce to the Galilean transforms. This is an important feature of the Lortentz transforms, as it meets the requirements of the Correspondence Principle.

Loss of Simultaneity The fact that

$$t' = \gamma(t - vx/c^2) \tag{2.40}$$

immediately shows the relativity of simultaneity, namely that two events with the same t but different x will not transform into two events with the same t', which expresses the loss of simultaneity predicted by special relativity.

Time Dilation The Lorentz factor γ is greater than 1, and since

$$t' = \gamma t \tag{2.41}$$

we have

$$t' > t \tag{2.42}$$

This is referred to as time dilation. Time dilation has been established observationally.

Length contraction Similarly, since

$$l' = \frac{l}{\gamma} \tag{2.43}$$

which is the effect referred to as 'length contraction' in special relativity. There are no good methods as yet to observe this phenomenon directly.

Velocity addition As shown in Figure 3 above, if two reference frames, S and S' are moving relative to each other with a velocity v_2, then an object moving at v_1 in the S' frame would be moving at $u \equiv v_1 + v_2$ relative to the frame S if there were no relativistic considerations, and this is consistent with our everyday experience at typical speeds. However, because of the loss of simultaneity imposed by special relativity, the speed is actually

$$u = \frac{v_1 + v_2}{1 + v_1 v_2/c^2} \tag{2.44}$$

The Invariant Interval Although the coordinates of the same event are different in different reference frames, the distance between the two events, s, in spacetime does not change and is given by:

$$s^2 = -ct^2 + x^2 + y^2 + z^2 \tag{2.45}$$

The minus sign in the time term above ($-ct^2$) has enormous consequences in the physics of general relativity as it mandates that the shortest distance between two points in spacetime also has the longest time.

Relativistic Dynamics Dynamics refers to considerations regarding momentum and energy, as modified by special relativity.

In short, momentum, which is usually written as $p = mv$, is written as

$$\mathbf{p} = \gamma m \mathbf{v} \tag{2.46}$$

using the value of γ as defined above. Energy is written as

$$E = \gamma m c^2 \tag{2.47}$$

and, this leads to the famous consequence of relativity known to most schoolchildren, namely that

$$E = mc^2 \tag{2.48}$$

2.3 General Relativity

Most major theories in physics are the result of a need to explain experimental observations. Quantum mechanics is a beautiful example of this, which has its foundations in the Bohr atom, Einstein's photoelectric effect and the Schrödinger wave equation. Quantum mechanics was developed because the existing theories could not explain the rapidly expanding experimental evidence.

General relativity stands in stark contrast, having been the product of the thinking of one man, without the need to explain any particularly troubling experimental evidence. At the time he developed the General Theory of Relativity, there was no specific need for a new explanation of existing experimental evidence. Newtonian physics did quite well in explaining the observations made until that time, perhaps with the exception of the advance of the perihelion of Mercury. It is said that most physicists of the day were willing to overlook this disparity. It was the genius of Einstein, who was not satisfied with the theoretical explanations of Newtonian gravity and who nearly single-handedly began a nearly ten year quest to explain gravity in a more elegant fashion. The result of that quest was the General Theory of Relativity.

Newtonian Gravity

Einstein was dissatisfied with the concept of gravity as described by Sir Isaac Newton, hundreds of years before. General Relativity is closely related to Special Relativity, which Einstein considered to be its basis (the two-story building analogy above). Based on special relativity, Einstein realized that "action at a distance" and the instantaneous transfer of information, both of which are mandated by Newtonian gravitation, are not possible. He therefore set out to develop a new theory of gravity, based on these concepts and not based on experimental evidence.

Foundations of General Relativity

General Relativity is based on three principles:

The Equivalence Principle In 1907, Einstein said he had his "happiest thought". While some references state that this was only a thought, other sources state that it actually happened. In any case, Einstein considered that a painter who fell from the roof would not feel his own weight. Thus was born the idea of the equivalence of inertial and gravitational mass. While this may seem intuitive, Einstein enunciated the "Strong Equivalence Principle" that codified this concept as a basic truth of nature, across all of physics, no longer limited to the motion of bodies as Galileo had considered it.

The Correspondence Principle : This name was coined by Niels Bohr in 1920, after General Relativity was described, but refers to the fact that General Relativity reduces to classical Newtonian physics in the weak field limit.

The Principle of Covariance : This requires that physics stays the same after coordinate transformations, and is the reason that General Relativity is expressed as tensors. The use of tensors was a considerable barrier for Einstein, who enlisted the aid of his college friend Marcel Grossman (who by then was a Professor of Mathematics and an expert in non-Euclidean Geometry) to teach him tensor calculus.

Gravitation and Geometry

Einstein focussed on the fact that freely falling frames are locally the same as inertial frames. Things were tricky for measurements across a finite distance. Consider, for example, the reference frame of a freely falling person. Suppose that this person holds out a rock and releases it. The rock is then also a freely falling object, and the rock is initially at rest with respect to the person. This is the idea contained in the Equivalence Principle.

The issue is that we would like to think of the freely falling worldlines as inertial worldlines. We would like to consider them as being 'straight lines in spacetime.' However, We must draw them on a spacetime diagram as curved. We can straighten out any one of them by using the reference frame of an observer moving along that worldline. However, this makes the other freely falling worldlines appear curved.

Eventually Einstein found a useful analogy with something that at first sight appears quite different, a curved surface. The idea is captured by the question, What is a straight line on a curved surface? Mathematicians made up a new word for this idea, the geodesic. A geodesic can be thought of as the straightest possible line on a curved surface. More precisely, we can define a geodesic as a line of minimal distance, the shortest line between two points. The idea is that we can define a straight line to be the shortest line between two points. Actually, there is another definition of geodesic that is even better, but requires more mathematical machinery to state precisely. Intuitively, it captures the idea that the geodesic is 'straight.' It tells us that a geodesic is the path on a curved surface that would be traveled, for example, by an ant (or a person) walking on the surface who always walks straight ahead and does not turn to the right or left [17]

The concept of a geodesic as the straightest possible line on a curved surface is central to Einstein's formulation of gravity as the curvature of space-time. Straight lines (geodesics) on a curved surface act like freely falling worldlines in a gravitational field. It is useful to think of this analogy at one more level: Consider two people standing on the surface of the earth. We know that these two people remain the same distance apart as time passes. Why do they do so? Because the earth itself holds them apart and prevents gravity from bringing them together.

The next central concept in the geometry of space-time is that curved surfaces are locally flat. Mathematically speaking, gravity is locally Lorentzian. In small areas of space-time, physics is defined by the Lorentz transforms. Putting these small areas of space-time together

results in general relativity. This is the same phenomenon one experiences when drawing a map of the earth on a flat piece of paper. We see that something like the equivalence principle holds for curved surfaces, flat maps are very accurate in small regions, but not over large ones.

The point is that this process of building a curved surface from flat ones is just exactly what we want to do with gravity! We want to build a gravitational field out of little pieces "flat" inertial frames. We might say that gravity is the curvature of spacetime. This gives us the new language that Einstein was looking for [17]:

Inertial Frames We can draw it on our flat paper and geodesics behave like straight lines. This is exactly the Minkowskian geometry of special relativity.

Worldlines of Freely Falling Observers Follow straight lines in Spacetime

Gravity The Curvature of Spacetime

In fact, with the following assumptions, we can derive the basic ideas of general relativity:

Gravity Gravity is the curvature of space-time

Covariance Physics is independent of the choice of coordinates

Metric The basic equations of general relativity give the dynamics of the metric which describe the curvature of space-time

Energy is conserved

Equivalence Principle

Correspondence Principle In the weak field limit, general relativity reduces to Newtonian physics.

Mathematical Introduction

We will begin now to describe the mathematics of general relativity, which is done in the language of tensors. By using tensors to describe gravity, Einstein was freed from the limitations imposed by specific coordinate systems. Tensors allow Physics to be described in a coordinate-free notation. We begin by describing some of the basics of tensor mathematics.

Tensor Operations:

- ⋆ Addition: $A^{\alpha\beta}_{\mu\nu} + B^{\alpha\beta}_{\mu\nu} = C^{\alpha\beta}_{\mu\nu}$
- ⋆ Subtraction: $A^{\alpha\beta}_{\mu\nu} - B^{\alpha\beta}_{\mu\nu} = D^{\alpha\beta}_{\mu\nu}$
- ⋆ Tensor Product: $A^{\alpha\beta}_{\mu\nu}\ B^{\gamma\delta}_{\eta\xi} = F^{\alpha\beta\gamma\delta}_{\mu\nu\eta\xi}$
- ⋆ Contraction: $A^{\alpha\psi}_{\psi\gamma} = H^{\alpha}_{\gamma}$ (summed over ψ)
- ⋆ Inner Product: $A^{\alpha\beta}_{\mu\nu}\ B^{\nu\gamma}_{\delta\eta} = P^{\alpha\beta\nu\gamma}_{\mu\nu\delta\eta} = K^{\alpha\beta\gamma}_{\mu\delta\eta}$

Tensors and Physics:
When the equations of motion are written in tensor form, they are invariant under some appropriately-defined transformations. For example:

- ⋆ Newtonian Mechanics: 3 - vectors $(x, y, z) = (x^1, x^2, x^3)$ are invariant under Galilean transformations.
- ⋆ Special Relativity: 4 - vectors $(t, x, y, z) = (x^0, x^1, x^2, x^3)$ are invariant under Lorentz transformations.
- ⋆ General Relativity: 4 - vectors $(t, x, y, z) = (x^0, x^1, x^2, x^3)$ are invariant under general coordinate transformations.

We now use the notation of tensors to describe flat space and space-time, and then use these concepts to put into mathematical terms the basic underlying principles of general relativity including curved three dimensional space, the covariant derivative and the Principle of General Covariance.

Flat Euclidean space

We generally think in terms of a flat space metric (Euclidean), where parallel lines never cross and the sum of the interior angles of a triangle is 180^0.

In this case, the invariant line element of space in Cartesian coordinates $(x, y, z) = (x^1, x^2, x^3)$ is:

$$ds^2 = (dx^1)^2 + (dx^2)^2 + (dx^3)^2, \tag{2.49}$$

and space is flat.

An equivalent way of writing the above metric is:

$$ds^2 = \delta_{ij} dx^i dx^j, \tag{2.50}$$

where $\delta_{\alpha\beta}$ is the Kronecker delta function defined as:

$$\delta_{\alpha\beta} = \begin{cases} 1 & \text{for } \alpha = \beta, \\ 0 & \text{for } \alpha \neq \beta. \end{cases} \tag{2.51}$$

Therefore, the Euclidean space metric tensor for Cartesian coordinates is:

$$\delta_{ij} = \begin{pmatrix} 1 & 0 & 0 \\ 0 & 1 & 0 \\ 0 & 0 & 1 \end{pmatrix}. \tag{2.52}$$

An invariant line element in an arbitrary coordinate system in flat space, can be written in terms of Cartesian coordinates (via change of variables):

$$ds^2 = \delta_{ij} dx^i dx^j = \delta_{ij} \left(\frac{\partial x^i}{\partial x'^k} dx'^k \right) \left(\frac{\partial x^j}{\partial x'^l} dx'^l \right) = \delta_{ij} \frac{\partial x^i}{\partial x'^k} \frac{\partial x^j}{\partial x'^l} dx'^k dx'^l \equiv p_{kl} dx'^k dx'^l. \tag{2.53}$$

where p_{kl} is the metric of the new coordinate system.

Since the line element is invariant under the interchange of dx' and dx, we may, without loss of generality, take the metric tensor to be symmetric in general relativity.

Consider an example of spherical coordinates (r, θ, ϕ), Fig. (2.4), where we are at the center of the spherical coordinate system. As we look out into the "cosmos," the flat space part of the metric (line element) is given by the following line element:

$$ds^2 = dr^2 + r^2 \left(d\theta^2 + \sin^2\theta d\phi^2\right), \tag{2.54}$$

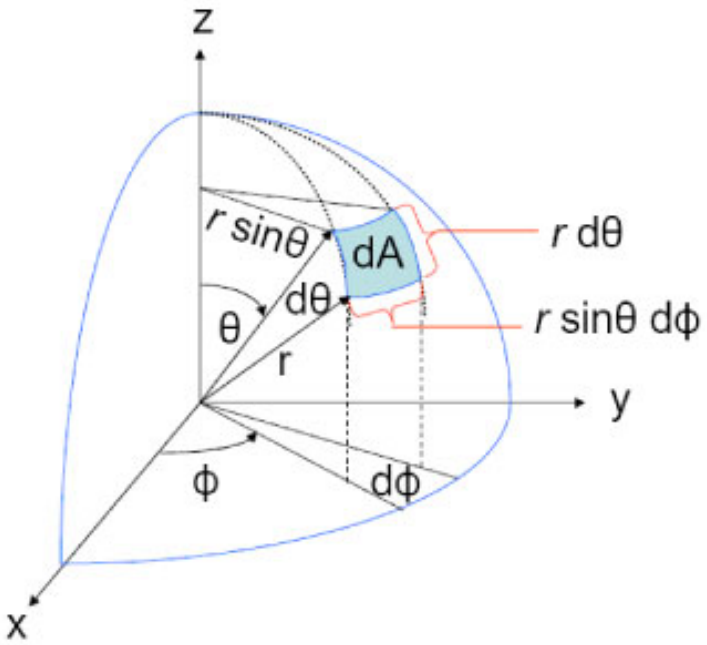

Figure 2.4: Spherical coordinate system. Figure shows r = constant surface, hence, $dr = 0$ on the surface [20].

where θ is now measured from the north pole and is π at the south pole.
It is useful to abbreviate the term between parenthesis as:

$$d\Omega^2 = d\theta^2 + \sin^2\theta d\phi^2, \tag{2.55}$$

because it is a measure of angle on the sky of the observer.

Flat Minkowski Spacetime

We can now generalize the interval to 4-dimensional flat spacetime (x^0, x^1, x^2, x^3) [20]:

$$ds^2 = -(dx^0)^2 + (dx^1)^2 + (dx^2)^2 + (dx^3)^2, \tag{2.56}$$

which can be written as:

$$ds^2 = \eta_{\alpha\beta} dx^\alpha dx^\beta, \tag{2.57}$$

where $\eta_{\alpha\beta}$ is the Minkowski (flat) spacetime metric tensor:

$$\eta_{\alpha\beta} = \begin{pmatrix} -1 & 0 & 0 & 0 \\ 0 & 1 & 0 & 0 \\ 0 & 0 & 1 & 0 \\ 0 & 0 & 0 & 1 \end{pmatrix}. \tag{2.58}$$

Curved Three-Dimensional Space

For a general (possibly curved) covariant spacetime metric tensor $g_{\alpha\beta}$, the invariant line element is given by

$$ds^2 = g_{\alpha\beta} dx^\alpha dx^\beta. \tag{2.59}$$

The contravariant spacetime metric tensor $g^{\alpha\beta}$ is the inverse of the covariant tensor $g_{\alpha\beta}$:

$$g^{\alpha\beta} g_{\beta\gamma} = \delta^\alpha_\gamma. \tag{2.60}$$

This implies that whenever the metric tensor is diagonal:

$$g^{\alpha\beta} = (g_{\alpha\beta})^{-1}. \tag{2.61}$$

One can take inner products of tensors with the metric tensor, thus lowering or raising indices:

$$A_{\alpha\beta} = g_{\alpha\mu} A^\mu_\beta, \qquad A^{\alpha\beta} = g^{\alpha\mu} A^\beta_\mu. \tag{2.62}$$

For the spatial part of $g_{\alpha\beta}$, as proven by Robertson and Walker, the alternative line elements, that obey both isotropy and homogeneity is:

$$ds^2 = dr^2 + S_k(r)^2 d\Omega^2, \tag{2.63}$$

where the function $S_k(r)$ is a function of space curvature given by:

$$S_k(r) = \begin{cases} \frac{1}{\sqrt{k}} \sin\left(\sqrt{k}\, r\right) & \text{for } k > 0 \\ r & \text{for } k = 0 \\ \frac{1}{\sqrt{-k}} \sinh\left(\sqrt{-k}\, r\right) & \text{for } k < 0 \end{cases}, \tag{2.64}$$

This means that the circumference of a sphere around us with radius r, for $k \neq 0$, is no longer equal to $C = 2\pi r$, but is smaller for $k > 0$ and larger for $k < 0$. Also, the surface area of that sphere is no longer $S = 4\pi r^2$, but is smaller for $k > 0$ and larger for $k < 0$. For small r (to be precise, for $r \ll |k|^{1/2}$) the deviation from $C = 2\pi r$ and $S = 4\pi r^2$ is small, but as r approaches $|k|^{1/2}$ the deviation can become very large. This can be checked by writing the Taylor series expansion of Eq. (2.64). This is very similar to the 2-dimensional example of the Earths surface [20].

If we stand on the North Pole, and use r as the distance from us along the sphere (i.e. the longitudinal distance) from the north pole and $d\phi$ as the 2-dimensional version of $d\Omega$, then the circumference of a circle at $r = 10000$ km (i.e. a circle that is the equator in this case) is just 40000 km instead of $2\pi \times 10000 = 62831$ km, i.e. a factor of 0.63 smaller than it would be on a flat surface.

The constant k is the curvature constant. We can also define a "radius of curvature", as:

$$R_{\text{curvature}} = |k|^{-1/2}, \tag{2.65}$$

which, for our 2-dimensional example of the Earths surface, is the radius of the Earth. In our 3-dimensional Universe it is the radius of a 3-dimensional "surface" of a 4-dimensional "sphere" in 4-dimensional space.

Note that the expression given in Eq. (2.63) is not the only way to write the metric in curved space. For instance, if we switch to a very commonly used parametrization in which we change the radial coordinate from r to $x \equiv S_k(r)$, then from Eq. (2.64):

$$r = \begin{cases} \frac{1}{\sqrt{k}} \sin^{-1}\left(\sqrt{k}\ x\right) & \text{for } k > 0 \\ x & \text{for } k = 0 \\ \frac{1}{\sqrt{-k}} \sinh^{-1}\left(\sqrt{-k}\ x\right) & \text{for } k < 0 \end{cases}, \tag{2.66}$$

which implies that:

$$dr = \begin{cases} \frac{1}{\sqrt{k}} \left(\frac{\sqrt{k}}{\sqrt{1-\left(\sqrt{k}x\right)^2}} dx \right) & \text{for } k > 0 \\ dx & \text{for } k = 0 \\ \frac{1}{\sqrt{-k}} \left(\frac{\sqrt{-k}}{\sqrt{1+\left(\sqrt{-k}x\right)^2}} dx \right) & \text{for } k < 0 \end{cases}. \tag{2.67}$$

By squaring both sides of Eq. (2.67) we get:

$$dr^2 = \begin{cases} \frac{1}{1-kx^2} dx^2 & \text{for } k > 0 \\ dx^2 & \text{for } k = 0 \\ \frac{1}{1-kx^2} dx^2 & \text{for } k < 0 \end{cases}. \tag{2.68}$$

Then, the metric for homogeneous, isotropic, 3-dimensional space can be written as

$$ds^2 = \frac{dx^2}{1-kx^2} + x^2 d\Omega^2, \tag{2.69}$$

which we can rewrite, by changing the name of the variable from x to r, as

$$ds^2 = \frac{dr^2}{1-kr^2} + r^2 d\Omega^2, \tag{2.70}$$

$$\Rightarrow ds^2 = \frac{dr^2}{1-kr^2} + r^2 \left(d\theta^2 + \sin^2\theta d\phi^2\right). \tag{2.71}$$

Note that this metric is different only in the way we choose our coordinate r; it is not different in any physical way from Eq. (2.63).

The Covariant Derivative

Consider a vector $\vec{A}$ given in terms of its components along the basis vectors $\hat{e}_\alpha$ as:

$$\vec{A} = A^\alpha \hat{e}_\alpha. \tag{2.72}$$

Differentiating the vector $\vec{A}$ using the standard Leibniz rule for the differentiation of the product of functions $(fg)' = f'g + fg'$, we get:

$$\frac{\partial \vec{A}}{\partial x^\alpha} = \frac{\partial}{\partial x^\alpha}\Big(A^\beta \hat{e}_\beta\Big) = \frac{\partial A^\beta}{\partial x^\alpha}\hat{e}_\beta + A^\beta \frac{\partial \hat{e}_\beta}{\partial x^\alpha}. \tag{2.73}$$

In flat Cartesian coordinates the basis vectors are constant. However, this is not the case in general curved spaces. In general, the derivative in the last term will not vanish, and it will itself be given in terms of the original basis vectors:

$$\frac{\partial \hat{e}_\beta}{\partial x^\alpha} \equiv \Gamma^\nu_{\alpha\beta}\hat{e}_\nu, \tag{2.74}$$

where $\Gamma^\nu_{\alpha\beta}$ is called Christoffel symbol, which is written in terms of the metric tensor $g_{\mu\nu}$ as (see [18]):

$$\Gamma^\nu_{\alpha\beta} \equiv \frac{1}{2}g^{\nu\gamma}\Big(g_{\alpha\gamma,\beta} + g_{\gamma\beta,\alpha} - g_{\alpha\beta,\gamma}\Big). \tag{2.75}$$

Here it is important to note that Christoffel symbols are not tensors.

Taking the curvature of the ambient manifold into account when taking derivatives of a scalar field ϕ, a vector A^α, or a co-vector A_α will yield covariant derivatives:

$$\partial_{;\mu}\phi \equiv \partial_{,\mu}\phi, \qquad A_{\alpha;\beta} \equiv A_{\alpha,\beta} - \Gamma^\nu_{\alpha\beta}A_\nu, \qquad A^\alpha_{;\beta} \equiv A^\alpha_{,\beta} + \Gamma^\nu_{\alpha\beta}A^\nu, \tag{2.76}$$

where we have used the short hand notation $\partial_{,\mu}\phi \equiv \frac{\partial\phi}{\partial x^\mu}$, $A_{\alpha,\beta} \equiv \frac{\partial A_\alpha}{\partial x^\beta}$ and $A^\alpha_{,\beta} \equiv \frac{\partial A^\alpha}{\partial x^\beta}$. Other covariant derivatives of second rank contravariant and covariant tensor are defined as

$$\nabla_\rho A^{\mu\nu} \equiv A^{\mu\nu}_{;\rho} \equiv A^{\mu\nu}_{,\rho} + \Gamma^\mu_{\rho\alpha}A^{\alpha\nu} + \Gamma^\nu_{\rho\beta}A^{\mu\beta}, \tag{2.77}$$

$$\nabla_\rho A_{\mu\nu} \equiv A_{\mu\nu;\rho} \equiv A_{\mu\nu,\rho} - \Gamma^\alpha_{\rho\mu}A_{\alpha\nu} - \Gamma^\beta_{\rho\nu}A_{\mu\beta}, \tag{2.78}$$

respectively. The covariant derivative of mixed tensor is defined as

$$\nabla_\rho A^\mu_\nu \equiv A^\mu_{\nu;\rho} \equiv A^\mu_{\nu,\rho} + \Gamma^\mu_{\rho\alpha}A^\alpha_\nu - \Gamma^\beta_{\rho\nu}A^\mu_\beta, \tag{2.79}$$

where $A^{\mu\nu}_{,\rho} = \frac{\partial A^{\mu\nu}}{\partial x^\rho}$, $A_{\mu\nu,\rho} = \frac{\partial A_{\mu\nu}}{\partial x^\rho}$, and $A^\mu_{\nu,\rho} = \frac{\partial A^\mu_\nu}{\partial x^\rho}$.

For vector A^α, and co-vector A_α, defined along a curve $x^\beta = x^\beta(s)$, the covariant derivative along this curve are

$$\frac{DA^\alpha}{Ds} \equiv \frac{dA^\alpha}{ds} + \Gamma^\alpha_{\beta\gamma}\frac{dx^\gamma}{ds}A^\beta, \qquad \frac{DA_\alpha}{Ds} \equiv \frac{dA_\alpha}{ds} - \Gamma^\beta_{\alpha\gamma}\frac{dx^\gamma}{ds}A_\beta, \tag{2.80}$$

The covariant derivative in a curved spacetime is the analog to the ordinary derivative in Cartesian coordinates in flat spacetime (from [20]).

The Principle of General Covariance

This principle states that all tensor equations valid in Special Relativity will also be valid in General Relativity if:

- ⋆ The Minkowski metric $\eta_{\alpha\beta}$ is replaced by a general curved metric $g_{\alpha\beta}$.

$$ds^2 = \eta_{\alpha\beta}dx^\alpha dx^\beta \quad \Rightarrow \quad ds^2 = g_{\alpha\beta}dx^\alpha dx^\beta \tag{2.81}$$

$$\eta_{\alpha\beta}u^\alpha u^\beta = -1 \quad \Rightarrow \quad g_{\alpha\beta}u^\alpha u^\beta = -1, \tag{2.82}$$

⋆ All the partial derivatives are replaced by covariant derivatives; in simple language the commas in the equations will be replaced by semicolon (, → ;). E.g.,

$$T^{\alpha\beta}_{\ ,\beta} = 0 \quad \Rightarrow \quad T^{\alpha\beta}_{\ ;\beta} = 0. \tag{2.83}$$

from [20]

The Einstein Field Equations

Having stated in mathematical terms the underlying principles of general relativity, including the geometry of flat spacetime, curved space-time, the covariant derivative, and the principle of covariance, we will now go on to describe the various tensors which make up the Einstein Field Equations including the Riemann tensor, the Ricci Tensor, and the Stress-Energy tensor. After gaining a basic mathematical grasp of these concepts, we can then see how Einstein arrived at the famous field equation which bears his name. There is no attempt to rigorously derive the field equations, but only to describe them in basic mathematical terms.

Einstein's field equations, the general relativity generalization of Poisson's equation for gravity, is a set of 10 equations that describe gravity. Einstein's general theory of relativity describes the fundamental interaction of gravitation as a result of spacetime being curved by matter and energy. First published by Einstein in 1915 as a tensor equation, the Einstein field equation equates local spacetime curvature (expressed by the Einstein tensor $G_{\mu\nu}$) to the local energy and momentum within that spacetime (expressed by the stress-energy tensor $T_{\mu\nu}$) [20]

Similar to the way that electromagnetic fields are determined from the source charges and currents through Maxwell's equations, Einstein's field equations are used to determine the spacetime geometry resulting from the presence of mass-energy and linear momentum (sources), that is, they determine the metric tensor of spacetime for a given arrangement of stress-energy in the spacetime. The relationship between the metric tensor and the Einstein tensor allows the Einstein field equations to be written as a set of non-linear partial differential equations. The solutions of the Einstein field equations are the components of the metric tensor. The trajectories of particles and radiation in the resulting geometries are then calculated using the geodesic equation.[20]

The Riemann tensor

The Riemann curvature tensor, or Riemann-Christoffel tensor, is the most common tensor used to describe the curvature of Riemannian manifolds. It associates a tensor to each point of a Riemannian manifold (i.e., it is a tensor field) that measures the extent to which the metric tensor is not locally isometric to a Euclidean flat space and so specifies the geometrical properties of spacetime. More precisely, the Riemann tensor governs the evolution of a vector on a displacement parallel propagated along a geodesic. It is defined in terms of Christoffel symbols as

$$R^{\alpha}_{\beta\gamma\delta} \equiv \Gamma^{\alpha}_{\beta\delta,\gamma} - \Gamma^{\alpha}_{\beta\gamma,\delta} + \Gamma^{\nu}_{\beta\delta}\Gamma^{\alpha}_{\nu\gamma} - \Gamma^{\nu}_{\beta\gamma}\Gamma^{\alpha}_{\nu\delta}, \tag{2.84}$$

where $\Gamma^{\alpha}_{\beta\delta,\gamma} \equiv \frac{\partial \Gamma^{\alpha}_{\beta\delta}}{\partial x^{\gamma}}$.

Spacetime is considered flat if the Riemann tensor vanishes everywhere. The Riemann tensor can also be written directly in terms of the spacetime metric

$$R_{\alpha\beta\gamma\delta} \equiv \frac{1}{2}\left(g_{\beta\gamma,\alpha\delta} + g_{\alpha\delta,\beta\gamma} - g_{\beta\delta,\alpha\gamma} - g_{\alpha\gamma,\beta\delta}\right) + g_{\mu\nu}\Gamma^{\nu}_{\alpha\gamma}\Gamma^{\mu}_{\beta\delta} - g_{\mu\nu}\Gamma^{\nu}_{\alpha\delta}\Gamma^{\mu}_{\beta\gamma}. \tag{2.85}$$

The Riemann tensor has skew symmetry and interchange symmetry. Because of these symmetries, the Riemann tensor in 4-dimensional spacetime has only 20 independent components out of $4^4 = 256$ [20].

The Ricci tensor

The Ricci tensor, or the Ricci curvature tensor, governs the evolution of a small volume parallel propagated along a geodesic. It is obtained from the Riemann tensor by contracting over two of the indices,

$$R_{\alpha\beta} \equiv R^{\gamma}_{\alpha\gamma\beta}. \tag{2.86}$$

It is symmetric, which means that it has at most 10 independent components out of $4 \times 4 = 16$. For the case of vacuum we will see later, the field equation is $R_{\mu\nu} = 0$.

The Ricci scalar

The Ricci scalar $\mathcal{R}$ is obtained by contracting the Ricci tensor over the remaining two indices and is denoted by :

$$\mathcal{R} \equiv g^{\alpha\beta}R_{\alpha\beta} = R^{\alpha}_{\alpha}. \tag{2.87}$$

The Einstein tensor

The Einstein tensor is defined in terms of the Ricci tensor and Ricci scalar as

$$G_{\alpha\beta} \equiv R_{\alpha\beta} - \frac{1}{2}g_{\alpha\beta}\mathcal{R}. \tag{2.88}$$

One can use Bianchi identities to derive a very important property of the Einstein tensor, $G_{\alpha\beta;\alpha} = 0$ [20].

The Stress-Energy Tensor

In the Newtonian approximation, the gravitational field is directly proportional to mass. In general relativity, mass is just one of several sources of spacetime curvature. The stress-energy (energy-momentum) tensor, denoted by $T^{\mu\nu}$, includes all possible forms of sources (energy) that can curve spacetime, and it describes the density and flow of the 4-momentum $(-E, p_{\mathrm{x}}, p_{\mathrm{y}}, p_{\mathrm{z}},)$.[18] In simple terms, the stress-energy tensor quantifies everything that causes spacetime to curve, and thus contributes to the gravitational field.

More rigorously, the components $T^{\mu\nu}$ of the stress-energy tensor is the flux of the μ component of the four momentum crossing the surface of constant x^{ν}. A surface of constant x^{ν} is simply a 3-plane perpendicular to the x^{ν}-axis. Hence, the stress-energy tensor is the flux of a 4-momentum across a surface of a constant coordinate. The stress-energy tensor describes the density of energy and momentum and the flux of energy and momentum in a region. Since, under the mass-energy equivalence principle, we can convert mass units to energy units and vice-versa, then the stress-energy tensor can describe all the mass and energy in a given region of spacetime [20]

The stress-energy tensor, being a tensor of rank two in four-dimensional spacetime, has sixteen components that can be written as a 4×4 matrix, and has the following structure in an orthonormal basis

$$T^{\mu\nu} = \begin{pmatrix} T^{00} & T^{01} & T^{02} & T^{03} \\ T^{10} & T^{11} & T^{12} & T^{13} \\ T^{20} & T^{21} & T^{22} & T^{23} \\ T^{30} & T^{31} & T^{32} & T^{33} \end{pmatrix}. \tag{2.89}$$

Note that the components T^{00}, T^{10}, T^{20} and T^{30} are interpreted as densities. A density is what you get when you measure the flux of 4-momentum across a 3-surface of constant time, which means the instantaneous value of 4-momentum flux is density.

We now consider several energy-momentum tensors frequently used in General Relativity including classical vacuum and dust.

Vacuum: This is the simplest possible stress-energy tensor in which all the values are zero:

$$T^{\mu\nu} = 0. \tag{2.90}$$

This tensor represents a region of space in which there is no matter, energy, or fields. This is not just at a given instant, but over the entire period of time in which we're interested in. Nothing exists in this region, and nothing happens in this region.

Dust: Imagine a time-dependent distribution of identical, massive, non-interacting, electrically neutral particles. In general relativity, such a distribution is called a dust.

To fully describe the dust we need to write its energy-momentum tensor, which is given by

$$T^{\mu\nu} = \rho u^{\mu} u^{\nu}. \tag{2.91}$$

For a comoving observer, the 4-velocity is given by $\vec{u} = (1, 0, 0, 0)$, so the stress-energy tensor reduces to

$$T^{\mu\nu} = \begin{pmatrix} \rho & 0 & 0 & 0 \\ 0 & 0 & 0 & 0 \\ 0 & 0 & 0 & 0 \\ 0 & 0 & 0 & 0 \end{pmatrix}. \tag{2.92}$$

Dust is an approximation to the content of the Universe at later times, when radiation is negligible.

The Einstein Field Equations

Just as Maxwell's equations govern the electric and magnetic field response to electric charges and current (sources), Einstein's field equations describe how the metric is governed by energy and momentum (sources). There are two basic parts of this equation, which describe the motion of particles and the generation of the gravitational field.

The effect of gravity on the motion of partices is described by the geodesic equation

$$\frac{d^2 x^{\nu}}{d\lambda^2} + \Gamma^{\nu}_{\gamma\delta} \frac{dx^{\gamma}}{d\lambda} \frac{dx^{\delta}}{d\lambda} = 0, \tag{2.93}$$

which is analogous to Newton's second law of motion $\vec{F} = m\vec{a}$.

The generation of a gravitational field by a source of mass energy involves finding the analog of the Poisson equation

$$\nabla^2 \Phi(\vec{x}) = 4\pi G \rho(\vec{x}), \tag{2.94}$$

which specifies how matter (or energy in general relativity) curves spacetime. Here $\nabla^2 = \delta^{ij}\partial_i\partial_j$ is the Laplacian in space and ρ is the mass density [the explicit form of $\phi = -GM/r$ is the solution of Eq. (2.94) for the case of a spherically symmetric mass distribution].

In classical Newtonian gravity, gravitational effects are produced by a mass at rest. In modified Newtonian gravity, which we can call special relativity, we learned that rest mass is also a form of energy. Thus special relativity put mass and energy on an equal footing. Extending this idea, one should expect that in general relativity, all sources of both energy and momentum contribute in generating spacetime curvature. On the left hand side of Eq. (2.94) a second order differential operator acts on the gravitational potential and on the right hand side is a measure of mass density. The relativistic generalization of the Poisson equation should be the relationship between tensors. The tensor generalization of mass density can be $T^{\mu\nu}$. This means that we consider the stress-energy tensor $T^{\mu\nu}$ as the source of spacetime curvature (with an unknown scaling factor), in the same sense that the mass density ρ is the source for the potential Φ in Newtonian gravity. Hence, the right hand side of the general relativity analog of the Poisson equation should be $\kappa T^{\mu\nu}$ (where κ is an unknown constant to be determined later.) [20]

Regarding the left hand side of the general relativity analog of the Poisson equation, we have shown that the spacetime metric in the Newtonian limit is modified by a term that is proportional to Φ. Extending this idea, the general relativity counterpart of $\nabla^2\Phi(\vec{x})$ contains terms having the second derivative of the metric tensor, for example:

$$\Big[\nabla^2\ g\Big]_{\mu\nu} = \kappa T^{\mu\nu}. \tag{2.95}$$

However, this should be a tensor equation and the left-hand side of Eq. (2.95) is not a tensor. It is just simplistic notation that indicates we need something on the left hand side that should have the second derivative of the metric.

The Riemann tensor $R_{\alpha\beta\gamma\delta}$, and consequently its contractions, the Ricci tensor $R_{\alpha\beta} = R^{\gamma}_{\alpha\gamma\beta}$, and the Ricci scalar $\mathcal{R} = R^{\alpha}_{\alpha}$, contain the second derivative of the metric and therefore is a candidate for the left hand side of Einstein's field equations.

Following this line of thought, Einstein originally suggested that the field equations might be

$$R_{\mu\nu} = \kappa T_{\mu\nu}, \tag{2.96}$$

but one can see directly that this can not be correct. While the conservation of energy and momentum require $T^{\mu\nu}_{\ ;\mu} = 0$, the same in general is not true for the Ricci tensor $R^{\mu\nu}_{\ ;\mu} \neq 0$. However Einstein's tensor, $G_{\mu\nu} = R_{\mu\nu} - \frac{1}{2}g_{\mu\nu}\mathcal{R}$, which is a combination of the Ricci tensor and scalar, satisfies the divergence-less condition $\nabla^\mu G_{\mu\nu} = 0$. Therefore, Einstein's field equations become

$$G_{\mu\nu} \equiv R_{\mu\nu} - \frac{1}{2}g_{\mu\nu}\mathcal{R} = \kappa T_{\mu\nu}. \tag{2.97}$$

This equation satisfies all of the obvious requirements: the right-hand side of is a covariant expression of the energy and momentum density in the form of a symmetric and conserved tensor, while the left-hand side is also a symmetric and conserved tensor constructed from the first and second derivatives of the metric tensor and the metric tensor itself. The only issue that remains is to fix the constant κ. By matching Einstein's equation in the Newtonian limit to the Poisson equation, the constant κ was found to $8\pi G$, where G is the Newtonian gravitational constant. Then Eq. (2.97) takes the form

$$G_{\mu\nu} \equiv R_{\mu\nu} - \frac{1}{2} g_{\mu\nu} \mathcal{R} = 8\pi G T_{\mu\nu}.$$

In summary, Einstein's equations for the gravitational field came from requiring that the equations of motion are generally covariant under coordinate transformations and reduced to the Newtonian form in weak stationary gravitational fields. The field equation relates the Ricci tensor, that is made up of second derivatives of the metric tensor, to the Ricci scalar formed by contracting the Ricci tensor, and to the energy-momentum content of the Universe [20].

Newtonian Gravity as the Weak Field Limit of General Relativity

That General Relativity reduces to Newtonian gravity in the weak field limit is a necessary consequence of the Correspondence Principle, which Einstein saw as an essential ingredient to General Relativity. We shall demonstrate this mathematically in this section.

In order to check that General Relativity reduces to Newton's Theory of Gravity, we must do two things [3].

Relate the geodesic equation to Newton's law of motion

Relate Einstein's field equations to the Newton-Poisson equation

We start with the definition of the interval, based on the metric

$$ds^2 = g_{\mu\nu} dx^\mu dy^\nu. \tag{2.98}$$

The Einstein field equation is

$$G_{\mu\nu} = -8\pi G T_{\mu\nu}. \tag{2.99}$$

The Newtonian potential for a point-like mass is

$$\Phi = \frac{-Gm}{r}. \tag{2.100}$$

The Newtonian equation of motion is

$$\frac{d^2 x^i}{dt^2} = F^i = -\frac{\partial \Phi}{\partial x^i}. \tag{2.101}$$

In the weak field limit

$$G_{00} = -2\nabla^2 \Phi \tag{2.102}$$

and

$$T_{00} = \rho. \tag{2.103}$$

Combining these two terms for the weak field limit with the Einstein field equation we then have

$$-2\nabla^2 \Phi = -8\pi G \rho \tag{2.104}$$

which reduces to the Newton-Poison equation

$$\nabla^2\Phi = 4\pi G\rho \tag{2.105}$$

showing that the Einstein field equation in the weak field limit, reduces to Newtonian gravity as a demonstration of the compliance of General Relativity with the correspondence principle.

Tests of General Relativity

Over the years, there have been a number of experimental tests of general relativity proposed. We shall discuss four of the classic tests of this theory. The first three including the gravitational deflection of light, the precession of perihelia and gravitational redshift were suggested by Einstein. The subject of bending of light by the sun is very briefly mentioned here and then developed in an extensive manner throughout this dissertation. The other three tests of general relativity are mentioned very briefly here for completeness but not developed mathematically.

These first three tests are considered the "classic" tests of general relativity. The fourth was added by Shapiro in 1964. There are other tests as well, which will not be described here. While it may not be common knowledge, many people depend daily on the results predicted by both special and general relativity in their daily lives, as the Global Positioning System requires corrections for both special relativistic effects (time dilation) and general relativistic effects (gravitational redshift). Without these small but critical correction factors, the GPS system would be useless to guide our cars or the missiles it was initially developed for [2].

Bending of Light by the Sun This will only be mentioned briefly here as it is the subject of Chapter 3, and in fact, the subject of the rest of this dissertation. Of specific interest regarding this particular test is that Einstein calculated a value for the bending of light by the sun, and published it in 1911. This result was in fact incorrect and his publication in 1915 of a value of 1.74arcsec which was the result verified in 1919 by Eddington. Had the planned expedition in 1914 gone forth, Einstein's fame may never have materialized. Also of interest is that this test was conducted after the general theory of relativity had been completely described, again emphasizing the unusual development of relativity where theory preceded experiments.

Advance of the Perihelion of Mercury It was well-known at the end of the nineteenth century that the orbit of Mercury did not exactly follow Newtonian mechanics. The perihelion of an elliptical orbit is its point of closest approach to the Sun. The precession of perihelia reflects the fact that noncircular orbits in general relativity are not perfect closed ellipses. Before general relativity, there were several attempts to explain the discrepancy, including a mythical, unobserved planet referred to as Vulcan that exerted a gravitational effect on Mercury disturbing its orbit. The major axis of Mercury's orbit precesses at a rate of 43arcsec every 100 years, which is exactly the value calculated by Einstein and published in 1916 [30].

Gravitational Redshift Einstein predicted the gravitational redshift of light based on the equivalence principle in 1907, but it is very difficult to measure astrophysically. Although it was measured in 1925, it was only conclusively tested by the Pound-Rebka experiment in 1959 which measured the relative redshift of two sources at the top and bottom of Harvard University's Jefferson tower using the Mössbauer effect. The result was in excellent agreement with general relativity. This was one of the first precision experiments testing general relativity [30].

Gravitational Time Delay Shapiro proposed another test, beyond the classical tests, which could be performed within the solar system. He predicted a relativistic time delay (Shapiro delay) in the round-trip travel time for radar signals reflecting off other planets. The mere curvature of the path of a photon passing near the Sun is too small to have an observable delaying effect (when the round-trip time is compared to the time taken if the photon had followed a straight path), but general relativity predicts a time delay which becomes progressively larger when the photon passes nearer to the Sun due to the time dilation in the gravitational potential of the sun. Observing radar reflections from Mercury and Venus just before and after it will be eclipsed by the Sun gives agreement with general relativity theory at the 5% level. More recently, the Cassini probe has undertaken a similar experiment which gave agreement with general relativity at the 0.002% level. Very Long Baseline Interferometry has measured velocity-dependent (gravitomagnetic) corrections to the Shapiro time delay in the field of moving Jupiter and Saturn [30].

A Comparison of Newtonian and Einsteinian Mechanics

Newtonian and Einsteinian mechanics, from [20].

Newtonian Mechanics	**Einsteinian Mechanics**
Absolute time and absolute space	Dynamical spacetime, one entity
Galilean invariance of space (simultaneity)	Lorentz invariance of spacetime (time dilation, length contraction, no simultaneity)
Existence of preferred inertial frames (at rest or moving at constant velocity with respect to absolute space).	No preferred frames (physics is the same everywhere).
Infinite speed of light c (instantaneous action at a distance)	Finite and fixed speed of light c (nothing physical can propagate faster than c)
There is no upper limit on the speed with which mass can travel.	There is an upper limit of speed with which mass can travel, c.
Gravity is a force.	Gravity is a distortion of the geometry of spacetime.
Newton's Second Law: $\frac{d^2x^i}{dt^2} = -\delta^{ij}\frac{\partial\Phi}{\partial x^j}$.	Geodesic equation: $\frac{d^2x^\nu}{d\lambda^2} = -\Gamma^\nu_{\gamma\delta}\frac{dx^\gamma}{d\lambda}\frac{dx^\delta}{d\lambda}$.
Poisson equation: $\nabla^2\Phi(x) = 4\pi G\rho_m$	Einstein's field equation: $G_{\mu\nu} = 8\pi G T_{\mu\nu}$
Mass produces a field Φ causing a force on the other mass m given by: $\vec{F} = -\vec{\nabla}\Phi$.	Spacetime is curved and mass particles move along curved geodesics defined by metric: $ds^2 = g_{\mu\nu}(x)dx^\mu dx^\nu$.
Absolute space acts on matter but is not acted upon.	Mass tells space-time how to curve and space-time tells matter how to move (from JA Wheeler)

A Summary of General Relativity

There are three essential ideas underlying general relativity [4]:

Space-time may be described as a curved four dimensional mathematical structure called a pseudo-Riemannian manifold. In brief, time and space together comprise a curved four dimensional non-Euclidean geometry. The laws of physics must be expressed in a form that is valid independent of any coordinate system used to label points in space-time.

At every space-time point there exist locally inertial reference frames corresponding to locally flat coordinates carried by freely falling observers in which the physics of general relativity is locally indistinguishable from that of special relativity. This is Einstein's strong equivalence principle and it makes general relativity an extension of special relativity to a curved space-time.

Mass, as well as mass and momentum flux, curves space-time in a manner described by the Einstein Field Equations. Mass moves in space-time under the influence of gravity along geodesics.

Pictorially, the concept of space-time curvature is often invoked as a rubber sheet. While this is may not be entirely accurate, it serves as a useful way to visualize the idea that a "sheet" of space-time is deformed by mass, resulting in a change in the geometry. It is perhaps best described in the "Parable of the Apple" [18].

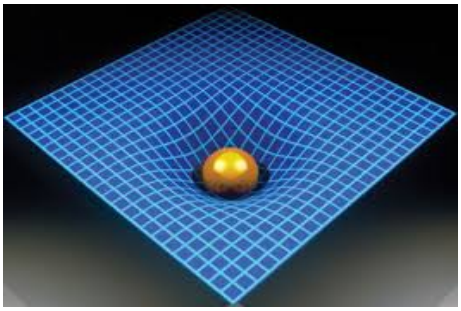

Figure 2.5: The geometry of space-time is changed by the presence of mass

General relativity can be stated in the formal tensor expression of Einstein's Field Equations:

$$G_{\mu\nu} = 8\pi T_{\mu\nu} \tag{2.106}$$

but is most eloquently summarized in the simple words of John Archibald Wheeler:

"Mass tells space-time how to curve and space-time tells matter how to move"

2.4 Fundamentals of Cosmology

The purpose of this section is to provide a brief introduction to Cosmology, particularly areas that relate closely to Relativity and Gravitational Lensing. There is no attempt here to be exhaustive, but only to introduce major concepts that serve as important background for studies in gravitational lensing.

The Cosmological Principle

Cosmology is the study of the structure and evolution of the Universe as a whole. We can write down equations for the evolution of the Universe by making a powerful assumption known as the cosmological principle. The cosmological principle states that the Universe appears isotropic (it looks the same in all directions) and homogeneous (properties such as density or temperature do not vary with position) to any observer.

As an assumption, the cosmological principle cannot be proven. But no observation performed so far is inconsistent with this assumption, on scales over 100MPc, at least no observation of the distant Universe. The density of galaxies appears to be independent of direction. The intensity of the cosmic background radiation (the microwave radiation from the early hot Universe) is highly isotropic. There appears to be no significant variation with direction.

We would expect intuitively that at any given time the universe ought to look the same to observers in all typical galaxies, and in whatever direction they look. (Hereafter we will use the label "typical" to indicate galaxies that do not have any large peculiar motion of their own, but are simply carried along with the general cosmic flow of galaxies.) This hypothesis is so natural (at least since Copernicus) that it has been called the Cosmological Principle by the English astrophysicist Edward Arthur Milne [1].

The Hubble Parameter

In the late 1920's, Hubble discovered that the spectral lines of galaxies were shifted towards the red by an amount proportional to their distances. If the redshift is due to the Doppler effect, this means that the galaxies move away from each other with velocities proportional to their separations. The importance of this observation is that it is just what we should predict according to the simplest possible picture of the flow of matter in an expanding universe [1]. In terms of the redshift $z \equiv (\lambda' - \lambda)/\lambda$, the "linear" Hubble law can be written as

$$z \approx (H_0/c)\, r \ , \tag{2.107}$$

where c is the speed of light, H_0 is the present value of the Hubble constant and r the distance to the galaxy. For small velocities ($V \ll c$), the Doppler redshift is $z \approx V/c$. Therefore, $V \approx H_0 r$, which is the most commonly used form of Hubble law. The present day Hubble expansion rate is $H_0 = 100\ h\ \mathrm{km\,s^{-1}\,Mpc^{-1}}$, where $h = 0.71^{+0.04}_{-0.03}$.

A particularly useful quantity to define from the scale factor is the *Hubble parameter* (sometimes referred to as the Hubble constant), given by

$$H \equiv \frac{\dot{a}}{a} \ . \tag{2.108}$$

The Hubble parameter relates how fast the most distant galaxies are receding from us to their distance from us via Hubble's law,

$$v \simeq Hd. \tag{2.109}$$

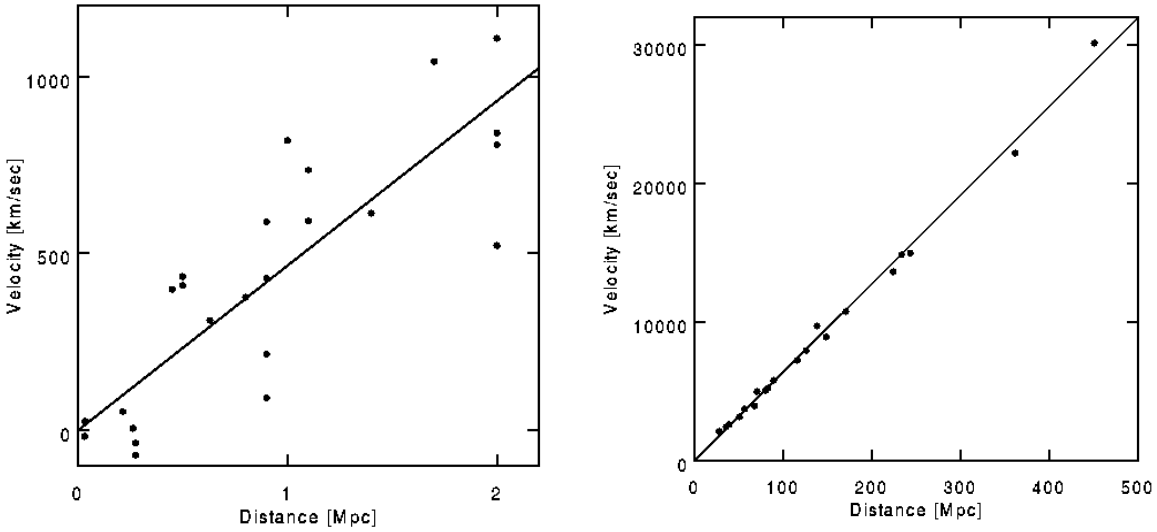

Figure 2.6: Hubble diagrams showing the relationship between recessional velocities of distant galaxies and their distances. The left plot shows the original data of Hubble. The right plot shows more recent data, using significantly more distant galaxies (note difference in scale) from [28]

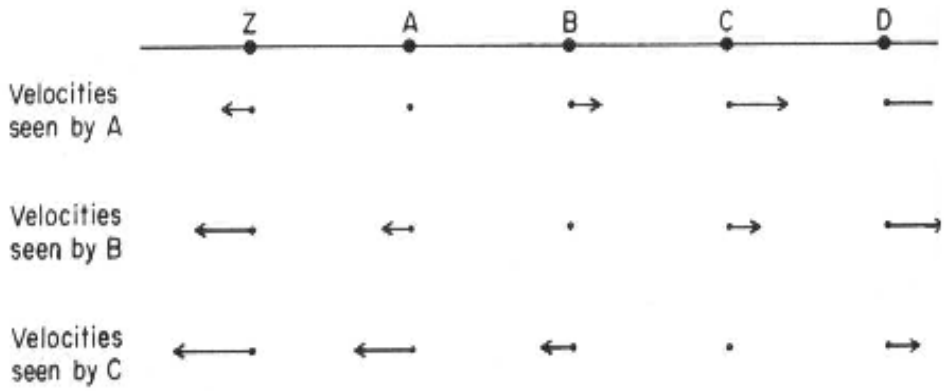

Figure 2.7: Homogeneity and the Hubble Law: A string of equally spaced galaxies Z, A, B, C, ... are shown with velocities as measured from A or B or C indicated by the lengths and directions of the attached arrows. The principle of homogeneity requires that the velocity of C as seen by B is equal to the velocity of B as seen by A, adding these two velocities gives the velocity of C as seen by A, indicated by an arrow twice as long. Proceeding in this way we can fill out the whole pattern of velocities shown in the figure. As can be seen the velocities obey the Hubble law: the velocity of any galaxy, as seen by others is proportional to the distance between them. This is the only pattern of velocities consistent with the principle of homogeneity. from [1]

This is the relationship that was discovered by Edwin Hubble, and has been verified to high accuracy by modern observational methods (see figure 2.6) [28].

As applied to the galaxies themselves, the Cosmological Principle requires that an observer in a typical galaxy should see all the other galaxies moving with the same pattern of velocities, whatever typical galaxy the observer happens to be riding in. It is a direct mathematical consequence of this principle that the relative speed of any two galaxies must be proportional to the distance between them, just as found by Hubble. To see this consider three typical galaxies A, B, and C, strung out in a straight line, as shown in Fig. 2.7. Suppose that the distance between A and B is the same as the distance between B and C. Whatever the speed of B as seen from A, the Cosmological principle requires that C should have the same speed relative to B. But note that C, which is twice away from A as is B, is also moving twice as fast relative to A as is B. We can add more galaxies in our chain, always with the result that the speed of recession of any galaxy relative to any other is proportional to the distance between them [1].

As often happens in science, this argument can be used both forward and backward. Hubble, in observing a proportionality between the distances of galaxies and their speeds of recession, was indirectly verifying the Cosmological Principle. Contrariwise, we can take the Cosmological Principle for granted on *a priori* grounds, and deduce the relation of proportionality between distance and velocity. In this way, through the relatively easy measurement of Doppler shifts, we are able to judge the distance of very remote objects from their velocities [1].

Before proceeding any further, two qualifications have to be attached to the Cosmological Principle. First, it is obviously not true on small scales – we are in a Galaxy which belongs to

a small local group of other galaxies, which in turn lies near the enormous cluster of galaxies in Virgo. In fact, of the 33 galaxies in Messier's catalogue, almost half are in one small part of the sky, the constellation of Virgo. The Cosmological Principle, comes into play only when we view the universe on a scale at least as large as the distance between clusters of galaxies, or about 100 million light years. Second, in using the Cosmological Principle to derive the relation of proportionality between galactic velocities and distances, we suppose the usual rule for adding $V \ll c$. This, of course, was not a problem for Hubble in 1929, as none of the galaxies he studied then had a speed anywhere near the speed of light. Nevertheless, it is important to stress that when one thinks about really large distances characteristic of the universe, as a whole, one must work in a theoretical framework capable of dealing with velocities approaching the speed of light.

Relativity in Cosmology

To derive the equations of the evolution of the Universe, we combine the cosmological principle with the complete theory of gravity, General Relativity. The Einstein Field Equations consist of ten nonlinear partial differential equations. They are incredibly hard to solve and for almost a century there have been many attempts at finding solutions which might describe real world phenomena. We are going to focus on one set of solutions which apply in a very particular regime. We will solve the Field Equations for the whole Universe under the assumption that it is homogeneous and isotropic. Homogeneity and isotropy are distinct yet inter-related concepts. For example a universe which is isotropic will be homogeneous while a universe that is homogeneous may not be isotropic. A universe which is only isotropic around one point is not homogeneous. A universe that is both homogeneous and isotropic is said to satisfy the Cosmological Principle. It is believed that our Universe satisfies the Cosmological Principle. [12]

Homogeneity severely restrict the metrics that we are allowed to work with in the Einstein field equation. For a start, they must be independent of space, and solely functions of time. Furthermore, we must restrict ourselves to spaces of constant curvature of which there are only three: a flat euclidean space, a positively curved space and a negatively curved space. We will look at curved spaces in a later lecture and will restrict ourselves to a flat geometry here. [12]

In the next sections, we will consider the Schwarzschild solution to the Einstein Field Equations because they are of great historical significance. We then consider the Robertson-Walker metric and Friedman equations as a way to bring together the General Theory of Relativity with the Cosmological Principle. The Robertson-Walker metric is defined for any behavior of the scale factor $a(t)$. This metric is then plugged into the Einstein Field Equations which relate the scale factor to the energy-momentum of the Universe.

The Schwarzschild Solution and Black Holes

In the fall of 1915, Karl Schwarzschild was already a well-known German astronomer, serving as Director of the Astrophysical Observatory in Potsdam and a member of the Prussian Academy of Sciences. At the outbreak of World War I, he volunteered for service despite being over 40 years of age, and served in France and Russia.

While on the eastern front, he contracted pemphigus, a rare auto-immune skin disease. While in the hospital, he attempted to find exact solutions of Einsteins equations of general relativity, newly published in November 1915. He obtained the solution for both a spherically symmetric star of uniform density and of a mass point. His results were published in early 1916, and Schwarzschild soon died of the disease, in May, 1916 [14].

The Schwarzschild solution to the Einstein Field Equations provided the basis for considering a black hole (this term was coined by JA Wheeler in the mid-1960s). The simplest description of black holes says a black hole is a region of spacetime from which gravity prevents anything, including light, from escaping. It is an object created when a massive star collapses to a size smaller than twice its geometrized mass, thereby creating such strong spacetime bending that its interior can no longer communicate with the external universe.

Black holes were first predicted using solutions of the equations of General Relativity. These equations predict specific properties for their external geometry. If the black hole is non-rotating, then its exterior metric is be that of Schwarzschild, which is the exact, unique, static and spherically symmetric solution of Einstein's equation in vacuum. In Schwarzschild coordinates, the line element for the Schwarzschild metric has the form

$$\mathrm{d}s^2 = -\left(1 - 2Gm/r\right)\mathrm{d}t^2 + \frac{\mathrm{d}r^2}{1 - 2Gm/r} + r^2\left(\mathrm{d}\theta^2 + \sin^2\theta\ \mathrm{d}\phi^2\right)\ , \tag{2.110}$$

where G is Newton's constant and we use units in which $c = 1$. The surface of the black hole, i.e., the horizon, is located at $r = 2Gm$. Only the region on and outside the black hole's surface, $r \geq 2Gm$, is relevant to external observers. Events inside the horizon can never influence the exterior.

In that region of spacetime, $r >> 2Gm$, where the geometry is nearly flat, Newton's theory, $\mathrm{d}v/\mathrm{d}t = \nabla\Phi(r)$, where $\Phi(r)$ is the Newtonian gravitational potential, can be obtained from the approximate line element

$$\mathrm{d}s^2 = -\left(1 - 2Gm/r\right)\mathrm{d}t^2 + \mathrm{d}r^2 + r^2\left(\mathrm{d}\theta^2 + \sin^2\theta\ \mathrm{d}\phi^2\right)\ . \tag{2.111}$$

For Schwarzschild metric, in the limit $r \gg 2Gm$, $\Phi(r) = -Gm/r$. Consequently, m is the mass that governs the Keplerian motions of test masses in the distant, Newtonian gravitational field and we can call m in Eq. (2.110) *Keplerian mass* of the black hole.

If the black hole is rotating with angular momentum J, its exterior geometry is given by the Kerr metric. The Kerr metric is given in Boyer-Lindquist coordinates, which are a generalization of Schwarzschild coordinates, by

$$\begin{aligned}\mathrm{d}s^2 \quad = \quad & -\left(1 - \frac{2Gmr}{\Sigma^2}\right)\mathrm{d}t^2 + \frac{\Sigma^2}{\Delta}\mathrm{d}r^2 + \Sigma^2\mathrm{d}\theta^2 - \frac{4Gmra}{\Sigma^2}\sin^2\theta\mathrm{d}t\mathrm{d}\phi \\ & + \left(r^2 + a^2 + \frac{2Gmra^2\sin^2\theta}{\Sigma^2}\right)\sin^2\theta d\phi^2\,,\end{aligned} \tag{2.112}$$

where a is the Kerr parameter, related to the angular momentum J by $a \equiv J/m$; $\Sigma^2 = r^2 + a^2\cos^2\theta$, and $\Delta = r^2 + a^2 - 2Gmr$. We will assume throughout that a is positive.

The Roberston-Walker Metric and the Friedman Equations

In 1917 Albert Einstein presented a model of the universe based on his theory of General Relativity. It described a geometrically symmetric (spherical) space with finite volume but no boundary. In accordance with the Cosmological Principle, the model was homogeneous and isotropic. It was also static: the volume of the space did not change.

In order to obtain a static model, Einstein had to introduce a new repulsive force in his equations. The size of this cosmological term is given by the cosmological constant Λ. Einstein presented his model before the redshifts of the galaxies were known, and taking the universe to be static was then reasonable. When the expansion of the universe was discovered, this

argument in favor of a cosmological constant vanished. Einstein himself later called it the biggest blunder of his life. Nevertheless the most recent observations seem to indicate that a non-zero cosmological constant has to be present.

The St. Petersburg physicist Alexander Friedmann studied the cosmological solutions of Einstein equations. If $\Lambda = 0$, only evolving, expanding or contracting models of the universe are possible. The general relativistic derivation of the law of expansion for the Friedmann models will not be given here. It is interesting that the existence of three types of models and their law of expansion can be derived from purely Newtonian considerations, with results in complete agreement with the relativistic treatment. Moreover, the essential character of the motion can be obtained from a simple energy argument, which we discuss next. [1]

Consider a spherical region of galaxies of radius r. We also assume $\Lambda = 0$.) The mass of this sphere is its volume times the cosmic mass density,

$$M = \frac{4\,\pi\,r^3}{3}\,\rho\,. \tag{2.113}$$

We can now consider the motion of a galaxy of mass m at the edge of our spherical region. According to Hubble's law, its velocity will be $V = Hr$ and the corresponding kinetic energy

$$K = \frac{1}{2}mV^2\ . \tag{2.114}$$

In a spherical distribution of matter, the gravitational force on a given spherical shell depends only on the mass inside the shell. The potential energy at the edge of the sphere is

$$U = -\frac{GMm}{r} = -\frac{4\pi m r^2 \rho G}{3}\,, \tag{2.115}$$

where $G = 6.67 \times 10^{-8}$ cm^3 g^{-1}s^{-2} is Newton's constant of gravitation. Hence, the total energy is

$$E = K + U = \frac{1}{2}m\,V^2 - \frac{G\,M\,m}{r}\ , \tag{2.116}$$

which has to remain constant as the universe expands. The value of ρ corresponding to $E = 0$ is called the critical density ρ_c. We have,

$$\begin{aligned} E &= \frac{1}{2}mH^2r^2 - \frac{GMm}{r} \\ &= \frac{1}{2}mH^2r^2 - Gm\frac{4\pi}{3}r^2\rho_c \\ &= mr^2\left(\frac{1}{2}H^2 - \frac{4\pi}{3}G\rho_c\right) = 0 \end{aligned} \tag{2.117}$$

where we define

$$\rho_c = \frac{3H^2}{8\pi G}\,. \tag{2.118}$$

The density parameter Ω is defined as $\Omega = \rho/\rho_c$.

Now consider two points at separation r, such that their relative velocity is V. Let $R(t)$ be a time dependent quantity representing the scale of the universe. If R increases with time, all distances, including those between galaxies, will grow. Then

$$r = \frac{R(t)}{R(t_0)}r_0\ , \tag{2.119}$$

and

$$V = \dot{r} = \frac{\dot{R}(t)}{R(t_0)}\, r_0 \ , \tag{2.120}$$

where dots denote derivative with respect to t. Therefore, the Hubble constant is

$$H = \frac{V}{r} = \frac{\dot{R}(t)}{R(t)} \ . \tag{2.121}$$

From the conservation of mass it follows that $\rho_0 R_0^3 = \rho R^3$. Using Eq. (2.118) for the critical density one obtains

$$\Omega = \frac{8\pi G}{3}\, \frac{\rho_0 R_0^3}{R^3 H^2} \ . \tag{2.122}$$

The deceleration expansion is described by the deceleration parameter q defined as

$$q = -\frac{R\ddot{R}}{\dot{R}^2} \ . \tag{2.123}$$

The deceleration parameter describes the change of expansion $\dot{R}$. The additional factors have been included in order to make it dimensionless, i.e., independent of the choice of units of length and time.

The expansion of the universe can be compared to the motion of a mass launched vertically from the surface of a celestial body. The form of the orbit depends on the initial energy. In order to compute the complete orbit, the mass M of the main body and the initial velocity have to be known. In cosmology, the corresponding parameters are the mean density and the Hubble constant.

The $E = 0$ model corresponds to the "flat" Friedmann model, so-called Einstein-de Sitter model. If the density exceeds the critial density, the expansion of any spherical region will turn to a contraction and it will collapse to a point. This corresponds to the closed Friedmann model. Finally, if $\rho < \rho_c$, the ever-expanding hyperbolic model is obtained.

These three models of the universe are called the standard models. They are the simplest relativistic cosmological models for $\Lambda = 0$. Models with $\Lambda \neq 0$ are mathematically more complicated, but show the same behaviour.

The simple Newtonian treatment of the expansion problem is possible because Newtonian mechanics is approximately valid in small regions of the universe. However, although the resulting equations are formally similar, the interpretation of the quantities involved is not the same as in the relativistic context. The global geometry of Friedmann models can only be understood within the general theory of relativity.

What is meant by a curved space? To answer this question, recall that our normal method of viewing the world is via Euclidean plane geometry. In Euclidean geometry there are many axioms and theorems we take for granted. Non-Euclidean geometries which involve curved space have been independently imagined by Carl Friedrich Gauss (1777-1855), Janos Bólyai (1802 - 1860), and Nikolai Ivanovich Lobachevski (1793-1856). Let us try to understand the idea of a curved space by using two dimensional surfaces. [1]

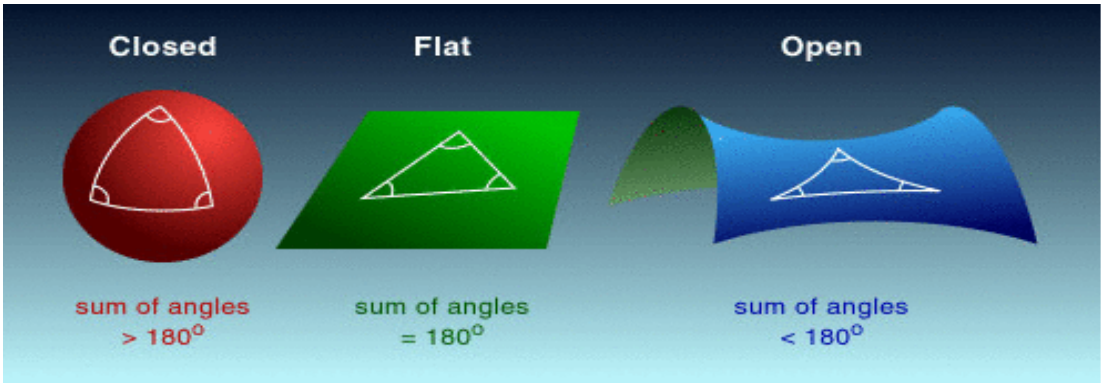

Figure 2.8: The two dimensional analogues of the Friedmann models. A spherical surface, a plane, and a pseudo-sphere. Note that the global geometry of the universe affects the sum of angles of a triangle. From [1]

Consider for example, the two-dimensional surface of a sphere. It is clearly curved, at least to us who view it from outside – from our three dimensional world. But how do the hypothetical two-dimensional creatures determine whether their two-dimensional space is flat (a plane) or curved? One way would be to measure the sum of the angles of a triangle. If the surface is a plane, the sum of the angles is 180°. But if the space is curved, and a sufficiently large triangle is constructed, the sum of the angles would not be 180°.

To construct a triangle on a curved surface, say the sphere of Fig. 2.8, we must use the equivalent of a straight line: that is the shortest distance between two points, which is called a geodesic. On a sphere, a geodesic is an arc of great circle (an arc in a plane passing through the center of the sphere) such as Earth's equator and longitude lines. Consider, for example, the triangle whose sides are two longitude lines passing from the north pole to the equator, and the third side is a section of the equator. The two longitude lines form 90° angles with the equator. Thus, if they make an angle with each other at the north pole of 90°, the sum of the angles is 270°. This is clearly not Euclidean space. Note, however, that if the triangle is small in comparison to the radius of the sphere, the angles will add up to nearly 180°, and the triangle and space will seem flat. On the saddlelike surface, the sum of the angles of a triangle is less than 180°. Such a surface is said to have negative curvature. [1]

On a large scale what is the overall curvature of the universe? Does it have positive curvature, negative curvature or is it flat? By solving Einstein equations, Robertson and Walker, showed that the three hypersurfaces of constant curvature (the hyper-sphere, the hyper-plane, and the hyper-pseudosphere) are indeed possible geometries for a homegeneous and isotropic universe undergoing expansion.

If the universe had a positive curvature, the universe would be closed, or finite in volume. This would not mean that the stars and galaxies extended out to a certain boundary, beyond which there is empty space. There is no boundary or edge in such a universe. If a particle were to move in a straight line in a particular direction, it would eventually return to the starting point – perhaps eons of time later. On the other hand, if the curvature of the space was zero or negative, the universe would be open. [1]

In an expanding universe, the galaxies were once much nearer to each other. If the rate of expansion had been unchanging, the inverse of the Hubble constant, $t_{\rm age} = H_0^{-1}$, would represent the age of the universe. In Friedmann-Robertson-Walker models, however, the expansion

is gradually slowing down (i.e., $q < 0$), and thus the Hubble constant gives an upper limit on the age of the universe, $t_{\rm age} \approx 14$ Gyr. Of course, if $\Lambda \neq 0$ this upper limit for the age of the universe no longer holds.

In an expanding universe the wavelength of radiation is proportional to R, like all other lengths. If the wavelength at the time of emission, corresponding to the scale factor R, is λ, then it will be λ_0 when the scale factor has increased to R_0: $\lambda_0/\lambda = R_0/R$. The redshift is

$$z = \frac{\lambda_0 - \lambda}{\lambda} = \frac{R_0}{R} - 1 \ ; \tag{2.124}$$

i.e., the redshift of a galaxy expresses how much the scale factor has changed since the light was emitted.

The Age-Redshift Relationship

If we see a source at redshift z, how old was the universe when the light left the source? In the FRW universe we have

$$dt = \frac{da}{\dot{a}} = \frac{da}{a}\frac{1}{H} = -\frac{dz}{1+z}\frac{1}{H} \tag{2.125}$$

so the age of the universe at redshift z is

$$t(z) = \int_0^t dt' = \int_z^\infty \frac{dz'}{1+z'}\frac{1}{H(z')} \tag{2.126}$$

Putting z = 0 gives the present age of the universe,

$$t_0 = \int_0^\infty \frac{dz'}{1+z'}\frac{1}{H(z')} \tag{2.127}$$

Subtracting the two tells us for how long the photons travelled to come to our detectors:

$$\Delta t = t_0 - t(z) = \int_0^z \frac{dz'}{1+z'}\frac{1}{H(z')} \tag{2.128}$$

Note that whereas time t is a coordinate whose origin is in the past (in usual cosmological models it is chosen to be at the beginning of the universe), the origin of the redshift is set to be today. Conceptually, t is just like Newtonian time, so it is simple to use. For example, if we discuss two different cosmological models, it is straightforward to compare them when the universe has the same age (assuming both have a beginning of time). In contrast, comparing them at the same redshift doesnt make sense unless you specify by which criteria you select today in the two models. Observationally, however, it is difficult to determine the age of the universe, while it is easy to measure the redshift. (Assuming we dont know beforehand what the function $H(z)$ is, i.e. how the universe expands.) The redshift is useful when it is expressed in relation to some parameter which is easy to measure, such as distances.

The Distance-Redshift Relation

The Friedmann equation may be solved most simply in parametric form, by recasting it in terms of the conformal time $d\eta = cdt/R$ (denoting derivatives with respect to η by primes): [21]

$$R'^2 = \frac{8\pi G}{3c^2}\rho R^4 - kR^2 \tag{2.129}$$

Because $H_0^2 R_0^2 = kc^2/(\Omega - 1)$, the Friedmann equation becomes

$$a'^2 = \frac{k}{\Omega - 1}[\Omega_t + \Omega_m a - (\Omega - 1)a^2 + \Omega_v a^4] \tag{2.130}$$

which is straightforward to integrate provided that $\Omega_v = 0$. Solving the Friedmann equation for $R(t)$ in this way is important for determining global quantities such as the present age of the universe, and explicit solutions for particular cases are considered below. However, from the point of view of observations, and in particular the distanceredshift relation, it is not necessary to proceed by the direct route of determining $R(t)$.

To the observer, the evolution of the scale factor is most directly characterized by the change with redshift of the Hubble parameter and the density parameter; the evolution of $H(z)$ and $\Omega(z)$ is given immediately by the Friedmann equation in the form $H^2 = 8\pi G\rho/3kc^2/R^2$. Inserting the model dependence of ρ on a gives

$$H^2(a) = H_0^2[\Omega_v + \Omega_m a^{-3} + \Omega_t^{-4} - (\Omega - 1)a^{-2}]. \tag{2.131}$$

This is a crucial equation, which can be used to obtain the relation between redshift and comoving distance. The radial equation of motion for a photon is $Rdr = cdt = cdR/\dot{R} = cdR/RH$. With $R = R_0/(1 + z)$, this gives

$$R_0 = \frac{c}{H(z)}dz \tag{2.132}$$

$$= \frac{c}{H_0}[\Omega_v + \Omega_m a^{-3} + \Omega_t^{-4} - (\Omega - 1)a^{-2}]^{-1/2}dz. \tag{2.133}$$

This relation is arguably the single most important equation in cosmology, since it shows how to relate comoving distance to the observables of redshift, Hubble constant and density parameters. The comoving distance determines the apparent brightness of distant objects, and the comoving volume element determines the numbers of objects that are observed. These aspects of observational cosmology are discussed in more detail below.

Lastly, using the expression for $H(z)$ with $\Omega(a) - 1 = kc^2/H^2R^2$ gives the redshift dependence of the total density parameter:

$$\Omega(z) - 1 = \frac{\Omega - 1}{1 - \Omega + \Omega_v a^2 + \Omega_m a^{-1} + \Omega_t a^{-2}} \tag{2.134}$$

This last equation is very important. It tells us that, at high redshift, all model universes apart from those with only vacuum energy will tend to look like the $\Omega = 1$ model.

If $\Omega \neq 1$, then in the distant past $\Omega(z)$ must have differed from unity by a tiny amount: the density and rate of expansion needed to have been finely balanced for the universe to expand to the present. This tuning of the initial conditions is called the flatness problem and is one of the motivations for the applications of quantum theory to the early universe. [21]

The Cosmological Constant

In cosmology, the cosmological constant (usually denoted by Λ) is the value of the energy density of the vacuum of space. It was originally introduced by Albert Einstein in 1917 as an addition to his theory of general relativity to achieve a static universe, which was the accepted view at the time. Einstein abandoned the concept after Hubble's 1929 discovery that all galaxies outside our own Local Group are moving away from each other, implying an overall expanding universe. From 1929 until the early 1990s, most cosmology researchers assumed the cosmological constant to be zero. Einstein was quoted by George Gamow as saying that the cosmological constant

was the "biggest blunder" of his life (The authenticity of this quote is sometimes questioned). [31]

Since the 1990s, several developments in observational cosmology, especially the discovery of the accelerating universe from distant supernovae in 1998, and also independent evidence from the cosmic microwave background and large galaxy redshift surveys, have shown that the mass-energy density of the universe includes around 70% in dark energy. While dark energy is poorly understood at a fundamental level, the main required properties of dark energy are that it dilutes much more slowly than matter as the universe expands, and that it clusters much more weakly than matter, or perhaps not at all. The cosmological constant is the simplest possible form of dark energy since it is constant in both space and time, and this leads to the current standard model of cosmology known as the ΛCDM model, which provides a good fit to many cosmological observations. [31]

In fact, adding the cosmological constant to Einstein's equations does not lead to a static universe at equilibrium because the equilibrium is unstable: if the universe expands slightly, then the expansion releases vacuum energy, which causes yet more expansion. Likewise, a universe that contracts slightly will continue contracting. However, the cosmological constant has remained a subject of theoretical and empirical interest. Empirically, cosmological data in the past decades strongly suggests that our universe has a positive cosmological constant. The explanation of this small but positive value is an outstanding theoretical challenge. [31]

General relativity is an example of a scientific theory of impressive power and simplicity, while the cosmological constant, is an example of a modification, originally introduced to help fit the data, which appears at least on the surface to be superfluous. Its original role, to allow static homogeneous solutions to Einstein's equations in the presence of matter, turned out to be unnecessary when the expansion of the universe was discovered by Hubble, and there have been a number of subsequent episodes in which a nonzero cosmological constant was put forward as an explanation for a set of observations and later withdrawn when the observational case evaporated. The energy density is the sum of a number of apparently unrelated contributions, each of magnitude much larger than the upper limits on the cosmological constant today. The reason that the observed vacuum energy is so small in comparison to the scales of particle physics has become a major focus if research, although it is usually thought to be easier to imagine an unknown mechanism which would set it precisely to zero than one which would suppress it by just the right amount to yield an observationally accessible cosmological constant. [6]

The history of the cosmological constant has led to a reluctance to further consider a nonzero cosmological constant. However, recent years have provided the best evidence yet that this elusive quantity does play an important dynamical role in the universe. It is worthwhile to review the physics and astrophysics of the cosmological constant (and its modern equivalent, vacuum energy). [6]

Einstein's field equations are

$$R_{\mu\nu} - \frac{1}{2}Rg_{\mu\nu} = 8\pi G T_{\mu\nu} \ . \tag{2.135}$$

The universe is spatially homogeneous and isotropic which implies that its metric takes the Robertson-Walker form

$$\mathrm{d}s^2 = -\mathrm{d}t^2 + a^2(t)R_0^2\left[\frac{\mathrm{d}r^2}{1-kr^2} + r^2\mathrm{d}\Omega^2\right] \ , \tag{2.136}$$

where $\mathrm{d}\Omega^2 = \mathrm{d}\theta^2 + \sin^2\theta\mathrm{d}\phi^2$ is the metric on a two-sphere.

To obtain a Robertson-Walker solution to Einstein's equations, the rest frame of the fluid must be that of a comoving observer in the metric (2.151); in that case, Einstein's equations

reduce to the two Friedmann equations

$$H^2 \equiv \left(\frac{\dot{a}}{a}\right)^2 = \frac{8\pi G}{3}\rho - \frac{k}{a^2 R_0^2} \ , \tag{2.137}$$

where we have introduced the Hubble parameter $H \equiv \dot{a}/a$, and

$$\frac{\ddot{a}}{a} = -\frac{4\pi G}{3}(\rho + 3p) \ . \tag{2.138}$$

Einstein was interested in finding static ($\dot{a} = 0$) solutions, both due to his hope that general relativity would embody Mach's principle that matter determines inertia, and simply to account for the astronomical data as they were understood at the time. A static universe with a positive energy density is compatible with (2.137) if the spatial curvature is positive ($k = +1$) and the density is appropriately tuned; however, (2.138) implies that $\ddot{a}$ will never vanish in such a spacetime if the pressure p is also nonnegative (which is true for most forms of matter, and certainly for ordinary sources such as stars and gas). Einstein therefore proposed a modification of his equations, to

$$R_{\mu\nu} - \frac{1}{2}R g_{\mu\nu} + \Lambda g_{\mu\nu} = 8\pi G T_{\mu\nu} \ , \tag{2.139}$$

where Λ is a new free parameter, the cosmological constant [7]. Indeed, the left-hand side of (2.139) is the most general local, coordinate-invariant, divergenceless, symmetric, two-index tensor we can construct solely from the metric and its first and second derivatives. With this modification, the Friedmann equations become

$$H^2 = \frac{8\pi G}{3}\rho + \frac{\Lambda}{3} - \frac{k}{a^2 R_0^2} \ . \tag{2.140}$$

and

$$\frac{\ddot{a}}{a} = -\frac{4\pi G}{3}(\rho + 3p) + \frac{\Lambda}{3} \ . \tag{2.141}$$

These equations admit a static solution with positive spatial curvature and all the parameters ρ, p, and Λ nonnegative. This solution is called the "Einstein static universe."

The discovery by Hubble that the universe is expanding eliminated the empirical need for a static world model (although the Einstein static universe continues to thrive in the toolboxes of theorists, as a crucial step in the construction of conformal diagrams). It has also been criticized on the grounds that any small deviation from a perfect balance will rapidly grow into a runaway departure from the static solution. [7]

The cosmological constant Λ is a parameter with units of (length)$^{-2}$. From the point of view of classical general relativity, there is no preferred choice for what the length scale defined by Λ might be. Particle physics, however, brings a different perspective to the question. The cosmological constant turns out to be a measure of the energy density of the vacuum — the state of lowest energy — and although we cannot calculate the vacuum energy with any confidence, this identification allows us to consider the scales of various contributions to the cosmological constant [7].

The cosmological constant is an energy associated with the vacuum, that is, with empty space. The possibility of a nonzero cosmological constant has been entertained in the past for theoretical and observational reasons. Recent supernovae results (Perlmutter et al 1998, Riess et al 1998) have made a strong case for a nonzero and possibly quite large cosmological constant. Their results have encouraged increased interest in the properties of a universe with nonzero cosmological constant. Several other observations of various cosmological phenomena

are also planned or underway which will further constrain the range of allowed values for the cosmological constant. [8].

The Equation of State

The Friedmann equation relates the rate of increase of the scale factor, as described by the Hubble parameter, to the total energy density of all matter in the universe. The Friedmann equation defines, at any given time, a critical energy density,

$$\rho_c \equiv \frac{3H^2}{8\pi G} \ , \tag{2.142}$$

for which the spatial sections must be precisely flat ($k = 0$). We then define the density parameter

$$\Omega_{\text{total}} \equiv \frac{\rho}{\rho_c} \ , \tag{2.143}$$

which allows us to relate the total energy density in the universe to its local geometry

$$\begin{aligned} \Omega_{\text{total}} > 1 \quad &\Leftrightarrow \quad k = +1 \\ \Omega_{\text{total}} = 1 \quad &\Leftrightarrow \quad k = 0 \\ \Omega_{\text{total}} < 1 \quad &\Leftrightarrow \quad k = -1 \ . \end{aligned} \tag{2.144}$$

It is often convenient to define the fractions of the critical energy density in each different component by

$$\Omega_i = \frac{\rho_i}{\rho_c} \ . \tag{2.145}$$

Energy conservation is expressed in GR by the vanishing of the covariant divergence of the energy-momentum tensor,

$$\nabla_\mu T^{\mu\nu} = 0 \ . \tag{2.146}$$

Applying this to our assumptions – the RW metric (2.151) and perfect-fluid energy-momentum tensor – yields a single energy-conservation equation,

$$\dot{\rho} + 3H(\rho + p) = 0 \ . \tag{2.147}$$

This equation is actually not independent of the Friedmann and acceleration equations, but is required for consistency. It implies that the expansion of the universe (as specified by H) can lead to local changes in the energy density. Note that there is no notion of conservation of "total energy," as energy can be interchanged between matter and the spacetime geometry. [28]

The relationship of the pressure and energy density are now considered. Within the fluid approximation used here, we may assume that the pressure is a single-valued function of the energy density $p = p(\rho)$. It is often convenient to define an equation of state parameter, w, by

$$p = w\rho \ . \tag{2.148}$$

This should be thought of as the instantaneous definition of the parameter w; it need represent the full equation of state, which would be required to calculate the behavior of fluctuations. Many useful cosmological matter sources do obey this relation with a constant value of w.

For example, $w = 0$ corresponds to pressureless matter, or dust – any collection of massive non-relativistic particles would qualify. Similarly, $w = 1/3$ corresponds to a gas of radiation, whether it be actual photons or other highly relativistic species.[28]

A constant w leads to a great simplification in solving our equations. The energy density evolves with the scale factor according to

$$\rho(a) \propto \frac{1}{a(t)^{3(1+w)}} \ . \tag{2.149}$$

The Standard Model

The success of the Big Bang rests on three observational pillars: the Hubble diagram exhibiting expansion; light element abundances which are in accord with Big Bang nucleosynthesis; and the blackbody radiation left over from the first few hundred thousand years, the cosmic microwave background [10]. We shall discuss each of these three pillars in the following three sections.

The Expanding Universe

Einstein's original field equations are

$$R_{\mu\nu} - \frac{1}{2} R g_{\mu\nu} = 8\pi G T_{\mu\nu} \ . \tag{2.150}$$

On very large scales the universe is spatially homogeneous and isotropic to an excellent approximation, which implies that its metric takes the Robertson-Walker form

$$\mathrm{d}s^2 = -\mathrm{d}t^2 + a^2(t) R_0^2 \left[\frac{\mathrm{d}r^2}{1 - kr^2} + r^2 \mathrm{d}\Omega^2 \right] \ , \tag{2.151}$$

where $\mathrm{d}\Omega^2 = \mathrm{d}\theta^2 + \sin^2\theta \mathrm{d}\phi^2$ is the metric on a two-sphere.

The curvature parameter k takes on values $+1$, 0, or -1 for positively curved, flat, and negatively curved spatial sections, respectively. The scale factor characterizes the relative size of the spatial sections as a function of time. It is written in a normalized form $a(t) = R(t)/R_0$, where the subscript 0 refers to a quantity evaluated at the present time. The redshift z undergone by radiation from a comoving object as it travels to us today is related to the scale factor at which it was emitted by

$$a = \frac{1}{(1+z)} \ . \tag{2.152}$$

The energy-momentum sources may be modeled as a perfect fluid, specified by an energy density ρ and isotropic pressure p in its rest frame. The energy-momentum tensor of such a fluid is

$$T_{\mu\nu} = (\rho + p) U_\mu U_\nu + p g_{\mu\nu} \ , \tag{2.153}$$

where U^μ is the fluid four-velocity.

To obtain a Robertson-Walker solution to Einstein's equations, the rest frame of the fluid must be that of a comoving observer in the metric (2.151). In that case, Einstein's equations reduce to the two Friedmann equations

$$H^2 \equiv \left(\frac{\dot{a}}{a} \right)^2 = \frac{8\pi G}{3} \rho - \frac{k}{a^2 R_0^2} \ , \tag{2.154}$$

where we have introduced the Hubble parameter

$H \equiv \dot{a}/a$, and

$$\frac{\ddot{a}}{a} = -\frac{4\pi G}{3}(\rho + 3p) \ . \tag{2.155}$$

Einstein was interested in finding static ($\dot{a} = 0$) solutions, both due to his hope that general relativity would embody Mach's principle that matter determines inertia, and to account for the astronomical data as they were understood at the time. A static universe with a positive energy density is compatible with (2.154) if the spatial curvature is positive ($k = +1$) and the density is appropriately tuned; however, (2.155) implies that $\ddot{a}$ will never vanish in such a spacetime if the pressure p is also non-negative (which is true for most forms of matter, and certainly for ordinary sources such as stars and gas) [6].

Einstein therefore proposed a modification of his equations, to

$$R_{\mu\nu} - \frac{1}{2}Rg_{\mu\nu} + \Lambda g_{\mu\nu} = 8\pi G T_{\mu\nu} \ , \tag{2.156}$$

where Λ is a new free parameter, the cosmological constant.

Indeed, the left-hand side of (2.156) is the most general local, coordinate-invariant, symmetric, two-index tensor without divergence that we can construct solely from the metric and its first and second derivatives. With this modification, the Friedmann equations become

$$H^2 = \frac{8\pi G}{3}\rho + \frac{\Lambda}{3} - \frac{k}{a^2 R_0^2} \ . \tag{2.157}$$

and

$$\frac{\ddot{a}}{a} = -\frac{4\pi G}{3}(\rho + 3p) + \frac{\Lambda}{3} \ . \tag{2.158}$$

These equations admit a static solution with positive spatial curvature and all the parameters ρ, p, and Λ nonnegative, and is referred to as the "Einstein static universe."

Two independent groups undertook searches for distant supernovae in order to measure cosmological parameters: the High-Z Supernova Team (Riess et al) and the Supernova Cosmology Project (Perlmutter et al). A plot of redshift vs. corrected apparent magnitude from the original SCP data is shown in Figure 2.9.

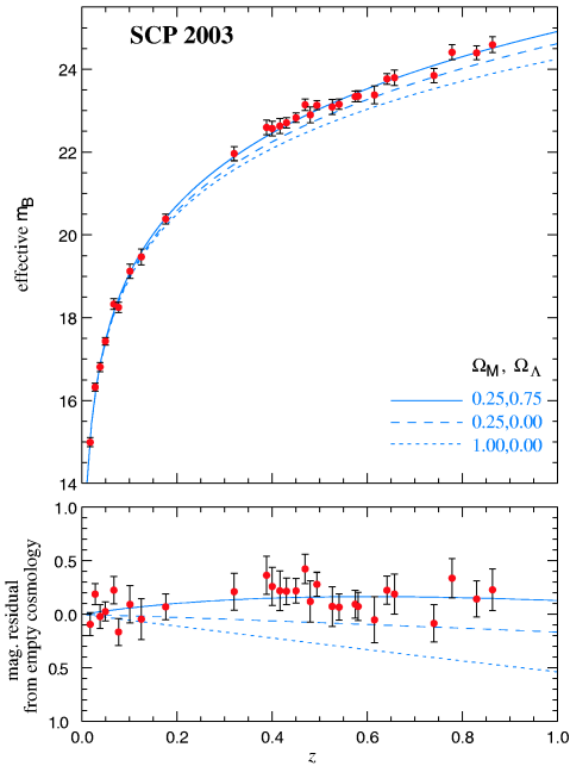

Figure 2.9: Hubble diagram from the Supernova Cosmology Project, from [28].

The data are much better fit by a universe dominated by a cosmological constant than by a flat matter-dominated model. In fact the supernova results alone allow a substantial range of possible values of $\Omega_{\rm M}$ and Ω_Λ; however, if we think we know something about one of these parameters, the other will be tightly constrained. In particular, if $\Omega_{\rm M} \sim 0.3$, we obtain

$$\Omega_\Lambda \sim 0.7 \ . \tag{2.159}$$

This corresponds to a vacuum energy density

$$\rho_\Lambda \sim 10^{-8} \ {\rm erg/cm^3} \sim (10^{-3} \ {\rm eV})^4 \ . \tag{2.160}$$

The supernova studies provided direct evidence for a nonzero value of Einstein's cosmological constant.

If general relativity is correct, cosmic acceleration implies there must be a dark energy density which diminishes relatively slowly as the universe expands. This can be seen directly from the Friedmann equation, which implies

$$\dot{a}^2 \propto a^2 \rho + {\rm constant} \ . \tag{2.161}$$

From this relationship, it is clear that the only way to get acceleration ($\dot{a}$ increasing) in an expanding universe is if ρ falls off more slowly than a^{-2}; neither matter ($\rho_{\rm M} \propto a^{-3}$) nor radiation ($\rho_{\rm R} \propto a^{-4}$) will do the trick. Vacuum energy is, of course, strictly constant; but the data are consistent with smoothly-distributed sources of dark energy that vary slowly with time.

There are good reasons to consider dynamical dark energy as an alternative to an honest cosmological constant. First, a dynamical energy density can be evolving slowly to zero, allowing for a solution to the cosmological constant problem which makes the ultimate vacuum energy vanish exactly. Second, it poses an interesting and challenging observational problem to study the evolution of the dark energy, from which we might learn something about the underlying physical mechanism. Perhaps most intriguingly, allowing the dark energy to evolve opens the possibility of finding a dynamical solution to the coincidence problem, if the dynamics are such as to trigger a recent takeover by the dark energy (independently of, or at least for a wide range of, the parameters in the theory). To date this hope has not quite been met, but dynamical mechanisms at least allow for the possibility (unlike a true cosmological constant).

The simplest possibility along these lines involves the same kind of source typically invoked in models of inflation in the very early universe: a scalar field ϕ rolling slowly in a potential, sometimes known as "quintessence" [28]. The energy density of a scalar field is a sum of kinetic, gradient, and potential energies,

$$\rho_\phi = \frac{1}{2}\dot{\phi}^2 + \frac{1}{2}(\nabla\phi)^2 + V(\phi) \ . \tag{2.162}$$

For a homogeneous field ($\nabla\phi \approx 0$), the equation of motion in an expanding universe is

$$\ddot{\phi} + 3H\dot{\phi} + \frac{dV}{d\phi} = 0 \ . \tag{2.163}$$

If the slope of the potential V is quite flat, we will have solutions for which ϕ is nearly constant throughout space and only evolving very gradually with time; the energy density in such a configuration is

$$\rho_\phi \approx V(\phi) \approx \text{constant} \ . \tag{2.164}$$

Thus, a slowly-rolling scalar field is an appropriate candidate for dark energy.

However, introducing dynamics opens up the possibility of introducing new problems, the form and severity of which will depend on the specific kind of model being considered. Most quintessence models feature scalar fields ϕ with masses of order the current Hubble scale,

$$m_\phi \sim H_0 \sim 10^{-33} \text{ eV} \ . \tag{2.165}$$

(Fields with larger masses would typically have already rolled to the minimum of their potentials.) In quantum field theory, light scalar fields are unnatural; renormalization effects tend to drive scalar masses up to the scale of new physics. The well-known hierarchy problem of particle physics amounts to asking why the Higgs mass, thought to be of order 10^{11} eV, should be so much smaller than the grand unification/Planck scale, 10^{25}-10^{27} eV. Masses of 10^{-33} eV are correspondingly harder to understand. In addition, light scalar fields give rise to long-range forces and time-dependent coupling constants that should be observable even if couplings to ordinary matter are suppressed by the Planck scale [28]. We therefore need to invoke additional fine-tunings to explain why the quintessence field has not already been experimentally detected.

To date, many investigations have considered scalar fields with potentials that asymptote gradually to zero, of the form $e^{1/\phi}$ or $1/\phi$. These can have cosmologically interesting properties, including "tracking" behavior that makes the current energy density largely independent of the initial conditions. They do not, however, provide a solution to the coincidence problem, as the era in which the scalar field begins to dominate is still set by finely-tuned parameters in the theory. One way to address the coincidence problem is to take advantage of the fact that matter/radiation equality was a relatively recent occurrence (at least on a logarithmic

scale); if a scalar field has dynamics which are sensitive to the difference between matter- and radiation-dominated universes, we might hope that its energy density becomes constant only after matter/radiation equality. Instead of a conventional kinetic energy $K = \frac{1}{2}(\dot{\phi})^2$, in k-essence the form

$$K = f(\phi)g(\dot{\phi}^2) \ , \tag{2.166}$$

has been suggested, where f and g are functions specified by the model. For certain choices of these functions, the k-essence field naturally tracks the evolution of the total radiation energy density during radiation domination, but switches to being almost constant once matter begins to dominate. Unfortunately, it seems necessary to choose a finely-tuned kinetic term to get the desired behavior [28].

An alternative possibility is that there is nothing special about the present era; rather, acceleration is just something that happens from time to time. In these models the potential takes the form of a decaying exponential (which by itself would give scaling behavior, so that the dark energy remained proportional to the background density) with small perturbations superimposed:

$$V(\phi) = e^{-\phi}[1 + \alpha\cos(\phi)] \ . \tag{2.167}$$

On average, the dark energy in such a model will track that of the dominant matter/radiation component; however, there will be gradual oscillations from a negligible density to a dominant density and back, on a timescale set by the Hubble parameter, leading to occasional periods of acceleration. Unfortunately, in neither the k-essence models nor the oscillating models do we have a compelling particle-physics motivation for the chosen dynamics, and in both cases the behavior still depends sensitively on the precise form of parameters and interactions chosen. Nevertheless, these theories stand as interesting attempts to address the coincidence problem by dynamical means.

One of the interesting features of dynamical dark energy is that it is experimentally testable.

In principle, different dark energy models can yield different cosmic histories, and, in particular, a different value for the equation of state parameter, both today and its redshift-dependence. Since the CMB strongly constrains the total density to be near the critical value, it is sensible to assume a perfectly flat universe and determine constraints on the matter density and dark energy equation of state; see Figure 2.10 for some recent limits.

As can be seen in Figure 2.10, one possibility that is consistent with the data is that $w < -1$. Such a possibility violates the dominant energy condition, but possible models have been proposed. However, such models run into serious problems when one takes them seriously as a particle physics theory. Even if one restricts one's attention to more conventional matter sources, making dark energy compatible with sensible particle physics has proven tremendously difficult.

Given the challenge of this problem, it is worthwhile considering the possibility that cosmic acceleration is not due to some kind of dark energy, but rather arises from new gravitational physics. there are a number of different approaches to this and we will not review them here.

Big Bang Nucleosynthesis

When the universe was much hotter and denser, when the temperature of order an MeV/k_B, there were no neutral atoms or even bound nuclei. The vast amounts of radiation in such a hot environment ensured that any atom or nucleus produced would be immediately destroyed by a high energy photon. As the universe cooled well below the binding energies of typical nuclei, light elements began to form. Knowing the conditions of the early universe and the

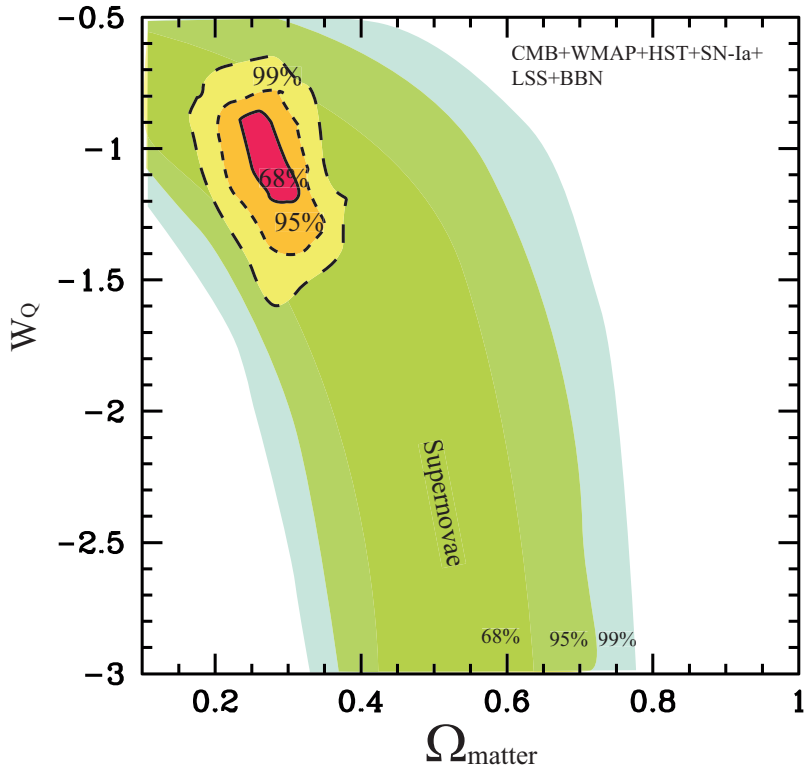

Figure 2.10: Constraints on the dark-energy equation-of-state parameter, as a function of Ω_M, assuming a flat universe. These limits are derived from studies of supernovae, CMB anisotropies, measurements of the Hubble constant, large-scale structure, and primordial nucleosynthesis. From [28].

relevant nuclear cross-sect ions, we can calculate the expected primordial abundances of all the elements. [10]

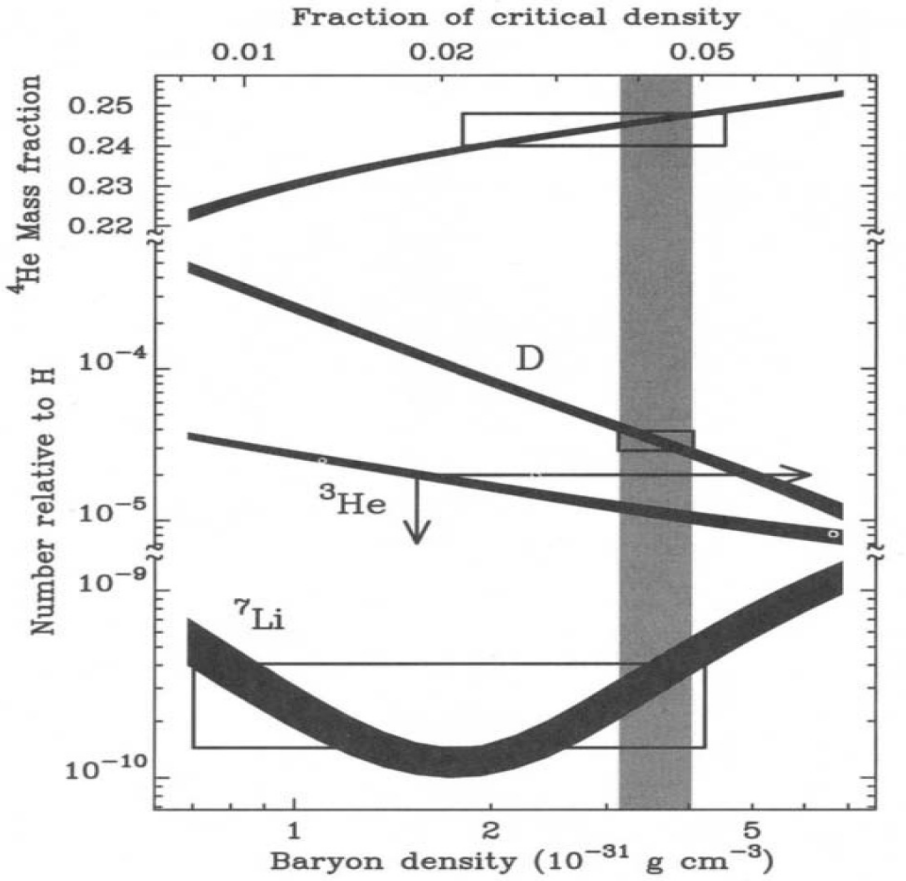

Figure 2.11: Constraint on the baryon density from Big Bang Nucleosynthesis. Predictions are shown for four light elements. The solid vertical band is fixed by measurements of primordial deuterium. The boxes are the observations; there is only an upper limit on the primordial abundance of ^3He. From [10]

Figure 2.11 shows the predictions of Big Bang Nucleosynthesis for the light element abundances. The boxes and arrows in Figure 2.11 show the current estimates for the light element abundances. These are consistent with the predictions, and this consistency test provides yet another ringing confirmation of the Big Bang. The measurements do even more though. The theoretical predictions, depend on the density of protons and neutrons at the time of nucleosynthesis. The combined proton plus neutron density is called the baryon density since both protons and neutrons have baryon number one and these are the only baryons around at the time. Thus, Big Bang Nucleosynthesis gives us a way of measuring the baryon density in the universe. Since we know how those densities scale as the universe evolves (they fall as A^{-3}), we can turn the measurements of light element abundances into measures of the baryon density today. In particular, the measurement of primordial deuterium pins down the baryon

density extremely accurately to only a few of the critical density. Ordinary matter (baryons) contributes at most 5 of the critical density. Since the total matter density today is almost certainly larger than this. Direct estimates give values on the order of 20-30. Nucleosynthesis provides a compelling argument for nonbaryonic dark matter. [10]

The deuterium measurements are the new developments in the field. These measurements are so exciting because they explore the deuterium abundance at redshifts of order 3-4, well before much processing could have altered the primordial abundances. The basic idea is that light from distant QSOs is absorbed by intervening neutral hydrogen systems. The key absorption feature arises from transition from the (n = 1) ground state of hydrogen to the first excited state (n = 2), requiring a photon with wavelength A = 1215.7 A. Since photons are absorbed when exciting hydrogen in this fashion, there is a trough in the spectrum at A = 1215.7 A, redshifted by a factor of 1 + 2. The corresponding line from deuterium should be (i) shifted over by 0.33 1 + z) and (ii) much less damped since there is much less deuterium. The steep decline in deuterium as a function of baryon density helps. Even relatively large errors in D measurements translate into small errors on the baryon density. [10]

The Cosmic Microwave Background

The Cosmological Principle has observational support of another sort, apart from the measurements of the Doppler shifts. After making due allowances for the distortions due to our own Galaxy and the rich nearby cluster of galaxies in the constellation of Virgo, the universe seems remarkably isotropic; that is, it looks the same in all directions. Now, if the universe is isotropic around us, it must also be isotropic about every typical galaxy. However, any point in the universe can be carried into another point by a series of rotations around fixed centers, so if the universe is isotropic around every point, it is necessary also homogeneous. In what follows we will discuss how the observation of the cosmic microwave background (CMB) provides convincing evidence for an isotropic universe. [1]

The expansion of the universe seems to suggest that typical objects in the universe were once much closer together than they are right now. This is the idea for the basis that the universe began about 13.7 billion years ago as an expansion from a state of very high density and temperature known affectionately as the Big Bang.

The Big Bang was not an explosion, because an explosion blows pieces out into the surrounding space. Instead, the Big Bang was the start of an expansion of space itself. The volume of the observable universe was very small at the start and has been expanding ever since. The initial tiny volume of extremely dense matter is not to be thought of as a concentrated mass in the midst of a much larger space around it. The initial tiny but dense volume was the universe – the entire universe. There would not have been anything else. When we say that the universe was once smaller than it is now, we mean that the average separation between galaxies (or other objects) was less. Therefore, it is the *size of the universe itself* that has increased since the Big Bang. [1]

In 1964, Arno Penzias and Robert Wilson were experiecing difficulty with what they assumed to be background noise, or "static," in their radio telescope . Eventually, they became convinced that it was real and that it was coming from outside the Galaxy. They made precise measurements at wavelength $\lambda = 7.35$ cm, in the microwave region of the electromagnetic spectrum. The intensity of this radiation was found initially not to vary by day or night or time of the year, nor to depend on the direction. It came from all directions in the universe with equal intensity, to a precision of better than 1%. It could only be concluded that this radiation came from the universe as a whole.

The intensity of this CMB as measured at $\lambda = 7.35$ cm corresponds to a blackbody radia-

tion at a temperature of about 3 K. When radiation at other wavelengths was measured, the intensities were found to fall on a blackbody curve, corresponding to a temperature of 2.725 K. [1]

The CMB provides strong evidence in support of the Big Bang, and gives us information about conditions in the very early universe. In fact, in the late 1940s, George Gamow calculated that the Big Bang origin of the universe should have generated just such a CMB .

To understand why, let us look at what a Big Bang might have been like. The temperature must have been extremely high at the start, so high that there could not have been any atoms in the very early stages of the universe. Instead the universe would have consisted solely of radiation (photons) and a plasma of charged electrons and other elementary particles. The universe would have been opaque - the photons in a sense "trapped," travelling very short distances before being scattered again, primarily by electrons. Indeed, the details of the CMB provide strong evidence that matter and radiation were once in thermal equilibrium at very high temperature. As the universe expanded, the energy spread out over an increasingly larger volume and the temperature dropped. Only when the temperature had fallen to about 3,000 K was the universe cool enough to allow the combination of nuclei and electrons into atoms. (In the astrophysical literature this is usually called "recombination," a singularly inappropriate term, for at the time we were considering the nuclei and electrons had never in the previous history of the universe been combined into atoms!) The sudden disappearence of electrons broke the thermal contact between radiation and matter, and the radiation continued thereafter to expand freely. [1]

At the moment this happened, the energy in the radiation field at various wavelengths was governed by the conditions of the thermal equilibrium, and was therefore given by the Planck blackbody formula for a temperature equal to that of the matter $\sim 3,000$ K. In particular, the typical photon wavelength would have been about one micron, and the average distance between photons would have been roughly equal to this typical wavelength.

What has happened to the photons since then? Individual photons would not be created or destroyed, so the average distance between photons would simply increase in proportion to the size of the universe, i.e., in proportion to the average distance between typical galaxies. But we saw that the effect of the cosmological redshift is to pull out the wavelength of any ray of light as the universe expands; thus the wavelength of any individual photon would also simply increase in proportion to the size of the universe. The photons would therefore remain about one typical length apart, just as for blackbody radiation. [1]

Before proceeding we will pursue this line of argument quantitavively. We can obtain the Planck distribution that gives the energy du of a blackbody radiation per unit volume, in a narrow range of wavelengths from λ to $\lambda + d\lambda$,

$$du = \frac{8\pi hc}{\lambda^5}\, d\lambda\, \frac{1}{e^{hc/\lambda kT} - 1} \ . \tag{2.168}$$

For long wavelengths, the denominator in the Planck distribution may be approximated by

$$e^{hc/\lambda kT} - 1 \simeq hc/\lambda kT \ , \tag{2.169}$$

Hence, in this wavelength region,

$$du = \frac{8\pi kT}{\lambda^4}\, d\lambda \ . \tag{2.170}$$

This is the Rayleigh-Jeans formula. If this formula held down to arbitrarily small wavelengths, $du/d\lambda$ would become infinite for $\lambda \to 0$, and the total energy density in the blackbody radiation would be infinite. Fortunately, as we saw before, the Planck formula for du reaches a maximum

at a wavelength $\lambda = 0.2014052\, hc/kT$ and then falls steeply off for decreasing wavelengths. The total energy density in the blackbody radiation is

$$u = \int_0^\infty \frac{8\pi hc}{\lambda^5}\, d\lambda\, \frac{1}{e^{hc/\lambda kT} - 1}\ . \tag{2.171}$$

Integrals of this sort can be looked up in standard tables of definite integrals; the result gives the Stefan-Boltzmann law

$$u = \frac{8\pi^5 (kT)^4}{15(hc)^3} = 7.56464 \times 10^{-15}\, (T/\mathrm{K})^4 \mathrm{erg/cm}^3\ . \tag{2.172}$$

(Recall that 1 J $\equiv 10^7$ erg $= 6.24 \times 10^{18}$ eV.)

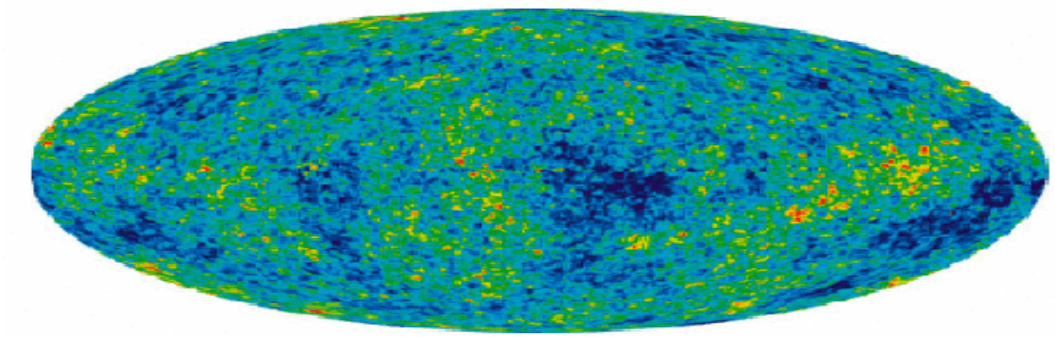

Figure 2.12: The CMB over the entire sky, color-coded to represent differences in temperature from the average 2.725 K: the color scale ranges from +300 μK (red) to −200 μK (dark blue), representing slightly hotter and colder spots (and also variations in density.) Results are from the WMAP satellite. The angular resolution is 0.2°. From [1].

The Planck distribution can be interpreted in terms of quanta of light or photons. Each photon has an energy $E = hc/\lambda$. Hence the number dn of photons per unit volume in blackbody radiation in a narrow range of wavelengths from λ to $\lambda + d\lambda$ is

$$dn = \frac{du}{hc/\lambda} = \frac{8\pi}{\lambda^4}\, d\lambda\, \frac{1}{e^{hc/\lambda kT} - 1}\,. \tag{2.173}$$

Then the total number of photons per unit volume is

$$\begin{aligned} n &= \int_0^\infty dn \\ &= 8\pi \left(\frac{kT}{hc}\right)^3 \int_0^\infty \frac{x^2\, dx}{e^x - 1}\,, \end{aligned} \tag{2.174}$$

where $x = hc/(\lambda kT)$. The integral cannot be expressed in terms of elementary functions, but it can be expressed as an infinite series

$$\int_0^\infty \frac{x^2\, dx}{e^x - 1} = 2\sum_{j=1}^\infty \frac{1}{j^3} \approx 2.4\ . \tag{2.175}$$

Therefore, the number photon density is

$$\begin{aligned} n &= 60.42198 \left(\frac{kT}{hc}\right)^3 \\ &= 20.28 \left(\frac{T}{\mathrm{K}}\right)^3 \text{ photons cm}^{-3} , \end{aligned} \tag{2.176}$$

and the average photon energy is

$$\langle E_\gamma \rangle = u/n = 3.73 \times 10^{-16} \, (T/\mathrm{K}) \text{ erg} . \tag{2.177}$$

Consider what happens to blackbody radiation in an expanding universe. If the size of the universe changes by a factor f, then doubles in size, then $f = 2$. As predicted by the Doppler effect, the wavelengths will change in proportion to the size of the universe to a new value $\lambda' = f\lambda$. After the expansion, the energy density du' in the new wavelength range λ' to $\lambda' + d\lambda'$ is less than the original energy density du in the old wavelength range $\lambda + d\lambda$, for two different reasons:
(i) Since the volume of the universe has increased by a factor of f^3, as long as no photons have been created or destroyed, the numbers of photons per unit volume has decreased by a factor of $1/f^3$.
(ii) The energy of each photon is inversely proportional to its wavelength, and therefore is decreased by a factor of $1/f$. It follows that the energy density is decreased by an overall factor $1/f^3 \times 1/f = 1/f^4$:

$$du' = \frac{1}{f^4} \, du = \frac{8\pi hc}{\lambda^5 f^4} \, d\lambda \, \frac{1}{e^{hc/\lambda kT} - 1} . \tag{2.178}$$

If we rewrite Eq. (2.178) in terms of the new wavelengths λ', it becomes

$$du' = \frac{8\pi hc}{\lambda'^5} \, d\lambda' \, \frac{1}{e^{hcf/\lambda' kT} - 1} , \tag{2.179}$$

which is exactly the same as the old formula for du in terms of λ and $d\lambda$, except that T has been replaced by a new temperature $T' = T/f$. Therefore, we conclude that freely expanding blackbody radiation remains described by the Planck formula, but with a temperature that drops in inverse proportion to the scale of expansion.

The existence of the thermal CMB gives strong support to the idea that the universe was extremely hot in its early stages. As can be seen in Fig. 2.12, the background is very nearly isotropic, supporting the isotropic and homogeneous models of the universe. Of course one would expect some small inhomogeneities in the CMB that would provide "seeds" around which galaxy formation could have started. These tiny inhomogeneities were first detected by the COBE (Cosmic Background Explorer) and by subsequent experiments with greater detail, culminating with the WMAP (Wilkinson Microwave Anisotropy Probe). [1].

The Cosmic Inventory

There is now a substantial observational basis for estimates of the cosmic mean densities of all the known and more significant forms of matter and energy in the present-day universe. The compilation of the energy inventory offers an overview of the integrated effects of the energy transfers involved in all the physical processes of cosmic evolution operating on scales ranging from the Hubble length to black holes and atomic nuclei. The compilation also offers a way

to assess how well we understand the physics of cosmic evolution, by the degree of consistency among related entries. Very significant observational advances, particularly from large-scale surveys including the *Two Degree Field Galaxy Redshift Survey*, the *Sloan Digital Sky Survey*, the *Two Micron All-Sky Survey*, the HI Parkes All Sky Survey, and the *Wilkinson Microwave Anisotropy Probe*, made it timely to compile what is known about the entire energy inventory, and was presented in a landmark publication by [15].

This inventory includes the mass densities in the various states of baryons. Most entries in this part of the inventory have not changed much, while substantial advances in the observational constraints have considerably reduced the uncertainties. It appears that most of the baryonic components are observationally well constrained, apart from the largest entry, for warm plasma, which still is driven by the need to balance the budget rather than more directly by the observations. [15]

The largest entries, for dark matter and the cosmological constant, or dark energy, are well constrained within a cosmological theory that is reasonably well tested, but the physical natures of these entries remain quite hypothetical. While the physical nature of magnetic fields and cosmic rays are understood, the theories of the evolution of these components, and the estimates of their contributions to the present energy inventory, are quite uncertain. The situation for most of the other entries tends to be between these extremes: the physical natures of the entries are adequately characterized, for the most part, and our estimates of their energy densities, while generally not very precise, seem to be meaningfully constrained by the observations. [15]

The inventory, which is presented in the following table, is arranged by categories and components within categories. We show here only a portion of the extensive inventory compiled by [15].

			Components[a]	Totals[a]
1	dark sector			0.954 ± 0.003
1.1	dark energy		0.72 ± 0.03	
1.2	dark matter		0.23 ± 0.03	
1.3	primeval gravitational waves		10^{-10}	
2	primeval thermal remnants			0.0010 ± 0.0005
2.1	electromagnetic radiation		$10^{-4.3\pm0.0}$	
2.2	neutrinos		$10^{-2.9\pm0.1}$	
2.3	prestellar nuclear binding energy		$-10^{-4.1\pm0.0}$	
3	baryon rest mass			0.045 ± 0.003
3.1	warm intergalactic plasma		0.040 ± 0.003	
3.1a	virialized regions of galaxies	0.024 ± 0.005		
3.1b	intergalactic	0.016 ± 0.005		
3.2	intracluster plasma		0.0018 ± 0.0007	
3.3	main sequence stars	spheroids and bulges	0.0015 ± 0.0004	
3.4		disks and irregulars	0.00055 ± 0.00014	
3.5	white dwarfs		0.00036 ± 0.00008	
3.6	neutron stars		0.00005 ± 0.00002	
3.7	black holes		0.00007 ± 0.00002	
3.8	substellar objects		0.00014 ± 0.00007	
3.9	HI + HeI		0.00062 ± 0.00010	
3.10	molecular gas		0.00016 ± 0.00006	
3.11	planets		10^{-6}	
3.12	condensed matter		$10^{-5.6\pm0.3}$	
3.13	sequestered in massive black holes		$10^{-5.4}(1+\epsilon_n)$	

Figure 2.13: The Cosmic Energy Inventory, part of Table 1 in [15]

The inventory in Figure 2.13 assumes the now standard relativistic Friedmann-Lemaître ΛCDM cosmology, in which space sections at fixed world time have negligibly small mean curvature. Einstein's cosmological term, Λ, is independent of time and position, the dark matter is an initially cold noninteracting gas, and primeval departures from homogeneity are adiabatic, Gaussian, and scale-invariant. Physics in the dark sector is not well constrained: Λ might be replaced with a dynamical component. The current limit on the index of the equation of state for the dark energy is $w = p/\rho < -0.78$ at 95%. The bound $w = -1.02^{+0.13}_{-0.19}$ is obtained from the Type Ia supernova Hubble diagram under the assumption of flat space curvature as in the models for dark energy now under discussion, the physics of the dark matter may prove to be more complicated than that of a free collisionless gas, and the initial conditions may not be adequately approximated by the present standard cosmology. If such complications were present we expect their effects on entries that are sensitive to the cosmological model would be slight, however, because the cosmological tests now offer close to compelling evidence that the ΛCDM model is a useful approximation to reality. [15]

The Dark Sector

The components in Category 1 (Figure 2.13) interact with the contents of the visible sector only by gravity, as far as is now known. This makes it difficult to check whether the dark energy — or Einstein's cosmological constant, Λ — and the dark matter really have the simple properties assumed in the ΛCDM cosmology. Future versions of the inventory might contain separate entries for the potential, kinetic and gradient contributions to the dark energy density, or a potential energy component in the dark matter.

There is abundant evidence that the total mass density — excluding dark energy — is well below the Einstein-de Sitter value. That means, among other things, that the consistency of cross-checks from the many ways to estimate the mass density provides close to compelling evidence that the gravitational interaction of matter at distances up to the large-scale flows is well approximated by the inverse square law, and that starlight is a good tracer of the mass distribution on scales to 100kpc. [15]

The other entries in the first category in Figure 2.13 are computed and estimates of the other significant contributions to the total mass density, under the assumption that the density parameters sum to unity, that is, space curvature is neglected.

Thermal Remnants

The components in Category 2 (Figure 2.13) include thermal remnants.

Entry 2.1 is based on the COBE measurement of the temperature of the thermal cosmic electromagnetic background radiation (the CMBR), $T_o = 2.725$ K. The COBE and UBC measurements show that the spectrum is very close to thermal. It has been slightly disturbed by the observed interaction with the hot plasma in clusters of galaxies. The limit on the resulting fractional increase in the radiation energy density is [15]

$$\delta u/u = 4y < 6 \times 10^{-5}. \tag{2.180}$$

This means that the background radiation energy density has been perturbed by the amount $\Delta\Omega < 10^{-8.5}$. The thermal background radiation has been perturbed also by the dissipation of the primeval fluctuations in the distributions of baryons and radiation on scales smaller than the Hubble length at the epoch of decoupling of baryonic matter and radiation. If the initial mass fluctuations are adiabatic and scale-invariant the fractional perturbation to the radiation energy per logarithmic increment of the comoving length scale is $\delta u/u \sim \delta_h^2$, where $\delta_h \sim 10^{-5}$ is

the density contrast appearing at the Hubble length. This is small compared to the subsequent perturbation by hot plasma.

Entry 2.2 uses the standard estimates of the relict thermal neutrino temperature, $T_\nu = (4/11)^{1/3} T_o$, and the number density per family, $n_\nu = 112$ cm^{-3}. They adopt the neutrino mass differences from oscillation experiments [15].

Nuclear binding energy was released during nucleosynthesis, and is shown in entry 2.3 as a negative value, meaning the comoving baryon mass density has been reduced and the energy density in radiation and neutrinos increased. The effect on the radiation background has long since been thermalized, of course, but the entry is worth recording for comparison to the nuclear binding energy released in stellar evolution. For the same reason, we compute the binding energy relative to free protons and electrons. The convention is artificial, because light element formation at high redshifts was dominated by radiative exchanges of neutrons, protons and atomic nuclei, and the abundance of the neutrons was determined by energy exchanges with the cosmic neutrino background. It facilitates comparison with category 6, however. The nuclear binding energy in entry 2.3 is the product

$$-\Omega_{\rm NB,He} = 0.0071\, Y_p\, \Omega_{\rm b} = 10^{-4.1}. \tag{2.181}$$

This is larger in magnitude than the energy in the CMBR today.

The Baryon Rest Mass

The entries in Category 3 (Figure 2.13) refer to the baryon rest mass. One must add the negative binding energies to get the present mass density in baryons. The binding energies are small and the distinction purely formal at the accuracy we can hope for in cosmology, of course, with the conceivable exception of the baryons sequestered in black holes.

They begin with the best-characterized components, the stars, star remnants, and planets, and then consider the diffuse components, and conclude this subsection with discussions of the baryons in groups and the intergalactic medium and the lost baryons in black holes. [15].

The baryon mass in stars is estimated from the galaxy luminosity density and the stellar mass-to-light ratio, $M_{\rm stars}/L$, along with a stellar initial mass function (the IMF) that allows us to estimate the mass fractions in various forms of stars and star remnants.

The mass in planets that are gravitationally bound to stars must be small, but it is of particular interest to us as residents of a planet. It is reported that about 6.5% of nearby FGKM stars have detected Jovian-like planets, and that an extrapolation to planets at larger orbital radii might be expected to roughly double this number. In the model for the PDMF the ratio of the number density of stars in the mass range 0.08 to 1.6 $m_\odot$ to the mass density in stars is $n/\rho = 2.1 m_\odot^{-1}$. The product of this quantity with the mass density in stars, the fraction 0.13, and the ratio of the mass of Jupiter to the Solar mass is

$$\Omega_{\rm planets} = 10^{-6.1}. \tag{2.182}$$

Stars with lower metallicity have fewer planets, but that may not introduce a serious error because there are fewer low metallicity stars. [15]

Entry 3.1, for the baryon mass outside galaxies and clusters of galaxies, is the difference between the adopted value of the baryon density parameter and the sum of all the other entries in category 3. Within standard pictures of structure formation this component could not be in a compact form such as planets, but rather must be a plasma, diffuse enough to be ionized by the intergalactic radiation or else shocked to a temperature high enough for collisional ionization, but not dense and hot enough to be a detectable X-ray source outside clusters and hot groups of galaxies.

We comment here on a simple picture for the cooling and settling of baryons onto galaxies. The sum of the baryon mass densities belonging to galaxies, in entries 3.3 to 3.13, is $\Omega_{\mathrm{b,g}} = 0.0035$. This is 8% of the total baryon mass. Suppose $\Omega_{\mathrm{b,g}}$ consists of all baryons gathered from radius r_g around $L \sim L_*$ galaxies, and it is supposed that we can neglect the addition of baryons by settling from further out and the loss by galactic winds. That is, we are supposing that at $r > r_g$ the ratio of the baryon density to the dark matter density is the cosmic mean value, and that the baryons closer in have collapsed onto the galaxies.

The Remainder

The interested reader is referred to the original publication [15] for a review of the rest of the cosmic inventory. By reviewing the dark sector and the baryon mass, we have discussed nearly 100.0% of the cosmic energy inventory. A summary chart is shown below in Figure 2.14 as a summary of the detailed description provided in [15].

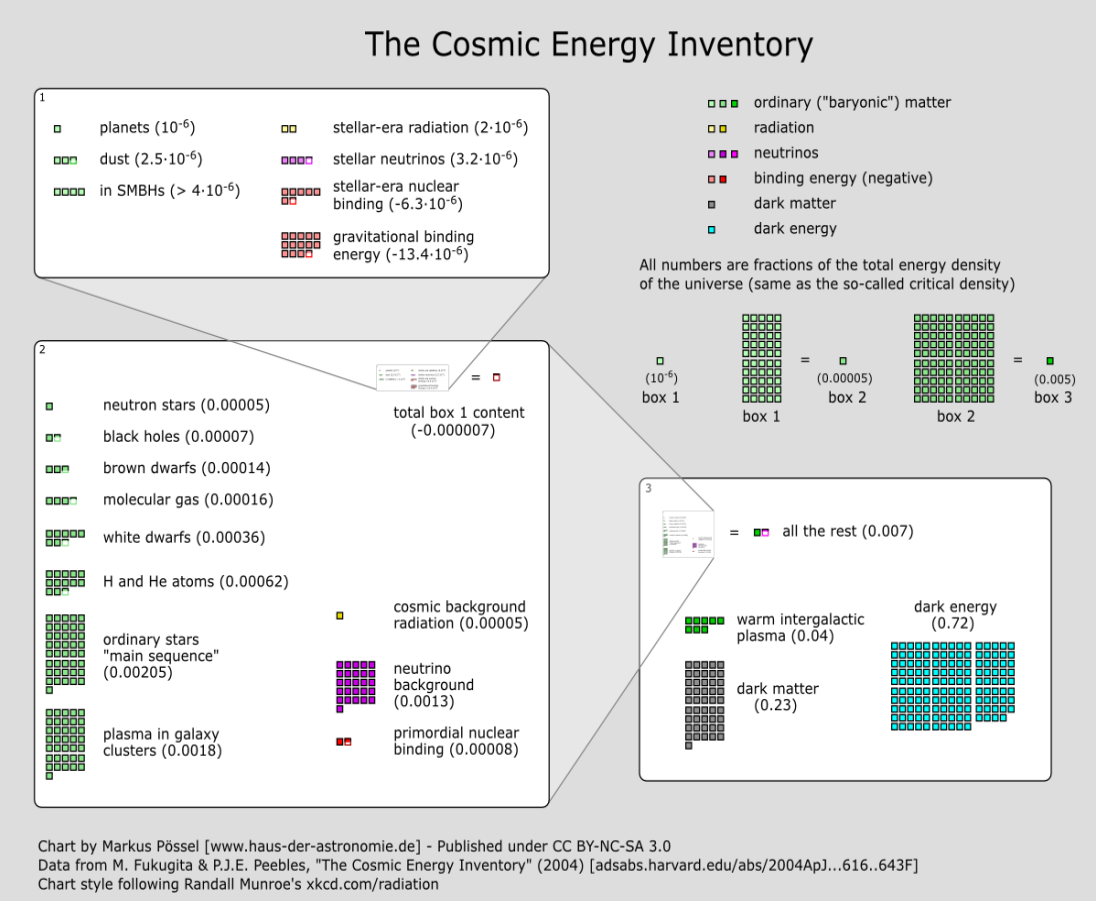

Figure 2.14: The Cosmic Energy Inventory, based on data from [15], as published by Pössel

The Cosmological Parameters

The discovery of the cosmic microwave background (CMB) by Penzias and Wilson in 1964 (Nobel Prize 1978) established the modern paradigm of the hot big bang cosmology. Almost immediately after this seminal discovery, searches began for anisotropies in the CMB – the primordial signatures of the fluctuations that grew to form the structure that we see today. Despite many attempts, the detection of higher-order anisotropies proved elusive until the first results from the *Cosmic Background Explorer* (*COBE*). The *COBE* results established the existence of a nearly scale-invariant spectrum of primordial fluctuations on angular scales larger than 7°, consistent with the predictions of inflationary cosmology, and stimulated a new generation of precision measurements of the CMB.

Rapid advances in observational cosmology have led to the establishment of a precision cosmological model, with many of the key cosmological parameters determined to one or two significant figure accuracy. Particularly prominent are measurements of cosmic microwave background (CMB) anisotropies, with the highest precision observations being those of the *Planck* Satellite which for temperature anisotropies supersede the iconic *WMAP* results. However the most accurate model of the Universe requires consideration of a range of different types of observation, with complementary probes providing consistency checks, lifting parameter degeneracies, and enabling the strongest constraints to be placed. [16]

The term 'cosmological parameters' encompasses an ever increasing range of parameters, and often includes the parameterization of some functions, as well as simple numbers describing properties of the Universe. The original usage referred to the parameters describing the global dynamics of the Universe, such as its expansion rate and curvature. Also now of great interest is how the matter budget of the Universe is built up from its constituents: baryons, photons, neutrinos, dark matter, and dark energy. We need to describe the nature of perturbations in the Universe, through global statistical descriptors such as the matter and radiation power spectra. There may also be parameters describing the physical state of the Universe, such as the ionization fraction as a function of time during the era since recombination. Typical comparisons of cosmological models with observational data now feature between five and ten parameters. [16]

With an isotropic and homogeneous matter background, described by a stress tensor T^{μ}_{ν} of a fluid in its rest frame. Thus $T^{\mu}_{\nu} = \mathrm{diag}(\rho, -p, -p, -p)$, where ρ is energy/matter density and p is pressure. The Einstein equations are

$$(\mathcal{R}_{\mu\nu} - \frac{1}{2} g_{\mu\nu}\mathcal{R}) = 8\pi G T_{\mu\nu} \ . \tag{2.183}$$

For a spacetime with metric and matter given above, and a cosmological constant Λ, these equations of motion yield

$$\left(\frac{\dot{R}}{R}\right)^2 = H^2 = \frac{8\pi G\rho}{3} - \frac{k}{R^2} + \frac{\Lambda}{3} \ . \tag{2.184}$$

Here, $\dot{R} = dR/dt$, etc. In addition the acceleration of $R(t)$ obeys

$$\frac{\ddot{R}}{R} = -\frac{4\pi G}{3}(\rho + 3p) + \frac{\Lambda}{3} \tag{2.185}$$

where p is pressure in the matter stress tensor above.

Write H_0 for the numerical value of H today, the Hubble constant, $H_0 = 100\,h$ km/s/Mpc and R_0 for the value of the scale factor today. [8] Then define

$$\begin{aligned} \Omega_k &= \frac{-k}{R_0^2 H_0^2} \\ \Omega_\rho &= \frac{8\pi G}{3H_0^2}\rho_0 \\ \Omega_\Lambda &= \frac{\Lambda}{3H_0^2}\ , \end{aligned} \tag{2.186}$$

constants corresponding to the values of these ratios today. The equation of motion, equation (2.184), implies [8]

$$1 = \Omega_k + \Omega_\rho + \Omega_\Lambda\ . \tag{2.187}$$

Ordinarily, the Universe is taken to be a perturbed Robertson–Walker space-time with dynamics governed by Einstein's equations. Using the density parameters Ω_i for the various matter species and Ω_Λ for the cosmological constant, the Friedmann equation can be written

$$\sum_i \Omega_i + \Omega_\Lambda - 1 = \frac{k}{R^2 H^2}\ , \tag{2.188}$$

where the sum is over all the different species of material in the Universe. This equation applies at any epoch, but later in this article we will use the symbols Ω_i and Ω_Λ to refer to the present values.

The complete present state of the homogeneous Universe can be described by giving the current values of all the density parameters and the Hubble constant h (the present-day Hubble parameter being written $H_0 = 100h\,\mathrm{km\,s^{-1}\,Mpc^{-1}}$). A typical collection would be baryons Ω_b, photons Ω_γ, neutrinos Ω_ν, and cold dark matter Ω_c (given charge neutrality, the electron density is guaranteed to be too small to be worth considering separately and is included with the baryons). The spatial curvature can then be determined from the other parameters using 2.188. The total present matter density $\Omega_\mathrm{m} = \Omega_\mathrm{c} + \Omega_\mathrm{b}$ is sometimes used in place of the cold dark matter density Ω_c. [16]

	Planck+WP +highL	*Planck*+WP +highL+BAO	*WMAP*9+eCMB +BAO
$\Omega_{\rm b}h^2$	0.02207 ± 0.00027	0.02214 ± 0.00024	0.02211 ± 0.00034
$\Omega_{\rm c}h^2$	0.1198 ± 0.0026	0.1187 ± 0.0017	0.1162 ± 0.0020
$100\,\theta_{\rm MC}$	1.0413 ± 0.0006	1.0415 ± 0.0006	—
$n_{\rm s}$	0.958 ± 0.007	0.961 ± 0.005	0.958 ± 0.008
τ	$0.091^{+0.013}_{-0.014}$	0.092 ± 0.013	$0.079^{+0.011}_{-0.012}$
$\ln(10^{10}\Delta^2_{\mathcal{R}})$	3.090 ± 0.025	3.091 ± 0.025	3.212 ± 0.029
h	0.673 ± 0.012	0.678 ± 0.008	0.688 ± 0.008
σ_8	0.828 ± 0.012	0.826 ± 0.012	$0.822^{+0.013}_{-0.014}$
$\Omega_{\rm m}$	$0.315^{+0.016}_{-0.017}$	0.308 ± 0.010	0.293 ± 0.010
Ω_Λ	$0.685^{+0.017}_{-0.016}$	0.692 ± 0.010	0.707 ± 0.010

Figure 2.15: Cosmological Parameters, from [16].

Parameter constraints reproduced from Table 1.1 in [16] are shown in Figure 2.15. All columns assume the ΛCDM cosmology with a power-law initial spectrum, no tensors, spatial flatness, and a cosmological constant as dark energy. *Planck* takes the sum of neutrino masses fixed to 0.06eV, while *WMAP* sets it to zero. Above the line are the six parameter combinations actually fit to the data in the *Planck* analysis ($\theta_{\rm MC}$ is a measure of the sound horizon at last scattering); those below the line are derived from these. Two different data combinations including *Planck* are shown to highlight the extent to which additional data improve constraints. The first column is a combination of CMB data only — *Planck* temperature plus *WMAP* polarization data plus high-resolution data from ACT and SPT — while the second column adds BAO data from the SDSS, BOSS, 6dF, and WiggleZ surveys. For comparison the last column shows the final nine-year results from the *WMAP* satellite, combined with the same BAO data and high-resolution CMB data (which they call eCMB). Note that the *WMAP* data uses Ω_Λ directly as a fit parameter, rather than $\theta_{\rm MC}$. The perturbation amplitude $\Delta^2_{\mathcal{R}}$ is specified at the scale $0.05\,{\rm Mpc}^{-1}$ for *Planck*, but $0.002\,{\rm Mpc}^{-1}$ for *WMAP*, so the spectral index $n_{\rm s}$ needs to be taken into account in comparing them. Uncertainties are shown at 68% confidence. [16]

These parameters allow us to track the history of the Universe back in time, at least until an epoch where interactions allow interchanges between the densities of the different species, which is believed to have last happened at neutrino decoupling, shortly before Big Bang Nucleosynthesis (BBN). To probe further back into the Universe's history requires assumptions about particle interactions, and perhaps about the nature of physical laws themselves. [16]

Large Scale Structure

The central unsolved riddle of cosmology has therefore become the question of how the near perfectly homogeneous, featureless, extremely hot and dense early Universe gave rise to the wealth and variety of structure which make our cosmos into such a fascinating world to live in. Instrumental in solving this puzzle is the realization that our Universe still contains cosmological fossils, structures and physical properties that still contain traces of the processes that have been responsible for the emergence of all the objects and structures populating our cosmos. The way in which matter has arranged itself on scales of a few up to several hundreds Megaparsec has evolved sufficiently far to yield observable manifestations of the growth process while its matter contents and internal motions have not yet been blended to such an extent that they do no longer contain any directly and objectively retrievable information on the structure formation processes. [29].

The hot and cold spots we see on the CMBR today were the high and low density regions at the time the radiation that we observe today was first emitted. Once matter took over as the dominant source of energy density, these perturbations were free to grow by accreting other matter from their surroundings. Initially, the collapsing matter would have just been dark matter since the baryons were still tied to the radiation. After the formation of the CMBR and decoupling, however, the baryons also fell into the gravitational wells set up by the dark matter and began to form stars, galaxies, galaxy clusters, and so on. Cosmologists refer to this distribution of matter as the "large scale structure" of the universe. [13]

Up to this point we have discussed the universe in terms of a homogeneous and isotropic FRW model. We now take the next step by explicitly considering small perturbations around the homogeneous and isotropic model (which we now refer to as the unperturbed or background universe). In cosmology, perturbation theory has wide applicability. Often the distribution of non-linear objects can be treated in terms of linear theory, even though their internal composition cannot, and even very non-linear structures such as planets, stars and galaxies have evolved from small initial perturbations under the influence of gravity. This growth is called structure formation, though sometimes the term is used to refer only to the situation when perturbations become of order unity and bound structures form. [23]

The growth of this small inhomogeneity into the present observable structure of the universe. This part is less speculative, since we have a well established theory of gravity, general relativity. However, there is uncertainty in this part too, since we do not know the precise nature of the dominant components to the energy density of the universe, the dark matter and the possible dark energy. The gravitational growth depends on the equations of state and the streaming lengths (particle mean free path between interactions) of these density components. Besides gravity, the growth is affected by pressure forces [23]

As a general rule, making predictions for the statistical properties of large scale structure can be very challenging. For the CMBR, the deviations from the mean temperature are very small and linear perturbation theory is a very good approximation. By comparison, the density of matter in our galaxy compared to the mean density of the universe is enormous. As a result, there are two basic options: either do measurements on very large physical scales where the variations in density are typically much smaller or compare the measurements to simulations of the universe where the non-linear effects of gravity can be modeled. Both of these options require significant investment in both theory and hardware, but the last several years have produced some excellent confirmations of the basic picture. [13]

The process that led to the generation of the acoustic peaks in the CMBR power spectrum was driven by the presence of a tight coupling between photons and baryons just prior to decoupling. This fluid would fall into the gravitational potential wells set up by dark matter (which does not interact with photons) until the pressure in the fluid would counteract the

gravitational pull and the fluid would expand. This led to hot spots and cold spots in the CMBR, but also led to places where the density of matter was a little higher thanks to the extra baryons being dragged along by the photons and areas where the opposite was true. Like with the CMBR, the size of these areas was determined by the size of the observable universe at the time of decoupling, so certain physical scales would be enhanced if you looked at the angular power spectrum of the baryons. Of course, once the universe went through decoupling, the baryons fell into the gravitational wells with the dark matter, but those scales would persist as "wiggles" on the overall matter power spectrum. [13]

Of course, as the size of the universe expanded, the physical scale of those wiggles increased, eventually reaching about 500 million light years today. Making a statistical measurement of objects separated by those sorts of distances requires surveying a very large volume of space. In 2005, two teams of cosmologists reported independent measurements of the expected baryon feature. As with the CMBR power spectrum, this confirmed that the model cosmologists have developed for the initial growth of large scale structure was a good match to what we see in the sky. [13]

The second method for understanding large scale structure is via cosmological simulations. The basic idea behind all simulations is this: if we were a massive body and could feel the gravitational attraction of all of the other massive bodies in the universe and the overall geometry of the universe, where would we go next? Simulations answer this question by quantizing both matter and time. A typical simulation will take N particles (where N is a large number; hence the term N-body simulation) and assign them to a three-dimensional grid. Those initial positions are then perturbed slightly to mimic the initial fluctuations in energy density from inflation. Given the positions of all of these particles and having chosen a geometry for our simulated universe, we can now calculate where all of these particles should go in the next small bit of time. We move all the particles accordingly and then recalculate and do it again. [13]

Obviously, this technique has limits. If we assign a given mass to all of our particles, then measurements of mass below a certain limit will be strongly quantized (and hence inaccurate). Likewise, the range of length scales is limited: above by the volume of the chunk of the universe we have chosen to simulate and below by the resolving scale of our mass particles. There is also the problem that, on small scales at least, the physics that determines where baryons will go involves more than just gravity; gas dynamics and the effects of star formation makes simulating baryons (and thus the part of the universe we can actually see!) challenging. Finally, we do not expect the exact distribution of mass in the simulation to tell us any thing in particular; we only want to compare the statistical properties of the distribution to our universe. This article discusses these statistical methods in detail as well as providing references to the relevant observational data. Still, given all of these flaws, efforts to simulate the universe have improved tremendously over the last few decades, both from a hardware and a software standpoint. [13]

The theory of cosmological perturbations has become a cornerstone of modern quantitative cosmology since it is the framework which provides the link between the models of the very early Universe such as the inflationary Universe scenario (which yield causal mechanisms for the generation of fluctuations) and the wealth of recent high-precision data on the spectrum of density fluctuations and cosmic microwave anisotropies.

Newtonian Theory of Cosmological Perturbations

The growth of density fluctuations is a consequence of the purely attractive nature of the gravitational force. Imagine (first in a non-expanding background) a density excess $\delta\rho$ localized about some point $\mathbf{x}$ in space. This fluctuation produces an attractive force which pulls the surrounding matter towards $\mathbf{x}$. The magnitude of this force is proportional to $\delta\rho$. Hence, by

Newton's second law

$$\ddot{\delta\rho} \sim G\delta\rho\,, \tag{2.189}$$

where G is Newton's gravitational constant. Hence, there is an exponential instability of flat space-time to the development of fluctuations.

Obviously, in General Relativity it is inconsistent to consider density fluctuations in a non-expanding background. If we consider density fluctuations in an expanding background, then the expansion of space leads to a friction term in (2.189). Hence, instead of an exponential instability to the development of fluctuations, the growth rate of fluctuations in an expanding Universe will be as a power of time. It is crucial to determine what this power is and how it depends both on the background cosmological expansion rate and on the length scale of the fluctuations. [5]

We will be taking the background space-time to be homogeneous and isotropic, with a metric given by

$$ds^2 \,=\, dt^2 - a(t)^2 d\mathbf{x}^2\,, \tag{2.190}$$

where t is physical time, $d\mathbf{x}^2$ is the Euclidean metric of the spatial hypersurfaces (here taken for simplicity to be spatially flat), and $a(t)$ denoting the scale factor, in terms of which the expansion rate is given by $H(t) = \dot{a}/a$. The coordinates $\mathbf{x}$ used above are "comoving" coordinates, coordinates painted onto the expanding spatial hypersurfaces. Note, however, that in the following two subsections $\mathbf{x}$ will denote the physical coordinates, and $\mathbf{q}$ the comoving ones.

In this context, matter is described by a perfect fluid, and gravity by the Newtonian gravitational potential φ. The fluid variables are the energy density ρ, the pressure p, the fluid velocity $\mathbf{v}$, and the entropy density S. The basic hydrodynamical equations are

$$\begin{aligned}
\dot{\rho} + \nabla\cdot(\rho\mathbf{v}) &= 0 \\
\dot{\mathbf{v}} + (\mathbf{v}\cdot\nabla)\mathbf{v} + \frac{1}{\rho}\nabla p + \nabla\varphi &= 0 \\
\nabla^2\varphi &= 4\pi G\rho \\
\dot{S} + (\mathbf{v}\cdot\nabla)S &= 0 \\
p &= p(\rho, S)\,.
\end{aligned} \tag{2.191}$$

The first equation is the continuity equation, the second is the Euler (force) equation, the third is the Poisson equation of Newtonian gravity, the fourth expresses entropy conservation, and the last describes the equation of state of matter.

The background is given by the background energy density ρ_o, the background pressure p_0, vanishing velocity, constant gravitational potential φ_0 and constant entropy density S_0. As mentioned above, it does **not** satisfy the background Poisson equation.

The equations for cosmological perturbations are obtained by perturbing the fluid variables about the background,

$$\begin{aligned}
\rho &= \rho_0 + \delta\rho \\
\mathbf{v} &= \delta\mathbf{v} \\
p &= p_0 + \delta p \\
\varphi &= \varphi_0 + \delta\varphi \\
S &= S_0 + \delta S\,,
\end{aligned} \tag{2.192}$$

where the fluctuating fields $\delta\rho, \delta\mathbf{v}, \delta p, \delta\varphi$ and δS are functions of space and time, by inserting these expressions into the basic hydrodynamical equations (2.191), by linearizing, and by combining the resulting equations which are of first order in time to obtain the following second

order differential equations for the energy density fluctuation $\delta\rho$ and the entropy perturbation δS

$$\begin{aligned} \ddot{\delta\rho} - c_s^2 \nabla^2 \delta\rho - 4\pi G \rho_0 \delta\rho &= \sigma \nabla^2 \delta S \\ \dot{\delta S} &= 0 \,, \end{aligned} \tag{2.193}$$

where the variables c_s^2 and σ describe the equation of state

$$\delta p = c_s^2 \delta\rho + \sigma \delta S \tag{2.194}$$

with

$$c_s^2 = \left(\frac{\delta p}{\delta \rho}\right)_{|_S} \tag{2.195}$$

denoting the square of the speed of sound.

The first conclusions from the basic perturbation equations (2.193) are that

1) entropy fluctuations do not grow,
2) adiabatic fluctuations are time-dependent, and
3) entropy fluctuations seed an adiabatic mode. [5]

Taking a closer look at the equation of motion (2.193) for $\delta\rho$, we see that the third term on the left hand side represents the force due to gravity, a purely attractive force yielding an instability of flat space-time to the development of density fluctuations (as discussed earlier, see (2.189)). The second term on the left hand side of (2.193) represents a force due to the fluid pressure which tends to set up pressure waves. In the absence of entropy fluctuations, the evolution of $\delta\rho$ is governed by the combined action of both pressure and gravitational forces. [5]

Restricting our attention to adiabatic fluctuations, we see from (2.193) that there is a critical wavelength, the Jeans length, whose wavenumber k_J is given by

$$k_J = \left(\frac{4\pi G \rho_0}{c_s^2}\right)^{1/2} . \tag{2.196}$$

Fluctuations with wavelength longer than the Jeans length ($k \ll k_J$) grow exponentially

$$\delta\rho_k(t) \sim e^{\omega_k t} \text{ with } \omega_k \sim 4(\pi G \rho_0)^{1/2} \tag{2.197}$$

whereas short wavelength modes ($k \gg k_J$) oscillate with frequency $\omega_k \sim c_s k$. Note that the value of the Jeans length depends on the equation of state of the background. For a background dominated by relativistic radiation, the Jeans length is large (of the order of the Hubble radius $H^{-1}(t)$), whereas for pressure-less matter the Jeans length goes to zero.

Relativistic Theory of Cosmological Fluctuations

The Newtonian theory of cosmological fluctuations discussed in the previous section breaks down on scales larger than the Hubble radius because it neglects perturbations of the metric, and because on large scales the metric fluctuations dominate the dynamics. [5]

Let us begin with a heuristic argument to show why metric fluctuations are important on scales larger than the Hubble radius. For such inhomogeneities, one should be able to approximately describe the evolution of the space-time by applying the first Friedmann-Lemâitre-Robertson-Walker (FLRW) equation of homogeneous and isotropic cosmology to the local Universe:

$$\left(\frac{\dot{a}}{a}\right)^2 = \frac{8\pi G}{3}\rho\,. \tag{2.198}$$

Based on this equation, a large-scale fluctuation of the energy density will lead to a fluctuation ("δa") of the scale factor a which grows in time. This is due to the fact that self gravity amplifies fluctuations even on length scales λ greater than the Hubble radius.

This argument is made rigorous in the following analysis of cosmological fluctuations in the context of general relativity, where both metric and matter inhomogeneities are taken into account. We will consider fluctuations about a homogeneous and isotropic background cosmology, given by the metric (2.190), which can be written in conformal time η (defined by $dt = a(t)d\eta$) as

$$ds^2 = a(\eta)^2\left(d\eta^2 - d\mathbf{x}^2\right). \tag{2.199}$$

The evolution of the scale factor is determined by the two FLRW equations,

$$\dot{\rho} = -3H(\rho + p)\,, \tag{2.200}$$

which determine the expansion rate and its time derivative in terms of the equation of state of the matter, whose background stress-energy tensor can be written as

$$T^{\mu}_{\nu} = \begin{pmatrix} \rho & 0 & 0 & 0 \\ 0 & -p & 0 & 0 \\ 0 & 0 & -p & 0 \\ 0 & 0 & 0 & -p \end{pmatrix}. \tag{2.201}$$

The theory of cosmological perturbations is based on expanding the Einstein equations to linear order about the background metric. The theory was initially developed in pioneering works by Lifshitz. Significant progress in the understanding of the physics of cosmological fluctuations was achieved by Bardeen who realized the importance of subtracting gauge artifacts from the analysis. [5]

To understand the generation and evolution of fluctuations in current models of the very early Universe, we need both Quantum Mechanics and General Relativity, i.e. quantum gravity. This is an intractable problem, since the theory of quantum gravity is not yet established. However, on large cosmological scales the fractional amplitude of the fluctuations is smaller than 1. Since gravity is a purely attractive force, the fluctuations must have been - at least in the context of an eternally expanding background cosmology - very small in the early Universe. Thus, a linearized analysis of the fluctuations is self-consistent. [5]

To briefly summarize the quantum theory of cosmological perturbations. In the linearized theory, fluctuations are set up at some initial time t_i mode by mode in their vacuum state. While the wavelength is smaller than the Hubble radius, the state undergoes quantum vacuum fluctuations. The accelerated expansion of the background redshifts the length scale beyond the Hubble radius. The fluctuations freeze out when the length scale is equal to the Hubble radius. On larger scales, the amplitude of v_k increases as the scale factor. This corresponds to the squeezing of the quantum state present at Hubble radius crossing (in terms of classical general

relativity, it is self-gravity which leads to this growth of fluctuations). It is the squeezing of the quantum vacuum state leads to the emergence of the classical nature of the fluctuations. [5]

The presiding discussion of Newtonian and Relativistic cosmological perturbations is intended to be a brief summary of this field. In order to further understand the nature of cosmological perturbations and the formation of large scale structure, it is necessary to delve into the quantum origins of cosmological perturbations. this can be further explored in [5] and the references therein.

Summary: Cosmology

Cosmology is the science concerned with the origins, structure and evolution of the Universe as a whole. It is based on the Cosmological Principle, which basically is an extension of the Copernican Principle that the earth is not a privileged location. On large scales, the universe is homogeneous and isotropic. As an assumption, the cosmological principle cannot be proven. But no observation performed so far is inconsistent with this assumption; at least no observation of the distant Universe. The density of galaxies appears to be independent of direction; the intensity of the cosmic background radiation (the microwave radiation from the early hot Universe) is highly isotropic; there is no significant variation with direction.

The physics of the Universe is best described, as we know today, by the General Theory of Relativity. The Robertson-Walker metric describes the kinematics of our homogeneous and isotropic Universe. The dynamics of the Universe are described by the Friedman equations. Galaxies have a redshift which is proportional to their distance. The Hubble constant expresses the rate of expansion of the Universe, according to Hubble's law. The "Big Bang" model of the Universe is supported collectively by three pillars, including studies of the Cosmic Microwave Background, the expansion of the Universe, and nucleosynthesis. The Cosmological Constant (Λ) is a way to express the increasing acceleration of the Universe, as was shown by supernovae studies. The standard model of the Universe is referred to as the ΛCDM model and can be described by the cosmological parameters. Large scale structure in the Universe is believed to be a result of gravitational instability. These density fluctuations, which left their trail in the Cosmic Microwave Background, result in gravitational collapse of over dense regions which the form the large scale structure in the Universe. [25]

Perhaps the most exciting way to end this brief survey of Cosmology is to acknowledge that while studies over the last 100 years have provided a great deal of insight into the origin, structure and evolution of the Universe, there remain an exponentially greater number of questions yet to be answered. What are the precise values of the cosmological parameters? What is the nature of Dark Energy and why is the Universe expanding? What is the nature of Dark Matter (to be discussed in Chapter 3)? What drove inflation in the early Universe?

2.5 Chapter Summary

The three vast subjects introduced in this chapter can be succinctly summarized in three statements:

Special Relativity The speed of light is constant.

General Relativity Mass tells space-time how to curve and space-time tells matter how to move (from JA Wheeler).

Cosmology The Universe is homogeneous and isotropic.

All else follows from these three statements which have vast repercussions for our understanding of the universe.

References

[1] L. A. Anchordoqui. Lectures on Astronomy, Astrophysics, and Cosmology. *ArXiv e-prints*, June 2007. x, xi, 37, 39, 42, 43, 44, 57, 58, 59, 60

[2] N Ashby. Relativity in the global positioning system. http://www.livingreviews.org/lrr-2003-1, January 2003. 33

[3] E. Bertschinger. *Gravitation in the Weak-Field Limit*. Massachusetts Institute of Technology, 2000. 32

[4] E. Bertschinger. *Introduction to Tensor Calculus for Relativity*. Massachusetts Institute of Technology, 2000. 36

[5] R. H. Brandenberger. Lectures on the Theory of Cosmological Perturbations. In N. Bretón, J. L. Cervantes-Cota, and M. Salgad, editors, *The Early Universe and Observational Cosmology*, **646** of *Lecture Notes in Physics, Berlin Springer Verlag*, pages 127–167, 2004. 70, 71, 72, 73

[6] S Carroll. The cosmological constant. http://www.livingreviews.org/lrr-2001-1, February 2001. 47, 51

[7] S. M. Carroll, W. H. Press, and E. L. Turner. The cosmological constant. *Ann Reviews Astr Astrophys*, **30**:499–542, 1992. 48

[8] J. D. Cohn. Living With Lambda. *ApJ Suppl*, **259**:213–234, August 1998. 49, 66

[9] J Cresser. *Lecture Notes in Special Relativity*. 2003. 11

[10] S. Dodelson. *Modern Cosmology*. Academic Press, 2003. x, 50, 56, 57

[11] R. Ferraro. From aether theory to Special Relativity. *ArXiv e-prints*, February 2013. x, 7, 8, 9, 10, 11

[12] P. Ferriera. *Lectures on General Relativity and Cosmology*. Oxford University, 2013. 40

[13] B Feuerbacher. Evidence for the big bang. http://www.talkorigins.org/faqs/astronomy/bigbang.html, January 2006. 68, 69

[14] P. Fromholz, E. Poisson, and C. M. Will. The Schwarzschild metric: It's the coordinates, stupid! *American Journal of Physics*, **82**:295–300, April 2014. 40

[15] M. Fukugita and P. J. E. Peebles. The Cosmic Energy Inventory. *Astrophys J*, **616**:643–668, December 2004. xi, 61, 62, 63, 64

[16] O. Lahav and A. R Liddle. The Cosmological Parameters 2014. *ArXiv e-prints*, January 2014. xi, 65, 66, 67

[17] D Marolf. *Notes on Relativity and Cosmology for PHY312*. Syracuse Univ, 2003. 8, 21, 22

[18] C. Misner, K. Thorne, and JA. Wheeler. *Gravitation*. WH Freeman, 1970. 18, 27, 29, 36

[19] D. Morin. *Introduction to Classical Mechanics*. Cambridge University Press, 2007. x, 14, 15, 18

[20] M. Omer Farooq. Observational constraints on dark energy cosmological model parameters. *ArXiv e-prints*, September 2013. x, 24, 25, 27, 28, 29, 31, 32, 35

[21] J. Peacock. *Cosmology: Standard Model*. Murdin, Encyclopedia of Astronomy and Astrophysics, 2006. 45, 46

[22] G. Preti, F. de Felice, and L. Masiero. On the Galilean non-invariance of classical electromagnetism. *Eur J Phys*, **30**:381, 2009. 10

[23] S. Rasanen. *Cosmology Notes*. University of Helsinki, 2011. 68

[24] W. Rindler. Special Relativity: Kinematics. *Scholarpedia*, **6**:8520, 2011. 12, 13

[25] B Ryden. *Introduction to Cosmology*. Addison-Wesley, 2002. 73

[26] A. Steane. *Relativity Made Relatively Easy*. Oxford University Press, 2012. 14, 16

[27] D Topper. *How Einstein Created Relativity from Physics and Astronomy*. Springer-Verlag, 2013. 6, 11

[28] M. Trodden and S. M. Carroll. TASI Lectures: Introduction to Cosmology. *ArXiv Astrophysics e-prints*, January 2004. x, 38, 39, 49, 50, 52, 53, 54, 55

[29] R. van de Weygaert. Large Scale Structure: Setting the Stage for the Galaxy Formation Saga. In H. J. A. Röttgering, P. N. Best, and M. D. Lehnert, editors, *The Most Distant Radio Galaxies*, page 341, 1999. 68

[30] Wikipedia. Tests of general relativity. `http://en.wikipedia.org/wiki/Tests_of_general_relativity`. 33, 34

[31] Wikipedia. Cosmological constant. `http://en.wikipedia.org/wiki/Cosmological_constant`, September 2014. 47

[32] C. M. Will. *Special Relativity: A Centenary Perspective*, pages 33–49. 2006. 12

Chapter 3

Gravitational Lensing: Models and Applications in Cosmology

3.1 Purpose and Organization of this Chapter

The information in this chapter can be found in any number of textbooks and major review articles, and has been collected here in one place to serve as a convenient summary of the rapidly growing field of gravitational lensing. This chapter is presented as background for what follows. There is no attempt to develop new aspects of science in this chapter. Much of the material in this chapter is derived from existing sources that are extensively cited.

There are many excellent comprehensive review articles about all facets of gravitational lensing. The interested reader is referred to [39], [63], [17], [61], [2] and others. Weak Gravitational lensing is extensively reviewed in [21], [50], [55], [4] and others.

After a review of distance measurements in cosmology (Section 3.2), we will briefly review the basic theory of gravitational lensing (Section 3.3), followed by an extensive discussion of Strong Gravitational Lensing (Section 3.4) and a brief discussion of Weak Gravitational Lensing (Section 3.5). Finally, we will highlight some of the issues and applications of gravitational lensing in contemporary cosmology research (Section 3.6) such as the Mass-Sheet Degeneracy (Section 3.6), using gravitational lensing to understand Dark Matter (Section 3.6), and using lensing as a "Cosmic Telescope" to detect objects that are otherwise impossible to detect (Section 3.6). Finally, we conclude with an introduction to gravitational lens models (Section 3.7) as a prelude to the remainder of this dissertation.

3.2 Distance Measurements in Cosmology

The measurement of distance on cosmological scales is a part of the foundation of gravitational lensing, and made somewhat counterintuitive because of the bending of space-time by a gravitational field. It is necessary to provide a brief review of this important subject.

Distance calculations were made using redshift values according to the methods described in [23]. This included distances to the lens, D_d, distance to the source, D_s and distance from the source to the lens, D_{ds}. The Hubble distance is defined by:

$$D_{\mathrm{H}} \equiv \frac{c}{H_0} = 3000\,h^{-1}\ \mathrm{Mpc} = 9.26 \times 10^{25}\,h^{-1}\ \mathrm{m} \tag{3.1}$$

In order to define the comoving distance, D_{C}, the function:

$$E(z) \equiv \sqrt{\Omega_{\mathrm{M}}\,(1+z)^3 + \Omega_k\,(1+z)^2 + \Omega_\Lambda} \tag{3.2}$$

is defined. The line-of-sight comoving distance, D_{C}, is then given by integration:

$$D_{\mathrm{C}} = D_{\mathrm{H}} \int_0^z \frac{dz'}{E(z')} \tag{3.3}$$

where D_{H} is the Hubble distance.

Since Ω_k=0 in this study, the transverse comoving distance, D_{M} is the same as D_{C}. The angular diameter distance, D_{A} is related to the transverse comoving distance, D_{M} by:

$$D_{\mathrm{A}} = \frac{D_{\mathrm{M}}}{1+z} \tag{3.4}$$

Therefore, the distance between two objects (D_{ds}) such as the lens (D_d) and source(D_s), with $\Omega_k \geq 0$ is given by:

$$D_{\mathrm{A12}} = \frac{1}{1+z_2}\left[D_{\mathrm{M2}}\sqrt{1+\Omega_k\,\frac{D_{\mathrm{M1}}^2}{D_{\mathrm{H}}^2}} - D_{\mathrm{M1}}\sqrt{1+\Omega_k\,\frac{D_{\mathrm{M2}}^2}{D_{\mathrm{H}}^2}}\right] \tag{3.5}$$

where D_{M1} and D_{M2} are the transverse comoving distances to z_1 and z_2, D_{H} is the Hubble distance, and Ω_k is the curvature density parameter. This calculation is significantly simplified in this study with Ω_k=0.

3.3 Gravitational Lensing: Basic Principles

Gravitational lensing depends solely on the projected, two-dimensional mass distribution of the lens, and is independent of the luminosity or composition of the lens. Lensing offers an ideal way to detect and study dark matter, and to explore the growth of structure in the universe.

Gravitational lensing is one of the most important probes of the universe, and has a long and rich history with large gaps in time. Although controversial, some claim that this phenomenon was predicted by Newton in Opticks. This seems to be open to interpretation. Early calculations of this effect were based on Newtonian mechanics, done by Cavendish (unpublished 1784) and separately by Soldner (1804).

We discuss gravitational lensing here under three main assumptions which are underlying the entire discussion. First, gravitational lensing is considered within the framework of general relativity. Second, we assume that lensing matter inhomogeneities have weak gravitational fields in the sense that their Newtonian gravitational potential is small, $\Phi \ll c^2$. Third, the sources of the potential are assumed to move slowly with respect to the mean cosmic flow, such that peculiar velocities are small compared with the speed of light. The assumption of weak, slowly moving gravitational lenses is well valid in all astrophysical applications except for light propagation near compact objects, which is not covered in this discussion. Lensing by moving and rotating astrophysical bodies has been discussed in the literature and generally been found to be negligibly small. Within the framework of these assumptions, gravitational lensing is considered to be a complete theory with fully developed theoretical aspects, including the mathematics of singularities in lens mapping [2].

The theory of gravitational lensing is best understood starting from Fermat's principle, which is well known from geometrical optics, which states that between a fixed source and a fixed observer, light will choose a path along which its travel time is extremal. Wave optics is typically unimportant for gravitational lensing because the wave length of light is much smaller than any structures in a gravitational lens.

The propagation of light in arbitrary curved spacetimes is a complicated theoretical problem. However, for almost all cases of relevance to gravitational lensing, we assume that the overall geometry of the universe is described by the Friedmann-Lemaître-Robertson-Walker metric and that matter inhomogeneities which cause lensing are just local perturbations. Light paths propagating from the source past the lens to the observer can then be broken up into three distinct zones. In the first zone, light travels from the source to a point close to the lens through unperturbed spacetime. In the second zone, near the lens, light is deflected. Finally, in the third zone, light again travels through unperturbed spacetime. To study light deflection close to the lens, we assume a locally flat, Minkowskian spacetime which is weakly perturbed by the Newtonian gravitational potential of the mass distribution constituting the lens. [39].

Using Newtonian mechanics, one can calculate based on the assumption that light has mass, and should undergo acceleration. The following derivation of the deflection angles is modified from [65] and [52]. For small deflections of a light ray, and the kinetic energy of the particle is much larger than its maximal potential energy in the gravitational field:

$$\frac{GmM}{\xi} \ll \frac{mv_0^2}{2} \tag{3.6}$$

or

$$\xi \gg r_g = \frac{2GM}{c^2} \tag{3.7}$$

Most gravitating bodies have sizes much larger than their gravitational radius, so that this

condition is always true. In the first order approximation:

$$\hat{a} \simeq -\frac{\Delta v_z}{c} \tag{3.8}$$

To obtain Δv_z we use the equation of motion, which along the z axis is written as

$$m\frac{dv_z}{dt} = -fcos\varphi = -\frac{f\xi}{r} \tag{3.9}$$

This leads to

$$\Delta v_z = -\xi GM \int_0^\infty \frac{dt}{r^3(t)} \tag{3.10}$$

By then using $dt = dx/c$ and integrating over φ we then obtain

$$\Delta v_z = -\frac{2GM}{\varphi c} \tag{3.11}$$

which can be written as:

$$\hat{a} = \frac{2GM}{\xi c^2} = \frac{r_g}{\xi} \tag{3.12}$$

where $\hat{a}$ is the angle of deflection. This formula shows the effect of the sun's gravitational field on light, using only Newtonian mechanics and a few assumptions, as shown above.

These calculations were also done by Einstein, and published in 1911, before his work on General Relativity was completed [13]. Einstein calculated a deflection by the sun of 0.83 arcseconds, based on the final formula above, the same result published by Soldner more than 100 years earlier! This formula did not account for the general relativistic considerations, which includes the curvature of space-time near the deflecting mass.

Einstein later recalculated the effect using the following formula, accounting for the curvature of space-time.

$$\hat{a} = \frac{4GM}{\xi c^2} = \frac{2r_g}{\xi} \tag{3.13}$$

where α is the deflection angle. Note that this result is exactly twice the result shown in the formula based on Newtonian mechanics.

We can now do a sample calculation to calculate the deflection angle of rays passing near the Sun's surface, so we set $\xi = R_\odot$. The sun's radius $R_\odot$ = 7 x 10^5km, so its gravitational (Schwarzschild) radius $r_{g\odot}$ = 2.96km.

Therefore

$$\hat{a} = \frac{2r_g}{\xi} = 8.4x10^{-6} = 1.74" \tag{3.14}$$

Gravitational lensing (by the sun) was the third test of the general theory of relativity, verified on a famous expedition in 1919 during a solar eclipse, by Sir Arthur Eddington. Eddington's results agreed with the second formula published by Einstein, to within 20 percent, which accounted for general relativity.

Prior to 1919, general relativity was able to explain gravitational redshift and the advance of the perihelion of mercury, which was the first observational test of general relativity. The bending of light by the sun observed during a solar eclipse was the third test. The remarkable feature of this experiment in 1919, and the reason that the results catapulted Einstein to the

top of the scientific heap, was that the bending of light by the sun was a *prediction* of relativity that was verified within acceptable error limits. The first laboratory test of General Relativity was the Pound Rebka experiment in 1960, to verify the gravitational redshift.

While it remains purely speculative, it is likely that World War I had a profound influence on the impact of Einstein and General Relativity at that time, because of the politics associated with a British scientist validating the results of a German. Furthermore, an earlier expedition was canceled because of the War, and if that expedition had gone forward, the results would have been compared with Einstein's 1911 work, and shown no agreement.

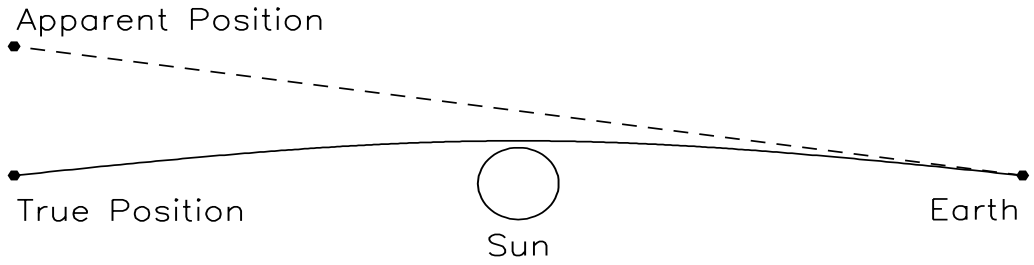

Figure 3.1: Angular deflection of a ray of light passing close to the limb of the Sun. Since the light ray is bent toward the Sun, the apparent positions of stars move away from the Sun. This is a schematic of what Eddington observed in 1919, which verified a prediction of General Relativity. [39]

The delay in the expedition until after the full formulation of general relativity and Einstein's recalculation was crucial to the Einstein's reputation. These results not only further verified general relativity but made Einstein a household name around the world. The deflection of light predicted by Newtonian gravity is exactly half that predicted by General Relativity, and Eddington's results were consistent with general relativity. It is ironic that in 1936, Einstein published his thoughts on gravitational lensing, stating 'Therefore, there is no great chance of observing this phenomenon' and yet it now is one of the most important tools in Cosmology [14]. The first gravitational lens was observed in 1979 by Walsh and colleagues.

Gravitational lensing analysis on background galaxies is a unique technique to map the mass distributions of any object, such as galaxies and clusters, regardless of their dynamical state. This enables us to explore substructures in primary halos and to measure their masses directly [46].

The Lens equation and Lens Potential

The mathematical basis of gravitational lensing is the lens equation using a thin-lens approximation, and is described by [39]. The reduced deflection angle is given by:

$$\vec{\alpha} = \frac{D_{\rm ds}}{D_{\rm s}} \vec{\hat{\alpha}} \, . \tag{3.15}$$

Since $\theta D_{\rm s} = \beta D_{\rm s} - \hat{\alpha} D_{\rm ds}$, the positions of the source and the image are given by

$$\vec{\beta} = \vec{\theta} - \vec{\alpha}(\vec{\theta}) \; . \tag{3.16}$$

This equation shows that the deflection is dependent on the ratio D_{ds}/D_s, and is generally referred to as the lensing equation. The lensing equation is perhaps the most important single equation in gravitational lensing as it is the basis for everything that follows.

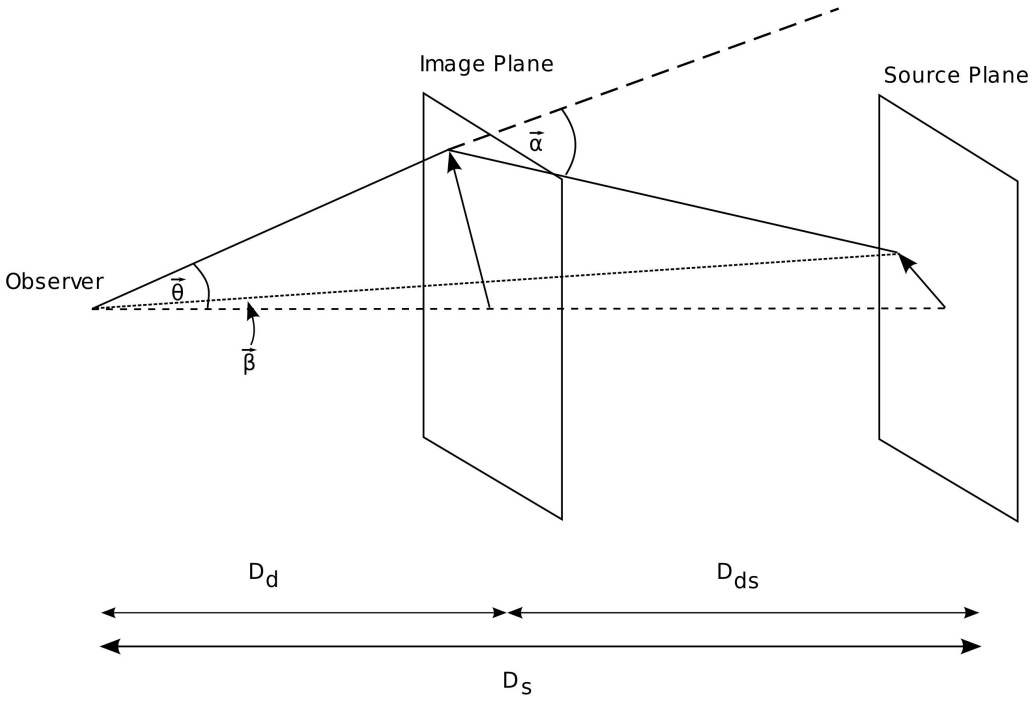

Figure 3.2: Schematic diagram of Gravitational Lensing [61]

If we define a scalar potential $\psi(\vec{\theta})$ which is an appropriately scaled, projected Newtonian potential of the lens, [39]

$$\psi(\vec{\theta}) = \frac{D_{\rm ds}}{D_{\rm d} D_{\rm s}} \frac{2}{c^2} \int \Phi(D_{\rm d}\vec{\theta}, z)\, dz \; . \tag{3.17}$$

The derivatives of ψ with respect to $\vec{\theta}$ have convenient properties. The gradient of ψ with respect to θ is the deflection angle:

$$\vec{\nabla}_\theta \psi = D_{\rm d} \vec{\nabla}_\xi \psi = \frac{2}{c^2} \frac{D_{\rm ds}}{D_{\rm s}} \int \vec{\nabla}_\perp \Phi \, dz = \vec{\alpha} \; , \tag{3.18}$$

while the Laplacian is proportional to the surface-mass density Σ:

$$\nabla^2_\theta \psi = \frac{2}{c^2} \frac{D_{\rm d} D_{\rm ds}}{D_{\rm s}} \int \nabla^2_\xi \Phi \, dz = \frac{2}{c^2} \frac{D_{\rm d} D_{\rm ds}}{D_{\rm s}} \cdot 4\pi G \, \Sigma = 2 \frac{\Sigma(\vec{\theta})}{\Sigma_{\rm cr}} \equiv 2\kappa(\vec{\theta}) \; , \tag{3.19}$$

where Poisson's equation relates the Laplacian of Φ to the mass density. The surface mass density scaled with its critical value $\Sigma_{\rm cr}$ is called the *convergence* $\kappa(\vec{\theta})$. Since ψ satisfies the two-dimensional Poisson equation $\nabla^2_\theta \psi = 2\kappa$, the effective lensing potential is written in terms of κ

$$\psi(\vec{\theta}) = \frac{1}{\pi} \int \kappa(\vec{\theta'}) \ln |\vec{\theta} - \vec{\theta'}| \, d^2\theta' \; . \tag{3.20}$$

As mentioned earlier, the deflection angle is the gradient of ψ, which is shown as:

$$\vec{\alpha}(\vec{\theta}) = \vec{\nabla}\psi = \frac{1}{\pi} \int \kappa(\vec{\theta'}) \frac{\vec{\theta} - \vec{\theta'}}{|\vec{\theta} - \vec{\theta'}|^2} \, d^2\theta' \; , \tag{3.21}$$

The local properties of the lens mapping are described by its Jacobian matrix $\mathcal{A}$:

$$\mathcal{A} \equiv \frac{\partial \vec{\beta}}{\partial \vec{\theta}} = \left(\delta_{ij} - \frac{\partial \alpha_i(\vec{\theta})}{\partial \theta_j} \right) = \left(\delta_{ij} - \frac{\partial^2 \psi(\vec{\theta})}{\partial \theta_i \partial \theta_j} \right) = \mathcal{M}^{-1} \; . \tag{3.22}$$

As indicated, $\mathcal{A}$ is the inverse of the magnification tensor $\mathcal{M}$. The matrix $\mathcal{A}$ is also called the inverse magnification tensor. The local solid-angle distortion due to the lens is given by the determinant of $\mathcal{A}$. A solid-angle element $\delta\beta^2$ of the source is mapped to the solid-angle element of the image $\delta\theta^2$, and so the magnification is given by [39]:

$$\frac{\delta\theta^2}{\delta\beta^2} = \det \mathcal{M} = \frac{1}{\det \mathcal{A}} \; . \tag{3.23}$$

This expression is an appropriate generalization when there is no symmetry.

Equation (3.22) shows that the matrix of second partial derivatives of the potential ψ (the Hessian matrix of ψ) describes the deviation of the lens mapping from the identity mapping. For convenience, we introduce the abbreviation [39]:

$$\frac{\partial^2 \psi}{\partial \theta_i \partial \theta_j} \equiv \psi_{ij} \; . \tag{3.24}$$

Since the Laplacian of ψ is twice the convergence, we have:

$$\kappa = \frac{1}{2} (\psi_{11} + \psi_{22}) = \frac{1}{2} \; \mathrm{tr} \; \psi_{ij} \; . \tag{3.25}$$

Two additional linear combinations of ψ_{ij} are important, and these are the components of the *shear* tensor:

$$\begin{aligned} \gamma_1(\vec{\theta}) &= \frac{1}{2} (\psi_{11} - \psi_{22}) \equiv \gamma(\vec{\theta}) \cos\left[2\phi(\vec{\theta})\right] \; , \\ \gamma_2(\vec{\theta}) &= \psi_{12} = \psi_{21} \equiv \gamma(\vec{\theta}) \sin\left[2\phi(\vec{\theta})\right] \; . \end{aligned} \tag{3.26}$$

With these definitions, the Jacobian matrix can be written:

$$\begin{aligned} \mathcal{A} &= \begin{pmatrix} 1 - \kappa - \gamma_1 & -\gamma_2 \\ -\gamma_2 & 1 - \kappa + \gamma_1 \end{pmatrix} \\ &= (1 - \kappa) \begin{pmatrix} 1 & 0 \\ 0 & 1 \end{pmatrix} - \gamma \begin{pmatrix} \cos 2\phi & \sin 2\phi \\ \sin 2\phi & -\cos 2\phi \end{pmatrix} \end{aligned} \tag{3.27}$$

Convergence and Shear

The meaning of the terms convergence and shear now becomes clear. Convergence alone causes an isotropic focusing of light rays, leading to an isotropic magnification of a source. The source is mapped onto an image with the same shape but larger size. Shear introduces anisotropy into the lens mapping. The quantity $\gamma = (\gamma_1^2 + \gamma_2^2)^{1/2}$ describes the magnitude of the shear and ϕ describes its orientation. As shown in Fig. 3.3, a circular source of unit radius becomes, in the presence of both κ and γ, an elliptical image with major and minor axes [39]:

$$(1 - \kappa - \gamma)^{-1} \ , \quad (1 - \kappa + \gamma)^{-1} \ . \tag{3.28}$$

The magnification is

$$\mu = \det \mathcal{M} = \frac{1}{\det \mathcal{A}} = \frac{1}{[(1-\kappa)^2 - \gamma^2]} \ . \tag{3.29}$$

Note that the Jacobian $\mathcal{A}$ is in general a function of position $\vec{\theta}$.

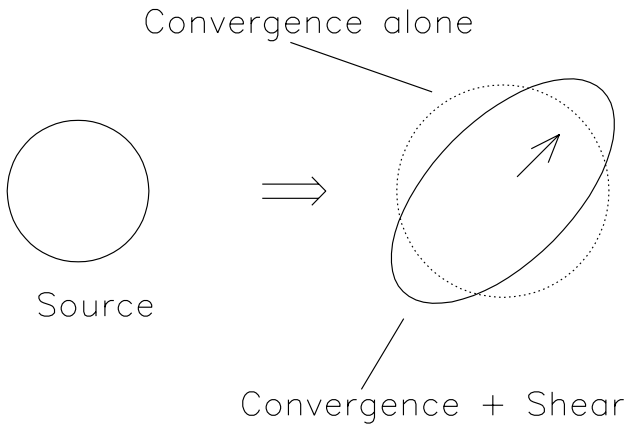

Figure 3.3: Illustration of the effects of convergence and shear on a circular source. Convergence magnifies the image isotropically, and shear deforms it to an ellipse. (From [39]).

As they travel from a background galaxy to the observer, photons get deflected by mass fluctuations along the line of sight. As a result, the apparent images of background galaxies are subject to a distortion that is characterized by the distortion matrix:

$$\Psi_{ij} \equiv \frac{\partial(\delta\theta_i)}{\partial\theta_j} \equiv \begin{pmatrix} \kappa + \gamma_1 & \gamma_2 \\ \gamma_2 & \kappa - \gamma_1 \end{pmatrix} , \tag{3.30}$$

where $\delta\theta_i(\theta)$ is the deflection vector produced by lensing on the sky. The convergence κ is proportional to the projected mass along the line of sight and describes overall dilations and

contractions. The shear γ_1 (γ_2) describes stretches and compressions along (at 45° from) the x-axis. Figure 3.4 illustrates the geometrical meaning of the two shear components. [50]

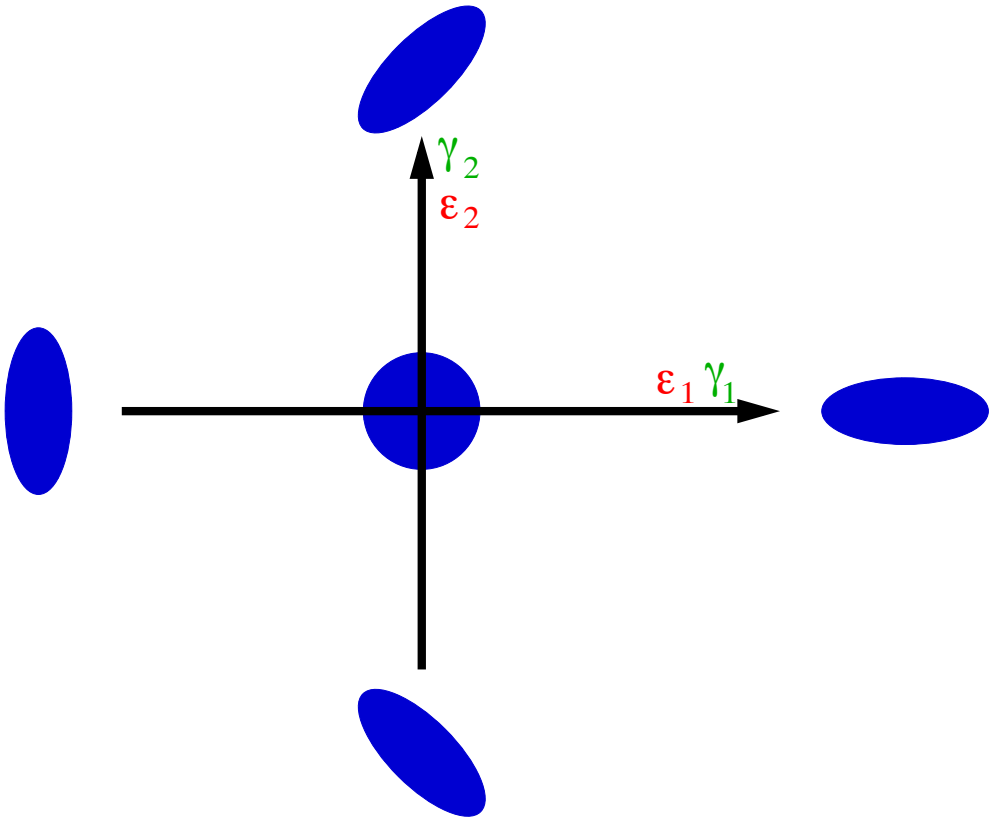

Figure 3.4: Illustration of the geometrical meaning of the shear γ_i and of the ellipticity ϵ_i. A positive (negative) shear component γ_1 corresponds to an elongation (compression) along the x-axis. A positive (negative) value of the shear component γ_2 corresponds to an elongation (compression) along the $x = y$ axis. The ellipticity of an object is defined to vanish if the object is circular (*center*). The ellipticity components ϵ_1 and ϵ_2 correspond to compression and elongations similar to those for the shear components. From [50]

Consequences of Gravitational Lensing

Strong lensing occurs when Equation 3.16 has multiple solutions corresponding to multiple images. Examples of the most common configurations of strong gravitational lensing by galaxies are shown in Figure 3.5 and explained with an optical analogy in Figure 3.6. This analogy is easily reproduced with a wine glass!

For a given deflector the solid angle in the source plane that produces multiple images is called the strong-lensing cross section. For a given population of deflectors, the optical depth is the fraction of the sky where distant sources appear to be multiply-imaged. [61].

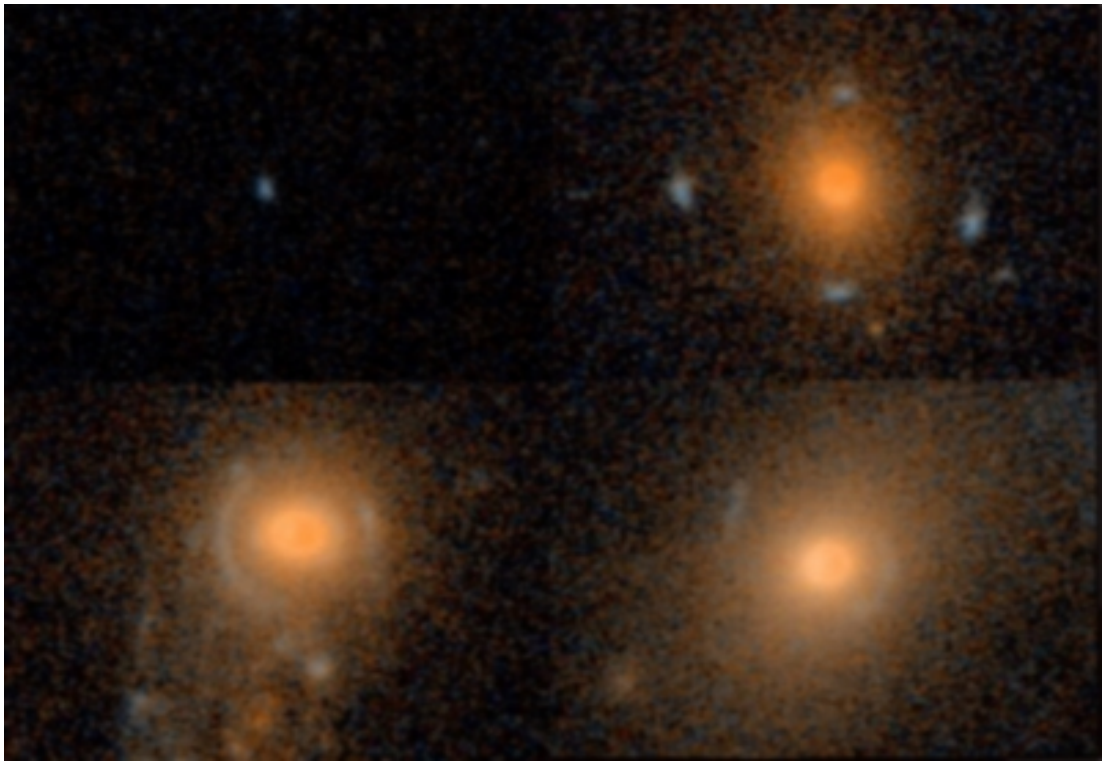

Figure 3.5: Examples of the most common configurations of galaxy-scale gravitational lens systems. A background source (top left) can produce four visible images (a “quad”; top right), an (incomplete) Einstein ring (bottom left), or two visible images (a “double”; bottom right), depending on the ellipticity of the projected mass distribution of the deflector and on the relative alignment between source and deflector [61]

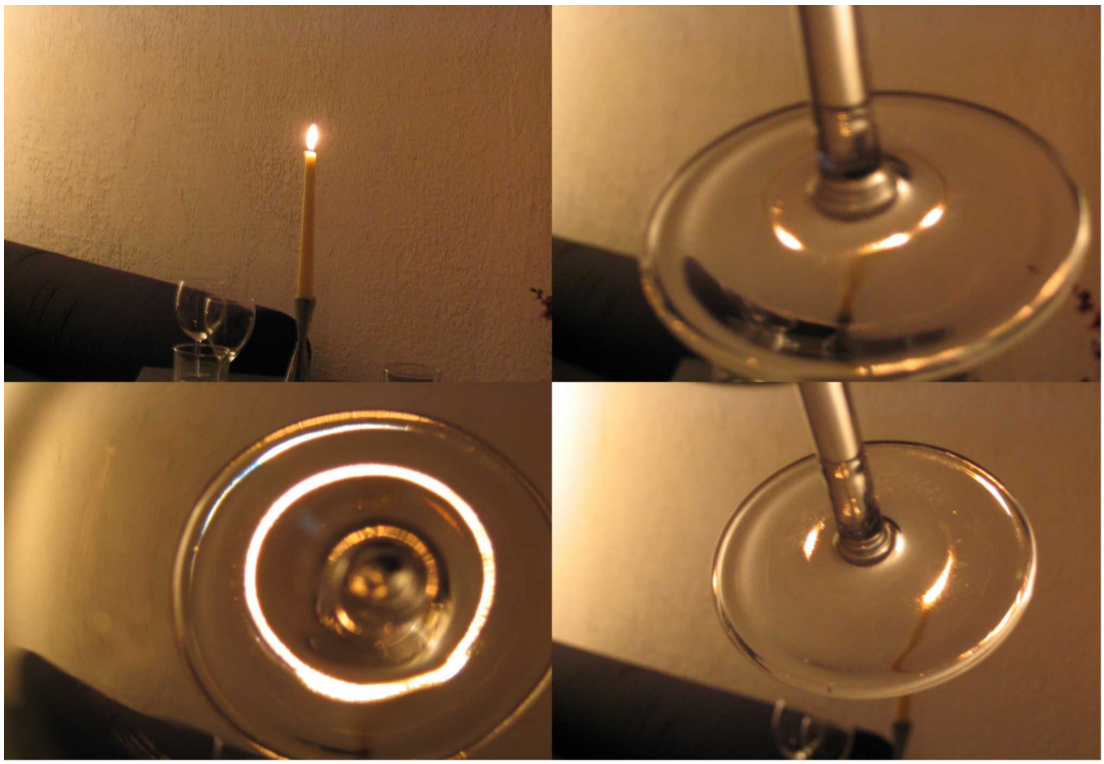

Figure 3.6: Optical analogy to illustrate the gravitational lensing phenomenon. The optical properties of the stem of a wineglass are similar to those of a typical galaxy scale lens. Viewed through a wineglass, a background compact source such as distant candle (top left), can reproduce the quad (top right), Einstein ring (bottom left), and double (bottom rights) configurations observed in gravitational lensing and shown in Figure 3.5. [61].

Change of Position

The deflection shifts the apparent location of a star, galaxy or quasar in the sky. In most cases, this makes little difference to observers, because they do not know where the object would have been in the absence of lensing. But if the sourcelens alignment changesfor instance, if either is movingastronomers can directly measure the displacement.

Magnification

The deflection and focusing of light rays affect the apparent brightness of the background star or quasar. Although most cosmic sources are demagnified slightly, some are magnified by varying degrees. Observers have measured magnifications of more than 100 times

Deformation

Extended cosmic objects (such as galaxies) often appear stretched along a circle centered on the lens, producing banana-shaped arcs. Point sources (such as stars and quasars, which are either too small or too distant to see in detail) typically remain points.

Multiplication

Strong gravitational lensing can produce multiple images. Additional images always emerge in pairs, and one of these images is mirrorinverted. Although the number of images must be odd, one image is usually obscured, so observers see an even number.

Lens Mapping

In the vicinity of an arbitrary point, the lens mapping as shown by the lens equation (Equation 3.16) can be described by its Jacobian matrix $\mathcal{A}$:

$$\mathcal{A} = \frac{\partial \vec{\beta}}{\partial \vec{\theta}} = \left(\delta_{ij} - \frac{\partial \alpha_i(\vec{\theta})}{\partial \theta_j} \right) = \left(\delta_{ij} - \frac{\partial^2 \psi(\vec{\theta})}{\partial \theta_i \partial \theta_j} \right). \tag{3.31}$$

Where we used the fact that the deflection angle can be expressed as the gradient of an effective two-dimensional scalar potential ψ: $\vec{\nabla}_\theta \psi = \vec{\alpha}$, where

$$\psi(\vec{\theta}) = \frac{D_{LS}}{D_L D_S} \frac{2}{c^2} \int \Phi(\vec{r}) dz \tag{3.32}$$

and $\Phi(\vec{r})$ is the Newtonian potential of the lens.

The determinant of the Jacobian $\mathcal{A}$ is the inverse of the magnification:

$$\mu = \frac{1}{\det \mathcal{A}}. \tag{3.33}$$

Let us define

$$\psi_{ij} = \frac{\partial^2 \psi}{\partial \theta_i \partial \theta_j}. \tag{3.34}$$

The Laplacian of the effective potential ψ is twice the convergence:

$$\psi_{11} + \psi_{22} = 2\kappa = \text{tr } \psi_{ij}. \tag{3.35}$$

With the definitions of the components of the external shear γ:

$$\gamma_1(\vec{\theta}) = \frac{1}{2}(\psi_{11} - \psi_{22}) = \gamma(\vec{\theta}) \cos[2\varphi(\vec{\theta})] \tag{3.36}$$

and

$$\gamma_2(\vec{\theta}) = \psi_{12} = \psi_{21} = \gamma(\vec{\theta}) \sin[2\varphi(\vec{\theta})] \tag{3.37}$$

(where the angle φ reflects the direction of the shear-inducing tidal force relative to the coordinate system) the Jacobian matrix can be written

$$\mathcal{A} = \begin{pmatrix} 1 - \kappa - \gamma_1 & -\gamma_2 \\ -\gamma_2 & 1 - \kappa + \gamma_1 \end{pmatrix} = (1 - \kappa) \begin{pmatrix} 1 & 0 \\ 0 & 1 \end{pmatrix} - \gamma \begin{pmatrix} \cos 2\varphi & \sin 2\varphi \\ \sin 2\varphi & -\cos 2\varphi \end{pmatrix}. \tag{3.38}$$

The magnification can now be expressed as a function of the local convergence κ and the local shear γ:

$$\mu = (\det \mathcal{A})^{-1} = \frac{1}{(1 - \kappa)^2 - \gamma^2}. \tag{3.39}$$

Caustic and Critical Curves

In strong lensing, reference is often made to 'caustics' in the source plane and 'critical curves' in the image/lens plane. Critical curves formally correspond to the solutions of det A = 0 in the lens/image plane; i.e. formally infinite magnification (in practice there is a limit to the magnification, due to the finite source size and the breakdown of geometrical optics). The lens equation maps these curves onto corresponding caustics in the source plane. The location of a source relative to the caustics determines how many images are produced, and their magnifications. A source located just inside a caustic has very magnified images, straddling the critical curve in the lens/image plane. As a source crosses a caustic, image pairs are created or destroyed. The area contained within caustics is related to the probability for a certain number of images. [27].

Both panels of Figure 3.7 show critical curves (lens plane, left-hand side) and caustics (source plane, right-hand side) for an elliptical mass distribution. A source (violet and light blue, respectively) is moved inwards towards the center of mass (red) in four (three) steps. The corresponding images in the lens plane are plotted in the same color on the left-hand side of each panel. Left-hand side: the light-blue source has crossed the outer caustic and two additional images radially emerge from the inner critical curve, which is a radial critical curve therefore. The corresponding caustic is a radial caustic. Moving the source further inwards (to the dark-blue point), results in the additional images moving away from the radial critical curve (the one going inwards gets smaller and fainter). Crossing the next caustic (green) two further images separate tangentially along the outer critical curve (tangential critical curve). The fifth image is very close to the centre and so small and faint that it is no longer seen in the figure. If the source is exactly on the optical axis (red), then four circularly distributed images occur (plus one in the centre that is invisible). If the mass distribution in the lens is spherically symmetric we would see a circle instead of the four red images the Einstein circle of the lens. [57]

In the case illustrated on the right panel the source is not moved across a straight fold of the tangential caustic but across a cusp. Then, (from blue to green) three images emerge out of one. Images emerging from a fold are called fold-arcs while those related to a cusp are called cusp-arcs. In general cusp-arcs are larger and more strongly curved and therefore more spectacular than fold-arcs.

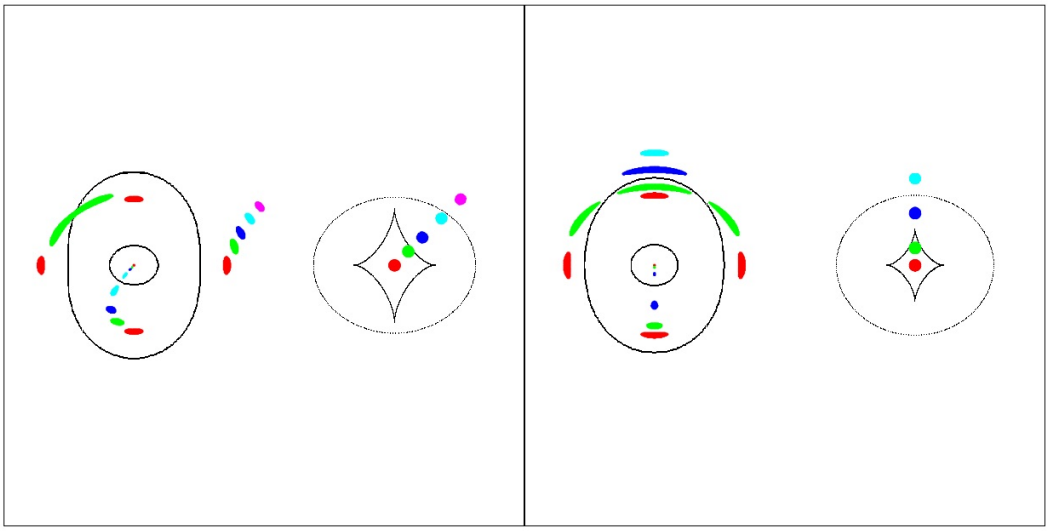

Figure 3.7: Compact source moving away from the center of an elliptical lens. Left panel: source crossing a fold caustic; right panel: source crossing a cusp caustic. Within each panel, the diagram on the left shows critical lines and image positions and the diagram on the right shows caustics and source positions. From [39]

According to Figure 3.8 the number of images always changes by two if the source crosses a critical curve. This is a generic result for non-singular mass distributions, for which the number of images must therefore be odd. While Figure 3.7 is intended to illustrate how arcs and multiple images form, typical image configurations for realistic lens models are shown in Figure 3.8. In the four panels the core radius (the steepness of the mass profile and the surface mass density in the centre) is varied. Small core radii favor multiple images and the appearance of arcs. The positions of images at a radial critical curve roughly measures the core radius (and therefore the flattening of the density distribution), while the images along the tangential critical curve determine the amplitude of the potential.

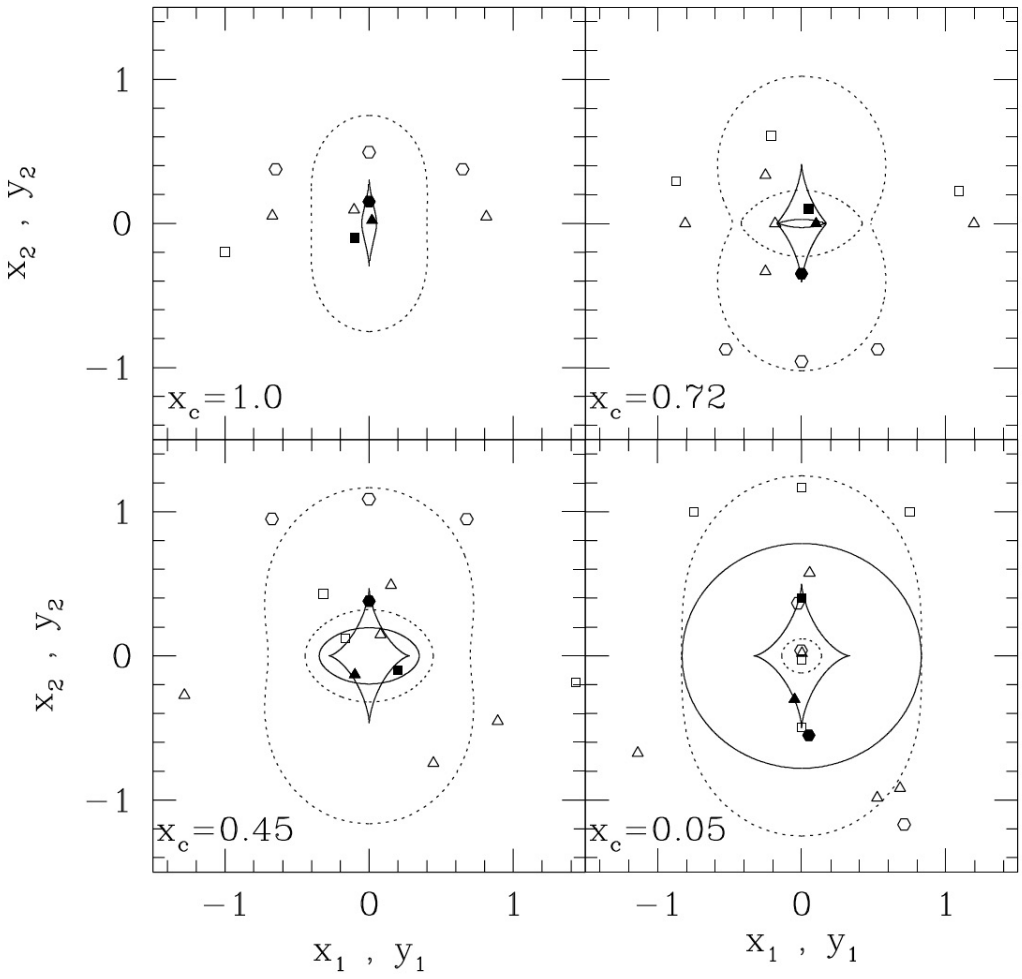

Figure 3.8: This figure illustrates possible multiple-image configurations in a typical lens. An isothermal sphere with additional external shear was assumed. The core radius varies in the four panels. Caustics are solid, critical curves dashed. Filled symbols represent the source position while the corresponding images are indicated by the open symbols. If the core radius is large $x_c = 2.0$, then only one tangential critical curve appears, the second (radial) critical curve gives rise to radial arcs or four or five, respectively, images. From [57]

The previous considerations have shown that an isolated lens typically has two critical curves, one defined by the total mass enclosed and the other defined by the slope of the mass profile. The caustics, i.e. the images of the critical curves, have several generic types. Most important are the so-called fold lines and the cusp points. When a source approaches a cusp from outside, an image pair is formed in addition to the existing image. The three images together are responsible for the largest distorted images we know. When a source approaches a fold line from outside, an additional image is formed in the interior of the fold. The two images straddling a fold critical curve are equally magnified, but they have opposite parity. Of the three images next to a cusp critical curve, the two outer ones have equal magnification and

equal parity, while the middle image has twice that magnification and the opposite parity. These statements are very important for our understanding of strong gravitational lenses because they hold independently of the actual lens model. [3].

The Einstein Radius and Einstein Ring

When a lens galaxy is spherically symmetric, it can redistribute the light of a background quasar or galaxy into a complete circle, which is referred to as an Einstein Ring. The diameter of the ring is proportional to the square root of the lensing massproviding a very elegant way of determining the mass of the lens galaxy. About a dozen Einstein rings are now known.

It is convenient to define the Einstein radius. For a circular deflector it is the radius of the region inside which the average surface-mass density equals the critical density. A point source perfectly aligned with the center of a circular mass distribution will be lensed into a circle of radius equal to the Einstein radius, or Einstein ring (see Figure 3.5).

The effect of alignment on the formation of an Einstein Ring is shown in Figure 3.9.

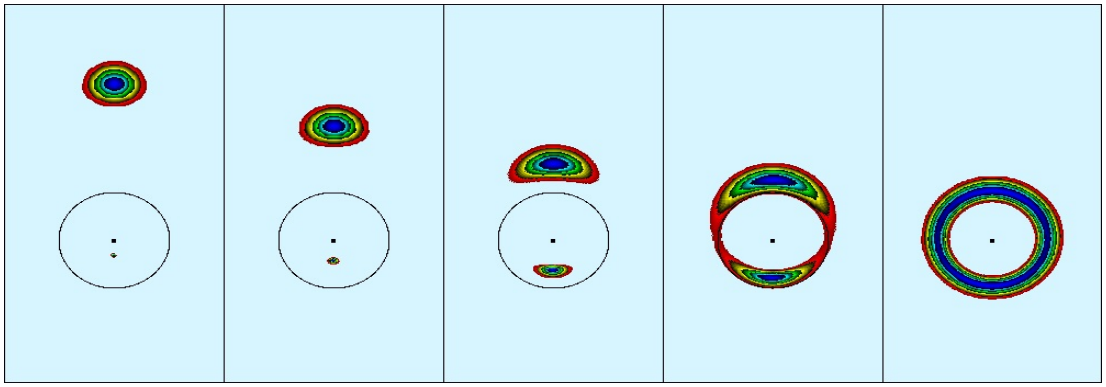

Figure 3.9: Five snapshots of a gravitational lens situation: From left to right the alignment between lens and source gets better and better, until it is perfect in the rightmost panel. This results in the image of an "Einstein ring". [63]

The size of the Einstein radius depends on the enclosed mass as well as on the redshifts of deflector and source. The definition of Einstein radius needs to be modified for non-circular deflectors.

Once appropriately defined, the Einstein radius is a most useful quantity to express the lensing strength of an object, and it is usually very robustly determined via strong lens models. As a consequence, the mass enclosed in the cylinder of radius equal to the Einstein radius can be measured to within 1-2%, including all random and systematic uncertainties. [61].

Consider now a circularly symmetric lens with an arbitrary mass profile. The lens equation reads

$$\beta(\theta) = \theta - \frac{D_{\rm ds}}{D_{\rm d} D_{\rm s}} \frac{4GM(\theta)}{c^2\,\theta} \,. \tag{3.40}$$

Due to the rotational symmetry of the lens system, a source which lies exactly on the optic axis ($\beta = 0$) is imaged as a ring if the lens is supercritical. Setting $\beta = 0$ in eq. (3.40) we obtain the radius of the ring to be

$$\theta_{\rm E} = \left[\frac{4GM(\theta_{\rm E})}{c^2}\,\frac{D_{\rm ds}}{D_{\rm d}D_{\rm s}}\right]^{1/2} .$$

This is the mathematical definition of the *Einstein radius*. Figure 3.10 illustrates the situation. Note that the Einstein radius is not just a property of the lens, but depends also on the various distances in the problem. [39].

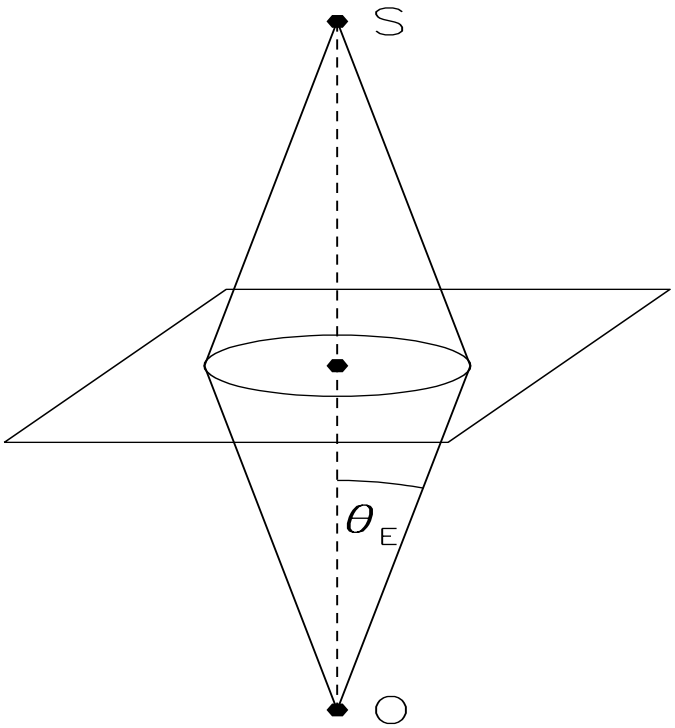

Figure 3.10: A source S on the optic axis of a circularly symmetric lens is imaged as a ring with an angular radius given by the Einstein radius $\theta_{\rm E}$. [39]

The Einstein radius provides a natural angular scale to describe the lensing geometry for several reasons. In the case of multiple imaging, the typical angular separation of images is of order $2\theta_{\rm E}$. Further, sources which are closer than about $\theta_{\rm E}$ to the optic axis experience strong lensing in the sense that they are significantly magnified, whereas sources which are located well outside the Einstein ring are magnified very little. In many lens models, the Einstein ring also represents roughly the boundary between source positions that are multiply-imaged and those that are only singly-imaged. The mean surface mass density inside the Einstein radius is the critical density $\Sigma_{\rm cr}$. [39].

For a point mass M, the Einstein radius is given by

$$\theta_{\rm E} = \left(\frac{4GM}{c^2}\,\frac{D_{\rm ds}}{D_{\rm d}D_{\rm s}}\right)^{1/2} . \tag{3.41}$$

To give two illustrative examples, we consider lensing by a star in the Galaxy, for which $M \sim M_\odot$ and $D \sim 10$ kpc, and lensing by a galaxy at a cosmological distance with $M \sim 10^{11}\, M_\odot$ and $D \sim 1$ Gpc. The corresponding Einstein radii are

$$\begin{aligned} \theta_{\rm E} &= (0.9\,{\rm mas}) \left(\frac{M}{M_\odot}\right)^{1/2} \left(\frac{D}{10\,{\rm kpc}}\right)^{-1/2}, \\ \theta_{\rm E} &= (0\farcs9) \left(\frac{M}{10^{11}\,M_\odot}\right)^{1/2} \left(\frac{D}{\rm Gpc}\right)^{-1/2}. \end{aligned} \tag{3.42}$$

Mass density profiles

Another quantity of interest is the average logarithmic slope of the three-dimensional total mass density profile $d\log\rho_{\rm tot}/d\log r \equiv -\gamma'$. An isothermal mass model has $\gamma' = 2$. The total mass density profile for a spherical model is often expressed in terms of the equivalent circular velocity

$$v_c \equiv \sqrt{\frac{GM(<r)}{r}}, \tag{3.43}$$

which facilitates comparison with the literature on spiral galaxies and on numerical simulations. For a spherical power-law density profile, γ' is simply related to the slope of the rotation curve by the relation $d\log v_c/d\log r = (2-\gamma')/2$. For this reason, an isothermal profile is sometimes referred to as a flat rotation curve. [61]

The basic result on this topic is that $\gamma' \approx 2$, i.e. early-type lens galaxies have approximately isothermal mass density profiles, or close-to-flat equivalent rotation curves. This has been known since at least the early nineties, both on the basis of lensing studies and on local kinematics. However, in order to understand the mass structure of galaxies with sufficient level of precision to constrain formation models, we need to ask more detailed questions. What is the average γ' and its intrinsic scatter for the overall population of early-type galaxies? How does γ' depend on the galactic radius or other global properties? Does it depend on the environment, as expected if halos were tidally truncated? Does γ' evolve with redshift? Determining the mass profiles of lens galaxies to high accuracy is essential for many applications to cosmography. [61]

In the past few years, the large number of lenses discovered and the high level of precision attainable with lensing has enabled substantial breakthroughs. Joint lensing and dynamical studies of the SLACS sample have shown that $\gamma' = 2.08 \pm 0.02$ with an intrinsic scatter of less than 10%. This result is valid in the sense of an average slope inside one effective radius or less, the typical size of the Einstein radius of SLACS lenses. For higher redshift deflectors, Einstein radii are typically larger than the effective radius and reach out to 5 R_e. Although the high redshift samples with measured velocity dispersions are small, they seem to suggest a somewhat larger intrinsic scatter around $\gamma' = 2$. No significant dependency on galactic radius, global galaxy parameter, or redshift has been found so far based on lensing and dynamical analysis. The small scatter around $\gamma' = 2$ is remarkable, considering that neither the DM halo, nor the stellar mass are well described by a simple power-law profile. Nevertheless, the two components add up to an isothermal profile (Fig. 3.11). This effect is similar to the disk-halo conspiracy responsible for the flat rotation curves of spiral galaxies, and it is therefore been dubbed the 'bulge-halo conspiracy'. Detailed dynamical studies of the two-dimensional velocity field of deflector galaxies in conjunction with strong gravitational lensing confirm this picture to higher accuracy. [61]

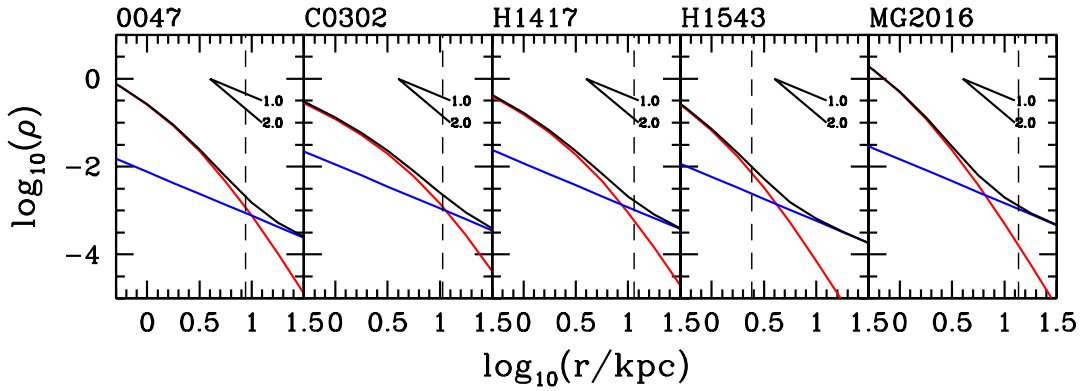

Figure 3.11: Mass density profiles of lens galaxies inferred from a strong lensing and dynamical analysis. In addition to the mass associated with the stars (red line), the data require a more extended mass component, identified as the dark matter halo (blue line). Although neither component is a simple power-law, the total mas profile is close to isothermal, i.e. $\gamma' = 2$. The vertical dashed line identifies the location of the Einstein radius. [61]

Similar and consistent results can be obtained directly from gravitational lens models, both for lensed sources covering a significant radial range or when a gravitational time delay has been measured and the cosmology is fixed by independent measurements.

The Double Einstein Ring

Given the already small optical depth for strong lensing, the lensing of multiple background sources by a single foreground galaxy is an extremely rare event. At Hubble Space Telescope (HST) resolution (FWHM $\sim 0\farcs12$) and depth ($I_{AB} \sim 27$) it is expected that one massive early-type galaxy (which dominate the lensing cross-section) in about 200 is a strong lens. Taking into account the strong dependence of the lensing cross-section on lens galaxy velocity dispersion ($\propto \sigma^4$), and the population of lens galaxies, it is estimated that about one lens galaxy in $\sim 40 - 80$ could be a double source plane strong gravitational lens.

For these reasons, at most a handful of double lenses are to be found in the largest spectroscopic surveys of early-type galaxies such as the luminous red galaxies of the Sloan Digital Sky Survey. However, future high resolution imaging surveys will increase the number of known lenses by 2-3 orders of magnitude, and hence should be able to provide large statistical samples of double source plane gravitational lenses, opening up the possibility of qualitatively new applications of gravitational lensing for the study of galaxy formation and cosmography.

The discovery of the first double source plane partial Einstein Ring was reported in 2008 [18]. The gravitational lens system SDSSJ0946+1006, was discovered as part of the Sloan Lens ACS (SLACS) Survey. The object was first selected by the presence of multiple emission lines at higher redshift in the residuals of an absorption line spectrum from the SDSS database as described by and then confirmed as a strong lens by high resolution imaging with the Advanced Camera for Surveys aboard HST. In addition to an Einstein ring due to the source (source 1) responsible for the emission lines detected in the SDSS spectrum, the Hubble image also shows a second multiply imaged system forming a broken Einstein Ring with a larger diameter then the inner ring (source 2). This configuration can only arise if the two lensed systems are at different redshifts and well aligned with the center of the lensing galaxy. [18]

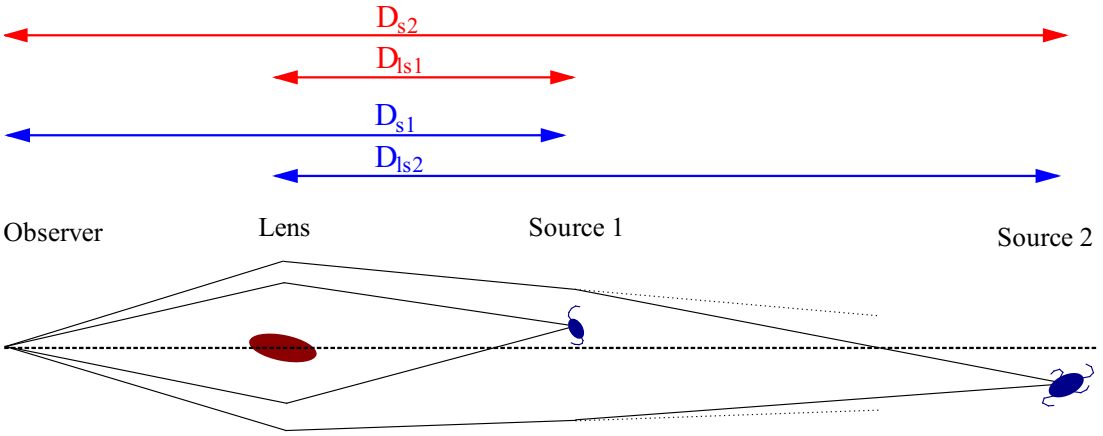

Figure 3.12: Sketch of a double source plane lens system. The cosmological scaling factor β is the product of $D_{\rm ls1}$ and $D_{\rm s2}$ (both in red) divided by the product of $D_{\rm ls2}$ and $D_{\rm s1}$ (both in blue). For a singular isothermal sphere, where the first source has no mass, β is the ratio of Einstein radii. Figure from [9].

Two concentric partial ring-like structures are clearly seen at radii $1.43 \pm 0.01''$ and $2.07 \pm 0.02''$ from the center of the lens galaxy. Such a peculiar lensing configuration – with widely different image separations of nearly concentric multiple image systems – implies that the rings come from two sources at different redshift, the innermost (Ring 1) corresponding to the nearest background source 1 and the outermost (Ring 2) being significantly further away along the optical axis. [18]

This was the first report of the discovery of the first galaxy-scale double lensing event made of a foreground lens galaxy at redshift $z_{\rm L} = 0.222$, a first source at redshift $z_{\rm s1} = 0.609$ (Ring 1) and a more distant source (Ring 2) with unknown redshift, despite an attempt to measure its redshift with deep optical spectroscopy using LRIS on the Keck I Telescope. The detection of Ring 2 in a single orbit HST-ACS F814W filter image, sets an upper limit to its redshift $z_{\rm s2} < 6.9$. [18]

Modeling the geometry of the lensed features at different source planes allowed determination of the mass density profile of the lens galaxy which was found to be close to isothermal. The best fit lens model predicts a stellar velocity dispersion in very good agreement with that measured from SDSS spectroscopy. The model requires a relatively large amount of dark matter inside the effective radius $f_{\rm DM,2D}(< R_{\rm eff}) \simeq 73 \pm 9\%$ (corresponding to a projected total mass-to-light ratio $M/L_V = 11.54 \pm 0.13\, h_{70}\ (M/L_V)_{\odot}$). Along with the complex isophotes of the lens galaxy and the presence of several other (less luminous) galaxies at similar photometric redshifts, the high dark matter fraction suggests that the lens may be the central galaxy of a group scale halo. The high precision of this measurement – far superior to that attainable from a single multiply imaged systems – demonstrates that double source plane lenses are extremely valuable tools to study the mass profile of galaxies and groups.

In this system, the presence of two multiply-imaged sources at different redshifts constrains the projected mass density slope to be $\gamma' = 2.00 \pm 0.03$, based purely on lens modeling. The lack of central images also constrains the slope of the total density profile to be steep (e.g.,

$\gamma' = 2$) in the central regions of deflectors. It should be noted that lensing is mostly sensitive to the projected mass density slope at the location of the images, rather than the average inside the images. Therefore, a direct comparison with the lensing and dynamical results is only valid to the extent that a pure power-law profile is a good model for the data.[61]

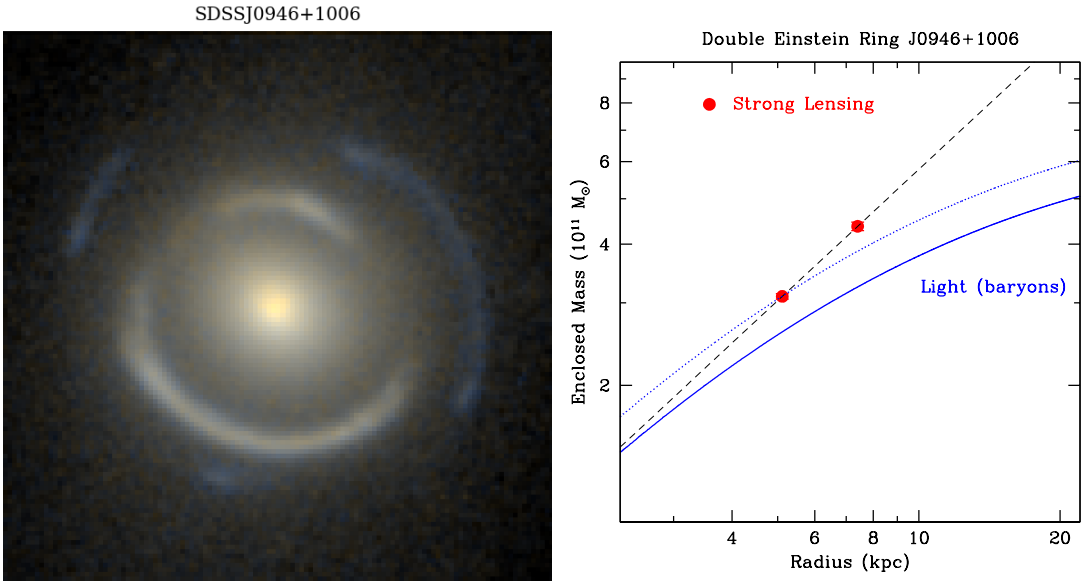

Figure 3.13: Double Einstein ring compound lens SDSSJ0946+1006. **Left:** color composite HST image. Note the foreground main deflector in the center, the bright ring formed by the images of the intermediate galaxy, and the fainter ring formed by the images of the background galaxy lensed by the two intervening objects. **Right:** Enclosed mass profile as inferred from the Einstein radii of the two rings (red solid points - the error bars are smaller than the points). The enclosed mass increases more steeply with radius than the enclosed light (solid blue line; rescaled by the best fit stellar mass-to-light ratio), indicating the presence of a more extended dark matter component. Even a "maximum bulge" solution (dotted blue line) cannot account for the mass at the outer Einstein radius. [61]

In a further study of J0946, this interesting system was used to determine cosmological parameters [9]. The authors present constraints on the equation of state of dark energy, w, and the total matter density, $\Omega_{\rm M}$, derived from SDSSJ0946+1006, the first cosmological measurement with a galaxy-scale double-source-plane lens. By modeling the primary lens with an elliptical power-law mass distribution, and including perturbative lensing by the first source, they were able to constrain the cosmological scaling factor in this system to be $\beta^{-1} = 1.404 \pm 0.016$, which implies $\Omega_{\rm M} = 0.33^{+0.33}_{-0.26}$ for a flat ΛCDM cosmology. Combining with a CMB prior from Planck, they found that $w = -1.17^{+0.20}_{-0.21}$ assuming a flat wCDM cosmology. This inference shifts the posterior by 1σ and improves the precision by 30 per cent with respect to Planck alone, and demonstrates the utility of combining simple, galaxy-scale multiple-source-plane lenses with other cosmological probes to improve precision and test for residual systematic biases.

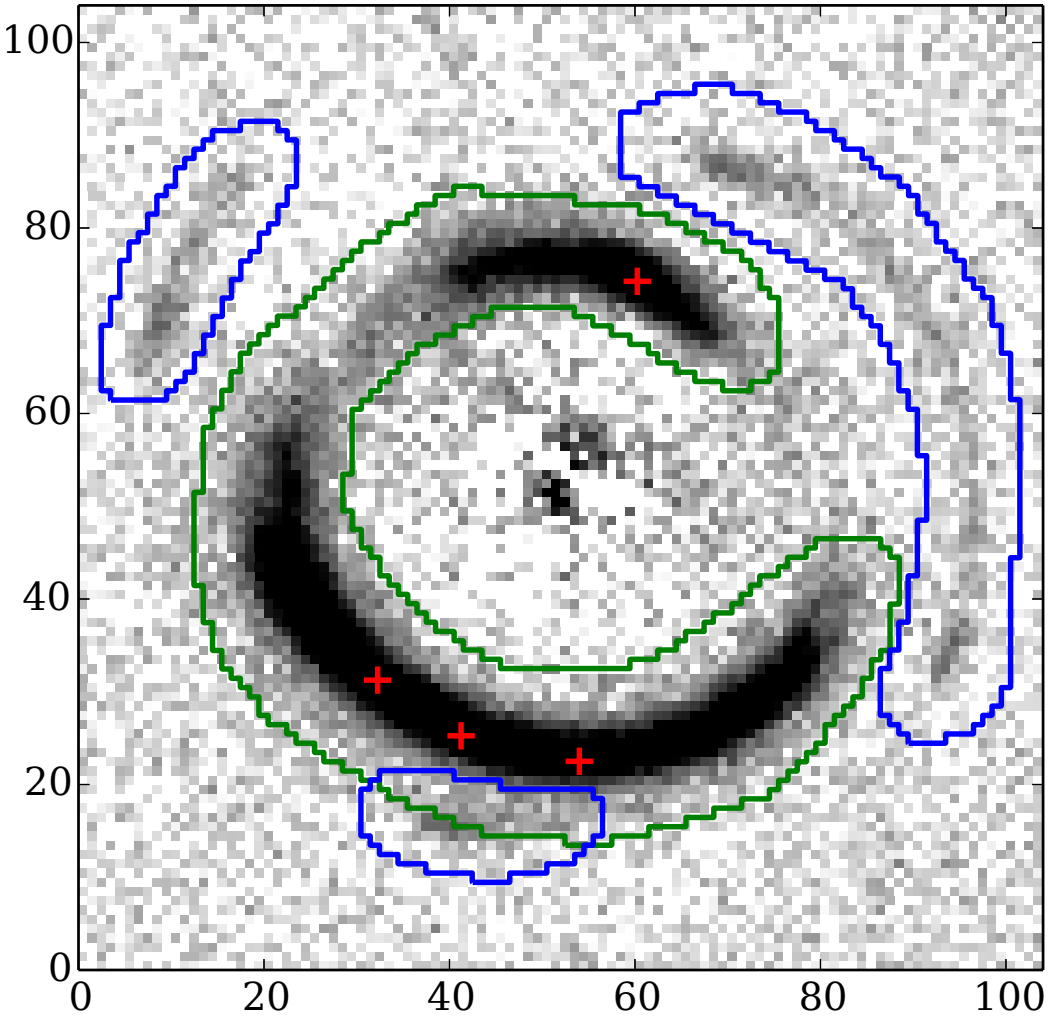

Figure 3.14: The galaxy-subtracted *HST* F814W image of SDSSJ0946+1006. The first source is modeled as only contributing to the flux observed within the green mask, and the second source is assumed to only have non-zero flux within the blue mask. The red crosses mark the 4 pixels which we map back on to the first lens plane and use to determine the centroid of the first source's mass. Figure from [9].

This is the first derivation of cosmological constraints from a galaxy-scale double-source-plane lens (DSPL). The measurement of β is completely independent of other cosmological probes, and can easily be combined with other datasets to produce tighter cosmological parameter estimates, lift parameter degeneracies, and test for the presence of unknown systematics. Because of the complementarity of DSPLs with the CMB, the measurement with just a single DSPL improves the precision of the inference on w by approximately one third. More precise inferences have been made by combining the CMB with, e.g., baryon acoustic oscillation (BAO) measurements (combining Planck with the BAO results from yields $w = -1.12^{+0.10}_{-0.11}$), but we

note that the number of DSPLs that will be useful for cosmological inference will increase by orders of magnitude with Euclid, dramatically improving the precision but also helping to uncover systematic biases. For example, combining Planck with *either* J0946 or BAO measurements causes the inference on w to shift closer to -1 by around 1σ. [9]

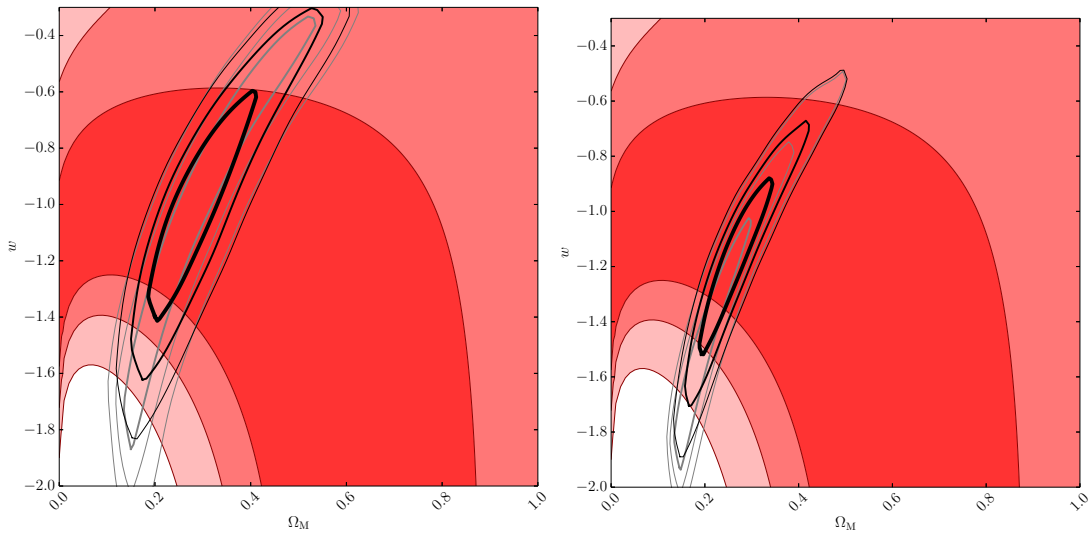

Figure 3.15: The w and $\Omega_{\rm M}$ plane. Red shows the 68, 95 and 99.7 per cent confidence constraints derived from our measurement of the cosmological scale factor in J0946. In the left, panel grey shows the WMAP9 constraints whilst the Planck 2013 constraints are shown on the right. In both panels, black shows the combined constraint from J0946 and the CMB prior. Figure from [9].

The lens model that they presented is robustly constrained, but the inference on β depends on the assumption that the observed lensing is entirely due to an elliptical power-law mass distribution at $z = 0.222$ and an isothermal mass distribution at $z = 0.609$. The latter point is not a significant concern here, since the highest redshift source has an impact parameter with respect to the $z = 0.609$ source that is more than three times larger than the Einstein radius $\theta^{\rm E}_{\rm s1}$. Similarly, the power-law description for the central total mass density distribution is motivated by the absence of any correlation between the power-law indices and radii of strong lenses, as well as the power-law behavior of the total mass distribution over a large range of scales from the ensemble weak lensing mass profile of lenses and mass profiles of massive X-ray-bright galaxies. [9]

Although multiple-source-plane lenses largely break this degeneracy for true mass sheets, it has been shown that a ring of mass (in addition to the mass from the power-law model) between the Einstein radii of the two sources can mimic the mass-sheet degeneracy even for multiple-source-plane lenses. However, it is not clear what physical process would be responsible for significant ring-like projected over- (or under-) densities and we therefore neglect this possibility. Lensing by line-of-sight structures is also not included in our model, and if these objects introduce a positive external convergence then our estimate of β will be low. The authors estimate that ignoring the external convergence results in a ~ 1 per cent systematic uncertainty on β (i.e., comparable to the statistical uncertainty) which would degrade the precision of our

inference on w by ≈ 25 per cent. However, directly modeling the line of sight using the existing SDSS and *HST* imaging and including the velocity dispersion profile will significantly decrease this systematic uncertainty. Furthermore, modeling the strong lensing with all of the available *HST* data will reduce our statistical uncertainty while allowing us to further test for residual systematics by comparing our inference on β between the different *HST* filters. [9]

Although there is still room for improvement of the measurement of β for J0946, the most significant obstacle for DSPL cosmological constraints is the scarcity of simple multiple-source-plane lenses. It is suggested [18] that one in $40 - 80$ galaxy-scale strong lenses should be a DSPL, and tentative Euclid forecasts of ~ 100000 galaxy-galaxy strong lenses, this analysis of J0946 demonstrates the significant degeneracy-breaking power of even a single DSPL.

Details of Image Formation

It is possible to classify the images in a simple way. We distinguish two kinds of images: *ordinary* and *critical* ones. Ordinary images occur at the points where the lens equation is verified and where the amplification is finite. On the contrary, for some critical points the lens mapping is not invertible and the amplification is infinite. These points form on the lens plane closed curves, named *critical curves*, and if we map them to the source plane we get other closed curves, named *caustics*. We can distinguish two kinds of critical curves: radial and tangential ones, but the second ones are crucial in our case to analyze the formation of images. Limiting the attention to the case of a single lens: for *spherical mass distribution* the critical curves are circular, the tangential caustic is point-like and the radial one is circular, in this case, in addition to a central image, two images form; for *elliptical mass distribution* the critical curves are not circular, the tangential caustic becomes an astroid with folds and cuspids (see Fig. 3.16) and in addition to an eventual central image, we can have 2 or 4 images. [60]

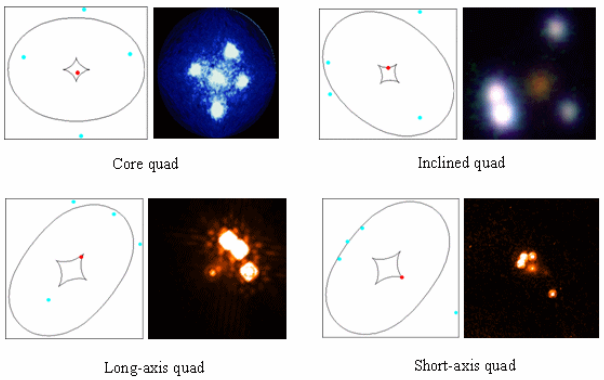

Figure 3.16: Image configurations in quadruply lensed events. For the double quasars, there are two possible configurations not shown here. [60]

In particular, when a source approaches the astroid from the inner side, two images fuse and disappear, thus passing from a 4-images to a 2-images configuration. In typical lensing events, when the source is near a fold, we observe two nearby images, one on a side of the critical curves and another to the other side (see inclined quad in Fig. 3.16), on the contrary, when the source is near a cusp, 3 images form near the critical curves (see lower panels in Fig. 3.16). These images are magnified respect to the other ones, as can be easily verified in real cases by

an inspections of the quasars in Fig. 3.16. More complex configurations with a higher number of images are possible when more than one lens are considered. [60]

Circularly Symmetric Lenses

Figures 3.17 and 3.18 show typical image configurations. The right halves of the figures display the source plane, and the left halves show the image configuration in the lens plane. Since $\mathcal{A}$ is a 2×2 matrix, a typical circularly symmetric lens has two critical lines where $\det \mathcal{A}$ vanishes, and two corresponding caustics in the source plane. The caustic of the inner critical curve is a circle while the caustic of the outer critical curve degenerates to a critical point because of the circular symmetry of the lens. A source which is located outside the outermost caustic has a single image. Upon each caustic crossing, the image number changes by two, indicated by the numbers in Fig. 3.17. The source shown as a small rectangle in the right panel of Fig. 3.17 has three images as indicated in the left panel. Of the three image, the innermost one is usually very faint; in fact, this image vanishes if the lens has a singular core (the curvature of the time delay function then becomes infinite) as in the point mass or the singular isothermal sphere. [39]

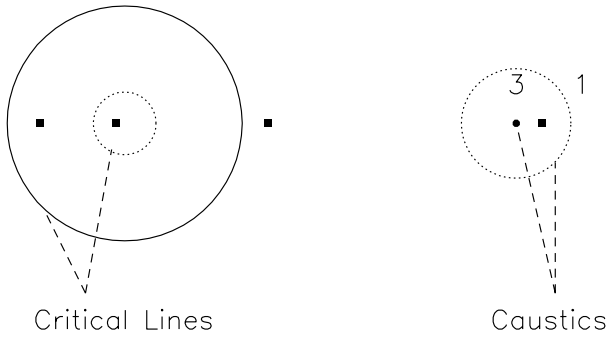

Figure 3.17: Imaging of a point source by a non-singular, circularly-symmetric lens. Left: image positions and critical lines; right: source position and corresponding caustics. [39]

Figure 3.18 shows the images of two extended sources lensed by the same model as in Fig. 3.17. One source is located close to the point-like caustic in the center of the lens. It is imaged onto the two long, tangentially oriented arcs close to the outer critical curve and the very faint image at the lens center. The other source is located on the outer caustic and forms a radially elongated image which is composed of two merging images, and a third tangentially oriented

image outside the outer caustic. Because of the image properties, the outer critical curve is called *tangential*, and the inner critical curve is called *radial*. [39]

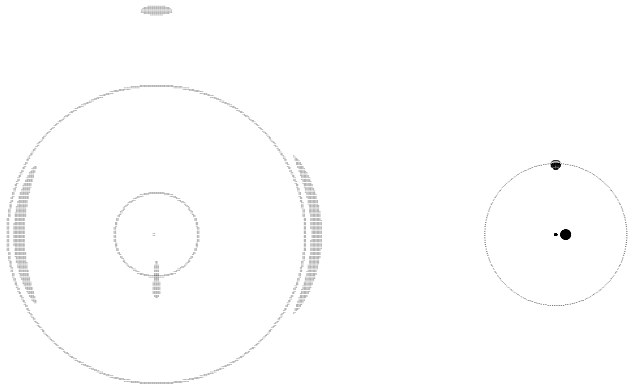

Figure 3.18: Imaging of an extended source by a non-singular circularly-symmetric lens. A source close to the point caustic at the lens center produces two tangentially oriented arc-like images close to the outer critical curve, and a faint image at the lens center. A source on the outer caustic produces a radially elongated image on the inner critical curve, and a tangentially oriented image outside the outer critical curve. Because of these image properties, the outer and inner critical curves are called *tangential* and *radial*, respectively.
[39].

Non-circular Lenses

A circularly symmetric lens model is much too idealized and is unlikely to describe real galaxies. Therefore, considerable work has gone into developing non-circularly symmetric models. The breaking of the symmetry leads to qualitatively new image configurations. [39]

Elliptical Galaxy Model

To describe an elliptical galaxy lens, we should ideally consider elliptical isodensity contours. A straightforward generalization of the isothermal sphere with finite core gives

$$\Sigma(\theta_1, \theta_2) = \frac{\Sigma_0}{[\theta_c^2 + (1-\epsilon)\theta_1^2 + (1+\epsilon)\theta_2^2]^{1/2}} \ , \tag{3.44}$$

where θ_1, θ_2 are orthogonal coordinates along the major and minor axes of the lens measured from the center. The potential $\psi(\theta_1, \theta_2)$ corresponding to this density distribution has been

calculated but is somewhat complicated. For the specific case when the core radius θ_c vanishes, the deflection angle and the magnification take on a simple form:

$$\alpha_1 = \frac{8\pi G\Sigma_0}{\sqrt{2\epsilon}c^2}\tan^{-1}\left[\frac{\sqrt{2\epsilon}\cos\phi}{(1-\epsilon\cos 2\phi)^{1/2}}\right] ,$$
$$\alpha_2 = \frac{8\pi G\Sigma_0}{\sqrt{2\epsilon}c^2}\tanh^{-1}\left[\frac{\sqrt{2\epsilon}\sin\phi}{(1-\epsilon\cos 2\phi)^{1/2}}\right] ,$$
$$\mu^{-1} = 1 - \frac{8\pi G\Sigma_0}{c^2(\theta_1^2+\theta_2^2)^{1/2}(1-\epsilon\cos 2\phi)^{1/2}} , \tag{3.45}$$

where ϕ is the polar angle corresponding to the vector position $\vec{\theta} \equiv (\theta_1, \theta_2)$.

Instead of the elliptical density model, it is simpler and often sufficient to model a galaxy by means of an elliptical effective lensing potential [39]

$$\psi(\theta_1,\theta_2) = \frac{D_{ds}}{D_s}\,4\pi\frac{\sigma_v^2}{c^2}\left[\theta_c^2 + (1-\epsilon)\theta_1^2 + (1+\epsilon)\theta_2^2\right]^{1/2} , \tag{3.46}$$

where ϵ measures the ellipticity. The deflection law and magnification tensor corresponding to this potential can be calculated. When ϵ is large, the elliptical potential model is inaccurate because it gives rise to dumbbell-shaped isodensity contours, but for small ϵ, it is a perfectly viable lens model. [39]

External Shear

The environment of a galaxy, including any cluster surrounding the primary lens, will in general contribute both convergence and shear. The effective potential due to the local environment then reads

$$\psi(\theta_1,\theta_2) = \frac{\kappa}{2}(\theta_1^2+\theta_2^2) + \frac{\gamma}{2}(\theta_1^2-\theta_2^2) \tag{3.47}$$

in the principal axes system of the external shear, where the convergence κ and shear γ are locally independent of $\vec{\theta}$. An external shear breaks the circular symmetry of a lens and therefore it often has the same effect as introducing ellipticity in the lens. It is frequently possible to model the same system either with an elliptical potential or with a circular potential plus an external shear. [39]

Image Configurations with a Non-Circularly Symmetric Lens

In contrast to the circularly symmetric case, for a non-circular lens the source, lens and images are not restricted to lie on a line. Therefore, it is not possible to analyze the problem via sections of the time delay surface. Fermat's principle and the time delay function are still very useful but it is necessary to visualize the full two-dimensional surface $t(\vec{\theta})$.

Figure 3.19 illustrates the wide variety of image configurations produced by an elliptical galaxy lens (or a circularly symmetric lens with external shear). In each panel, the source plane with caustics is shown on the right, and the image configurations together with the critical curves are shown on the left. Compared to the circularly symmetric case, the first notable difference introduced by ellipticity is that the central caustic which was point-like is now expanded into a diamond shape; it is referred to as the *astroid* caustic (also tangential caustic). Figure 3.19 shows the images of a compact source moving away from the lens center along a symmetry line (right panel) and a line bisecting the two symmetry directions (left panel). A source behind

the center of the lens has five images because it is enclosed by two caustics. One image appears at the lens center, and the four others form a cross-shaped pattern. When the source is moved outward, two of the four outer images move toward each other, merge, and disappear as the source approaches and then crosses the astroid (or tangential) caustic. Three images remain until the source crosses the radial caustic, when two more images merge and disappear at the radial critical curve. A single weakly distorted image is finally left when the source has crossed the outer caustic. When the source moves toward a cusp point (right panel of Figure 3.19), three images merge to form a single image. All the image configurations shown in Figure 3.19 are exhibited by various observed cases of lensing of QSOs and radio quasars. [39]

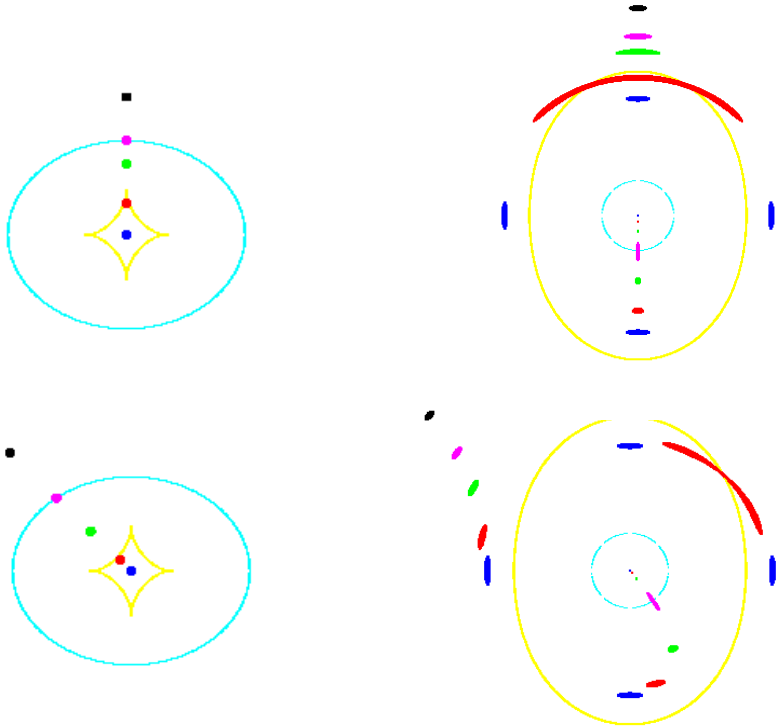

Figure 3.19: The caustic and critical lines of an elliptical lens. The left and right panels describe the caustic and the critical curves respectively. The upper panels show the relationship between source positions and the shapes of images around the cusp. Lower panels are the same but around the fold. [19] and [17].

Classification of Gravitational Lensing

Gravitational lensing is usually considered in one of several categories, or regimes, based on the nature of the observed effects. Strong gravitational lensing occurs when a single source is seen as several images. In addition to the source itself, there are usually two or four additional images. These distortions are easily visible as dramatic effects which also includes high magnification, luminous arcs, and sometimes a complete 'Einstein Ring'.

In weak lensing, the distortions of the background sources are much smaller and are therefore

detected by statistical analysis of large numbers of sources. In these cases, the center of the lens is further away from the observer's line of sight, to $\Theta \gg \Theta_E$. The orientations can be averaged to measure the shear of the lensing field. The shear can then be used to reconstruct the mass distribution in the area, particularly the background distribution of dark matter. Weak lensing is more common than strong lensing.

In microlensing, there is no change in shape of the image, but the amount of light received changes over time. Unlike macrolensing and millilensing, microlensing is a transient effect such that it is observable through monitoring a source for a period of time and recording its light curve. The apparent brightness of the source varies over time as the alignment of the lens system changes due to the moving lens.

Last, is the category referred to as millilensing. Millilensing (sometimes called mesolensing) effects, may be produced by satellite galaxies or their dark counterparts, dark matter subhalos, as well as small-scale objects such as intermediate-mass black holes, with typical multiple image separations in the order of milliarcseconds. Therefore, lensing effects in this regime potentially address one of the small-scale issues of the CDM theory, the so-called "missing satellites problem" which is discussed below, in the section on Dark Matter substructure [1].

Measurement of gravitational lensing in clusters is usually limited to strong and weak lensing. Strong lensing produces drastic lensing events with highly elongated arcs or multiple images of background objects. Weak lensing uses statistical measurements of small distortions in the shapes of background galaxies produced by a massive, foreground cluster. Weak lensing studies of low-redshift clusters provides us with a good opportunity to detect and measure smaller subhalo masses in clusters [46].

Since strong and weak lensing probe mass distributions at different radii, the combination of these two is powerful and essential for the full understanding and detailed mapping of the gravitational potential of clusters. While the combined strong and weak lensing analysis allows accurate and robust measurements of the concentration parameter, the current main limitation is the small number of clusters available for such a detailed combined analysis [44]. Umetsu and colleagues have developed a precise cluster mass profile which is averaged from combined strong and weak lensing data [62]. They outline their methods for obtaining high precision mass profiles, combining independent weak-lensing distortion, magnification, and strong-lensing measurements. For massive clusters the strong and weak lensing regimes contribute equal logarithmic coverage of the radial profile. The utility of high-quality data is limited by the cosmic noise from large scale structure along the line of sight. This noise is overcome when stacking clusters, as too are the effects of cluster asphericity and substructure, permitting a stringent test of theoretical models. This technique combines all possible lensing information available in the cluster regime. This study concentrates on those clusters for which high-quality data is available in both regimes.

Umetsu and coworkers have developed a method for improving the statistical precision of cluster mass profiles, combining independent weak-lensing distortion, magnification, and strong-lensing measurements. This extends recent weak-lensing work by to include the central strong-lensing information in a stacking analysis, for full radial coverage. This exciting methods takes into account the cosmic covariance from uncorrelated large scale structure projected along the line of sigt, as well as the effect of different cluster redshifts, so that error propagation in terms of lensing efficiency of individual clusters can be properly averaged.

The technique of stacked lensing analysis can be used to combine strong and weak lensing data, and can also be applied to weak lensing alone. This is discussed below, in the discussion of analyzing the effects of dark matter on the density profile, as analyzed by gravitational lensing.

3.4 Strong Gravitational Lensing

Three properties make strong gravitational lensing useful to measure and understand the universe. Firstly, strong lensing observables - such as relative positions, flux ratios, and time delays between multiple images - depend on the gravitational potential of the foreground galaxy (lens or deflector) and its derivatives. Secondly, the lensing observables also depend on the overall geometry of the universe via angular diameter distances between observer, deflector, and source. Thirdly, the background source often appears magnified to the observer, sometimes by more than an order of magnitude. As a result, gravitational lensing can be used to address three major astrophysical issues: i) understanding the spatial distribution of mass at kpc and sub-kpc scale where baryons and DM interact to shape galaxies as we see them; ii) determining the overall geometry, content, and kinematics of the universe; iii) studying galaxies, black holes, and active nuclei that are too small or too faint to be resolved or detected with current instrumentation. [61].

Discovery of Strong Gravitational Lenses

There are three key steps that must be taken to confirm the lensing hypothesis and study a sample in detail: a redshift measurement for the lens (typically from optical spectroscopy); a distinct redshift for the background source (typically from radio or (sub-)mm wave spectroscopy); and spatially-resolved imaging of the source that is consistent with strong lensing [8]

The strong lensing applications described in the literature span a broad range of astrophysical phenomena, observational, and theoretical challenges. However, they all share a common limitation: the relatively small number of systems to which they can be applied. Although there are 200 systems known, they are not all suitable for all applications. Studies must rely on at most a few tens of cases to infer results of general interest.

Fortunately, a number of large surveys are expected to take place in the next decade, providing an ideal dataset to mine for rare objects such as strong lenses. The challenge will consist in developing fast and robust algorithms to find new lenses, and then in mustering the resources needed to study them.

Imaging-based searches

Imaging-based searches can be divided into catalog-based and pixel-based. Catalog-based searches look for objects in a lensing-like configuration. They are most effective at detecting sharp multiply-imaged features such as multiply-imaged quasars, but they can also be used for extended sources, provided the image separation is large enough for deblending. Pixel-based searches start from a set of pixels, and look for lensing-like configurations. Lenses are identified on the basis of characteristic geometries or by actually modeling every system as a possible lens. The pixel-based method is slower and more computationally intensive than catalog-based searches, but in principle can be used to push the detection limit to smaller angular separations, beyond the level where source and deflector can be deblended by general-purpose cataloging softwares. Visual searches can be considered as pixel-based, with the human brain as lens-modeling tool. Algorithms need to be adjusted to reach an optimal balance between completeness (false negative) and purity (false positive) appropriate for each dataset and scientific goal. The best algorithms can currently achieve 90% completeness and purity searching through HST data. Although some human intervention is still necessary, this breakthrough makes it feasible to search through future surveys of 1000 $\deg^2$ or more. [61]

Time-domain surveys allow for a different image-based strategy: looking for variable resolved sources. At high galactic latitude, lensed quasars are more common than contaminants such as pairs of variable stars. Pairs of non-lensed quasars can be distinguished on the basis of their light curves and colors, while lensed supernovae are a welcome contaminant. A first application of the method to the SDSS Supernovae survey data show that the only known compelling lens candidate is recovered as a close pair of variable sources. Out of over 20,000 sources, only a handful of false positives are found, suggesting a "purity" of ∼20%. This is encouraging, although more tests on wider and deeper data are needed to further improve the method in view of upcoming surveys. [61]

Spectroscopy-based searches

Spectroscopic searches rely on identifying composite spectra with features coming from multiple redshifts. Follow-up high resolution information is then needed to identify the subset of events with detectable multiple-images, and to obtain astrometry for lens modeling. A strong advantage of the method is that lenses come with redshifts by construction. After the early serendipitous discoveries, the method started to bear large numbers of lenses only with the SDSS spectroscopic database. The recent searches highlight the quality of spectroscopic data as the key element for success. High signal-to-noise ratios are needed to identify faint spectral features, close-to Poisson limited sky subtraction is needed to reduce false positives, spectral resolution better than 100 $\mathrm{km\,s^{-1}}$ is need to resolve line multiplets, and wide wavelength coverage increases the redshift range for the search. It is a testament to the high quality of the SDSS database that the confirmation rate is $\sim 60-70$ %, after a very strict initial selection (approximately 1/1000 SDSS galaxies are selected as a candidate for follow-up by SLACS). [61]

Time Delays

Refsdal [51] pointed out that if the background source is variable, it is possible to measure an absolute distance within the system and therefore the Hubble constant. Consider the light paths from the source to the observer corresponding to the individual lensed images. Although each is at a stationary point in the Fermat time delay surface, the absolute light travel time for each will generally be different, with one of the Fermat minima having the smallest travel time. Therefore, if the source brightens, this brightening will reach the observer at different times corresponding to the two different light paths. Measurement of the time delay corresponds to measuring the difference in the light travel times, each of which is individually given by [24]:

$$\tau = \frac{D_\mathrm{l} D_\mathrm{s}}{c D_\mathrm{ls}} (1+z_\mathrm{l}) \left(\frac{1}{2}(\theta-\beta)^2 + \psi(\theta) \right), \tag{3.48}$$

where α, β and θ are angles defined above in Figure 3.2, D_l, D_s and D_ls are angular diameter distances also defined in Figure 3.2, z_l is the lens redshift, and $\psi(\theta)$ is a term representing the Shapiro delay of light passing through a gravitational field. Fermat's principle corresponds to the requirement that $\nabla\tau = 0$. Once the differential time delays are known, we then calculate the ratio of angular diameter distances which appears in the above equation. If the source and lens redshifts are known, H_0 follows immediately. From this equation, we can derive a useful rule for the case of a 2-image lens, if we make the assumption that the matter distribution is

isothermal [1] and $H_0 = 70$ km s^{-1} Mpc^{-1}, is

$$\Delta\tau = (14 \text{ days})(1 + z_l)Ds^2 \left(\frac{f-1}{f+1}\right), \tag{3.49}$$

where z_l is the lens redshift, s is the separation of the images (approximately twice the Einstein radius), $f > 1$ is the ratio of the fluxes and D is the value of $D_s D_l / D_{ls}$ in Gpc. A larger time delay implies a correspondingly lower H_0. [24]

The first gravitational lens was discovered in 1979 and monitoring programs began soon afterwards to determine the time delay. This turned out to be a long process involving a dispute between proponents of a $\sim 400-$day and a $\sim 550-$day delay, and ended with a determination of 417 ± 2 days. Since that time, at least 17 more time delays have been determined (see Table 3.1). In the early days, many time delays were measured at radio wavelengths by studying systems in which a radio-loud quasar was the multiply imaged source. Recently, optically-measured delays have dominated, due to the fact that only a small optical telescope in a site with good seeing is needed for the photometric monitoring, whereas radio time delays require large amounts of time on long-baseline interferometers which do not commonly exist. [24].

Table 3.1 shows the currently measured time delays, of a number of systems. Since the most recent review an extra half-dozen have been added, and there is every reason to suppose that the sample will continue to grow at a similar rate. The person who wants to measure time delays is faced with a dilemma, in terms of whether to justify the proposal in terms of measuring H_0, given the previously mentioned problems with mass modeling, or in terms of determining mass models by assuming $H_0 = 71$ km s^{-1} Mpc^{-1} (or whatever). From [24].

Consider a galaxy lensing a time-variable source like a quasar or a supernova. Under the thin lens approximation, multiple images will be observed to vary with a delay which depends on the gravitational potential as well on a ratio of angular diameter distance. The ratio of angular diameter distances is mostly sensitive to the Hubble Constant H_0 (hereafter h in units of 100 km s^{-1}Mpc^{-1}). However, time delays also contain non-negligible information about other cosmological parameters, especially if one considers a sample of deflectors and sources spanning a range of redshifts. Therefore, although it is convenient to think in terms of the Hubble constant as the primary parameter, time-delays provide constraints in the multidimensional cosmological parameter space. When combined with other cosmology probes like the CMB power spectrum, time-delays are very effective at breaking degeneracies such as that between H_0 and w [61].

From a practical point of view, cosmography with time-delays can be broken into two separate problems: measuring time delays and modeling the lensing potential, including matter along the line of sight. Uncertainties in these two terms dominate the error budget and they are independent. Therefore, in order to measure H_0 to 1% accuracy from one lens system one needs to know both quantities with sub percent accuracy. Or, for a sample of N lenses, one needs unbiased measurements with approximately half $\sqrt{N}\%$ uncertainty on both quantities [61].

Measuring time delays

Measuring time delays requires properly sampled light curves of duration significantly longer than the time-delay between multiple images. Once an approximate time-delay is known, the measurement can generally be refined by adapting the monitoring strategy, e.g. with dense sampling triggered after an event on the leading image. Typical time delays for galaxy lens

[1] An isothermal model is one in which the projected surface mass density decreases as $1/r$. An isothermal galaxy will have a flat rotation curve, as is observed in many galaxies.

Lens system	Time delay [days]
CLASS 0218+357	10.5 ± 0.2
HE 0435-1-223	$14.4^{+0.8}_{-0.9}$ (AD)
SBS 0909+532	45^{+1}_{-11} (2σ)
RX 0911+0551	146 ± 4
FBQ 0951+2635	16 ± 2
Q 0957+561	417 ± 3
SDSS 1004+4112	38.4 ± 2.0 (AB)
HE 1104–185	161 ± 7
PG 1115+080	23.7 ± 3.4 (BC)
	9.4 ± 3.4 (AC)
RX 1131–1231	$12.0^{+1.5}_{-1.3}$ (AB)
	$9.6^{+2.0}_{-1.6}$ (AC)
	87 ± 8 (AD)
CLASS 1422+231	8.2 ± 2.0 (BC)
	7.6 ± 2.5 (AC)
SBS 1520+530	130 ± 3
CLASS 1600+434	51 ± 2
	47^{+5}_{-6}
CLASS 1608+656	31.5^{+2}_{-1} (AB)
	36^{+1}_{-2} (BC)
	77^{+2}_{-1} (BD)
SDSS 1650+4251	49.5 ± 1.9
PKS 1830–211	26^{+4}_{-5}
HE 2149–2745	103 ± 12
Q 2237+0305	$2.7^{+0.5}_{-0.9}$ h

Table 3.1: Time delays, with 1-σ errors, from the literature. In some cases multiple delays have been measured in 4-image lens systems, and in this case each delay is given separately for the two components in brackets. From [24]

systems are in the range weeks to months (with tails on both ends out to hours to years) and minimum detectable amplitudes from the ground are of order ∼5%, limited by photometric accuracy for crowded sources and microlensing. Thus, accurate time-delays typically require several seasons of dedicated monitoring effort.

After the first "heroic" campaigns of the nineties and early 2000, which yielded of order 10 time-delays, several groups are now trying to take this effort to the next level with the help of queue mode scheduling and robotic telescopes. A recent summary of published time-delay measurements is given by [24]. Taking the published time-delay uncertainties at face value, the present sample contributes to the error budget on H_0 a little less than 1%. Time-domain astronomy is a rapidly growing field and it is likely that many of the logistical problems faced by time-delay hunters so far will be solved in the next decade. [61]

Lens Statistics

The abundance of galaxy lenses has often been used for constraining the cosmological constant Λ. While early studies typically found *upper* limits of $\Lambda \lesssim 0.7$, more recent investigations find values which are better compatible with other determinations, finding spatially-flat model universes with low matter density ($\Omega_0 \simeq 0.3$) preferred. The reason for this change is that gradually more realistic galaxy luminosity functions were used for estimating the expected number of lenses, rather than error-prone extrapolations of local galaxy number densities towards high redshift [2].

The Sloan Digital Sky Survey has allowed the definition of a homogeneously selected quasar sample from which cosmological parameters were derived. Assuming a spatially flat universe, a value of $\Omega_{\Lambda 0} = 0.74^{+0.17}_{-0.16}$ was derived for the cosmological constant, where statistical and systematic errors were combined in quadrature. Allowing a free equation-of-state parameter gave $w = -1.1^{+0.67}_{-0.78}$ and a matter-density parameter of $\Omega_{\mathrm{m}0} = 0.26 \pm 0.08$ when combined with independent cosmological constraints.

Halos are expected to have a continuous mass spectrum in universes dominated by cold dark matter, which is described by mass functions. Thus, one would expect a continuous distribution of splitting angles between fractions of an arc second to several ten arc seconds. The observed image-splitting distribution was studied to determine if it was consistent with expectations from CDM. Observation and theory agreed if selection effects were taken into account. Others found that the splitting-angle distribution in CDM is grossly incompatible with microwave-background constraints in a model universe with high matter density and vanishing cosmological constant, but that both could be comfortably reconciled in a spatially-flat, low-density CDM model. [2]

Occasionally, therefore, lens systems should be detected with splitting angles of ten or more arc seconds. Some have interpreted the absence of wide-separation lenses in the CLASS survey as being due to low central mass concentrations in group- and cluster-sized halos. It was perceived as a further confirmation of the CDM paradigm when a quadruply imaged quasar was detected in the Sloan Digital Sky Survey with a splitting angle of 14.62 arc seconds, for which others derived a lens mass of $(5 \pm 1) \times 10^{13}\, h^{-1}\, M_\odot$ within a radius of $100\, h^{-1}$ kpc based on a non-parametric lens model. The triaxiality of CDM halos must be taken into account in probability and mass estimates for the formation of wide-separation lens systems, which is familiar from other studies of strong lensing in galaxy clusters. [2]

Clearly, cosmological parameters from the statistics of strong gravitational lensing by galaxies are generally no longer competitive compared to those based on observations of the cosmic microwave background because the uncertainties in lens models and sample selection are considerable. It should be kept in mind, however, that the cosmic microwave background does not independently measure the Hubble constant, but the expansion rate during the time of

recombination. Hence, independent measurements in particular of the Hubble constant are and remain most important. [2]

Estimation of the Hubble Constant

The lens equation is dimensionless, and the positions of images as well as their magnifications are dimensionless numbers. Therefore, information on the image configuration alone does not provide any constraint on the overall scale of the lens geometry or the value of the Hubble constant. Refsdal [51] realized that the time delay, however, is proportional to the absolute scale of the system and does depend on H_0 (cf. Fig. 3.20). [39]

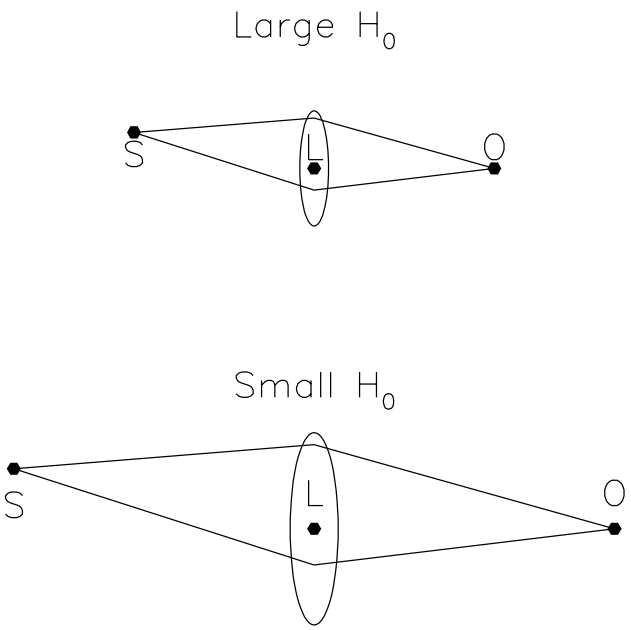

Figure 3.20: Sketch of the dependence of the overall scale of a lens system on the value of the Hubble constant [39].

To see this, we first note that the geometrical time delay is simply proportional to the path lengths of the rays which scale as H_0^{-1}. The potential time delay also scales as H_0^{-1} because the linear size of the lens and its mass have this scaling. Therefore, for any gravitational lens system, the quantity

$$H_0 \, \Delta\tau \tag{3.50}$$

depends only on the lens model and the geometry of the system. A good lens model which reproduces the positions and magnifications of the images provides the scaled time delay $H_0 \, \Delta\tau$ between the images. Therefore, a measurement of the time delay $\Delta\tau$ will yield the Hubble constant H_0. [39]

To measure the time delay, the fluxes of the images need to be monitored over a period of time significantly longer than the time delay in order to achieve reasonable accuracy. In fact,

the analysis of the resulting light curves is not straightforward because of uneven data sampling, and careful and sophisticated data analysis techniques have to be applied. QSO 0957+561 has been monitored both in the optical and radio wavebands. Unfortunately, analysis of the data has led to two claimed time delays [39] :

$$\Delta\tau = (1.48 \pm 0.03) \text{ years} \tag{3.51}$$

and

$$\Delta\tau \simeq 1.14 \text{ years} \tag{3.52}$$

The discrepancy appears to have been resolved in favor of the shorter delay. In addition to a measurement of the time delay, it is also necessary to develop a reliable model to calculate the value of $H_0\Delta\tau$. QSO 0957+561 has been studied by a number of groups over the years, with recent work incorporating constraints from VLBI imaging. The Hubble constant is estimated to be

$$H_0 = (82 \pm 6)\,(1-\kappa)\left(\frac{\Delta\tau}{1.14 \text{ yr}}\right)^{-1} \text{km s}^{-1}\,\text{Mpc}^{-1} \tag{3.53}$$

where κ refers to the unknown convergence due to the cluster surrounding the lensing galaxy. Since the cluster κ cannot be negative, this result directly gives an upper bound on the Hubble constant ($H_0 < 88$ km s^{-1} Mpc^{-1} for $\Delta\tau = 1.14$ years). Actually, κ can also be modified by large scale structure along the line of sight. In contrast to the effect of the cluster, this fluctuation can have either sign, but the rms amplitude is estimated to be only a few per cent. It is confirmed that large-scale structure does not modify the functional relationship between lens observables, and therefore does not affect the determination of H_0. [39]

To obtain an actual value of H_0 instead of just an upper bound, we need an independent estimate of κ. Studies of weak lensing by the cluster give $\kappa = 0.24 \pm 0.12$ (2σ) at the location of the lens. This corresponds to $H_0 = 62^{+12}_{-13}$ km s^{-1} Mpc^{-1}. Another technique is to measure the velocity dispersion σ_{gal} of the lensing galaxy, from which it is possible to estimate κ used the Keck telescope to measure $\sigma_{\text{gal}} = 279 \pm 12$ km s^{-1}, which corresponds to $H_0 = 66 \pm 7$ km s^{-1} Mpc^{-1}. Although most models of QSO 0957+561 are based on a spherically symmetric galaxy embedded in an external shear (mostly due to the cluster), introduction of ellipticity in the galaxy, or a point mass at the galaxy core, or substructure in the cluster seem to have little effect on the estimate of H_0 [39].

A measurement of the time delay has also been attempted in the Einstein ring system B 0218+ 357. In this case, a single galaxy is responsible for the small image splitting of $0''.3$. The time delay has been determined to be 12 ± 3 days (1σ confidence limit) which translates to $H_0 \sim 60$ km s^{-1} Mpc^{-1} [39].

The determination of H_0 through gravitational lensing has a number of advantages over other techniques. [39].

1 The method works directly with sources at large redshifts, $z \sim 0.5$, whereas most other methods are local (observations within $\sim$ 100 Mpc) where peculiar velocities are still comparable to the Hubble flow.

2 While other determinations of the Hubble constant rely on distance ladders which progressively reach out to increasing distances, the measurement via gravitational time delay is a one-shot procedure. One measures directly the geometrical scale of the lens system. This means that the lens-based method is absolutely independent of every other method and at the very least provides a valuable test of other determinations.

3 The lens-based method is based on fundamental physics (the theory of light propagation in General Relativity), which is fully tested in the relevant weak-field limit of gravity. Other methods rely on models for variable stars (Cepheids) or supernova explosions (Type II), or empirical calibrations of standard candles (Tully-Fisher distances, Type I supernovae). The lensing method does require some information on the "shapes" of galaxies which is used to guide the choice of a parameterized lens model.

Cosmological Constant

A large cosmological constant Λ_0 increases the volume per unit redshift of the universe at high redshift. This means that the relative number of lensed sources for a fixed comoving number density of galaxies increases rapidly with increasing Λ_0. Turning this around it is possible to use the observed probability of lensing to constrain Λ_0. The current limit is $\Lambda_0 < 0.65$ (2σ confidence limit) for a universe with $\Omega_0 + \Lambda_0 = 1$. With a combined sample of optical and radio lenses, this limit could be slightly improved to $\Lambda_0 < 0.62$ (2σ; [39].

A completely independent approach considers the redshift distribution of lenses. For a given source redshift, the probability distribution of z_d peaks at higher redshift with increasing Λ_0. Once again, by comparing the observations against the predicted distributions one obtains an upper limit on Λ_0. This method is less sensitive than the first, but gives consistent results. [39]

Another technique consists in comparing the observed QSO image separations to those expected from the redshifts of lenses and sources and the magnitudes of the lenses, assuming certain values for Ω_0 and Λ_0. The cosmological parameters are then varied to optimize the agreement with the observations. Applying this approach to a sample of seven lens systems, it was found that $\Lambda_0 = 0.64^{+0.15}_{-0.26}$ (1σ confidence limit) assuming $\Omega_0 + \Lambda_0 = 1$. [39]

3.5 Weak Gravitational Lensing

The main subject of this dissertation is strong lensing models. However, for the sake of completeness of this introductory material, it is essential to discuss the subject of weak gravitational lensing as well. There is no generally applicable definition of weak lensing despite the fact that

it constitutes a flourishing area of research. The common aspect of all studies of weak gravitational lensing is that measurements of its effects are statistical in nature. While a single multiply-imaged source provides information on the mass distribution of the deflector, weak lensing effects show up only across ensembles of sources. One example was given above: The shape distribution of an ensemble of galaxy images is changed close to a massive galaxy cluster in the foreground, because the cluster's tidal field polarizes the images. We shall see later that the size distribution of the background galaxy population is also locally changed in the neighborhood of a massive intervening mass concentration. [4]

Until very recently, weak lensing has been considered by a considerable fraction of the community as 'black magic' (or to quote one member of a PhD examination committee: "You have a mass distribution about which you don't know anything, and then you observe sources which you don't know either, and then you claim to learn something about the mass distribution?"). Most likely the reason for this is that weak lensing is indeed weak. One cannot 'see' the effect, nor can it be graphically displayed easily. Only by investigating many faint galaxy images can a signal be extracted from the data, and the human eye is not sufficient to perform this analysis. This is different even from the analysis of CMB anisotropies which, similarly, need to be analyzed by statistical means, but at least one can display a temperature map of the sky. However, weak lensing has gained a lot of credibility, not only because it has contributed substantially to our knowledge about the mass distribution in the Universe, but also because different teams, with different data set and different data analysis tools, agree on their results. [55]

Magnification and distortion effects due to weak lensing can be used to probe the statistical properties of the matter distribution between us and an ensemble of distant sources, provided some assumptions on the source properties can be made. For example, if a *standard candle* at high redshift is identified, its flux can be used to estimate the magnification along its line-of-sight. It can be assumed that the orientation of faint distant galaxies is random. Then, any coherent alignment of images signals the presence of an intervening tidal gravitational field. As a third example, the positions on the sky of cosmic objects at vastly different distances from us should be mutually independent. A statistical association of foreground objects with background sources can therefore indicate the magnification caused by the foreground objects on the background sources.

All these effects are quite subtle, or weak, and many of the current challenges in the field are observational in nature. A coherent alignment of images of distant galaxies *can* be due to an intervening tidal gravitational field, but *could* also be due to propagation effects in the Earth's atmosphere or in the telescope. A variation in the number density of background sources around a foreground object *can* be due to a magnification effect, but *could* also be due to non-uniform photometry or obscuration effects. These potential systematic effects have to be controlled at a level well below the expected weak-lensing effects. [4]

The principles of weak gravitational lensing

Distortion of faint galaxy images

Images of distant sources are distorted in shape and size, owing to the tidal gravitational field through which light bundles from these sources travel to us. Provided the angular size of a lensed image of a source is much smaller than the characteristic angular scale on which the tidal field varies, the distortion can be described by the linearized lens mapping, i.e., the Jacobi matrix $\mathcal{A}$. The invariance of the surface brightness by gravitational light deflection, $I(\boldsymbol{\theta}) = I^{(\mathrm{s})}[\boldsymbol{\beta}(\boldsymbol{\theta})]$,

together with the locally linearized lens equation,

$$\boldsymbol{\beta} - \boldsymbol{\beta}_0 = \mathcal{A}(\boldsymbol{\theta}_0) \cdot (\boldsymbol{\theta} - \boldsymbol{\theta}_0) \; , \tag{3.54}$$

where $\boldsymbol{\beta}_0 = \boldsymbol{\beta}(\boldsymbol{\theta}_0)$, then describes the distortion of small lensed images as

$$I(\boldsymbol{\theta}) = I^{(\mathrm{s})}[\boldsymbol{\beta}_0 + \mathcal{A}(\boldsymbol{\theta}_0) \cdot (\boldsymbol{\theta} - \boldsymbol{\theta}_0)] \; . \tag{3.55}$$

We recall (see IN) that the Jacobi matrix can be written as

$$\mathcal{A}(\boldsymbol{\theta}) = (1-\kappa) \begin{pmatrix} 1-g_1 & -g_2 \\ -g_2 & 1+g_1 \end{pmatrix} \; , \text{ where } \; g(\boldsymbol{\theta}) = \frac{\gamma(\boldsymbol{\theta})}{[1-\kappa(\boldsymbol{\theta})]} \tag{3.56}$$

is the reduced shear, and the g_α, $\alpha = 1, 2$, are its Cartesian components. The reduced shear describes the shape distortion of images through gravitational light deflection. The (reduced) shear is a 2-component quantity, most conveniently written as a complex number,

$$\gamma = \gamma_1 + \mathrm{i}\gamma_2 = |\gamma| \, \mathrm{e}^{2\mathrm{i}\varphi} \; ; \quad g = g_1 + \mathrm{i}g_2 = |g| \, \mathrm{e}^{2\mathrm{i}\varphi} \; ; \tag{3.57}$$

its amplitude describes the degree of distortion, whereas its phase φ yields the direction of distortion. The reason for the factor '2' in the phase is the fact that an ellipse transforms into itself after a rotation by 180°. Consider a circular source with radius R); mapped by the local Jacobi matrix, its image is an ellipse, with semi-axes

$$\frac{R}{1-\kappa-|\gamma|} = \frac{R}{(1-\kappa)(1-|g|)} \quad ; \quad \frac{R}{1-\kappa+|\gamma|} = \frac{R}{(1-\kappa)(1+|g|)}$$

and the major axis encloses an angle φ with the positive θ_1-axis. Hence, if sources with circular isophotes could be identified, the measured image ellipticities would immediately yield the value of the reduced shear, through the axis ratio

$$|g| = \frac{1-b/a}{1+b/a} \quad \Leftrightarrow \quad \frac{b}{a} = \frac{1-|g|}{1+|g|}$$

and the orientation of the major axis φ. In these relations it was assumed that $b \leq a$, and $|g| < 1$. We shall discuss the case $|g| > 1$ later. [55]

However, faint galaxies are not intrinsically round, so that the observed image ellipticity is a combination of intrinsic ellipticity and shear. The strategy to nevertheless obtain an estimate of the (reduced) shear consists in locally averaging over many galaxy images, assuming that the intrinsic ellipticities are *randomly oriented*. In order to follow this strategy, one needs to clarify first how to define 'ellipticity' for a source with arbitrary isophotes (faint galaxies are not simply elliptical); in addition, seeing by the atmospheric turbulence will blur – and thus circularize – observed images, together with other effects related to the observation procedure. From [55].

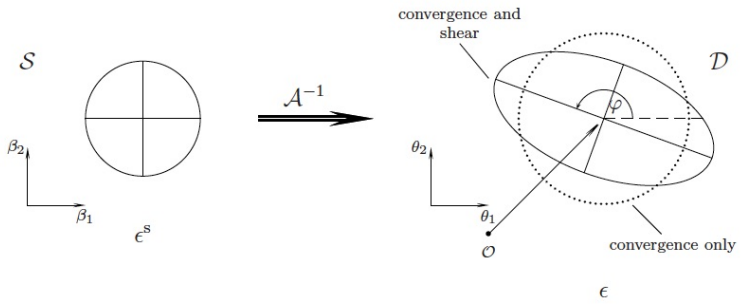

Figure 3.21: A circular source, shown at the left, is mapped by the inverse Jacobian $\mathcal{A}^{-1}$ onto an ellipse. In the absence of shear, the resulting image is a circle with modified radius, depending on κ. Shear causes an axis ratio different from unity, and the orientation of the resulting ellipse depends on the phase of the shear. From [55]

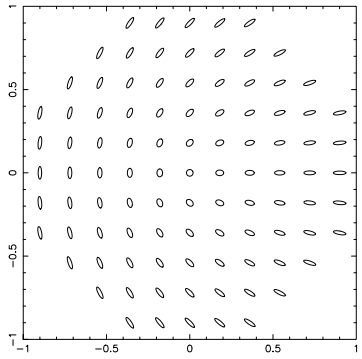

Figure 3.22: The shape of image ellipses for a circular source, in dependence on their two ellipticity components χ_1 and χ_2; a corresponding plot in term of the ellipticity components ϵ_i would look quite similar. Note that the ellipticities are rotated by 90° when $\chi \to -\chi$ From [55]

Which of these two definitions is more convenient depends on the context; one can easily transform one into the other,

$$\epsilon = \frac{\chi}{1 + (1 - |\chi|^2)^{1/2}} , \quad \chi = \frac{2\epsilon}{1 + |\epsilon|^2} . \tag{3.58}$$

In fact, other (but equivalent) ellipticity definitions have been used in the literature, but the two given above appear to be most convenient.

From source to image ellipticities.

In total analogy, one defines the second-moment brightness tensor $Q_{ij}^{(\mathrm{s})}$, and the complex ellipticities $\chi^{(\mathrm{s})}$ and $\epsilon^{(\mathrm{s})}$ for the unlensed source. From

$$Q_{ij}^{(\mathrm{s})} = \frac{\int \mathrm{d}^2\beta \; I^{(\mathrm{s})}(\boldsymbol{\theta})\, q_I[I^{(\mathrm{s})}(\boldsymbol{\beta})]\,(\beta_i - \bar{\beta}_i)\,(\beta_j - \bar{\beta}_j)}{\int \mathrm{d}^2\beta \; I^{(\mathrm{s})}(\boldsymbol{\theta})\, q_I[I^{(\mathrm{s})}(\boldsymbol{\beta})]} \;, \quad i,j \in \{1,2\} \;, \tag{3.59}$$

one finds with $\mathrm{d}^2\beta = \det \mathcal{A}\, \mathrm{d}^2\theta$, $\boldsymbol{\beta} - \bar{\boldsymbol{\beta}} = \mathcal{A}\left(\boldsymbol{\theta} - \bar{\boldsymbol{\theta}}\right)$, that

$$Q^{(\mathrm{s})} = \mathcal{A}\, Q\, \mathcal{A}^T = \mathcal{A}\, Q\, \mathcal{A} \;, \tag{3.60}$$

where $\mathcal{A} \equiv \mathcal{A}(\bar{\boldsymbol{\theta}})$. Using the definitions of the complex ellipticities, one finds the transformations

$$\chi^{(\mathrm{s})} = \frac{\chi - 2g + g^2\chi^*}{1 + |g|^2 - 2\Re(g\chi^*)} \;; \quad \epsilon^{(\mathrm{s})} = \begin{cases} \dfrac{\epsilon - g}{1 - g^*\epsilon} & \text{if } |g| \le 1 \;; \\ \dfrac{1 - g\epsilon^*}{\epsilon^* - g^*} & \text{if } |g| > 1 \;. \end{cases} \tag{3.61}$$

The inverse transformations are obtained by interchanging source and image ellipticities, and $g \to -g$ in the foregoing equations.

Estimating the (reduced) shear.

In the following we make the assumption that the intrinsic orientation of galaxies is random,

$$\mathrm{E}\left(\chi^{(\mathrm{s})}\right) = 0 = \mathrm{E}\left(\epsilon^{(\mathrm{s})}\right) \;, \tag{3.62}$$

which is expected to be valid since there should be no direction singled out in the Universe. This then implies that the expectation value of ϵ is [as obtained by averaging the transformation law (3.61) over the intrinsic source orientation]

$$\mathrm{E}(\epsilon) = \begin{cases} g & \text{if } |g| \le 1 \\ 1/g^* & \text{if } |g| > 1 \;. \end{cases} \tag{3.63}$$

This is a remarkable result, since it shows that each image ellipticity provides an unbiased estimate of the local shear, though a very noisy one. The noise is determined by the intrinsic ellipticity dispersion

$$\sigma_\epsilon = \sqrt{\left\langle \epsilon^{(\mathrm{s})} \epsilon^{(\mathrm{s})*} \right\rangle} \;,$$

in the sense that, when averaging over N galaxy images all subject to the same reduced shear, the 1-σ deviation of their mean ellipticity from the true shear is $\sigma_\epsilon/\sqrt{N}$. A more accurate estimate of this error is

$$\sigma = \sigma_\epsilon \left[1 - \min\left(|g|^2, |g|^{-2}\right)\right] / \sqrt{N} \tag{3.64}$$

Hence, the noise can be beaten down by averaging over many galaxy images; however, the region over which the shear can be considered roughly constant is limited, so that averaging over galaxy images is always related to a smoothing of the shear. Fortunately, we live in a Universe where the sky is 'full of faint galaxies', as was impressively demonstrated by the Hubble Deep Field images and previously from ultra-deep ground-based observations. Therefore, the accuracy of a shear estimate depends on the local number density of galaxies for which a shape can

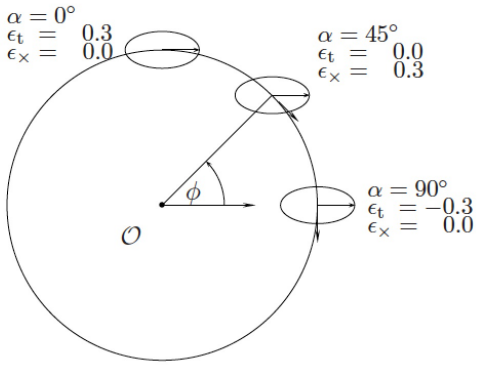

Figure 3.23: Illustration of the tangential and cross-components of the shear, for an image with $\epsilon_1 = 0.3$, $\epsilon_2 = 0$, and three different directions ϕ with respect to a reference point. From [55]

be measured. In order to obtain a high density, one requires deep imaging observations. As a rough guide, on a 3 hour exposure with a 4-meter class telescope, about 30 galaxies per arcmin^2 can be used for a shape measurement.

In fact, considering (3.63) we conclude that the expectation value of the observed ellipticity is the same for a reduced shear g and for $g' = 1/g^*$. It has been shown that one cannot distinguish between these two values of the reduced shear from a purely local measurement, and term this fact the 'local degeneracy'; this also explains the symmetry between $|g|$ and $|g|^{-1}$ in (3.64). Hence, from a local weak lensing observation one cannot tell the case $|g| < 1$ (equivalent to $\det \mathcal{A} > 0$) from the one of $|g| > 1$ or $\det \mathcal{A} < 0$. This local degeneracy is, however, broken in large-field observations, as the region of negative parity of any lens is small (the Einstein radius inside of which $|g| > 1$ of massive lensing clusters is typically $\lesssim 30''$, compared to data fields of several arcminutes used for weak lensing studies of clusters), and the reduced shear must be a smooth function of position on the sky.

Whereas the transformation between source and image ellipticity appears simpler in the case of χ than ϵ – see (3.61), the expectation value of χ cannot be easily calculated and depends explicitly on the intrinsic ellipticity distribution of the sources. In particular, the expectation value of χ is not simply related to the reduced shear (Schneider & Seitz 1995). However, in the weak lensing regime, $\kappa \ll 1$, $|\gamma| \ll 1$, one finds

$$\gamma \approx g \approx \langle \epsilon \rangle \approx \frac{\langle \chi \rangle}{2} \,. \tag{3.65}$$

Tangential and cross component of shear

The shear components γ_1 and γ_2 are defined relative to a reference Cartesian coordinate frame. Note that the shear is *not* a vector (though it is often wrongly called that way in the literature), owing to its transformation properties under rotations: Whereas the components of a vector are multiplied by $\cos\varphi$ and $\sin\varphi$ when the coordinate frame is rotated by an angle φ, the shear components are multiplied by $\cos(2\varphi)$ and $\sin(2\varphi)$, or simply, the complex shear gets multiplied by $\mathrm{e}^{-2\mathrm{i}\varphi}$. The reason for this transformation behavior of the shear traces back to its original definition as the traceless part of the Jacobi matrix $\mathcal{A}$. This transformation behavior is the same as that of the linear polarization; the shear is therefore a *polar*. In analogy with vectors, it is often useful to consider the shear components in a rotated reference frame, that is, to measure them w.r.t. a different direction; for example, the arcs in clusters are tangentially aligned, and so their ellipticity is oriented tangent to the radius vector in the cluster. From [55].

If ϕ specifies a direction, one defines the *tangential* and *cross components* of the shear *relative to this direction* as

$$\gamma_{\rm t} = -\Re\left[\gamma\,{\rm e}^{-2{\rm i}\phi}\right] \quad , \quad \gamma_\times = -\Im\left[\gamma\,{\rm e}^{-2{\rm i}\phi}\right] \;; \tag{3.66}$$

For example, in case of a circularly-symmetric matter distribution, the shear at any point will be oriented tangent to the direction towards the center of symmetry. Thus in this case choose ϕ to be the polar angle of a point; then, $\gamma_\times = 0$. In full analogy to the shear, one defines the tangential and cross components of an image ellipticity, $\epsilon_{\rm t}$ and $\epsilon_\times$.

The sign in (3.66) is easily explained (and memorized) as follows: consider a circular mass distribution and a point on the θ_1-axis outside the Einstein radius. The image of a circular source there will be stretched in the direction of the θ_2-axis. In this case, $\phi = 0$ in (3.66), the shear is real and negative, and in order to have the tangential shear positive, and thus to define tangential shear in accordance with the intuitive understanding of the word, a minus sign is introduced. Negative tangential ellipticity implies that the image is oriented in the radial direction. We warn the reader that sign conventions and notations have undergone several changes in the literature, and the current author had his share in this. From [55].

Minimum lens strength for its weak lensing detection.

As a first application of this decomposition, we consider how massive a lens needs to be in order that it produces a detectable weak lensing signal. For this purpose, consider a lens modeled as an SIS with one-dimensional velocity dispersion σ_v. In the annulus $\theta_{\rm in} \le \theta \le \theta_{\rm out}$, centered on the lens, let there be N galaxy images with positions $\boldsymbol{\theta}_i = \theta_i(\cos\phi_i, \sin\phi_i)$ and (complex) ellipticities ϵ_i. For each one of them, consider the tangential ellipticity

$$\epsilon_{{\rm t}i} = -\Re\left(\epsilon_i\,{\rm e}^{-2{\rm i}\phi_i}\right) \;. \tag{3.67}$$

The weak lensing signal-to-noise for the detection of the lens obtained by considering a weighted average over the tangential ellipticity is

$$\begin{aligned} \frac{\rm S}{\rm N} &= \frac{\theta_{\rm E}}{\sigma_\epsilon}\sqrt{\pi n}\,\sqrt{\ln(\theta_{\rm out}/\theta_{\rm in})} \\ &= 8.4\left(\frac{n}{30\,{\rm arcmin}^{-2}}\right)^{1/2}\left(\frac{\sigma_\epsilon}{0.3}\right)^{-1}\left(\frac{\sigma_v}{600\,{\rm km\,s}^{-1}}\right)^2 \\ &\times \qquad \left(\frac{\ln(\theta_{\rm out}/\theta_{\rm in})}{\ln 10}\right)^{1/2}\left\langle\frac{D_{\rm ds}}{D_{\rm s}}\right\rangle \;, \end{aligned} \tag{3.68}$$

where $\theta_{\rm E} = 4\pi(\sigma_v/c)^2(D_{\rm ds}/D_{\rm s})$ is the Einstein radius of an SIS, n the mean number density of galaxies, and the average of the distance ratio is taken over the source population from which the shear measurements are obtained. Hence, the S/N is proportional to the lens strength (as measured by $\theta_{\rm E}$), the square root of the number density, and inversely proportional to σ_ϵ, as expected. From this consideration we conclude that clusters of galaxies with $\sigma_v \gtrsim 600\,{\rm km/s}$ can be detected with sufficiently large S/N by weak lensing, but individual galaxies ($\sigma_v \lesssim 200\,{\rm km/s}$) are too weak as lenses to be detected individually. From [55].

Mean tangential shear on circles.

In the case of axi-symmetric mass distributions, the tangential shear is related to the surface mass density $\kappa(\theta)$ and the mean surface mass density $\bar\kappa(\theta)$ inside the radius θ by $\gamma_{\rm t} = \bar\kappa - \kappa$. It

is remarkable that a very similar expression holds for general matter distributions. To see this, we start from Gauss' theorem, which states that

$$\int_0^\theta \mathrm{d}^2\vartheta\, \nabla\cdot\nabla\psi = \theta \oint \mathrm{d}\varphi\, \nabla\psi\cdot\boldsymbol{n}\ ,$$

where the integral on the left-hand side extends over the area of a circle of radius θ (with its center chosen as the origin of the coordinate system), ψ is an arbitrary scalar function, the integral on the right extends over the circle with radius θ, and $\boldsymbol{n}$ is the outward directed normal on this circle. Taking ψ to be the deflection potential and noting that $\nabla^2\psi = 2\kappa$, one obtains

$$m(\theta) \equiv \frac{1}{\pi}\int_0^\theta \mathrm{d}^2\vartheta\, \kappa(\boldsymbol{\vartheta}) = \frac{\theta}{2\pi}\oint \mathrm{d}\varphi\, \frac{\partial\psi}{\partial\theta}\ , \tag{3.69}$$

where we used that $\nabla\psi\cdot\boldsymbol{n} = \psi_{,\theta}$. Differentiating this equation with respect to θ yields

$$\frac{\mathrm{d}m}{\mathrm{d}\theta} = \frac{m}{\theta} + \frac{\theta}{2\pi}\oint \mathrm{d}\varphi\, \frac{\partial^2\psi}{\partial\theta^2}\ . \tag{3.70}$$

Consider a point on the θ_1-axis; there, $\psi_{,\theta\theta} = \psi_{11} = \kappa + \gamma_1 = \kappa - \gamma_\mathrm{t}$. This last expression is independent on the choice of coordinates and must therefore hold for all φ. Denoting by $\langle\kappa(\theta)\rangle$ and $\langle\gamma_\mathrm{t}(\theta)\rangle$ the mean surface mass density and mean tangential shear on the circle of radius θ, (3.70) becomes

$$\frac{\mathrm{d}m}{\mathrm{d}\theta} = \frac{m}{\theta} + \theta\left[\langle\kappa(\theta)\rangle - \langle\gamma_\mathrm{t}(\theta)\rangle\right]\ . \tag{3.71}$$

The dimensionless mass $m(\theta)$ in the circle is related to the mean surface mass density inside the circle $\bar\kappa(\theta)$ by

$$m(\theta) = \theta^2\,\bar\kappa(\theta) = 2\int_0^\theta \mathrm{d}\vartheta\ \vartheta\ \langle\kappa(\vartheta)\rangle\ . \tag{3.72}$$

Together with $\mathrm{d}m/\mathrm{d}\theta = 2\theta\,\langle\kappa(\theta)\rangle$, (3.71) becomes, after dividing through θ,

$$\langle\gamma_\mathrm{t}\rangle = \bar\kappa - \langle\kappa\rangle\ , \tag{3.73}$$

a relation which very closely matches the result mentioned above for axi-symmetric mass distributions. One important immediate implication of this result is that from a measurement of the tangential shear, averaged over concentric circles, one can determine the azimuthally-averaged mass profile of lenses, even if the density is not axi-symmetric. From [55].

Magnification effects

A magnification μ changes source counts according to

$$n(>S,\boldsymbol{\theta},z) = \frac{1}{\mu(\boldsymbol{\theta},z)}\, n_0\left(>\frac{S}{\mu(\boldsymbol{\theta},z)},z\right)\ , \tag{3.74}$$

where $n(>S,z)$ and $n_0(>S,z)$ are the lensed and unlensed cumulative number densities of sources, respectively. The first argument of n_0 accounts for the change of the flux (which implies that a magnification $\mu > 1$ allows the detection of intrinsically fainter sources), whereas the prefactor in (3.74) stems from the change of apparent solid angle. In the case that $n_0(S) \propto S^{-\alpha}$, this yields

$$\frac{n(>S)}{n_0(>S)} = \mu^{\alpha-1}\ , \tag{3.75}$$

and therefore, if $\alpha > 1$ (< 1), source counts are enhanced (depleted); the steeper the counts, the stronger the effect. In the case of weak lensing, where $|\mu - 1| \ll 1$, one probes the source counts only over a small range in flux, so that they can always be approximated (locally) by a power law. Provided that $\kappa \ll 1$, $|\gamma| \ll 1$, a further approximation applies,

$$\mu \approx 1 + 2\kappa \; ; \quad \text{and} \quad \frac{n(> S)}{n_0(> S)} \approx 1 + 2(\alpha - 1)\kappa \; . \tag{3.76}$$

Thus, from a measurement of the local number density $n(> S)$ of galaxies, κ can in principle be inferred directly. It should be noted that $\alpha \sim 1$ for galaxies in the B-band, but in redder bands, $\alpha < 1$; therefore, one expects a depletion of their counts in regions of magnification $\mu > 1$. Broadhurst et al. (1995) have discussed in detail the effects of magnification in weak lensing. Not only are the number counts affected, but since this is a redshift-dependent effect (since both κ and γ depend, for a given physical surface mass density, on the source redshift), the redshift distribution of galaxies is locally changed by magnification.

Since magnification is merely a stretching of solid angle, it has been pointed out that magnified images at fixed surface brightness have a larger solid angle than unlensed ones; in addition, the surface brightness of a galaxy is expected to be a strong function of redshift [$I \propto (1+z)^{-4}$], owing to the Tolman effect. Hence, if this effect could be harnessed, a (redshift-dependent) magnification could be measured statistically. Unfortunately, this method is hampered by observational difficulties; it seems that estimating a reliable estimate for the surface brightness from seeing-convolved images is even more difficult than determining image shapes. From [55].

Shape Measurements and PSF Correction

The typical change in ellipticity due to gravitational lensing is much smaller than the intrinsic shape of the source, even in the case of clusters of galaxies. Although this can be dealt with by averaging the shapes of many galaxies, the shear signal can be overwhelmed by instrumental effects, which may be difficult to assess on an object-by-object basis. Hence the study of algorithms that can accurately determine the shapes of faint galaxies has been a major part of the development of weak gravitational lensing as a key tool for cosmology.

The problem is highlighted by comparing the "true" image of an object to the "observed" version shown in Figure 3.24. The main source of bias that needs to be corrected for is the blurring of the images by the point spread function (PSF). Unless the pixels are large with respect to the PSF, the pixellation is not a major source of concern. As it is easier to measure properties when the noise is low, the S/N ratio is another key parameter determining how well shapes can be measured. In the case of space-based observations, due to the combination of low sky background and radiation damage, charge transfer inefficiency may also be an important effect. [21]

One approach to recover the true galaxy shapes is to adopt a suitable model of the surface brightness distribution. An estimate of the lensing signal is obtained by shearing the model and convolving it with the PSF, comparing the result to the observed image until a best fit is found. A model for the PSF is typically obtained by analyzing the shapes of a sample of stars in the actual data. An important advantage of this approach is that instrumental effects can be incorporated in a Bayesian framework. As the modeling requires many calculations and thus is computationally expensive, the use of model-fitting algorithms has only recently become more prominent. Some examples of this approach are `lensfit` which was used to analyze the CFHTLenS data, and `im3shape`. There are challenges as well: the model needs to accurately describe the surface brightness of the galaxies, while having a limited number of parameters in

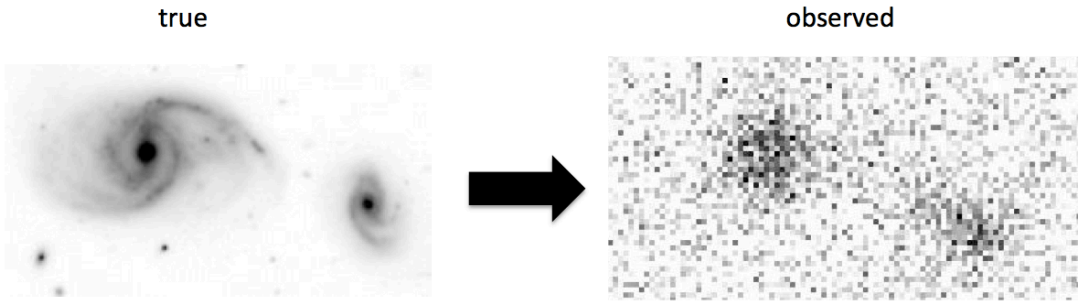

Figure 3.24: We need to infer accurate information about the shape of the true surface brightness distribution (left) from images that have been corrupted by various sources of bias, such as pixellation, seeing and noise. Given a good description of the instrumental effects it is possible to simulate their effects and thus examine the performance of shape measurement algorithms. [21]

order to avoid fitting the noise. A model that is too rigid will lead to model bias, as does a model that is too flexible. [21]

Galaxy shapes can also be quantified by computing the moments of the galaxy images. Such methods have been applied to data extensively, especially the KSB method. The shapes can be quantified by the polarization

$$e_1 = \frac{I_{11} - I_{22}}{I_{11} + I_{22}}, \text{ and } e_2 = \frac{2I_{12}}{I_{11} + I_{22}}, \tag{3.77}$$

where the quadrupole moments I_{ij} are given by

$$I_{ij} = \frac{1}{I_0} \int \mathrm{d}^2\mathbf{x}\; x_i x_j W(\mathbf{x}) f(\mathbf{x}), \tag{3.78}$$

where $f(\mathbf{x})$ is the observed galaxy image, $W(\mathbf{x})$ a suitable weight function to suppress the noise and I_0 the weighted monopole moment. It is also convenient to define $R^2 = I_{11} + I_{22}$ as a measure of the size of the galaxy. Both model-fitting and moment-based methods are used to measure the weak lensing signal and further development is ongoing. In these notes we continue with a closer look at the use of moments, because it is somewhat easier to see how the results are impacted by instrumental effects.

Observational distortions

The observed moments are changed by the blurring of the PSF: the PSF has a width which leads to rounder images and typically is anisotropic, which leads to a preferred orientation. If that were not enough, noise in the images leads to additional biases. The various sources of bias can be grouped into two kinds: a multiplicative bias m that scales the shear, and an additive bias c that reflects preferred orientations that are introduced. The observed shear and true shear are thus related by:

$$\gamma_i^{\mathrm{obs}} = (1 + m)\gamma_i^{\mathrm{true}} + c, \tag{3.79}$$

where we implicitly assumed that the biases are the same for both shear components. The additive bias is a major source of error for cosmic shear studies because the PSF patterns can

overwhelm the lensing signal. Studies of clusters and galaxies use the tangential shear averaged using many lens-source pairs, and much of the additive biases tend to average away. As we discuss below it is possible to test how well the correction for additive bias has performed, but the estimate of the multiplicative bias requires image simulations. [21]

If it were possible to ignore the effects of noise in the images, we could use unweighted moments. In this case the correction for the PSF is straightforward as the corrected moments are given by

$$I_{ij}^{\rm true} = I_{ij}^{\rm obs} - I_{ij}^{\rm PSF}, \tag{3.80}$$

i.e. one only needs to subtract the moments of the PSF from the observed moments. The result provides an unbiased estimate of the polarization, but to convert the result into a shear still requires knowledge of the unlensed ellipticity (distribution), although this could be established iteratively from the data.

From a pure statistical perspective it is more efficient to image large areas of the sky rather than take deep images of smaller regions. Hence the images of the sources are typically noisy and unweighted moments cannot be used. The optimal estimate is obtained by matching the weight function to the size (and shape) of the galaxy image. However, the correction for the change in moments due to both the weight function and the PSF is no longer simple, but involves higher order moments of the surface brightness distribution, which themselves are affected by noise. Note that limiting the expansion in moments is analogous to the model bias in model-fitting approaches.

In the simplified case of unweighted moments, the change in the observed ellipticity $\hat{\epsilon}$ due to small errors in the PSF size ($\delta R^2_{\rm PSF}$) or PSF ellipticity ($\delta\epsilon_{\rm PSF}$) can be expressed as

$$\hat{\epsilon}_{\rm gal} \approx \epsilon_{\rm gal} + \frac{\partial\epsilon_{\rm gal}}{\partial(R^2_{\rm PSF})}\delta(R^2_{\rm PSF}) + \frac{\partial\epsilon_{\rm gal}}{\partial\epsilon_{\rm PSF}}\delta\epsilon_{\rm PSF}, \tag{3.81}$$

which can be written as

$$\hat{\epsilon}_{\rm gal} \approx \left[1 + \frac{\delta(R^2_{\rm PSF})}{R^2_{\rm gal}}\right]\epsilon_{\rm gal} - \left[\frac{R^2_{\rm PSF}}{R^2_{\rm gal}}\delta\epsilon_{\rm PSF} + \frac{\delta(R^2_{\rm PSF})}{R^2_{\rm gal}}\epsilon_{\rm PSF}\right]. \tag{3.82}$$

The first term shows the multiplicative bias caused by errors in the PSF size, relative to the galaxy size. The second term corresponds to the additive bias and is determined by errors in the PSF model $\delta\epsilon_{\rm PSF}$ and residuals in the correction for the PSF anisotropy (last term). However, the PSF is not the only source of bias, especially when considering weighted moments and hence the expression for the multiplicative bias (idem for the additive one) becomes more involved when more effects are included. In particular new contributions arise that are related to the correction method (method bias). As is already clear from the expression reproduced above, a small PSF is important in order to minimize the biases. Although small PSF anisotropy is preferable, a good model of the PSF size and shape is critical. [21]

PSF model

Although much effort has been spent on improving the correction for the PSF, without an accurate model for the spatial variation of the PSF, the resulting signal will nonetheless be biased (e.g. In ground-based data the PSF changes from exposure to exposure due to changing atmospheric conditions and gravitational loads on the telescope. The PSF of HST observations changes due to the change in thermal conditions as it orbits around the Earth. If a sufficient number of stars can be identified in the images, these can be used to model the PSF. As can be

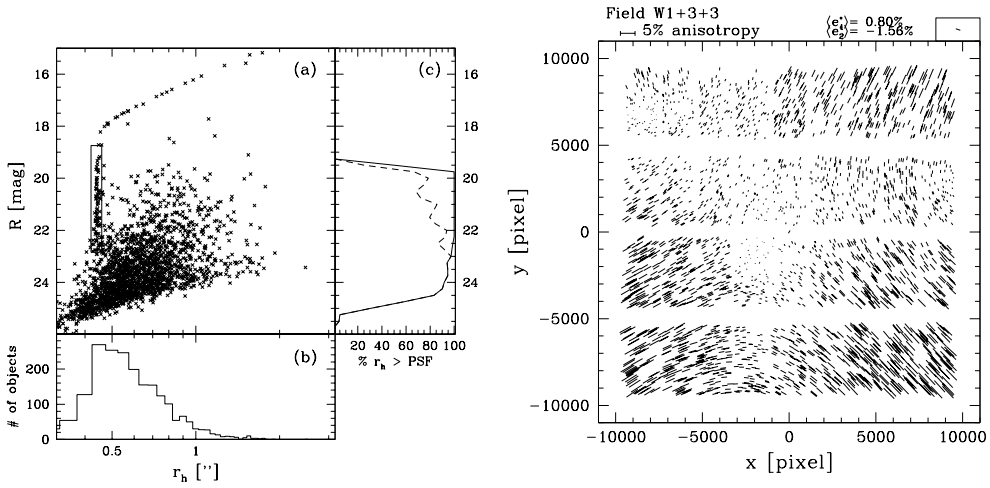

Figure 3.25: *Left panel:* Plot of the apparent magnitude versus half-light radius for RCS data. The rectangle indicates the sample of stars that can be used to model the PSF variation. Brighter stars saturate and their observed sizes increase as can be seen as well. *Right panel:* An example of the pattern of PSF anisotropy for MegaCam on CFHT. The sticks indicate the direction of the major axis of the PSF and the length is proportional to the PSF ellipticity. A coherent pattern across the field-of-view is clearly visible. [21]

seen from Figure 3.25 stars can be identified by plotting magnitude versus size. As the stars are the smallest objects, they occupy a clear vertical locus. If the star saturates, charge leaks into neighboring pixels and the size increase which explains the trail towards larger sizes, whereas the size and shape estimates become noisy for faint stars. After selecting a sample of suitable stars (not too bright such that they are saturated but also not too faint such that they cannot be separated from faint, small sources) the resulting PSF pattern can be modeled. The right panel in Figure 3.25 shows an example for MegaCam on the Canada-France-Hawaii Telescope (CFHT), which shows a coherent pattern across the field-of-view.

Most studies to date fit an empirical model to the measurements of a sample of stars to capture the spatial variation. As the PSF pattern is determined by (inevitable) misalignments in the optics, the overall pattern varies relatively smoothly. However, to efficiently image large areas of sky, observations are carried out using mosaic cameras. For instance, Megacam on CFHT consists of 36 chips. Misalignments and flexing of the chips will lead to small additional PSF patterns on the scale of the chips. A single low-order model fit to the full focal plane cannot capture these small scale variations. Instead a low-order (typically second-order) polynomial is used for each chip, but this may lead to over-fitting on small scales due to the limited number of stars per chip. Whether a model based on the typical optical distortions can be used to model the PSF pattern of the Subaru telescope has also been evaluated. The global pattern, which varies from exposure to exposure, can indeed be described fairly well. By combining many observations, one can also try to account for the misalignments of the individual chips. [21]

To obtain deeper images and to fill in the gaps between the chips, exposures are dithered and combined into a stack. As the observing conditions typically vary between exposures, the combined PSF pattern becomes very complicated (especially at the location of the chip gaps). It is important to account for this, for instance by modeling the PSF of each exposure and keeping track which PSFs contribute to the stack at a particular location. Alternatively one can model each exposure.

The true shapes of galaxies should not correlate with the PSF pattern, although chance alignments of the shear and the PSF may occur. This enables an important test of the fidelity of the correction for PSF anisotropy: we can measure the correlation between the corrected galaxy shapes and the PSF ellipticity, the star-galaxy correlation. The detection of a significant correlation points to an inadequate correction, which may be due to the method itself or the PSF model. Importantly, this test does not depend on cosmology, while being very sensitive to one of the most dominant sources of bias in cosmic shear studies. In the analysis of the CFHTLenS data, this was used to identify and omit fields that showed significant systematics. [21]

Cluster Mass Reconstruction with Weak Gravitational Lensing

The study of cosmic shear has been the main science driver of most recent weak lensing studies, but in this section we highlight some of the applications to galaxy and cluster lensing which pertain to cosmology and the study of dark matter.

Mapping the distribution of dark matter

The observed weak lensing shear field provides estimates of the derivatives of the lensing potential It is possible to invert this problem to obtain a parameter-free reconstruction of the surface density distribution: it is possible to make an ‘image’ of the dark matter distribution.

The surface density (up to an arbitrary contant κ_0) can be written as:

$$\kappa(\boldsymbol{\theta}) - \kappa_0 = \frac{1}{\pi} \int d^2\boldsymbol{\theta}' \frac{\zeta(\boldsymbol{\theta}' - \theta)\gamma(\boldsymbol{\theta}')}{(\boldsymbol{\theta}' - \theta)^2}, \tag{3.83}$$

where the convolution kernel $\zeta(\theta)$ is given by

$$\zeta(\boldsymbol{\theta}) = \frac{\theta_2^2 - \theta_1^2 + 2i\theta_1\theta_2}{|\boldsymbol{\theta}|^4}. \tag{3.84}$$

The proper evaluation of this integral requires data out to infinity, which is impractical. This complication spurred the development of finite-field inversion methods.

The intrinsic shapes of the sources add significant noise to the reconstruction and as a result only the distribution of matter in massive clusters of galaxies can be studied in detail using weak lensing mass reconstructions. Of particular interest is the study of merging systems, where dynamical techniques cannot be used. Figure 3.26 shows a reconstruction of the mass distribution of the Bullet cluster based on HST observations. The reconstructed (dark) matter distribution is offset from the hot X-ray gas, but agrees well with the distribution of galaxies. These observations provide some of the best evidence for the existence of dark matter. This is because in alternative theories of gravity the hot X-ray gas should be the main source of the lensing signal. In the near future we can expect improved constraints on the properties of dark matter particles based on a systematic study of merging systems. [22]

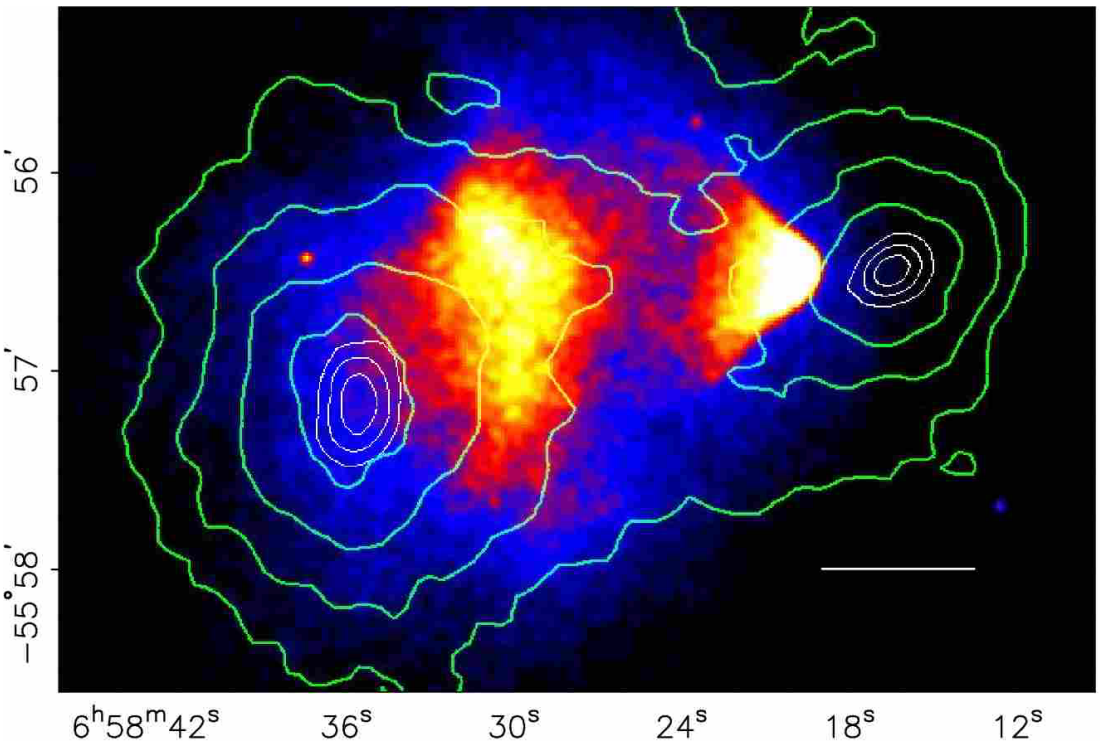

Figure 3.26: X-ray emission from the 'Bullet' cluster of galaxies as observed by Chandra. The eponymous bullet is a small galaxy cluster which has passed through the larger cluster and whose hot gas is seen in X-rays as the triangular shape on the right. The contours correspond to the previous mass reconstruction. The dark matter distribution is clearly offset from the gas, which contains the majority of baryonic matter, but agrees well with the distribution of galaxies – as expected if both the dark matter and stars in galaxies are effectively collisionless. From [22]

Cosmology with galaxy clusters

Since clusters trace the highest peaks in the density, their number density as a function of mass and redshift depends strongly on the underlying cosmology, making it an interesting complementary probe for dark energy studies. Although conceptually straightforward, the implementation of this method has proven difficult.

One reason is that precise measurements of cosmological parameters require cluster catalogs with well-defined selection functions. In principle clusters can be identified in mass reconstructions from large weak lensing surveys, but projections along the line-of-sight lead to a relatively high false positive rate. Hence, either one must work with a statistic that includes projection effects, or with samples derived from optical, X-ray or radio observations.

Even in the latter case it is essential to have a well-determined relation between the observed cluster properties and mass. This is where weak lensing studies of large cluster samples can play an important role. The determination of the mean relation between the quantity of interest (e.g., richness, X-ray temperature) and cluster mass can be done statistically. For instance, the ensemble averaged weak lensing signal has been measured as a function of richness and luminosity using data from Sloan Digital Sky Survey (SDSS). Unfortunately, the mass-observable is

expected to have an intrinsic scatter as well, which is the result of differences in formation history, etc. The precise characterization of this unknown scatter is important to ensure accurate measurements of cosmological parameters. Individual weak lensing masses can be derived for massive clusters. We note, however, that ultimately the accuracy of these mass measurements is limited by projections along the line of sight. [22]

Multi-wavelength observations of samples that contain up to ~ 50 massive clusters have only recently started. These comprehensive studies, which also combine data at other wavelengths, will not only help quantify the scatter, but will also improve our understanding of cluster physics. This in turn will increase the reliability of other cluster mass estimators (such as the X-ray temperature). Evidence has recently been found that the outer regions of clusters are not in hydrostatic equilibrium, suggesting that additional pressure may be provided by bulk motion of the plasma. Cluster cosmology is an evolving field, and the hope is that with large samples of clusters observed in multiple wavelengths their internal physics will be modeled well enough for cosmological applications. [22]

Properties of dark matter halos

Simulations of hierarchical structure formation in CDM cosmologies have shown that the density profiles of virialized halos over a wide range in mass have a nearly universal profile with radius – the Navarro-Frenk-White (NFW) profile. The only difference between halos of galaxies and clusters of different mass is their concentration, which reflects the central density of the halo. Gravitational lensing provides us with powerful tools to test a range of predictions of the CDM paradigm via the structure of halos. For instance, the dark matter dominated outer regions can be uniquely probed by weak lensing, whereas strong gravitational lensing can be used to study the density profile on small scales.

Central regions: In the context of CDM, simulations indicate a power law density profile $\rho \propto r^{-\beta}$ as $r \to 0$. The original studies found a slope of $\beta = 1$, but the exact value is still debated. Without a complete treatment of the effects of baryons, observational results will be difficult to interpret. Despite these complications, much effort is devoted to determine the slope of the density profile observationally, as it can provide unique constraints on physical properties of the dark matter particle, such as its interaction cross section. [22]

Dynamical studies of galaxies have proven useful, and much of the current controversy about the central slope is based on observations of the rotation curves of low surface brightness galaxies, which suggest that the dark matter distribution has a central core. Strong lensing by galaxies can provide limited information because the typical Einstein radius is large compared to the region of interest. Nevertheless, the combination of strong lensing and dynamics has shown to be extremely useful for the study of the stars and dark matter in galaxies and to test general relativity.

Strong lensing can be used to study the inner density profiles of clusters, although results are still somewhat ambiguous. Of particular interest are clusters that show both tangential and radial arcs, because these can help to constrain the density profile. An analysis of such systems suggests an average slope $\beta \sim 0.5$. [22]

Outer regions: The value for the outer slope of the density profile is expected to be $\beta \sim 3$. A related prediction is that the mean central density of the halo decreases with virial mass, i.e., lower mass systems are more concentrated. The average dark matter profile of galaxy clusters has been studied using SDSS. These results agree well with predictions from ΛCDM models, as do studies of individual clusters such as Abell 1689.

The study of the outer parts of galaxies is more difficult, because the signal of an individual galaxy is too small to be detected. The interpretation of the observed signal, also known as the galaxy-mass cross-correlation function is complicated by the fact that it is the convolution of the galaxy dark matter profile and the (clustered) distribution of galaxies. Despite these limitations, galaxy-galaxy lensing studies provide a number of useful tests of the cold dark matter paradigm.

One such test is the measurement of the extent of dark matter halos. Pioneering studies were unable to provide constraints because of the small numbers of lens-source pairs. Large surveys, such as SDSS, RCS and CFHTLShave measured the lensing signal with much higher precision, enabling determination of the extent of dark matter halos around field galaxies. Note that these measurements use the small scale end of the galaxy-shear cross-correlation. [22]

Another area where galaxy-galaxy lensing studies will have a great impact is the study of the shapes of dark matter halos. CDM simulations predict that halos are tri-axial. This is supported by the findings that show the dark matter halos are on average aligned with the light distribution with a mean axis ratio that is in broad agreement with the CDM predictions. A similar result was obtained recently using CFHTLS data. Both these studies lacked the multi-color data to separate lenses by galaxy type. Such a separation was done using SDSS data. They did not detect a significant flattening, although their data do suggest a positive alignment for the brightest ellipticals.

The accuracy of these measurements is expected to improve significantly over the next few years as more data is collected as part of cosmic shear surveys. An accurate measurement of the anisotropy of the lensing signal around galaxies (i.e, the signal of flattened halos in CDM) is also a powerful way to test alternative theories of gravity. [22]

3.6 Gravitational Lensing in Cosmology

Gravitational lensing is an important tool for determining the values of cosmological parameters, for the characterization of dark matter and more recently used as "cosmic telescopes" to image objects that would otherwise not be visible. Strong gravitational lensing by galaxies and clusters provides one of the most striking confirmations of Einstein's theory of General Relativity. In the case of galaxy-galaxy lensing, the chance alignment of two galaxies along the line of sight

provides information about both the lens and the source that cannot be obtained in any other way. The angular separation of multiple images of a lensed galaxy is typically parameterized in terms of the angular Einstein radius and provides an unambiguous measurement of the total mass of the lens (baryonic plus non-baryonic) as long as the distances to the lens and source are known. At the same time, lensing increases the apparent size of the background source and conserves surface brightness in the process [8].

The Mass-Sheet Degeneracy

When modeling lensed quasars, on the basis of a few quasar images, one attempts to model the whole two-dimensional gravitational potential of the lensing galaxy or galaxies. There is no unique solution to the problem: too few observational constraints are available and several mass models giving each one a different time-delay can reproduce a given image configuration, its astrometry and flux ratios. In other words, lens models are degenerate.

Degeneracies have been described and blamed abundantly in the literature for being the main source of uncertainty in lens models. Whatever precision on the measured astrometry and time-delay, several mass models will predict several time-delays and hence several H_0. One must devise techniques to break the degeneracies or find quasars that are less affected by them.

The main degeneracy one has to face in quasar lensing is called the mass sheet degeneracy: when adding to a given mass model, a sheet of constant mass density (i.e., constant convergence), one does not change any of the observables, except for the time-delay. The additional mass can be internal to the lensing galaxy (e.g., ellipticity does not change the total mass within the Einstein radius, but does change at the position of the images) or due to intervening objects along the line of sight. The exact mass introduced by the mass sheet increases the total mass of the lens, but one can re-scale it and locally change its slope at the position of the images. The result is that the image configuration does not change, but the convergence, at the position of the images does change, and modifies the time-delay. Therefore, knowledge of the the slope of the mass profile of the lensing galaxy, whether it be under the form of a model or of a measurement, is one of the keys to having a "good" model. [10]

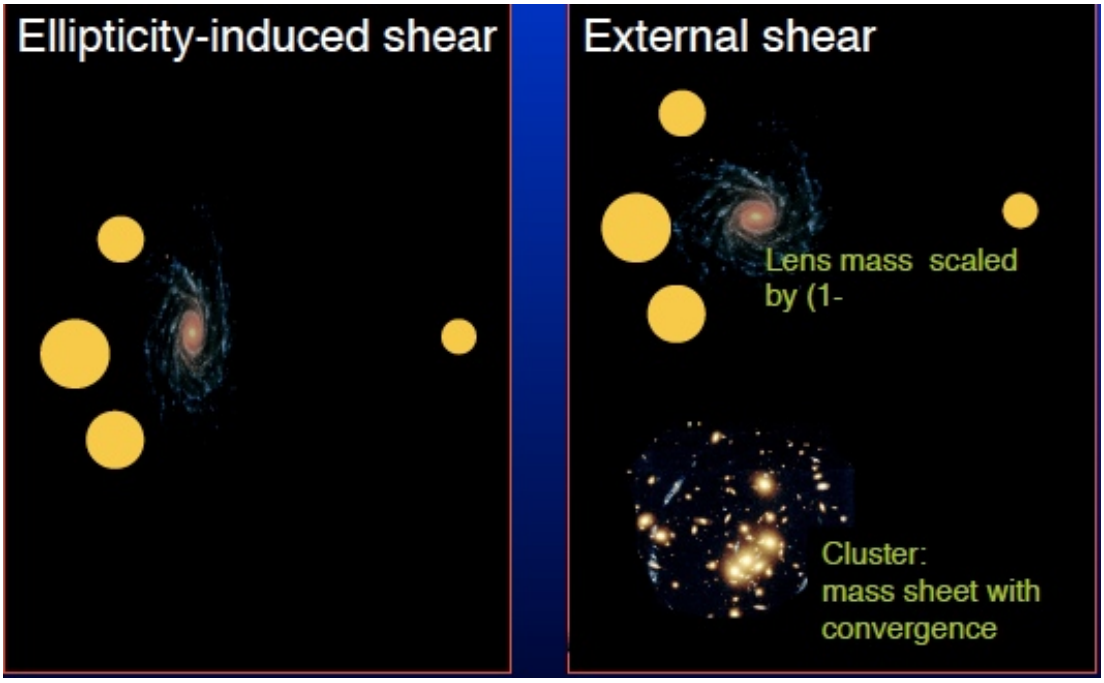

Figure 3.27: Two ways of obtaining a given image configuration. The left panel displays a system with four images, with an elliptical lens that introduces convergence and shear at the position of the images. On the right panel, is shown the same image geometry and flux ratios, but the lens is now circular. One would in principle only obtain two images with such a lens. The shear required to obtain four images is introduced by the nearby cluster. The mass density of the cluster is represented through its convergence . The mass of the main lens is scaled accordingly by $1/(1-\kappa)$ so that the image configuration remains the same as in the left panel: the mass in the main lens and in the cluster are degenerate. If no independent measurement is available for at least one of the components (main lens or cluster), it is often difficult to know, from the modeling alone, what exactly are their respective contributions.[10].

Adding convergence also modifies the shear, hence the ellipticity of the main lens. There are several ways of reproducing a given combination of shear and convergence at the position of the images, as illustrated in Figure 3.27. In the left panel of the figure, the shear is produced only by the main elliptical lensing galaxy. In the right panel, the total shear is a combination of the lens-induced shear and of that of the nearby galaxy cluster. In principle, it is even possible to model a given system equally with either one single elliptical lens or with a completely circular lens and an intervening cluster responsible for an "external" source of shear.

Both types of degeneracies can be broken or, at least, their effect can be strongly minimized, by constraining in an independent way (1) the mass profile of the main lens, and (2) the total mass (and possibly also the radial mass profile) of any intervening cluster along the line of sight. This work can be done with detailed imaging, spectroscopy of all objects along the line of sight, and by using numerical multi-components models for the total lensing potential

The Mass Sheet Degeneracy has its origin in the transformation shown here. Consider a strong lensing system with images coming from a single source. A uniform sheet of mass with

density Σ_s produces a deflection described by

$$\vec{\alpha}_s(\vec{\theta}) = \frac{D_s}{D_{ds}} \frac{\Sigma_s}{\Sigma_{cr}} \vec{\theta}, \tag{3.85}$$

in which the critical mass density for the current geometry is defined as follows:

$$\Sigma_{cr} = \frac{c^2}{4\pi G D_d} \frac{D_s}{D_{ds}}. \tag{3.86}$$

Note that Σ_{cr} depends on the redshift of the source via the angular diameter distances D_s and D_{ds}. Let $\Sigma_0(\vec{\theta})$ be a mass distribution that is compatible with the observed images. This means that the corresponding lens equation

$$\vec{\beta}_0(\vec{\theta}) = \vec{\theta} - \frac{D_{ds}}{D_s} \vec{\alpha}_0(\vec{\theta}) \tag{3.87}$$

projects the images onto the source plane in such a way that they overlap exactly. Without further constraints, this immediately yields an infinite number of alternative solutions. Indeed, if the mass distribution is replaced by

$$\Sigma_1(\vec{\theta}) = \lambda \Sigma_0(\vec{\theta}) + (1 - \lambda)\Sigma_{cr}, \tag{3.88}$$

the new lens equation becomes

$$\vec{\beta}_1(\vec{\theta}) = \vec{\theta} - \lambda \frac{D_{ds}}{D_s} \vec{\alpha}_0(\vec{\theta}) - (1 - \lambda) \frac{D_{ds}}{D_s} \vec{\alpha}_s(\vec{\theta}) = \lambda \vec{\beta}_0(\vec{\theta}). \tag{3.89}$$

The transformation (3.88) describes the so-called mass-sheet degeneracy and simply rescales the source plane by the factor λ, producing an equally acceptable source reconstruction. Note that merely adding a mass-sheet is not sufficient; one also needs to rescale the original mass distribution by the same factor λ, which justifies the alternative name of steepness degeneracy. The density of the mass-sheet has to be precisely the critical mass density for this to work. For this reason, a mass-sheet cannot be used when there are sources at different redshifts, since these would require different critical densities. [33]

The mass sheet degeneracy can also be looked at from the point of view of redshifts [6]. In the simple case of background sources all having the *same redshift*, the mass-sheet degeneracy can be understood just using the above equations. Indeed, consider for a moment the transformation of the potential ψ

$$\psi(\vec{\theta}, z) \to \psi'(\vec{\theta}, z) = \frac{1 - \lambda}{2} \vec{\theta}^2 + \lambda \psi(\vec{\theta}, z) \ , \tag{3.90}$$

where λ is an arbitrary constant. κ and γ are related to the potential ψ through its second partial derivatives (denoted by subscript), namely

$$\kappa = \frac{1}{2}(\psi_{,11} + \psi_{,22}) \ , \ \gamma_1 = \frac{1}{2}(\psi_{,11} - \psi_{,22}) \ , \ \gamma_2 = \psi_{,12} \ . \tag{3.91}$$

From (3.90) it follows that κ transforms as

$$\kappa(\vec{\theta}, z) \to \kappa'(\vec{\theta}, z) = \lambda \kappa(\vec{\theta}, z) + (1 - \lambda) \ , \tag{3.92}$$

and similarly the shear changes as $\gamma(\vec{\theta}, z)$ to $\lambda\gamma(\vec{\theta}, z)$. Therefore the reduced shear $g(\vec{\theta}, z)$ remains invariant.

It has been shown that in the case of a known *redshift distribution*, a similar form of the mass-sheet degeneracy holds to a very good approximation for non-critical clusters, i.e. for clusters with $|g(\vec{\theta}, z)| \leq 1$ for all source redshifts z. In such a case the standard weak-lensing mass reconstruction is affected by the degeneracy

$$\kappa \to \kappa' \simeq \lambda\kappa + \frac{(1-\lambda)\ \langle Z(z)\rangle}{\langle Z^2(z)\rangle}\ , \tag{3.93}$$

where $\langle Z^n(z)\rangle$ denotes the n-th order moment of the distribution of cosmological weights. As a result, *standard* weak-lensing reconstructions are still affected by the mass-sheet degeneracy even for sources at different redshifts; moreover, simulations show that the degeneracy is hardly broken even for lenses close to critical. [6].

One usually factors out the similarity transformation by working with a scaled arrival time surface like so [53]

$$\tau(\boldsymbol{\theta}) = \frac{1}{2}(\boldsymbol{\theta}-\boldsymbol{\beta})^2 - 2\nabla_{\boldsymbol{\theta}}^{-2}\kappa(\boldsymbol{\theta}). \tag{3.94}$$

Here the scaled arrival time τ, the scaled surface density (or convergence) κ and the operator $\nabla_{\boldsymbol{\theta}}^{-2}$ are all dimensionless. The physical arrival time and density are

$$t(\boldsymbol{\theta}) = (1+z_{\rm L})\frac{D_{\rm L}D_{\rm S}}{cD_{\rm LS}}\tau(\boldsymbol{\theta}), \qquad \Sigma(\boldsymbol{\theta}) = \frac{c^2}{4\pi G}\frac{D_{\rm S}}{D_{\rm LS}D_{\rm L}}\kappa(\boldsymbol{\theta}). \tag{3.95}$$

The usual lensing potential is $\psi = 2\nabla_{\boldsymbol{\theta}}^{-2}\kappa$ and the bending angle is $\boldsymbol{\alpha} = \nabla_{\boldsymbol{\theta}}\psi$.

We now rewrite (3.94) by discarding a $\frac{1}{2}\boldsymbol{\beta}^2$ term, since it is constant over the arrival-time surface, and using $\nabla_{\boldsymbol{\theta}}^2\boldsymbol{\theta}^2 = 4$, to get

$$\tau(\boldsymbol{\theta}) = 2\nabla_{\boldsymbol{\theta}}^{-2}(1-\kappa) - \boldsymbol{\theta}\cdot\boldsymbol{\beta}. \tag{3.96}$$

The transformation

$$1-\kappa \to s(1-\kappa), \qquad \boldsymbol{\beta} \to s\boldsymbol{\beta}. \tag{3.97}$$

clearly just rescales time delays while keeping the image structure the same; but since the source plane is rescaled by s all magnifications are scaled by $1/s$, leaving relative magnifications unchanged. The effect on the lens is to rescale the lensing mass and then add or subtract a constant mass sheet. This is (3.97) a magnification transformation, but it is usually referred to as the 'mass-sheet degeneracy' [53]

For a circular lens, the mass-sheet degeneracy preserves the total mass inside an Einstein radius $\theta_{\rm E}$. We can see this by invoking the two-dimensional analog of Gauss's flux law in electrostatics, which in lens notation becomes

$$\oint \boldsymbol{\alpha}\times d\mathbf{l} = 2\int \kappa\, d^2\boldsymbol{\theta}, \tag{3.98}$$

or that the normal component of $\boldsymbol{\alpha}$, integrated along any closed loop, is proportional to the enclosed mass. Along an Einstein ring, $\boldsymbol{\alpha}$ is always radial and hence normal to the ring; also, its magnitude always equals $\theta_{\rm E}$ (since a source at the centre is imaged onto the ring). Hence, the left hand integral in Eq. (3.98) depends only on $\theta_{\rm E}$. Meanwhile the right hand integral gives twice the enclosed mass. Thus, fixing the Einstein radius fixes the enclosed mass.

The mass-sheet degeneracy is broken if there are sources at more than one redshift. The reason is that we can no longer factor out the source-redshift dependence as we did in Eqs. (3.94) and (3.95). Instead, we can replace (3.94) and (3.95) with

$$\tau(\boldsymbol{\theta}) = \frac{1}{2}(\boldsymbol{\theta}-\boldsymbol{\beta})^2 - 2\frac{D_{\rm LS}}{D_{\rm S}}\nabla_{\boldsymbol{\theta}}^{-2}\kappa(\boldsymbol{\theta}), \qquad t(\boldsymbol{\theta}) = (1+z_{\rm L})\frac{D_{\rm L}}{c}\tau(\boldsymbol{\theta}), \quad \Sigma(\boldsymbol{\theta}) = \frac{c^2}{4\pi G}\frac{1}{D_{\rm L}}\kappa(\boldsymbol{\theta}), \tag{3.99}$$

and replace Eq. (3.96) with

$$\tau(\boldsymbol{\theta}) = 2\nabla_{\boldsymbol{\theta}}^{-2}\left(1 - \frac{D_{\rm LS}}{D_{\rm S}}\kappa\right) - \boldsymbol{\theta}\cdot\boldsymbol{\beta}, \tag{3.100}$$

Sources at different redshifts imply simultaneous equations of the type (3.100) but with different factors of $D_{\rm LS}/D_{\rm S}$, which prevents a transformation like (3.97). [53]

The mass distribution $\kappa(\boldsymbol{\theta})$ and each of the distributions

$$\kappa_\lambda(\boldsymbol{\theta}) = \lambda\,\kappa(\boldsymbol{\theta}) + (1-\lambda)\,, \tag{3.101}$$

together with an (in most cases unobservable; see below) isotropic scaling of the source plane coordinates $\beta \to \lambda\,\beta$, yields exactly the same dimensionless observables, i.e., image positions, image shapes, magnification ratios, etc. This is called the mass-sheet degeneracy (MSD). In other words, from the observed image positions and flux ratios, one cannot distinguish between the original κ and any of the mass distributions in (3.101). Weak gravitational lensing cannot break the MSD, since image shapes are unaffected. However, the product of the time delay and the Hubble constant is affected, $H_0\,\Delta t \to \lambda\,H_0\,\Delta t$, but leaving time delay ratios again invariant. [56]

Breaking the mass-sheet degeneracy

The mass-sheet transformation (MST) leaves the critical curves invariant, also the curves on which $\kappa = 1$. Furthermore, it leaves the shapes of the isodensity contours invariant, just the value of κ on these contours changes according to (3.101).

As is clear from the transformation of $H_0\,\Delta t$, in order to get a reliable estimate of the Hubble constant from gravitational lensing, one first needs to break the MSD. Several ways have been suggested in the literature. Some of these make use of the fact that the MST (3.101) affects the magnification, $\mu \to \mu/\lambda^2$, hence if the magnification can be estimated, the value of λ can be constrained (this magnification corresponds to the aforementioned isotropic scaling of the source plane coordinates). For AGN as sources, which have a very broad distribution of intrinsic luminosities, this cannot be easily accomplished. It has been shown that the correlation between AGN variability properties and luminosity can be used as a tool for estimating source luminosities, and hence lensing magnification, the scatter of the variability–luminosity relation is large and can only be employed in a statistical way.

Another possibility to break the MSD in strong lensing systems is based on independent mass estimates of the lens. Combining lensing measurements with spectroscopy of the lens galaxy, the MSD can be broken.For early-type galaxies (most lenses are of that type), the stellar velocity dispersion yields an estimate of the mass inside the effective radius of the lens, which together with the precise (and unaffected by the MST) determination of the mass inside the Einstein radius of the lens allows one to determine the mean slope γ' of the mass profile between the effective radius and the Einstein radius. [56]

In general, the velocity dispersion measurement in individual systems is derived with typically 10% uncertainty, which translates into an uncertainty of the same order on the logarithmic slope of the profile The radial/tangential anisotropy of the stars commonly encoded in the anisotropy parameter $\beta = 1 - (\bar{\sigma_\theta^2}/\bar{\sigma_r^2})$ also systematically affects the estimate of the slope to a level which can reach 15%. The impact of anisotropy may in practice be smaller, i.e. less than 5%.

In any case, the MST to first order corresponds to a scaling of the three-dimensional mass distribution by a factor λ – with the constant $(1-\lambda)$-term corresponding to a larger-scale 3-D mass component which contributes little to the gravitational potential inside the effective radius.

Since $\sigma^2 \propto M$, we find that $\Delta H_0/H_0 = \Delta\lambda/\lambda = \Delta M/M = 2\Delta\sigma/\sigma$. Thus an uncertainty of 6% in the stellar velocity dispersion translates into a $\sim$ 12% uncertainty in the Hubble constant, even if we ignore uncertainties regarding orbit anisotropies and triaxiality of the mass distribution.

[6] uses the information of *individual redshifts* of background sources to break this degeneracy. As an illustration of the effect, suppose that half of the background sources are located at a known redshift $z^{(1)}$, and the other half at another known redshift $z^{(2)}$. Then, the weak lensing reconstructions based on the two populations will provide two different mass maps, $\kappa'(\vec{\theta}, z^{(1)})$ and $\kappa'(\vec{\theta}, z^{(2)})$, leading to two different forms of the mass-sheet degeneracy. In other words, the two mass reconstructions ($i = 1, 2$) are given by

$$\kappa'(\vec{\theta}, z^{(i)}) = \lambda^{(i)}\kappa_{\rm t}(\vec{\theta}, z^{(i)}) + \left(1 - \lambda^{(i)}\right) \tag{3.102}$$

where they denote $\kappa_{\rm t}(\vec{\theta}, z^{(i)})$ the true projected κ of the lens at the angular position $\vec{\theta}$ for sources at redshift $z^{(i)}$. Since the transformation (3.102) holds for any $\vec{\theta}$, we have a system of equations to be solved for $\lambda^{(1)}$ and $\lambda^{(2)}$. The relation between $\kappa_{\rm t}(\vec{\theta}, z^{(1)})$ and $\kappa_{\rm t}(\vec{\theta}, z^{(2)})$ is known, and it follows

$$\kappa_{\rm t}(\vec{\theta}, z^{(1)})Z(z^{(2)}) = \kappa_{\rm t}(\vec{\theta}, z^{(2)})Z(z^{(1)}). \tag{3.103}$$

If one measures both $\kappa'(\vec{\theta}, z^{(i)})$ at N different positions $\vec{\theta}_j$, this gives us a system of $2N$ equations to be solved for $\lambda^{(i)}$ and $\kappa_{\rm t}(\vec{\theta}_j)$. The mass-sheet degeneracy is therefore at least in theory lifted. [6]

It is interesting to observe that this argument only applies to relatively "strong" lenses. Indeed, for "weak" lenses, i.e. lenses for which we can use a first order approximation in κ and γ, the expectation value of measured image ellipticities is $\langle\epsilon(z)\rangle = \gamma(\vec{\theta}, z)$. In such case the degeneracy of the form

$$\psi(\vec{\theta}, z) \to \psi'(\vec{\theta}, z) = \frac{1-\lambda}{2}\vec{\theta}^2 + \psi(\vec{\theta}, z) \tag{3.104}$$

leaves the observable $\gamma(\vec{\theta}, z)$ unchanged. As a result, the method described above cannot be used to break the mass-sheet degeneracy for these lenses. Only when the $(1 - Z(z)\kappa)$ term in the reduced shear becomes important and $g(\vec{\theta}, z)$ can be distinguished from $\gamma(\vec{\theta}, z)$ in the (noisy) data, is it possible to make unbiased cluster mass reconstructions. [6]

[59] describe two methods for breaking the mass-sheet degeneracy:

i. *Stellar dynamics of the lens galaxy.* Stellar dynamics can be used jointly with lensing to break the internal mass-sheet degeneracy by providing an estimate of the enclosed mass at a radius different from the Einstein radius, which is approximately the radius of the lensed images from the lens galaxy. We note that for a given stellar velocity dispersion, there is a degeneracy in the mass and the stellar orbit anisotropy (which characterizes the amount of tangential velocity dispersion relative to radial dispersion). Nonetheless, the mass-isotropy degeneracy is nearly orthogonal to the mass-sheet degeneracy, so a combination of the mass within the effective radius (from the stellar velocity dispersion) and the mass within the Einstein radius (from lensing) effectively breaks both the mass-isotropy and the internal mass-sheet degeneracies.

ii. *Studying the environment and the line of sight to the lens galaxy.* Observations of the field around lens galaxies allow a rough picture of the projected mass distribution to be built up. Many lens galaxies lie in galaxy groups, which can be identified either by their spectra or, more cheaply (but less accurately), by their colors and magnitudes. By modeling the

mass distribution of the groups and galaxies in the lens plane and along the line of sight to the lens galaxy, one can estimate the external convergence κ_{ext} at the redshift of the lens. The group modeling requires (i) identification of the galaxies that belong to the group of the lens galaxy, and (ii) estimates of the group centroid and velocity dispersion. A number of recipes can be followed. Two extremes can be considered: (i) the group is described by a single smooth mass distribution, and (ii) the masses are associated with individual galaxy group members with no common halo. The realistic mass distribution for a galaxy group should be somewhere between these two extremes. The experience to date is that modeling lens environments accurately is very difficult, with uncertainties of 100% typical.

[59] emphasizes that the mass-sheet degeneracy is simply one of the several parameter degeneracies in the lens modeling that has been given a special name. When power-laws ($\kappa \sim bR^{1-\gamma'}$, where R is the radial distance from the lens center, b is the normalization of the lens, and γ' is the radial slope in the mass profile) are used to describe the lens mass distribution, one often finds a H_0-γ' degeneracy in addition to the H_0-b-$\kappa_{\rm ext}$ (mass-sheet) degeneracy (for fixed $\Omega_{\rm m}$, Ω_Λ and w; more generally, $D_{\Delta {\rm t}}$ would be in place of H_0). These two degeneracies are of course related via H_0. The H_0-γ' degeneracy primarily occurs in lens systems with symmetric configurations due to a lack of information on γ'. In contrast, lens systems with images spanning a range of radii or with extended images provide information on γ', and so the H_0-γ' degeneracy is broken. Nonetheless, the H_0-b-$\kappa_{\rm ext}$ degeneracy is still present unless information from dynamics and lens environment studies is provided.

Dark Matter and Gravitational Lensing

The discussion of dark matter will begin with a definition (3.6, followed by some general ideas to characterize dark matter (3.6). We will then discuss some of the problems in the CDM model that are brought about by the concept of dark matter (3.6), and then discuss methods for detecting dark matter. Last, we will look at four effects of dark matter on the universe and how those effects can be used to determine the nature of dark matter (3.6).

Definition

Dark matter has been defined as any form of matter whose existence is inferred solely on the basis of its gravitational effects. The existence of dark matter in galaxy clusters was predicted by Fritz Zwicky in the 1930's, who observed that galaxies in clusters are moving faster than predicted by their mass estimates. This preceded the pioneering work of Vera Rubin, who accurately measured the rotation curves of galaxies and found that experimental results required the existence of dark matter. This research took a great leap forward in the 1990s when numerical simulations of structure formation with CDM were performed. Dark matter does not emit or absorb light in any form, thus it does not interact electromagnetically.

Characterization of Dark Matter

Dark matter is characterized as ordinary matter (i.e. baryonic matter, e.g. MACHOs) or some other kind of matter (i.e. non-Baryonic matter, e.g. WIMPs). Most research has looked at these two main groups of particles. At this time, many investigators believe that WIMPs or other non-baryonic particles appear to be the most promising possibility among a long list of possibilities [58]. The search to characterize the properties of dark matter is one of the most important lines of investigations in cosmology today, and is seen as an integral part of verifying the existing models of cosmology.

According to the standard model, baryonic dark matter is required to make up the difference between the visible matter density and the baryon density as required by standard BBN models. Exactly where these baryons might be hiding depends on the nature of the objects being studied.

Characterization of non-baryonic dark matter is done in one of two ways, either direct or indirect. Direct searches depend on dark matter particles actually passing through detectors and physically interacting with them. Indirect searches look for secondary products produced when dark matter particles annihilate each other elsewhere. Direct searches can, in principle, be used to look for neutrinos, axions and WIMPs, whereas only WIMPs are accessible indirectly [58]. These methods will be discussed below in Section 2.3, Specific Dark Matter Detection Techniques.

Problems with DM in the ΛCDM model of Cosmology

On large scales, the ΛCDM simulations work quite well, while on galaxy scales there are 3 main problems that arise when comparing observational results with those predicted by the models. An understanding of these 3 problems which result from the comparing the numerical simulations to observation is essential to understand the nature of dark matter in galaxies.

1. Core-Cusp problem: The core-cusp problem arises from the CDM simulations that suggest that CDM forms "cusp distributions", meaning that they increase sharply to a high value at a central point. This would suggest that the center of the galaxy has a higher dark matter density, but this has not been observed [11]. There have been three suggested ways to interpret the constraints of the core-cusp problem including: (a) CDM halos do in fact have cusps, constraining cosmological parameters, (b) Something eliminates the cusps (feedback, modified dark matter), or (c) The CDM simulations which show cusp formations are wrong [64].

2. Angular momentum problem: The angular momentum problem is a result of the types of models used to describe the CDM universe. This includes three basic issues: disks rotate too fast at a given luminosity, mass (dark and luminous) is too concentrated and that disks are too small at a given rotation speed [7]. This was worked out by Navarro and Steinmetz, who concluded that the dark halos are much less centrally concentrated than those formed in the CDM models they investigated, suggesting the need for extreme feedback [40].

3. Missing satellite problem: The existence of dark matter is based on a number of lines of evidence, including the rotation curves of spiral galaxies, x-ray halos in elliptical galaxies, kinematics of galaxy clusters and gravitational lensing toward galaxy clusters. One goal of determining the nature of dark matter is to better understand the true history of structure formation of the universe and to basically "build better models". The magnitude of this problem is suggested by model predictions of 10,000 satellite galaxies in the Milky Way galaxy, while only 30 have been identified.

Since our understanding of the universe is based currently on the CDM model, these three problems which are a result of the models currently in use, represent significant areas of research in cosmology today, and motivate attempts to further understand dark matter.

Dark Matter- Evidence

The existence of dark matter is based on a number of lines of evidence. Basically, since dark matter is not directly observable (yet), we rely on observing its effects to infer its existence. Continuing research related to dark matter is basically in two tracks. Next, we will look at ways of studying the effects of dark matter on various aspects of the Universe including

- Mass Distribution

- Dark Matter and Global Shape
- Density Profile
- Dark Matter Substructure

While many lines of evidence support the existence of dark matter, at this time we have only been able to observe its effects and have not directly observed or characterized dark matter. This evidence and the observed effects are all based on gravitational effects. It is of course possible that our understanding and/or characterization of gravity is fundamentally flawed, which leads us to erroneously attribute these observations to dark matter.

Mass Distribution

In a simple calculation based on the mechanics of Kepler's third law, it is easy to show that

$$M = \frac{V^2 r}{G} \tag{3.105}$$

If we solve this equation for our own solar system with the radius of the sun's orbit and velocity of the sun, then this predicts that there are about 1 x 10^8 solar masses inside the sun's orbit. Clearly, something is wrong! This is a very simple and fast illustration of why the concept of dark matter has been invoked. Other data has also been used more convincingly.

Until the 1970s, rotation data for spiral galaxies came from optical observations which do not extend beyond the luminous inner regions. At that time, the optical rotation curves seemed consistent with the distribution of luminous matter. With the construction of radio telescopes, it became possible to measure the distribution and rotation of the H I in spiral galaxies, which showed that the H I in many spirals extended far beyond the starlight, and that the H I rotation curves in such galaxies showed nearly constant rotational velocity out to the radial limits of the data [16].

This was unexpected, because a flat rotation curve means that the total mass of the spiral within some radius r increases linearly with r, while the total luminosity approaches a finite asymptotic limit as r increases. It soon became clear that a large amount of invisible gravitating mass (more than 90 per cent of the total mass in some examples) is needed to explain these flat rotation curves (see Figure 3 below). At the radial limit of the data, the dark halo is providing most of the total gravitational field. In almost every example, a massive dark halo that dominates the enclosed mass M(r) at large r is needed to explain the observed rotation curves. The nature of this dark matter remains unknown, and is one of the great problems of modern astrophysics [16].

The studies of the masses of spiral galaxies are based on the 21cm emission line of hydrogen in spiral galaxies, to trace orbital motions. The rotation curve is then used to determine the total amount of mass as a function of distance from the center. Rotation curves measure the mass distribution of a galaxy. This is discussed further below in the section 'Dynamical Effects of Dark Matter on Visible Structure'. Spiral galaxies all tend to have flat rotation curves indicating large haloes of dark matter.

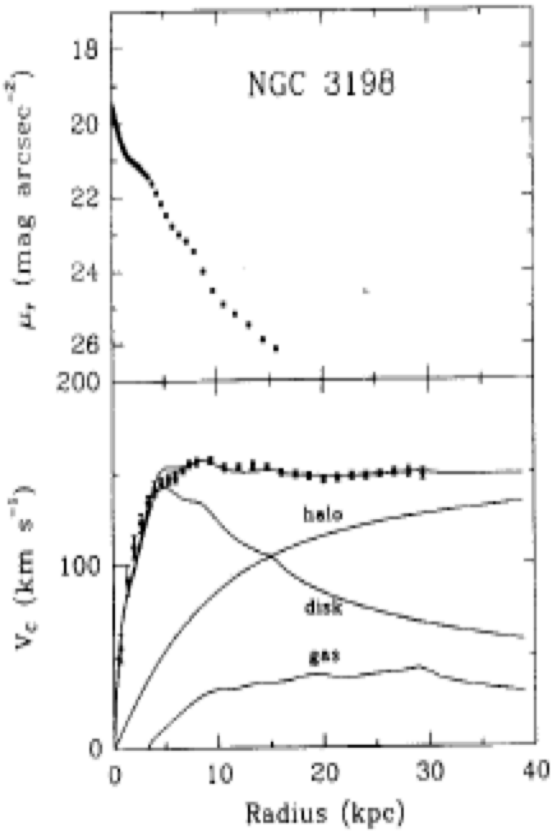

Figure 3.28: Rotation curve for a typical galaxy from [16]. The lower panel hows the H1 rotation curve (points). The curve labelled disk shows the expected rotation curve if the surface density distribution followed the surface brightness distribution in the upper panel. The curve labelled gas is the contribution to the rotation curve from the observed gas. The curve labelled halo is the rotation curve of the adopted dark halo model: the three labelled rotation curves, when added in quadrature, produce the total rotation curve that passes through the observed points.

Measuring mass in elliptical galaxies is slightly different, since ellipticals have very little gas which makes it impossible to use the 21cm H line, as is done with spiral galaxies. Elliptical galaxies are not supported by rotation, so rotation curves cannot be used to study their dark matter content. Elliptical galaxies are studies with the broadening of stellar spectral lines. Broader lines generally indicate faster star movement.

Measuring mass in galaxy clusters is somewhat different. The velocities of galaxies are studied by their Doppler shifts. Up to 50 times the mass of the stars is found in clusters. Another method of measuring cluster mass is based on the fact that clusters contain large amounts of hot x-ray emitting gas. The temperature of this hot gas measures the cluster's mass because the gas is held it the cluster by gravitational forces. Cluster masses obtained by x-ray measurements agree well with the galactic velocity method. A third method of determining the mass in galaxy clusters is using gravitational lensing, discussed further below.

Especially for galaxy clusters, the mass function is an important tool of the theoretician.

The mass function describes the halo mass distribution in the Universe. The evolution of the mass function is sensitive to cosmology because matter density controls the rate of the growth of structure. There have been a number of analytic methods used to calculate the mass function for dark matter halos, which can show the evolution of the mass function with different cosmologies, for example standard CDM with Ω_m=1.0, Open CDM with Ω_m=0.3 and Ω_Λ=0, or ΛCDM with ω=-0.8. Two of the mass functions that have been used are the Press-Schechter and the Sheth-Tormen types. These are then used in simulations to understand the mass function of dark matter halos. The halos present a set of specific difficulties in calculating the mass function [20].

Studies of mass-to-light ratios show that as one proceeds farther from the center, there is more mass per light. Thus, most matter is not luminous and it is not concentrated centrally.

The existence of galactic halos of dark matter is mainly derived from studies of stars and gas in spiral galaxies. It is acknowledged that much less is known about dark matter around elliptical galaxies. In an interesting study of gravitational lensing to derive the masses of elliptical galaxies, Magain and Chantry found that the mass to light ratios in these galaxies does not depend on radius and that the mass does not exceed the value predicted by stellar population models by more than a factor of two [35]. They conclude that these results can be explained by baryonic matter alone, without the need for dark matter. These results are in sharp contrast to what is found from the rotation curves of spiral galaxies.

Testing predictions from numerical dark matter simulations and probing dark energy require precise measurements of galaxy cluster masses, however it is nontrivial to define what is meant by the mass of a cluster because clusters do not have any clear boundary between themselves and the surrounding large-scale structure. By convention cluster mass has been defined as the mass enclosed within a three-dimensional sphere of a given radius with respect to the halo center such as the virial mass. Given a working definition of mass, a method of mass measurement must be chosen, each of which suffers a number of advantages and disadvantages [48]. The problem of cluster mass determination is being studied intensively with gravitational lensing.

Dark Matter and Global Shape

The shapes of the dark matter halos are not expected to be spherical. One of the general predictions of structure formation within the prevailing cold dark matter (CDM) paradigm is that galaxy-scale dark matter haloes should be described by a triaxial density ellipsoid [29]. Despite the near-ubiquitous predictions of triaxiality from such simulations, there has not been much observational evidence to confirm triaxiality in specific individual galaxies, although gravitational lensing and X-ray observations have indicated that non-sphericity appears to be common in dark matter haloes, such studies are sensitive only to the integral of the density profile along the line of sight and do not provide real three dimensional information [29]. The Milky Way Galaxy provides perhaps the best laboratory for testing predictions of halo sphericity since the tidal stream remnants of dwarf satellites orbiting in the Galactic halo can be traced in three dimensions and provide sensitive probes of the underlying mass distribution. Observations of the lengthy tidal streams produced by the destruction of the Sagittarius dwarf spheroidal are capable of providing strong constraints on the shape of the Galactic gravitational potential. However, previous work, based on modeling different stream properties in axisymmetric Galactic models has yielded conflicting results: while the angular precession of the Sgr leading arm is most consistent with a spherical or slightly oblate halo, the radial velocities of stars in this arm are only reproduced by prolate halo models. Law and colleagues [29] demonstrated that this apparent paradox can be resolved by instead adopting a triaxial potential. Their new Galactic halo model, which simultaneously fits all well-established phase space constraints from the Sgr

stream, provides the first conclusive evidence for, and tentative measurement of, triaxiality in an individual dark matter halo.

Since the natural shape of dark matter is triaxial as is confirmed as well from the cosmologicial N-body simulations, it is surprising at first sight that disk galaxies are roughly axisymmetric in the outer parts. Yet this has been shown with very high quality HI data. This suggests strongly that the process of disk galaxy formation is such that the original triaxial dark matter halo shape is modified by the formation of the disk, e.g. due to dissipation. The shape of the dark matter halo close to the disk should be either oblate or prolate [5].

The application of gravitational lensing to determine the shape of dark matter halos was nicely demonstrated in a landmark study by Oguri and colleagues [45], who observed 20 massive clusters of galaxies with the Subaru Telescope's Prime Focus Camera (Suprime-Cam). Clusters of galaxies are ideal sites for studying the distribution of dark matter, because they contain thousands of galaxies and are known to accompany a large amount of dark matter. The superb light-collecting power and excellent image quality of the Subaru Telescope gave the researchers an extra advantage. By using Suprime-Cam at prime focus, they could capture objects in a particularly wide field-of-view.

Observations with Suprime-Cam yielded wide-field images of 20 massive clusters of galaxies (typically located at 3 billion light years from Earth), which were then used to measure and analyze dark matter distributions. From their detailed analysis of gravitational lensing effects in the images, they obtained clear evidence that the distribution of dark matter in the clusters has, on average, an extremely flattened shape rather than a simple spherical contour. The measured degree of the flattening is quite large, corresponding to 2:1 in terms of the ratio of major to minor axes of the ellipse.

This finding represents the first direct and clear detection of flattening in the dark matter distribution with the use of gravitational lensing. In addition to the promise of using gravitational lensing for exploring the nature of dark matter, this research contributes to the theoretical modeling of dark matter. Detailed comparisons of the team's findings with theoretical model predictions of the distribution of dark matter show that the observed degree of the flattening is in excellent agreement with theoretical expectations [43].

Density Profile

In the 1990s, numerical simulations were used to fit an analytic density profile to density distributions to predict a density profile, called the NFW profile (Navarro, Frenk and White). Other density profiles have been evaluated to fit the rotation curves. A major motivation is to test key predictions from the cold dark matter theory of structure formation: (1) the density profile of the dark matter halos posited to host galaxies and cluster of galaxies is predicted to be universal and follow a simple 2-parameter model and (2) massive galaxy cluster-scale dark matter halos have concentrations that are less concentrated than less massive halos [47].

Gravitational lensing has been used as a probe of the dependence of cluster density on cluster-centric radius, which is known as the density profile. This has been done with three different approaches including statistics of multiply lensed QSOs, time delay statistics and arc statistics [41; 42].

The mass and internal structure of galaxy clusters reflect the properties of primordial density perturbations and the nature of dark matter. One of the most interesting predictions from numerical simulations based on the cold dark matter (CDM) model of structure formation is that dark matter halos can be described by the NFW profile [48]. These results have shown that cluster-scale halos should have relatively shallow, low-concentration mass profiles, where the power-law slope of density profile becomes more negative with increasing radius, approaching

an asymptotic slope of ?3 around the virial radius.

One of the most recent methods to probe the mean mass density profile of cluster-scale dark matter halos was reported by Okabe and colleagues, using stacked weak-lensing [47]. In this study, a mass-selected sample of clusters at z 0.2 was analyzed using a stacked weak lensing analysis, based on Subaru observational data. An NFW model was used to fit the data. This study is important because it shows the potential for weak lensing techniques to be used to determine the mean mass density profiles of cluster-scale dark matter halos.

Dark matter substructure

The cold dark matter (CDM) paradigm predicts the presence of numerous substructures in dark halos on any scale, because less massive objects form earlier and become more massive through mergers. High- resolution N-body simulations have shown an assembly history that subhalos continually fall into larger halos [46].

The missing satellite problem, where cosmological simulations of CDM predict a significantly larger fraction of lower mass satellites around galaxies than is detected, represents a major puzzle in the study of structure formation [34]. The SDSS has found additional faint satellites in the Milky Way, but the numbers are much lower than the predicted abundances of sub haloes [34]. One approach to finding these dark satellites is through gamma rays emitted by dark matter annihilation. Gravitational lensing is am alternative way to detect subhaloes. Using gravitational lensing, there are several approaches including the effect on image positions, and their effect on time delays in the case of massive satellites.

Quadruply gravitationally lensed quasars are extremely useful objects for lensing studies because they provide a large number of constraints on the models of the mass distribution of the lensing galaxies. Simple models for the gravitational potentials – a monopole plus a quadrupole – are extremely good at reproducing the positions of the quasar images. However, there are some cases where they fail to produce the observed fluxes of the images. This is termed a flux ratio anomaly and is most likely due to small scale structure in the mass distribution of the lens. The idea is that there is some mass condensation in the smooth dark matter distribution of the lensing galaxy, and this object further perturbs the light from the background quasar through its own gravitational influence. Although the angular deflection due to such an object is undetectable with current telescopes, the change in brightness is detectable, leading to the observed flux ratio anomaly [49]. Many lenses have flux ratio anomalies, where the relative brightnesses cannot be explained by simple central lens galaxies. Mid-IR observations have been used in the search for substructure and using this technique in a multiply lensed galaxy, the observed flux-ratio anomaly is used as evidence of low-mass substructure [34].

The study of MG0414+0534 is interesting as an example of using flux ratio anomalies to study substructure. This quadruply lensed quasar (zs=2.64, zl=0.96) is radio-loud, and was discovered in 1989 by Hewitt. The fact that it is a radio loud quasar makes it unusual, and important for study because the radio data can be compared with optical data.

It was then studied by Falco and coworkers who reported that the flux ratios were different comparing the optical and radio data [15]. The system was analyzed using four different gravitational lens models. They suggested microlensing as a possible explanation for this difference. Keeton et al then discussed the origin of shear in gravitational lenses, including a discussion of MG0414 [26]. They concluded that the most important source of ellipticity in gravitational lenses is the primary lens galaxy. This system was also reviewed by Mao and Schneider, who clearly state that the difference in flux ratios observed may be a result of small scale structure within the lens galaxy [36]. By this time, no one had yet applied the term flux ratio anomaly to this phenomenon.

This quasar was studied by Minezaki et al [38] who found a flux ratio anomaly at mid-IR wavelengths that suggests a millilensing structure. Mid-IR is used because image fluxes can be affected by extinction and microlensing in the primary lens at the easily observed wavelengths. At mid-IR, both extinction and microlensing are negligible [34]. The models of Minezaki et al were extended to a more detailed model in the work by MacLeod and colleagues [34] who used Lensmodel software, and found that the model had a significantly improved fit with the addition of a third lens near image A2. MacLeod and colleagues found a flux ratio of 0.93 ± 0.02 for the A2/A1 images. This ratio should be 1.00 since they are bright, close images, if one assumes a smooth lens model. The fact that they are 5σ apart is the flux ratio anomaly, which suggests substructure. The results of MacLeod are very close to those observed my Minezaki. The fact that the anomaly persists into the mid-IR is considered evidence that it is a result of substructure in the lens (millilensing) which is concluded both by MacLeod and Minezaki.

MacLeod and colleagues not only did detailed observational studies, but they then used lensmodel software to model the system. They started with G1 and G2, as in previous studies and then added a third lens galaxy (G3) with an SIS profile at various positions surrounding the lens, searching for a better fit to the observed flux ratios. This third galaxy distorts the critical curves near images A1 and A2 (see their Fig 6), bringing their flux ratio back into agreement with the mid-IR data. The exact nature of G3 is not yet known [34].

Summary: The nature of dark matter

The existence of dark matter is inferred from its gravitational effects, and has not been observed directly. There have been many attempts to characterize dark matter, and non-baryonic particles are considered to be strong possibilities. Searches for dark matter are characterized as direct or indirect. Considerations of dark matter within the CDM model of cosmology have led to three problems including

- The core-cusp problem
- The angular momentum problem
- The missing satellite problem

Efforts to understand dark matter are focused on (a) methods to detect dark matter and (b) understanding the effects of dark matter on galactic structure.

There are several methods being used to identify and determine the nature of dark matter including:

- WIMP annihilation: WIMPS may be the non-baryonic matter which comprises dark matter, but cannot be observed directly. Annihilation of WIMPS in the dark matter halos produce high energy particles, which if observed, could be evidence that WIMPS exist.
- Dynamical effects on visible galactic structure: The effect of dark matter on the kinematics of galaxies and clusters is used as evidence that dark matter exists. For galaxy clusters, mass of the cluster is calculated based on the virial theorem. These dynamical effects have been used to determine the mass of galaxies and clusters.
- Gravitational lensing: Gravitational lensing was the second observational test of general relativity in 1919, and has become one of the most important tools in modern cosmology. The deflection of light from a background source by an intervening galaxy is categorized as strong, weak or micro-lensing. Analysis of the images formed can lead to quantitative

methods to calculate many cosmological parameters of interest, including galactic mass, shape, density profiles, and the locations of dark matter substructure.

These three techniques described above are then being used to investigate the effects of dark matter on the universe, including such features as:

- Mass distribution: On a basic level, this is how the existence of dark matter was originally inferred, by looking at the rotation curves of galaxies and noting that they were "flattened" suggesting the existence of much more matter than is explained by luminous matter.
- Shape: Gravitational lensing has been used recently to verify an extremely flattened shape for the distribution of dark matter in clusters.
- Density Profile: Stacked weak lensing has recently been used to determine the mean mass density profiles of cluster-scale dark matter halos.
- Dark matter substructure: Recent studies of the quadruply lensed radio-loud quasar MG0414 used detailed mid-IR measurements to identify the flux ratio anomaly in this object, confirming the previous results of Minezaki and colleagues [38] and then use lens modeling to suggest the position of dark matter (G3) to explain the observed flux ratio anomaly.

Gravitational Lensing as Cosmic Telescopes

In a typical galaxy-scale strong lens system, the background source is magnified by an order of magnitude. Exploiting this effect, lensed galaxies at intermediate and high redshift can be studied with the same level of detail as non-lensed galaxies in the local universe (§ 3.6). Furthermore, the host galaxies of bright active galactic nuclei are "stretched away" from the wings of the point spread function, enabling precise measurements of their luminosity and size, and ultimately of the cosmic evolution of the relation between host galaxy and central black hole (§ 3.6). Finally, microlensing by stars provides us with unique spatial information on the scale of the accretion disk, which is orders of magnitudes smaller than anything that can be resolved from the ground at any wavelength (§ 3.6).

Small and faint galaxies

The resolution of HST and the sensitivity of radio interferometers mean that we know very little about the distant ($z >> 0.1$) universe on scales below $\sim$ 1 kpc. Indeed, even in the nearby universe ($z \sim 0.1$), large ground based surveys such as SDSS do not provide much sub-kpc scale information. Yet, we know from the local volume that small and faint galaxies are an essential ingredient of the universe, acting as building blocks of more massive systems. Only with the aid of gravitational lensing we can resolve sub-kpc scales and determine the morphology and size, and kinematics of small galaxies as well as trace the location of star formation and the pattern of chemical abundances. Furthermore, flux magnification enables detailed spectroscopic studies that would be prohibitive in the absence of lensing. These pilot studies show that intrinsic properties can be robustly recovered via lens modeling. The rapid increase in the number of known lenses should soon provide the large statistical samples needed for high impact studies. [61]

Host galaxies of lensed active nuclei

In the local universe, massive galaxies are found to harbor central supermassive black holes. Remarkably, the mass of the black hole correlates with kpc-scale properties of the host bulge, such as velocity dispersion, luminosity and stellar mass. This family of correlations has been interpreted as evidence that black hole growth and energy feedback from active galactic nuclei play an important role in galaxy formation and evolution. However, the physics of the interaction as well as the relative timing of galaxy formation and black hole growth are poorly understood. Although the local relations are an important constraint, observing their cosmic evolution is necessary to answer some fundamental questions. Are the local relations only the end-point of evolution, or are they established early-on? Which comes first, the black hole or the host bulge?

It is challenging to answer these questions observationally. Direct dynamical black hole mass measurements can only be done in the very local universe. At intermediate and high-z redshift, one needs to rely on indirect methods such as the empirically calibrated relation with continuum luminosity and line width observed for type-1 active galactic nuclei (AGN). However, the presence of bright luminous point sources hampers the study of the host galaxy. Strong lensing helps by stretching the host galaxy of distant lensed quasars primarily along the tangential direction. Of course, the quasar is also magnified, but one generally wins because the surface brightness of the point spread function falls off more rapidly than linearly. Using this method, showed that the bulges of host galaxies of distant quasars are more luminous than expected based on the local relation, consistent with a scenario where bulge formation predates black hole growth, at least for some objects. Similar results have been found for non-lensed AGN. However, without the aid of lensing, studies have to be limited to lower redshifts and lower luminosity AGNs. [61]

Structure of active galactic nuclei

Understanding the physics of accretion disks and the regions surrounding supermassive black holes is essential to explain the AGN phenomenon with all its implications for galaxy formation and evolution. However, the scales involved are extremely small by astronomical standards (for a typical 10^9 $M_\odot$ black hole, the Schwarzschild radius is $\approx 3 \cdot 10^{14}$ cm, the broad line region is $\sim 10^{17-18}$ cm), and therefore impossible to resolve with conventional imaging techniques.

Microlensing is perhaps the only tool capable of probing the small scales of the accretion disk. The Einstein radius of a star of mass M_s, corresponds to approximately $4 \cdot 10^{16} \sqrt{M_s/M_\odot}cm\approx$ $0.01 \sqrt{M_s/M_\odot}$pc when projected at the redshift of a typical lensed quasar. The inner parts of the accretion disk will be smaller than this scale and therefore subject to microlensing, while the broad line region and the outer dusty torus should be largely unaffected. The characteristic timescale for variation is given by the microlensing caustic crossing time, typically of order years, although it can be shorter for special redshift combinations such as that of Q2237+030. [61]

Based on this principle, one can infer the characteristic size of the accretion disk as a function of wavelength. Long-light curves – where the gravitational time delay between multiple images can also be determined – provide the most stringent limit, but interesting information can also be obtained from single epoch data on a statistical basis.

The inferred absolute size of the accretion disk can be known up to a factor of order unity, which depends on $\langle M_s \rangle$ and on the relative transverse speeds between the stars, the deflector, and the source. However, the slope of the relation between accretion disk temperature and size is independent of that factor and can thus be determined more precisely. Current results indicate that the accretion disk is approximately the size expected for disks, although discrepancies of

order a factor of a few have been reported. Assuming that the size scales as $\lambda^{1/\eta}$, η is found to be in the range $0.5 - 1$, whereas $\eta = 0.75$ is expected for a disk. Long wavelength data imply the presence of a second spectral component, consistent with the hypothesis of a dusty torus of size much larger than the microlensing scale.

These first exciting results are just the beginning, because very few light curves obtained so far are long enough to harness the full power of microlensing. With the rapid development of time-domain astronomy predicted for the next decade, multiwavelength monitoring campaigns of several years for tens of objects should become feasible. [61]

A $z \sim 10$ Galaxy Discovered Using a Gravitational Lens

In an extremely exciting recent development, [66] report the discovery of a $z \sim 10$ Lyman-break galaxy multiply imaged by the massive galaxy cluster A2744, which has been observed to an unprecedented depth with *HST* as part of the Hubble Frontier Fields campaign. This report demonstrates the power of gravitational lenses as cosmic telescopes.

HFF observations of A2744 ($z = 0.308$) were obtained. These data consisted of 70 orbits with WFC3/IR in the F105W, F125W, F140W, and F160W near-infrared filters, and 70 orbits with ACS/WFC in the F435W, F606W, and F814W optical bandpasses. These observations were supplemented with archival ACS data.

The investigators initially identified the high-redshift galaxy candidate as a J-band dropout near the center of A2744 (referred to as JD1A). A preliminary estimate of JD1A's photometric redshift suggested it was most likely at $z \sim 10$, although there was a non-negligible probability of it being a lower-redshift ($z \sim 2 - 3$) interloper.

In order to assess these two possibilities, and motivated by the vicinity to the critical curves, the investigators used an updated version of a publicly available *light traces mass* (LTM) gravitational lensing model of A2744. The LTM model assumes that both the baryonic and dark matter mass distributions can be traced by the cluster's light distribution, where the latter mass component is a smoothed version of the former. This method has been most successful at uncovering large numbers of multiply imaged galaxies in other galaxy clusters. Compared to the publicly accessible LTM model of A2744, the new LTM model uses an updated catalog of multiple images, spanning the redshift range $z \sim 1 - 7$.

Using the LTM model, the investigators delens JD1A to the source-plane and back, considering both the low- and high-redshift hypotheses. A source redshift of $z \sim 2$ predicts a counter-image $\sim 3arcsec$ northeast of the position of JD1A, and a second counter-image approximately $20arcsec$ west of the southern core of the cluster. However, no other objects are located at either of these predicted positions within $\sim 1 - 2arcsec$ (the image reproduction precision *rms* of the model is $\sim 1\farcs3$). A source redshift of $z \sim 10$, on the other hand, yields the same positional symmetry of multiple images as in the $z \sim 2$ case, but—as expected—with larger deflection angles. Remarkably, they found faint J-band dropout galaxies near both predicted counter-image locations, although note that this identification is tentative due to this object's faintness.

Several independent lensing models were used to verify the positions of the predicted multiple images. First, they constructed a second model with the updated pipeline, which adopts the LTM assumption only for the galaxies, yet follows an analytical form for the dark matter, namely (projected) elliptical NFW distributions for the main mass clumps. This model (hereafter, "NFW") is basically identical to the ZITRIN NFW model released as part of the Hubble Frontier Fields, but has been updated using the multiple-image catalog. Finally, they checked the results against the lensing model of A2744 supplied by the `CATS` team, constructed using the parametric `Lenstool` algorithm, and against a free-form lensing model, which combines both parametric

and non-parametric techniques.

The authors found that all four lensing models yield consistent results regarding the predicted multiple image positions of JD1. Quantitatively, the LTM model yields $z \gtrsim 4$ for the candidate, while the "NFW" model requires $z \gtrsim 8$, both with 95% confidence based on more than ten thousand Monte-Carlo Markov Chain (MCMC) steps. The `Lenstool` model yielded similar results. This analysis shows that a high-redshift solution for the candidate is clearly favored over the lower-redshift ($z \sim 2-3$) alternative.

The LTM model implies magnifications of $10.01^{+1.1}_{-0.86}$, $11.25^{+4.8}_{-2.5}$, and $3.57^{+0.33}_{-0.03}$ (95% confidence intervals) for JD1A, JD1B, and JD1C, respectively. These values are broadly consistent with the magnifications predicted by the updated "NFW" model, and with the magnifications inferred using the `Lenstool` lensing model, although these can reach up to ~ 2 times higher magnifications for images A and B, and $\sim 50\%$ lower magnification for image C, and the reader should refer to these as the typical systematic uncertainties here. For calculating the source properties, they used the magnifications from the LTM model, which renders the calculation conservative in the sense that higher magnifications for A and B yield an even smaller and fainter source than inferred.

Finally, the magnification by the lens models indicate that the intrinsic apparent magnitude is 29.9 AB (F160W), and the rest-frame UV (~ 1500 $\AA$) absolute magnitude is $M_{UV,AB} = -17.6$, corresponding to ~ 0.1 $L^*_{z=8}$, or ~ 0.2 $L^*_{z=10}$ (extrapolated with $dM^*/dz \sim 0.45$). This makes this galaxy one of the least luminous $z \sim 10$ candidates ever discovered, supplying a first taste of the upcoming achievements of the HFF observational effort – reaching deeper into the faint end of the high-redshift luminosity function.

In summary, this remarkable discovery was only possible because of the power of a gravitational lens as a cosmic telescope.

3.7 Gravitational Lens Models

The gravitational deflection of light is a simple physical phenomenon with a rich phenomenology and history. The fact that many different observable effects arise from a few key physical principles gives gravitational lensing broad reach in astrophysics, cosmology, relativity, and even mathematics. This section of the basic review will focus on strong lensing systems in

which light bending by a distant, massive galaxy creates multiple, resolvable images of a more distant source.

We now turn to highlight a core component of strong lensing studies: lens modeling. One of the problems with lensing, is that we cannot see everything we need to understand in order to interpret lens data. We cannot avoid making some assumptions about how the mass in lens galaxies is distributed. To a large extent the assorted modeling methods that have emerged in recent years differ as to what assumptions are made and how they are used. [25]

As we will see, there can be assumptions about both the lens galaxy and the background source.With the source, the choice of point-like or extended is governed by the data, but if it is extended we need to decide what kind of symmetries and/or smoothness criteria to impose.With the lens, the fundamental choice is how to apply independent astrophysical knowledge. One approach is to define a modest space of models based on a careful analysis of what we think we know about the properties of galaxies that are important for lensing. A second approach is to give the lens models much more freedom and flexibility, and to supplement the lens data with explicit constraints on the form and/or smoothness of the lens model in order to obtain a reasonable set of acceptable models.

The goal of this section is to review various lens modeling methods and see if we can discuss them in a common framework especially in the context of Bayesian statistics. In Bayesian language, we draw conclusions from the posterior probability distribution for a model, which can be decomposed into two factors: the likelihood of the data given the model, and priors on the model. The form of the likelihood is guided by the nature of the data. The form of the priors, by contrast, depends on the choice of models. The two approaches mentioned above boil down to using astrophysical priors to narrow the model space before we encounter any lens data, or keeping the model space large and using priors in conjunction with lens data to constrain the posterior distribution. The distinction is often distilled into light traces mass" (LTM, formerly called parametric) versus non-Lignt Traces Mass" (non-LTM, formerly called non-parametric) models. [25]

Having outlined how lenses constrain the mass distribution, we turn to the problem of actually fitting data. The simplest approach for a casual user is simply to down load a modeling package, read the manual, try some experiments, and then apply it intelligently. There are many such packages available, as described later in Chapter 4.

In most cases we are interested in the problem of fitting the positions $\vec{\theta}_i$ of $i = 1 \cdots n$ images where the image positions have been measured with accuracy σ_i. We may also know the positions and properties of one or more lens galaxies. Time delay ratios also constrain lens models but sufficiently accurate ratios are presently available for relatively few systems. Flux ratios constrain the lens model, but we are so uncertain of their systematic uncertainties due to extinction in the ISM of the lens galaxy, and the effects of substructure that we can never impose them with the accuracy needed to add a significant constraint on the model. [37]

The basic issue with lens modeling is whether or not to invert the lens equations ("source plane" or "image plane" modeling). The lens equation supplies the source position

$$\vec{\beta}_i = \vec{\theta}_i - \vec{\alpha}(\vec{\theta}_i, \vec{p}) \tag{3.106}$$

predicted by the observed image positions $\vec{\theta}_i$ and the current model parameters $\vec{p}$. Particularly for LTM models it is easy to project the images on to the source plane and then minimize the difference between the projected source positions. This can be done with a χ^2 fit statistic of

the form

$$\chi^2_{src} = \sum_i \left(\frac{\vec{\beta} - \vec{\beta}_i}{\sigma_i} \right)^2 \tag{3.107}$$

where we treat the source position $\vec{\beta}$ as a model parameter.

The astrometric uncertainties σ_i are typically a few milli-arcseconds. Moreover, where VLBI observations give significantly smaller uncertainties, they should be increased to approximately 0.″001–0.″005 because low mass substructures in the lens galaxy can produce systematic errors on this order. *Astrometric constraints can be imposed to no greater accuracy than the largest deflection scales produced by lens components which are not included in the models.* The advantage of χ^2_{src} is that it is fast and has excellent convergence properties. The disadvantages are that it is wrong, cannot be used to compute parameter uncertainties, and may lead to a model producing additional images that are not actually observed. [37]

The reason it is wrong and cannot be used to compute parameter errors is that the uncertainty σ_i in the image positions does not have any meaning on the source plane. This is easily understood if we Taylor expand the lens equation near the projected source point $\vec{\beta}_i$ corresponding to an image

$$\vec{\beta} - \vec{\beta}_i = M_i^{-1}(\vec{\theta} - \vec{\theta}_i) \tag{3.108}$$

where M_i^{-1} is the inverse magnification tensor at the observed location of the image. In the frame where the tensor is diagonal, we have that $\Delta\beta_\pm = \lambda_\pm \Delta\theta_\pm$ so a positional error $\Delta\beta_\pm$ on the source plane corresponds to a positional error $\lambda_\pm^{-1}\Delta\beta_\pm$ on the image plane. Since the observed lensed images are almost always magnified (usually $\lambda_+ = 1 + \kappa + \gamma \sim 1$ and $0.5 > |\lambda_- = 1 + \kappa - \gamma| < 0.05$) there is always one direction in which small errors on the source plane are significantly magnified when projected back onto the image plane. Hence, if you find solutions with $\chi^2_{src} \sim N_{dof}$ where N_{dof} is the number of degrees of freedom, you will have source plane uncertainties $\Delta\beta \lesssim \sigma_i$. However, the actual errors on the image plane are $\mu = |M|$ larger, so the χ^2 on the image plane is $\sim \mu^2 N_{dof}$ and you in fact have a terrible fit.

If you assume that in any interesting model you are close to having a good solution, then this Taylor expansion provides a means of using the easily computed source plane positions to still get a quantitatively accurate fitting statistic,

$$\chi^2_{int} = \sum_i \frac{\left(\vec{\beta} - \vec{\beta}_i\right) \cdot M_i^2 \cdot \left(\vec{\beta} - \vec{\beta}_i\right)}{\sigma_i^2}, \tag{3.109}$$

in which the magnification tensor M_i is used to correct the error in the source position to an error in the image position. This procedure will be approximately correct provided the observed and model image positions are close enough for the Taylor expansion to be valid.

Finally, there is the exact statistic where for the model source position $\vec{\beta}$ you numerically solve the lens equation to find the exact image positions $\vec{\theta}_i(\vec{\beta})$ and then compute the goodness of fit on the image plane

$$\chi^2_{img} = \sum_i \left(\frac{\vec{\theta}_i(\vec{\beta}) - \vec{\theta}_i}{\sigma_i} \right)^2. \tag{3.110}$$

This will be exact even if the Taylor expansion of χ^2_{int} is breaking down, and if you find all solutions to the lens equations you can verify that the model predicts no additional visible images. Unfortunately, using the exact χ^2_{img} is also a much slower numerical procedure.

As we discussed earlier, even though lens models provide the most accurate mass normalizations in astronomy, they can constrain the mass distribution only if the source is more complex than a single compact component. For most lenses, obtaining information on the radial density profile requires some other information such as a dynamical measurement, a time delay measurement or a lensed extended component of the source. Even for these systems, it is important to remember that the actual constraints on the density structure really only apply over the range of radii spanned by the lensed images – the mass interior to the images is constrained but its distribution is not, while the mass exterior to the images is completely unconstrained. This is not strictly true when we include the angular structure of the gravitational field and the mass distribution is quasi-ellipsoidal.

It is also important to keep some problems with LTM models in mind. First, models that lack the degrees of freedom needed to describe the actual mass distribution can be seriously in error. Second, models with too many degrees of freedom can be nonsense. We can illustrate these two limiting problems with the sad history of Q0957+561 for the first problem and attempts to explain anomalous flux ratios with complex angular structures in the density distribution for the dark matter for the second. [37]

Q0957+561, the first lens discovered and the first lens with a well measured time delay, is an ideal lens for demonstrating the trouble you can get into using LTM models without careful thought. The lens consists of a cluster and its brightest cluster galaxy with two lensed images of a radio source bracketing the galaxy. VLBI observations resolve the two images into thin, multi-component jets with very accurately measured positions (uncertainties as small as 0.1 mas, corresponding to deflections produced by a mass scale $\sim 10^{-8}$ of the primary lens!). Models developed along two lines. One line focused on models in which the cluster was represented as an external shear while the other explored more complex models for the cluster and argued that external shear models had too few parameters to represent the mass distribution given the accuracy of the constraints. The latter view was born out by the morphology of the lensed host galaxy and direct X-ray observations of the cluster which showed that the lens galaxy was within about one Einstein radius of the cluster center where a tidal shear approximation fails catastrophically. The origin of the problem is that as a two-image lens, Q0957+561 is critically short of constraints unless the fine details of the VLBI jet structures are included in the models. Many studies imposed these constraints to the limit of the measurements while not including all possible terms in the potential which could produce a deflection on that scale (i.e. the precision should have been restricted to milli-arcseconds rather than micro-arcseconds). Models would adjust the positions and masses of the cluster and the lens galaxy in order to reproduce the small scale astrometric details of the VLBI jets without including less massive components of the mass distribution that also affects the VLBI jet structure on these angular scales. Lens models must contain all reasonable structures producing deflections comparable to the scale of the measurement errors.

Nomenclature for Lens Model Studies

One of the difficult problems in the strong gravitational lensing literature is variability in terminology. The first characteristic of a lens model is whether it is LTM or non-LTM. In strong gravitational lensing, there are a several observables such as the relative positions of images, relative fluxes of images and time delays among the lensed images. These observables depend not only on the mass distribution of the source but also on cosmological parameters. The LTM method assumes a simple but physically reasonable model of potential such as an isothermal sphere, NFW model, elliptical pseudo-isothermal model and so on with parameters that have clear physical meanings, based on the assumption that light traces mass. Physically

reasonable means that one can infer the shape of the lensing potential from the image position as well as the lens position and shape assuming the existence of a correlation between light and mass (thus "LTM"). In the case of a galaxy lens, the relative position of the images and the presence of arcs gives us enough information to determine the form of the potential. [17]

The other method is called the non-LTM method, which is sometimes referred to as the "grid-based" method because one does not assume the potential shape from the beginning. This method has become widely used since deep observations using 8-10 m telescopes and the HST reveal detailed shape information of images for galaxy lenses, and a multitude of arcs and images for cluster lenses. This information allows us to establish the grid by grid correspondence between the image plane and the source plane. The basic principle of the non-LTM method is the conservation of the surface brightness. The surface brightness of two grids related by the lens equation is the same. [17]

Another important characterization for lens model studies is whether the comparison is direct or indirect. Direct studies are conducted by the same investigator, and two or more models are compared directly in the same investigation. Indirect studies are conducted by comparing results with results that already exist in the literature.

A third parameter for comparative studies is whether the data is the same in the two models, a semi-independent study, or the exact data used to construct the model of the same object is different, an independent study.

Characterization of lens studies according to these three parameters as a unified consistent nomenclature was suggested in a previous study [30]. It is hope that adoption of such a consistent terminology will allow more consistent comparisons of lens studies.

LTM and non-LTM Lens Models

Lens inversion procedures are often divided into two categories: LTM and non-LTM methods. LTM techniques approximate the mass distribution of the lens by a function that is characterized by a small number of parameters. They then optimize these parameters to provide the best possible fit to the observed data. Several such algorithms have been proposed (e.g. LENSCLEAN), and several software packages are publicly available (e.g. GRAVLENS and LENSTOOL. Lens model software packages are discussed extensively in Chapter 4 of this dissertation and [31]. Non-parametric inversion methods try to avoid this restriction, for example by pixellizing the mass distribution, pixellizing the lens potential or by dynamically adjusting the number of basis functions used. [32].

There remains a great deal of controversy about the use of these two techniques, and some argue that one is more "correct" than the other. LTM techniques seem to be used most commonly. This is motivated by the fact that the data usually do not contain more than a few arcs. This is not enough to constrain the mass distribution without the help of a parametrization. LTM methods rely heavily on assumptions or priors on the mass distribution. A common prior is the assumption that there is a smooth dark matter component which is correlated spatially with the centroid of the luminous matter in the cluster. The mass is then ususally modeled by a large smooth dark matter halo placed on top of the central galaxy or the centroid of the luminous matter, as well as smaller dark matter haloes located in the positions of the other luminous galaxies. The parameters of each halo are then adjusted to best reproduce the observations. [12].

There is some subjectivity involved in this process, particularly in the addition of the dominant dark matter component to the cluster. The assumption that the dark matter follows the luminosity is necessary but remains the Achilles heel of LTM lens modeling. For large clusters the number of parameters in the LTM lens model quickly becomes large but there is still no

guarantee that the LTM model used, is in fact capable of reproducing well the mass distribution. It is not hard to imagine complications such as dark matter substructure, asymmetric galaxy profiles, interactions between individual galaxies and the cluster or even dark matter haloes without significant luminosity all of which would not be well represented by the typical LTM methods. In these cases, where the number of parameters is large, we may want to consider alternative non-LTM methods where all the previous problems do not have any effect on any of the assumptions. Also is in these situations where the number of parameters in both LTM and non-LTM methods is comparable. When the number of parameters is comparable in both cases, it is interesting to explore non-LTM methods since they do not rely on the same assumptions [12]. This strongly supports the conduct of comparative studies in gravitational lensing.

LTM Models

The oldest approach to lens modeling is to assume the density distributions of lens galaxies can be approximated by functions with a modest number of free parameters. Astrophysical knowledge is built into the careful selection of functions and parameters, in two ways. First, we can consider density distributions derived from other observational and theoretical studies of galaxies: the list includes isothermal, power law, de Vaucouleurs, Hernquist, and NFW models, etc. [25]

Table 3.2 compiles formulae for the effective lensing potential and deflection angle of four commonly used circularly symmetric lens models including the point mass, singular isothermal sphere, isothermal sphere with a softened core, and constant density sheet. In addition, one can have more general models with non-isothermal radial profiles, e.g. density varying as radius to a power other than -2. [39]

From [39].

Lens Model	$\psi(\theta)$	$\alpha(\theta)$
Point mass	$\frac{D_{\rm ds}}{D_{\rm s}}\frac{4GM}{D_{\rm d}c^2}\ln\lvert\theta\rvert$	$\frac{D_{\rm ds}}{D_{\rm s}}\frac{4GM}{c^2 D_{\rm d}\lvert\theta\rvert}$
Singular isothermal sphere	$\frac{D_{\rm ds}}{D_{\rm s}}\frac{4\pi\sigma^2}{c^2}\lvert\theta\rvert$	$\frac{D_{\rm ds}}{D_{\rm s}}\frac{4\pi\sigma^2}{c^2}$
Softened isothermal sphere	$\frac{D_{\rm ds}}{D_{\rm s}}\frac{4\pi\sigma^2}{c^2}\left(\theta_{\rm c}^2+\theta^2\right)^{1/2}$	$\frac{D_{\rm ds}}{D_{\rm s}}\frac{4\pi\sigma^2}{c^2}\frac{\theta}{(\theta_{\rm c}^2+\theta^2)^{1/2}}$
Constant density sheet	$\frac{\kappa}{2}\theta^2$	$\kappa\lvert\theta\rvert$

Table 3.2: Examples of circularly symmetric lenses. The effective lensing potential $\psi(\theta)$ and the deflection angle $\alpha(\theta)$ are given. The core radius of the softened isothermal sphere is $\theta_{\rm c}$.

The gravitational time-delay functions $t_{\rm grav}(\theta) \propto -\psi(\theta)$ of the models in Table 3.2 are illustrated in Fig. 3.29. Note that the four potentials listed in Tab. 3.2 all are divergent for $\theta \to \infty$. (Although the three-dimensional potential of the point mass drops $\propto r^{-1}$, its projection along the line-of-sight diverges logarithmically.) The divergence is, however, not serious since images always occur at finite θ where the functions are well-behaved. [39]

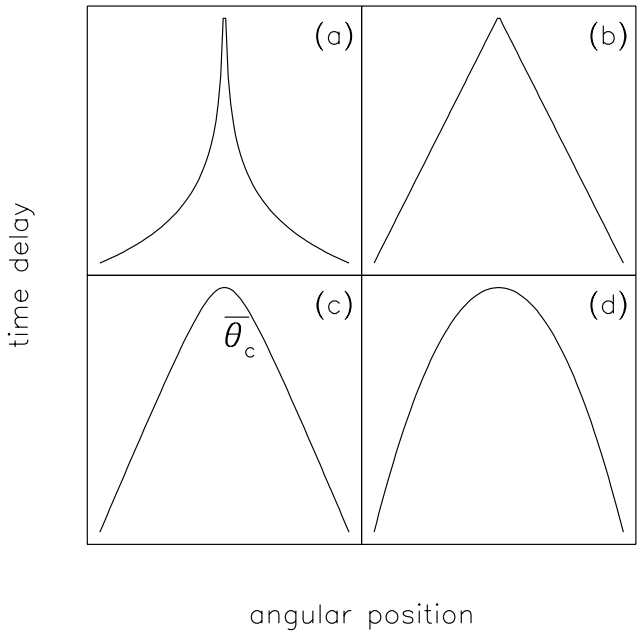

Figure 3.29: Gravitational time-delay functions for the four circularly symmetric effective potentials listed in Tab. 3.2. (a) point mass; (b) singular isothermal sphere; (c) softened isothermal sphere with core radius θ_c; (d) constant density sheet.

There are a number of general principles that have emerged from LTM lens modeling. The Einstein radius, and the mass within it, are robust measurements with model uncertainties at the percent level. It can be difficult to constrain the radial density profile from strong lensing alone, especially in 4-image lenses. By combining strong lensing with other astrophysical evidence, it has been found that the total density profiles of lens galaxies are close to isothermal, although they might not be perfectly isothermal at all radii and there may be some intrinsic scatter We cannot assume that lens galaxies are spherical or isolated. Image position data, especially in 4-image lenses and rings, are good enough to detect and even distinguish quadrupole moments due to ellipticity in the lens galaxy and tidal shear from the lens galaxys environment. Smooth lens models often fail to reproduce the observed flux ratios in 4-image lenses. The failures can usually be attributed to elements missing from the smooth models, namely microlensing by stars and/or millilensing by dark matter substructure. [25]

LTM lens models can be used with all of the different source modeling methods discussed so far. Indeed, LTM lens models have been used with point-like sources, with Einstein rings modeled using elliptical sources, with extended sources in LensClean, and with pixelated sources. The principles discussed above have been drawn from the full range of LTM lens modeling studies. [25]

One final point about LTM lens modeling is that we do not always think about it in a Bayesian sense because we do not necessarily have to deal with explicit priors. Nevertheless, it is straightforward and even attractive to place LTM modeling in a Bayesian framework. We might want to do that in order to impose additional astrophysical constraints (for example, on the shape and mass-to-light ratio of the stellar distribution if we are modeling the stars and dark matter separately).

Non-LTM Models

An alternative to selecting parametric models is to expand the lens potential using some appropriate set of basis functions:

$$\phi(x) = \sum_v a_v f_v(x) \tag{3.111}$$

and then fit for the coefficients a_v. While such models were formerly called non-parametric, that term is highly misleading because there are in fact parameters (namely the expansion coefficients) [25]. These models are now referred to as non-LTM, to reflect the physics involved. Some authors use the term free-form because it highlights the point that the models are given more freedom to deviate from preconceptions. As opposed to LTM strong lens modelling, which often indicates that the source and lens-potential model of the lens system can be described by a small set of parameters (e.g. image positions, flux-ratios, time-delays for the lensed images, and lens strength, ellipticity, scale, etc. for the lens potential model), grid-based strong lensing means that the source and lens-potential models are described by a large set of parameters that directly quantify a grid of source-brightness and/or lens-potential values. Hence in short summary: Non-parametric really means lots of parameters! . This is one of the reasons that the term non-parametric has been dropped in favor of "non-LTM". [28].

There have been various approaches to non-LTM models that use different choices of basis functions and priors, and different data that lead to the models being over- or under-constrained.

In many cases LTM strong lens modeling can not be used. For example, there are lens systems with extended and complex lensed images for which one can not easily relate structure in one lensed image to structure in another lensed image (this is often trivial in case of point images and jets). Besides this, grid-based strong lensing (non-LTM) makes few to no assumptions about the structure of the source (and possibly the lens potential as well, although the solutions often require regularization because the number of free parameters can be large. non-LTM lensing analysis makes use of all (or most) information available in the lensed images or even absence of information; i.e. the prediction of lensed images that are not present in the data are penalized. Finally, non-LTM analysis allows structure of the source to be separated from structure in the lens potential, in a statistical (i.e. Bayesian) sense. [28]

There are many approaches to non-LTM models, as stated above. A nice summary of the grid-based approach is given in [28]. First, a data-model is build, which describes the observed data as a function of a set of (non)linear parameters. The source is described by a set of linear parameters (i.e. their surface brightness values on a predefined source grid), whereas the lens-potential is described by a set of nonlinear parameters that parametrically describe the lens potential in the image plane. To solve for the linear parameters (given a fixed potential model), a quadratic penalty function is defined, using the above data-model, the first part of which is a standard χ^2 term and the second part is a regularization term that results in the smoothest source model allowed by the data. The minimum of this penalty function is found through standard linear-algebra techniques. Once a good starting model has been found, the relative weight (λ) between the χ^2 and regularization terms in the penalty function is found through an Bayesian evidence optimization, subsequently marginalizing over this nuisance parameter, giving the evidence of the set of non-linear model parameters. The best non-linear parameters are then found by maximizing the evidence penalty-function, using standard non-linear optimization methods, like Downhill-Simplex, Conjugate-Gradient methods, etc. Finally, the lens-equations can be linearized to include a linear correction to the lens-potential in the equations. This fully-linear equation can then iteratively be solved. The above outline indicates what can be done in grid-based lensing techniques, although simplified version are possible (e.g.

modeling can be done without Bayesian evidence optimization) or more complicated version (e.g. adaptive grids).

Another approach is the pixelated mass map. Saha and Williams have developed free-form models in which the basis functions correspond to mass pixels [54]. The PixeLens code applies to point-image lenses and uses position and time delay constraints, so the problem is fully linear (in the pixel densities, the source position, the time scale factor t_0^{-1}, and also the external shear amplitudes). With even modest spatial resolution in the mass map, the mass pixels outnumber the constraints so the problem is under-constrained. Saha and Williams deal with the resulting solution space in two ways. First, they impose priors to eliminate models that are grossly unphysical:

- 1. All pixel densities must be non-negative.
- 2. The density gradient must point within 45 degrees of the lens center.
- 3. No pixel value may exceed the average of its neighbors by more than a factor of two (except for the central pixel).
- 4. The projected density profile must be steeper than $r^{-1/2}$.
- 5. If desired, the mass map may be required to have inversion symmetry.

These priors restrict the solution space but are otherwise non-informative, so the posterior is uniform over the allowed models. The second step is to use Monte Carlo techniques to generate an ensemble of models drawn from the posterior. The ensemble average is itself a successful model (since the constraints are linear, any linear combination of good models is also good) that gives a sense of the typical properties of the solutions. The statistics of the ensemble then characterize the range of successful models. [25]

Another approach to non-LTM modelling has been referred to as the hybrid approach. Non-LTM modeling has not been applied to lenses with general extended sources, because the source reconstruction method is non-linear in the lens parameters, and it is impractical to undertake a non-linear optimization of a large number of free-form modes. Instead, hybrid models have been introduced to accommodate extended sources while still allowing a (quasi-)linear analysis of general lens potentials. In hybrid models we obtain an arbitrary potential, $\phi = \phi_0 + \delta\phi$ as a combination of a reference model ϕ_0 and perturbations $\delta\phi$. The reference model is taken to have some restricted, parametric form, so it provides amodest number of non-linear parameters that must be searched explicitly. The perturbations, by contrast, are allowed to be fully free. The idea is that if the potential perturbations are small, we can do a Taylor series expansion and work to lowest order in $\delta\phi$, and thus linearize the problem. As we will see, there are several reasons why it may be necessary to iterate a few times, but at each step the analysis is linear. [25]

Hybrid models have been used to handle the complexity in B1608+656 associated with having two galaxies inside the Einstein radius. The analysis started with a parametric two-galaxy model and then refined it using pixelated potential reconstruction. (They also accounted for many other details including light from the lens galaxies, and extinction of the lensed images by dust in the lens galaxies.) The joint Bayesian analysis of constraints from lensing and WMAP supports a wide range of conclusions involving the mass distribution of the lens galaxies and their environment, the Hubble constant, and curvature and dark energy parameters. Hybrid models have also been used as the basis of a method to search for unseen mass clumps in lens galaxies and place constraints on dark matter substructure. A mass clump near the Einstein radius will distort an extended image in a characteristic way that can be uncovered by simultaneously reconstructing the (pixelated) source and potential. [25]

References

[1] S. Asadi. *Gravitational Millilensing as a Probe of Dark Halo Substructure*. Master's thesis, Stockholm University, 2012. 105

[2] M. Bartelmann. TOPICAL REVIEW Gravitational lensing. *Classical and Quantum Gravity*, **27**[23]:233001, December 2010. 77, 79, 110, 111

[3] M Bartelmann. Three introductory lectures on gravitational lensing. https://lss.bao.ac.cn/lens11/images/b/b0/Bartelmann_LectureNotes.pdf, July 2011. 92

[4] M. Bartelmann and P. Schneider. Weak gravitational lensing. *Phys Rep*, **340**:291–472, January 2001. 77, 114

[5] A Bosma. The dark matter problem. http://ned.ipac.caltech.edu/level5/Bosma2/Bos3_4.html, December 1998. 141

[6] M. Bradač, M. Lombardi, and P. Schneider. Mass-sheet degeneracy: Fundamental limit on the cluster mass reconstruction from statistical (weak) lensing. *Astr Astrophys*, **424**:13–22, September 2004. 132, 133, 135

[7] A Brooks. The role of gas in the formation of disk galaxies. http://astro.fnal.gov/events/Seminars/Slides/Brooks_111510.pdf, July 2013. 137

[8] R. S. Bussmann, I. Perez-Fournon, S. Amber, J. Calanog, M. A. Gurwell, H. Dannerbauer, F. De Bernardis, H. Fu, A. I. Harris, M. Krips, A. Lapi, A. Omont, D. Riechers, J. Wardlow, A. J. Baker, M. Birkinshaw, J. Bock, N. Bourne, D. L. Clements, A. Cooray, G. De Zotti, L. Dunne, S. Dye, S. Eales, D. Farrah, R. Gavazzi, J. Gonzalez Nuevo, R. Hopwood, E. Ibar, R. J. Ivison, S. Maddox, M. Michalowski, M. Negrello, S. J. Oliver, I. G. Roseboom, D. Scott, S. Serjeant, A. J. Smith, M. Smith, E. Valiante, P. van der Werf, A. Verma, J. D. Vieira, L. Wang, and D. Wilner. Gravitational Lens Models Based on Submillimeter Array Imaging of Herschel-selected Strongly Lensed Sub-millimeter Galaxies. *ArXiv e-prints*, September 2013. 106, 130

[9] T. E. Collett and M. W. Auger. Cosmological constraints from the double source plane lens SDSSJ0946+1006. *MNRAS*, **443**:969–976, September 2014. xii, 96, 97, 98, 99, 100

[10] F Courbin. The mass model and degeneracies. http://ned.ipac.caltech.edu/level5/March03/Courbin/Courbin3_3.html. xiii, 130, 131

[11] W. J. G. de Blok. The Core-Cusp Problem. *Advances in Astronomy*, **2010**, 2010. 137

[12] J. M. Diego, P. Protopapas, H. B. Sandvik, and M. Tegmark. Non-parametric inversion of strong lensing systems. *Mon Not Royal Astr Soc*, **360**:477–491, June 2005. 151, 152

[13] A. Einstein. Ueber den einfluss der schwerkraft auf die ausbreitung des lichtes. *Annalen der Physik*, **35**:898, 1911. 80

[14] A. Einstein. Lens-like action of a star by the deviation of light in a gravitational field. *Science*, **84**:506, 1936. 81

[15] E. E. Falco, J. Lehar, and I. I. Shapiro. HST Observations and Models of the Gravitational Lens System MG 0414+0534. *Astron J*, **113**:540, February 1997. 142

[16] K Freeman. *Encyclopedia of Astronomy and Astrophysics*. Nature Publishing Company, 2001. xiv, 138, 139

[17] T. Futamase. Gravitational lensing in cosmology. book by WT Ni, Centennial General Relativity Book, 2015. xiii, 77, 104, 151

[18] R. Gavazzi, T. Treu, L. V. E. Koopmans, A. S. Bolton, L. A. Moustakas, S. Burles, and P. J. Marshall. The Sloan Lens ACS Survey. VI. Discovery and Analysis of a Double Einstein Ring. *Astrophys J*, **677**:1046–1059, April 2008. 95, 96, 100

[19] M. Hattori, J. Kneib, and N. Makino. Gravitational Lensing in Clusters of Galaxies. *Progress of Theoretical Physics Supplement*, **133**:1–51, 1999. xiii, 104

[20] K. Heitmann. Dark matter halos, mass functions and cosmology. http://cosmology.lbl.gov/talks/Heitmann_08.pdf, July 2013. 140

[21] H. Hoekstra. Weak gravitational lensing. *ArXiv e-prints*, December 2013. xiii, 77, 121, 122, 123, 124, 125

[22] H. Hoekstra and B. Jain. Weak Gravitational Lensing and Its Cosmological Applications. *Annual Review of Nuclear and Particle Science*, **58**:99–123, November 2008. xiii, 126, 127, 128, 129

[23] D. W. Hogg. Distance measures in cosmology. *ArXiv Astrophysics e-prints*, May 1999. 78

[24] N. Jackson. The Hubble Constant. *Living Reviews in Relativity*, **10**:4, September 2007. 107, 108, 109, 110

[25] CharlesR. Keeton. On modeling galaxy-scale strong lens systems. *General Relativity and Gravitation*, **42**[9]:2151–2176, 2010. 148, 152, 153, 154, 155

[26] C.R. Keeton, C.S. Kochanek, and U. Seljak. Shear and ellipticity in gravitational lenses. *Astrophys.J.*, **482**:604–620, 1997. 142

[27] L. King. Gravitational lensing lecture 14. http://, April 2007. 89

[28] L Koopmans. Grid-based strong gravitational lensing. http://www.cpt.univ-mrs.fr/~cosmo/EcoleCosmologie/DossierCours11/Koopmans-2.pdf. 154

[29] David R. Law, Steven R. Majewski, and Kathryn V. Johnston. Evidence for a Triaxial Milky Way Dark Matter Halo from the Sagittarius Stellar Tidal Stream. *Astrophys.J.*, **703**:L67–L71, 2009. 140

[30] A. T. Lefor and T. Futamase. Comparison of Strong Gravitational Lens Model Software I. Time delay and mass calculations are sensitive to changes in redshift and are model dependent. *ArXiv e-prints*, July 2013. 151

[31] A. T. Lefor, T. Futamase, and M. Akhlaghi. A systematic review of strong gravitational lens modeling software. *New Astr Rev*, **57**:1–13, July 2013. 151

[32] J. Liesenborgs, S. de Rijcke, H. Dejonghe, and P. Bekaert. Non-parametric inversion of gravitational lensing systems with few images using a multi-objective genetic algorithm. *Mon Not Royal Astr Soc*, **380**:1729–1736, October 2007. 151

[33] J. Liesenborgs, S. de Rijcke, H. Dejonghe, and P. Bekaert. A generalization of the mass-sheet degeneracy producing ring-like artefacts in the lens mass distribution. *Mon Not Roy Astr Soc*, **386**:307–312, May 2008. 132

[34] C. L MacLeod, R. Jones, E. Agol, and C. S. Kochanek. Detection of Substructure in the Gravitationally Lensed Quasar MG0414+0534 using Mid-Infrared and Radio VLBI Observations. *ArXiv e-prints*, December 2012. 142, 143

[35] P. Magain and V. Chantry. Gravitational lensing evidence against extended dark matter halos. *ArXiv e-prints*, March 2013. 140

[36] Shu-de Mao and Peter Schneider. Evidence for substructure in lens galaxies? *Mon.Not.Roy.Astron.Soc.*, **295**:587–594, 1998. 142

[37] G. Meylan, P. Jetzer, P. North, P. Schneider, C. S. Kochanek, and J. Wambsganss, editors. *Gravitational Lensing: Strong, Weak and Micro*, 2006. 148, 149, 150

[38] Takeo Minezaki, Masashi Chiba, Nobunari Kashikawa, Kaiki Taro Inoue, and Hirokazu Kataza. Subaru Mid-infrared Imaging of the Quadruple Lenses. II. Unveiling Lens Structure of MG0414+0534 and Q2237+030. *Astrophys.J.*, **697**:610–618, 2009. 143, 144

[39] R. Narayan and M. Bartelmann. Lectures on Gravitational Lensing. *ArXiv Astrophysics e-prints*, June 1996. xi, xii, xiii, 77, 79, 81, 82, 83, 84, 90, 93, 101, 102, 103, 104, 111, 112, 113, 152

[40] J. F. Navarro and M. Steinmetz. Dark Halo and Disk Galaxy Scaling Laws in Hierarchical Universes. *Astrophys J*, **538**:477–488, August 2000. 137

[41] M Oguri. Resolving the central density profile of dark matter halos with gravitational lensing. http://www-utap.phys.s.u-tokyo.ac.jp/obscosm/files/master_oguri_presen.pdf, January 2002. 141

[42] M Oguri. *Resolving the Central Density Profile of Dark Matter Halos with Gravitational Lensing Statistics*. Master's thesis, University of Tokyo, 2002. 141

[43] M. Oguri. Research illuminates the shape of dark matter's distribution. http://www.naoj.org/Pressrelease/2010/04/26/, April 2010. 141

[44] M. Oguri, M. B. Bayliss, H. Dahle, K. Sharon, M. D. Gladders, P. Natarajan, J. F. Hennawi, and B. P. Koester. Combined strong and weak lensing analysis of 28 clusters from the Sloan Giant Arcs Survey. *Mon Not. Royal Astr Soc*, **420**:3213–3239, March 2012. 105

[45] M. Oguri, M. Takada, N. Okabe, and G. P. Smith. Direct measurement of dark matter halo ellipticity from two-dimensional lensing shear maps of 25 massive clusters. *Mon Not. Royal Astr Soc*, **405**:2215–2230, July 2010. 141

[46] N. Okabe, Y. Okura, and T. Futamase. Weak-lensing Mass Measurements of Substructures in Coma Cluster with Subaru/Suprime-cam. *AstrophysJ*, **713**:291–303, April 2010. 81, 105, 142

[47] N. Okabe, G. P. Smith, K. Umetsu, M. Takada, and T. Futamase. LoCuSS: The Mass Density Profile of Massive Galaxy Clusters at z = 0.2. *Astrophys J Lett*, **769**, June 2013. 141, 142

[48] N. Okabe, M. Takada, K. Umetsu, T. Futamase, and G. P. Smith. LoCuSS: Subaru Weak Lensing Study of 30 Galaxy Clusters. *Proc Astr Soc Japan*, **62**:811–, June. 140, 141

[49] D. Pooley. Gravitational flux ratio anomalies. http://www.deadlyastroninja.com/research/node3.html, July 2013. 142

[50] A. Refregier. Weak Gravitational Lensing by Large-Scale Structure. *Ann Rev Astro*, **41**:645–668, 2003. xi, 77, 85

[51] S. Refsdal. On the possibility of determining Hubble's parameter and the masses of galaxies from the gravitational lens effect. *Monthly Notices Royal Astr Soc*, **128**:307, 1964. 107, 111

[52] W. Rindler. *Essential Relativity*. Springer-Verlag, 1977. 79

[53] P. Saha. Lensing Degeneracies Revisited. *Astr J*, **120**:1654–1659, October 2000. 133, 134

[54] P. Saha and L. L. R. Williams. Qualitative Theory for Lensed QSOs. *Astr J*, **125**:2769–2782, June 2003. 155

[55] P. Schneider. Weak Gravitational Lensing. *ArXiv Astrophysics e-prints*, September 2005. xiii, 77, 114, 115, 116, 118, 119, 120, 121

[56] P. Schneider and D. Sluse. Mass-sheet degeneracy, power-law models and external convergence: Impact on the determination of the Hubble constant from gravitational lensing. *Astron Astrophys*, **559**:A37, November 2013. 134

[57] S Seitz. Astrophysics lab: Strong gravitational lensing. http://www.usm.lmu.de/people/stella/stella.html. xi, 89, 91

[58] T Sumner. Experimental searches for dark matter. http://relativity.livingreviews.org/Articles/lrr-2002-4/, July 2002. 136, 137

[59] S. H. Suyu, P. J. Marshall, M. W. Auger, S. Hilbert, R. D. Blandford, L. V. E. Koopmans, C. D. Fassnacht, and T. Treu. Dissecting the Gravitational lens B1608+656. II. Precision Measurements of the Hubble Constant, Spatial Curvature, and the Dark Energy Equation of State. *Astrophys J*, **711**:201–221, March 2010. 135, 136

[60] C. Tortora. Strong Lensing, dark matter and H_0 estimate. *ArXiv Astrophysics e-prints*, February 2007. xii, 100, 101

[61] T. Treu. Strong Lensing by Galaxies. *Ann Reviews AA*, **48**:87–125, September 2010. xi, xii, 77, 82, 85, 86, 87, 92, 94, 95, 97, 106, 107, 108, 110, 144, 145, 146

[62] K. Umetsu, T. Broadhurst, A. Zitrin, E. Medezinski, D. Coe, and M. Postman. A Precise Cluster Mass Profile Averaged from the Highest-quality Lensing Data. *Astrophys J*, **738**:41, September 2011. 105

[63] J. Wambsganss. Gravitational Lensing in Astronomy. *Living Reviews in Relativity*, **1**:12, August 1998. xii, 77, 92

[64] Wikipedia. Cuspy halo problem. http://en.wikipedia.org/wiki/Cuspy_halo_problem, July 2013. 137

[65] C. Will. Henry cavendish, johan von soldner and the deflection of light. *Am J Physics*, **56**:413, 1988. 79

[66] A. Zitrin, W. Zheng, T. Broadhurst, J. Moustakas, D. Lam, X. Shu, X. Huang, J. M. Diego, H. Ford, J. Lim, F. E. Bauer, L. Infante, D. D. Kelson, and A. Molino. A Geometrically Supported z ˜ 10 Candidate Multiply Imaged by the Hubble Frontier Fields Cluster A2744. *ApJ Letters*, **793**:L12, September 2014. 146

Chapter 4

A Systematic Review of Strong Gravitational Lens Model Software

4.1 Purpose and Organization of this Chapter

In order to effectively compare strong gravitational lens models, it is necessary to first have an inventory of available software. [1]. This chapter is the result of an attempt to be comprehensive and describe as many lens model software packages as possible. The literature was extensively reviewed and multiple search methodologies employed. Having done this, there were 26 strong gravitational lens model software packages identified, which are reviewed in this chapter. The extent of the review of each software package depended on its availability and the ability to install and use the software.

This chapter is organized as follows. In section §4.3, we review the classification of gravitational lens models and the methodology used to review the available software. In section §4.4, we review 17 software packages that have been used extensively in gravitational lens research. Following this, in section §4.5, we review nine programs that are useful in education for gravitational lensing. In section §4.6 we discuss several factors of importance in selecting and comparing available software and in section §4.7 we make suggestions for the next generation of software to support future gravitational lens research based on this review.

The data from this study was used as the basis of the Software Review in the Orphan Lens Project [12]. In addition, several software packages were added to the web site by other contributors after completion of this study, and then added to this study from the Orphan Lens web site.

4.2 Introduction

Gravitational lensing has great promise to provide new insights into the structure and history of the universe. Gravitational lensing has yielded many exciting results by mapping dark matter

[1] Portions of this chapter were published in *Lefor AT, Futamase T. and Akhlaghi M. A systematic review of strong gravitational lens modeling software. New Astronomy Reviews 2013. 57:1-13* [30] doi:10.1016/j.newar.2013.05.001. Permission to use this published material granted by the Publisher, License 3571220164041

distributions, and the recent use of strong gravitational lensing data has added a new dimension to this research [14]. Gravitational lensing is a very active area of investigation, and research is highly dependent on computer modeling. In some areas of contemporary astrophysics research, there is software that is a *de facto* standard for many investigators (e.g. SExtractor [8] [1], GALFIT [50] [2], etc.). While gravitational lens modeling software has been written, there are no standards and no easily accessible source of information about existing software. The lack of standard software may be a virtue of the gravitational lensing community, allowing more flexibility and creativity. The lack of a single standard program makes it more important to compare existing software used for modeling strong gravitational lenses. Information regarding existing software will be helpful to those developing new approaches and interfaces.

This review was undertaken to identify available strong lens modeling software, and review the installation, use, and the nature of inputs and data outputs. This paper serves as a guide to available software and provides useful information to both new and established investigators in this field. The availability of source code may be a useful starting point for anyone writing their own modeling software.

4.3 Classification and Review Methodology

Modeling of gravitational lenses starts with a list of observables such as relative positions of the components, relative fluxes of the images, time delays between the images and other lens properties. Gravitational lens modeling can be considered a "forward" or a "reverse" problem. In the forward problem, images are predicted based on a known source and lensing mass. More commonly, the reverse problem is considered, using observed images to reconstruct a model of the mass density based on the images, usually approached using non-parametric methods.

In Light Traces Mass (LTM, formerly known as parametric) models, a clear physical parameterization is used to construct the model from the outset, while non-LTM (formerly known as non-parametric) models are often "grid-based", although there are other methods used. Both LTM and non-LTM models are valuable, since some features of individual lenses are model independent while others are very model dependent [58]. A major distinction is whether the calculation is "model-based" (LTM or parametric) or "model-free" (non-LTM or non-parametric) at the start of the process [15]. The recent approach to model classification avoids the confusion of parametric vs. non-parametric (since all models use parameters) and classifies models as LTM or non-LTM [14].

Light Traces Mass Models

Light Traces Mass models are generally used to solve the "forward" problem, taking a source and lensing mass, and then predicting the resulting image. LTM models are also known as simply-parameterized models, and assume a physical model which fits the data with relatively few defined parameters [23]. In LTM models, the data is fitted to a physical object (e.g. Point Mass, Singular Isothermal Sphere, Singular Isothermal ellipsoid, De Vaucouleurs model, Navarro-Frank-White Model, etc.) and a model of the lensing mass made using that physical object to predict the effect on the light from the source.

[1] http://astroa.physics.metu.edu.tr/MANUALS/sextractor/
[2] http://users.obs.carnegiescience.edu/peng/work/galfit/galfit.html

Non-Light Traces Mass Models

Non-LTM models are often used to solve the more complex "reverse" problem, also called lens inversion, of taking a lensed image and from it, predicting the nature of the lensing mass. The lens inversion problem is complicated by the fact that there are huge degeneracies in the parameter space which make several models able to fit observed data [40]. The degeneracy problem is inherent in lens inversion, because the constraints on the potential are local [2]. The principle underlying non-LTM gravitational lens models is that the effective lens potential and the deflection equations are linear functions of the surface density [43]. These models reconstruct the mass distribution or lens potential as a map defined on a grid of pixels [23]. By using a large number of parameters these models are very flexible, but conversely, the large number of parameters can lead to over-fitting the data. The parameters are usually in the form of basis functions, and given the large number used, the term "non-parametric" is somewhat paradoxical, although it refers to the lack of a discrete physical model being used in the solution of the problem [36]. It is only recently that lens inversion is studied using strong gravitational lensing data.

Lens inversion methods are classified into 3 types: (i) model dependent reconstructions, (ii) potential reconstruction on a grid and (iii) expansion of the potential functions. Degeneracy must be dealt with using any of these techniques [2]. Further examples of these techniques include the maximum entropy method [65], genetic algorithms [10; 36], Bayesian analysis [11; 62], the semilinear technique [66], and perturbative reconstruction [2].

The ideal lens inversion algorithm (i) should be free of assumptions regarding mass or luminosity distributions, (ii) should not depend on prior information, (iii) should not produce models that are physically impossible, (iv) should be free of uncontrollable parameters, and (v) should be extendable to any kind of data [31]. The fact that there are so many techniques being used to investigate lens inversion, indicates that there is no single "best" technique. The theoretical underpinnings of these various methods have been reviewed and shown to be essentially different methods of doing the same thing [11].

Education and Research Modeling Software

Gravitational lens modeling software can also be arbitrarily classified into packages used for education and those used for research. Those classified for research in this review have been used in published studies of gravitational lensing. Those classified as educational have not been used for studies.

Review Methodology

There are two main goals when evaluating gravitational lens modeling software [69]. The first is to determine if the software can recover the lens model parameters of a known lens, and with what accuracy. The second regards the accuracy of the source reconstruction. The accomplishment of these two goals must be considered against the background of software usability and efficiency.

Gravitational lens modeling software was identified by using search engines on the Internet as well as searching the literature on arXiv.org. The software reviewed here was chosen based on availability for download and the ability to install and execute the programs. Another resource for gravitational lens modeling software is the Astro-Code Wiki, which includes links for several of the modeling codes reviewed here [5]. Information regarding release dates and versions was obtained from the web sites. Each of the software packages described here was downloaded, compiled (when necessary) and installed. Sample data files were used when

available, and output shown here is directly from the downloaded version. All of the software functioned as described by their developers. Documentation was also downloaded directly from the internet. This review was not intended to be all inclusive; other lens modeling packages are not reviewed. Several of these programs, although web sites for download were identified on line or in publications, were no longer available for download. Others had significant issues when attempting to compile and execute the programs, precluding their use. There are likely other software packages being used by individuals but not available for download on the internet. The software reviewed here is representative of what is available in regard to algorithms, types of models available and feature sets. Features of the software reviewed relating to installation and use are summarized in Table 4.1, for the software that was fully evaluated. Software not fully evaluated is summarized in Table 4.2. Features of the software relating to lensing models and algorithms are summarized in Table 4.3.

Package	Year	Source	Exec	Platform	Ref
gravlens	2008	No	Yes	PPC, Linux, OS X	[26]
lensmodel	2008	No	Yes	PPC, Linux, OS X	[26]
Lensview	2008	Yes	No	OS X/Linux	[67]
Lenstool	2006	Yes	No	OS X/Linux	[23]
LensPerfect	2007	Yes	No	Python	[15]
glafic	2012	No	Yes	OS X/Linux	[46]
PixeLens	2007	Yes	Yes	Java	[57; 70]
SimpLens	2003	Yes	Yes	Java	[58]
GRALE	2008	Yes	No	OS X/Linux	[31]
GravLensHD	2011	No	Yes	iOS	[55]
G-Lens	1998	No	Yes	DOS	[9]
Gravitational Lensing	2002	No	Yes	Win/HP-49	[63]
lens	2002	Yes	No	MATLAB	[45]
MOWGLI	2013	No	Yes	Java	[44]

Table 4.1: A summary of the features of 14 strong gravitational lens model software packages which were fully evaluated. Source indicates that the source code is provided, Exec indicates that a downloadable executable file is provided and Platform indicates the computing platform that the executable works on. (PPC=PowerPC, Dates are the current version available, Exec=available executable code). Software in the upper portion of the table is considered 'Research' and that in the lower portion is considered 'Educational'.

Package	Year	Source	Exec	Platform	Ref
IGLOO	2004	Yes	No	Linux	[21]
GLAMROC	2008	Yes	No	Linux	[6]
GLASS	2013	Yes	No	Python	[17]
Mirage	2011	No	No	MATLAB	[54]
ZB	2009	No	No	MATLAB	[71]
WSLAP	2004	No	No	-	[18]
SaWLens	2009	No	No	Linux	[41; 42]
GLEE	2010	No	No	Linux	[20; 61]
Gravitational Lenser	2000	Yes	Yes	Adobe Photoshop	[51]
WFPC2	2001	No	No	Web	[48]
XFGLenses	2008	Yes	No	Linux	[19]
Gravitational Lensing Model	2011	Yes	Yes	Java	[59]

Table 4.2: A summary of the features of 12 strong gravitational lens model software packages which were not fully evaluated in this study for various reasons but are summarized below. Source indicates that the source code is provided, Exec indicates that a downloadable executable file is provided and Platform indicates the computing platform that the executable works on. (PPC=PowerPC, Dates are the current version available, Exec=available executable code). Software in the upper portion of the table is considered 'Research' and that in the lower portion is considered 'Educational'.

4.4 Research Software

Strong gravitational lens modeling software for research use is in this category. There were 17 such packages identified in the literature and on the internet. The first nine software packages described here have been used to analyze experimental data in published studies, and were available for download and testing. These nine have complete descriptions of software features and lensing features. The remaining eight software packages are described briefly, but were not tested, either because the authors do not make them available or because the software simply could not be compiled.

gravlens

Gravlens is a subset of lensmodel. The lensmodel software uses the gravlens kernel and adds functionality, and was also described by [26]. The description of these two packages is combined below, with the understanding that the Gravlens kernel is limited in functionality compared with lensmodel. The details are described in the User Manual [24].

lensmodel

Software features

The GRAVLENS- Software for gravitational lensing package was first released in 2001, and is now in version 1.99 dated 2008[1]. The software is available as a download, with executable files provided for PPC and Linux architectures. Source code is not available. Documentation is also available as a 101 page user manual [24]. The lensmodel program is available as a download, with executable files provided for PPC and Linux architectures. Source code is not available. The lensmodel software uses the gravlens kernel and adds functionality, and was also described by [26]. A tutorial is provided with the user manual. The user interface is character based and input is through a text file with text commands. There are two on-line tutorials that illustrate many of the features of the software. While gravlens includes basic lensing calculations, lensmodel includes added routines to model strong lenses [24].

Lensing features

The lensmodel software uses a parametric model, and has been used in a number of research studies [1; 4; 7; 16; 38; 60]. GRAVLENS was first described along with a new algorithm that allowed calculation of lensing parameters for a generalized mass model, allowing implementation of multiple parameterized models [26]. GRAVLENS is a sophisticated software package that is accompanied by a large catalog of parametric lensing models [25]. Both programs in GRAVLENS includes a wide range of basic lensing calculations which are based on tiling of the image. The heart of the code is a general algorithm for solving the lens equation and is fully described in [26]. This algorithm involves tiling the image and source planes, and using these tiles to determine the number and approximate positions of all lensed images associated with a given source. Performing a calculation requires specifying the details of the tiling and the parameters of the mass model. The code uses a polar grid centered on the main galaxy. Default values work with most calculations. Optionally, a critical curve grid can be used in which critical curves are used to determine where to place radial zones. Various options for plotting the output are available, and the output is a file of macros for input into the SuperMongo plotting program. The lensmodel software expands on the capabilities of gravlens, to

[1] http://redfive.rutgers.edu/ keeton/gravlens/

include routines that make it easy to fit models to observed lens systems. The central portion of lensmodel computes a χ^2 value for a set of models. A wide variety of lens models are available in the catalog [25]. The software can also calculate the Hubble constant using time delays. The available tutorials are very helpful for illustrating and explaining the complex commands that are used in gravlens and lensmodel.

Gravlens was used to model strong gravitational lenses in an interesting study which examined the cusp and fold relations as a gauge of substructure [1]. This was a theoretical investigation to look at the sensitivity of these relations to the presence of substructure in the lens. The authors found that the fold relation is a more robust indicator of substructure than the cusp. Gravlens provided an excellent analytical tool for this study. A newly discovered elliptical galaxy at z=0.0345 was investigated and modeled with gravlens/lensmodel [60]. The model was created with a SIE, and was found to be in close agreement with the light distribution observed.

In a study of a bright strongly lensed z=2 galaxy in the SDSS DR5, Lin and colleagues used Lensview to model a lensing system [38]. However, since Lensview uses the full image information, they employed gravlens/lensmodel to fit an SIE model using only the image positions. The resulting model showed a very good fit to the image positions. This study is one of the very few *direct comparisons* of strong gravitational lens modeling software in the literature.

The ten image radio lens, B1933+503 was modeled using gravlens by Cohn and coworkers [16]. The mass distribution of this system was modeled with a wide variety of parameterized ellipsoidal density distributions. The models were constrained using the relative positions of the lens galaxy and the lensed images and the flux ratios between the images. The mass distribution was concluded to have an approximately flat rotation curve based on this analysis. The gravlens program was used to model the cluster lens MS0451.6-0305 by Alba and colleagues [7]. A simple elliptical lens model (SIE) with external shear was used. They used an NFW profile for the cluster mass distribution which was consistent with observations. The model reproduced the positions of the Extremely Red Object images and the radio images very well. This model was used to test if the configuration of the observed radio emission could be understood as a result of gravitational lensing, and was able to explain the morphology of the radio map as a result of the three lensed background sources. Gravlens was also used to model a strongly lensed Lyman Break galaxy at z=2.73, identified in the SDSS DR4 imaging data [4]. The authors assumed a SIE and used gravlens/lensmodel to perform fits to the data. The fitted values showed excellent agreement with observed values from the SDSS DR4 database.

Summary

Both gravlens and lensmodel require no installation as they are provided as executable binary files. They are somewhat complicated to use because of the character based interface and extensive command set. They would benefit from a graphical user interface which is described in a web site but the code has not been available [3] [1]. The lack of source code is also a limiting factor for those wishing to study the computational techniques used. Finally, the programs are limited by requiring an outside plotting package to view graphical results. The required plotting package is expensive and somewhat outdated. Both gravlens and lensmodel have an extensive catalog of available mass models that can work with complex datasets, and perform very well in regard to comparing the models generated with observational results. Overall, they are excellent strong gravitational lens modeling software packages.

[1] http://cinespa.ucr.ac.cr/software/xfgl/index.html

Lensview

Software features

Lensview was first released in 2006 and he current version 1.1.2 is dated 2008 [1]. This software is distributed as source code, and has dependencies on CFITSIO, GSL and the FFTW libraries, as well as an optional dependency on fastsell. It can be installed in Linux or OS X. There is a web site where the software can be downloaded, with information regarding installation and use, but there is no separate user manual [67]. The user interface is character based and input is through a text file with text commands. The software is described as running in two modes, "simple projection" and "normal" (fit an observed image).

Lensing features

Lensview is based on the LensMEM algorithm [65], which finds the best fitting lens mass model and source brightness distribution using a maximum entropy constraint [69]. Lensview is used to study lens inversion, obtaining a model of the source based on lensed images. It uses a parametric model for solving the lens inversion problem. The main features of the software include: (i) projection between image and source plane conserving surface brightness, (ii) compound lens models which can contain several basic components, (iii) reconstruction of the unlensed source brightness profile and corresponding model image using a non-parametric source, (iv) iterative source reconstruction process incorporating a maximum entropy metric, and (v) statistical evaluation of the model image given by the current lens model parameters.

In simple mode, Lensview takes as input: a source, a lens model, a data image (optional) and projects the source onto the image. The projected image and χ^2 are output. A log file is also produced. A variety of lens model components are supported, including pseudo-isothermal potential (PIEP), SIE, point mass, power-law mass distribution, NFW, constant density mass sheet, external shear, exponential disc and a Sérsic mass distribution. Sample templates for each of these mass distributions are given on the website [67]. To use the software, one needs a data image, a PSF image and a mask image, all of which need to be the same size. There are no sample data files provided with the software, but there are some examples available through the website. Output from the program can be a FITS image, or a file for input into IDL and plotting the χ^2 surfaces.

In their study, Wayth and Webster first used Lensview with simulated optical images to determine optimal pixel size, accuracy of lens model parameters, distinguishing power of the image and overall goodness-of-fit [69]. Model images were created with a two-component source having two regions of different size and peak brightness. A PSF was generated and convolved with the simulated image. They found that an image to source pixel scale ratio of at least 2 is required to reproduce the data and a ratio of 3 was optimal. A sufficiently large source plane of approximately 15x15 pixels was adequate. All lens model parameters were well recovered using this data. A comparison of various models showed that the image could distinguish between lens models although the differences were quite small.

Lensview was used to analyze the Einstein Ring ER 0047-2808 [68]. This study modeled the system using six different models, including PIEP, SIS+γ, SIE, SPEMD, M/L and NFW. This study showed that the SIS+γ, M/L and NFW (25kpc) could not reproduce the data, but that the other models could. The differences between the other, successful models, were subtle. The data showed that the lensed image has four distinct bright regions, and that Lensview was able to generate a best-fitting image and reconstructed the source brightness profile using a non-parametric model.

[1] https://www.cfa.harvard.edu/ rwayth/lensview/

Lensview was also used to analyze the optically lensed arc HST J15433+5352 [69]. This lens was modeled with a PIEP model, including an external shear. The final source plane used was 10x10 pixels, with a source-to-image plane pixel scale ratio of 1/2. The resulting model was somewhat surprising in that a purely elliptical model reproduced the data equally to a model including shear. They found a critical radius (b) of 0.525, which differed somewhat from data previously reported with a critical radius of 0.58 [29]. Some of this difference could be accounted for the fact that the Lensview study is a non-parametric model, while Knudson et al [29] used a parametric model.

Lin et al used Lensview to study a bright strongly lensed galaxy in the SDSS DR5 [38]. Lensview provided an excellent model, but as the authors pointed out, Lensview uses the full image information which precludes determination of how well the image positions are determined. They then used Lensmodel to fit an SIE model using only the image positions. This study illustrates both the strengths and weaknesses of this approach, but more importantly also suggests the need for using multiple approaches to modeling.

Summary

Lensview is a comprehensive modeling program, with a large number of features and options. It is not straightforward to use, although the sample data files and suggestions provided on the website do facilitate gaining proficiency with the software. Due to its comprehensive nature, it is possible to specify very complicated lens models based on one or more components.

Lenstool

Software features

Lenstool was first written in 1993, and is now released as version 6.7.1, dated 2006[1]. Lenstool is distributed as source code with dependencies on WCSTOOLS, PGPLOT and CFITSIO, and the latest version is available on the Lenstool Project web site [27]. Installation is somewhat tedious but can be accomplished with available standard libraries, and can be installed in Linux or OS X. The user interface is character based and input is through a text file with text commands. A 61-page user manual as well as a 41 page document entitled "Lenstool for Dummies" are available for download [39]. The documentation is excellent for this complex and comprehensive strong gravitational lens modeling software.

Lensing features

Input to Lenstool is a character based input file. Each line consists of a command and appropriate data. Keywords are either first identifiers or second identifiers. A number of input files are necessary. The first is a PAR file, containing the basic parameters for the model, a list of the arcs for which Lenstool will predict counter images, and specification of requested optimization. The remainder of the input includes multiple image files and a cluster members file. The available options and commands are extensive, and testing the software with the files available for download is an excellent way to gain familiarity with the complex input required.

Lenstool is referenced in at least 11 manuscripts [e.g. 22; 23; 28; 37; 52; 53]. These manuscripts are listed on the Lenstool website [27], and many of them include downloadable files of the lens models used in the research. Strong lens galaxy clusters are modeled with parametric methods, and ranked using Bayesian evidence. Although Lenstool was initially developed in 1993 with a downhill χ^2 minimization, modeling of complex systems become inefficient due to

[1] http://www.oamp.fr/cosmology/lenstool/

the sensitivity of the technique to local minima. The computational method used by Lenstool was then changed to use a publicly available Markov Chain Monte-Carlo sampler, avoiding local minima in the likelihood functions. The merits of this method on simulated strong lensing clusters is demonstrated by Jullo et al [23].

Using a multi-scale model with a hybrid approach of LTM and non-LTM modeling in the Lenstool software, Jullo and Kneib were able to model Abell 1689, but only for a limited subset of images [22]. The key feature is that Lenstool uses a multi-scale model, allowing sharper contrast in regions of higher density. This arrangement of potentials of different sizes allows Lenstool to produce a high-resolution model with a minimum number of parameters. In this study, a mass reconstruction was created using Lenstool. The model combined a grid of radial basis functions and galaxy scale clumps with cluster member galaxies. A grid was built from a mass map based on 2 cluster-scale and 60 galaxy-scale clumps of mass, instead of the 190 galaxy-scale clumps used in previous studies [37]. A catalog of 28 images in 12 systems of multiple images were selected for this analysis. There were 122 parameters, which took 15 days to produce 2000 MCMC samples on a 2.4GHz processor. The results of this study confirmed the ability of a multi-scale model to be used as a lens model. The authors report that the errors between the positions of observed and predicted images were halved, compared to previous studies.

The nature of the mass distribution in Abell 1703 was studied using Lenstool [52]. This demonstrated the ability to model the inner mass distribution of massive galaxy clusters. This study used a spectroscopic survey to confirm photometric redshifts and precisely constrain the mass distribution in Abell 1703. Lenstool was used to constrain a parametric mass model with the identified multiple systems. The positions of the multiply imaged systems were used to optimize parameters describing the mass distribution, using a Pseudo Isothermal Elliptical Mass Distribution (PIEMD) using the profile derived from photometry. The Bayesian approach in Lenstool provides a large number of models which sample the probability density function of all the parameters. Results were compared to previous weak-lensing studies, and were found to have a very good fit. This strong lensing analysis using Lenstool and a simple NFW component for the large scale dark matter distribution, was able to reproduce the large number of images in Abell 1703, as well as demonstrate consistency with previous weak-lensing analyses.

Summary

Lenstool is a comprehensive program for gravitational lens modeling. The software is relatively easy to install and use, and is accompanied by extensive documentation. It has been extensively used in the modeling of observed gravitational lenses. The availability of the input files from previous studies increases the utility of this software. The software uses a novel technique to combine the strengths of both LTM and non-LTM models, by using a multi-scale model that allows sharper contrast in areas of high density. The flexibility of this approach allows improved prediction of image positions compared to previous studies.

LensPerfect

Software features

LensPerfect was released in 2007 and is available for download [1]. The software is written in Python and the source code is included. Dependencies include Numpy, Scipy, Matplotlib and Pyfits. Installation of the software is slightly complicated by the fact that the software will not work with the latest version of Python. There are numerous sample data files provided

[1] http://http://www.its.caltech.edu/ coe/LensPerfect/

to demonstrate the features of the software. Output from analysis of one of the sample files is shown in Fig 4.1. Documentation is available on two web sites including one which details installation and use of the software [13], although there is no separate user manual. The user interface is character based and input is through a text file with text commands.

Lensing features

The software was developed by Coe [15] and has also been used in one more research study [14]. LensPerfect uses a parametric model but is also "model-free" as described by its developers, who further characterize it as non-LTM. LensPerfect solutions are given as sums of basis functions. While most parametric models are based on a physical object, the basis functions used by LensPerfect have no physical interpretation. Input to the program is via a text file and graphical output is shown immediately on the display.

LensPerfect represents a new approach to gravitational lens mass map reconstruction, and is the first method to do so using strong gravitational lensing data (multiple images). This new approach uses direct inversion to obtain assumption-free mass map solutions which perfectly reproduce all multiple image positions. This was developed using a new mathematical approach, using a curl-free interpolation of vectors given at scattered data points. One of the key features in any model is the measure of "physicality" of the model. The developers of LensPerfect use a new measure of physicality, with the following traits: (i) positive mass everywhere within the convex hull, (ii) low mass scatter in each radial bin, (iii) no "tunnels", (iv) overall smoothness and (v) average mass in radial bins decreases outwards. The only rigid constraint among these is the first trait, requiring positive mass. A complete discussion of these traits is available in the reference [15].

LensPerfect provides an accurate mass map even when there are many lensed galaxies, by using several novel approaches. A weighted average of predicted source positions is used to determine each new source position. The solution is rebuilt at each iteration as new sources are added. This process is fast, and results in an accurate mass map. Both source and image positions are always perfectly constrained.

The galaxy cluster Abell 1689 is one of the most studied gravitational lens systems, and thus is ideal for comparisons among lensing models. The large number of multiple images in Abell 1689 also make detailed analysis a challenging problem. In a followup investigation after introducing the method and software, LensPerfect was applied to the analysis of Abell 1689 using the positions of 168 multiple images. The non-LTM models from LensPerfect were able to reproduce the observed input positions of 168 multiple images of 55 knots residing within 135 images of 42 galaxies [14]. The computing problem associated with analyzing Abell 1689 is obvious, since it has 100+ strong lensing features. The software must produce a mass model with correct amounts of mass to deflect light from 30+ background galaxies into multiple paths to arrive at the 100+ observed positions. LensPerfect did this, using direct matrix inversion to find solutions based on the input data. The optimization took two weeks to run on a Macbook Pro (Apple Corp., Cupertino CA) laptop computer. This study demonstrates the robustness of the algorithm and its computing efficiency.

A mass map of Abell 1689 produced by LensPerfect using NFW and Sérsic fits had a recovered mass profile which matched the input mass profile extremely well [14]. The NFW fit parameters compare very well to previous studies of Abell 1689 using strong lensing data as well as studies using a combination of strong and weak lensing data.

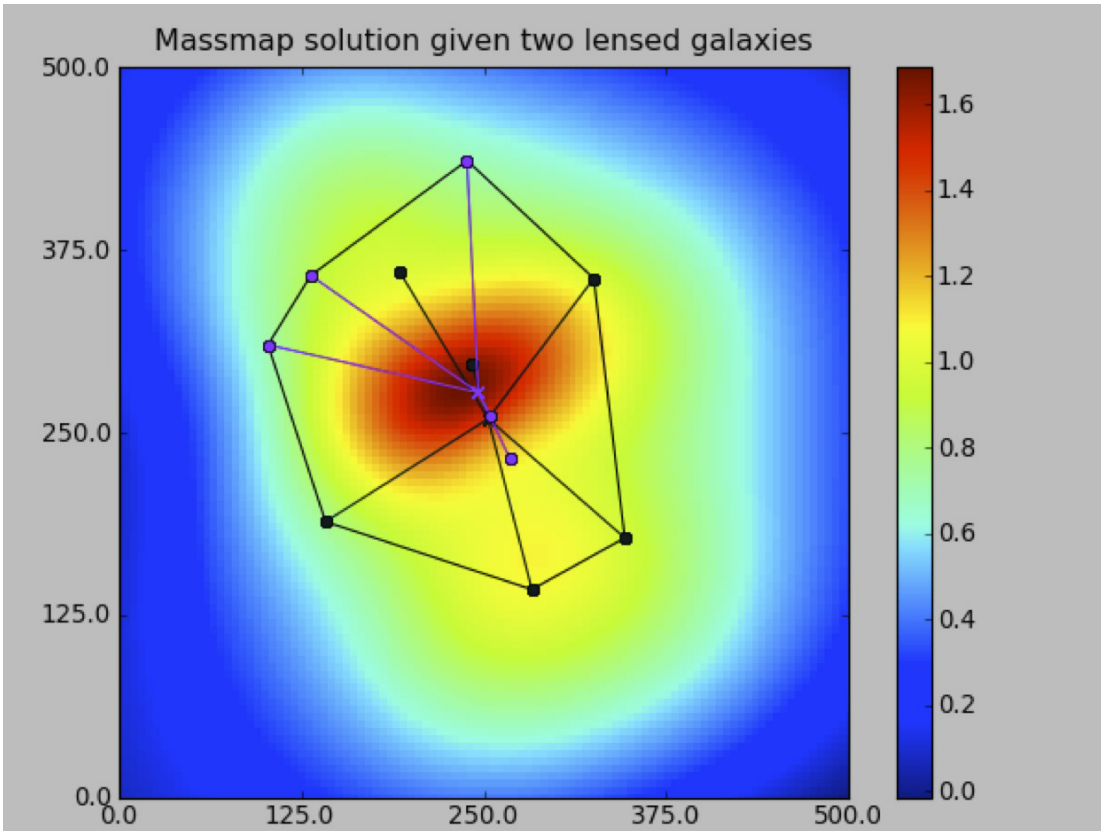

Figure 4.1: Sample output from LensPerfect using a supplied test dataset

Summary

LensPerfect is a full-featured program that is extremely capable of producing a mass map based on lensed images, even when there are many galaxies as demonstrated in the followup study of Abell 1689. It is distributed as source code, written in Python, which is available for many platforms. The new approach taken by LensPerfect results in fast and accurate modeling, even of complex systems. The output is graphical and displayed directly. LensPerfect does an excellent job of accurate reconstruction of the sources and lensed images. The ability of LensPerfect to accurately produce a mass map using strong lensing data represents an important advance in gravitational lens research, and will likely lead to further advances.

glafic

Software features

The current release of glafic was written in 2012, and is provided as a downloadable executable file which is unpacked from a .tar file [1]. Several sample input files (also in a single .tar file) and a detailed 51 page Users manual are provided. Source code is not provided. There is no installation procedure since it is provided as an executable file for OS X. The program runs without any modifications necessary. The user interface is character based and input is through a text file with text commands. The program runs in the command line interface using OS X. There is no graphical interface.

Lensing features

Glafic uses a parametric model that can be used for a wide variety of gravitational lensing analyses [46]. It includes computation of lensed images for both point and extended sources, handling of multiple sources, a wide variety of lens potentials and a technique for mass modeling. Commands are entered in a simple text file, which begins with a list of primary parameters (omega, lambda, Hubble, lens redshift z, pixel size, etc.) and then an optional list of secondary parameters (optional data files, output format desired, extended source normalizations, etc). Point sources are defined simply by their redshift and x- and y-coordinates. Each lens is defined by the lens model and seven parameters. A large catalog of lens models is available (including point mass, Hernquist, NFW, Einsato, Sérsic, etc.). Extended sources can be Gaussian, Sérsic, top hat, Moffat or multiple sources. After defining the parameters and the lens models, parameters to be varied in the χ^2 minimizations are specified. Following this, the desired commands are issued such as computing various lensing properties, Einstein radius, write lensing properties to a FITS file (see sample output in Fig 4.2), etc. Various types of optimization are permitted. The commands are well described and illustrated in the User's manual. Commands can be entered as a batch using an input file, or entered on a command line. A number of sample data files are provided which illustrate a number of the major features of glafic.

Glafic was used to perform a strong lens analysis of SDSS J1004+4112 [46]. This is a particularly interesting quasar lens because it is one of only two known examples of a cluster-scale quasar lens, and contains multiply imaged galaxies at z $\sim$ 3. The authors include an indirect comparison with multiple previous mass models of this interesting lens. This study used a parametric model, with the main halo of the lensing cluster modeled with the generalized NFW profile. A standard χ^2 minimization was used to find the best-fit mass model. The best-fit radial mass profile generated is in good agreement with strong lensing data inferred from Chandra X-ray observations. The model used several new constraints including positions

[1] http://www.slac.stanford.edu/ oguri/glafic/

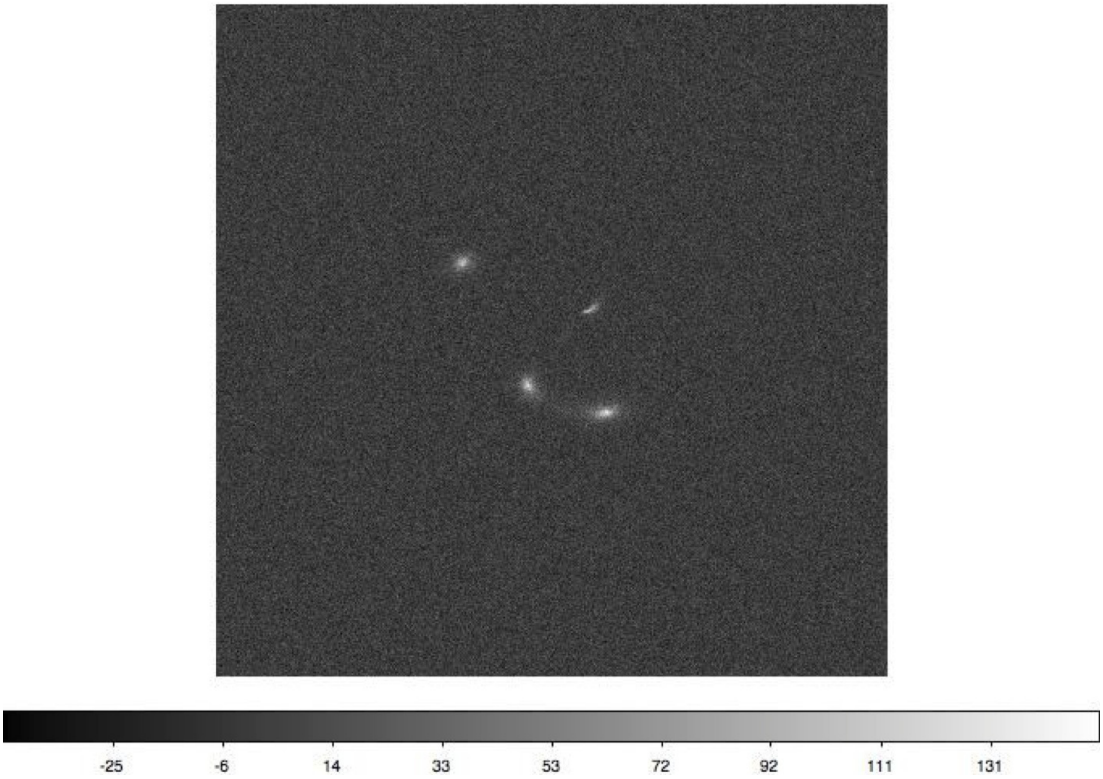

Figure 4.2: FITS image output by glafic for a sample model with a single point source, two lenses and two extended sources

of spectroscopically confirmed multiple imaged galaxies, time delays between quasar images, and faint central images. The model thus generated was able to successfully reproduce all observations including time delays.

Summary

The glafic program is a well-designed, flexible and easy to use lens modeling program. It includes a wide variety of lens models and is extremely flexible in the types of models it accepts. The User's manual is helpful and complete. Output consists of a variety of possible data files including FITS images. Glafic can accurately recover lens model parameters of known lensing systems.

PixeLens

Software features

PixeLens was written in 2007, and is available to run in a web browser or as a stand alone java applet which can be downloaded from the website [1]. There is no installation needed. This

[1] http://www.qgd.uzh.ch/projects/pixelens/

program was used at the ANGLES School for Gravitational Lensing in 2007. The source code is provided in the downloadable .jar file. Information is also available on the website. Sample input data is provided. A paper (19 pages) and tutorial (14 pages) detailing the software and underlying theory are available on the website, and serve as excellent documentation with numerous examples. The user interface is a single window with several entry panels in the window. Input is done in the window, or through an input file.

Lensing Features

This program uses a non-parametric model, with Bayesian statistics. Input to the program consists of model constants (red shifts, pixel size, etc) and image data. The radius of the mass map in pixels and the redshifts for the lens and source must be given. Optional inputs include setting the mass map as symmetric or asymmetric, the radius of the mass map, external shear, the number of models allowed, and several others. Image data includes x- and y- locations and the time delays. Type of output can be selected as text or eps files. Sample output is shown in Fig. 4.3, showing the image directly on the display.

[57] used PixeLens using non-LTM models to perfectly reproduce some of the data for Abell1689, but computational limitations restricted PixeLens to fitting 30 multiple images at a time, because of the requirement for exact fits to the image data. This could be considered a virtue allowing the data to be split into two sets as pointed out in the study. In this study, PixeLens had been enhanced to use multiple-source redshifts. PixeLens had some advantages in the models generated, particularly in handling the inherent problem of degeneracy. While some software uses one or a few models, PixeLens generates a large ensemble of models which explore the possible mass distributions that can reproduce the data. Data from PixeLens was compared to independent datasets for consistency [57]. PixeLens has also been used to model the giant quadruple quasar SDSS J1004+4112 [57; 70]. In addition to the lensing data (image positions), six kinds of constraints were applied to limit the ensemble to lenses that could plausibly be galaxies or clusters. The result was free-form reconstructions allowed detection of structure in the lens associated with cluster galaxies [70]. J1004+4112 was reconstructed using 13 images from 4 sources.

Summary

PixeLens is an easy to use program for non-parametric modeling of gravitational lenses. There is ample documentation available. It is based on reconstruction of a pixellated mass map by generating large ensembles of models with a Metropolis algorithm. It can model several lenses simultaneously, which is a rare feature of modeling software. The code has been tested with a number of fake models and correctly recovers both the mass distributions of the lens and H0 within uncertainties. PixeLens has been used in several published studies to analyze gravitational lenses [56; 57].

SimpLens

Software features

SimpLens was written in 2003, and is available to run in a web browser or as a stand alone java applet which can be downloaded from the website [1]. There is no installation procedure needed. The source code is provided in the downloadable .jar file. The user interface is a single

[1] http://www.physik.uzh.ch/ psaha/lens/simplens.php

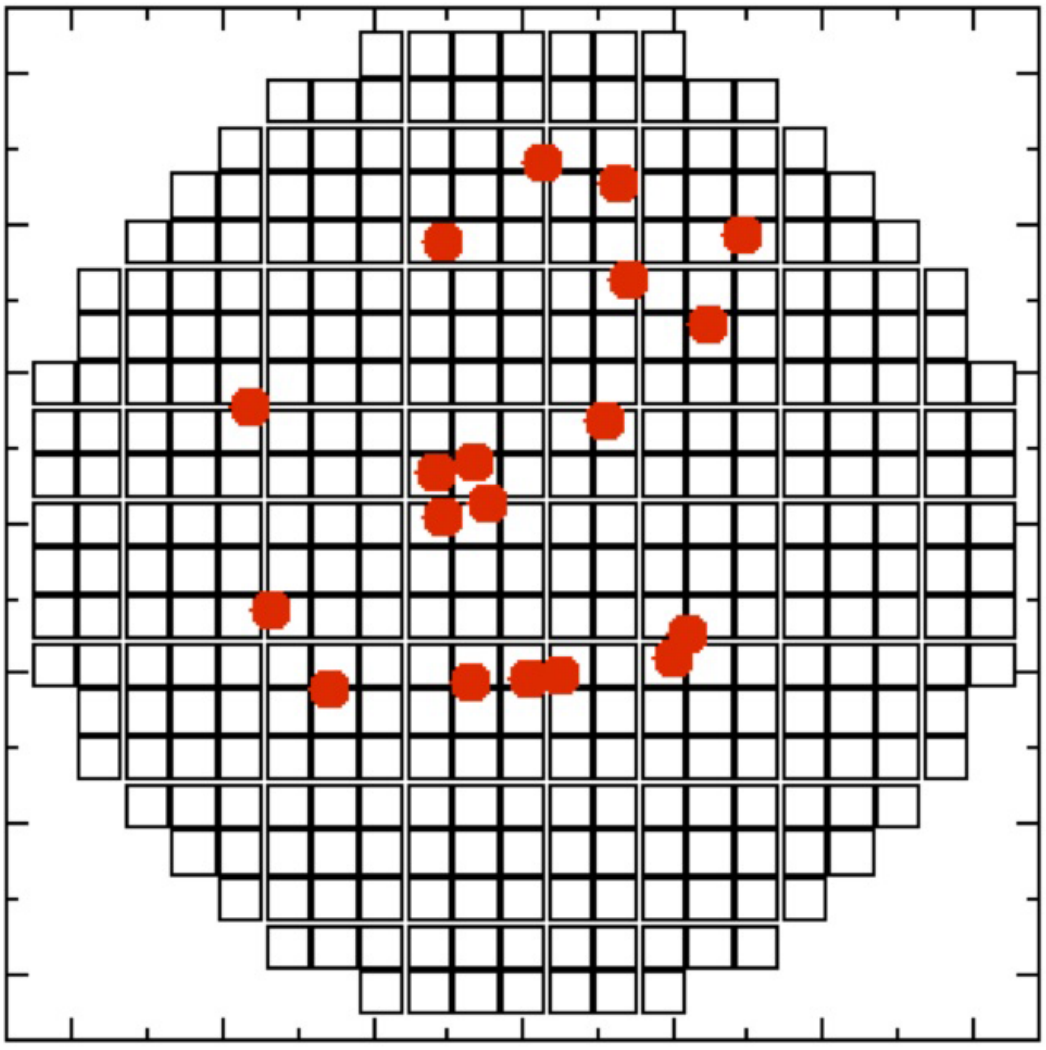

Figure 4.3: Sample output from PixeLens

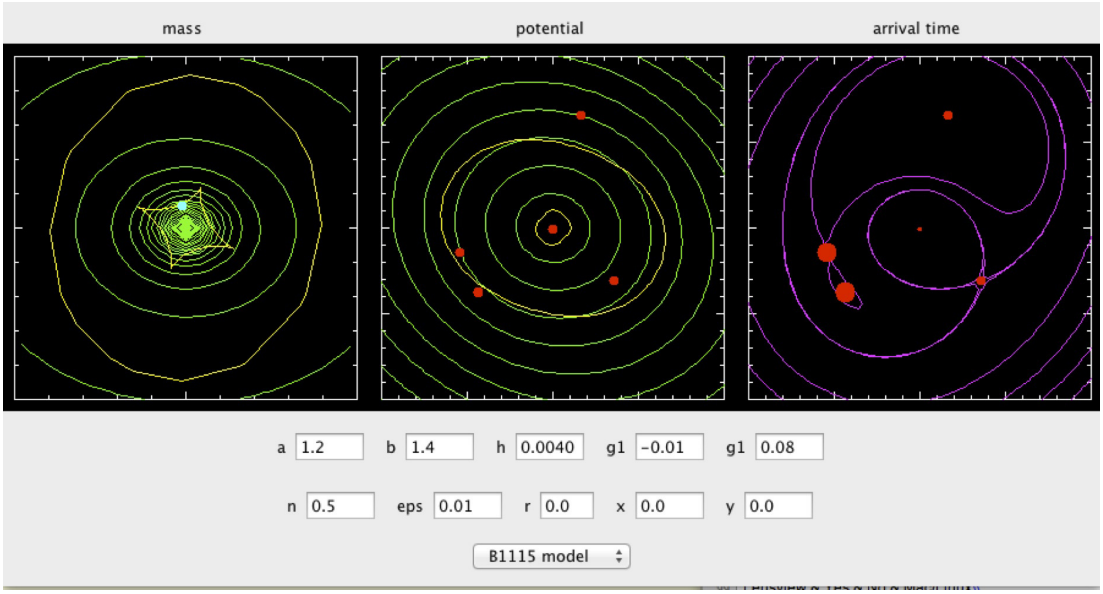

Figure 4.4: Sample data entry and output from SimpLens

window which displays graphs of mass, potential and arrival time. There is no formal written documentation, but the web site provides adequate information.

Lensing features

SimpLens uses a non-parametric model, and the algorithm is explained in an article written by the developer [58]. That article also demonstrates some of the analytic capabilities of SimpLens. The user can enter values for a,b,h,g1, g2, n, eps, r, x, and y. The parameters a, b, and h specify an elliptical mass distribution, while g1 and g2 refer to the external mass. By clicking the computer mouse, the source position can be changed (see Fig 4.4 left panel) and the effect of that change instantly visualized on the display. The graphs display caustics, saddle point contours and critical curves. A number of sample data sets are provided which are easily selected in a pull-down menu. The various parameters from the sample data can then be varied to instantly observe the effect of the alteration on the three graphs. For example, the sample data allows one to easily observe the effect of added shear.

Summary

SimpLens is a simple interactive program which allows one to instantly demonstrate the effect of changing parameters on caustics, saddle points and critical curves for mass, potential and arrival time. It is very easy to use and very instructive.

GRALE

Software features

The current version of GRALE is 0.9.0, released in 2008 [1]. It is provided as source code which must be compiled and linked using the CMAKE utility. The installation procedure is fairly straightforward, and the GSL and CFITSIO libraries are necessary. The software can be installed in Linux, or OS X. The GRALE library is easily run under GRALESHELL, which provides an interactive environment. The software runs in a single window and text commands are entered in a panel at the bottom of the window. Output is obtained using GNUPLOT (see Fig. 4.5) or optionally as a FITS image. Documentation consists of a website dedicated to this software, but there is no separate user manual.

Lensing features

GRALE can be used to simulate gravitational lenses and to invert lensing systems. The GRALE algorithm uses a non-parametric technique to infer the mass distribution of a gravitational lens system with multiple strong lensed systems [31]. To start simulating a gravitational lens, the user first decides which type of lens to use. There are a variety to select from including a point mass lens, a SIS, SIE, projected Plummer sphere, square shaped region of constant density, a two dimensional gaussian density profile, and others. The lens parameters include mass, distance and others as appropriate. Commands and parameters are entered line by line in GRALESHELL. Next, the distances to the source plane are specified and then the mapping from the image plane to the source plane is specified. Sources can then be added. A sample lens model is shown in Fig. 4.5. Lens parameters can be optionally saved and retrieved. The program directly outputs a file which is used by GNUPLOT to generate visual output.

GRALE has been used in a number of published studies to analyze various lenses. GRALE functions well in modeling systems with few images, and thus less information [32]. GRALE was used in a study using strong lens modeling to search for dark matter [34].

GRALE was used to model the system Cl 0024+1654, and infer the mass maps using a non-parametric technique [33]. This represents the first time that image information alone was used to reconstruct the mass distribution of this cluster in the strong lensing region. No information about the positions of cluster members was used. Image data for sources A and B as previously described was used for the inversion procedure to reconstruct the source. Source A was mapped onto five images and source B mapped onto two images. A mass map was obtained by averaging 28 solutions. The only bias in the technique is that the user must specify a square shaped area for the algorithm to search mass distribution, assuming that no mass is outside the boundaries of that region. Using the inversion procedure in GRALE, an averaged mass map was obtained that displayed the features seen in the ACS images.

Models of the well known system SDSS J1044+4112 were also created using GRALE [35]. This study looked at five spectroscopically confirmed images and position information was used from existing studies. One of the images was uncertain (A5) and was not included in the first inversion. A second inversion was then performed with the addition of image A5, which allowed reconstruction of the source shapes after projecting back onto the source planes. Calculation of the total mass within 60Kpc and 110Kpc compared well to results in existing studies. Comparison was also made to the best fit NFW model, and the configuration of the cluster corresponded to that reported previously [47].

[1] http://research.edm.uhasselt.be/ jori/page/index.php?n=Physics.Grale

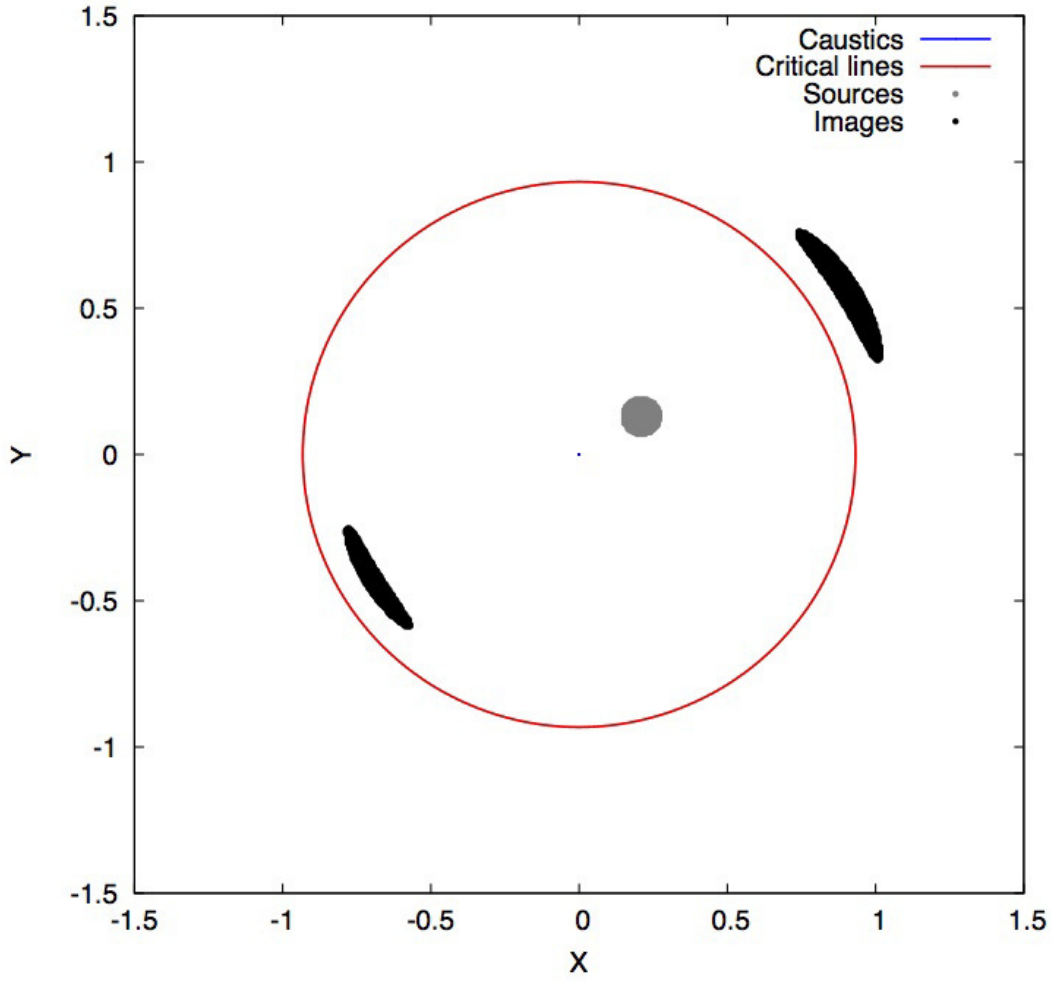

Figure 4.5: Output from GRALE for one of the supplied sample data files

Summary

GRALE is easily installed and straightforward to use. Commands are text-based and relatively intuitive. A variety of lens models is available for simulations. A large number of lens and source parameters can be entered by the user, allowing one to perform complex lens simulations. In several studies, GRALE did an excellent job of recovering lens parameters and accurately reconstructing the source parameters. GRALE has been tested with models of C 0024+1654 and SDSS J1004+4112 and gives results compatible with previous studies.

IGLOO

The IGLOO (Interactive Gravitational Lens Optimization Olgorithm) code, developed at the University of Manchester, is different from other lens modeling software (e.g. GravLens, Lenstool, etc.) in philosophy. It sacrifices richness of features (and sophistication of algorithm) to user-friendliness and small size of code. It is an LTM model code. There have not been any studies to date using this code. It was not possible to compile this code or test it because of its many dependencies, some of which are no longer available.

This software can be downloaded at the URL given. It is dependent on GSL and PGPLOT. Some documentation is available at the website [21]. The documentation includes a user manual, some sample data as well as a description of the software design. Optimizations are performed with the AMOEBA downhill-simplex method. The interface includes a number of function buttons and a graphical output.

Glamroc

Glamroc is an adaptive mesh ray tracing code, using a non-LTM algorithm [6]. The source code is available. It has been used in one study [49]. It does not have data-fitting capability and is therefore useful for theoretical investigations. The software is accompanied by documentation and sample data files. This code could not be compiled or tested.

GLASS

GLASS is the Gravitational Lensing AnalysiS Software, and was released in 2013. It is a non-LTM code that uses an under-constrained adaptive grid of mass pixels to model a lens [17]. It extends and develops some of the concepts from the free form modeling tool PixeLens, but with all new code. The most computationally intensive portion was written in C but Python was chosen because of its extensibility as a language and for its large scientic library support. The flexibility allows GLASS to have quite sophisticated behavior while at the same time simplifying the user experience and reducing the overall development time. One of the striking features is that the input file to GLASS is itself a Python program.

The software is freely available for download and includes excellent documentation including sample input files and a User Manual.

At the heart of GLASS lies a new algorithm for sampling the high dimensional linear space that represents the modeling solution space. Each prior is a simple function that adds linear constraints that operate on either a single lens object or the entire ensemble of objects. GLASS currently describes the lens mass as a collection of pixels, but the code has been designed to support alternative methods. In particular, there are future plans to develop a module using Bessel functions. The algorithm for generating models in GLASS samples a convex polytope in a high dimensional space whose interior points satisfy both the lens equation and other physically motivated linear priors. [17].

Mirage

Mirage is a non-LTM models software that is written in MATLAB. It could not be tested because it is not publicly available. It has been used in several studies. Mirage determines the parameters of pixelated source intensity distributions for a given lens model. This technique enables including the effects of spatially variant point-spread functions using the iterative procedures in this lensing code.

The authors have developed a method to include the effects of a spatially variant PSF in gravitational lens modeling [54]. Including these effects in the standard semilinear method would be difficult due to the complicated blurring matrix required. These complications are overcome by incorporating the algorithm used. This approach can accommodate large lensing problems, which limits the applicability of the direct semilinear approach. Techniques to include the effects of spatially variant PSFs are important, as the response varies over the detector area for many astronomical instruments. The algorithm used allows this effect to be included in lensing problems, thus improving the quality of reconstructions when the variability of the PSF is significant. The CGLS and SD algorithms allow a regularized inversion to be found quickly by truncated iteration.

ZB

ZB is an LTM strong gravitational lens model code with a minimum number of free parameters [71]. It is somewhat less flexible than other methods because of the LTM assumption and the use of few free parameters. Inputs to the program are (a) the position and flux of the [red sequence] cluster members and (b) a list of multiple image systems and their redshift. The user also defines other minor factors such as cosmology, etc. The output is the mass model, kappa/mass density map, magnification map, critical curves, deflection fields, mass profile, model optimized redshifts for the arcs if requested, rms and chi-sqaured, the potential and time delays if requested, etc.

ZB strong lens model software excels in physically finding multiple-image systems. It uses a simple parametrization and and a minimum of free parameters. In the original modeling method, it adopts a power-law surface mass density for the galaxies scaled by their light and smooths the superposition of this (unnormalized) galaxy contribution to represent the DM, with either a 2D spline interpolation whose polynomial degree is a free parameter, or with a Gaussian whose width is a free parameter. The overall resulting deflection field is then simply normalized to a certain redshift / multiple-image system where the normalization is another free parameters. For some more flexibility / ellipticity, external shear is added which introduces two additional free parameters. Therefore the procedure adheres to the light-traces-mass (LTM) assumption, yet this very simple procedure yields excellent results. The method can be implemented via a grid minimization - which is faster but somewhat cruder, or via an MCMC.

ZB has been used in a large number of published studies, analyzing dozens of cluster lenses, including some direct comparisons with other lensing software. Some of these include CL0024, MACS0717, MACS1149, A1703, A2261, A383, and MS1358. This MATLAB-based software is however, not available for distribution.

WSLAP

WSLAP was introduced in 2004, and is a non-LTM lens model software. This software is not available for distribution, and is used almost solely by its author [18].

This software revisits the issue of non-parametric gravitational lens reconstruction and presents a new method to obtain the cluster mass distribution using strong lensing data without using any prior information on the underlying mass. The method relies on the decomposition of the lens plane into individual cells. The problem in this approximation can be expressed as a system of linear equations for which a solution can be found. Moreover, it is proposed to include information about the null space. That is, the software makes use of the pixels in which there are no arcs above the sky noise. The only prior information is an estimation of the physical size of the sources. No priors on the luminosity of the cluster or shape of the haloes are needed, making the results very robust. In order to test the accuracy and bias of the method the software makes use of simulated strong lensing data. This method reproduces accurately both the lens mass and source positions and provides error estimates.

SaWLens

Nonparametric analysis of gravitational lenses combining both weak and strong lensing information. A detailed analysis of the software's application is provided in Section 5 of Merten [41]. This software was designed to combine mutiple observational constraints into a joint reconstruction method in a consistent way.

The software is written as about 12,000 lines of C++ code, with multiple dependencies including GSL, MPI, ATLAS, LAPACK, CFITSIO, CCfits and LibAstroC++. It requires at least 8 CPU cores and about 1GB of memory per core. It runs under Linux and it is preferably run on 16-128 core Beowolf clusters. Similar performance can be reached on NVIDIA Tesla GPU cards. For example, CLASH reconstructions are run on a 24 core 2 node system with about 1 day runtime per lens. Linux installations running the code need to have an MPI environment installed even if the code is just running on a single task. This software is not available for distribution, and has only been used in studies published by its author.

This software has been used in a number of studies [42].

GLEE

GLEE (Gravitational Lens Efficient Explorer) is used to probe cosmology through gravitational lens time delays and to study the mass structure of galaxies/clusters [20; 61]. A variety of simply-parametrized profiles can be used to describe the lens mass distributions. The sources can be either point-like or spatially extended; pixelated grids are used to describe the surface brightness of spatially extended sources. The lens parameters can be either optimized or sampled.

GLEE uses simultaneous modeling of lens light distribution, lens mass distribution and source light distribution, and is applicable to galaxy, group and cluster-scale strong lenses. The spatially extended source modeling is computationally intensive. The lens parameters can be either optimized or sampled. Pixelated grids are used to describe the surface brightness of spatially extended sources.

GLEE has been used in a number of studies, but the software is not available for distribution and is used only by its authors.

4.5 Educational Software

Programs suited for education are useful to demonstrate the basic principles of lensing. Categorization as educational software is arbitrary and based on the fact that there were no studies found in the literature that used these nine software packages for data analysis in published

studies. Of these nine software packages, the first five were available for download and testing and are fully described. The remaining four were not fully tested and are only briefly described.

GravLens HD

Software features

GravLensHD is available for iOS devices and is obtained from the Apple (Cupertino CA) App Store, at no cost [1]. The source code is not provided. There is a help-screen with some suggested exercises to demonstrate the features of a gravitational lens. The web site has some additional information [55]. There is no formal documentation. The interface is limited to a single touch screen. Installation is simple using the App Store application.

Lensing Features

This software uses a single mass as a lens, and is categorized as a parametric model. The software uses a simulated source and a foreground lensing mass to draw arcs or an Einstein ring as one moves the lensing mass relative to the star digitally on the touch screen. The lensing mass can be made invisible leaving the lensed image of the source. The ellipticity of the lensing mass can be changed through a few preset shapes. The size of the lensing mass can be changed with on-screen gestures. The images can be saved to the devices library.The background image can be changed to any picture of the user's choice, giving an excellent way to show the effect of a lens on a known image. Some technical material is also available within the application. It uses a singular isothermal sphere (SIS) model with external shear. The maximum shear permitted is 0.6.

Summary

In summary, this software provides an excellent demonstration of the effect of a gravitational lens, and may serve as a tool to stimulate young minds to think about astronomy. The concepts used are the same as those for any gravitational lensing system. There is no option for numerical input, and all interaction with the software is through the touch screen. Further information is available on a web site dedicated to this software [55].

G-Lens

Software features

G-Lens was written by Boughen in 1998 (as part of an undergraduate honors thesis), and is available as an on-line download as a single executable file [2]. The program will only run in a DOS or early Windows environment, but can be used with more modern operating systems in DOS emulators, such as DOSBox which runs in OS X [64]. Source code is not provided. There is no installation, as one needs only to execute the .exe file provided. The software was reviewed in the June 2000 issue of Sky and Telescope [9]. Along with the software, there is a one-page instruction sheet available, but no other documentation. The user interface is a single character based text box where the values of parameters are entered.

[1] Available on iOS devices though the App Store application
[2] http://uv.vuchorsens.dk/r/AC/doc/Ast

Lensing Features

The lens mass is varied and is modeled as a single point mass, characterizing this software as a parametric model. Input to the program is performed by providing the lensing mass (in solar masses), the lens and source distances (in Mpc) and then selecting among three options for geometry of the lens (circle, ellipse and grid). Output is immediately shown on the display. The image can be optionally printed.

Summary

This software simulates a simple point mass lens and allows numerical input regarding basic system geometry. The output is graphical showing the image resulting from the lens designed by the user. The ability to specify basic parameters numerically makes this a good program for demonstration of basic lens effects.

Gravitational Lensing

Software features

Gravitational Lensing was written in 2002 and is distributed as an executable file which runs in Windows, and also as a C program for use on an HP-49 calculator. The software is available for download on the website [1]. There is no installation, as one needs only to run the .exe file provided. Source code for the Windows version is not distributed. Documentation is available to explain the science of lensing, written in Dutch. There is no documentation for running the software. The interface is a single window, and a "File" menu. The program has an "About" screen but no on-line help. The options in the "File" menu allows changing parameters of the lens model. After changing the parameters, the result is displayed in the window.

Lensing features

The mass can be varied on the data entry screen and is modeled as a point mass, characterizing this as a parametric model. Sample output is shown in Fig 4.6. The mass of the source and lens can be set individually (as multiples of solar masses). Distances from the observer to source and lens are set in Mpc. The position of the source can be set as an offset from center, and the angle of view can be varied. Models include a Plummer model or isothermal sphere. The Einstein radius can be optionally set. A set of default values is also available to show the capabilities of the program.

Summary

This simulation is simple to install and use. Various parameters are easily set in a menu screen and the resulting lens model instantly visualized. There are two optional models that can be used. This software is very useful as an educational tool, but not sufficiently robust for research analysis.

lens

Software features

Lens was released in 2002, and is written in MATLAB, and therefore the MATLAB (The MathWorks Inc, Natick MA USA) software is required. The source code is distributed and

[1] http://www.kwakkelflap.com/gravlens.html

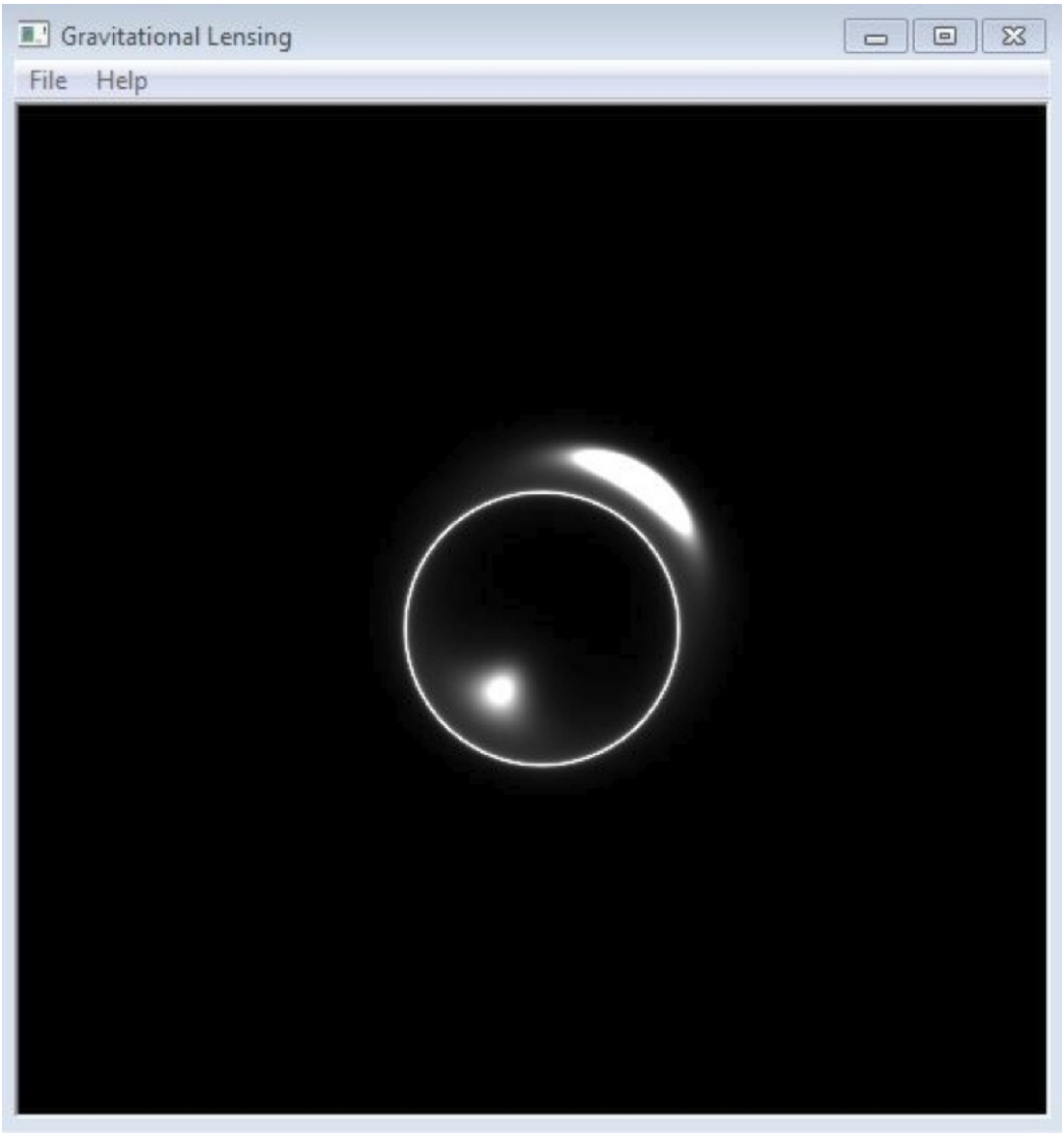

Figure 4.6: Sample output from Gravitational Lensing

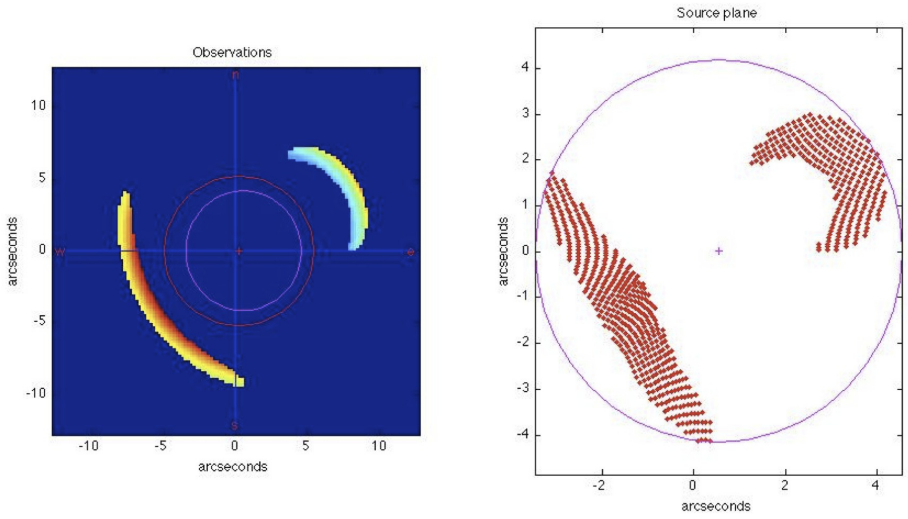

Figure 4.7: Sample output from Lens showing the image plane (left) and the generated source plane (right)

easily installed in MATLAB (these tests conducted with version R2010a). The source code and sample data files (SIS1 and SIS2) are available for download [1]. The package includes two programs written in MATLAB, lens ("forward" modeling) and invert (which solves the lens inversion problem). The information on the website includes a tutorial, and serves as excellent documentation. The user interface is through the MATLAB screen. Installation is accomplished using MATLAB. Sample data files are provided to test the software.

Lensing features

Lens is a hybrid program, which demonstrates both the "forward" problem as well as lens inversion. For modeling the lensed images, lens uses a parametric model as a SIS, and the algorithm is described in an accompanying article [45] which is easily available following a link from the website. Various model parameters of the SIS can be changed in the parameter file, as detailed on the website. The input data file specifies observation parameters, lens parameters (sigma, z) and source parameters (z,x,y, ellipticity, flux) and produces the lensed image (the "forward" problem") (left panel, Fig 4.7). Resulting images are shown directly on the display with no further intervention. The program optionally writes a data file which can then be used as input to the inversion routine to solve the "reverse" problem. The user estimates the center of the lensing mass with the computer mouse, and an image of the source plane is created (right panel, Fig 4.7).

Summary

This program is easy to use, but requires MATLAB. The program demonstrates a solution to the basic problems of gravitational lensing including the forward and reverse problems. Input

[1] http://www.astro.ubc.ca/people/newbury/siam/lens.html

files are easy to create and the output graphics are quickly generated and illustrate the solution. The software could be easily modified, and is supplied with ample comments.

MOWGLI

Software features

MOWGLI is available as a Java applet, accessed through a web browser [1]. The web site includes a Quick-start guide on-screen with easy to follow directions. The interface is intuitive and requires minimal training to use. There is no documentation as all information is described on the web site.

Lensing features

MOWGLI is designed for interactive manual modeling of strong gravitational lenses, as described on the web site. Objects such as lenses, sources or masks are added to the screen through an easy to use interface. One can upload a .jpg image of the system for which modeling is desired. By clicking and dragging on the screen, the objects can be moved into various positions as desired. Once the objects are positioned, there are two buttons labeled 'predicted' and 'residual' to view these two images on the right hand panel of the interface. The residual can be minimized by adjusting the Chi square with an on-screen button.

Summary

This software is easy to use and easily accessible as a Java applet. According to the website, a paper has been submitted to further describe the features.

Gravitational Lenser

Gravitational Lenser (version 1.3) is a plug-in for Adobe Photoshop that demonstrates the basic principles of lensing and allows the user the vary several parameters to observe the effect of changing the parameters on the image produced by the lens [51]. It is available for download, but according to the web site, runs only in the Windows environment at present. Source code is available. Parameters are adjusted with six slider controls.

WFPC2

WFPC2 is a web-based app that allows the user to set a variety of parameters on a control panel, and see the effect of the various parameters on the resulting images [48]. The user can select from six parameterized lens potentials. The software has images for six lenses that were observed with HST, and the user can then do a side-by-side comparison of the simulation with the HST image. This software is excellent for demonstrating the effects of various parameters on the images.

XFGLenses

XFGLenses can be downloaded from the web site [3] and is fully described in a paper [19]. The software is a GUI control panel with numerous parameters that can be specified and the effect

[1] http://www.ephysics.org/mowgli/

of these parameters on lensed images can then be observed. The control panel includes a model menu, a source menu, a source positioner, as well as counters, buttons and sliders.

Compiling the software requires XForms, OpenGL and Image Library which make it extremely difficult to compile into working software. Part of this project includes a front-end interface for gravlens and lensmodel (described above).

Gravitational Lensing Model

The Gravitational Lensing Model simulates the result of the deflection of photons as they pass through the warped space-time of a gravitational field of stars, clusters of galaxies or dark matter. In the simulation one can examine the effect caused by a gravitational lens in three different cases: 1. A point-mass lens and a point mass source. 2. A point-mass lens and an extended source. 3. A softened isothermal sphere lens and an extended source.

The software is distributed as an open source Java applet, and can be downloaded from the web site [59]. It is a nice program to demonstrate some of the basics of gravitational lensing, and is easy to use.

Package	Model	Algorithm
gravlens	LTM	Image tiling
lensmodel	LTM	Image tiling
Lenstool	LTM/Non-LTM	MCMC
LensPerfect	LTM	Vector interpolation
glafic	LTM	Adaptive meshing
PixeLens	Non-LTM	Pixelated mass map
SimpLens	Non-LTM	-
Lensview	Non-LTM	LensMEM
GRALE	Non-LTM	Genetic
IGLOO	LTM	AMOEBA simplex
GLAMROC	Non-LTM	Adaptive Ray tracing
GLASS	Non-LTM	Adaptive Pixel Grid
Mirage	Non-LTM	Pixellated source intensity
ZB	LTM	Simple Parameterization / MCMC
WSLAP	non-LTM	Lens plane divided into cells
SaWLens	non-LTM	Strong and Weak Lensing
GLEE	LTM	Probes Cosmology through Time Delays
GravLensHD	LTM	-
G-Lens	LTM	-
Gravitational Lensing	LTM	-
lens	LTM/Non-LTM	-
MOWGLI	-	-
Gravitational Lenser	-	Lensing basics with Adobe Photoshop
WFPC2	LTM	Web-based with 6 Potentials
XFGLenses	LTM	GUI with 22 lens models
Gravitational Lensing Model	LTM	Three Models available

Table 4.3: Lensing features of gravitational lens modeling software. The type of lens models and algorithm used by each of the software packages is shown. Software in the upper portion of the table is considered 'Research' and that in the lower portion is considered 'Educational'.

4.6 Discussion

Most research using gravitational lens modeling software utilizes a single software package to model an observed lensing system. Results are then compared with observational data or other models from the literature. This is the first review to specifically examine strong gravitational lens modeling software. This information is of particular importance because there are no single standard programs used for modeling gravitational lenses.

Software Selection

There are a number of factors which are important when selecting appropriate software. Investigators wishing to develop their own may use existing software, especially if source code is provided, as a starting point for feature sets, data entry, etc. The computing platform may also be an important factor, although most of the research software reviewed here will run on a Linux system. Some of the software reviewed runs on a limited number of systems. The type of data used for input and the results provided are also important factors. Some of the programs

provide immediate display of output while others require another step, with other software, to display the results.

Software Comparisons

Comparisons of gravitational lens modeling software will be defined as *indirect comparisons* or *direct comparisons*. An indirect comparison is comparing results from various software, in different papers, modeling the same lensing system. This is relatively easy because the software is commonly tested using well-described lensing systems such as Cl0024+1654 (GRALE:[33]), SDSS J1004+4112 (glafic:[46], GRALE:[35] and PixeLens:[70]), and Abell1689 (Lenstool:[22], LensPerfect:[14], and PixeLens:[57]). Direct comparisons compare the models generated for a single lensing system using different software in the same publication. However, there are very few direct comparisons of software in the literature.

The modeling of Abell 1689 by PixeLens, LensPerfect and Lenstool has been compared qualitatively [14]. Lin and coworkers use Lensview to model a bright z=2 galaxy and then compared the results to another model made using Lenstool [38]. There is often no single ideal modeling software, as was illustrated in the study by Lin and colleagues who found that the Lensview model made it difficult to determine how well image positions alone are determined [38]. Further studies are needed to compare the ability of various software packages to model the same lensing system in order to enable meaningful comparisons. Understanding the underlying assumptions and limitations of the various software will be facilitated in the future by more direct comparison studies.

Future research in gravitational lens modeling will also require direct comparisons of the results of models using data from both strong and weak gravitational lensing analysis. Such analyses have already been reported for Abell1689 [14; 37].

The use of direct comparisons will enable better comparisons of software usability, feature sets as well as checking results against known software. Future studies in gravitational lens modeling will demand new approaches and sophistication.

4.7 Conclusions

There is a wide variety of gravitational lensing modeling software available. Many of the publications using these packages are written by the software developers, suggesting that the software is developed for their personal use. Software available only as executable files has the advantage of being rapidly usable, as long as the computing platform is available. Software distributed as source code may require significant time to compile and prepare given the vagaries of software libraries.

The comprehensiveness of this study is limited by the ability to identify existing software or studies related to the software reviewed. However, a fairly wide spectrum of software was available for review, and this analysis identifies opportunities for improvement based on existing software.

Awareness of available software may limit the need to develop proprietary software in the future. The source code is available for some applications which facilitates the development of custom software. Given the increased activity in gravitational lensing research, sharing of software and algorithms may result in significant time savings. The usability of available software is somewhat limited by the essentially consistent use of character based user interfaces. Future software should be modular in nature and use a graphical user interface for improved functionality.

Until recently, the construction of gravitational mass maps to detail dark matter distribution has depended on data from weak lensing. However, as shown in recent studies using LensPerfect, glafic and GRALE, accurate mass maps can be constructed using data from strong gravitational lensing data, and this may signal a new era in studies of strong gravitational lensing. New approaches to software development will be necessary to support this shift in research, especially with the advent of far more detailed images from the next generation of telescopes. Future studies should include direct comparisons with other available software in addition to indirect comparisons with previous studies of well-described lensing systems.

References

[1] A. B. Aazami and P. Natarajan. Substructure and the cusp and fold relations. *Mon Not Roy Astr Soc*, **372**:1692–1698, November 2006. 166, 167

[2] C. Alard. Perturbative reconstruction of a gravitational lens: when mass does not follow light. *Astr & Astrophys*, **506**:609–621, November 2009. 163

[3] F Alfaro. Keeton's interface. http://cinespa.ucr.ac.cr/software/xfgl/index.html, February 2008. 167, 187

[4] S. S. Allam, D. L. Tucker, H. Lin, H. T. Diehl, J. Annis, E. J. Buckley-Geer, and J. A. Frieman. The 8 O'Clock Arc: A Serendipitous Discovery of a Strongly Lensed Lyman Break Galaxy in the SDSS DR4 Imaging Data. *ApJ Lett*, **662**:L51–L54, June 2007. 166, 167

[5] AstroCode. Astro-code wiki webpage. http://www.astrosim.net/code/doku.php?id=home:code:lensing:strong, 2013. 163

[6] E Baltz. Glamroc web page. http://kipac.stanford.edu/collab/research/lensing/glamroc/, 2008. 165, 180

[7] A. Berciano Alba, M. A. Garrett, L. V. E. Koopmans, and O. Wucknitz. Highly-magnified, multiply-imaged radio counterparts of the sub-mm starburst emission in the cluster-lens MS0451.6-0305. *Astr & Astrophys*, **462**:903–911, February 2007. 166, 167

[8] E. Bertin and S. Arnouts. SExtractor: Software for source extraction. *Astr and Astrophysics*, **117**:393–404, June 1996. 162

[9] M Boughen. Software review. Sky and Telescope Magazine June 2000 p68, 2000. 165, 183

[10] B. J. Brewer and G. F. Lewis. When Darwin Met Einstein: Gravitational Lens Inversion with Genetic Algorithms. *Proc Am Soc Astr*, **22**:128–135, 2005. 163

[11] B. J. Brewer and G. F. Lewis. Strong Gravitational Lens Inversion: A Bayesian Approach. *ApJ*, **637**:608–619, February 2006. 163

[12] J Brownstein. Orphan lens project web page. http://admin.masterlens.org, 2014. 161

[13] D Coe. Lensperfect web page. http://www.its.caltech.edu/~coe/LensPerfect/download/, May 2012. 171

[14] D. Coe, N. Benítez, T. Broadhurst, and L. A. Moustakas. A High-resolution Mass Map of Galaxy Cluster Substructure: LensPerfect Analysis of A1689. *ApJ*, **723**:1678–1702, November 2010. 162, 171, 190

[15] D. Coe, E. Fuselier, N. Benítez, T. Broadhurst, B. Frye, and H. Ford. LensPerfect: Gravitational Lens Mass Map Reconstructions Yielding Exact Reproduction of All Multiple Images. *ApJ*, **681**:814–830, July 2008. 162, 165, 171

[16] J. D. Cohn, C. S. Kochanek, B. A. McLeod, and C. R. Keeton. Constraints on Galaxy Density Profiles from Strong Gravitational Lensing: The Case of B1933+503. *ApJ*, **554**:1216–1226, June 2001. 166, 167

[17] J. P. Coles, J. I. Read, and P. Saha. Gravitational lens recovery with GLASS: measuring the mass profile and shape of a lens. *Mon Not Roy Astr Soc*, **445**:2181–2197, December 2014. 165, 180

[18] J. M. Diego, P. Protopapas, H. B. Sandvik, and M. Tegmark. Non-parametric inversion of strong lensing systems. *Mon Not Roy Astr Soc*, **360**:477–491, June 2005. 165, 181

[19] F. Frutos-Alfaro. A Computer Program to Visualize Gravitational Lenses. *ArXiv Astrophysics e-prints*, April 2002. 165, 187

[20] A. Halkola, H. Hildebrandt, T. Schrabback, M. Lombardi, M. Bradač, T. Erben, P. Schneider, and D. Wuttke. The mass distribution of RX J1347-1145 from strong lensing. *Astro Astrophys*, **481**:65–77, April 2008. 165, 182

[21] N Jackson. Igloo web page. http://www.jb.man.ac.uk/research/gravlens/igloo/idoc.pdf, July 2004. 165, 180

[22] E. Jullo and J.-P. Kneib. Multiscale cluster lens mass mapping - I. Strong lensing modelling. *Mon Not Roy Astr Soc*, **395**:1319–1332, May 2009. 169, 170, 190

[23] E. Jullo, J.-P. Kneib, M. Limousin, Á. Elíasdóttir, P. J. Marshall, and T. Verdugo. A Bayesian approach to strong lensing modelling of galaxy clusters. *New Journal of Physics*, **9**:447, December 2007. 162, 163, 165, 169, 170

[24] C Keeton. Software for gravitational lensing. http://redfive.rutgers.edu/~keeton/gravlens/, January 2004. 166

[25] C. R. Keeton. A Catalog of Mass Models for Gravitational Lensing. *ArXiv Astrophysics e-prints*, February 2001. 166, 167

[26] C. R. Keeton. Computational Methods for Gravitational Lensing. *ArXiv Astrophysics e-prints*, February 2001. 165, 166

[27] J-P Kneib. Lenstool project web page. http://lamwws.oamp.fr/lenstool/, May 2012. 169

[28] J.-P. Kneib, R. S. Ellis, I. Smail, W. J. Couch, and R. M. Sharples. Hubble Space Telescope Observations of the Lensing Cluster Abell 2218. *ApJ*, **471**:643, November 1996. 169

[29] A. Knudson, K. U. Ratnatunga, and R. E. Griffiths. Investigation of Gravitational Lens Mass Models. *AJ*, **122**:103–112, July 2001. 169

[30] A. T. Lefor, T. Futamase, and M. Akhlaghi. A Systematic Review of Strong Gravitational Lens Modeling Software. *ArXiv e-prints*, June 2012. 161

[31] J. Liesenborgs, S. De Rijcke, and H. Dejonghe. A genetic algorithm for the non-parametric inversion of strong lensing systems. *Mon Not Roy Astr Soc*, **367**:1209–1216, April 2006. 163, 165, 178

[32] J. Liesenborgs, S. de Rijcke, H. Dejonghe, and P. Bekaert. Non-parametric inversion of gravitational lensing systems with few images using a multi-objective genetic algorithm. *Mon Not Roy Astr Soc*, **380**:1729–1736, October 2007. 178

[33] J. Liesenborgs, S. de Rijcke, H. Dejonghe, and P. Bekaert. Non-parametric strong lens inversion of Cl 0024+1654: illustrating the monopole degeneracy. *Mon Not Roy Astr Soc*, **389**:415–422, September 2008. 178, 190

[34] J. Liesenborgs, S. de Rijcke, H. Dejonghe, and P. Bekaert. The search for dark matter via strong lens inversions of galaxy clusters using genetic algorithms. In *Proceedings of Science*, 2008. 178

[35] J. Liesenborgs, S. de Rijcke, H. Dejonghe, and P. Bekaert. Non-parametric strong lens inversion of SDSS J1004+4112. *Mon Not Roy Astr Soc*, **397**:341–349, July 2009. 178, 190

[36] Jori Liesenborgs. *Genetic algorithms for the non-parametric inversion of gravitational lenses*. PhD thesis, Unversiteit Hasselt, 2009. 163

[37] M. Limousin, J. Richard, E. Jullo, J.-P. Kneib, B. Fort, G. Soucail, Á. Elíasdóttir, P. Natarajan, R. S. Ellis, I. Smail, O. Czoske, G. P. Smith, P. Hudelot, S. Bardeau, H. Ebeling, E. Egami, and K. K. Knudsen. Combining Strong and Weak Gravitational Lensing in Abell 1689. *ApJ*, **668**:643–666, October 2007. 169, 170, 190

[38] H. Lin, E. Buckley-Geer, S. S. Allam, D. L. Tucker, H. T. Diehl, D. Kubik, J. M. Kubo, J. Annis, J. A. Frieman, M. Oguri, and N. Inada. Discovery of a Very Bright, Strongly Lensed z = 2 Galaxy in the SDSS DR5. *ApJ*, **699**:1242–1251, July 2009. 166, 167, 169, 190

[39] M McCourt. Lenstool for dummies. http://www.oamp.fr/cosmology/lenstool/, October 2006. 169

[40] M Meneghetti. Introduction to gravitational lensing. http://pico.bo.astro.it/~massimo/pico/Teaching.html, May 2012. 163

[41] J Merten. An advanced method to recover the mass distribution of galaxy clusters. http://www.mpia.de/imprs-hd/theses/thesis_merten.pdf, 2009. 165, 182

[42] J. Merten, M. Cacciato, M. Meneghetti, C. Mignone, and M. Bartelmann. Combining weak and strong cluster lensing: applications to simulations and MS 2137. *Ast Astrophys*, **500**:681–691, June 2009. 165, 182

[43] G. Meylan, P. Jetzer, P. North, P. Schneider, C. S. Kochanek, and J. Wambsganss, editors. *Gravitational Lensing: Strong, Weak and Micro*, 2006. 163

[44] MOWGLI. Moewgli web page. http://www.ephysics.org/mowgli/, May 2012. 165

[45] P Newbury. Inverting gravitational lenses. Society for industrial and applied mathematics March 2002, 2002. 165, 186

[46] M. Oguri. The Mass Distribution of SDSS J1004+4112 Revisited. *Proc Astr Soc Japan*, **62**:1017–, August 2010. 165, 173, 190

[47] M. Oguri, N. Inada, C. R. Keeton, B. Pindor, J. F. Hennawi, M. D. Gregg, R. H. Becker, K. Chiu, W. Zheng, S.-I. Ichikawa, Y. Suto, E. L. Turner, J. Annis, N. A. Bahcall, J. Brinkmann, F. J. Castander, D. J. Eisenstein, J. A. Frieman, T. Goto, J. E. Gunn, D. E. Johnston, S. M. Kent, R. C. Nichol, G. T. Richards, H.-W. Rix, D. P. Schneider, E. S. Sheldon, and A. S. Szalay. Observations and Theoretical Implications of the Large-Separation Lensed Quasar SDSS J1004+4112. *ApJ*, **605**:78–97, April 2004. 178

[48] L Ondra. Wfpc2 hst gravitational lens image creator. http://virtual-universe.org/ego_cgi.html, 2001. 165, 187

[49] G. Orban de Xivry and P. Marshall. An atlas of predicted exotic gravitational lenses. *Mon Not Royal Astr Soc*, **399**:2–20, October 2009. 180

[50] C. Y. Peng, L. C. Ho, C. D. Impey, and H.-W. Rix. Detailed Decomposition of Galaxy Images. II. Beyond Axisymmetric Models. *AJ*, **139**:2097–2129, June 2010. 162

[51] K. Ratnatunga. Gravitational lenser 1.3. http://leo.astronomy.cz/grlens/grl0.html, 2000. 165, 187

[52] J. Richard, L. Pei, M. Limousin, E. Jullo, and J. P. Kneib. Keck spectroscopic survey of strongly lensed galaxies in Abell 1703: further evidence of a relaxed, unimodal cluster. *Astr & Astrophys*, **498**:37–47, April 2009. 169, 170

[53] J. Richard, D. P. Stark, R. S. Ellis, M. R. George, E. Egami, J.-P. Kneib, and G. P. Smith. A Hubble and Spitzer Space Telescope Survey for Gravitationally Lensed Galaxies: Further Evidence for a Significant Population of Low-Luminosity Galaxies beyond z=7. *ApJ*, **685**:705–724, October 2008. 169

[54] A. Rogers and J. D. Fiege. Strong Gravitational Lens Modeling with Spatially Variant Point-spread Functions. *Astrophys J*, **743**:68, December 2011. 165, 181

[55] E Rykoff. Gravlens web page. http://sites.google.com/site/erykoff/, May 2012. 165, 183

[56] P. Saha, J. Coles, A. V. Macciò, and L. L. R. Williams. The Hubble Time Inferred from 10 Time Delay Lenses. *ApJ Lett*, **650**:L17–L20, October 2006. 175

[57] P. Saha, J. I. Read, and L. L. R. Williams. Two Strong-Lensing Clusters Confront Universal Dark Matter Profiles. *ApJ Lett*, **652**:L5–L8, November 2006. 165, 175, 190

[58] P. Saha and L. L. R. Williams. Qualitative Theory for Lensed QSOs. *AJ*, **125**:2769–2782, June 2003. 162, 165, 177

[59] M. Sancho. Gravitational lensing model. http://www.opensourcephysics.org/items/detail.cfm?ID=11451, 2014. 165, 188

[60] R. J. Smith, J. P. Blakeslee, J. R. Lucey, and J. Tonry. Discovery of Strong Lensing by an Elliptical Galaxy at z = 0.0345. *ApJ Lett*, **625**:L103–L106, June 2005. 166, 167

[61] S. H. Suyu and A. Halkola. The halos of satellite galaxies: the companion of the massive elliptical lens SL2S J08544-0121. *Astr Astrophys*, **524**:A94, December 2010. 165, 182

[62] S. H. Suyu, P. J. Marshall, M. P. Hobson, and R. D. Blandford. A bayesian analysis of regularized source inversions in gravitational lensing. *Monthly Notices of the Royal Astronomical Society*, **371**[2]:983–998, 2006. 163

[63] W Vandenbroucke. Gravitational lensing web page. http://www.kwakkelflap.com/gravlens.html, May 2012. 165

[64] P Veenstra. Dosbox software website. http://www.dosbox.com, June 2012. 183

[65] S. Wallington, C. S. Kochanek, and R. Narayan. LensMEM: A Gravitational Lens Inversion Algorithm Using the Maximum Entropy Method. *ApJ*, **465**:64, July 1996. 163, 168

[66] S. J. Warren and S. Dye. Semilinear Gravitational Lens Inversion. *ApJ*, **590**:673–682, June 2003. 163

[67] R. Wayth. Lensview web page. https://www.cfa.harvard.edu/~rwayth/lensview, May 2012. 165, 168

[68] R. B. Wayth, S. J. Warren, G. F. Lewis, and P. C. Hewett. The lens and source of the optical Einstein ring gravitational lens ER 0047-2808. *Mon Not Roy Astr Soc*, **360**:1333–1344, July 2005. 168

[69] R. B. Wayth and R. L. Webster. LENSVIEW: software for modelling resolved gravitational lens images. *Mon Not Roy Astr Soc*, **372**:1187–1207, November 2006. 163, 168, 169

[70] L. L. R. Williams and P. Saha. Models of the Giant Quadruple Quasar SDSS J1004+4112. *AJ*, **128**:2631–2641, December 2004. 165, 175, 190

[71] A. Zitrin, T. Broadhurst, K. Umetsu, D. Coe, N. Benítez, B. Ascaso, L. Bradley, H. Ford, J. Jee, E. Medezinski, Y. Rephaeli, and W. Zheng. New multiply-lensed galaxies identified in ACS/NIC3 observations of Cl0024+1654 using an improved mass model. *Mon Not Roy Astr Soc*, **396**:1985–2002, July 2009. 165, 181

Chapter 5

Time delay and mass calculations are sensitive to changes in redshift and are model dependent

5.1 Purpose and Organization of this Chapter

The purpose of this chapter is to conduct a direct comparison of strong gravitational lens models [1]. In particular we wanted to compare the results of four different strong gravitational lens model software packages in the calculations of time delay and mass for two different systems. The models were as identical as possible, and used as input to each of the software packages evaluated. The purpose of this portion of the study was to determine how variable the results are for two commonly evaluated parameters, time delay and mass.

This chapter is organized as follows. In section §5.3 we review the models used for the two systems studied and the selection of redshift values tested, including a mock model and the model for SDSSJ1004+4112. In section §5.4 we present the results for the calculation of time delay and mass for each of the two model systems used, calculated by each of the four strong gravitational lensing codes selected in this study, at nine different geometries. A summary of data comparing changes in each parameter to changes in $D_{\rm d}D_{\rm s}/D_{\rm ds}$ at each geometry tested is also presented. In section §5.5 the nomenclature for lens model comparisons is defined, and a review of existing comparative studies conducted. The results of the direct comparisons in this study are discussed. In section §5.6 we make suggestions for the next generation of software to support future gravitational lens research based on this study.

5.2 Introduction

The present is referred to as the "Golden Age" of Precision Cosmology [6]. Strong gravitational lensing data is a rich source of information about the structure and dynamics of the universe, and these data are contributing significantly to this notion of precision cosmology. Strong lensing is becoming a powerful tool to investigate three major issues in astrophysics: understanding

[1] Portions of this chapter were published in *Lefor AT and Futamase T. Comparison of strong gravitational lens model software I. Redshift and model dependence of time delay and mass calculations. Astronomy and Computing 2014. 6:28-40* [20]. doi:10.1016/j.ascom.2014.04.006. Permission to use this published material granted by the Publisher, License 3571220329348

the spatial distribution of mass, determining the overall geometry, content and kinematics of the universe, and studying distant galaxies, black holes and galactic nuclei that are otherwise too faint to study with current instrumentation [46]. The use of time delays calculated from gravitational lens systems has been used for some time to obtain cosmological constraints [e.g. 7; 10; 39; 44]. Data from strong gravitational lensing has also been used to establish the value of H_0 [e.g. 27; 42; 43], and is being combined with other datasets to obtain other cosmological constraints such as Ω_m and w_x [e.g. 16]. More recently, strong gravitational lensing data is being used to evaluate the gas phase metallicity of lensed galaxies [1], as a probe of the particle nature of gravity and dark matter [19; 30], and as a test of scalar-tensor gravity [32]. Future strong gravitational lensing studies promise to further expand our understanding of the physics of the universe. A comprehensive database of 646 strong gravitational lens systems (accessed 23 Feb 2014) is maintained and provides extensive information about each of these systems [29]. Further understanding of the systematic errors in strong gravitational lens modeling, beginning with the software, is essential as more lens systems are identified.

Comparison of strong gravitational lens models

Strong gravitational lens models allow determination of the value of various cosmological constraints. However, data analysis is complicated by the various types of models used as well as the many different software codes that have been used [21]. The strong gravitational lens modeling codes in use are not necessarily mutually exclusive, and there is no one software package that appears to be ideal.

While the use of strong gravitational lens models as a probe of the fundamental features of the universe continues to increase, most studies to date utilize a single model analyzed with a single software code to understand a particular system. Each model consists of one or more files, usually text files, as input to the modeling software that encode the characteristics of the lensing system. There are number of barriers to greater use of multiple codes in a single study, including the complexity of each model as well as the fact that the model used for each code is often very different from that used for other codes. There are very few existing studies which compare the results of analysis of one system using multiple software codes.

Effect of changes in the model on results

There are many differences among the software codes used for strong gravitational lens models, which perhaps start with their initial classification, as parametric and non-parametric. While this classification is commonly used, it is actually somewhat of a misnomer since all models use parameters. More recently, parametric models are usually referred to as "Light Traces Mass" (LTM), and non-parametric models are referred to as "Non-Light Traces Mass" (Non-LTM) [3]. However, each of the codes can behave in a different way, which may lead to different results. The redshift of the lens and the source are critically important starting points for any lens model, but there have been few studies to determine the effect of changes in these important parameters on the final results of a lens model.

Purpose of this study

The purpose of this study is to investigate the effect of changes in system geometry, specifically the effect of varying redshift, on the value of time delay and mass as calculated by four different strong gravitational lens modeling codes. Although spectroscopic redshifts are becoming more available, there may be systems for which preliminary investigations necessitate the use of photometric redshifts. If the results of lens model calculations show little change with small

changes in redshift, the results of lens model calculations using photometric redshifts may be more useful.

Changes in redshift used in this study are based on the results in [5], which estimate the errors in photometric redshifts to be:

$$\Delta z_{lens} \sim 0.04(1 + z_{lens}) \tag{5.1}$$

$$\Delta z_{source} \sim 0.10(1 + z_{source}) \tag{5.2}$$

These studies are performed to understand how each software code behaves under the conditions of changing values of redshift, and compare those changes to changes in $D_{\rm d}D_{\rm s}/D_{\rm ds}$ at the same redshift values, tin order to understand the variability in results using different lens model software. A review of existing comparative strong gravitational lens studies is included to define the current state of comparative studies and define nomenclature for future studies.

5.3 Methods

Software

Models for each system are evaluated using two LTM lens model codes, Lenstool (version 6.7.1) [18](Lenstool actually has both LTM and non-LTM components [3])and glafic (version 1.1.6) [34], as well as two non-LTM codes, GRALE (version 0.12.1) [22] and PixeLens (version 2.17) [38]. The software in this study was obtained by download from public web sites. Input files for SDSSJ1004+4112 for Lenstool, and input files for all four software packages for the mock model were written for this study. The GRALE model of SDSSJ1004+4122 was used in a previous study by [24]. The glafic files were previously used in a study by [35], and the PixeLens model was previously used by [49]. For the purpose of the models in this study, Ω_m is set to 0.24, and Ω_Λ set to 0.76, h=0.70, with a flat universe (Ω_k=0) [e.g. 33; 45] and $H_0 = 100h\,\mathrm{km\,s^{-1}Mpc^{-1}}$. All models are run on an Intel (Santa Clara, CA) processor using Scientific Linux version 6.4.

Lens models

Two different systems are investigated with each of four strong lens modeling codes, including a simple four-image mock model, and the giant gravitational quasar SDSSJ1004+4112. For each model, time delays and enclosed mass are calculated. The time delays are calculated as the difference in arrival time of the images. PixeLens directly calculates the time delays for each image and the enclosed mass. The time delays for each image and the mass enclosed within the Einstein radius is directly calculated by glafic and GRALE. Lenstool calculates the time delays for each image, and produces a mass map as a FITS file from which the mass inside the Einstein radius is obtained.

The mock model includes one potential, as a Singular Isothermal Ellipsoid (SIE) located at the center (0.0, 0.0). Also at the center (0.0, 0.0) is a single point source. The SIE has a velocity dispersion of 300 km s^{-1} and an ellipticity of 0.5 with a position angle of 0. Four images are located equidistant from the center at 1.3". All models are similarly parameterized.

The models for SDSSJ1004+4112 modeled with Pixelens [49], glafic [35] and GRALE [24] were used unchanged from the published studies. Details of the parameterization of each model are available in the original studies. The model for Lenstool was prepared for this study, and follows the parameterization used in the glafic model. Time delays and enclosed mass within the Einstein radii are calculated and compared as percent change from the values obtained with

the actual lens system, $z_{lens} = 0.68$ and $z_{source} = 1.734$. The z_{source} for the source located at z=1.734 was varied, while the redshifts for the other sources were not changed. Time delays of the images from that source were compared.

Varying lens system parameters

After creating the model files for the two systems they are used as input to PixeLens, GRALE, Lenstool, and glafic. Lens system geometry, specifically z_{lens} and z_{source}, is varied by directly editing the input files and the models re-calculated. The geometry of the mock model is set at z_{lens}=0.3, and z_{source}=2.5 as initial (baseline) redshift values. The value of z_{lens} and z_{source} are each varied through a range of four values (according to Equations 1 and 2 as described by [5], and based on the extrapolation of empirical findings [33]), resulting in five models at z_{lens}=0.3 while varying z_{source}, and five models at z_{source}=2.5 while varying z_{lens}. Similarly, the SDSSJ1004+4112 model was varied, with a total of five models at z_{lens}=0.68 while varying z_{source}, and five models at z_{source}=1.734 while varying z_{lens}. A total of nine models (baseline plus four varying z_{lens} and four varying z_{source}) are calculated using each of the four modeling software packages in the study, to evaluate the mock model (Tables 5.1-5.4) and the SDSSJ1004+4112 model (Tables 5.5-5.8). The purpose of using these nine models is to "stress"' the software to observe the effect of changes in redshift on output parameters.

Throughout this study, efforts were made to parameterize all models similarly. In each of the comparison calculations, the only parameter altered was the z_{lens} or z_{source}, depending on the portion of the study. In all cases, source position, velocity dispersion, ellipticity, etc. were left unchanged in all of the calculations.

Distance Calculations

Distance calculations were made using redshift values according to the methods described in [12]. This includes distances to the lens, $D_{\rm d}$, distance to the source, $D_{\rm s}$ and distance from the source to the lens, $D_{\rm ds}$. The Hubble distance ($D_{\rm H}$) is defined by:

$$D_{\rm H} \equiv \frac{c}{H_0} = 3000\,h^{-1}\ {\rm Mpc} = 9.26 \times 10^{25}\,h^{-1}\ {\rm m} \tag{5.3}$$

In order to define the comoving distance, $D_{\rm C}$, the function:

$$E(z) \equiv \sqrt{\Omega_{\rm M}\,(1+z)^3 + \Omega_k\,(1+z)^2 + \Omega_\Lambda} \tag{5.4}$$

is defined. The line-of-sight comoving distance, $D_{\rm C}$, is then given by integration:

$$D_{\rm C} = D_{\rm H} \int_0^z \frac{dz'}{E(z')} \tag{5.5}$$

where $D_{\rm H}$ is the Hubble distance.

Since Ω_k=0 in this study, the transverse comoving distance, $D_{\rm M}$ is the same as $D_{\rm C}$. The angular diameter distance, $D_{\rm A}$ is related to the transverse comoving distance, $D_{\rm M}$ by:

$$D_{\rm A} = \frac{D_{\rm M}}{1+z} \tag{5.6}$$

Therefore, the distance between two objects ($D_{\rm ds}$) such as the lens ($D_{\rm d}$) and source($D_{\rm s}$), with $\Omega_k \geq 0$ is given by:

$$D_{\rm A12} = \frac{1}{1+z_2}\left[D_{\rm M2}\sqrt{1+\Omega_k\frac{D_{\rm M1}^2}{D_{\rm H}^2}} - D_{\rm M1}\sqrt{1+\Omega_k\frac{D_{\rm M2}^2}{D_{\rm H}^2}}\right] \tag{5.7}$$

where D_{M1} and D_{M2} are the transverse comoving distances to z_1 and z_2, D_H is the Hubble distance, and Ω_k is the curvature density parameter. This calculation is significantly simplified in this study with Ω_k=0.

Time Delay Calculations

Time delays are calculated for each of the two models using each of the four lens modeling software packages tested, to evaluate the effect of a change in system geometry on the calculated parameters. The mathematical basis of gravitational lensing is the lens equation, and is described by [31]. The reduced deflection angle α and the actual deflection angle $\hat{\alpha}$ are related by eq. (5.8).

$$\vec{\alpha} = \frac{D_{ds}}{D_s}\,\vec{\hat{\alpha}}\ . \tag{5.8}$$

The angle between the optic axis and the true source position is defined as $\vec{\beta}$, and the angle between the optic axis and the image is defined as $\vec{\theta}$ [31]. Since $\theta D_s = \beta D_s - \hat{\alpha} D_{ds}$, the positions of the source and the image are given by

$$\vec{\beta} = \vec{\theta} - \vec{\alpha}(\vec{\theta})\ . \tag{5.9}$$

This equation shows that the deflection is dependent on the ratio D_{ds}/D_s, and is generally referred to as the lensing equation. If we consider a lens with a constant surface-mass density. The (reduced) deflection angle is then:

$$\alpha(\theta) = \frac{D_{ds}}{D_s}\,\frac{4G}{c^2\xi}\,(\Sigma\pi\xi^2) = \frac{4\pi G\,\Sigma}{c^2}\,\frac{D_d D_{ds}}{D_s}\,\theta\ , \tag{5.10}$$

where $\xi = D_d\theta$. In this case, the lens equation is linear, meaning that $\beta \propto \theta$. We then define a critical surface-mass density

$$\Sigma_{cr} = \frac{c^2}{4\pi G}\,\frac{D_s}{D_d D_{ds}} = 0.35\,\mathrm{g\,cm^{-2}}\left(\frac{D}{1\,\mathrm{Gpc}}\right)^{-1}\ , \tag{5.11}$$

where the effective distance D is defined as the combination of distances

$$D = \frac{D_d D_{ds}}{D_s}\ . \tag{5.12}$$

For a lens with a constant surface mass density Σ_{cr}, the deflection angle is $\alpha(\theta) = \theta$, and so $\beta = 0$ for all θ.

A complete equation to calculate time delays involves unobservable quantities [33], indicating that time delays in general depend on the details of mass models. The time delay is related by [50]:

$$\Delta t_{ij} \propto \frac{D_d D_s}{D_{ds}} \tag{5.13}$$

for a given value of z_{lens}. Thus, the relationship between D_d, D_s and D_{ds} should determine the behavior of a time delay calculation when the system geometry is altered. Based on this relationship, the percent change in D_d, D_s and D_{ds} for each of the redshifts in this study is also calculated and used as a basis of comparison of the changes in results calculated for each of the models.

Mass calculations

Each of the modeling software codes tested also calculates the mass of the lens. The relative projected mass density is determined by [18]:

$$\kappa(\xi^I, z^s) = \frac{\nabla^2\varphi(\xi^I, z^s)}{2} = \frac{\Sigma(\xi^I, z^s)}{\Sigma_{crit}} \tag{5.14}$$

The critical density is defined by:

$$\Sigma_{crit}(z^s, z^d) = \frac{c^2}{4\pi G}\frac{D_{\rm s}}{D_{\rm ds}D_{\rm d}} \tag{5.15}$$

The Newtonian projected potential is given by ϕ, and the lens-normalized projected potential is given by φ. The absolute projected mass density is then:

$$\Sigma(\xi^I) = \Sigma_{crit}\frac{\nabla^2\varphi}{2} = \frac{\nabla^2\phi(\xi^I)}{4\pi G} \tag{5.16}$$

Since this value is absolute, it does not depend on z_{source}.

The mass inside the Einstein radius (M($<R_E$)) for a Singular Isothermal Sphere is given by [51]:

$$M(<R_E) = R_E^2\frac{D}{8\pi G} \tag{5.17}$$

This relationship shows that the mass inside the Einstein radius is mostly dependent on the value of the Einstein radius.

Data Analysis and Presentation

The calculated values for time delay and enclosed mass are shown in Tables 5.1-5.4 (mock model) and Tables 5.5-5.8 (SDSSJ1004+4112). However, due to differences in the models, it is difficult to compare the absolute values calculated. Furthermore, the goal of this analysis was to observe the effects of changing geometry on changes in the calculated parameters. Therefore, the percent change in each value at each geometry is calculated compared to the values at the baseline geometry for each system. Based on the relationship between time delay and $D_{\rm d}D_{\rm s}/D_{\rm ds}$, the percent change in $D_{\rm d}D_{\rm s}/D_{\rm ds}$ at each redshift is also calculated and used as a basis of comparison of the changes in results calculated for each of the models. If time delay is related to $D_{\rm d}D_{\rm s}/D_{\rm ds}$ by a simple proportion, then the percent change in time delay should change similarly with the percent change in $D_{\rm d}D_{\rm s}/D_{\rm ds}$ at each geometry. The percent change in each calculated value is plotted with the percent change in $D_{\rm d}D_{\rm s}/D_{\rm ds}$ in Figures 5.1-5.4 (mock model) and Figures 5.5-5.8 (SDSSJ1004+4112).

5.4 Results

Mock Model

A mock model is used with a single lens potential as a SIE at z_{lens}=0.3 and z_{source}=2.5. This model generates four equidistant images. Since this is mock data, the same model is used as input for all four software codes evaluated, and is thus a direct, semi-independent lensing comparison. The results from all four codes tested are shown, at each of the nine geometries evaluated, with the values for time delay and mass, in Tables 5.1-5.4. For comparison, the values of $D_{\rm d}D_{\rm s}/D_{\rm ds}$ are shown at each geometry investigated. The differences in arrival times,

time delays, are shown for images 2, 3 and 4 as TD2, TD3 and TD4, respectively, relative to image 1, as calculated by each of the software models. All time delays are shown in days.

In order to compare the effect of changes in redshift among the models tested against changes in $D_{\rm d}D_{\rm s}/D_{\rm ds}$, the values calculated for each parameter at each geometry are compared to the value using the baseline geometry and the percent change determined. The percent change in the values of $D_{\rm d}D_{\rm s}/D_{\rm ds}$ were also calculated, and shown on each graph. Figures 5.1 and 5.2 show the effect of changes in redshift on time delay calculations. The values for the time delay of images 2 and 4 are shown in all of the graphs. In both constant z_{lens} and z_{source} evaluations, there is considerable variability in the time delay calculations. The calculated values with each code are generally quite different from the changes in $D_{\rm d}D_{\rm s}/D_{\rm ds}$ alone, although the results with PixeLens and Lenstool with a fixed z_{lens}=0.30 follow the changes in $D_{\rm d}D_{\rm s}/D_{\rm ds}$ most closely at all geometries tested.

The summary of results for the mass calculations are shown in Figures 5.3 and 5.4 with constant z_{lens} and z_{source} respectively. In the studies with a constant z_{lens}=0.30 (Figure 5.3), PixeLens and Lenstool calculated a mass value that exactly follows true changes in $D_{\rm d}D_{\rm s}/D_{\rm ds}$, while GRALE which showed no change in the calculated mass value, and changes calculated by glafic were opposite in slope. Similarly, the calculations with geometries having a constant z_{source}=2.50 (Figure 5.4) show results that follow $D_{\rm d}D_{\rm s}/D_{\rm ds}$ closely, although the slope of the line for GRALE calculations is in the opposite direction. A review above in Section 5.3, shows that the critical mass density is directly proportional to the distances as shown in equation 5.15. However, the absolute projected mass-density shows no dependence on z_{source} as shown in equation 5.16 and likely explains the results in Figure 5.3.

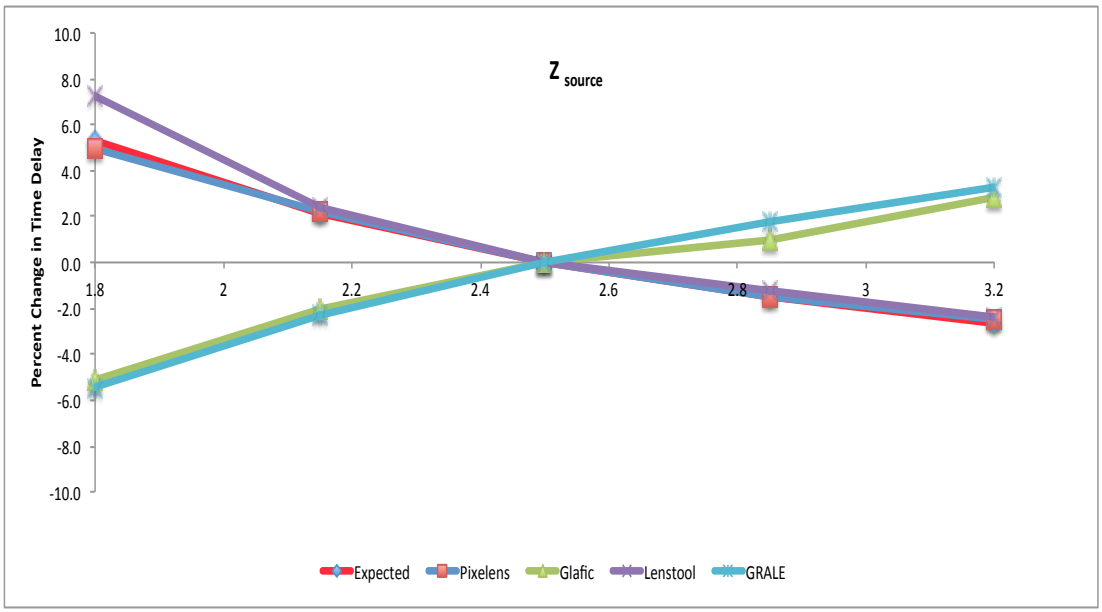

Figure 5.1: The effect of changes in redshift on percent change in time delay for the mock model with z_{lens}=0.30 and varying z_{source}. Expected shows changes in the value of $D_{\rm d}D_{\rm s}/D_{\rm ds}$ with the changes in redshift.

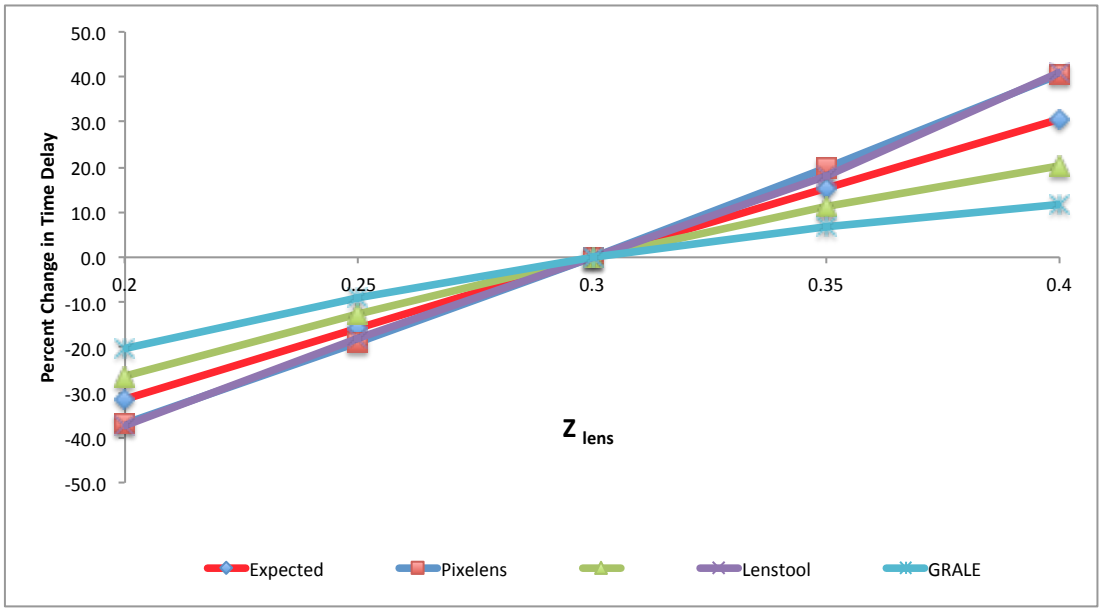

Figure 5.2: The effect of changes in redshift on percent change in time delay for the mock model with z_{source}=2.50 and varying z_{lens}. Expected shows changes in the value of $D_{\rm d}D_{\rm s}/D_{\rm ds}$ with the changes in redshift.

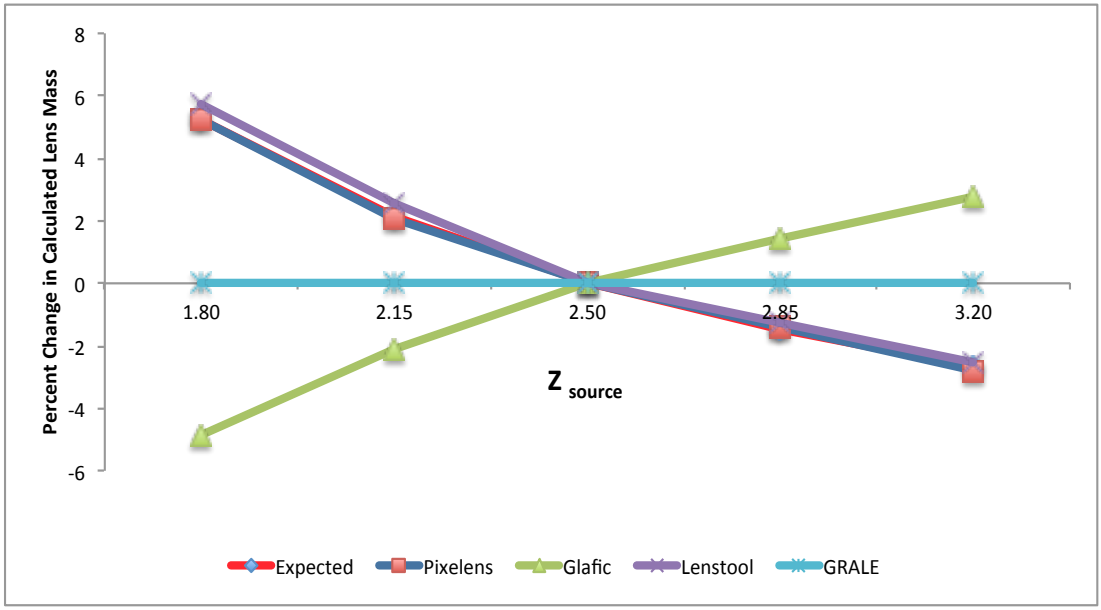

Figure 5.3: The effect of changes in redshift on percent change in calculated mass inside the Einstein radius (M($<R_E$)) for the mock model with z_{lens}=0.30 and varying z_{source}. Expected shows changes in the value of $D_{\rm d}D_{\rm s}/D_{\rm ds}$ with the changes in redshift.

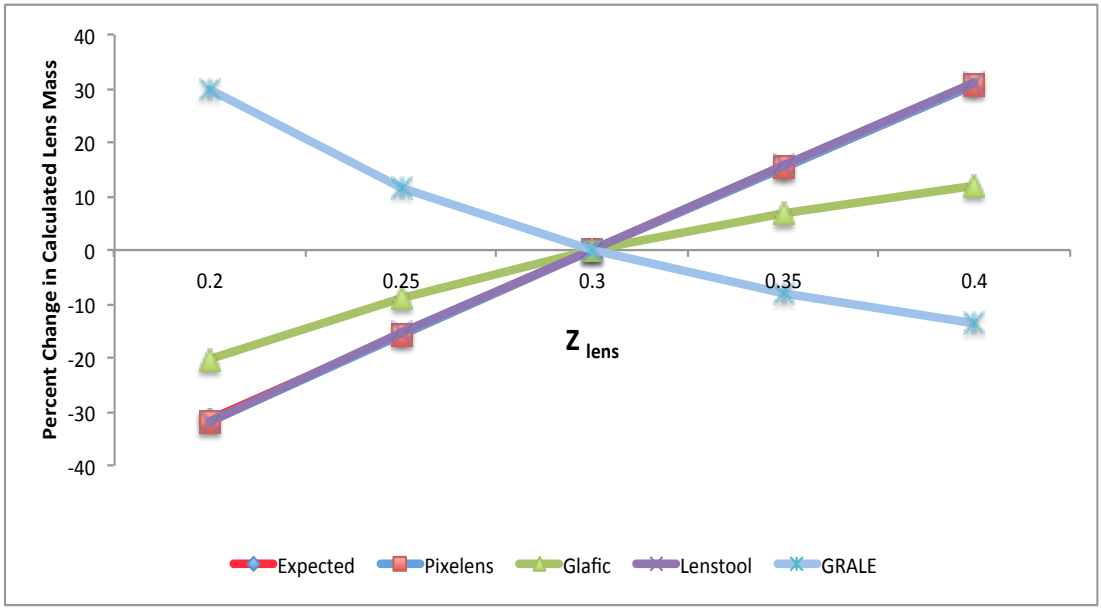

Figure 5.4: The effect of changes in redshift on percent change in calculated mass inside the Einstein radius (M($<R_E$)) for the mock model with z_{source}=2.50 and varying z_{lens}. Expected shows changes in the value of $D_{\rm d}D_{\rm s}/D_{\rm ds}$ with the changes in redshift.

PixeLens

PixeLens version 2.17 is used in this study [38]. PixLens is a non-LTM strong gravitational lens modeling code for solving lens inversions using a pixelated mass map. The program generates an ensemble of models, and the default of 100 models is used in this study. PixeLens was previously used in a study of SDSSJ1004+4112, and the model from that published study was used in the present study [49].

The results of the PixeLens analysis with the mock model are shown in Table 5.1. These results show very little change in any of the time delays for changes in z_{source}, while maintaining z_{lens} at z=0.3. The changes in time delays are similar to the proportional changes in z_{lens}, and the $D_{\rm d}D_{\rm s}/D_{\rm ds}$ is very similar in all of these models. However, similar proportional changes in z_{lens} result in significant changes in the time delays, while maintaining z_{source} at z=2.5. There were no changes in image positions for the PixeLens models. The changes in the time delays are greatest in geometries with the greatest changes in $D_{\rm d}D_{\rm s}/D_{\rm ds}$. The changes is $D_{\rm d}D_{\rm s}/D_{\rm ds}$ do not always predict changes in the time delays in this data, which is seen in Figure 5.2 comparing the curve for PixeLens with the expected curve.

z_{lens}	z_s	$D_{\rm d}D_{\rm s}/D_{\rm ds}$	TD_2	TD_3	TD_4	M($<R_E$)
0.30	1.80	1.218	4.21	0	4.21	3.02E11
0.30	2.15	1.182	4.10	0	4.10	2.93E11
0.30	2.50	1.157	4.01	0	4.01	2.87E11
0.30	2.85	1.140	3.92	0	3.92	2.83E11
0.30	3.20	1.126	3.91	0	3.91	2.79E11
0.20	2.50	0.792	2.53	0	2.53	1.96E11
0.25	2.50	0.976	3.25	0	3.25	2.42E11
0.30	2.50	1.157	4.01	0	4.01	2.87E11
0.35	2.50	1.336	4.80	0	4.80	3.31E11
0.40	2.50	1.514	5.64	0	5.64	3.75E11

Table 5.1: A mock model with four images modeled using PixeLens demonstrating the effect of changes in z_{lens} and z_{source} (z_s) on calculated parameters including time delay (TD, days) and mass enclosed in the Einstein radius (in $M_\odot$) (baseline system geometry highlighted in gray)

glafic

Glafic version 1.1.6 was used in these studies. Glafic is an LTM lens modeling code, and has been used extensively in previous studies. The mock model input files for glafic were written using a command file and a file with the image data for the geometry of the four images of the model. The lens was modeled as a SIE. The results for the mock model are shown in Table 5.2. The time delays for two of the four images have small absolute changes at the geometries investigated, including those with a large change in $D_{\rm d}D_{\rm s}/D_{\rm ds}$. The time delay calculations with glafic do not generally follow the changes in $D_{\rm d}D_{\rm s}/D_{\rm ds}$ for models where z_{lens} is held constant (Figure 5.1), but do generally follow the changes in $D_{\rm d}D_{\rm s}/D_{\rm ds}$ when z_{source} is constant (Figure 5.2). The positions of the images calculated by the glafic models change as the geometry of the lens system changes. The values of mass inside the Einstein radius do not closely follow the changes in $D_{\rm d}D_{\rm s}/D_{\rm ds}$ as shown in Figures 5.3 and 5.4.

z_{lens}	z_s	$D_{\rm d}D_{\rm s}/D_{\rm ds}$	TD_2	TD_3	TD_4	M($<R_E$)
0.30	1.80	1.218	36.7	0	36.7	4.09E11
0.30	2.15	1.182	37.9	0	37.9	4.21E11
0.30	2.50	1.157	38.7	0	38.7	4.30E11
0.30	2.85	1.140	39.3	0	39.3	4.36E11
0.30	3.20	1.126	39.8	0	39.8	4.42E11
0.20	2.50	0.792	28.5	0	28.5	3.43E11
0.25	2.50	0.976	33.9	0	33.9	3.91E11
0.30	2.50	1.157	38.7	0	38.7	4.30E11
0.35	2.50	1.336	43.0	0	43.0	4.59E11
0.40	2.50	1.514	46.6	0	46.6	4.81E11

Table 5.2: A mock model with four images modeled using glafic demonstrating the effect of changes in z_{lens} and z_{source} (z_s) on calculated parameters including time delays (TD, days) and mass enclosed in the Einstein radius (in $M_\odot$) (baseline system geometry highlighted in gray)

Lenstool

The Lenstool analysis of the mock model is performed using the same geometry used with the other modeling software in this study, and similarly parameterized as a SIE. Lenstool readily

provided time delay data for each of the images, which is shown in Table 5.3. These data show very little change in the time delays when z_{source} is varied, maintaining z_{lens} at z=0.3, and followed the changes in $D_{\rm d}D_{\rm s}/D_{\rm ds}$ very closely as shown in Figure 5.1. There were no changes in image positions for the Lenstool models. Lenstool showed greater variability from changes in $D_{\rm d}D_{\rm s}/D_{\rm ds}$ when the z_{source} was fixed as shown in Figure 5.2. Lenstool calculations of mass enclosed within the Einstein radius followed changes in $D_{\rm d}D_{\rm s}/D_{\rm ds}$ very closely for all models tested.

z_{lens}	z_s	$D_{\rm d}D_{\rm s}/D_{\rm ds}$	TD_2	TD_3	TD_4	M($<R_E$)
0.30	1.80	1.218	8.9	0	8.9	1.66E11
0.30	2.15	1.182	8.5	0	8.5	1.61E11
0.30	2.50	1.157	8.3	0	8.3	1.57E11
0.30	2.85	1.140	8.2	0	8.2	1.55E11
0.30	3.20	1.126	8.1	0	8.1	1.53E11
0.20	2.50	0.792	5.2	0	5.2	1.07E11
0.25	2.50	0.976	6.8	0	6.8	1.33E11
0.30	2.50	1.157	8.3	0	8.3	1.57E11
0.35	2.50	1.336	9.8	0	9.8	1.82E11
0.40	2.50	1.514	11.7	0	11.7	2.06E11

Table 5.3: A mock model with four images modeled using Lenstool demonstrating the effect of changes in z_{lens} and z_{source} (z_s) on the calculated time delays (TD, days) and mass enclosed within the Einstein radius (in $M_\odot$) (baseline geometry highlighted in gray)

GRALE

The GRALE analysis of the mock model is shown in Table 5.4. The GRALE model is a SIE, as in the other models. The time delay calculations with GRALE do not generally follow the changes in $D_{\rm d}D_{\rm s}/D_{\rm ds}$ for models where z_{lens} is held constant (Figure 5.1), but do generally follow the changes in $D_{\rm d}D_{\rm s}/D_{\rm ds}$ when z_{source} is constant (Figure 5.2), in a manner quite similar to the glafic models. The positions of the images calculated by the GRALE models change as the geometry of the lens system changes. There was no effect on changes in z_{source} on calculations of mass density as shown in Figure 5.3. Changes in mass density for changes in z_{lens} were opposite in slope to changes in $D_{\rm d}D_{\rm s}/D_{\rm ds}$ as shown in Figure 5.4 .

z_{lens}	z_s	$D_{\rm d}D_{\rm s}/D_{\rm ds}$	TD_2	TD_3	TD_4	M($<R_E$)
0.30	1.80	1.218	5.74	0	5.74	55.31
0.30	2.15	1.182	5.93	0	5.93	55.31
0.30	2.50	1.157	6.07	0	6.07	55.31
0.30	2.85	1.140	6.18	0	6.18	55.31
0.30	3.20	1.126	6.27	0	6.27	55.31
0.20	2.50	0.792	4.83	0	4.83	71.68
0.25	2.50	0.976	5.53	0	5.53	61.74
0.30	2.50	1.157	6.07	0	6.07	55.31
0.35	2.50	1.336	6.49	0	6.49	50.89
0.40	2.50	1.514	6.78	0	6.78	47.73

Table 5.4: A mock model with four images modeled using GRALE demonstrating the effect of changes in z_{lens} and z_{source} (z_s) on calculated parameters including time delays (TD, days), and total mass density as calculated by GRALE (baseline system geometry highlighted in gray)

Previous models of SDSSJ1004+4112

SDSSJ1004+4112 has been extensively studied and is therefore an excellent system for this comparative study [24; 35; 49]. The large gravitationally lensed quasar SDSSJ1004+4112 was first extensively described in 2003 as quadruple images separated by 14.62 arc seconds [15]. This is a particularly important finding, since the large separation between the components supported the idea that this object was dominated by dark matter. The four components had a consistent redshift of z=1.734. The lensing object was identified as an early type galaxy at a redshift of z=0.68. Spectroscopic follow-up observations and a mass modeling study of this system were then reported by Oguri [36]. The mass model was studied using Lensmodel , described by Keeton [17], and showed that a wide range of lens models are consistent with the data. The models also suggested significant substructure in the cluster and uncertainty in the time delays. A fifth image in this complex system was then reported in 2005 based on HST imaging [14]. The fifth image was then spectroscopically confirmed by Inada and colleagues [13]. Sharon and coworkers then reported multiply imaged galaxies at z=3.32 and z=2.74 which were spectroscopically confirmed as well as a third, unconfirmed galaxy [41]. Time delays for the system were evaluated with Lensmodel [11]. In 2010, Oguri and colleagues performed a complete analysis of the system using glafic [35], and include a summary of the previous models of this complex system. This system was also modeled using GRALE (non-LTM), and the model used in that study was used in the present work to evaluate GRALE [24].

Lens models of SDSS J1004+4112 in this study

The models for PixeLens, glafic and GRALE were all previously used in published studies and used in their original form. Thus, the analysis of SDSSJ1004+4112 is a direct, independent lensing comparison. Results at each geometry tested are shown for each of the four software codes tested, with calculated results for time delay and mass. Time delays are for the images in the original model at z_{lens}=1.734 (or at the varied geometry). All time delays are shown in days. Mass values shown are the mass within the Einstein radius for z_{lens}=1.734 (or at the varied geometry). For comparison, the calculated values of $D_{\rm d}D_{\rm s}/D_{\rm ds}$ are shown at each geometry investigated. In order to facilitate comparison between these models which are parameterized somewhat differently, the percent change in calculated values is compared.

The values calculated for each parameter at each geometry are compared to the values using the baseline geometry and the percent change determined. For comparison, the percent change in the values of $D_{\rm d}D_{\rm s}/D_{\rm ds}$ is also calculated, and shown on each graph. The results for time delay calculations are shown in Figures 5.5 and 5.6 at constant z_{lens} and z_{source}, respectively. The results for enclosed mass calculations with the SDSSJ1004+4112 models are shown in Figures 5.7 and 5.8 with constant z_{lens} and z_{source}, respectively.

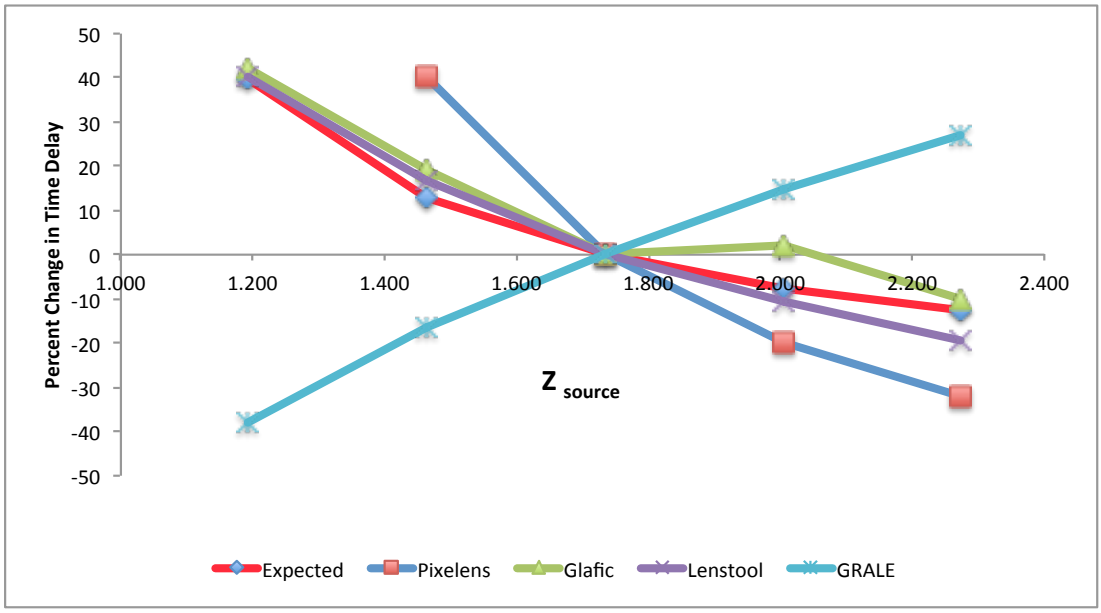

Figure 5.5: The effect of changes in redshift on calculated time delays for SDSSJ1004 with z_{lens}=0.68 and varying z_{source}. Expected shows changes in the value of $D_{\rm d}D_{\rm s}/D_{\rm ds}$ with the changes in redshift.

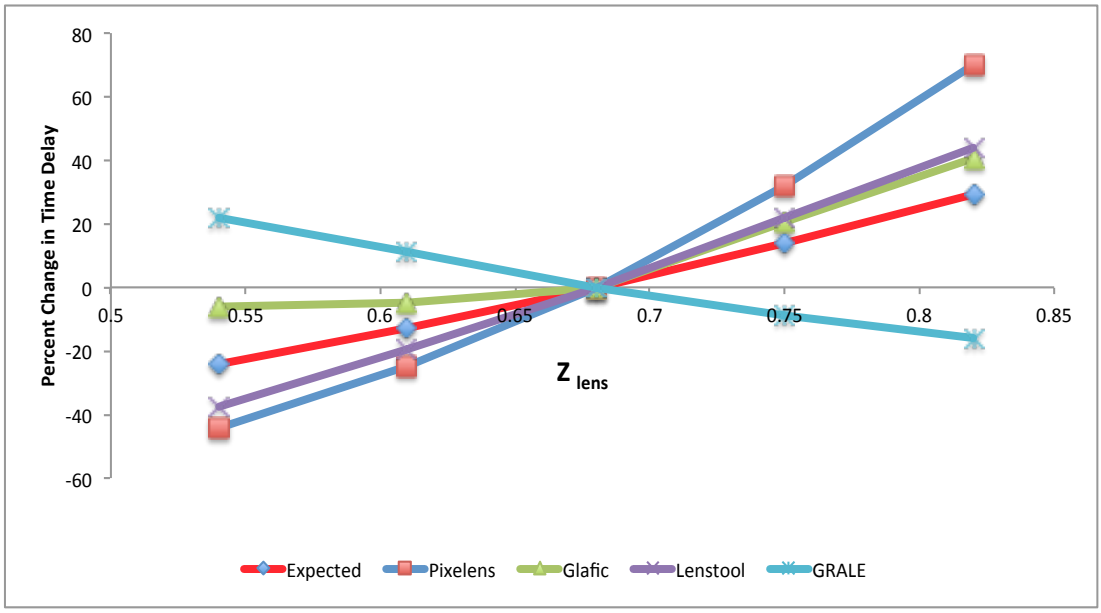

Figure 5.6: The effect of changes in redshift on calculated time delays for SDSSJ1004 with z_{source}=1.734 and varying z_{lens}. Expected shows changes in the value of $D_{\rm d}D_{\rm s}/D_{\rm ds}$ with the changes in redshift.

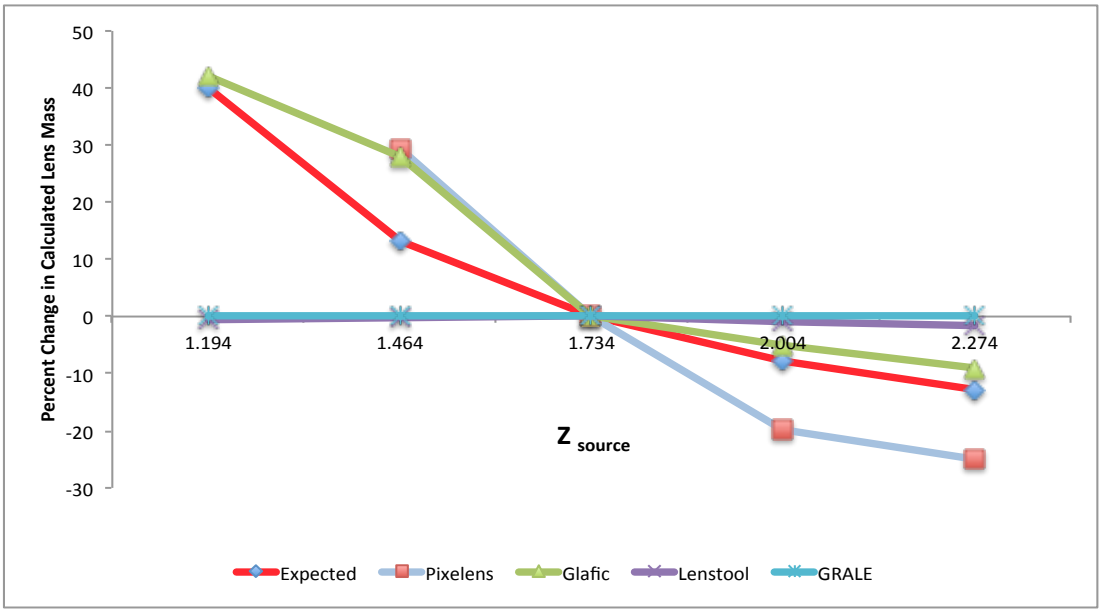

Figure 5.7: The effect of changes in redshift on percent change in calculated mass inside the Einstein radius (M($<R_E$)) for SDSSJ1004 with z_{lens}=0.68 and varying z_{source}. Expected shows changes in the value of $D_{\rm d}D_{\rm s}/D_{\rm ds}$ with the changes in redshift.

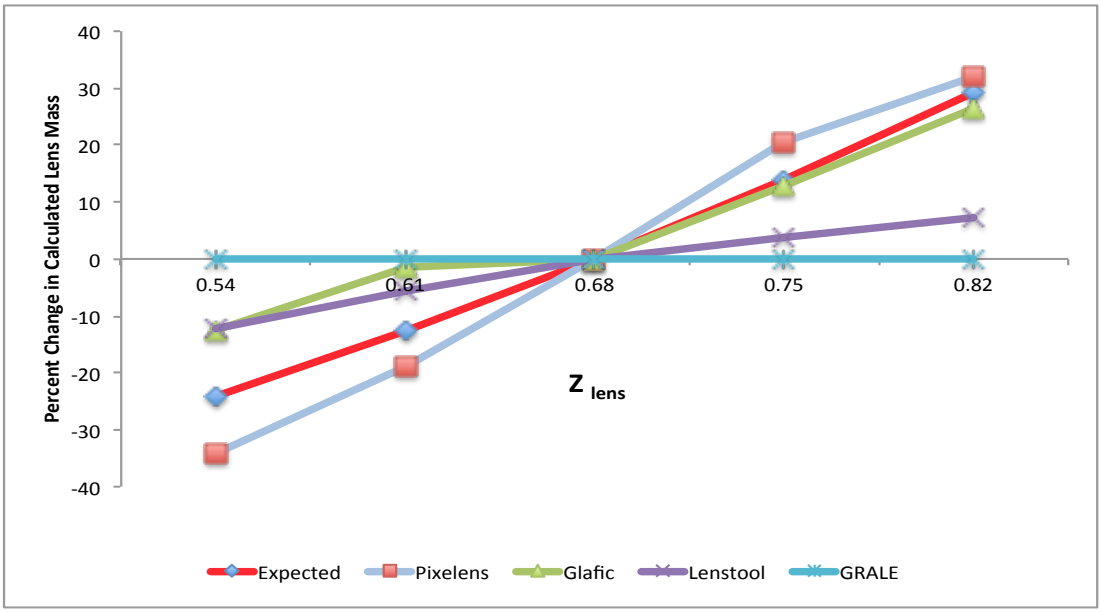

Figure 5.8: The effect of changes in redshift on percent change in calculated mass inside the Einstein radius (M($<R_E$)) for SDSSJ1004 with z_{source}=1.734 and varying z_{lens}. Expected shows changes in the value of $D_{\rm d}D_{\rm s}/D_{\rm ds}$ with the changes in redshift.

PixeLens

The results of the PixeLens analysis of SDSSJ1004+4112 are shown in Table 5.5. The model used from [49] has four sources at a range of redshifts with a total of 13 images. In the model for SDSSJ1004+4112, the full data set was used with 13 images, but when z_{source} was varied, only the distance for the four images at z=1.734 were varied. In addition to the 4 images at z=1.734, there were 5 images at z=3.32, 2 images at z=2.74 and 2 images at z=2.94.

PixeLens is unable to generate a model with z_{lens}=0.68 and z_{source}=1.194 because of the unusual system geometry. The behavior of the calculated time delays in this model are quite different than those with the mock model. In the first set of data with a constant z_{lens}=0.68, even with variation of the z_{source}, the value of $D_{\rm d}D_{\rm s}/D_{\rm ds}$ changes somewhat, and yet the time delays change a great deal, getting progressively smaller as z_{source} increases, which is easily seen in Figures 5.5 and 5.6. In the second data set, with a constant z_{source}=1.734, as z_{lens} increases, the time delays also increase progressively, with $D_{\rm ds}/D_{\rm s}$ getting smaller. The changes in $D_{\rm d}D_{\rm s}/D_{\rm ds}$ in this model are more pronounced than with the mock model, thus making correlation with these values somewhat more clear. The time delays shown in Table 5.5 are those for the 4 images at the setting of z_{source}, while there are 9 other images in the model not shown, which were left at a fixed value of z, from the observational data. The values of these time delays (not shown) varies in a manner similar to the time delays shown for the four images. The enclosed mass calculations are comparable to those published with this model, and with other published models of this system [24; 49]. The enclosed mass calculated by the model varies a relatively small amount in the first dataset with a constant z_{lens}=0.68 and a $D_{\rm d}D_{\rm s}/D_{\rm ds}$ that varies little. In the second data set, despite a wide variation in $D_{\rm ds}/D_{\rm s}$, the enclosed mass varies much less.

z_{lens}	z_s	$D_{\rm d}D_{\rm s}/D_{\rm ds}$	TD_2	TD_3	TD_4	M($<R_E$)
0.68	1.194	4.198	–	–	–	–
0.68	1.464	3.392	351.2	33.5	1433.2	1.63E12
0.68	1.734	3.000	251.5	18.5	886.4	1.26E12
0.68	2.004	2.769	194.7	12.9	614.3	1.01E12
0.68	2.274	2.617	174.2	9.33	483.0	8.34E11
0.54	1.734	2.276	146.2	10.7	493.8	8.30E11
0.61	1.734	2.622	194.7	14.7	668.7	1.02E12
0.68	1.734	3.000	251.5	18.5	886.4	1.26E12
0.75	1.734	3.414	340.7	24.5	1168.4	1.52E12
0.82	1.734	3.878	432.6	32.0	1506.5	1.85E12

Table 5.5: The PixeLens model of SDSSJ1004+4112 demonstrates the effect of changes in z_{lens} and z_{source} (z_s) on calculated parameters including time delays (TD, days) and enclosed mass within the Einstein radius (in $M_\odot$), with the actual system geometry highlighted in gray

glafic

The glafic model used in this study is considerably more complex than the PixeLens model, and was used in the previous extensive study of SDSSJ1004+4112 by [35]. The model uses a total of seven lens potentials and eight point sources. The point sources in the baseline model are at z=1.734 (1 source), 2.74 (2 sources), 3.28 (2 sources) and 3.33 (3 sources). There are no extended sources in the model. The seven lens potentials include one external perturbation and three multipole perturbations as well as a Pseudo-Jaffe Ellipsoid (jaffe), an NFW density profile (nfw) and a multiple galaxies component (gals). The redshift of the first point source (baseline model at z=1.734) is varied in the models in this study, as shown in Table 5.6. The glafic model used has 5 images at z=1.734.

The result of the glafic analysis is shown in Table 5.6, showing the time delays (TD), and mass. Glafic uses a single lens plane, so the redshift of that plane is varied in the study. The mass of the pseudo-Jaffe ellipsoid potential is shown within the Einstein radius as calculated directly by glafic. Changes in TD2 and TD5 did change with $D_{\rm d}D_{\rm s}/D_{\rm ds}$, while there was very little variation in TD3. The changes in TD5, compared to changes in $D_{\rm d}D_{\rm s}/D_{\rm ds}$, are easily seen in figures 5.5 and 5.6, where the time delay calculated by glafic changes in a manner similar to $D_{\rm d}D_{\rm s}/D_{\rm ds}$, with a constant z_{lens}, until z_{source} goes above the baseline value. Glafic calculations of mass change in a manner quite different from $D_{\rm d}D_{\rm s}/D_{\rm ds}$ as shown in Figures 5.7 and 5.8.

z_{lens}	z_s	$D_{\rm d}D_{\rm s}/D_{\rm ds}$	TD_2	TD_3	TD_4	TD_5	M($<R_E$)
0.68	1.194	4.198	1071	812.6	2212.8	3551.6	7.50E11
0.68	1.464	3.392	900.1	821.8	2368.1	2983.7	6.76E11
0.68	1.734	3.000	754.0	821.5	2042.3	2499.1	5.28E11
0.68	2.004	2.769	769.1	821.3	1915.6	2652.0	5.02E11
0.68	2.274	2.617	678.6	820.9	2888.3	2987.6	4.80E11
0.54	1.734	2.276	708.4	821.3	1941.1	2347.9	4.62E11
0.61	1.734	2.622	716.0	821.4	1943.1	2373.3	5.20E11
0.68	1.734	3.000	754.0	821.5	2042.3	2499.1	5.28E11
0.75	1.734	3.414	908.0	821.5	2450.9	3009.6	5.96E11
0.82	1.734	3.878	1060.7	822.1	2686.5	3515.8	6.67E11

Table 5.6: glafic model of SDSSJ1004+4112 demonstrates the effect of changes in z_{lens} and z_{source} (z_s) on calculated parameters including time delays (TD, days) and mass (in units of $M_\odot$) (actual system geometry highlighted in gray)

Lenstool

To date, there have been no studies of SDSSJ1004+4112 using Lenstool in the literature. The model used here was written for this study and uses the five main images in the lensing system at z=1.734, as well as the other images used above in the glafic model. Position data for the model was obtained from previous studies [35]. The results of this analysis are shown in Table 5.7. Changes in time delay calculated by Lenstool followed closely with changes in $D_{\rm d}D_{\rm s}/D_{\rm ds}$ (Figures 5.5 and 5.6). Changes in the mass inside the Einstein radius (Figures 5.7 and 5.8) are more exaggerated than changes in $D_{\rm d}D_{\rm s}/D_{\rm ds}$.

z_{lens}	z_s	$D_{\rm d}D_{\rm s}/D_{\rm ds}$	TD_2	TD_3	TD_4	TD_5	M($<R_E$)
0.68	1.194	4.198	1686	6875	8179	3009	8.48E11
0.68	1.464	3.392	1409	5517	6803	1828	8.49E11
0.68	1.734	3.000	1204	4647	5831	1057	8.48E11
0.68	2.004	2.769	1071	4050	5199	422	8.48E11
0.68	2.274	2.617	975	3630	4699	-54.0	8.48E11
0.54	1.734	2.276	746.7	2805	3640	-255.0	7.60E11
0.61	1.734	2.622	975.2	3663	4707	348	8.08E11
0.68	1.734	3.000	1204	4647	5831	1057	8.48E11
0.75	1.734	3.414	1468	5727	7117	1755	8.84E11
0.82	1.734	3.878	1733	6908	8411	2548	9.13E11

Table 5.7: The Lenstool analysis of SDSSJ1004+4112 demonstrates the effect of changes in z_{lens} and z_{source} (z_s) on calculated parameters including time delay (TD, days), and enclosed mass inside the Einstein radius (in $M_\odot$) (actual system geometry highlighted in gray)

GRALE

The GRALE model used in this study was previously published with a complete evaluation by [24]. The results of this analysis are shown in Table 5.8. Calculations of time delays are significantly different with GRALE compared to changes in $D_{\rm d}D_{\rm s}/D_{\rm ds}$, with an opposite slope in the line (Figures 5.5 and 5.6). There are no changes in mass at any of the geometries tested with GRALE (Figures 5.7 and 5.8), as is seen with a constant z_{lens} with the mock model.

z_{lens}	z_s	$D_{\rm d}D_{\rm s}/D_{\rm ds}$	TD_2	TD_3	TD_4	TD_5	M($<R_E$)
0.68	1.194	4.198	708	1097	641	937	81.0
0.68	1.464	3.392	955	1963	855	1465	81.0
0.68	1.734	3.000	1142	2658	1045	1902	81.0
0.68	2.004	2.769	1313	3227	1199	2283	81.0
0.68	2.274	2.617	1450	3691	1306	2602	81.0
0.54	1.734	2.276	1393	3623	1240	2552	81.0
0.61	1.734	2.622	1270	3128	1158	2212	81.0
0.68	1.734	3.000	1142	2658	1045	1902	81.0
0.75	1.734	3.414	1039	2223	937	1634	81.0
0.82	1.734	3.878	959	1820	847	1403	81.0

Table 5.8: The GRALE analysis of SDSSJ1004+4112 demonstrates the effect of changes in z_{lens} and z_{source} (z_s) on calculated parameters including time delay (TD, days), and the mass density within the Einstein radius (actual system geometry highlighted in gray)

5.5 Discussion

General and Nomenclature

This purpose of this study is to review the status of comparative evaluations of gravitational lens models and compare the effect of changes in redshift on two models using four different strong gravitational lens modeling software codes. The nomenclature for lens model comparisons has not been standardized, and the following three parameters will be used in describing comparison studies. Strong gravitational lens models are classified as LTM or non-LTM. Comparisons between different software are referred to as "direct" if the models are used and compared in the same paper, and "indirect" when comparisons are made to previously published data [21]. Comparisons are also categorized as "independent" if the models use different input data for the same lens system, and "semi-independent" when the same input data is used for two different models in the same paper [e.g. 47]. These three parameters should be used to classify all future lens model comparisons.

The results of this study show significant differences in the calculations of time delays and enclosed mass among the different software code compared. The calculated values are different, but in addition the response of the calculated values to changes in system geometry are also different as demonstrated by comparing the percent change in calculated values. The origins of these differences are in part due to differences in the way that the software models the lens system. In addition, the various software codes have different approaches to paramaterization of a lens system. The catalog of available lens potentials is different in glafic and Lenstool, for example. Awareness of these intrinsic differences in the various strong gravitational lens models suggests the need for caution in interpreting the results. Differences observed between different lens models may reflect differences in the software alone, even when models are parameterized as similarly as possibe. The specific assumptions made by each of the software models used must be taken into account when interpreting results.

Comparative Studies of Strong Gravitational Lens Models

Of the 646 strong gravitational lenses currently in the Orphan Lens database [29], many have been studied using one of the available strong gravitational lens modeling software codes available. There have been several studies that compare strong gravitational lensing analyses with

X-ray analyses [e.g. 8; 28]. Coe at al compared their results using Lensperfect (Non-LTM) with previous results modeling Abell 1689 [3; 4]. An indirect comparison of results for strong gravitational lensing analysis of SDSS J1004 using glafic (LTM) is included in the study by Oguri and colleagues [35]. There are very few studies which include models of a single lens system using more than one of the software codes available in the same paper, as "direct" comparisons. A review of these existing studies was undertaken to illustrate the present situation in lens model comparisons.

Lin et al described SDSS J120602.09+514229.5 as a bright star forming galaxy at z=2.0, strongly lensed by a foreground galaxy at z=0.42 [26]. The system was modeled using Lensview (Non-LTM), originally described in 2006 [48]. The system was modeled using a singular isothermal ellipsoid (SIE) as the mass model. The authors correctly point out that smooth mass models fit the image positions well, but not always the flux ratios of the images. They found $\Theta_{Ein} = 3.82 \pm 0.03$, which translates to $R_{Ein}=14.8 \pm 0.1 h^{-1}$. Lensview uses the full image information, so the authors performed a direct, semi-independent comparison using GravLens / Lensmodel (LTM), which allows fitting an SIE model using only image positions [17]. This showed a very good fit to the image positions, in agreement with the Lensview fit. They also found that the predicted flux for the A3 image in the Lensmodel fit was smaller than the measured flux by a factor of 2 [26].

A direct, semi-independent comparison of results obtained with GravLens (LTM) with those obtained using Lensview (Non-LTM) was also performed in an analysis of SDSS J1430+4105 [9]. The lens mass distribution was first studied using Gravlens assuming point sources, and then with Lensview using the 2-dimensional surface brightness distribution of the same system. The authors conducted an extensive modeling study with Gravlens, using five separate models including a one component SIE, Power law, a de Vaucouleurs component with a dark matter halo, and two further models to show that the result was unaffected by taking the environment into account. Following this modeling with Gravlens, Lensview was used because it is well-suited to systems with extended flux such as the one studied. Overall, the authors found good agreement among the models generated and the information from Lensview, which fits lens models to image data and uses the best-fitting lens model to reconstruct the source and image, was complementary to that obtained with Gravlens.

In a direct comparison of independent lens models, Abell 1703 was studied using ZB software (LTM), and GRALE (Non-LTM)[29; 54]. ZB software has been used in a number of studies, and identified multiple images in high quality ACS images. It uses only 6 free parameters, so that the number of multiple images exceeds the number of free parameters [52; 54]. The non-LTM technique used by GRALE employs an adaptive grid inversion technique and a genetic algorithm for non-LTM inversion [22; 25]. GRALE has been used to analyze a number of systems including SDSSJ1004+4112 [24] and CL0024+1654 [23]. The LTM model using ZB software accurately reproduced all multiply-lensed images, which led the authors to conclude that their preliminary assumption that mass traces light is reasonable. The non-LTM technique of GRALE, for which no prior information regarding the the distribution of cluster galaxies or mass is given, resulted in a very similar 2D mass distribution to that generated using ZB [54]. The authors generated a subtraction map of the two results demonstrating the similarities of the two results, and were able to explain the small differences observed. The authors conclude that the LTM model may at times be less flexible than the non-LTM model. This study may be a landmark study in direct comparisons of strong lensing techniques because it is the first to have a complete analysis by two independent modeling methods.

In another direct comparison of ZB and GRALE, Zitrin and coworkers performed a strong lensing analysis of MS 1358.4+6245 [53]. This detailed analysis using ZB software demonstrated a shallow mass distribution of the central region by uncovering 19 multiply-lensed images that

were previously undetected. In this direct, semi-independent comparison of ZB and GRALE, results with the non-LTM adaptive grid method of GRALE also yielded a similarly shallow profile. This is an important study demonstrating the value of a direct comparison with two different modeling techniques.

More recently, an accurate mass distribution of the galaxy cluster MACS J1206.2-0847 was described using the combination of weak-lensing distortion, magnification, and strong-lensing analysis of wide field Subaru imaging and HST data as part of the Cluster Lensing and Supernova survey with Hubble (CLASH) program [47]. The authors used complementary strong gravitational lensing analyses with ZB (LTM), Lenstool (LTM), Lensperfect (non-LTM), PixeLens (non-LTM) and SaWLens (LTM) [29]. This study is probably the most comprehensive direct comparison of strong gravitational lens modeling software to date. The positions and redshifts were based on a previous study [55], and is thus a semi-independent study. The study primarily depended on the ZB software, then used other software to verify the identification of multiple images and independently assess the level of inherent systematic uncertainties in the analyses. ZB software included a Markov Chain Monte Carlo (MCMC) implementation where the BCG mass is allowed to vary. Seven free parameters were used in total which led to a fully constrained fit since the number of multiple images is greater than the number of free parameters. The new MCMC results were in good agreement with those previously obtained [55]. The authors then performed complementary strong lensing analyses in a direct comparison using Lenstool, Lensperfect, PixeLens and SaWLens, using the multiple images previously identified [55] and the same spectroscopic and photometric redshift information. The SaWLens software uses combined strong gravitational lensing constraints with weak lensing distortion constraints. Finally, the authors compare the resulting projected integrated mass profiles derived from these direct strong-lensing analyses along with the primary strong lensing results based on [55]. This extensive direct, semi-independent comparison of strong gravitational lensing models shows clear consistency among a wide variety of analytic techniques with different systematics, supporting the reliability of the analyses in this study [47].

The Hubble Space Telescope (HST) Frontier Fields project is reporting preliminary results [2]. This important deep field observing program will combine the power of the HST with gravitational lenses. Lens models in the Frontier Fields project will include models from a number of software codes including ZB, GRALE, Lenstool, and two other non-LTM lens model software codes which will facilitate direct comparison of results from a number of lens models rather than depending on a single model from which to draw conclusions. This approach represents an important step in the use of data from lens models.

This review of existing literature shows that direct comparisons of strong gravitational lens modeling codes are not plentiful, and suggests that this is an important goal for future studies.

Mock Model

A simple mock model is used in this study because it facilitates comparison across a variety of software as a direct semi-independent study. This model allowed identical parameterization across the four software models compared, within the limitations of the software. A total of nine models were used with each of the software packages evaluated. A summary of the results for the mock models is shown in Figures 5.1 and 5.2 (time delay) and Figure 5.3 and 5.4 (mass). The models studied used a fixed z_{lens}=0.3 and varied z_{source} (Figures 5.1 and 5.3) and a fixed z_{source}=2.5 with varied z_{lens} (Figures 5.2 and 5.4).

In examining the results of the mock model, the most striking difference is seen in Figure 5.1, where the percent change for Lenstool, PixeLens and the expected values (reflecting changes in $D_{\rm d}D_{\rm s}/D_{\rm ds}$) are all of similar magnitude, and the curves all have a have similar slope, while

the curves showing the changes in the glafic and GRALE models have an inverse slope, and are nearly identical to each other. Although the differences in the curves are only a few percent, this difference is easily visible.

The Einstein radius, R_E, for a Singular Isothermal Sphere is defined as [51]:

$$R_E = 4\pi \left(\frac{v_d}{c}\right)^2 * \frac{D_{\rm ds}}{D_{\rm s}} \tag{5.18}$$

and thus, with each new model geometry, R_E changes as a result of the change in $D_{\rm ds}/D_{\rm s}$. The separation between multiple images is set by R_E, which leads to a change in image position at each geometry. Thus, changes in image position are expected to scale according to $D_{\rm ds}/D_{\rm s}$, and time delays would not scale simply as $D_{\rm d}D_{\rm s}/D_{\rm ds}$.

In the PixeLens models with fixed z_{lens}, calculations of $D_{\rm d}D_{\rm s}/D_{\rm ds}$ show that $D_{\rm d}D_{\rm s}/D_{\rm ds}$ varies very little despite the wide range of z_{source} used. Among these models there are very small variations in the calculated time delays, or the total enclosed mass. The PixeLens models do not have a change in image positions with changes in model geometry. In the second group of models with fixed z_{source} and varying z_{lens}, the changes in both the time delays and enclosed mass calculation are small when the change in $D_{\rm d}D_{\rm s}/D_{\rm ds}$ is small, but as that changes more significantly, so does the change in time delay and enclosed mass. In general, the calculated time delays are similar to changes in $D_{\rm d}D_{\rm s}/D_{\rm ds}$ for all of the PixeLens models tested.

The glafic models tested have the same distribution of z_{lens} and z_{source} as used in the tests with PixeLens. The glafic models show slight changes in time delay calculations with a constant value of z_{lens}, and greater changes with a constant z_{source}. The changes in enclosed mass scale according to the changes in $D_{\rm d}D_{\rm s}/D_{\rm ds}$. The changes in enclosed mass calculated by glafic are similar to those seen in the PixeLens models.

The glafic models with a constant value of z_{lens} (Figure 5.1) show changes that do not follow the changes in $D_{\rm d}D_{\rm s}/D_{\rm ds}$, in fact the line has an inverse slope to the changes in $D_{\rm d}D_{\rm s}/D_{\rm ds}$. The glafic models with a constant z_{lens} change image positions at each of the various geometries tested, which scale exactly the same (percent change) as the calculated time delays when z_{lens} is held constant. These changes in time delay scale according to $D_{\rm ds}/D_{\rm s}$, based on the changes in image position as discussed above. In contrast, although the image positions with a constant z_{source} change in a manner which scales similarly to $D_{\rm ds}/D_{\rm s}$, the changes in time delays with a constant z_{source} (Figure 5.2) scale more closely to $D_{\rm d}D_{\rm s}/D_{\rm ds}$. This change in image position with glafic models explains the observation that the time delays with the glafic models scale as $D_{\rm ds}/D_{\rm s}$ when z_{lens} is constant (Figure 5.1).

The Lenstool models show very little change in calculated time-delays compared to changes in $D_{\rm d}D_{\rm s}/D_{\rm ds}$ at a wide range of geometries tested. However, when the change in $D_{\rm d}D_{\rm s}/D_{\rm ds}$ is larger, the change in time delay is more marked for one of the images. These changes are similar to the pattern seen with PixeLens in that small changes in $D_{\rm d}D_{\rm s}/D_{\rm ds}$ result in negligible changes in the time delays. The image positions compared among the various models are the same.

The calculations of time delay with GRALE show little variation with a fixed value of z_{lens}, similar in magnitude to results with glafic. The calculation of mass with a fixed z_{source} show no changes which may be a result of the use of absolute projected mass density (Equation 5.16) calculation which does not depend on z_{source}. The GRALE models also have a change in image position at the various geometries studied, similar to the glafic models, and the changes in image position for all nine models studied scale according to $D_{\rm ds}/D_{\rm s}$, similar to the results with glafic. The changes in time delay calculated by GRALE scale the same as changes in image position for models with z_{lens} held constant (Figure 5.1), but scale more closely to changes in $D_{\rm d}D_{\rm s}/D_{\rm ds}$ with models where z_{source} is held constant (Figure 5.2), similar to the results with

glafic.

The calculations of lens mass with a fixed z_{lens}=0.30 shown in Figure 5.3, for PixeLens and Lenstool, all follow the expected result very closely, showing that the mass calculation varies exactly as does $D_{\rm d}D_{\rm s}/D_{\rm ds}$. The results with a fixed z_{source}=2.50, although fairly close among PixeLens, glafic and Lenstool, show slightly greater variation, as seen in Figure 5.4 .

The results with glafic and GRALE show that the time delays scale similarly to the changes in image position rather than $D_{\rm d}D_{\rm s}/D_{\rm ds}$, when z_{lens} is constant. The observed differences in time-delay calculations is consistent with the fact that the software depends on other factors in these calculations and that for glafic and GRALE, the time delay calculations vary with changes in the image position which follow the changes in the model geometry. The time delays calculated by PixeLens and Lenstool follow the general pattern of changes in $D_{\rm d}D_{\rm s}/D_{\rm ds}$, and there are no changes in image position calculated by these models.

SDSSJ1004+4112 Model

Effect of changes in redshift on calculated time delays and mass with SDSSJ1004+4112

Similar to the studies of the mock model above, five models with z_{lens} fixed at z=0.68 and varied z_{source}, and five models with z_{source} fixed at z=1.734, and varied z_{lens} are evaluated, using the baseline geometries for the system, for a total of nine different models tested. Figures 5.5 and 5.6 show a summary of the time delay calculations for all four software packages compared to the expected variation calculated from changes in $D_{\rm d}D_{\rm s}/D_{\rm ds}$. A summary of the results for the mass calculations is shown in Figures 5.7 and 5.8.

PixeLens has been used in several studies of this system [40; 49]. The model used has four sources at a range of redshifts with a total of 13 images, and was obtained from the tutorial document [37]. In contrast to the range of redshifts used in this study for the mock model, calculations of $D_{\rm d}D_{\rm s}/D_{\rm ds}$ showed a fairly wide variation. As a check of model consistency, the calculated enclosed mass for the actual system geometry was identical to that in reported studies at 6.1E13 within 110kpc [24; 49]. In the first PixeLens model of this system, the models allowed the detection of structures in the lens associated with cluster galaxies [49]. This non-LTM model was in good agreement with the LTM model previously reported by Oguri [36]. It is interesting that the time delays in the mock model vary very little, with small changes in $D_{\rm d}D_{\rm s}/D_{\rm ds}$, while with similar small changes in $D_{\rm d}D_{\rm s}/D_{\rm ds}$ for SDSSJ1004+4112, there is a wide variation in the time delays. The enclosed mass calculation also has a wider variation in the SDSSJ1004+4112 model than the mock model. PixeLens was also used to model the more complete description of SDSSJ1004+4112 with 13 images coming from four sources, which is the data set used in this study [40]. The calculated time delays with PixeLens show much wider variation than the variation in $D_{\rm d}D_{\rm s}/D_{\rm ds}$, although this variation is much less marked in the systems tested where z_{source} was fixed (Figure 5.5) than when z_{lens} was fixed (Figure 5.4).

The glafic model input files from the study by Oguri are used in the present study to evaluate SDSSJ1004+4112 using glafic [35] at various geometries. The glafic model incorporated new observational data, including multiple galaxies and time delays. The halo component model used a generalized NFW profile, and reproduced all observations. There is little effect on calculations of time delays, despite wide variations in geometry, but there are significant effects on parameters of the three lens profiles used in the model showing changes in mass. Time delays 3 and 4 do vary based on changes in $D_{\rm d}D_{\rm s}/D_{\rm ds}$, while the others do not (Table 5.6). As was observed in the study of the mock model, the image positions calculated by the glafic models do change with changes in system geometry. These changes in image position may partially explain the fact that the time delays do not scale simply as $D_{\rm d}D_{\rm s}/D_{\rm ds}$.

The Lenstool model used in this study was developed for this study, as there are no previous studies which used Lenstool to evaluate SDSSJ1004+4112. The time delays follow the expected results quite closely at nearly all geometries tested, indicating that the time delays depend on $D_{\rm d}D_{\rm s}/D_{\rm ds}$. There are essentially no changes in calculated mass with a fixed z_{lens}, consistent with absolute projected mass density (Equation 5.16).

The previously reported GRALE model of SDSSJ1004+4112 demonstrated a central image of a second galaxy where an object is visible in the ACS images [24]. The GRALE model reproduced the calculations of enclosed mass reported in other studies, with virtually no changes at all geometries tested. While there were very small changes in image position calculated with the GRALE model, these changes were almost insignificant and could not explain the differences in time delay calculations observed.

Comparing the results of the four models with the variation in $D_{\rm d}D_{\rm s}/D_{\rm ds}$, shows that while PixeLens, glafic and Lenstool show similar trends to changes in $D_{\rm d}D_{\rm s}/D_{\rm ds}$, there are still considerable differences of more than 20 percent in some cases. Lenstool is very close to following the changes in $D_{\rm d}D_{\rm s}/D_{\rm ds}$, especially with a fixed value of z_{lens} (Figure 5.5). Changes in time delays calculated with the GRALE model were significantly different from the changes in $D_{\rm d}D_{\rm s}/D_{\rm ds}$. Although changes in image position were similar in direction and magnitude to changes in the time delay calculated by glafic and GRALE with the mock model, similar changes were not observed with the models of SDSSJ1004+4112. This may be partially explained by the fact that the SDSSJ1004+4112 models have many more images and multiple potentials while the mock model is very simple with just one potential and four images.

Study Limitations

It is acknowledged that there are limitations to the methodology used to compare the models of SDSSJ1004+4112. Three of the four models used were from previous studies, the original models are used in order to obtain results consistent with the previous studies. In contrast to the study here with the mock model, the parameterization of the models of SDSSJ1004+4112 is somewhat different, including the number of images used in the model and other factors. Thus, these models differ in their basic parameterization as well as the limitations imposed by the various software such as potentials available to be used in the model. For this reason, percent change in results rather than the absolute values were compared.

5.6 Conclusions

This is the first systematic evaluation of the behavior of strong gravitational lens modeling software to evaluate the effect of changes in redshift on time delay and mass calculations. This study is not intended to demonstrate superiority of one modeling software over another, but rather to illustrate differences through a systematic evaluation of the results of strong gravitational lens model calculations of time delay and mass with changes in redshift, and to compare with changes in $D_{\rm d}D_{\rm s}/D_{\rm ds}$. A consistent nomenclature for gravitational lens model studies is suggested using three parameters. Although there are many studies of strong gravitational lens systems, a review of the literature shows that few of them include direct analyses with different software models. The results of this study show that even small changes in redshift significantly affect the calculated values of time delays and mass using four strong gravitational lens modeling codes. The changes in calculated time delays and mass are different from the changes in $D_{\rm d}D_{\rm s}/D_{\rm ds}$, suggesting that the calculations are dependent on other factors, and these changes are different among the software packages used in this study. This is explained

in part, for models using glafic and GRALE, that the image positions change with system geometry resulting in changes in time delay that do not scale as $D_{\rm d}D_{\rm s}/D_{\rm ds}$. There are intrinsic differences in some software which limits the ability to parameterize two models in exactly the same way.

Future studies of strong gravitational lensing should include more direct comparisons to evaluate the results with different software, as is planned for the Hubble Space Telescope Frontier Fields Project. Strong gravitational lens modeling software requires systematic study to understand its functions and limitations, and this study is an initial effort to further this understanding.

References

[1] S. Belli, T. Jones, R. S. Ellis, and J. Richard. Testing the Universality of the Fundamental Metallicity Relation at High Redshift Using Low-Mass Gravitationally Lensed Galaxies. *ArXiv e-prints*, February 2013. 198

[2] M. Bradac, H. Ebeling, J. Merten, K. Sharon, L. Williams, and A. Zitrin. Frontier fields lensing models. http://www.stsci.edu/hst/campaigns/frontier-fields/Lensing-Models, November 2013. 218

[3] D. Coe, N. Benítez, T. Broadhurst, and L. A. Moustakas. A High-resolution Mass Map of Galaxy Cluster Substructure: LensPerfect Analysis of A1689. *ApJ*, **723**:1678–1702, November 2010. 198, 199, 217

[4] D. Coe, E. Fuselier, N. Benítez, T. Broadhurst, B. Frye, and H. Ford. LensPerfect: Gravitational Lens Mass Map Reconstructions Yielding Exact Reproduction of All Multiple Images. *ApJ*, **681**:814–830, July 2008. 217

[5] D. Coe and L. A. Moustakas. Cosmological Constraints from Gravitational Lens Time Delays. *ApJ*, **706**:45–59, November 2009. 199, 200

[6] Daniel Coe. *Towards an understanding of dark matter: Precise gravitational lensing analysis complemented by robust photometric redshifts*. PhD thesis, Johns Hopkins Univ, 2007. 197

[7] F. Courbin, V. Chantry, Y. Revaz, D. Sluse, C. Faure, M. Tewes, E. Eulaers, M. Koleva, I. Asfandiyarov, S. Dye, P. Magain, H. van Winckel, J. Coles, P. Saha, M. Ibrahimov, and G. Meylan. COSMOGRAIL: the COSmological MOnitoring of GRAvItational Lenses. IX. Time delays, lens dynamics and baryonic fraction in HE 0435-1223. *AstrAstrophys*, **536**:A53, December 2011. 198

[8] A. Donnarumma, S. Ettori, M. Meneghetti, R. Gavazzi, B. Fort, L. Moscardini, A. Romano, L. Fu, F. Giordano, M. Radovich, R. Maoli, R. Scaramella, and J. Richard. Abell 611. II. X-ray and strong lensing analyses. *AAP*, **528**:A73, April 2011. 217

[9] T. Eichner, S. Seitz, and A. Bauer. Golden gravitational lensing systems from the Sloan Lens ACS Survey. II. SDSS J1430+4105: A precise inner total mass profile from lensing alone. *ArXiv e-prints*, September 2012. 217

[10] R. Fadely, S. S. Allam, A. J. Baker, H. Lin, D. Lutz, A. E. Shapley, M.-S. Shin, J. Allyn Smith, M. A. Strauss, and D. L. Tucker. Mid-infrared Spectroscopy of Two Lensed Star-forming Galaxies. *ApJ*, **723**:729–736, November 2010. 198

[11] J. Fohlmeister, C. S. Kochanek, E. E. Falco, J. Wambsganss, N. Morgan, C. W. Morgan, E. O. Ofek, D. Maoz, C. R. Keeton, J. C. Barentine, G. Dalton, J. Dembicky, W. Ketzeback, R. McMillan, and C. S. Peters. A Time Delay for the Largest Gravitationally Lensed Quasar: SDSS J1004+4112. *ArXiv Astrophysics e-prints*, July 2006. 209

[12] D. W. Hogg. Distance measures in cosmology. *ArXiv Astrophysics e-prints*, May 1999. 200

[13] N. Inada, M. Oguri, E. E. Falco, T. J. Broadhurst, E. O. Ofek, C. S. Kochanek, K. Sharon, and G. P. Smith. Spectroscopic Confirmation of the Fifth Image of SDSS J1004+4112 and Implications for the M_{BH}–σ_* Relation at z = 0.68. *ProcAstrSocJapan*, **60**:L27, October 2008. 209

[14] N. Inada, M. Oguri, C. R. Keeton, D. J. Eisenstein, F. J. Castander, K. Chiu, P. B. Hall, J. F. Hennawi, D. E. Johnston, B. Pindor, G. T. Richards, H.-W. R. Rix, D. P. Schneider, and W. Zheng. Discovery of a Fifth Image of the Large Separation Gravitationally Lensed Quasar SDSS J1004+4112. *ProcAstrSocJapan*, **57**:L7–L10, June 2005. 209

[15] N. Inada, M. Oguri, B. Pindor, J. F. Hennawi, K. Chiu, W. Zheng, S.-I. Ichikawa, M. D. Gregg, R. H. Becker, Y. Suto, M. A. Strauss, E. L. Turner, C. R. Keeton, J. Annis, F. J. Castander, D. J. Eisenstein, J. A. Frieman, M. Fukugita, J. E. Gunn, D. E. Johnston, S. M. Kent, R. C. Nichol, G. T. Richards, H.-W. Rix, E. S. Sheldon, N. A. Bahcall, J. Brinkmann, Ž. Ivezić, D. Q. Lamb, T. A. McKay, D. P. Schneider, and D. G. York. A gravitationally lensed quasar with quadruple images separated by 14.62arcseconds. *Nature*, **426**:810–812, December 2003. 209

[16] E. Jullo, P. Natarajan, J.-P. Kneib, A. D'Aloisio, M. Limousin, J. Richard, and C. Schimd. Cosmological Constraints from Strong Gravitational Lensing in Clusters of Galaxies. *Science*, **329**:924–927, August 2010. 198

[17] C. R. Keeton. Computational Methods for Gravitational Lensing. *ArXiv Astrophysics e-prints*, February 2001. 209, 217

[18] J-P Kneib. Lenstool project web page. `http://lamwws.oamp.fr/lenstool/`, May 2012. 199, 202

[19] L. V. E. Koopmans, M. Barnabe, A. Bolton, M. Bradac, L. Ciotti, A. Congdon, O. Czoske, S. Dye, A. Dutton, A. Elliasdottir, E. Evans, C. D. Fassnacht, N. Jackson, C. Keeton, J. Lasio, L. Moustakas, M. Meneghetti, S. Myers, C. Nipoti, S. Suyu, G. van de Ven, S. Vegetti, O. Wucknitz, and H.-S. Zhao. Strong Gravitational Lensing as a Probe of Gravity, Dark-Matter and Super-Massive Black Holes. In *astro2010: The Astronomy and Astrophysics Decadal Survey*, **2010** of *ArXiv Astrophysics e-prints*, page 159, 2009. 198

[20] A. T. Lefor and T. Futamase. Comparison of Strong Gravitational Lens Model Software I. Time delay and mass calculations are sensitive to changes in redshift and are model dependent. *ArXiv e-prints*, July 2013. 197

[21] A. T. Lefor, T. Futamase, and M. Akhlaghi. A Systematic Review of Strong Gravitational Lens Modeling Software. *ArXiv e-prints*, June 2012. 198, 216

[22] J. Liesenborgs, S. De Rijcke, and H. Dejonghe. A genetic algorithm for the non-parametric inversion of strong lensing systems. *MonNotRoyalAstrSoc*, **367**:1209–1216, April 2006. 199, 217

[23] J. Liesenborgs, S. de Rijcke, H. Dejonghe, and P. Bekaert. Non-parametric strong lens inversion of Cl 0024+1654: illustrating the monopole degeneracy. *MonNotRoyalAstrSoc*, **389**:415–422, September 2008. 217

[24] J. Liesenborgs, S. de Rijcke, H. Dejonghe, and P. Bekaert. Non-parametric strong lens inversion of SDSS J1004+4112. *MonNotRoyalAstrSoc*, **397**:341–349, July 2009. 199, 209, 213, 215, 217, 220, 221

[25] Jori Liesenborgs. *Genetic algorithms for the non-parametric inversion of gravitational lenses*. PhD thesis, Unversiteit Hasselt, 2009. 217

[26] H. Lin, E. Buckley-Geer, S. S. Allam, D. L. Tucker, H. T. Diehl, D. Kubik, J. M. Kubo, J. Annis, J. A. Frieman, M. Oguri, and N. Inada. Discovery of a Very Bright, Strongly Lensed z = 2 Galaxy in the SDSS DR5. *ApJ*, **699**:1242–1251, July 2009. 217

[27] Y. Mellier. Cosmological Applications of Gravitational Lensing. In M. Lachièze-Rey, editor, *NATO ASIC Proc. 541: Theoretical and Observational Cosmology*, page 211, 1999. 198

[28] M. Meneghetti, E. Rasia, J. Merten, F. Bellagamba, S. Ettori, P. Mazzotta, K. Dolag, and S. Marri. Weighing simulated galaxy clusters using lensing and X-ray. *AAP*, **514**:A93, May 2010. 217

[29] L. Moustakas and J. Brownstein. The orphan lens project. `http://www.masterlens.astro.utah.edu`, February 2013. 198, 216, 217, 218

[30] L. A. Moustakas, K. Abazajian, A. Benson, A. S. Bolton, J. S. Bullock, J. Chen, E. Cheng, D. Coe, A. B. Congdon, N. Dalal, J. Diemand, B. M. Dobke, G. Dobler, O. Dore, A. Dutton, R. Ellis, C. D. Fassnacht, H. Ferguson, D. Finkbeiner, R. Gavassi, F. W. High, T. Jeltema, E. Jullo, M. Kaplinghat, C. R. Keeton, J.-P. Kneib, L. V. E. Koopmans, S. M. Koishiappas, M. Kuhlen, A. Kusenko, C. R. Lawrence, A. Loeb, P. Madae, P. Marshall, R. B. Metcalf, P. Natarajan, J. R. Primack, S. Profumo, M. D. Seiffert, J. Simon, D. Stern, L. Strigari, J. E. Taylor, R. Wayth, J. Wambsganss, R. Wechsler, and A. Zentner. Strong gravitational lensing probes of the particle nature of dark matter. In *astro2010: The Astronomy and Astrophysics Decadal Survey*, **2010** of *Astronomy*, page 214, 2009. 198

[31] R. Narayan and M. Bartelmann. Lectures on Gravitational Lensing. *ArXiv Astrophysics e-prints*, June 1996. 201

[32] T. Narikawa, T. Kobayashi, D. Yamauchi, and R. Saito. Testing general scalar-tensor gravity and massive gravity with cluster lensing. *ArXiv e-prints*, February 2013. 198

[33] M. Oguri. Gravitational Lens Time Delays: A Statistical Assessment of Lens Model Dependences and Implications for the Global Hubble Constant. *ApJ*, **660**:1–15, May 2007. 199, 200, 201

[34] M. Oguri. The Mass Distribution of SDSS J1004+4112 Revisited. *ProcAstrSocJapan*, **62**:1017–, August 2010. 199

[35] M. Oguri. The Mass Distribution of SDSS J1004+4112 Revisited. *ProcAstrSocJapan*, **62**:1017–, August 2010. 199, 209, 214, 215, 217, 220

[36] M. Oguri, N. Inada, C. R. Keeton, B. Pindor, J. F. Hennawi, M. D. Gregg, R. H. Becker, K. Chiu, W. Zheng, S.-I. Ichikawa, Y. Suto, E. L. Turner, J. Annis, N. A. Bahcall, J. Brinkmann, F. J. Castander, D. J. Eisenstein, J. A. Frieman, T. Goto, J. E. Gunn, D. E. Johnston, S. M. Kent, R. C. Nichol, G. T. Richards, H.-W. Rix, D. P. Schneider, E. S. Sheldon, and A. S. Szalay. Observations and Theoretical Implications of the Large-Separation Lensed Quasar SDSS J1004+4112. *ApJ*, **605**:78–97, April 2004. 209, 220

[37] J Read. Pixelens tutorial. http://www.itp.uzh.ch/~justin/Astro/Lectures/PixeLens/tutorial.pdf, September 2012. 220

[38] J Read. Pixelens web page. http://www.qgd.uzh.ch/projects/pixelens/, May 2012. 199, 206

[39] S. Refsdal. On the possibility of determining Hubble's parameter and the masses of galaxies from the gravitational lens effect. *MonNotRoyalAstrSoc*, **128**:307, 1964. 198

[40] P. Saha, J. I. Read, and L. L. R. Williams. Two Strong-Lensing Clusters Confront Universal Dark Matter Profiles. *ApJLett*, **652**:L5–L8, November 2006. 220

[41] K. Sharon, E. O. Ofek, G. P. Smith, T. Broadhurst, D. Maoz, C. S. Kochanek, M. Oguri, Y. Suto, N. Inada, and E. E. Falco. Discovery of Multiply Imaged Galaxies behind the Cluster and Lensed Quasar SDSS J1004+4112. *ApJLett*, **629**:L73–L76, August 2005. 209

[42] S. H. Suyu, P. J. Marshall, M. W. Auger, S. Hilbert, R. D. Blandford, L. V. E. Koopmans, C. D. Fassnacht, and T. Treu. Dissecting the Gravitational lens B1608+656. II. Precision Measurements of the Hubble Constant, Spatial Curvature, and the Dark Energy Equation of State. *ApJ*, **711**:201–221, March 2010. 198

[43] S. H. Suyu, T. Treu, R. D. Blandford, W. L. Freedman, S. Hilbert, C. Blake, J. Braatz, F. Courbin, J. Dunkley, L. Greenhill, E. Humphreys, S. Jha, R. Kirshner, K. Y. Lo, L. Macri, B. F. Madore, P. J. Marshall, G. Meylan, J. Mould, B. Reid, M. Reid, A. Riess, D. Schlegel, V. Scowcroft, and L. Verde. The Hubble constant and new discoveries in cosmology. *ArXiv e-prints*, February 2012. 198

[44] S. H. Suyu, T. Treu, S. Hilbert, A. Sonnenfeld, M. W. Auger, R. D. Blandford, T. Collett, F. Courbin, C. D. Fassnacht, L. V. E. Koopmans, P. J. Marshall, G. Meylan, C. Spiniello, and M. Tewes. Cosmology from gravitational lens time delays and Planck data. *ArXiv e-prints*, June 2013. 198

[45] M. Tegmark, D. J. Eisenstein, M. A. Strauss, D. H. Weinberg, M. R. Blanton, J. A. Frieman, M. Fukugita, J. E. Gunn, A. J. S. Hamilton, G. R. Knapp, R. C. Nichol, J. P. Ostriker, N. Padmanabhan, W. J. Percival, D. J. Schlegel, D. P. Schneider, R. Scoccimarro, U. Seljak, H.-J. Seo, M. Swanson, A. S. Szalay, M. S. Vogeley, J. Yoo, I. Zehavi, K. Abazajian, S. F. Anderson, J. Annis, N. A. Bahcall, B. Bassett, A. Berlind, J. Brinkmann, T. Budavari, F. Castander,

A. Connolly, I. Csabai, M. Doi, D. P. Finkbeiner, B. Gillespie, K. Glazebrook, G. S. Hennessy, D. W. Hogg, Ž. Ivezić, B. Jain, D. Johnston, S. Kent, D. Q. Lamb, B. C. Lee, H. Lin, J. Loveday, R. H. Lupton, J. A. Munn, K. Pan, C. Park, J. Peoples, J. R. Pier, A. Pope, M. Richmond, C. Rockosi, R. Scranton, R. K. Sheth, A. Stebbins, C. Stoughton, I. Szapudi, D. L. Tucker, D. E. vanden Berk, B. Yanny, and D. G. York. Cosmological constraints from the SDSS luminous red galaxies. *PhysRevD*, **74**[12]:123507, December 2006. 199

[46] T. Treu. Strong Lensing by Galaxies. *AnnRevAstr*, **48**:87–125, September 2010. 198

[47] K. Umetsu, E. Medezinski, M. Nonino, J. Merten, A. Zitrin, A. Molino, C. Grillo, M. Carrasco, M. Donahue, A. Mahdavi, D. Coe, M. Postman, A. Koekemoer, N. Czakon, J. Sayers, T. Mroczkowski, S. Golwala, P. M. Koch, K.-Y. Lin, S. M. Molnar, P. Rosati, I. Balestra, A. Mercurio, M. Scodeggio, A. Biviano, T. Anguita, L. Infante, G. Seidel, I. Sendra, S. Jouvel, O. Host, D. Lemze, T. Broadhurst, M. Meneghetti, L. Moustakas, M. Bartelmann, N. Benítez, R. Bouwens, L. Bradley, H. Ford, Y. Jiménez-Teja, D. Kelson, O. Lahav, P. Melchior, J. Moustakas, S. Ogaz, S. Seitz, and W. Zheng. CLASH: Mass Distribution in and around MACS J1206.2-0847 from a Full Cluster Lensing Analysis. *ApJ*, **755**:56, August 2012. 216, 218

[48] R. B. Wayth and R. L. Webster. LENSVIEW: software for modelling resolved gravitational lens images. *MonNotRoyalAstrSoc*, **372**:1187–1207, November 2006. 217

[49] L. L. R. Williams and P. Saha. Models of the Giant Quadruple Quasar SDSS J1004+4112. *AstrJ*, **128**:2631–2641, December 2004. 199, 206, 209, 213, 220

[50] H. J. Witt, S. Mao, and C. R. Keeton. Analytic Time Delays and H_0 Estimates for Gravitational Lenses. *ApJ*, **544**:98–103, November 2000. 201

[51] E Wright. Arclets in clusters. http://ned.ipac.caltech.edu/level5/Mellier/Mellier2_3.html, May 2014. 202, 219

[52] A. Zitrin, T. Broadhurst, R. Barkana, Y. Rephaeli, and N. Benítez. Strong-lensing analysis of a complete sample of 12 MACS clusters at z0.5: mass models and Einstein radii. *MonNotRoyalAstrSoc*, **410**:1939–1956, January 2011. 217

[53] A. Zitrin, T. Broadhurst, D. Coe, J. Liesenborgs, N. Benítez, Y. Rephaeli, H. Ford, and K. Umetsu. Strong-lensing analysis of MS 1358.4+6245: New multiple images and implications for the well-resolved z= 4.92 galaxy. *MonNotRoyalAstrSoc*, **413**:1753–1763, May 2011. 217

[54] A. Zitrin, T. Broadhurst, K. Umetsu, Y. Rephaeli, E. Medezinski, L. Bradley, Y. Jiménez-Teja, N. Benítez, H. Ford, J. Liesenborgs, S. de Rijcke, H. Dejonghe, and P. Bekaert. Full lensing analysis of Abell 1703: comparison of independent lens-modelling techniques. *MonNotRoyalAstrSoc*, **408**:1916–1927, November 2010. 217

[55] A. Zitrin, P. Rosati, M. Nonino, C. Grillo, M. Postman, D. Coe, S. Seitz, T. Eichner, T. Broadhurst, S. Jouvel, I. Balestra, A. Mercurio, M. Scodeggio, N. Benítez, L. Bradley, H. Ford, O. Host, Y. Jimenez-Teja, A. Koekemoer, W. Zheng, M. Bartelmann, R. Bouwens, O. Czoske, M. Donahue, O. Graur, G. Graves, L. Infante, S. Jha, D. Kelson, O. Lahav, R. Lazkoz, D. Lemze, M. Lombardi, D. Maoz, C. McCully, E. Medezinski, P. Melchior,

M. Meneghetti, J. Merten, A. Molino, L. A. Moustakas, S. Ogaz, B. Patel, E. Regoes, A. Riess, S. Rodney, K. Umetsu, and A. Van der Wel. CLASH: New Multiple Images Constraining the Inner Mass Profile of MACS J1206.2-0847. *ApJ*, **749**:97, April 2012. 218

Chapter 6

HydraLens: Computer-Assisted Strong Gravitational Lens Model Generation and Translation

6.1 Purpose and Organization of this Chapter

The purpose of this chapter is to describe the HydraLens Software Package that was written as part of this dissertation. HydraLens is a program to directly translate lens models to facilitate comparative studies using various lens model software packages. A User Manual is included as Appendix A. [1]. [2]

This chapter is organized as follows. In section §6.3 we discuss the detailed organization of the HydraLens software. In section §6.3 we discuss the command structure and input files used by each of the four lens model software codes implemented in order to delineate the issues in lens model translation. In section §6.4, we discuss the details of lens model generation and translation as implemented in HydraLens. In section §6.5 we discuss issues in comparative lens model studies as well as limitations and future development of HydraLens.

6.2 Introduction

The present time has been referred to as the "Golden Age" of Precision Cosmology [2]. Strong gravitational lensing data is a rich source of information about the structure and dynamics of the universe, and these data are contributing significantly to this notion of precision cosmology. Strong gravitational lens studies are highly dependent on the software used to create the models and analyze the components such as lens mass, Einstein radius, time delays etc. A comprehensive review of available software has been conducted by [12]. While many such software packages exist, most studies to date utilize only a single software package for analysis. Furthermore, most authors of strong gravitational lensing studies use their own software only.

[1] Portions of this chapter were published in *Lefor AT. Comparison of strong gravitational lens model software II. HydraLens: Computer-assisted strong gravitational lens model generation and translation. Astronomy and Computing 2014. 5:28-34* [10] doi:10.1016/j.ascom.2014.04.002. Permission to use this published material granted by the Publisher, License 3571220094415

[2] The software is available for download from the Astronomy Source Code Library at http://ascl.net/1402.023

More recently, the status of comparative studies of strong gravitational lens models has been reviewed by [11].

One of the barriers to conducting comparative studies is the heterogeneity of the lens modeling software that currently exists, which includes data input, calculation algorithms, and data output. This heterogeneity is not surprising since all of the software has been independently developed. There are also some common elements among the software being used. This heterogeneity presents one of the greatest barriers to the use of multiple modeling codes in the study of strong gravitational lenses. The data files used by each model code are quite different, and the formats can be confusing for someone wanting to use an unfamiliar lens modeling code. This is a major barrier to comparative studies. Until the present time, software designed to facilitate model entry is only available for Gravlens [1]. Using this program is somewhat hampered by the difficulty in compiling it with multiple dependencies. For all other existing lens model software, lens models files are entered as a simple free text file, and the user must be careful to count exactly the number of parameters entered on each line and carefully set the values of dozens of numerical flags. Small errors in entry of the file will make the results unpredictable and unusable.

Some of the software used in lensing studies remains inaccessible to all investigators except the one who developed the software [21]. In addition to preventing other investigators from duplicating analyses, the lack of availability of software presents another barrier to comparative studies. The Orphan Lens Database [14] contains a database of 24 strong gravitational lens modeling software codes. Of these, 16 have been identified as being used in research studies, of which five (Mirage, ZB, WSLAP, SaWLens and GLEE) are not publicly distributed and are used almost exclusively by their developers. The remaining 11 strong gravitational lens model software packages are available for download by interested investigators (Lenstool, Lensview, Gravlens, Lensmodel, GRALE, PixeLens, SimpLens, glafic, LensPerfect, IGLOO and GLAMROC). An extensive review of strong gravitational lens model software is presented in Chapter 4.

HydraLens Software

The software described herein is called "HydraLens" in reference to the multi-headed creature of Greek mythology, and it directly addresses the difficulties associated with writing a lens model for four different, publicly available strong gravitational lens model codes. HydraLens is freely available, and easy to compile with no-cost compilers, as a single, unified program. There are no dependencies on other software or interfaces. HydraLens facilitates the entry of lens model files for the four codes implemented, by using a simple graphical user interface (GUI) instead of entering multiple parameters in simple text files. Models are entered using a GUI, which has common elements and layout for all four model codes implemented, largely obviating the need for manuals and references. In addition, HydraLens can translate lens model files among the four software packages implemented. HydraLens serves two purposes. First, the ability of HydraLens to translate among modeling codes may assist in the conduct of comparative studies. Second, HydraLens is useful for those learning about strong gravitational lens models, enabling straightforward creation of multiple input files.

6.3 Methods

Strong Gravitational Lens Models

Each lens model software package uses a different input data format to construct the model. They do have some features in common, and some are more similar than others. All of them use simple text files as input, but the format of the text files, available functionality and command structures are very dependent on the particular software. Some of the lens model software uses multiple accessory files to provide other data. Each of them has a unique list of commands, with great variability. For example, Lenstool uses a number of commands in the French language. The fact that they use a wide range of flags, with a wide range of meanings, makes writing a lens model file difficult, especially for the uninitiated. HydraLens was written to simplify the process of creating lens model input files to facilitate direct comparison studies, and to assist those starting in the field.

HydraLens Software Development

The use of a simple GUI was considered essential in the development of HydraLens, which was implemented in Visual Basic (VB, Microsoft Corp, Redmond WA USA) since VB offers a commonly recognized and easy to code GUI, as well as the fact that VB software runs in nearly any Windows (Microsoft Corp) environment. VB compilers are available at no cost. HydraLens is easily read and modified making HydraLens more generally useful to the astrophysics community. There are extensive comments embedded in the code to allow customization as desired and a user manual supplied.

Overview of HydraLens

For each lens model software implemented, HydraLens has four basic functions: model generation, model write, model parsing and model translation. Each of these functions is implemented using a modular approach, for each of the four strong gravitational lens software packages in the system. Each of these four basic modules interacts with a common set of data structures that are configured specifically for the lens model software, as shown in Figure 6.1.

The model generation function accepts input from the user from a GUI window, and fills in a data structure with the information for that type of model. Alternatively, the data structure can be filled in by a parsing an existing model by reading each line, then putting the commands and data into the same data structures as the model generation function uses. For example, one might have an existing model for a particular lens system written for Lenstool. This existing model can be read in by HydraLens (model parsing) and then translated to any or all of the other three model types supported. Once the model information is in the model-specific data structure (through model generation or through model parsing), it can be written out as a lens model input file, or it can be translated.

Common Parameter Entry

Most of the information for each model type is entered on a single GUI screen, visible after the user selects the model type to be generated. However, some of the models require the user to enter a number of parameters for each of many lines, such as the .obs file used in glafic which has up to eight parameters for each image for each of the sources entered in glafic. Entering these in a simple text editor is acceptable, but requires the user to be aware of what is typed in each column, with no assistance. For each group of parameters needed, in each program, the

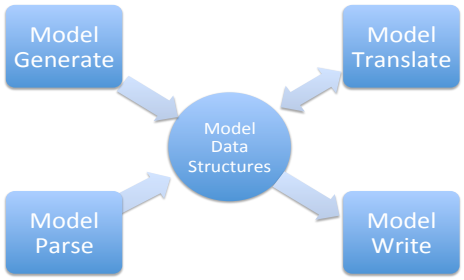

Figure 6.1: Basic data structure of HydraLens showing the interactions of the four modules with the data arrays

software uses a common screen for parameter entry that simply labels each text box, allowing the user to enter text in an appropriately labeled area, then generating the appropriate line for the data file. This parameter entry screen is common to all routines in HydraLens, and greatly simplifies data input (Figure 6.2).

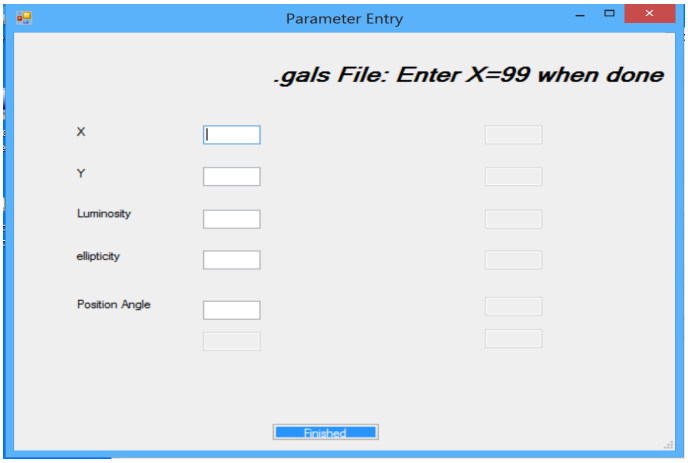

Figure 6.2: Parameter entry is greatly facilitated using a common parameter window, obviating the need to count columns as parameters are entered into labeled text boxes

Lens Model Input files

In this section, we discuss the model files for each of the four lens model codes implemented, focusing on aspects of the input file format important for the generation and translation of the model. Since HydraLens is concerned only with writing lens model files, there is no discussion of output from any of the software. In order to understand the scope of the models available

with each of the software packages implemented, it is important to review in some detail the design of each model and the commands available.

Lenstool

Lenstool (http://ascl.net/1102.004) was developed by Kneib, described in 1997 and has undergone several improvements to its algorithms [4]. It has been used in many studies in the literature, and uses a combination of light traces mass (LTM, previously known as 'parametric') and non-light traces mass (non-LTM, previously known as 'non-parametric') approaches. Lenstool is available for download as source code and has dependencies on several other software packages to build the software. It is accompanied by a User's Manual [9], and there is also a manual written by a third-party which is very useful [13]. Sample lens model input files are available for download.

The Lenstool command structure consists of first and second identifiers. The first identifiers are a group of 15 keywords that are basically groups, under which the second identifiers are stated along with values of the parameters. For each of the first identifiers, there is a group of specific second identifiers. Each second identifier is followed by parameters unique to that second identifier such as numerical flags or file names. Each model file does not necessarily contain all of the first identifiers.

The 15 first identifiers in Lenstool include: (Descriptions from the Lenstool Users manual [9])

i. runmode: Reference coordinates can be set (reference), images and arclets (image, arclet) can be defined with the name of input files, a source file (source) can be specified, as well as other second identifiers.

ii. grille: this defines parameters such as number of potential modes, grid mode, polar / rectangular shape of the grid, number of clumps that define the lens potential, and size of the grid.

iii. potentiel: Defines the gravitational potential. The profile used is identified by a number, and includes SIS, circular sphere, elliptical sphere, pseudo-elliptical, point mass, PIEMD, plane mass, and NFW profile. For the potential selected, the user specifies a position, ellipticity, angle, and z_{lens}. Each different mass model is defined by a numerical flag. Position, mass, ellipticity, velocity dispersion are also set here.

iv. limit: Defines constraints on the potential and is used for optimization.

v. potfile: Default parameters for galaxy scale mass components that account for perturbations to the cluster potential by the galaxies. This includes a filename of the galaxy catalog, mass profile (PIEMD is the default), velocity dispersion, r_{core}, r_{cut} among others.

vi. cline: Parameters to compute critical and caustic lines, including the location of the source plane, area to search for critical lines and step between searches.

vii. cosmologie: Specifies the value of constants such as Ω_m, Λ, H_0.

viii. champ: Define size of the field used in some calculations such as dimension of the grid

ix. grande: Define representation of the computer deformation of objects

x. observ: Define noise (seeing or Poisson) that is added to a gravitational image.

xi. source: Specifies details of the source, including z_{source}.

xii. image: Specifies the input data file (object file, with secondary parameter 'multfile') and characteristics of images, multiple images or arclets.

xiii. cleanlens: Define parameters to retrieve the shape of the source knowing a pixel-frame of the image

xiv. image: Define characteristics of images, multiple images or arclets

xv. fini: Tells Lenstool to stop reading the .par file. This is mandatory.

Lenstool also uses a group of input data files, including:

Object File A list of objects characterized by their position, shape and redshift with an integer identifier for each object and six parameters. This format is used for arclets or sources.

Marker File A list of marker points in the image plane, with an identifier and xy-coordinate for each.

IPX Pixel Image File IPX is a simple format for pixel-images data with a 4 line header.

FITS pixel image File This controls the reading of FITS pixel-frames.

A basic Lenstool model includes the model parameter file (.par file) with primary and secondary identifiers as well as an image file (.cat, in the format of an object file) to define the source images.

gravlens/lensmodel

Gravlens/lensmodel (http://ascl.net/1102.003) was developed by Keeton, and described in 2001 [8]. These two codes are similar, sharing the same command structure, except that lensmodel adds functionality to the Gravlens kernel. These use a LTM approach to lens models. A paper detailing the mathematics of the mass models in GRAVLENS is also available [7]. The GRAVLENS package is available for download as two executable files, and is accompanied by a User Manual [6]. The two executables include gravlens and lensmodel.

Sample data files are available for download. Basic commands include:

Set commands These are used to set the values of parameters such as Ω, Λ, z_{lens} and z_{source}. There are also a set of flags for gravlens regarding grid format, parity checking, source plane χ^2, tiling and others. In the main data entry screen these values are pre-populated with typical values.

Data This command specifies the name of the input data file to use.

Startup Specifies the number of galaxies for each mass model and the number of mass models, which is followed by a line to specify the mass model selected and the flags for parameters that will be optimized. Once the user selects a particular lens model, the parameters screen opens and the parameters specific to that model are listed with labeled text boxes for entry. Optimization flags are entered separately on the main GUI screen.

Commands Gravlens has many commands available for use. Some of them require entry of numerous parameters and some are standalone words. The commands allow optimization, varying parameters, data plotting, checking the code, and simple lensing calculations. Common commands are used to set the type of tiling (grid mode), compute the lensing properties on the specified grid (maketab), check the code (checkder, check mod), create plots of data (plotgrid, plotcrit), and perform simple lensing calculations (calcRein, finding).

The data file specifies the image data for the lens, including:

- Number of galaxies
- Position, R_{eff}, PA and e for each galaxy
- Number of sources
- Number of images for that source
- Location, flux, and time delays for each image as well as an identifier

A basic gravlens/lensmodel lens model consists of two files. The first is the input file, specifying parameters and data file name, the mass model to use with optimization parameters, and commands. The second file is the data file which specifies the data for each galaxy and source, as well the images for each of the sources. HydraLens facilitates the creation of both of these files with a GUI interface.

glafic

Glafic (http://ascl.net/1010.012) was developed by Oguri and described in 2010 [15]. It has been used in a wide range of studies, and is a LTM approach to strong gravitational lens models, using an adaptive mesh method with increased resolution near the critical curves. Glafic uses functional lens model optimizations with many options. It is available for download as an executable file, and is accompanied by a detailed User Manual [16]. Sample lens models are available for download as well. The structure of glafic is somewhat close in appearance to gravlens. A glafic input file has three parts. The first part sets the values of various parameters such as Ω_m and Λ. The second part defines the lenses, extended sources and point sources. The third part is the list of commands. There is an optional section to define optimizations.

Parameter settings in glafic:

Primary parameters Each of the primary parameters is associated with a flag, file name, etc. These include Ω, Λ, H_0, z_{lens}, output file name, rectangular region of the lens plane, pixel size for extended sources and point sources, and adaptive meshing recursion level.

Secondary parameters These include the name of the gals data file, the extended source model arcs file, seed for random number generation, and a number of other parameters and flags that control the behavior of glafic.

Definition of lenses, extended sources and point sources in glafic:

lenses There are 21 different lens mass models in glafic. Each is stored with its name and up to eight parameters. A single lens plane is supported. Most are characterized by a mass scale, x and y coordinates, ellipticity and position angle, and other parameters as needed for the specific mass model.

extended sources There are five different extended source types, each of which has up to 8 parameters, including source redshift, coordinates and up to 5 other parameters as indicated.

point sources Point sources are stored only as redshift with x and y coordinates.

Glafic uses a number of secondary files as data for the model, including a galaxy file (galfile.dat), a source file (srcfile.dat), an observation file (obs), and a priors file (prior). Each of these is saved simply as strings based on how many parameters are used in each line.

Data files used by glafic include:

obs file File with data of an image of lensed arcs read with command readobs_point or readobs_extend (for point sources, extended sources)

gals file Mass model gals data file (galfile.dat) contains coordinates, luminosity, ellipticity and position angle of each galaxy

src file Data file used to enter extended source model arcs (srcfile.dat)

prior file List of priors on parameters, read by 'parprior' command

flux file Read with the command 'point_flux', this file contains fluxes for point sources

mask file Optional file read by 'readobs_extend'

sigma file A list of σ values for Markov-Chain Monte Carlo optimization, read by 'mcmc_sigma'

Optimization Commands in glafic:

Preparation read an image of lensed arcs from a file, calculate noise from observed image, read data file for point source optimization, read text file of priors

Setting optimization parameters Perform model optimization, randomize optimization parameters, calculate a one dimensional χ^2 slice, vary cosmological parameters.

Commands in glafic:

Lens properties Compute various lensing properties for an image, compute Einstein radii for a source redshift, compute mass, write lensing properties to an output file, compute convergences

Extended sources Write images of lensed extended sources to an output file, calculate total flux, peak count and peak location, and write time delay surfaces

Point sources Find lensed images for point sources, move source position, compute critical curves and caustics, write mesh pattern, and write time delay surfaces

Other Commands Other commands are available for composite sources, morsel optimization, and other optimization commands.

Utilities available in glafic:

Markov-Chain Monte-Carlo Read a list of σ values for model parameters, perform MCMC calculations, read a resulting chain file. Needs a file of σ values.

General Utility functions Change a parameter value, change optimization flags, moving lens positions, print model parameters or optimization flags, and compute a physical critical surface mass density

A basic glafic lens model includes a parameter / command file (.input) and an image (obs) file.

PixeLens

PixeLens (http://ascl.net/1102.007) was developed by Saha and described in 2006 [19]. PixeLens is a non-LTM lens model code, and is written in Java which is downloaded as a .jar file and run locally [18]. It is accompanied by explanatory documentation as well as a tutorial explaining the details of the input file [17]. Sample model files are available on the website. The model files for Pixelens are the simplest among the four codes implemented in HydraLens. Model input can be done through a GUI or through the command line as a batch file that is called when Pixelens in invoked through Java. The model consists of a group of constants and image data.

Constants Pixelens requires an object name, the radius of the mass map in pixels and z_{lens} and z_{source} to be specified. Optionally, one can specify the map symmetry, radius of the mass amp, shear, number of models, Hubble time, minimum steepness, maximum steepness, annular density and cosmological parameters such as Ω_m and Ω_Λ.

Image Data Images are given in double or quad format. For each image, one specifies the x and y coordinates as well as the time delay. The redshifts are specified in the first section above. Images must be listed in arrival time order. There is also a 'multi' format used for cluster lenses, useful if there are several source redshifts, or if the image is not a double or quad image.

A PixeLens model can be entered directly into the Java GUI, or saved as a single text file which contains all the information. HydraLens generates the text file for input to the Java applet.

6.4 Implementation

When HydraLens is started, the user is presented with an input screen (see Figure 6.3) to define the name of the model, the directory to store the model and then select the target software from available choices. After selecting the type of model to generate, the user is brought to screens specific for each model.

Lens Model Generation

Lenstool

The user first generates any accessory files needed including image file, source file or arclet file. Selecting a button for each file type brings the user to a special screen to build that file type. Upon return to the main model entry screen, the user is presented with detailed entry panels for each of seven commonly used primary parameters in Lenstool, including runmode, grille, potential, limit, cosmologie, image and source. The entry panel for each primary identifier is pre-populated with commonly used values, and parameters are selected using check boxes. When the 'finished' button is pressed, the final lens model is created in the directory selected by the user in the initial screen.

gravlens/lensmodel

HydraLens creates the model file (.input), starting with setting the basic parameter which are on the main gravlens screen pre-populated with typical values. After finalizing the primary

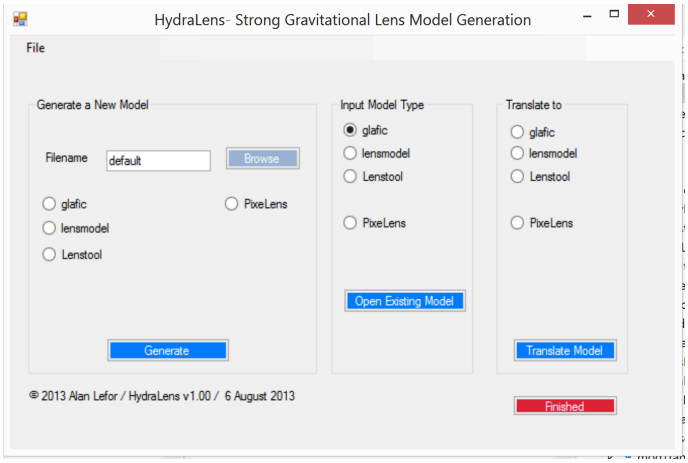

Figure 6.3: The opening screen allows the user to choose to generate a new model, read in an existing model, and translate a model

parameters, that part of the window becomes invisible, leading the user to enter secondary parameters. The user then specifies secondary parameters as desired. Last, the desired commands are entered from a scrolled list of available commands. The resulting model file has four sections, including primary parameters, secondary parameters, models / optimizations and commands. The 'data' command loads the data from a specified file. Once the data command is entered, a button appears on the screen to allow entry of the data file containing the information for each lens galaxy, source, and images for that source. The data file is written, including appropriate comment lines.

glafic

After selecting a glafic model, the user selects the type of file to generate (Main model, gals, obs, priors or source) and then goes to a screen specific for that file type. The main model file has a panel for the primary and secondary parameters. Lens models with extended sources and points sources are constructed next followed by entry of desired commands. All available commands are divided into basic calculations, sources, optimization and utilities and selected from lists on the screen.

PixeLens

After selecting a PixeLens model, the user is brought to the PixeLens screen (see Figure 6.4). The values of required and optional parameters are entered on the left and mage data is entered on the right. Note that the 'action' buttons in the middle and right panels are 'grayed out'. These buttons become active as the user finishes each portion of building the model, to lead them through each step of the process. When the 'Finished' (red, lower right) is pressed, the model is written to the file.

Completion

After going through the software specific screens to generate the model, the user is informed that the file has been written and is then brought back to the main screen. At this point the

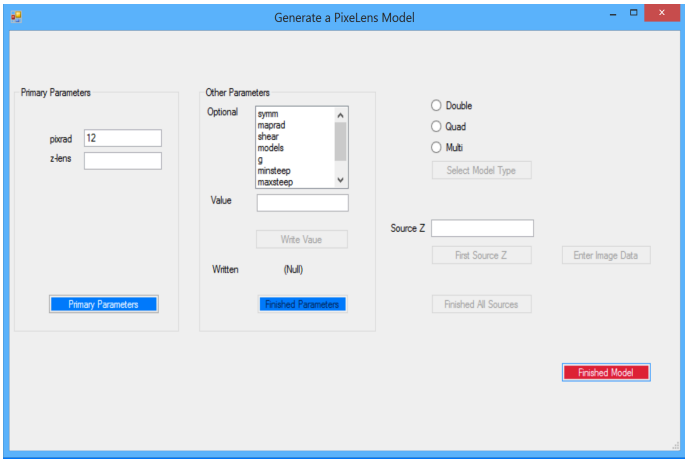

Figure 6.4: The PixeLens model generation entry screen

user's only choice is to stop, having generated the model, or to translate it into one of the other three model types.

Lens Model Translation

The process of translation is performed with no user interaction. After generating a model or specifying the file path to an existing model, and returning to the main HydraLens window, the user selects the software target for translation. The software generates a new model, with an appropriate file name extension and returns to the main HydraLens window so the user can exit. There are four model types supported in HydraLens, so there are 12 different translation modules. Each translation module reads the model that the user just generated from the data structure for that model, translates the parameters and puts them in the data structure for the target model type, then calls the model write routine to write new target model file from the data structure.

As an example of using HydraLens for translation, a simple model can be easily written and tested in PixeLens, as a way of "rapid prototyping". This simple model can then be translated to models for Lenstool, Lensmodel and glafic in a matter of minutes. The models generated will be functional, but may need modification since many features in glafic, for example, do not exist in PixeLens such as optimizations. The user must then edit the glafic model to set the optimization parameters as desired. In most cases, this is still much faster and simpler than starting with an empty screen in a basic text editing program. Similarly, translation to PixeLens will often result in a simpler model than the original. Another example of information that cannot be translated relates to specific limitations of the codes. In Lenstool, each potential can have its own lens plane, while in the other three codes, only one lens plane is permitted. Thus, translating from Lenstool with such a model necessarily will not include the multiple lens planes.

It is not possible to transfer all data and/or commands from one type of model to another because of differences in the requirements of each model code. Despite the possible loss of information, the models produced by HydraLens will generally work, and then may need minor modifications to allow for differences in the lens model codes.

Another difficulty associated with translation is the differences in commands used by the

various codes. For example, glafic will calculate the Einstein radius and mass inside the Einstein radius for a Single Isothermal Ellipsoid model by ignoring the ellipticity. Lensmodel generates an error message when one tries to calculate the Einstein radius for a Single Isothermal Ellipsoid model. Due to the wide range of commands, HydraLens does not translate commands, but rather gives each model a standard group of functioning commands that can be modified by the user.

The model translation feature offers two important advantages over writing a model using a text editor. First, when creating a new type of model, the image coordinates are easily transferred into the target model, without concern for typing long lists of numbers and counting columns of parameters with proper formatting of the image files. Second, an input file is created with many of the important fields already populated. A minor review of the resulting input file may be necessary, but based on testing to date, the models created will be functional in the target software.

6.5 Discussion

HydraLens facilitates creation of strong gravitational lens models for more than one lens model code, in order to facilitate direct comparison studies of strong gravitational lens models. In view of the paucity of direct comparative studies in the literature [11; 12], HydraLens may help increase the number of future comparative studies by simplifying the process of model development. Additionally, HydraLens may serve an important role in education where students are just starting to use strong gravitational lens modeling codes . HydraLens allows students to easily explore a number of available software packages. The study of strong gravitational lensing is no longer limited to investigators, but has now extended to being a part of the curriculum in some undergraduate and graduate programs [5; 20], as well as being taught to students in specialized intensive education programs [3]. The use of lens model software by students may be enhanced by using a tool such as HydraLens to facilitate the writing of lens model input files.

The use of HydraLens, by both investigators to facilitate comparative studies and by students to use the available software in their studies, is enhanced by the two main functions of HydraLens including lens model file generation and lens model file translation.

Limitations

The major limitation of HydraLens is that it is subject to the unbreakable rule of computing, "garbage-in, garbage-out". HydraLens cannot write a model in the absence of appropriate input data, and for this reason is referred to as computer-assisted model generation rather than "automatic" model generation. A person totally naive to lens models will not necessarily benefit from HydraLens, without some guidance. Similarly, a person who is an expert at writing lens models for a particular software may not benefit from HydraLens. The people most likely to find HydraLens of value are those who have begun to write lens models and have some minimal level of experience, or people who are capable with one model software and want to begin using another to conduct direct comparison studies.

The software described herein is functional and available, and facilitates the writing of lens model files for a variety of available strong gravitational lens model software. For the purpose of writing lens models, HydraLens could be viewed as a specialized text editor. In this role, its major advantage is that the user will rarely need to refer to a reference source for the meaning of most parameters as they are clearly described in the GUI at the time of entry. The input files for lens model software uses simple text files. When writing a model using only a text editor,

the user must be very careful about values of flags and parameters, which requires constant reference to users' manuals. HydraLens greatly simplifies that task by entering all fields using a GUI, but the models generated may require some editing. There is no substitute for scientific insight when writing a gravitational lens model.

In its role as lens model translation software, HydraLens may not always construct a perfect model. Another limitation of model translation is that features vary greatly from one lens model software to another, so that translation may necessitate the loss of some information or capabilities. For example, glafic accepts data on image flux which is not included in Lenstool models. The model created by HydraLens serves as a starting point and eliminates the need for starting the process with a blank piece of paper. Translated models from HydraLens greatly simplifies the tedium of writing an initial model file, especially in regard to image geometry. Generated models are easily edited since they are all simple text files.

6.6 Future Development and Conclusions

Further Development

HydraLens is undergoing further development, especially to improve internal consistency checking within the model. Due to its modular nature, other strong gravitational lens model codes are being built into the system to expand its repertoire of models to generate and translate. These features are being added, and will be included in future releases.

Conclusions

Previous reviews have shown that there are few comparative studies of strong gravitational lens models in the existing literature [12], yet such comparisons are very important to advance the field. Furthermore, given the differences in results from various strong gravitational lens model codes, such comparitive studies are of great importance [11].

Barriers to comparative studies include the lack of availability of some software, and the heterogeneity of the input files used in model codes which are available. HydraLens allows the user to enter a lens model with an easy-to-follow GUI rather than entering a tedious text file, for four commonly used strong gravitational lens modeling codes, all of which are freely available for download. Furthermore, HydraLens is capable of translating the data files among the four model codes implemented to allow rapid development and testing of other models for comparison. These features may serve to facilitate direct comparison studies, and also to enhance the educational application of strong gravitational lens model software. Further development is already underway to provide more features and improve the usability of HydraLens.

References

[1] F Alfaro. Keetons interface. http://cinespa.ucr.ac.cr/software/xfgl/index.html, February 2008. 230

[2] Daniel Coe. *Towards an understanding of dark matter: Precise gravitational lensing analysis complemented by robust photometric redshifts*. PhD thesis, Johns Hopkins Univ, 2007. 229

[3] E Gradolph. Canary islands winter school of astrophysics. http://www.iac.es/winterschool/2012/, January 2012. 240

[4] E. Jullo, J.-P. Kneib, M. Limousin, Á. Elíasdóttir, P. J. Marshall, and T. Verdugo. A Bayesian approach to strong lensing modelling of galaxy clusters. *New Journal of Physics*, **9**:447, December 2007. 233

[5] P Kalas. Lab 6 gravitational lensing. http://astro.berkeley.edu/~kalas/labs/documents/ay122_lab6_v2.pdf, November 2010. 240

[6] C Keeton. Software for gravitational lensing. http://redfive.rutgers.edu/~keeton/gravlens/, January 2004. 234

[7] C. R. Keeton. A Catalog of Mass Models for Gravitational Lensing. *ArXiv Astrophysics e-prints*, February 2001. 234

[8] C. R. Keeton. Computational Methods for Gravitational Lensing. *ArXiv Astrophysics e-prints*, February 2001. 234

[9] J-P Kneib. Lenstool project web page. http://lamwws.oamp.fr/lenstool/, May 2012. 233

[10] A. T. Lefor. Comparison of Strong Gravitational Lens Model Software II. HydraLens: Computer Assisted Generation of Lens Models. *Astronomy and Computing*, **5**:28–34, August 2014. 229

[11] A. T. Lefor and T. Futamase. Comparison of Strong Gravitational Lens Model Software I. Time delay and mass calculations are sensitive to changes in redshift and are model dependent. *ArXiv e-prints*, July 2013. 230, 240, 241

[12] A. T. Lefor, T. Futamase, and M. Akhlaghi. A Systematic Review of Strong Gravitational Lens Modeling Software. *ArXiv e-prints*, June 2012. 229, 240, 241

[13] M McCourt. Lenstool for dummies. http://www.oamp.fr/cosmology/lenstool/, October 2006. 233

[14] L. Moustakas and J. Brownstein. The orphan lens project. http://www.masterlens.astro.utah.edu, February 2013. 230

[15] M. Oguri. The Mass Distribution of SDSS J1004+4112 Revisited. *Proceedings Astr Soc Japan*, **62**:1017–, August 2010. 235

[16] M Oguri. glafic user's manual. http://www.slac.stanford.edu/oguri/glafic/, June 2013. 235

[17] J Read. Pixelens tutorial. http://www.itp.uzh.ch/~justin/Astro/Lectures/PixeLens/tutorial.pdf, September 2012. 237

[18] J Read. Pixelens web page. http://www.qgd.uzh.ch/projects/pixelens/, May 2012. 237

[19] P. Saha, J. I. Read, and L. L. R. Williams. Two Strong-Lensing Clusters Confront Universal Dark Matter Profiles. *ApJ Letters*, **652**:L5–L8, November 2006. 237

[20] S Seitz. Astrophysics lab: Strong gravitational lensing. http://www.usm.uni-muenchen.de/people/stella/praktikum/linsen/sl_english.pdf, July 2013. 240

[21] L. Shamir, J. F. Wallin, A. Allen, B. Berriman, P. Teuben, R. J. Nemiroff, J. Mink, R. J. Hanisch, and K. DuPrie. Practices in source code sharing in astrophysics. *ArXiv e-prints*, April 2013. 230

Chapter 7

A direct, semi-independent comparative study of four strong gravitational lenses: SDSS J1320+1644, COSMOS J095930+023427, SDSSJ1430, and J1000+0021

7.1 Purpose and Organization of this Chapter

The goal of this study is to directly compare the results of calculations among four model software codes in the evaluation of four lens systems, as a follow-up to the work presented in Chapter 5. [1] The present study has several unique features. This study is the first to use computer-aided lens model design, using HydraLens software (Chapter 6) to facilitate lens model generation.There are no previous single studies which compare the results for multiple lens systems using multiple lens model software. This study was designed to further evaluate comparative lens model analyses and includes both direct and indirect semi-independent studies of four lens systems using four different software models. Other studies have included indirect comparisons to previous lens model analyses, or direct comparisons of several lens models of a single lens system. This is the first study to also include combined indirect and direct analyses where previously published lens models were used for direct comparisons.

The two objects studied in Chapter 5 were evaluated with four software lens models. The results of each model were compared, specifically looking at time delays and lens mass. The study in this chapter was designed to evaluate four known lensing objects with each of four software models, specifically looking at best-fit lens parameters. There is no attempt to optimize the model for each lens model software used. Rather, we sought to use nearly identical software models and compare the results.

The nomenclature of lens model comparison studies, lens systems studied, previous lens

[1] The results in this chapter have been submitted to *The Astrophysical Journal*

model studies of these systems and the lens model software used are described in section §7.3. The results of the lens model studies for each of the four systems studied are presented in section §7.4 and a review of existing comparison studies along with the results of this study are presented in §7.5. Conclusions and suggestions for future lens model studies are in section §7.6.

7.2 Introduction

The present time has been referred to as the "Golden Age" of Precision Cosmology. Strong gravitational lensing data is a rich source of information about the structure and dynamics of the universe, and these data are contributing significantly to this notion of precision cosmology. Strong gravitational lens studies are highly dependent on the software used to create the models and analyze the components such as lens mass, Einstein radius, time delays etc. A comprehensive review of available software has been conducted by [19] (see also Chapter 4). While many such software packages are available, most studies utilize only a single software package for analysis. Furthermore, most authors of strong gravitational lensing studies use their own software only.

More recently, the status of comparison studies of strong gravitational lens models has been reviewed by [18] (see also Chapter 5). This study demonstrated that changes in redshift affect time delay and mass calculations in a model dependent fashion, with variable results with small changes in redshift for the same models.

An important resource for the conduct of comparison studies is the Orphan Lens Project, a compendium of information about strong lens systems that as of May 2014 contained data for 656 lens systems [22]. There are a number of barriers to the conduct of lens model comparisons. Ideally, a comparison study of a previously studied lens would include the original model for comparison, but this is sometimes impossible because the lens model code is not made publicly available. Another barrier to performing comparative studies is the complexity of the lens model files, since there are major differences among the commonly used model software available. In order to facilitate this step of the process the HydraLens program was developed to generate model files for multiple strong gravitational lens model packages [17] (see also Chapter 6).

To date, the largest comparison study of strong gravitational lens models was an analysis of MACSJ1206.2-0847 as part of the CLASH survey conducted by [32]. This study included four different strong gravitational lens models including Lenstool ([9]), PixeLens ([30]), LensPerfect ([3]) and SaWLens ([21]). The authors conducted five lens model analyses using the same data, and is thus categorized as a direct and semi-independent study. This type of study has great advantages in that all data and all models are available for direct comparison in a single study.

The Hubble Space Telescope (HST) Frontier Fields project is reporting preliminary results [1] [16]. This important deep field observing program will combine the power of the HST with gravitational lenses. Lens models in the Frontier Fields project will include models from a number of software codes including ZB, GRALE, Lenstool, and two other non-LTM lens model software codes which will facilitate direct comparison of results from a number of lens models rather than depending on a single model from which to draw conclusions.

[1] http://www.stsci.edu/hst/campaigns/frontier-fields/Lensing-Models

7.3 Methods

Nomenclature

The use of standardized nomenclature to describe lensing studies is useful to evaluate multiple studies. In this chapter we follow the nomenclature previously described [18]. Lens model comparison studies are referred to as direct when the comparison is made based on calculations using two software models in the same paper, and indirect when comparison is made to previously published data. In this study, we also use the actual models from published studies (kindly supplied by the investigators) so these are considered combined indirect/direct comparisons. Lens model comparisons using the same data are referred to as semi-independent, and when different data is used, the comparison is independent. Lastly, software is classified as Light Traces Mass (LTM, formerly known as parametric), or non Light Traces Mass (non-LTM, formerly known as non-parametric).

Lens Model Preparation

Each lens model software package uses a different input data format to describe the lens model. All of them use simple text files as input, but the format of the text files, available functionality and command structures are dependent on the particular software. Some lens model software uses multiple accessory files to provide other data. Each of them has a unique list of commands, with great variability. HydraLens [17] (Chapter 6 and Appendix A) [1] was written to simplify the process of creating lens model input files to facilitate direct comparison studies, and to assist those starting in the field.

The four lens systems were evaluated using four lens model codes, necessitating 16 different models. The Lenstool model for COSMOS J095930+023427 was kindly provided by Cao [2]. The glafic model for SDSS J1320+1644 was kindly provided by Rusu [29]. The remaining 14 models were written for this study using HydraLens. In the case of COSMOS J095930+023427 and SDSS J1320+1644, the two lens models we received from other investigators were used as input to HydraLens which generated the models for the other three software packages used in this study. In the case of SDSS J1430+4105 and J1000+0021, models were first written for PixelLens [2]. HydraLens was then used to translate the PixeLens model into the format for the other strong gravitational lens model software, including Lenstool [3], Lensmodel [4] and glafic [5]. The translated files output from HydraLens were edited to assure that parameters were fixed or free as appropriate, and that optimization parameters were correctly set. The lens model files were then used as input to the respective lens model software.

Gravitational Lenses Studied

The parameters used for the four lens systems was obtained from previous studies. The geometry for each system was identical in all four models evaluated, and therefore all studies conducted are classified as semi-independent lens analyses. Three of the lens systems studied are listed in the Orphan Lens Database [22] including COSMOS J095930+023427, SDSS J1320+1644 and SDSSJ1430+4105.

[1] http://ascl.net/1402.023
[2] http://ascl.net/1102.007
[3] http://ascl.net/1102.004
[4] http://ascl.net/1102.003
[5] http://ascl.net/1010.012

COSMOS J095930+023427

The lens COSMOS J095930 was first described by Jackson [7]. COSMOS J095930 is an early-type galaxy with four bright images of a distant background source. It is located at z_{lens}=0.892, and the background source is estimated at z_{source}=2.00. While the exact z_{source} is unknown, the value used by previous investigators is 2.00.

Models of this system were described by Faure using Lenstool [5]. This model used a Singular Isothermal Ellipsoid (SIE) with external shear ($+\gamma$) and found an Einstein radius of 0.79" and σ_V=255 km s^{-1}.

More recently, an extensive multi-wavelength study of this system was reported by Cao and colleagues [2], also using Lenstool. This analysis used four different models, an SIE with two Singular Isothermal Spheres (SIS) as well as a Pseudo-Isothermal Elliptical Mass Distribution (PIEMD) model with two SIS, both with and without external shear [10]. We selected the SIE+SIS+SIS model used by Cao as the basis of the present indirect comparison with their work as well as the direct comparisons with the four lens models studied here.

The Lenstool model developed by Cao and coworkers was kindly supplied for this study and used as a baseline model which was then translated into input files for the other software by HydraLens. The Lenstool model used by Cao included priors for the values of ellipticity ($\epsilon = [0.0, 0.9]$) and position angle (PA= [-90,90] for the SIE potential) and for the velocity dispersion ($\sigma = [100, 1000]$ for all three potentials). These same priors were used in the models of COSMOS J095930 for Lensmodel and glafic in this study. The Lenstool model developed by Cao uses optimization in the source plane.

The Lenstool model developed by Cao has five free parameters including the velocity dispersion of the three galaxies, and orientation and ellipticity of the SIE galaxy. The positions of the second and third galaxies (SIS) in the model were fixed. The models used here were similarly parameterized.

The present study is an indirect comparison with the analysis of Cao [2] as well as a direct comparison of the four lens models studied. Since we were provided the model used by Cao, it is a combined indirect/direct comparative analysis of COSMOS J095930. All four models of this system used a $\Omega_m = 0.3$, $\Omega_\Lambda = 0.7$, $H_0 = 70$ km s^{-1} cosmology, as was used by [2].

SDSS J1320+1644

SDSSJ1320+1644 was initially described by [25] and [6], and is a large separation lensed quasar candidate identified in the SDSS, with a separation of 8″.585 ±0″.002 at z_{source}=1.487 [29]. Both an elliptical and disk-like galaxy were identified almost symmetrically between the quasars at redshift z_{lens}=0.899.

A detailed lens model analysis of this system was conducted by Rusu and colleagues [29], using glafic software. Based on their analysis, they conclude that SDSSJ1320+1644 is a probable gravitationally lensed quasar, and if it is, this would be the largest separation two-imaged lensed quasar known. They show that the gravitational lens hypothesis implies that the galaxies are not isolated, but are embedded in a dark matter halo, using an NFW model and an SIS model. The SIS model has a σ_V=645±25 km s^{-1}. We use the 'SIS free' model as the basis of the comparison study, as defined by Rusu [29], which models the three galaxies (referred to as G1, G2 and G4) as SIS potentials and leaves the position of the dark matter halo (also modeled as a SIS) as a free parameter. The model used by Rusu includes priors for the velocity dispersion of the dark matter halo ($\sigma = [400, 800]$). The same priors were used in the models of SDSS J1320+1644 in this study. The analysis by Rusu uses optimization by glafic in the image plane.

Rusu considers models with 0 degrees of freedom, including 14 nominal constraints and the same number of nominal parameters, which fit with $\chi^2 << 1$. The ellipticity and position

angle are used when the position of the dark matter halo is fixed. The models developed for this study were similarly parameterized using the position of the dark matter halo as a free parameter ("SIS-free") and fixed to introduce ellipticity and position angle.

A number of glafic models developed by Rusu and coworkers were kindly supplied for this comparative analysis and used as a baseline model which was then translated by HydraLens into models for the other software. The present study includes an indirect comparison with the analysis of Rusu [29] as well as a direct comparison of the four software lens models studied. Since we were provided a model used by Rusu, this is a combined indirect/direct comparative analysis of SDSSJ1320+1644. All four models of this system used a $\Omega_m = 0.27$, $\Omega_\Lambda = 0.73$, $H_0 = 70$ km s^{-1} cosmology, as was used by [29].

SDSS J1430+4105

SDSS1430+4105 was first described by [1] as part of the SLACS survey. This system is at redshift z_{lens}=0.285 with z_{source}=0.575, and has a complex morphology with several subcomponents as described by [4]. Bolton reported an effective radius of 2.55" and a σ_{SDSS}=322 km s^{-1}.

A very detailed lens model analysis of this system was then conducted by [4]. This analysis was a direct, semi-independent comparative analysis using both Gravlens (LTM) and Lensview (non-LTM) software. The authors studied five different models using Gravlens/Lensmodel, including an SIE and a Power Law (PL) model as well as three two-component de Vaucouleurs plus dark matter models. Similar results were found with the two different lens model analyses. They also studied four models using Lensview [35] including an SIE and PL models with and without external shear. We use the Gravlens/Lensmodel SIE model as the basis of the indirect comparison with their work. The plane of optimization used in the Eichner model is not explicitly stated in the report [4].

The models developed in the previous study were not available, and thus all models used were written for this study. The results referred to as Model I by Eichner did not use any priors in the lens model for SDSS J1430+4105, although priors were used in the development of the model with results within the error limits reported. Similarly, priors were not used in the models in this study. The free parameters used by Eichner et al included the lensing strength b, the ellipticity and the orientation of the single-component SIE lens. These same free parameters were used in the models developed for this study.

This is both an indirect comparison (compared with the SIE model in the published study of [4]) and direct comparisons of the four lens models studied here. All four models of this system used a $\Omega_m = 0.3$, $\Omega_\Lambda = 0.7$, $H_0 = 70$ km s^{-1} cosmology, as was used by [4].

J1000+0021

Using imaging data from CANDELS and the large binocular telescope, van der Wel and colleagues recently reported the quadruple galaxy-galaxy lens J100018.47+022138.74 (J1000+0221), which is the first strong galaxy lens at $z_{lens} > 1$ [34]. This interesting system has a z_{lens}=1.53 and a z_{source}=3.417.

In the paper [34], the system was analyzed in the manner described by [33]. They reported an Einstein radius of $R_E = 0.35$" with an enclosed mass of $M_E = (7.6 \pm 0.5) \times 10^{10}\ M_\odot$ with an upper limit on the dark matter fraction of 60%. The highly magnified (40×) source galaxy has a very small stellar mass ($\sim 10^8\ M_\odot$). The $z = 1.53$ lens is a flattened, quiescent galaxy with a stellar mass of $\sim 6 \times 10^{10}\ M_\odot$.

There have been no other lens model analyses of this system using software models and therefore all models were developed for this study using data from [34], and is thus is a direct

comparison of the four lens software models studied. There were no priors used in the lens models of J1000+0021 in this study. The free parameter in the SIS models was only the velocity dispersion. In the SIE models, free parameters included the velocity dispersion, orientation and ellipticity.

All four models of this system used a $\Omega_m = 0.3$, $\Omega_\Lambda = 0.7$, $H_0 = 70$ km s^{-1} cosmology.

Lens Models

The analyses in this study were performed with four strong gravitational lens model software packages that have been used extensively in the literature. All four systems were modeled with all four lens model software packages. Lenstool and Lensmodel were executed under Scientific Linux version 6.4 (except as noted for Lensmodel in section §7.4), and PixeLens and glafic were executed under OS/X version 10.9. All of these lens model software codes were reviewed in the Orphan Lens Project and the descriptions of the software are from the web site [22] as well as from a review of lens model software [19].

Error calculations were performed according to the method of Rusu et al [29]. The errors quoted for the calculated parameters (ellipticity, orientation, magnification, time delay, etc.) reflect the calculations corresponding to calculations within the 1σ confidence interval for velocity dispersions.

The fit of the models is assessed by χ^2 optimization and the RMS uncertainty. The RMS is calculated by:

$$RMS^2_{images} = \sum_i ((x_i^{'} - x_i)^2 + (y_i^{'} - y_i)^2) \ / \ N_{images}, \tag{7.1}$$

where $x_i^{'}$ and $y_i^{'}$ are the locations given by the model, and x_i and y_i are the real images location, and the sum is over all N_{images} images. The χ^2 results are calculated for the models by Lenstool, Lensmodel and glafic, and are reported in the data tables. The RMS value is reported by Lenstool directly, while a manual calculation was necessary for models using Lensmodel and glafic.

PixeLens

PixeLens is a non-LTM strong gravitational lens model software that is available for download [4] as a Java program which runs in a browser window [30]. Version 2.7 was used in these studies. PixeLens is accompanied by a manual [27] and a tutorial [28]. PixeLens reconstructs a pixelated mass map for the lens in terms of the arrival time surface and has been used in several studies [30].

PixeLens employs a built-in MCMC approach and creates an ensemble of 100 lens models per given image configuration. The pixelated mass map offers the advantage of being linear in the unknown. Since all equations are linear in the unknowns, the best-fitting model and its uncertainties are obtained by averaging over the ensemble [15; 30].The pixelated mass map differentiates PixeLens from the other software used in this study which fit parametric functional forms.

Lenstool

Lenstool has been used in many different studies and is available for download [5] [9]. Version 6.7.1 was used in these studies. Lenstool has features of both LTM and non-LTM modeling and uses a Bayesian approach to strong lens modeling and has been well-described in the literature [8; 9]. There are several resources available for writing lens models for Lenstool [14; 20].

Lenstool can optimize most of the parameters in a model. Models produced by HydraLens for Lenstool were modified slightly to add appropriate optimization parameters and then used with Lenstool. Lenstool optimization is performed with MCMC, and χ^2 optimization for all models was conducted in the source plane. Lenstool uses the geometry of the images given and then finds counter-images. The image positions are recomputed and the time delays determined.

Gravlens

The Gravlens package includes two codes, Gravlens and Lensmodel [13] accompanied by a user manual [11]. Version 1.99o was used in these studies, under the Linux operating system, downloaded from the Astrophysics Source Code Library [6]. However, the Darwin (Macintosh) executable file provided for version 1.99o will only run on the now obsolete PowerPC architecture. A newer version to run on the Macintosh platform under OS/X 10.9 (Gravlens version dated November 2012) was kindly provided by Professor Keeton, for these studies. Lensmodel is an extension of Gravlens and was used for all analyses here. It is fully described in two publications by Keeton [12; 13], and has been used extensively.

Lensmodel is an LTM lens model software, which optimizes the selected lens parameters and uses a tiling algorithm and a simplex method with a polar grid centered on the main galaxy. The tiles are used to determine the image positions, and then uses a recursive sub-gridding algorithm to more accurately determine image positions. Optimization for all models in this study were conducted in the source plane.

glafic

Glafic is an LTM lens model software, and includes computation of lensed images for both point and extended sources, handling of multiple sources, a wide variety of lens potentials and a technique for mass modeling [23] with multiple component mass models. Version 1.1.5 was used on the OS/X platform and version 1.1.6 was used with Linux in these studies[7].

Each lens is defined by the lens model and seven parameters. A large catalog of lens models is available (including point mass, Hernquist, NFW, Einsato, Sersic, etc.). After defining the parameters and the lens models, parameters to be varied in the χ^2 minimizations are specified. Following this, the desired commands are issued such as computing various lensing properties, Einstein radius, write lensing properties to a FITS file, etc [24]. Glafic has been used in a large number of lens model studies, including SDSSJ1004 [23], and performs lens model optimization.

Glafic uses a downhill simplex method of optimization, and all models in this study were optimized in the source plane. The image plane is divided using square grids by an adaptive meshing algorithm. The level of adaptive meshing is set as an optional parameter.

7.4 Results

Each of the four lens systems was modeled with all four lens model software codes including PixeLens, Lenstool, Lensmodel, and glafic. Best-fit lens model parameters from previous studies are presented along with the results from this study for each system. The results reported for each lens were intended to follow the format of the data for best-fit lens parameters as reported in previous studies, and therefore there are some differences in the data presented for the four lens systems. Lenstool and glafic directly calculate the velocity dispersion and then calculate the Einstein radius and mass within the Einstein radius. Lensmodel directly calculates the Einstein radius, from which the other values were deduced. PixeLens calculates mass at various distances from the lens mass.

COSMOS J095930+023427

Best-fit lens model parameters for COSMOS J095930+023427 are shown in Figure 7.1 (Table 1). The data reported in [2] are at the upper portion of the table, and show the results of the Lenstool model. The results in this study using the Lenstool model are somewhat different because the model in this study used optimization in the image plane, rather than the source plane optimization used by Cao. The glafic model was also conducted with optimization in the image plane, while the Lensmodel model is conducted with source plane optimization because image plane optimization did not yield a satisfactory model. Direct comparisons of the four software models evaluated are shown next. The models used here were based on the SIE+SIS+SIS model used by [2]. The Lenstool model includes an SIE potential at z_{lens}=0.892, and two SIS potentials at z_{lens}=0.7, as described by [2].

The PixeLens model used image coordinates from [2], and calculated an enclosed mass inside the Einstein radius very close to that calculated by the Lenstool model. The Lenstool model optimized the ellipticity, position angle and velocity dispersion for the single SIE potential, and only the velocity dispersion for the two SIS potentials, as done by [2] as free parameters. The Lensmodel model sets all three lens potentials at z_{lens}=0.892 because the software does not permit multiple lens planes. The ellipticities and position angles optimized by each of the three codes are quite different.

The Einstein radius of the SIE potentials are similar while there is some difference in the optimized velocity dispersions calculated by the three codes, particularly in the values calculated by glafic for the second potential. In an effort to understand this, the velocity dispersions of the first and second potentials were fixed at the values calculated by Lenstool at 238 and 391 km s^{-1} respectively and the velocity dispersion of the third potential allowed to optimize, using glafic. This resulted in a velocity dispersion of 634 km s^{-1} for the third potential. When the first and third values were fixed at 238 and 603 km s^{-1}, the second potential was optimized at 56.7 km s^{-1}. Magnifications and time delays for this model are shown in Figure 7.2 (Table 2). Both time delays and magnifications calculated by all four models show great variability.

The velocity dispersions shown in Figure 7.1 (Table 1) as calculated here are slightly different from those reported by [2], because of the different optimization technique. The velocity dispersions shown in Figure 7.1 (Table 1) as calculated here are exactly the same as those reported by [2], which is expected since the model file was identical. The velocity dispersion values shown for the Lensmodel and glafic models are somewhat different. The Lenstool model used by Cao [2] defined potentials at z_{lens}=0.892 and 0.7, although Lenstool allows only a single lens plane [14]. When the results were re-calculated defining all lenses in the same plane (z_{lens} = 0.892) using Lenstool, there was no effect on the calculation of the velocity dispersion. The wide variation in time delays calculated for this system are shown in Figure 7.2 (Table 2), and are consistent with the wide range in time delays reported in our previous study using different models [18]. There is a wide disparity in time delay calculations seen in all of the systems evaluated in this study.

The image planes for the four models are shown in Figure 7.3. The image positions have been changed from the input positions in glafic because of the image tracing algorithm used. This slight difference may account for the differences seen in time delay and magnification. Lenstool identified 16 images, although they are nearly superimposed on the image plane shown in Figure 7.3b.

Each of the models uses somewhat different optimization schemes, and the velocity dispersions are a result of optimization, which may explain some of the differences shown in Figure 7.1 (Table 1). The differences in the results among the three software programs is not surprising, since this model had all three velocity dispersions as free-parameters.

TABLE 1
BEST-FIT LENS MODEL PARAMETERS FOR COSMOS J095930+023427

Software	RA ($''$)	Dec ($''$)	χ^2 RMS($''$)	e	θ (deg)	R_E ($''$)	$M(< R_E)$ (10^{11} $M_\odot$)	σ_0 (km s^{-1})
Results from [2]								
Lenstool			1.7					
SIE	[0.0]	[0.0]		0.28	-10	0.79	$3.49^{+0.5}_{-0.3}$	238
SIS	[-10.98]	[0.474]		···	···	···	···	391
SIS	[3.52]	[13.2]		···	···	···	···	603
Direct Comparison of Lens Models (This Study)								
PixeLens	···	···		···	···	···	3.51	···
Lenstool			1.2					
SIE	[0.0]	[0.0]	0.06	0.33 ± 0.06	-12 ± 8	0.79 ± 0.03	3.49 ± 0.7	234 ± 23
SIS	[-10.98]	[0.474]		···	···	1.8	11.7	412 ± 32
SIS	[3.52]	[13.2]		···	···	4.3	67.9	632 ± 48
Lensmodel			2.2					
SIE	[0.0]	[0.0]	0.3	0.002 ± 0.002	84 ± 18	0.76 ± 0.06	1.91 ± 0.6	252 ± 23
SIS	[-10.98]	[0.474]		···	···	1.6	8.81	369 ± 36
SIS	[3.52]	[13.2]		···	···	2.3	18.1	442 ± 56
glafic			0.9					
SIE	[0.0]	[0.0]	0.2	0.50 ± 0.08	65 ± 2	0.79 ± 0.02	2.06 ± 0.8	256 ± 23
SIS	[-10.98]	[0.474]		···	···	0.00	*	0.60 ± 0.05
SIS	[3.52]	[13.2]		···	···	4.2	57.6	590 ± 48

NOTE. — Values shown in square brackets are fixed in the models. Values without brackets are the optimized/calculated values from the model. *Calculated mass at 6.10E+00$M_\odot$

Figure 7.1: Table 1

TABLE 2
MAGNIFICATION AND TIME DELAYS FOR FOUR IMAGES IN COSMOS J095930+023427

Software	A	B	C	D
PixeLens				
Time Delay	0	0.7	3.4	0.07
Lenstool				
Magnification	7.8 ± 4.3	6.3 ± 10	8.2 ± 6.2	7.9 ± 7.0
Time Delay	0	37 ± 22	31 ± 18	32 ± 21
Lensmodel				
Magnification	1.5 ± 1.5	1.3 ± 1.5	0.7 ± 2.5	0.9 ± 1.5
Time Delay	0	16 ± 12	9.4 ± 8.8	9.9 ± 7.5
glafic				
Magnification	-4.2 ± 1.1	9.2 ± 2.2	-102 ± 7.0	113 ± 23
Time Delay	0	28 ± 7	5.0 ± 1.4	4.9 ± 1.4

NOTE. — Time delay is shown in days

Figure 7.2: Table 2

SDSS J1320+1644

Best-fit lens model parameters for SDSS J1320+1644 are shown in Figure 7.4 (Table 3) with an indirect/direct comparison to the study of [29] and the four direct comparisons in this study. [29] utilized a glafic model that modeled the potentials of G1, G2 and G4 which were boosted by an embedding dark matter halo. One of the published models used four SIS potentials and fixed the locations of the first three, allowing the position of the fourth (the dark matter halo) to optimize ("SIS free"). Furthermore, they concluded that any reasonable mass model reproduced the observed image configuration. The values shown in Table 3 are those as presented in the paper, as the 'SIS free' model [29]. In this study, the values calculated by [29] and shown here were reproduced exactly using their model, and the $\pm$ values are at 1σ.

The PixeLens model has a much lower calculated time delay than the other models, and an enclosed mass within 1σ of the value reported by [29]. As performed by [29], the positions of the sources were kept fixed for the first three SIS potentials. The velocity dispersion and position of the last potential (the dark matter halo) were optimized. The optimized position of the fourth potential calculated in the Lenstool model is quite different, and the velocity dispersion is similar to other models. Lensmodel uses the Einstein radius, rather than velocity dispersion so the Einstein radii for the first three SIS potentials were fixed, and the fourth was a free parameter. The mass of the fourth potential calculated by Lensmodel is nearly identical to the values calculated using glafic by [29] as well as the Lenstool and glafic models reported

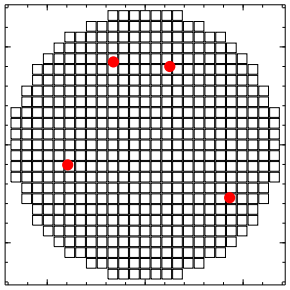

(a)

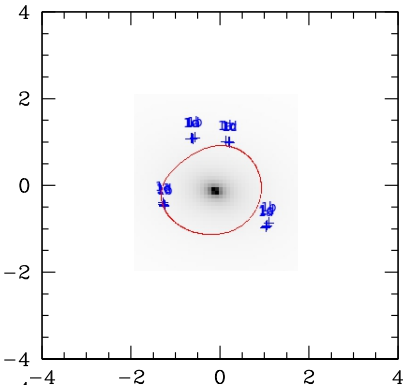

(b)

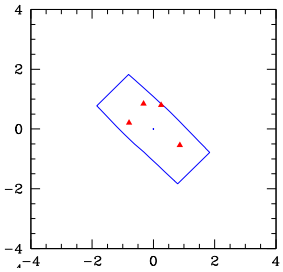

(c)

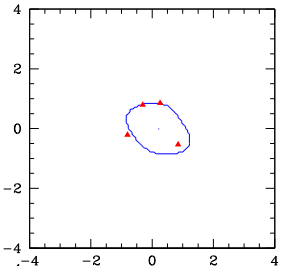

(d)

Figure 7.3: Image planes for COSMOS J095930+023427 calculated by (a)PixeLens, (b)Lenstool, (c)Lensmodel and (d)glafic. Red triangles show image positions. Axes are labeled in arc seconds.

here. The time delays and magnification values show more variability. The calculated models of SDSS J1320+1644 show similar optimization for the mass of the fourth SIS potential, with fairly similar positions calculated by Lensmodel and glafic, while the positions calculated by Lenstool show greater variability. There is great variability among the calculated time delays and magnifications.

The calculations performed in this study using glafic are the same as the glafic SIS-free model reported by [29]. Figure 7.4 (Table 3) shows that the mass calculated for the fourth SIS potential, which was a free parameter, optimized to the same value for Lenstool, Lensmodel and glafic. The optimized geometry was slightly different for Lenstool compared to the others. The Einstein radius calculated by all four models was almost the same for the first SIS potential. The fact that the velocity dispersion for the fourth lens potential was optimized to the same value in all of the models may reflect the fact that there was only a single free parameter in each model. This is different from the results above with COSMOS J095930+023427, which optimized three lens potentials as free parameters, with varying results among the models tested.

The model of SDSS J1320+1644 was straightforward including four SIS potentials which was reproduced in all software models without difficulty. The model used by Rusu [29] had 0 degrees of freedom and with a resulting $\chi^2 << 1$, due in part to the design of the model with 14 nominal constraints and 14 parameters. The similarity of the potentials used to model the system may have contributed to the close results for optimization of the mass. Despite this, position, magnification and time delay showed great variability among the four models. The velocity dispersion for only the fourth lens potential was left as a free parameter, with the other three fixed, which is likely a major factor in the close agreement found among the various models in the calculation of the velocity dispersion.

The image planes for the four models are shown in Figure 7.5. The image positions in the image planes are the same as the input positions in all models. Despite this, there is variability in the time delay and magnification calculations.

TABLE 3
BEST-FIT LENS MODEL PARAMETERS FOR SDSS J1320+1644

Software	RA ($''$)	Dec ($''$)	χ^2 RMS($''$)	μ	Δt (days)	R_E ($''$)	$M(< R_E)$ (10^{11} $M_\odot$)	σ_0 (km s^{-1})
Results from [29]								
glafic			$\chi^2 << 1$	37 ± 29	-860 ± 460			
SIS	[-4.991]	[0.117]				0.5 ± 0.2	2.1 ± 1.5	[237]
SIS	[-2.960]	[3.843]				...	...	[163]
SIS	[-9.169]	[5.173]				...	...	...
SIS	-4.687	1.149				...	...	645 ± 25
Direct Comparison of Lens Models (This Study)								
PixeLens	[0.0]	[0.0]		...	3.5	...	2.9	...
Lenstool			11.5	1.0 ± 1.2	-1 ± 10			
SIS	[-4.991]	[0.117]	2.3			[0.49]	1.1	[237]
SIS	[-2.960]	[3.843]				[0.23]	0.25	[163]
SIS	[-9.169]	[5.173]				[0.12]	0.07	[118]
SIS	-0.471	0.179				3.6	61	645 ± 25
Lensmodel			51.1	1.3 ± 2.0	485 ± 210			
SIS	[-4.991]	[0.117]	3.9			[0.49]	1.1	[237]
SIS	[-2.960]	[3.843]				[0.23]	0.25	[163]
SIS	[-9.169]	[5.173]				[0.12]	0.07	[118]
SIS	-3.93	2.43				2.9	53	576 ± 25
glafic			2.0E-06	37 ± 29	-860 ± 460			
SIS	[-4.991]	[0.117]	0.10			[0.5]	2.1 ± 1.5	[237]
SIS	[-2.960]	[3.843]				[0.23]	0.25	[163]
SIS	[-9.169]	[5.173]				[0.12]	0.070	[118]
SIS	-4.687	1.149				3.6 ± 0.2	61	645 ± 25

NOTE. — Values shown in square brackets are fixed in the models. Values without brackets are the optimized/calculated values from the model.

Figure 7.4: Table 3

SDSSJ1430+4105

The indirect comparison to the work of [4] and the results of the four direct comparisons in this study are shown in Figure 7.6 (Table 4). In [4] there are five different models tested for SDSSJ1430+4105. The models were tested with Gravlens/Lensmodel (LTM) [13] and Lensview (LTM) [35], and the results compared in a direct comparison.

The model used in the current study is based on Model I, as described in [4], which models the lens as an SIE, ignoring the environment of the lens. The best fitting parameters reported by [4] are shown in Figure 7.6 (Table 4). Their results are in good agreement with those by [1]. In the SIE model using Lensview as reported by [4], their results were very similar to those with the Lensmodel model. The input files for the model used by [4] were not available for this study, making this study both an indirect and direct comparison.

The enclosed mass calculated by PixeLens inside the Einstein radius, is slightly higher than the result published by [4]. The Einstein radii calculated by all the models are very close to each

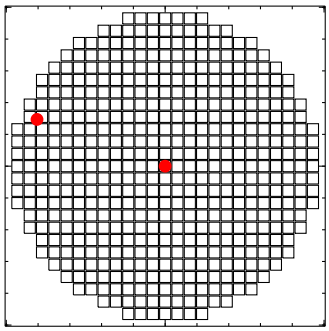

(a)

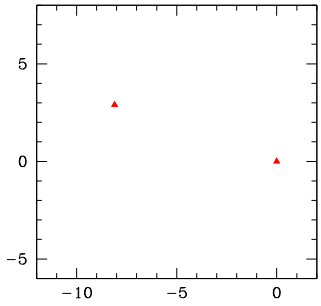

(b)

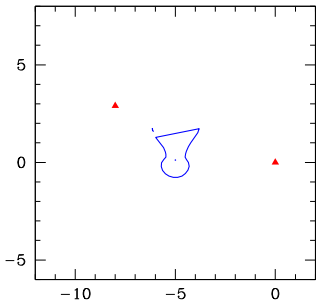

(c)

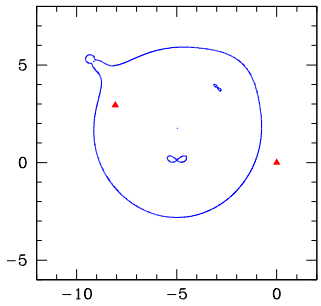

(d)

Figure 7.5: Image planes for SDSS J1320+1644 calculated by (a)PixeLens, (b)Lenstool, (c)Lensmodel and (d)glafic. Red triangles show image positions. Axes are labeled in arc seconds.

other as well as close to the result of [4]. As shown in other lens systems in this study, there is considerable variation in magnification and time delay calculations among the four models studied as shown in Figure 7.7 (Table 5). The optimized ellipticities among the four models are all quite close, but there is significant variability in the optimal position angles calculated.

The models used in this study (results shown in Tables 4 and 5) were written without detailed knowledge of the model used by [4]. Despite this, the models all had similar results, especially in regard to Einstein radius, enclosed mass and velocity dispersion calculations.

The image planes for the four models are shown in Figure 7.8. The image positions in the output image plane of the Lensmodel model (Figure 3c) are identical to those reported by Eichner [4]. The glafic (Figure 3d) model resulted in just 4 images in the output image plane. In addition, Lenstool (Figure 3b) identified a total of 28 images, although some of them are nearly superimposed in the image plane shown in Figure 7.8b.

The position angles were somewhat different but there was good agreement among the models for ellipticity calculations. As with other models in this study, there was variation in the calculation of time delays and magnifications.

One of the reasons for such close agreement among the models is that the models all used a single SIE potential, which allowed for comparable potentials among the four lens model codes tested. There was a single lens plane in all of the models.

TABLE 4
BEST-FIT LENS MODEL PARAMETERS FOR SDSSJ1430+4105

Software	RA ($''$)	Dec ($''$)	χ^2 RMS($''$)	e	θ (degrees)	R_E ($''$)	$M(< R_E)$ (10^{11} $M_\odot$)	σ_0 (km s^{-1})
Results from [4]								
Lensmodel SIE	[0.0]	[0.0]	11.5	$0.71^{+0.02}_{-0.02}$	$-21.6^{+2.5}_{-2.3}$	$1.49^{+0.02}_{-0.02}$	$5.35^{+0.07}_{-0.06}$	322 ± 22
Direct Comparison of Lens Models (This Study)								
PixeLens	[0.0]	[0.0]	...	...	...	...	6.04	...
Lenstool SIE	[0.0]	[0.0]	4.9 0.25	0.89 ± 0.03	82 ± 22	1.45 ± 0.02	3.59 ± 0.05	317 ± 22
Lensmodel SIE	[0.0]	[0.0]	15.9 0.30	0.53 ± 0.32	22 ± 32	1.42 ± 0.02	3.51 ± 0.05	309 ± 22
glafic SIE	[0.0]	[0.0]	2.4 0.29	0.52 ± 0.03	-10 ± 3.4	1.50 ± 0.02	3.67 ± 0.11	334 ± 22

NOTE. — Values shown in square brackets are fixed in the models

Figure 7.6: Table 4

TABLE 5
MAGNIFICATION AND TIME DELAYS FOR FIVE IMAGES IN SDSS J1430+4105

Software	A	B	C	D	E
PixeLens					
Time Delay	0	0	0	0	0
Lenstool					
Magnification	1.10 ± 0.2	2.66 ± 0.1	0.5 ± 0.5	2.7 ± 0.4	0.49 ± 0.3
Time Delay	0	82 ± 18	66 ± 22	90 ± 33	-16 ± 12
Lensmodel					
Magnification	1.0 ± 0.0	1.56 ± 0.2	0.7 ± 0.15	0.77 ± 0.15	0.36 ± 0.10
Time Delay	0	31 ± 2.5	32 ± 3.0	32 ± 3.0	39 ± 3.5
glafic					
Magnification	2.8 ± 0.02	-1.4 ± 0.02	-1.4 ± 0.02	1.1 ± 0.02	$\cdots$
Time Delay	0	34 ± 4	34 ± 4	0	$\cdots$

NOTE. — Time delay is shown in days

Figure 7.7: Table 5

J1000+0021

An analysis of this lens system was performed by [34] with a calculated Einstein radius of $R_E = 0.35$" (or 3.0 kpc) with an enclosed mass of $M_E = 7.6 \pm 0.5 \times 10^{10}\ M_\odot$. There have been no extensive lens model analyses of this system published to date. This is the first strong galaxy lens at z_{lens} >1. In all models, the position (both RA and Dec) of the lens galaxy was kept constant, and the mass was a free parameter optimized by the software. Further details of the model used were not provided, such as the model software used or the χ^2 calculation.

Results of the four direct comparisons done in this study are shown in Figure 7.9 (Table 6). This lens system was modeled both using an SIS and an SIE, with all lens model software tested. The PixeLens model calculated the enclosed mass the same as reported by [34]. Using an SIS potential, the Einstein radius, enclosed mass and velocity dispersion calculations were nearly the same for Lenstool, Lensmodel and glafic. The Einstein radii and velocity dispersions

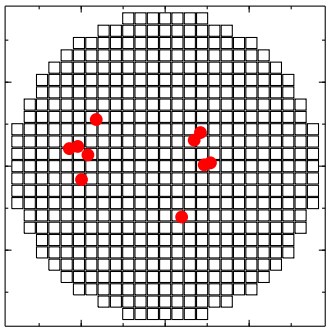

(a)

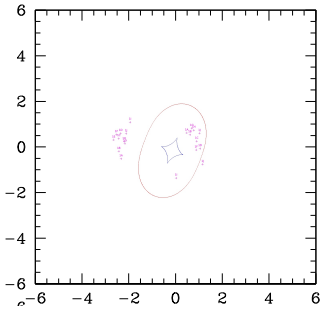

(b)

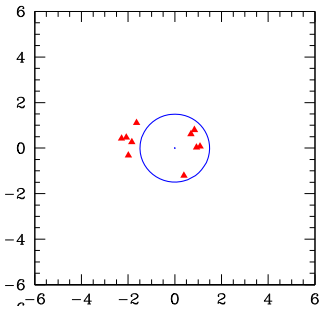

(c)

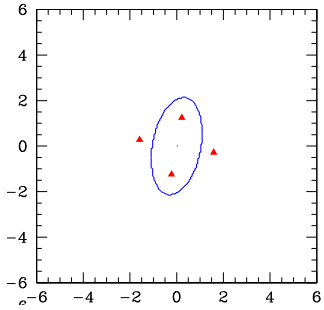

(d)

Figure 7.8: Image planes for SDSS J1430+4105 calculated by (a)PixeLens, (b)Lenstool, (c)Lensmodel and (d)glafic. Red triangles show image positions. Axes are labeled in arc seconds.

were very close to that reported by [34]. Calculations of magnification and time delay showed quite a bit of variability in these models.

The results of the models shown in Figure 7.9 (Table 6) show very similar results for the SIS and the SIE models. The enclosed mass within the Einstein radius is somewhat lower than that reported by [34] for Lenstool, Lensmodel and glafic although the PixeLens model reproduced the enclosed mass calculation very well. Similar to the models used for SDSSJ1430+4105, these models were all quite straightforward with a single potential located at the origin, which may have contributed to the concordance of results.

Comparing the results of the SIE models, the results with an SIE model using the four software packages were also nearly identical, although among the SIE models, there was some variability in the calculations of ellipticity and position angle.

The image planes of the four models are shown in Figure 7.10. This system is particularly interesting. The image positions in the Lensmodel and glafic (Figures 7.10c and d) models have an almost identical geometry, while the image positions in the Lenstool model (Figure 7.10b) are quite different. The time delays and magnifications in the Lensmodel and glafic models are very similar, while the Lenstool model values are quite different.

TABLE 6
BEST-FIT LENS MODEL PARAMETERS FOR J1000+0021

Software	RA ($''$)	Dec ($''$)	χ^2 RMS($''$)	μ	Δt (days)	R_E ($''$)	$M(<R_E)$ (10^{11} $M_\odot$)	σ_0 (km s^{-1})
Results from [34]								
				40 ± 2		0.35	0.76 ± 0.5	182 ± 10
Direct Comparison of Lens Models (This Study) - Singular Isothermal Sphere (SIS) Models								
PixeLens	[0.0]	[0.0]		...	2.3	...	0.8	...
Lenstool SIS	[0.0]	[0.0]	2.9 0.05	1.6 ± 3.3	-18 ± 22	0.4 ± 0.2	0.6 ± 0.2	200 ± 10
Lensmodel SIS	[0.0]	[0.0]	5.8 0.23	2.3 ± 0.4	0.1 ± 0.1	0.4 ± 0.4	0.6 ± 0.4	190 ± 10
glafic SIS	[0.0]	[0.0]	0.3 0.10	7.1 ± 12	3.8 ± 1.8	0.4 ± 0.05	0.6 ± 0.25	192 ± 10
Singular Isothermal Ellipsoid (SIE) Models								
Software	RA ($''$)	Dec ($''$)	χ^2 RMS($''$)	e	θ	R_E ($''$)	$M(<R_E)$ (10^{11} $M_\odot$)	σ_0 (km s^{-1})
Lenstool SIE	[0.0]	[0.0]	1.7 0.04	0.76 ± 0.4	19 ± 18	0.4 ± 0.05	0.6 ± 0.07	190 ± 10
Lensmodel SIE	[0.0]	[0.0]	1.7 0.12	0.26 ± 0.04	-71 ± 35	0.4 ± 0.1	0.6 ± 0.05	190 ± 10
glafic SIE	[0.0]	[0.0]	0.5 0.05	0.008 ± 0.003	-70 ± 19	0.4 ± 0.05	0.6 ± 0.22	189 ± 10

NOTE. — Values shown in square brackets are fixed in the models

Figure 7.9: Table 6

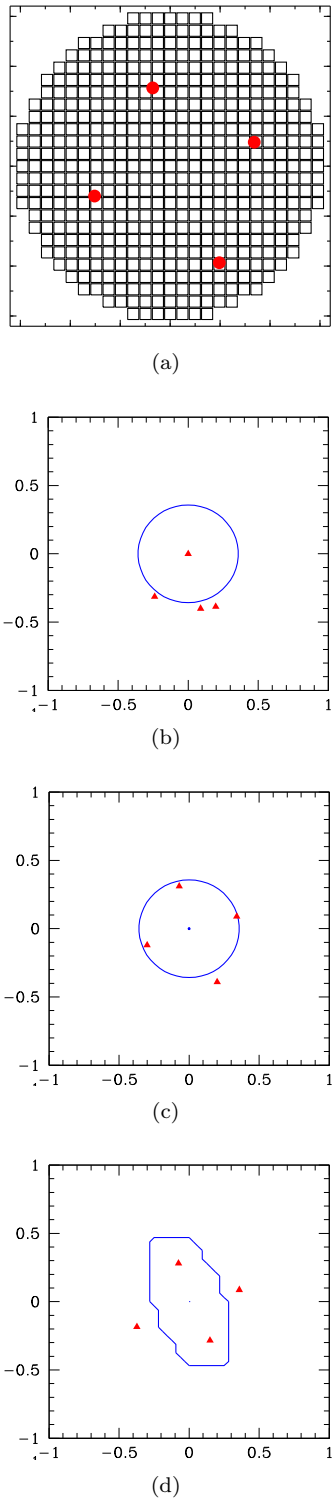

Figure 7.10: Image planes for J1000+0021 calculated by (a)PixeLens, (b)Lenstool, (c)Lensmodel and (d)glafic. Red triangles show image positions. Axes are labeled in arc seconds.

Comparison of Results

There are some generalizations that can be made comparing the results calculated from the models for each of the four lens systems studied. The Einstein radii and mass within the Einstein radii are quite close for the four models of each system. The Einstein radius is calculated from the average distance between the lens center and multiple images, and is insensitive to the radial density profile [26]. The conversion from the Einstein radius to the enclosed mass within the Einstein radius is dependent only on the lens and source redshifts, and is therefore model independent [26]. Thus, the similar results for Einstein radii and mass within the Einstein radii are expected since all models had the same system geometry of z_{lens} and z_{source}.

There is variation among the calculated time delays and magnifications comparing the models generated by each of the four lens model software programs. The image positions input to each model were identical. However, the image planes showing the output image positions of the 16 models studied show changes in image position due to the image tracing algorithms in each software model. These differences explain some of the variation seen in time delay and magnification.

There is also little agreement among calculations of ellipticity and position angle. The variation in results for calculated ellipticity and position angle may be a result of differences in the optimization algorithms used by Lenstool, Lensmodel and glafic.

The complexity of the model also has an impact on agreement among the calculated values for velocity dispersion. In the models for SDSS J1430+4105, J1000+0021and SDSS J1320+1644, there was only one potential with the velocity dispersion as a free-parameter for optimization. In all three of these systems, there was close agreement among the calculated values. In the model of COSMOS J095930+023427, there were three lens potentials which were optimized, with quite a bit of variation among the results from the three software programs used.

Comparison of Lens Model Software by Version

In order to evaluate the effect of software version and/or operating system / hardware platform, the model of SDSS J1320+1644 was evaluated with glafic and Lensmodel on two different hardware platforms. Glafic is distributed as an executable file with version 1.1.5 for the OS/X platform and version 1.1.6 for Linux. Lensmodel is available as an executable file only for download as version 1.99o for the Linux platform, and we were provided a version to run on OS/X.

Input files for the models of SDSS J1320+1644 were used unchanged. In the first test, the model was tested with the two versions of glafic. The mass of the first three SIS potentials were held as fixed parameters and the mass of the fourth potential, as well as its position, were free parameters to be optimized. Identical results were reported using either version of glafic, on both platforms. The results were identical including the numbers of models used for optimization in each run and the calculation of all parameters evaluated. The content of all output files produced by both versions was identical. The models for SDSS J1320+1644 were then tested with each of the two versions of Lensmodel. In this same test, optimizing the fourth SIS potential, results with Lensmodel were slightly different comparing the two versions. The optimized Einstein radius of the fourth potential using the Linux version is reported as 3.622605, and the OS/X version reports 3.622528. There are similarly small differences in the optimized position of the fourth potential.

In the next test, the mass of all four potentials was optimized. The results with glafic, on both hardware platforms, were again identical in regard to all parameters evaluated, to the accuracy of the last decimal place reported. The contents of all output files produced by glafic were identical with the Linux and OS/X versions. However, the two versions of Lensmodel

reported widely disparate results with the two versions tested. The Einstein radii of the four optimized SIS potentials using the Linux version are 1.851, 1.004, 0.3161 and 1.660. Using the OS/X version, the four potentials are optimized at 2.234, 1.818, 0.3139 and 2.006.

The hardware platform and/or operating system used in the calculations is not reported in any of the studies reviewed.

7.5 Discussion

Small changes in redshift have different effects on the calculation of time delays and mass by different lens model software codes [18]. In that study, a mock model with a single potential and four images as well as a model of SDSS J1004+4112 were evaluated and the effect of changes in redshift on changes in calculations of time delay and mass were determined. The study showed that changes in time delay and mass calculations are not always proportional to changes in $D_{\mathrm{d}}D_{\mathrm{s}}/D_{\mathrm{ds}}$, as would be predicted. The image positions in this study also changed as a result of the image tracing by the software, which was partly responsible for the differences in the values of time delay and mass in both systems when comparing the models from four different lens model software packages.

The present study was designed to specifically compare the results from different lens models, rather than changes in the results, to identify factors that affect the ability to compare results from different codes. The present study is the largest strong gravitational lens software comparison study performed to date, evaluating four different lens systems with four different lens model software codes in a single study, and is the first study to use HydraLens for the preparation of multiple models.

Indirect Comparison Studies

Parameters calculated using strong gravitational lens models and compared with other published results, are referred to as "indirect comparison studies". In the indirect comparison of COSMOSJ095930 performed by [2] and [5], both analyses were conducted with Lenstool, and had very similar results for Einstein radius, mass enclosed within the Einstein radius, and other parameters. It is difficult to discern the details of the model used by [5] with regard to number, type and geometry of the lens potentials used. Indirect comparisons are further complicated by a lack of available detail of the model used, making it difficult to reproduce previous results.

Direct Comparison Studies

Studies where different lens models are compared in the same study, are referred to as "direct comparison studies". The direct comparisons performed of Abell 1703, MS1358, MACSJ1206 and SDSS120602 have been described in detail in [18] . The information in these direct studies was complementary in nature, leading to a greater understanding of the lens system. The lens SDSSJ1430 was investigated by [4] who compared the results using Lensview and Lensmodel. The Lensmodel analysis assumes point sources while Lensview uses the two-dimensional surface brightness distribution of the same system. Both analyses led to the same conclusions regarding the mass distribution of the galaxy. The two lens model techniques were indeed complementary and led to similar results. In a comparative analysis of RX J1347.5-1145 using glafic and PixeLens, the authors note a 13 percent difference in the calculation of mass enclosed within the Einstein radius [15]. They suggest that the LTM model used by glafic may not be assigning sufficient mass to the profiles in the models used. We observed a similar underestimation of enclosed mass by non-LTM models as compared to PixeLens in the analysis of J1000+0021.

7.6 Conclusions

Indirect comparison studies are of value, but as some of the comparisons conducted in this study show, it may be difficult to reproduce the results of previous studies without previous model files available to create the models for other software, thus limiting the nature of the comparisons performed. In the analyses of COSMOS J095930+023427 and SDSS J1320+1644, being able to use the same models as used in the original studies, qualifies these as direct comparisons. This supports the importance of sharing lens model files in future studies.

Even in direct comparisons, the results with one model may not be exactly the same as with another because of the difficulty in translating some of the features of one model to another because of the differences in features of the available software. For example, it is not possible to parameterize a PixeLens model exactly the same as a Lenstool model because of inherent differences in the software. These differences may explain the observations of [15] as well as some of the results in this study. Despite best efforts to similarly parameterize two models, there still may be small differences. This suggests that using several models to understand a system may lead to improved understanding.

In seeking agreement among various models, the number of free parameters for the lens potentials is an important factor. While there was reasonable agreement among the calculated values for Einstein radius in single potential models, such as SDSS J1430+4105 and J1000+0021 in this study, there was less agreement in a more complicated model such as COSMOS J095930+023427, which may be a reflection of using more lens potentials to describe the system.

Differences noted in time delay and magnification calculations may be due to differences in the image tracing algorithms used by each of the software models. The input image positions are the same in all models. The software calculates new positions based on the software specific ray-tracing algorithm used going from the source plane back to the image plane, resulting in differences in time delay results. The differences in optimization algorithms used also leads to some of the observed differences among the software models, with great variation in the calculation of ellipticity and position angle.

These results demonstrate that there are significant differences in results using lens models prepared with different software, and are consistent with a previous study of differences in lens models [18]. There is no intention to suggest that a particular group of models are necessarily more correct, but only to suggest that future lensing studies should evaluate lens models using several approaches to understand the system more thoroughly, as already being conducted in the Hubble Frontier Fields project.

Based on the results of this study, in order to allow comparisons across studies, it will be important to use a consistent nomenclature for lensing studies, specifying indirect vs. direct comparisons, independent vs. semi-independent comparisons and the type of model being used as LTM vs. non-LTM, as we have previously described [18]. Furthermore, this study has shown at least in one situation that the software version used can significantly affect the results which stresses the importance of specifying the software version number being used in all future studies, in addition to the hardware/operating system platform. It is also suggested that more detail is provided in future studies to allow reproducibility of the models such as the number and types of potentials used along with the name of the potential used in the various software packages.

One of the most important aspects of any scientific experiment is reproducibility. In gravitational lens model studies, this is impossible in many cases because the software is not available to other investigators, or the lens model files are not available. Code-sharing of software in astrophysics is essential, as emphasized by [31]. Based on the studies reported here, the sharing

of lens model files in gravitational lens studies is also essential to assure reproducibility and increased transparency in future gravitational lensing studies. Another approach in lensing studies that has been successfully applied in weak lensing is computer challenges. The use of multiple approaches including comparative studies of lens models, open software, open lens model files, and computer challenges will help to assure increased transparency in future studies and enhance the results.

References

[1] A. S. Bolton, S. Burles, L. V. E. Koopmans, T. Treu, R. Gavazzi, L. A. Moustakas, R. Wayth, and D. J. Schlegel. The Sloan Lens ACS Survey. V. The Full ACS Strong-Lens Sample. *AstrophysJ*, **682**:964–984, August 2008. 248, 256

[2] S. Cao, G. Covone, M. Paolillo, and Z.-H. Zhu. A multi-wavelength study of the gravitational lens COSMOS J095930+023427. *Research in Astronomy and Astrophysics*, **13**:15–27, January 2013. 246, 247, 251, 265

[3] D. Coe, E. Fuselier, N. Benítez, T. Broadhurst, B. Frye, and H. Ford. LensPerfect: Gravitational Lens Mass Map Reconstructions Yielding Exact Reproduction of All Multiple Images. *AstrophysJ*, **681**:814–830, July 2008. 245

[4] T. Eichner, S. Seitz, and A. Bauer. Golden gravitational lensing systems from the Sloan Lens ACS Survey - II. SDSS J1430+4105: a precise inner total mass profile from lensing alone. *MonNotRoyalAstrSoc*, **427**:1918–1939, December 2012. 248, 256, 258, 265

[5] C. Faure, T. Anguita, D. Alloin, K. Bundy, A. Finoguenov, A. Leauthaud, C. Knobel, J.-P. Kneib, E. Jullo, O. Ilbert, A. M. Koekemoer, P. Capak, N. Scoville, and L. A. M. Tasca. On the evolution of environmental and mass properties of strong lens galaxies in COSMOS. *AAP*, **529**:A72, May 2011. 247, 265

[6] N. Inada, M. Oguri, M.-S. Shin, I. Kayo, M. A. Strauss, T. Morokuma, C. E. Rusu, M. Fukugita, C. S. Kochanek, G. T. Richards, D. P. Schneider, D. G. York, N. A. Bahcall, J. A. Frieman, P. B. Hall, and R. L. White. The Sloan Digital Sky Survey Quasar Lens Search. V. Final Catalog from the Seventh Data Release. *AstronomJ*, **143**:119, May 2012. 247

[7] N. Jackson. Gravitational lenses and lens candidates identified from the COSMOS field. *Mon N Roy Astr Soc*, **389**:1311–1318, September 2008. 247

[8] E. Jullo and J.-P. Kneib. Multiscale cluster lens mass mapping - I. Strong lensing modelling. *Mon Not Roy Astr Soc*, **395**:1319–1332, May 2009. 249

[9] E. Jullo, J.-P. Kneib, M. Limousin, Á. Elíasdóttir, P. J. Marshall, and T. Verdugo. A Bayesian approach to strong lensing modelling of galaxy clusters. *New Journal of Physics*, **9**:447, December 2007. 245, 249

[10] A. Kassiola and I. Kovner. Elliptic Mass Distributions versus Elliptic Potentials in Gravitational Lenses. *AstrophysJ*, **417**:450, November 1993. 247

[11] C Keeton. Gravlens user manual. `http://redfive.rutgers.edu/~keeton/gravlens/`, January 2004. 250

[12] C. R. Keeton. A Catalog of Mass Models for Gravitational Lensing. *ArXiv Astrophysics e-prints*, February 2001. 250

[13] C. R. Keeton. Computational Methods for Gravitational Lensing. *ArXiv Astrophysics e-prints*, February 2001. 250, 256

[14] J-P Kneib. Lenstool manual. http://lamwws.oamp.fr/lenstool/, May 2012. 249, 251

[15] F. Köhlinger and R. W. Schmidt. Strong lensing in RX J1347.5-1145 revisited. *ArXiv e-prints*, September 2013. 249, 265, 266

[16] N. Laporte, A. Streblyanska, B. Clement, I. Pérez-Fournon, D. Schaerer, H. Atek, F. Boone, J.-P. Kneib, E. Egami, P. Martínez-Navajas, R. Marques-Chaves, R. Pelló, and J. Richard. The first Frontier Fields cluster: 4.5 μm excess in a z ˜ 8 galaxy candidate in Abell 2744. *Astr & Astrophys*, **562**:L8, February 2014. 245

[17] A. T. Lefor. Comparison of Strong Gravitational Lens Model Software II. HydraLens: Computer Assisted Generation of Lens Models. *Astronomy and Computing*, **5**:28–34, August 2014. 245, 246

[18] A. T. Lefor and T. Futamase. Comparison of Strong Gravitational Lens Model Software I. Time delay and mass calculations are sensitive to changes in redshift and are model dependent. *ArXiv e-prints*, July 2013. 245, 246, 251, 265, 266

[19] A. T. Lefor, T. Futamase, and M. Akhlaghi. A systematic review of strong gravitational lens modeling software. *New Astr Rev*, **57**:1–13, July 2013. 245, 249

[20] M McCourt. Lenstool for dummies. http://www.oamp.fr/cosmology/lenstool/, October 2006. 249

[21] J. Merten, M. Cacciato, M. Meneghetti, C. Mignone, and M. Bartelmann. Combining weak and strong cluster lensing: applications to simulations and MS 2137. *AstrAstrophys*, **500**:681–691, June 2009. 245

[22] L. Moustakas and J. Brownstein. The orphan lens project. http://www.masterlens.astro.utah.edu, February 2013. 245, 246, 249

[23] M. Oguri. The Mass Distribution of SDSS J1004+4112 Revisited. *Proceedings Astr Soc Japan*, **62**:1017–, August 2010. 250

[24] M. Oguri. glafic user's manual. http://www.slac.stanford.edu/oguri/glafic/, June 2013. 250

[25] M. Oguri, N. Inada, M. A. Strauss, C. S. Kochanek, I. Kayo, M.-S. Shin, T. Morokuma, G. T. Richards, C. E. Rusu, J. A. Frieman, M. Fukugita, D. P. Schneider, D. G. York, N. A. Bahcall, and R. L. White. The Sloan Digital Sky Survey Quasar Lens Search. VI. Constraints on Dark Energy and the Evolution of Massive Galaxies. *AstronJ*, **143**:120, May 2012. 247

[26] M. Oguri, C. E. Rusu, and E. E. Falco. The stellar and dark matter distributions in elliptical galaxies from the ensemble of strong gravitational lenses. *ArXiv e-prints*, September 2013. 264

[27] J Read. Pixelens manual. http://www.qgd.uzh.ch/programs/pixelens/, September 2012. 249

[28] J Read. Pixelens tutorial. http://www.itp.uzh.ch/~justin/Astro/Lectures/PixeLens/tutorial.pdf, September 2012. 249

[29] C. E. Rusu, M. Oguri, M. Iye, N. Inada, I. Kayo, M.-S. Shin, D. Sluse, and M. A. Strauss. The Quasar-galaxy Cross SDSS J1320+1644: A Probable Large-separation Lensed Quasar. *AstroPhysJ*, **765**:139, March 2013. 246, 247, 248, 249, 253, 255

[30] P. Saha, J. I. Read, and L. L. R. Williams. Two Strong-Lensing Clusters Confront Universal Dark Matter Profiles. *ApJ Letters*, **652**:L5–L8, November 2006. 245, 249

[31] L. Shamir, J. F. Wallin, A. Allen, B. Berriman, P. Teuben, R. J. Nemiroff, J. Mink, R. J. Hanisch, and K. DuPrie. Practices in source code sharing in astrophysics. *Astronomy and Computing*, **1**:54–58, February 2013. 266

[32] K. Umetsu, E. Medezinski, M. Nonino, J. Merten, A. Zitrin, A. Molino, C. Grillo, M. Carrasco, M. Donahue, A. Mahdavi, D. Coe, M. Postman, A. Koekemoer, N. Czakon, J. Sayers, T. Mroczkowski, S. Golwala, P. M. Koch, K.-Y. Lin, S. M. Molnar, P. Rosati, I. Balestra, A. Mercurio, M. Scodeggio, A. Biviano, T. Anguita, L. Infante, G. Seidel, I. Sendra, S. Jouvel, O. Host, D. Lemze, T. Broadhurst, M. Meneghetti, L. Moustakas, M. Bartelmann, N. Benítez, R. Bouwens, L. Bradley, H. Ford, Y. Jiménez-Teja, D. Kelson, O. Lahav, P. Melchior, J. Moustakas, S. Ogaz, S. Seitz, and W. Zheng. CLASH: Mass Distribution in and around MACS J1206.2-0847 from a Full Cluster Lensing Analysis. *AstrophysJ*, **755**:56, August 2012. 245

[33] G. van de Ven, J. Falcón-Barroso, R. M. McDermid, M. Cappellari, B. W. Miller, and P. T. de Zeeuw. The Einstein Cross: Constraint on Dark Matter from Stellar Dynamics and Gravitational Lensing. *AstrophysJ*, **719**:1481–1496, August 2010. 248

[34] A. van der Wel, G. van de Ven, M. Maseda, H. W. Rix, G. H. Rudnick, A. Grazian, S. L. Finkelstein, D. C. Koo, S. M. Faber, H. C. Ferguson, A. M. Koekemoer, N. A. Grogin, and D. D. Kocevski. Discovery of a Quadruple Lens in CANDELS with a Record Lens Redshift z=1.53. *ArXiv e-prints*, September 2013. 248, 260, 262

[35] R. B. Wayth and R. L. Webster. LENSVIEW: software for modelling resolved gravitational lens images. *Mon Not Roy Astr Soc*, **372**:1187–1207, November 2006. 248, 256

Chapter 8

RXJ1131 and B1608: Comparative Studies of Time Delays for Two Well-Characterized Strong Gravitational Lenses

8.1 Purpose and Organization of this Chapter

In Chapter 5, we showed that strong gravitational lens models made with different software can yield significantly different results for the calculation of time delays for two different lens systems [13]. In that study we used a mock model and SDSSJ1004+4112 as the basis of a comparative study of lens models, evaluating time delay and mass calculations. This is a follow-up to the study in Chapter 5, to focus specifically on time delay calculations. The purpose of this chapter is to perform a study of two gravitational lenses, B1608+656 and RXJ1131-1231, for which there is a wealth of observational and lens model data available for comparison. These two systems have been extremely well characterized with regard to time delays in many previous studies (see below in Section 8.2). [1]

After an Introduction, and discussion of existing studies of B1608 and RXJ1131 in Section 8.2, we describe the lens models developed for these two lens systems in this study, in Section 8.3. The Results of studies using these lens models with Lenstool, PixeLens, Lensmodel and glafic are described in Section 8.4. A discussion of the results is in Section 8.5 including a detailed description of the implications of the variations found for using time delays to calculate cosmological parameters such as H_0 in Section 8.5. Finally, we will make some conclusions and discuss future plans to complete this study in Section 8.6.

[1] The results in this chapter represent a work in progress. Future plans are described in Section 8.6.

8.2 Introduction

These last few years are being called the era of precision cosmology. Many different analytic methods have resulted in data that supports what is commonly known as the concordance cosmology, characterized by a virtually flat geometry in a universe dominated by dark matter and dark energy [27]. With precision for parameters now reaching the few percent level, it is valuable to compare and contrast different methods of establishing the description of the Universe. A comparison of independent probes with similar precision allows one to test the accuracy of the measurements, and reveal uncertainties.

Gravitational lensing has been used as one such probe of the Universe. The use of lensing data is dependent not only on observations, but also on analysis of the data. Many of the analyses to date are done using a single software code to determine critical parameters. Often, this code is one written by the individual investigator conducting the study. While many of the well-known codes are available for public use, many are not available which makes it impossible to reproduce these studies [14].

Using Time Delays to Determine Cosmological Parameters

There is a brief discussion of Time Delays in Chapter 3, Section 3.4 of this dissertation, which is further expanded below in Section 8.2. The idea of using time delays is traced back to [20]. In principle, gravitational lensing provides an independent one-step method for Hubble constant determination. Refsdal suggested using time delays between the images of gravitationally-lensed supernovae long before discovery of the first gravitationally lensed quasar. Time delays are proportional to H_0^-1 and weakly depend on other cosmological parameters.

The accuracy of the method relies on the precision of the time delay determination, knowledge of the distances in the system and reconstruction of the mass distribution of the lens. Advances in spectroscopy combined with precise cosmology allow for distance measurement with great accuracy. The mass distribution of the lens can be reconstructed well using resolved radio and optical images. In addition, for lenses located at a low enough redshift, the velocity dispersion of the lens can be measured, which allows for independent confirmation of the mass distribution [1].

The dependence of the estimate of H_0 from a gravitational lens time delay on the mass distribution of the lens is well known, both from models of particular time delay lenses and from general analytic principles [8]. The most important trend is that the predicted time delays, or the inferred H_0, increase as the mass distribution becomes more centrally concentrated. In particular, it was shown that adding a constant surface density sheet to the mass distribution has no observable effect other than to rescale the time delay (the mass sheet degeneracy), and that the Hubble constants estimated from lens potentials of the form $\phi \propto R^{3-\eta}$ ($\rho \propto r^{-\eta}$) roughly scale as $H_0 \propto (\eta - 1)/\Delta t$, almost independent of the angular structure of the potential.

Gravitational lens time delays are determined by the Hubble constant, the positions of the lensed images, and the surface density in the annulus bounded by the images. The average surface density $\langle\kappa\rangle$ in the annulus is more important than its distribution. The relationship between time delays and the local surface density is exact for circular lenses. While this is not exactly true for non-circular lenses, it is true in practice. In two-image lenses, where the images lie on opposite sides of the lens galaxy, the delays are insensitive to the angular structure of the lens. In four-image lenses the delays are very sensitive to the quadrupole structure of the potential, but the image positions tightly constrain the quadrupole and leave the surface density as the only important variable [8].

Time Delay Basics

The observations of gravitationally lensed quasars are best understood in light of Fermat's principle. Intervening mass between a source and an observer introduces an effective index of refraction, thereby increasing the light-travel time. The competition between this Shapiro delay from the gravitational field and the geometric delay due to bending the ray paths leads to the formation of multiple images at the stationary points (minima, maxima, and saddle points) of the travel time [10].

As with glass optics, there is a thin-lens approximation that applies when the optics are small compared to the distances to the source and the observer. In this approximation, we need only the effective potential, $\psi(\vec{x}) = (2/c^2)(D_{ls}/D_s)\int dz\phi$, found by integrating the 3D potential ϕ along the line of sight. The light-travel time is

$$\tau\left(\vec{x}\right) = \left[\frac{1+z_l}{c}\right]\left[\frac{D_l D_s}{D_{ls}}\right]\left[\frac{1}{2}\left(\vec{x}-\vec{\beta}\right)^2 - \psi\left(\vec{x}\right)\right], \tag{8.1}$$

where $\vec{x} = (x, y) = R(\cos\theta, \sin\theta)$ and $\vec{\beta}$ are the angular positions of the image and the source, $\psi(\vec{x})$ is the effective potential, $(\vec{x}-\vec{\beta})^2/2$ is the geometric delay in the small-angle approximation, z_l is the lens redshift, and D_l, D_s, and D_{ls} are angular-diameter distances to the lens, to the source, and from the lens to the source, respectively. The only dimensioned quantity in the travel time is a factor of $H_0^{-1} \simeq 10h^{-1}$ Gyr arising from the H_0^{-1} scaling of the angular-diameter distances.

Images at the extrema of the time delay function are observed, which we find by setting the gradients with respect to the image positions equal to zero, $\vec{\nabla}_x\tau = 0$, and finding all the stationary points $(\vec{x}_A, \vec{x}_B, \cdots)$ associated with a given source position $\vec{\beta}$. The local magnification of an image is determined by the magnification tensor M_{ij}, whose inverse is determined by the second derivatives of the time delay function [10],

$$M_{ij}^{-1} = \vec{\nabla}_x\vec{\nabla}_x\tau(\vec{x}) = \begin{pmatrix} 1-\kappa-\gamma\cos 2\theta_\gamma & \gamma\sin 2\theta_\gamma \\ \gamma\sin 2\theta_\gamma & 1-\kappa+\gamma\cos 2\theta_\gamma \end{pmatrix}, \tag{8.2}$$

where the convergence $\kappa = \Sigma/\Sigma_c$ is the local surface density in units of the critical surface density $\Sigma_c = c^2 D_s/4\pi G D_l D_{ls}$, and γ and θ_γ define the local shear field and its orientation. The determinant of the magnification tensor is the net magnification of the image, but it is a signed quantity depending on whether the image has positive (maxima, minima) or negative (saddle points) parity.

A simple but surprisingly realistic starting point for modeling lens potentials is the singular isothermal sphere (the SIS model) in which the lens potential is simply

$$\psi(\vec{x}) = bR, \qquad \text{where} \qquad b = 4\pi\frac{D_{ls}}{D_s}\frac{\sigma^2}{c^2} = 1\farcs45\left(\frac{\sigma}{225\,\mathrm{km\ s^{-1}}}\right)^2\frac{D_{ls}}{D_s} \tag{8.3}$$

is a deflection scale determined by geometry and σ is the 1D velocity dispersion of the lens galaxy. For $|\vec{\beta}| < b$, the SIS lens produces two colinear images at radii $R_A = |\vec{\beta}| + b$ and $R_B = b - |\vec{\beta}|$ on opposite sides of the lens galaxy (as in Fig. 8.1 but with $\Delta\theta_{AB} = 180°$). The A image is a minimum of the time delay and leads the saddle point, B, with a time delay difference of

$$\Delta t_{SIS} = \tau_B - \tau_A = \frac{1}{2}\left[\frac{1+z_l}{c}\right]\left[\frac{D_l D_s}{D_{ls}}\right](R_A^2 - R_B^2). \tag{8.4}$$

Typical time delay differences of months or years are the consequence of multiplying the $\sim 10h^{-1}$ Gyr total propagation times by the square of a very small angle ($b \approx 3\times10^{-6}$ radians

so, $R_A^2 \approx 10^{-11}$). The SIS model suggests that lens time delay measurements reduce the determination of the Hubble constant to a problem of differential astrometry. This is almost correct, but we have made two idealizations in using the SIS model.

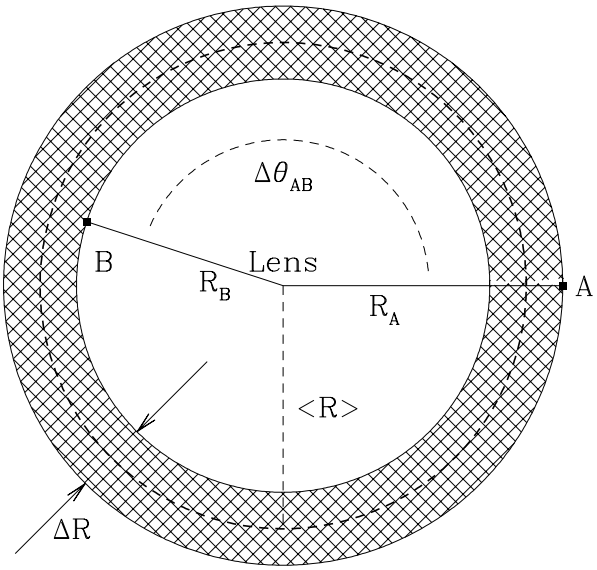

Figure 8.1: Schematic diagram of a two-image time delay lens. The lens lies at the origin, with two images A and B at radii R_A and R_B from the lens center. The images define an annulus of average radius $\langle R\rangle = (R_A + R_B)/2$ and width $\Delta R = R_A - R_B$, and the images subtend an angle $\Delta\theta_{AB}$ relative to the lens center. For a circular lens $\Delta\theta_{AB} = 180°$ by symmetry. From [10]

The first idealization was to ignore deviations of the radial (monopole) density profile from that of an SIS with density $\rho \propto r^{-2}$, surface density $\Sigma \propto R^{-1}$, and a flat rotation curve. The SIS is a special case of a power-law monopole with lens potential

$$\psi(\vec{x}) = \frac{b^2}{(3-\eta)}\left(\frac{R}{b}\right)^{3-\eta}, \tag{8.5}$$

corresponding to a (3D) density distribution with density $\rho \propto r^{-\eta}$, surface density $\Sigma \propto R^{1-\eta}$, and rotation curve $v_c \propto r^{(2-\eta)/2}$. For $\eta = 2$ we recover the SIS model, and the normalization is chosen so that the scale b is always the Einstein ring radius. Models with smaller (larger) η have less (more) centrally concentrated mass distributions and have rising (falling) rotation curves. The limit $\eta \to 3$ approaches the potential of a point mass. By adjusting the scale b and the source position $|\vec{\beta}|$, we can fit the observed positions of two images at radii R_A and R_B on opposite sides ($\Delta\theta_{AB} = 180°$) of the lens for any value of η [10].

The expression for the time delay difference can be well approximated by:

$$\Delta t(\eta) = \tau_B - \tau_A \simeq (\eta - 1)\Delta t_{SIS}\left[1 - \frac{(2-\eta)^2}{12}\left(\frac{\Delta R}{\langle R\rangle}\right)^2 \cdots\right], \tag{8.6}$$

where $\langle R\rangle = (R_A + R_B)/2 \simeq b$ and $\Delta R = R_A - R_B$ (see Fig. 8.1). While the expansion

assumes $\Delta R/\langle R\rangle$ (or $|\vec{\beta}|$) is small, we can usually ignore the higher-order terms. There are two important lessons from this model.

i. Image astrometry of simple two-image and four-image lenses generally cannot constrain the radial mass distribution of the lens.

ii. More centrally concentrated mass distributions (larger η) predict longer time delays, resulting in a larger Hubble constant for a given time delay measurement.

The second idealization was to ignore deviations from circular symmetry due to either the ellipticity of the lens galaxy or the local tidal gravity field from nearby objects. A very nice analytic example of a lens with angular structure is a singular isothermal model with *arbitrary* angular structure, where the effective potential is $\psi = bRF(\theta)$, and $F(\theta)$ is an arbitrary function. The model family includes the most common lens model, the singular isothermal ellipsoid (SIE). The time delays for this model family are simply Δt_{SIS}, *independent of the angular structure of the lens* [10].

The Gravitational Lens B1608+656

B1608+656 was discovered by [16] and has been very well characterized [5; 24; 25; 26]. B1608+656 was discovered as part of the Comic Lens All Sky Survey (CLASS), which was a survey designed to locate gravitational lens systems consisting of multiply imaged compact components with separations greater than $0.2''$. This was the first discovery of a gravitational lens in that survey, a quadruply imaged object with a maximum separation of $2.1''$.

The gravitational lens CLASS B1608+656 is one of very few four-image lens systems for which all three independent time delays have been measured and studied in detail. This makes the system an excellent candidate for a high-quality determination of H_0 at cosmological distances. However, the original measurements of the time delays had large (12–20%) uncertainties, due to the low level of variability of the background source during the monitoring campaign [5].

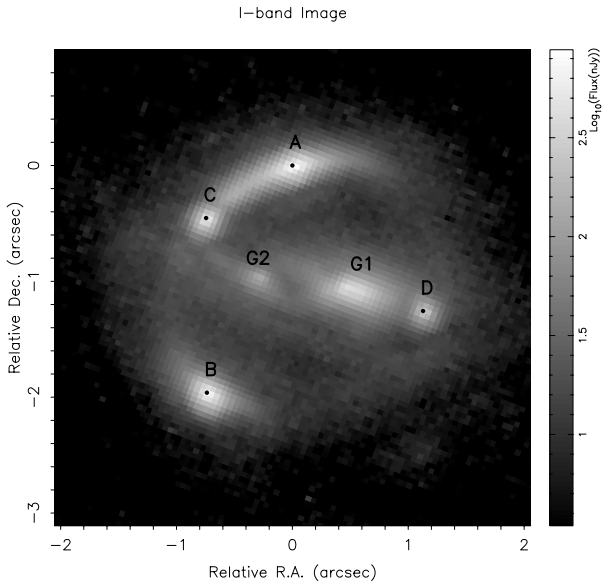

Figure 8.2: The original reduced *HST*/F814W image of B1608+656. The four images are labelled A, B, C, and D; the two lens galaxies are G1 and G2. From [24]

Table 3.1 shows a list of time delays that are available in the literature. Of these lens systems, CLASS B1608+656 is the only four-image system at that time for which all three independent time delays have been unambiguously measured. This makes this system ideal for further evaluation in a comparative lens model study.

The lens system is shown in Figure 8.2. This image shows the two lensing galaxies, as well as the four separate images. Koopmans performed a detailed study of the mass model of B1608, as shown in Figure 8.3. Their models included a variety of potentials, including SIE potentials and others.

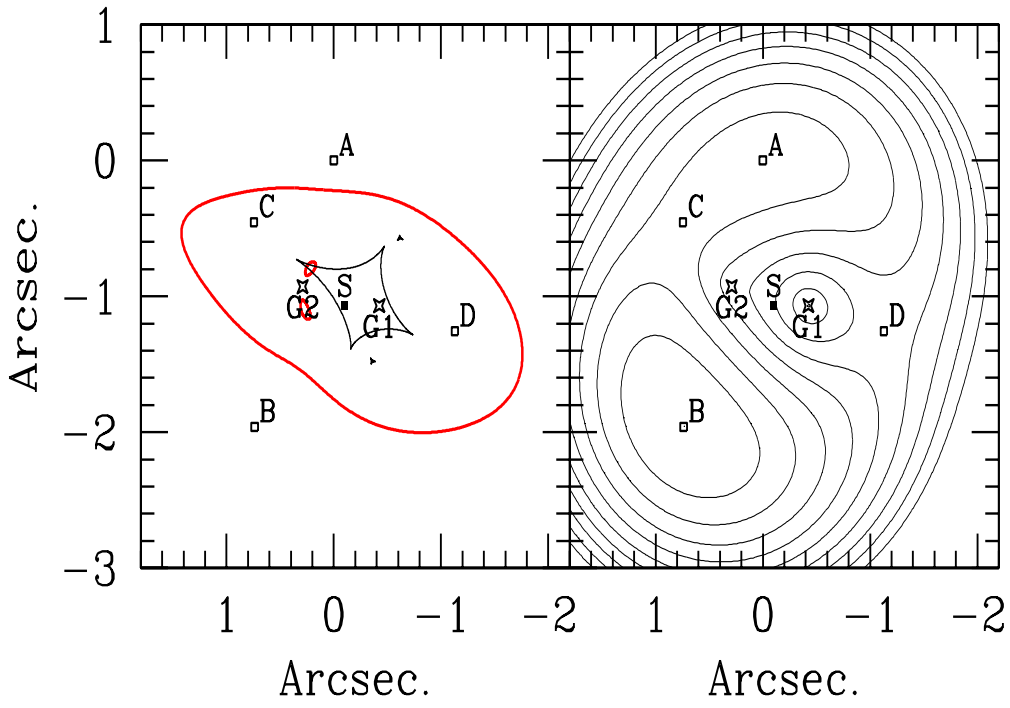

Figure 8.3: Left: Critical (thick) and caustic curves (thin) of the SPLE1+D model. The galaxy positions are indicated by stars, the images positions by open squares and the source by a closed square. Right: The contours indicate constant time delays starting at Δt=0 at image B and increasing in steps of 10 h^{-1} days. From [11]

They presented significantly improved and refined mass models of the gravitational lens B1608+656 – compared with previous modeling efforts – with the aim of determining a value of the Hubble Constant, that is less affected by previously known systematics (e.g. radial mass profile, dust extinction, etc.) [11].

Constraints on the mass model include: (i) the stellar velocity dispersion of the dominant lens galaxy (G1), as measured with ESI, (ii) the deconvolved Einstein Ring seen in the HST F160W and F814W images – the former of which is little affected by dust – corrected for the contribution from the lens galaxies, (iii) the extinction-corrected lens-galaxy centroids and structural parameters, the former being one of the major uncertainties in previous lens models and (iv) recent improvements in the determination of the three independent time delays in this four-image lens system.

Lens models have also been improved in allowing for many additional free parameters compared with previous modeling efforts, including the galaxy positions, the position angle of G1, an external shear and the density slopes of G1 and G2. Some of these parameters are constrained with observational priors. The freedom in the lens model (up to 22 free parameters) allows for a proper analysis of the error on the inferred value of H_0, including all observational errors and correlations between free parameters [11].

The Gravitational Lens RXJ1131-231

The discovery of a new quadruply imaged quasar surrounded by an optical Einstein ring candidate, RXJ1131−1231, was reported by [22]. Spectra of the different components of RXJ1131−1231 revealed a source at z = 0.658. At the time of its discovery, this object was the closest known gravitationally lensed quasar. The lensing galaxy is clearly detected, with a redshift measured at z = 0.295. This system has been extensively characterized by others as well, including [2; 3; 15; 23; 27; 28; 30].

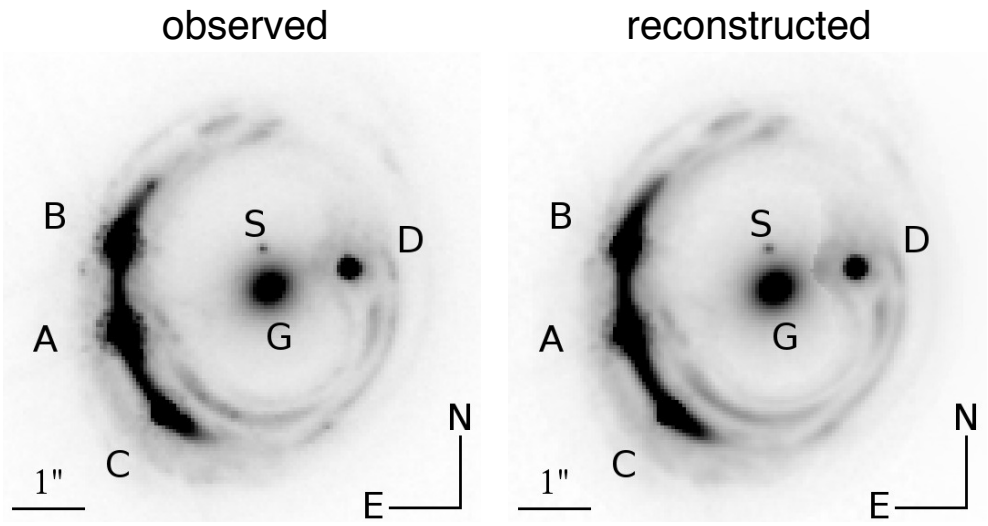

Figure 8.4: *HST* ACS image of RXJ1131−1231 in F814W filter. The background AGN is lensed into four images (A, B, C and D) by the primary lens galaxy G and its satellite S. Left: observed image. Right: reconstructed image based on the most probable composite model. From [27]

This lens system is shown in Figure 8.4, and includes a main lens galaxy (G), four images (A, B, C and D) as well as a small satellite galaxy, S. This Figure shows the primary lens galaxy G and a satellite lens galaxy S that are surrounded by the Einstein ring of the lensed source [3; 27]. This bright system brings together rare properties (i.e. quad, bright optical Einstein ring, small redshift, high amplification), nearly unique among the known gravitational lens systems [22].

A detailed analysis of nine years of observations of RXJ1131−1231 is presented by [29]. The R-band light curves of the four individual images of the quasar were obtained using deconvolution photometry for a total of 707 epochs. Several sharp quasar variability features strongly constrain the time delays between the quasar images. Using three different numerical techniques, they measure time delays for all possible pairs of quasar images while always processing the four light curves simultaneously. For all three methods, the delays between the three close images A, B, and C are compatible with being 0, while they measure the delay of image D to be 91 days, with a fractional uncertainty of 1.5% (1σ) including systematic errors.

8.3 Methods

We analyze strong gravitational lens models for two systems, including B1608+656 and RXJ1131−1231. Both systems are analyzed using Lenstool [6], Lensmodel [7], glafic [18] and PixeLens [19]. All four of these codes are publicly available for download and have been used extensively in the literature, as well as in our previous studies. PixeLens is a non-LTM code, while Lenstool, Lensmodel and glafic are all LTM codes.

The approach to comparative lens model studies here is similar to that used in our previous studies (Chapters 5 [13], and 7) . Specifically, we are using the same model in all four codes, to the greatest degree possible. While it is acknowledged that some features cannot be reproduced among the codes, this approach was taken to demonstrate intrinsic differences in the model codes. An alternative approach (not taken) would be to develop an optimal model in each code. However, this approach is avoided in these studies as it may not show the differences in the codes as well, although it may be an equally valid approach.

All models in this study use a $\Omega_m = 0.3$, $\Omega_\Lambda = 0.7$, $H_0 = 70$ km s^{-1} cosmology.

Models of B1608+656

This system has been well studied. The model used here was adapted from [21], which used the PixeLens code to study this system. This model was then translated into Lenstool, Lensmodel and glafic using the HydraLens code [12], which we developed to facilitate comparative lens model studies.

Our first set of models use a single SIE potential. This is admittedly a simplification of the true situation, since the observational data identifies two lens galaxies, G1 and G2. These models were used as a starting point for the study. The image positions used are from [11], and a single SIE potential is at [0.0,0.0]. The lens galaxy position is held constant, while the ellipticity, position angle and mass are free parameters.

The second set of models also uses image positions from [11], but uses two lens galaxies, G1 and G2, at the geometry from the same previous study. Both of these galaxies are modeled using SIE potentials. In these models, the lens galaxy positions are fixed, and the ellipticity, position angle, and mass are free parameters. These models are not analyzed with PixeLens, since PixeLens does not specify the lens potentials, so the results would be the same as with the models above.

Models of RXJ1131−1231

Models for RXJ1131−1231 were developed using the system geometry from [23]. The model includes a single SIE potential and four images. These initial models did not include the satellite lens galaxy, referred to as S, above. In these models, the lens galaxy positions are fixed, and the ellipticity, position angle, and mass are free parameters.

Starting with the initial system geometry, a model was written for PixeLens, which was then translated by HydraLens [12]for Lenstool, Lensmodel and glafic. The resulting models were modified slightly to adjust the parameters for optimization and the details of the lensing potential.

8.4 Results

The results for all models were assessed in several ways. The initial geometry was shown by the plot from PixeLens. Graphs of the critical and caustic curves generated by glafic were also

used.

The fit of the models was assessed using χ^2 and rms as figures-of-merit. The values of χ^2 for each model are calculated directly by Lenstool, Lensmodel and glafic. The values for the rms are calculated directly by Lenstool, and manually for models generated with Lensmodel and glafic.

The χ^2 is calculated by:

$$\chi^2 = \sum \frac{(y_f - y_i)^2}{\sigma_i^2} \tag{8.7}$$

where y_f is the model estimate, y_i are the individual measurements and σ_i is the uncertainty in the individual measurements.

The fit assessed by the rms uncertainty in the image plane is calculated by:

$$rms^2_{images} = \sum_i ((x_i^{'} - x_i)^2 + (y_i^{'} - y_i)^2) \ / \ N_{images}, \tag{8.8}$$

where $x_i^{'}$ and $y_i^{'}$ are the locations given by the model, and x_i and y_i are the real images location, and the sum is over all N_{images} images. The best-fit solution is obtained by the minimum rms, and the uncertainties are determined by the location of predicted images in the source plane [31].

The chi-square is computed assuming that noise within the data can be approximated by the square root of the signal recorded. The consequence of using a chi-square goodness-of-fit metric is to reduce the influence of the peak maximum when determining the parameters for the synthetic model. Notably, for high resolution data the use of chi-square to optimize the model may broaden the resulting full width at half maximum compared to the same model optimized using the rms. Different goodness-of-fit metrics offer alternative views from which an optimum for a model can be established, however neither statistic is a measure for how well a model itself relates to the true states present within the data.

Results of B1608+656 Lens Models

The image geometry of B1608+656 is shown here in Figure 8.5. The image positions and geometry are from [11], and have the same configuration as in that report. The image geometries used are the same in both the single and two potential model in this study.

Single Lens Potential Models of B1608+656

The results of the single potential models of B1608+656 are shown here in Table 8.1 (time delays) and Table 8.2 (Best Fit Lens Parameters). The critical and caustic lines for the lens model produced by glafic are shown in Figure 8.6. The time delays for this system are all on the same order of magnitude, although they are somewhat variable. The Lenstool model closely predicts the time delays for images A and C, while the time delay for image D is somewhat low.

A review of the best fit lens parameters shown in Table 8.2 shows that the χ^2 for the models is rather high, which probably reflects the fact that a single potential model is not adequate to describe this system with two known lenses, G1 and G2. However, these models were used as a simplistic starting point for the analysis, and it is not surprising that the models are not a good fit. The mass of each of the four models is not that different, although there range is notable. These results may have been different if the position of the lens mass was left as a free parameter, which will be addressed in future studies.

Software / Ref	A	B	C	D
Fassnacht [5]	31.5	···	36.0	77.0
PixeLens	7.9	···	0.4	48.2
Lenstool	38.0	···	32.4	56.5
Lensmodel	8.6	···	1.9	23.9
glafic	15.0	···	12.3	49.4

Table 8.1: Time Delays for four images in B1608. The three LTM models all use a single SIE potential for the lens. The time delay for all images is relative to image B, in days.

Software	RA ($''$)	Dec ($''$)	χ^2	rms ($''$)	e	θ (deg)	R_E ($''$)	$M(< R_E)$ ($10^{11}\ M_\odot$)	σ_0 (km s^{-1})
PixeLens	···	···	···	···	···	···	···	4.83	···
Lenstool	[0.0]	[0.0]	471	0.08	0.78	165	1.16	3.65	299
Lensmodel	[0.0]	[0.0]	754	0.21	0.58	69.4	1.02	2.77	280
glafic	[0.0]	[0.0]	89.3	0.11	0.42	65	1.26	4.28	312

Table 8.2: Best Fit Lens Parameters for B1608 models with a single SIE lens potential

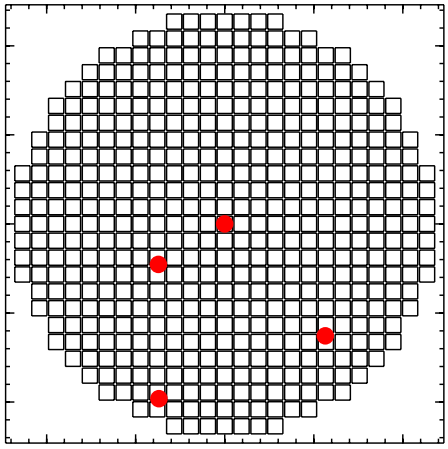

Figure 8.5: B1608 model made with Pixelens using geometry from [11].

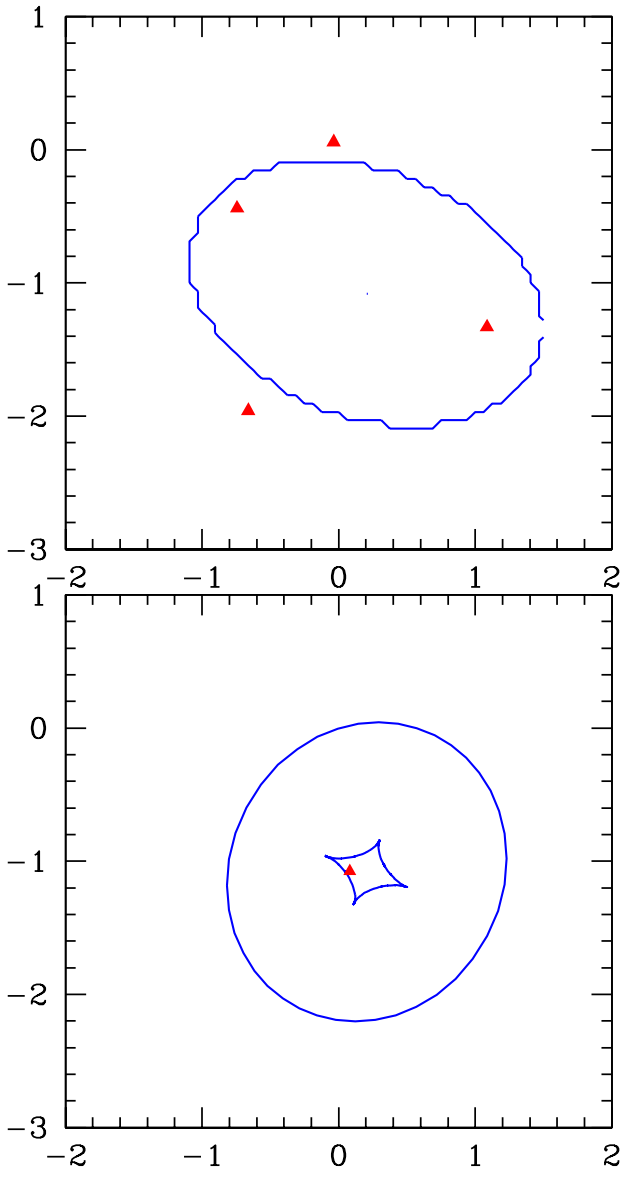

Figure 8.6: B1608 model made with glafic using geometry from [11] and a single lens potential. The image plane is shown in the upper panel and the source plane is in the lower panel.

Two Lens Potential Models of B1608+656

The results of the two potential models of B1608+656 are shown in Table 8.3 (time delays) and Table 8.4 (Best Fit Lens Parameters). The critical and caustic lines for the model produced by glafic is shown in Figure 8.7. The critical and caustic lines for this model should be compared with the results of [11] as shown in Figure 8.3. The critical an caustic lines are quite similar to that shown in Figure 8.3.

The PixeLens results in Table 8.3 are shown just for comparison, but there is no specification of potentials in the non-LTM code, PixeLens. The results from the other 3 codes are somewhat closer to the real values as reported by [5]. Despite this, there are still significant differences between the time delays of the models and the observational data. As above, if the position of the lens potentials varied, the results might be closer to the observational data.

In reviewing the best fit lens parameters in Table 8.4, the χ^2 values are much lower suggesting a better fit of the data. The rms values are also very small, consistent with a better fit. All three models predict a higher mass than that report din the model by [5], although all three have a larger mass for G1 compared to G2. The ellipticity and position angles show great variability in all models evaluated.

Software / Ref	A	B	C	D
Fassnacht [5]	31.5	···	36.0	77.0
PixeLens	7.9	···	0.4	48.2
Lenstool	26.6	···	36.7	51.2
Lensmodel	18.3	···	22.3	48.3
glafic	31.1	···	38.1	61.3

Table 8.3: Time Delays for four images in B1608+656. The 3 LTM models use two SIE potentials for the G1 and G2 components of the lens, using the geometry from Table 3 in [11]. Time delays for all images are relative to image B, in days.

Software / Reference	RA ($''$)	Dec ($''$)	χ^2	rms ($''$)	e	θ (deg)	R_E ($''$)	$M(< R_E)$ (10^{11} $M_\odot$)	σ_0 (km s^{-1})
[11]			99.8	···					
G1	[0.425]	[-1.059]			0.60	77	···	···	247
G2	[-0.291]	[-0.928]			0.32	68	···	···	60
Lenstool			8.1	0.008					
G1	[0.425]	[-1.059]			0.16	93	0.67	1.22	228
G2	[-0.291]	[-0.928]			0.99	151	0.46	0.58	189
Lensmodel			87.3	0.42					
G1	[0.425]	[-1.059]			0.17	79	0.69	1.28	231
G2	[-0.291]	[-0.928]			0.41	45	0.40	0.43	177
glafic			6.15	0.11					
G1	[0.425]	[-1.059]			0.10	127	0.71	1.35	233
G2	[-0.291]	[-0.928]			0.71	54	0.47	0.59	190

Table 8.4: Best Fit Lens Parameters for B1608+656 models with G1 and G2 lens potentials based on the model from [11], Table 3. Positions of the potentials were fixed (in brackets) while ellipticity, position angle and velocity dispersion were free parameters for both G1 and G2.

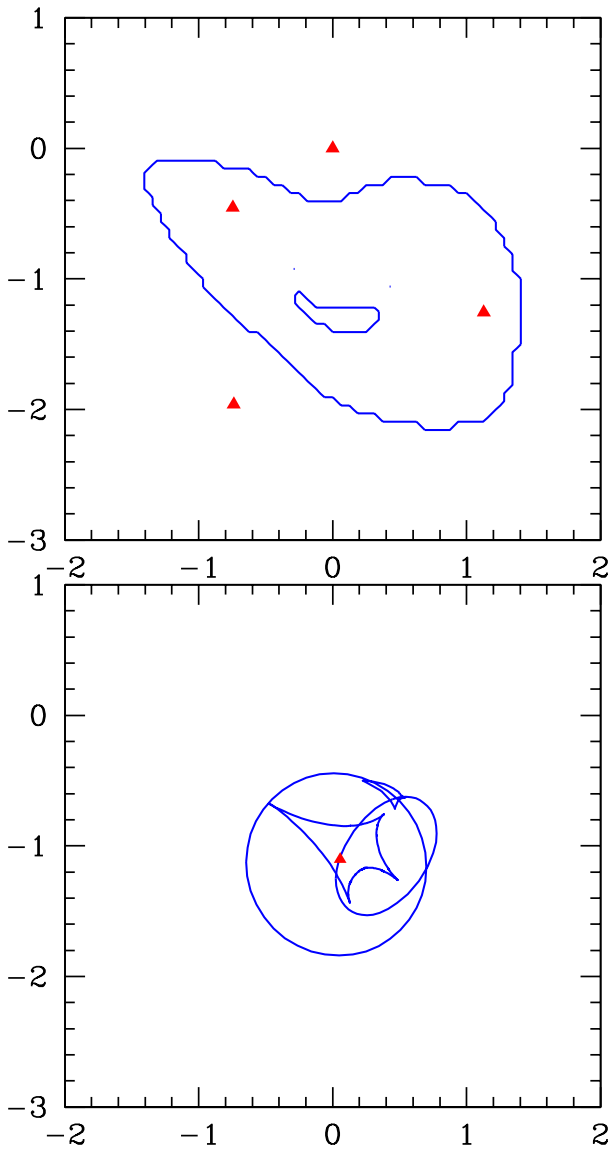

Figure 8.7: B1608 model made with glafic using geometry from [11] with two lens potentials, G1 and G2. The image plane is shown in the upper panel and the source plane is in the lower panel.

Results of RXJ1131−1231 Lens Models

The results for lens models of RXJ1131−1231 are shown here inTable 8.5 (time delays) and Table 8.6 (Best Fit Lens Parameters). The basic system geometry is shown below in Figure 8.8, and the critical and caustic lines from the glafic model are shown in Figure 8.9.

Time delays predicted by the PixeLens model are extremely close to those reported by

[23; 29]. The Lenstool model has a somewhat high time delay for Image C, but otherwise all of the models are fairly close to that reported previously. It may be possible to improve the results of the Lenstool model by using a different potential (e.g. PIEMD) or by allowing the position of the potential to be a free parameter.

The rms values for all models shown in Table 8.4 are fairly low, suggesting a good fit of the data, while the χ^2 values are somewhat high for the Lensmodel and glafic models. The Lenstool model has a fairly low value for χ^2. All of the models predict a similar mass to the [29] model, although the PixeLens model is higher than the rest. The critical and caustic lines for the model shown in Figure 8.9 are similar to that reported previously by [2].

Software / Ref	A	B	C	D
Suyu [23]	0.7 ± 1.4	$\cdots$	-0.4 ± 2.0	91.4 ± 1.5
Tewes [29]	0.7 ± 1.2	$\cdots$	0.4 ± 1.6	-91.4 ± 1.2
PixeLens	0.13	$\cdots$	0.2	90.6
Lenstool	2.4	$\cdots$	12.7	108.3
Lensmodel	1.6	$\cdots$	0.2	87.3
glafic	1.9	$\cdots$	0.15	110.9

Table 8.5: Time Delays for four images in RXJ1131−1231. The time delay for all images is relative to image B, in days.

Software / Reference	RA ($''$)	Dec ($''$)	χ^2	rms ($''$)	e	θ (deg)	R_E ($''$)	$M(< R_E)$ (10^{11} $M_\odot$)	σ_0 (km s^{-1})
[23]	$\cdots$	$\cdots$	$\cdots$	$\cdots$	0.76	115	1.64	$\cdots$	$\cdots$
[3]	-0.15	-0.41	272	$\cdots$	0.45	-73.6	1.823	$\cdots$	$\cdots$
PixeLens	$\cdots$	$\cdots$	$\cdots$	$\cdots$	$\cdots$	$\cdots$	$\cdots$	6.91	$\cdots$
Lenstool	[0.0]	[0.0]	14.1	0.02	0.80	17	1.88	5.19	359
Lensmodel	[0.0]	[0.0]	321	0.12	0.07	-71	1.80	5.01	350.6
glafic	[0.0]	[0.0]	406	0.40	0.39	106	1.82	5.09	353

Table 8.6: Best Fit Lens Parameters for RXJ1131−1231 models. All LTM models have a single SIE lens potential.

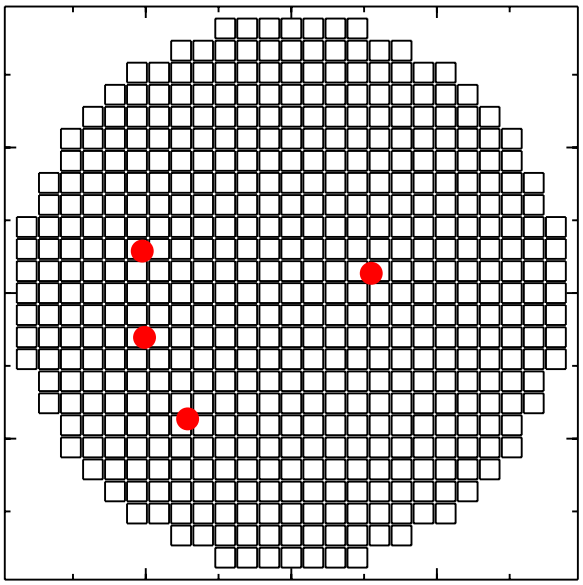

Figure 8.8: RXJ11311 model made with Pixelens

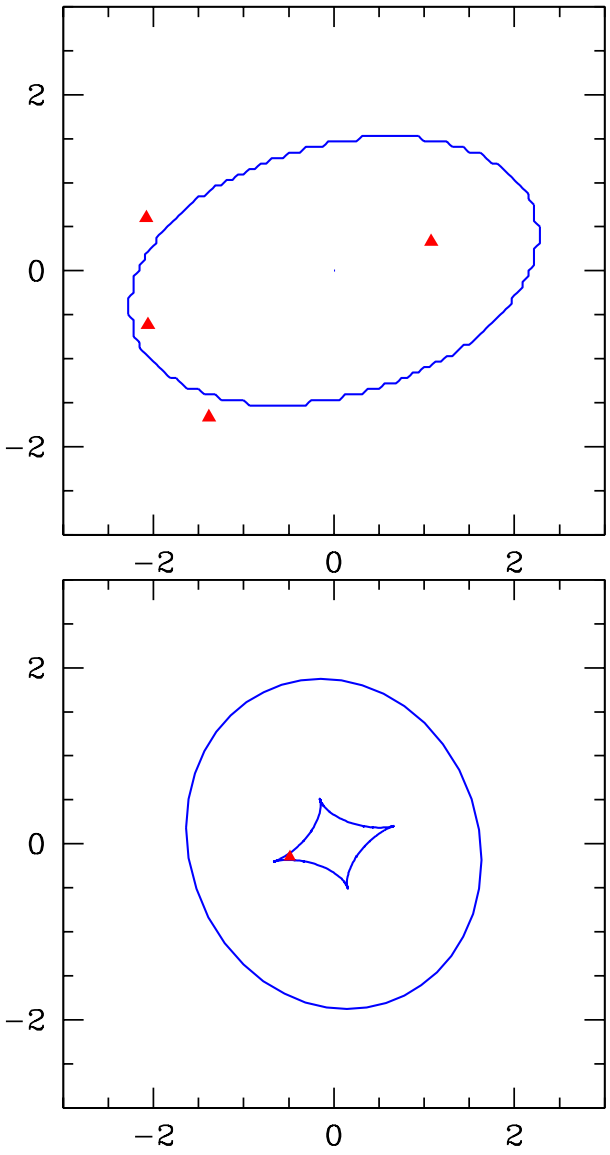

Figure 8.9: RXJ1131 model made with glafic using a single lens potential. The image plane is shown in the upper panel and the source plane is in the lower panel.

8.5 Discussion

Lens Models

This study evaluates lens models in a number of ways. The study of each of the three models considered begins with a check of the basic system geometry, which was done by comparing the image positions produced by the PixeLens model with the image positions in the literature.

The critical and caustic lines for the three systems evaluated were similar to those published in previous studies.

Time Delays

The use of lens model data to calculate time delays is important because of the potential for time dearly data to constrain calculation of H_0 as well as other cosmological parameters. These applications of time delay data are further discussed below.

The most important trend is that the predicted time delays, or the inferred H_0, increase as the mass distribution becomes more centrally concentrated. Time delays are controlled by a local property of the lens, the average surface density in the annulus between the lensed images. Reducing the model dependence of the time delay estimates to such a simple physical property of the lens leads to simple, accurate scaling laws for H_0, provides model-independent tests for the homogeneity of the time delay lenses, demonstrates that standard parametric models have the necessary degrees of freedom to study degeneracies in estimates of H0 from time delay measurements, and makes it easy to theoretically predict time delays for standard halo models [8].

The dependence of time delays on the radial and angular structure of the lens shows that standard parametric models, which can adjust both the radial mass distribution and the quadrupole structure of the lens, encompass the physical properties needed to study the dependence of Hubble constant estimates on the mass distribution of the lens.

It is interesting in this study, that the relatively simple model made with PixeLens, a non-LTM code, was able to very accurately reproduce the time delays for the system RXJ1131−1231. Most degrees of freedom in nonparametric models are not important for time delay estimates in simple lenses. Since the parametric models have the advantage of corresponding to physical models of galaxies, while most realizations of the nonparametric models do not, the use of nonparametric approaches is probably better suited to very complicated systems [8].

Lens Model Parameters

We use elliptically-symmetric distributions with power-law profiles to model the dimensionless surface mass density of the lens galaxies,

$$\kappa_{\rm pl}(\theta_1,\theta_2) = \frac{3-\gamma'}{2}\left(\frac{\theta_{\rm E}}{\sqrt{q\theta_1^2+\theta_2^2/q}}\right)^{\gamma'-1}, \tag{8.9}$$

where γ' is the radial power-law slope (with $\gamma' = 2$ corresponding to isothermal), $\theta_{\rm E}$ is the Einstein radius, and q is the axis ratio of the elliptical isodensity contours. Various studies have shown that the power-law profile provides accurate descriptions of lens galaxies. It has been shown that the grid-based lens potential corrections from power-law models were only $\sim 2\%$ for B1608+656 with interacting lens galaxies, thus validating the use of the simple power-law models even for complicated lenses. We note that the surface brightness of the main deflector in RXJ1131−1231 shows no signs of interaction and it is therefore much simpler than the case of B1608+656, further justifying the use of a simple power-law model to describe the mass distribution within the multiple images [23]

The Einstein radius in Equation (8.9) corresponds to the geometric radius of the critical curve, and the mass enclosed within the isodensity contour with the geometric Einstein radius is:

$$M_{\rm E} = \pi\theta_{\rm E}^2 D_{\rm d}^2 \Sigma_{\rm crit} \tag{8.10}$$

that depends only on $\theta_{\rm E}$, a robust quantity in lensing.

Time Delays and the Determination of H_0

It has been known that time delays between multiple images of strong gravitational lens systems offer an interesting method to measure the Hubble constant H_0, the most fundamental cosmological parameter that governs the length and time scale of our universe [20]. An advantage of this method is that it does not rely on so-called distance ladder and can measure the global Hubble constant independently of any local measurements. Motivated by this time delays have been measured in more than 10 lensed quasar systems [see, e.g., 9] [17]. The situation as it presents is, however, somewhat confusing and controversial. [8; 10] claimed from the analysis of several lens systems that the Hubble constant should be relatively low, $H_0 \sim 50\,{\rm km\,s^{-1}Mpc^{-1}}$. However, [11] performed systematic mass modeling of B1608+656 using all available data from radio to optical and found constrained the value of the Hubble constant to be $H_0 = 75^{+7}_{-6}\,{\rm km\,s^{-1}Mpc^{-1}}$. The analysis of the smallest separation lens B0218+357 yields $H_0 = 78 \pm 3\,{\rm km\,s^{-1}Mpc^{-1}}$. By combining time delays in 10 lensed quasar systems $H_0 = 72^{+8}_{-11}\,{\rm km\,s^{-1}Mpc^{-1}}$ was obtained. [17].

Implications of Comparative Lens Model Studies for the Determination of Cosmological Parameters using Time Delays

The idea to use time delay lenses to measure H_0 was first proposed by [20]. Strong gravitational lenses are elegant geometric consequences of how light travels through the universe while grazing massive galaxies. When the line of sight alignment is very close, light takes multiple paths around the curved space of the lens. These paths form multiple images, and the light takes a different amount of time to travel each path. Light passing closer to the lens is deflected by a larger angle (increasing its path length) and experiences a greater relativistic time dilation, further delaying its arrival. If the source flares up, or otherwise varies in intensity (e.g., if it is an active galactic nucleus, or AGN), we can observe these "time delays" between or among the images. These time delays are functions of the angular diameter distances between the source, lens, and observer, as well as the properties of the lens itself [4].

Future large ensembles of time delay lenses have the potential to provide interesting cosmological constraints complementary to those of other methods. In a flat universe with constant w including a Planck prior, LSST time delay measurements for $\sim 4,000$ lenses should constrain the local Hubble constant h to ~ 0.007 ($\sim 1\%$), Ω_{de} to ~ 0.005, and w to ~ 0.026 (all 1-σ precisions) [4].

To date, most efforts have focused on studies of individual time delay lenses. In theory, one might be able to control all systematics and constrain H_0 unambiguously given a single "golden lens". Such a lens would have a sufficiently simple and well-measured geometry. The closest to a golden lens may be B1608+656. In [26], the authors claim all systematics have been controlled to 5%. New estimates for H_0 based on this lens have been reported [4].

It is reasonable to expect that time delays will be reliably measured for large numbers of these lenses, whether through repeated observations in surveys (Pan-STARRS and LSST), auxiliary monitoring, and/or through tailored specific missions such as OMEGA [4].

Historically, analyses of individual lenses have yielded varying answers for H_0 This can be attributed to two factors, both of which, it appears, are now being overcome.

The first factor is simple intrinsic variation in lens properties (especially mass slope) and environment (lensing contributions from neighboring galaxies). Consider the following estimate from a simple empirical argument. If statistical uncertainties on H_0 decrease as $1/\sqrt{N}$ (as-

suming systematics can be controlled), and the current uncertainty from 16 lenses is $\sim 10\%$, then the uncertainty on a single lens might be $\sim 40\%$. Thus, assuming $h = 0.7$ (where $H_0 = 100h$ km s^{-1} Mpc^{-1}), individual lenses may be expected to yield a wide range of $h = 0.42$ – 0.98 (1-σ) [4].

The second factor in the wide range of reported H_0 values is that different analyses have assumed different mass profiles to model the lenses, including isothermal, de Vaucouleurs, and mass follows light. There is substantial weight of evidence that galaxy lenses are roughly isothermal on average, at least within approximately the scale radius. Theoretical work supports this idea, showing that a wide range of plausible luminous plus dark matter profiles all combine to yield roughly an isothermal profile *at the Einstein radius*, though the slope may deviate from isothermal beyond that radius [4].

8.6 Conclusions and Future Plans

[4] presented an analysis of the potential of gravitational lens time delays to constrain a broad range of cosmological parameters. The cosmological constraining power $\delta\mathcal{T}_{\mathcal{C}}$ was calculated for Pan-STARRS 1, LSST, and OMEGA based on expected numbers of lenses (including the quad-to-double ratio) as well as the expected uncertainties in lens models, photometric redshifts, and time delays. The Fisher matrix results in that study allow time delay constraints to be easily combined with and compared to constraints from other methods.

The importance of time delay data to advance the understanding of cosmological parameters underscores the importance of a further understanding of the calculation of time delays using strong gravitational lens models.

Future plans include further work with these models. Specifically:

- The two potential model for B1608+656: Vary positions of the potentials to obtain more constrained models.
- Use different types of potentials to optimize models
- Use the data to calculate H_0 from models for B1608+656 and RXJ1131−1231

References

[1] A. Barnacka, M. Geller, I. P. Dell'Antonio, and W. Benbow. Strongly Lensed Jets, Time Delays, and the Value of H0. *ArXiv e-prints*, August 2014. 272

[2] B. J. Brewer and G. F. Lewis. Unlensing HST observations of the Einstein ring 1RXS J1131-1231: a Bayesian analysis. *Mon Not Roy Astr Soc*, **390**:39–48, October 2008. 278, 286

[3] J.-F. Claeskens, D. Sluse, P. Riaud, and J. Surdej. Multi wavelength study of the gravitational lens system RXS J1131-1231. II. Lens model and source reconstruction. *Astr & Astrophys*, **451**:865–879, June 2006. 278, 286

[4] D. Coe and L. A. Moustakas. Cosmological Constraints from Gravitational Lens Time Delays. *ApJ*, **706**:45–59, November 2009. 290, 291

[5] C. D. Fassnacht, E. Xanthopoulos, L. V. E. Koopmans, and D. Rusin. A Determination of H_0 with the CLASS Gravitational Lens B1608+656. III. A Significant Improvement in the Precision of the Time Delay Measurements. *Astrophys J*, **581**:823–835, December 2002. 275, 281, 284

[6] E. Jullo, J.-P. Kneib, M. Limousin, Á. Elíasdóttir, P. J. Marshall, and T. Verdugo. A Bayesian approach to strong lensing modelling of galaxy clusters. *New Journal of Physics*, **9**:447, December 2007. 279

[7] C. R. Keeton. Computational Methods for Gravitational Lensing. *ArXiv Astrophysics e-prints*, February 2001. 279

[8] C. S. Kochanek. What Do Gravitational Lens Time Delays Measure? *ApJ*, **578**:25–32, October 2002. 272, 289, 290

[9] C. S. Kochanek, B. Mochejska, N. D. Morgan, and K. Z. Stanek. A Simple Method to Find All Lensed Quasars. *ApJ Lett*, **637**:L73–L76, February 2006. 290

[10] C. S. Kochanek and P. L. Schechter. The Hubble Constant from Gravitational Lens Time Delays. *Measuring and Modeling the Universe*, page 117, 2004. xv, 273, 274, 275, 290

[11] L. V. E. Koopmans, T. Treu, C. D. Fassnacht, R. D. Blandford, and G. Surpi. The Hubble Constant from the Gravitational Lens B1608+656. *Astrophys J*, **599**:70–85, December 2003. xv, xvi, 277, 279, 280, 282, 283, 284, 285, 290

[12] A. T. Lefor. Comparison of Strong Gravitational Lens Model Software II. HydraLens: Computer Assisted Generation of Lens Models. *Astronomy and Computing*, **5**:28–34, August 2014. 279

[13] A. T. Lefor and T. Futamase. Comparison of Strong Gravitational Lens Model Software I. Time delay and mass calculations are sensitive to changes in redshift and are model dependent. *ArXiv e-prints*, July 2013. 271, 279

[14] A. T. Lefor, T. Futamase, and M. Akhlaghi. A systematic review of strong gravitational lens modeling software. *New Astr Rev*, **57**:1–13, July 2013. 272

[15] N. D. Morgan, C. S. Kochanek, E. E. Falco, and X. Dai. Time-Delay Measurement for the Quadruple Lens RX J1131-1231. *ArXiv Astrophysics e-prints*, May 2006. 278

[16] S. T. Myers, C. D. Fassnacht, S. G. Djorgovski, R. D. Blandford, K. Matthews, G. Neugebauer, T. J. Pearson, A. C. S. Readhead, J. D. Smith, D. J. Thompson, D. S. Womble, I. W. A. Browne, P. N. Wilkinson, S. Nair, N. Jackson, I. A. G. Snellen, G. K. Miley, A. G. de Bruyn, and R. T. Schilizzi. 1608+656: A Quadruple-Lens System Found in the CLASS Gravitational Lens Survey. *Astrophys J Lett*, **447**:L5, July 1995. 275

[17] M. Oguri. Gravitational Lens Time Delays: A Statistical Assessment of Lens Model Dependences and Implications for the Global Hubble Constant. *ApJ*, **660**:1–15, May 2007. 290

[18] M. Oguri. The Mass Distribution of SDSS J1004+4112 Revisited. *Proceedings Astr Soc Japan*, **62**:1017–, August 2010. 279

[19] J Read. Pixelens web page. http://www.qgd.uzh.ch/projects/pixelens/, May 2012. 279

[20] S. Refsdal. On the possibility of determining Hubble's parameter and the masses of galaxies from the gravitational lens effect. *Monthly Notices Royal Astr Soc*, **128**:307, 1964. 272, 290

[21] P. Saha and L. L. R. Williams. A Portable Modeler of Lensed Quasars. *Astr J*, **127**:2604–2616, May 2004. 279

[22] D. Sluse, J. Surdej, J.-F. Claeskens, D. Hutsemékers, C. Jean, F. Courbin, T. Nakos, M. Billeres, and S. V. Khmil. A quadruply imaged quasar with an optical Einstein ring candidate: 1RXS J113155.4-123155. *Astr Astrophys*, **406**:L43–L46, July 2003. 278

[23] S. H. Suyu, M. W. Auger, S. Hilbert, P. J. Marshall, M. Tewes, T. Treu, C. D. Fassnacht, L. V. E. Koopmans, D. Sluse, R. D. Blandford, F. Courbin, and G. Meylan. Two Accurate Time-delay Distances from Strong Lensing: Implications for Cosmology. *Astrophys J*, **766**:70, April 2013. 278, 279, 286, 289

[24] S. H. Suyu and R. D. Blandford. The anatomy of a quadruply imaged gravitational lens system. *Mon Not Roy Astr Soc*, **366**:39–48, February 2006. xv, 275, 276

[25] S. H. Suyu, P. J. Marshall, M. W. Auger, S. Hilbert, R. D. Blandford, L. V. E. Koopmans, C. D. Fassnacht, and T. Treu. Dissecting the Gravitational lens B1608+656. II. Precision Measurements of the Hubble Constant, Spatial Curvature, and the Dark Energy Equation of State. *Astrophys J*, **711**:201–221, March 2010. 275

[26] S. H. Suyu, P. J. Marshall, R. D. Blandford, C. D. Fassnacht, L. V. E. Koopmans, J. P. McKean, and T. Treu. Dissecting the Gravitational Lens B1608+656. I. Lens Potential Reconstruction. *Astrophys J*, **691**:277–298, January 2009. 275, 290

[27] S. H. Suyu, T. Treu, S. Hilbert, A. Sonnenfeld, M. W. Auger, R. D. Blandford, T. Collett, F. Courbin, C. D. Fassnacht, L. V. E. Koopmans, P. J. Marshall, G. Meylan, C. Spiniello, and M. Tewes. Cosmology from Gravitational Lens Time Delays and Planck Data. *Astrophys J Lett*, **788**:L35, June 2014. xv, 272, 278

[28] M. Tewes, F. Courbin, G. Meylan, C. S. Kochanek, E. Eulaers, N. Cantale, A. M. Mosquera, P. Magain, H. Van Winckel, D. Sluse, G. Cataldi, D. Vörös, and S. Dye. COSMOGRAIL: the COSmological MOnitoring of GRAvItational Lenses. XIII. Time delays and 9-yr optical monitoring of the lensed quasar RX J1131-1231. *Astr & Astrophys*, **556**:A22, August 2013. 278

[29] M. Tewes, F. Courbin, G. Meylan, C. S. Kochanek, E. Eulaers, N. Cantale, A. M. Mosquera, P. Magain, H. Van Winckel, D. Sluse, G. Cataldi, D. Vörös, and S. Dye. COSMOGRAIL: the COSmological MOnitoring of GRAvItational Lenses. XIII. Time delays and 9-yr optical monitoring of the lensed quasar RX J1131-1231. *Astr & Astrophys*, **556**:A22, August 2013. 278, 286

[30] O. Wucknitz and F. Volino. The gravitational lens J1131-1231 - How to avoid missing an opportunity. *ArXiv e-prints*, November 2008. 278

[31] A. Zitrin, T. Broadhurst, R. Barkana, Y. Rephaeli, and N. Benítez. Strong-lensing analysis of a complete sample of 12 MACS clusters at z>0.5: mass models and Einstein radii. *Mon Not Roy Astr Soc*, **410**:1939–1956, January 2011. 280

Chapter 9

Cosmological Parameters from Strong Gravitational Lens Models: Studies of GRAMORs

9.1 Purpose and Organization of this Chapter

This study was undertaken to further understand the cluster lens MACSJ1149.5+2223. [1] [2]This fascinating lensing cluster is of interest for two major reasons. First, it is currently under intense study as one of the clusters in the Hubble Frontier Fields project, which means that it is being modeled by a number of independent modeling groups to obtain a deeper understanding of this cluster lens.

Second, this cluster contains the largest known lensed images of a single spiral galaxy which lies close to the center of the cluster (z=0.544). These images cover 150" and are magnified approximately 200 times, which qualify this as the first GRAMOR (GRAvitationally lensed yet MORphologically regular) image [18]. GRAMORs were first described in 1998, and offer a unique opportunity for study of cluster lenses [4]. Although described in 1998, MACSJ1149.5+2223 is the first GRAMOR observed, and offers a way to test the idea that GRAMORs can be used to constrain cosmological parameters.

In this study, we explore the idea that GRAMORs can be used to constrain cosmological parameters, specifically the Equation of State parameter, w_X. This chapter is organized as follows. In Section §9.3 we describe the lens models used to evaluate MACSJ1149.5+2223 including one with Lenstool and one with glafic. In Section §9.4 we describe the results obtained with the lens models. The meaning of the results are described in Section §9.5. Some final conclusions as well as a discussion of the next steps in this project are made in Section §9.6.

9.2 Introduction

Gravitational lensing provides a powerful tool to compare the predictions of cluster simulations with observations. Gravitational lensing by galaxy clusters is found at intermediate redshifts,

[1]The results in this chapter represent a work in progress, which is continuing. Future plans are described in Section 9.6.

[2]Results from this chapter were presented at the Yale Frontier Fields Workshop, Yale University, New Haven CT USA, Nov 12-14 2014, http://www.astro.yale.edu/yale_frontier_workshop/

including the most distant cluster discovered by Zwicky, Cl0024+17 (z = 0.39), and one of the richest clusters discovered by Abell, A1689 (z = 0.18), with the largest known Einstein ring, $r \sim 45$" [18]. For such clusters many tens of multiply lensed images have been identified in deep Hubble images, leading to accurately measured central surface mass distributions. The Einstein radii of these massive clusters are found to be larger than predicted in the context of the standard ΛCDM cosmological model. This discrepancy is empirically supported by the surprisingly concentrated mass profiles measured for such clusters, when combining the inner strong lensing with the outer weak lensing signal boosting the critical radius at a fixed virial mass. The large number of giant arcs may help constrain the total lensing cross-section and is considered by some to be at odds with standard ΛCDM [18].

The magnification generated by massive clusters has consistently led to the discovery of the highest redshift galaxies, with the current record standing at $z \sim 9.6$ for a galaxy behind A1689 and magnified by nearly a factor of ~ 10, further discussed below in Section 9.2. Although lens magnification reduces the accessible area of the source plane it enhances the flux of faint galaxies with a net positive effect for the most distant galaxies lying on the steep exponential tail of the luminosity function. Lensing provides additional spatial resolution by stretching images, producing spatially resolved details.

GRAMORs

One of the most powerful results from studies of strong gravitational lensing is the ability to determine the values of cosmological parameters. A GRAMOR image was discovered in the cluster MACS J1149.5+2223 at redshift 0.544 [18]. The GRAMOR image is a spiral galaxy at redshift 1.4906 with area 55□" and is observed near the center of the cluster as one of multiple images. The area of all lensed images covers 150□" with a magnification estimated to be ∼200 in total. Mass reconstruction using the multiple images showed a very flat mass profile [18]. This is consistent with the theoretical prediction that a mass distribution with a flat central core can easily produce undistorted images [16].

The other reason is the expectation that the statistics of GRAMORs will depend strongly on cosmological parameters. Lens statistics depends in general on the cosmological parameters, in particular the existence of dark energy [3; 4; 5]. Conditions for the formation of GRAMORs is highly restricted compared with giant luminous arcs, and thus the appropriate combination of the cosmological parameters will be more restrictive.

The Hubble Frontier Fields Project

Extending over three Hubble Space Telescope (HST) cycles, the Hubble Frontier Fields (HFF) initiative constitutes the largest commitment of HST time for the exploration of the distant Universe through gravitational lensing by massive galaxy clusters. The power of clusters as well-calibrated telescopes for studies of the distant Universe has become fully appreciated only in recent years. This important next step forward is now being taken in the form of the Hubble Frontier Fields (HFF), a recent initiative launched by the Space Telescope Science Institute. As part of the preparations for these unprecedented observations of lensing clusters, five independent teams have analysed existing imaging and spectroscopic data to provide the community with accurate mass models on each cluster [14].

The Hubble Frontier Fields is a revolutionary project to model six galaxy clusters [6]. These clusters were carefully selected because of their unique features. It is expected that gaining an understanding of these clusters will significantly advance our understanding of the Universe. Of great significance is that these six clusters are being modeled by multiple investigators,

each using different techniques including both LTM and non-LTM models. These six clusters include Abell 2744, MACS J0416.1-2403, MACS J0717.5+3745, MACS J1149.5+2223, Abell S1063, and Abell 370. The results of these extensive modeling efforts are immediately made public through the Hubble Frontier Fields web site.

Strong-lensing models, as well as mass and magnification maps, for the cores of the six HST Frontier Fields galaxy clusters are available on the web site [6]. The parametric lens models are constrained by the locations and redshifts of multiple image systems of lensed background galaxies. The studies use a combination of photometric redshifts and spectroscopic redshifts of the lensed background sources obtained by HFF investigators [7] (for Abell 2744 and Abell S1063), collected from the literature, or provided by the lensing community.

Using these data, the HFF investigators (1) compare the derived mass distribution of each cluster to its light distribution, (2) quantify the cumulative magnification power of the HFF clusters, (3) describe how our models can be used to estimate the magnification and image multiplicity of lensed background sources at all redshifts and at any position within the cluster cores, and (4) discuss systematic effects and caveats resulting from our modeling methods. These investigators specifically investigate the effect of the use of spectroscopic and photometric redshift constraints on the uncertainties of the resulting models.

In initial results, the investigators find that the photometric redshift estimates of lensed galaxies are generally in excellent agreement with spectroscopic redshifts, where available. However, the flexibility associated with relaxed redshift priors may cause the complexity of large-scale structure that is needed to account for the lensing signal to be underestimated. These findings underline the importance of spectroscopic arc redshifts, or tight photometric redshift constraints, for high precision lens models.

Previous Lens Models of MACSJ1149.5

Below are summaries of the four lens models of MACSJ1149.5+2223 that have been previously published and used in studies. The descriptions of the various lens models are obtained from each respective publication.

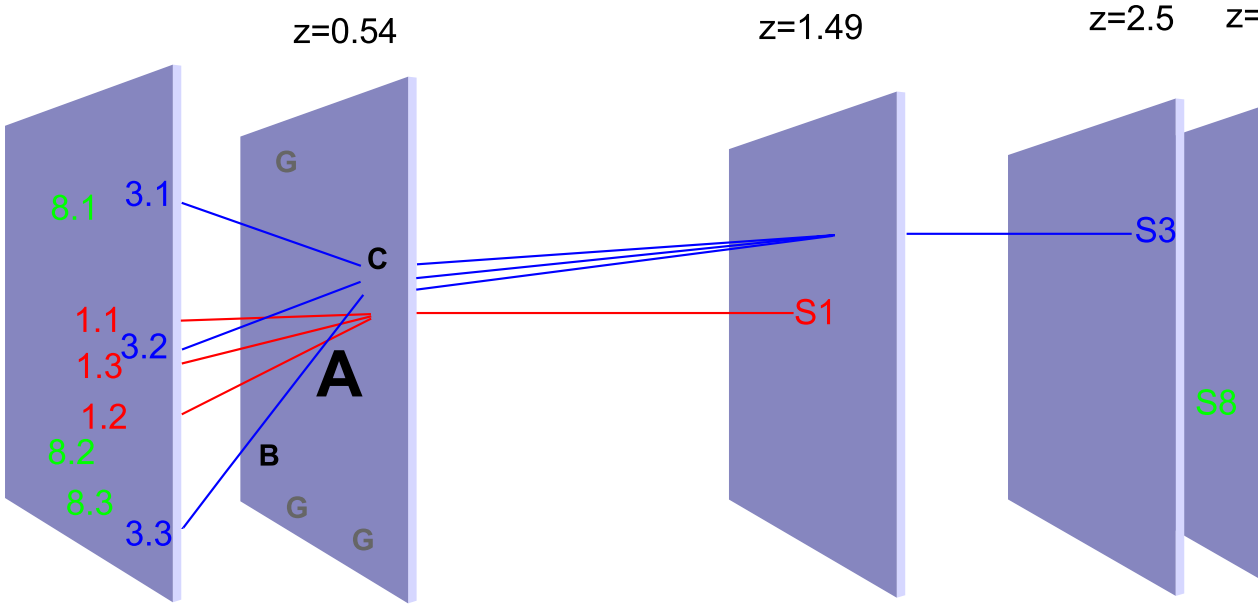

Figure 9.1: Geometry of the cluster lens and the sources S1, S3 and S8 and schematic light paths for sources S1 and S3 as an example. The lensing effect of the source S1 of the main image system 1 is shown, in the reconstruction of all other multiple images whose sources are at higher redshift. A,B,C denote individually modelled mass components in the cluster, G scaled galaxy mass contributions. From [13]

ZB Lens Model

There have been a number of lens model studies to date of MACSJ1149.5. The first model was that reported by Zitrin and Broadhurst [18] in their initial description of this fascinating lensing cluster. They apply their well-tested approach to lens modeling, which had been applied successfully to A1689 and Cl0024, uncovering unprecedentedly large numbers of multiply lensed images [20]. The full details of this approach can be found in previous papers from this group. Briefly, the basic assumption adopted is that mass approximately traces light, so that the photometry of the red cluster member galaxies is the starting point for our model.

Cluster member galaxies are identified as lying close to the cluster sequence by photometry. They approximate the large-scale distribution of matter by assigning a power-law mass profile to each galaxy, the sum of which is then smoothed. The degree of smoothing and the index of the power law are the most important free parameters. A worthwhile improvement in fitting the location of the lensed images is generally found by expanding to first order the gravitational potential of the smooth component, equivalent to a coherent shear, where the direction of the shear and its amplitude are free, allowing for some flexibility in the relation between the distribution of DM and the distribution of galaxies which cannot be expected to trace each other in detail.

All well-detected candidate lensed galaxies are then lensed back to the source plane using the derived deflection field, and then relens this source plane to predict the detailed appearance and location of additional counter images, which may then be identified in the data by morphology, internal structure, and color. The fit is assessed by the rms uncertainty in the image plane.

Importantly, this image-plane minimization does not suffer from the well-known bias involved with source plane minimization, where solutions are biased by minimal scatter toward shallow mass profiles with correspondingly higher magnification. The model is successively refined as additional sets of multiple images are identified and then incorporated to improve the model.

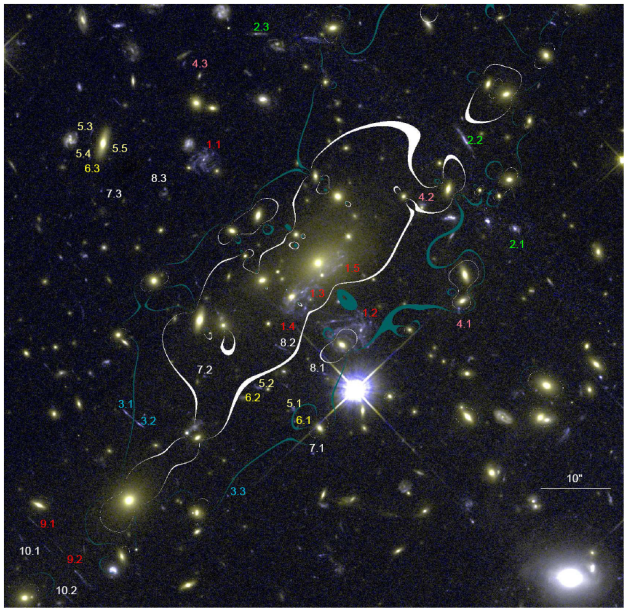

Figure 9.2: Model of MACSJ1149 by [18]. Large scale view of the multiply lensed galaxies identified by the model. In addition to the large spiral galaxy system 1, many other fainter sets of multiply lensed galaxies are uncovered by our model. The white curve overlaid shows the tangential critical curve corresponding to the distance of system 1. The larger critical curve overlaid in blue corresponds to the average distance of the fainter systems, passing through close pairs of lensed images in systems 2 and 3. This large scale elongated "Einstein ring" encloses a very large critically lensed region equivalent to 170 kpc in radius. For this cluster one arcsecond corresponds to 6.4 kpc/h_{70}, with the standard cosmology.

In the results of their analysis, the derived surface mass distribution is found to be very nearly uniform within the central 200kpc, with very little uncertainty, as is expected given the very large and undistorted images observed. The value of the uniform surface mass in this central region is the critical value for generating multiple images, about $0.5g/cm^2$ at the estimated redshift for the source.

The total magnification of the spiral galaxy derived is about 200, when summed over all five images, forming the largest known images of any lensed source, and is independent of the unknown source redshift, and given by the ratio of the area of images divided by the area subtended by the deprojected source.

Analysis of this model concludes that the unusually large and undistorted lensed images of a spiral galaxy uncovered requires a nearly uniform distribution of matter within the central $\sim 200kpc$ region covered by these images. The formation of multiple images requires the value of the central surface density to be nearly equal to the critical surface density for lensing.

Finally, they conclude that this cluster is unique in having near uniform density in projection,

at the critical level, thereby maximizing gravitational lens magnification. They calculate that the total area of sky exceeding a magnification, $\mu > 10$, is $\sim 2.8 arcmin^2$ corresponding to the current high-redshift limit of $z \sim 8$, which is over twice the equivalent area calculated for other massive clusters such as A1689 and Cl0024. This extreme magnification together with the lack of image distortion makes MACS J1149.5+2223 the most powerful known lens for accessing faint galaxies in the early universe. The power of MACSJ1149.5 was recently harnessed exactly as stated here to observe an object at $z \sim 9.6$ (see Section 9.2).

In summary, this model assumes that the mass approximately follows the light. The model consists of a superposition of power-law mass profiles for each galaxy in the cluster. As constraints, this model uses the multiple image positions from strong lensing. However, many of the details, are only reproduced approximately. Under the assumption that the BCG consists only of stellar mass, this models infers a nearly uniform DM surface mass density out to $\sim 200 kpc$.

A followup model of this system was published by [19]. This newer analysis took into account the spectroscopic redshifts and the presence of faint lensed galaxies. The published spectroscopic redshifts [15] were in full agreement with the predictions of their previous analysis. They assumed $z \simeq 1.5$ for the spiral-galaxy (system 1), and $z \simeq 2$ for the outer blue images (system 3), which were later verified to be at $z = 1.49$ and $z = 1.89$, respectively. Many other faint lensed galaxies are also visible, most of which were securely identified as belonging to 10 sets of multiply-lensed background galaxies. They also found that the critical curves for a source redshift of $z \simeq 2$ enclose a mass of $1.71 \pm 0.20 \times 10^{14} M_{\odot}$, and have an equivalent Einstein radius of $27 \pm 3 arcsec$.

Smith Lens Model

The second description of a lens model was reported by [15]. This model was based on their observational data of MACSJ1149.5, and was developed using Lenstool. Their goal was to constrain the shape of the mass distribution in the cluster core. They adopted stringent criteria for the inclusion of multiple-image systems as constraints on the lens model to guard against detection of spurious features in the mass distribution. To be included, a galaxy or morphological feature within a galaxy must be identified a minimum of three times, and the morphological and color match between the multiple images of the galaxy/feature must be unambiguous.

The mass distribution was initially parameterized as a superposition of 21 cluster galaxies, plus five cluster-scale components (which they referred to as halos) centered on the brightest galaxy in each of the light concentrations. All galaxies and halos were parameterized as smoothly truncated pseudo-isothermal elliptical mass distributions (PIEMD). This is the same parameterization we adopted in the model used here for the studies of constraining cosmological parameters.

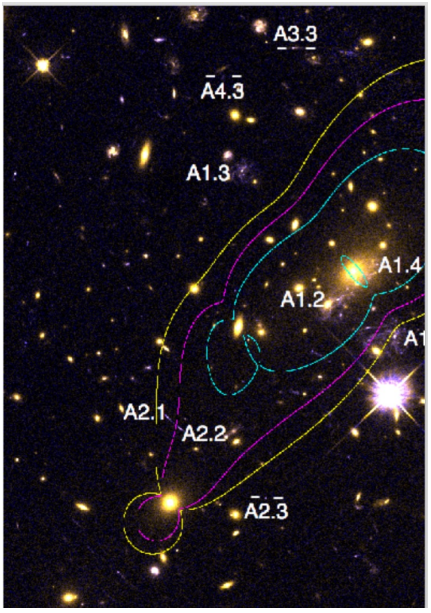

Figure 9.3: Model of MACSJ1149 by [15]. The central $\sim 80'' \times 80''$ of the cluster showing the multiple image systems discussed in the text. The cyan (outer), magenta and yellow curves show the $z = 1.491$, $z = 1.894$ and $z = 2.497$ tangential critical curves respectively. The inner cyan curve shows the radial critical curve for $z = 1.491$.

They then used the Bayesian evidence, i.e., the probability of the model given the data and the choice of the PIEMD parameterization, to determine whether the additional complexity of the five halo model is justified by the data. The result is summarized in Table 1 of the paper [15]. The probability of the four halo model exceeds that of the five halo model by a factor of 20. They therefore conclude that halo C is not justified by the data. They then tested whether even simpler models offer more probable descriptions of the data. In summary, models with ¡4 halos are less probable than the four halo model by 12-107 orders of magnitude, and therefore adopted the four halo model as the fiducial model, and list its parameters in Table 1 of the paper.

In summary, this model is also based on the image positions of multiply lensed bright clumps. However, it makes use of a larger number of bright clumps, hence a significantly larger number of constraints. The reconstructed image positions have a root mean square (rms) deviation from the observed positions of 0.5 arcsec. This model rules out the flat central profile proposed by [18].

Rau Lens Model

There is a third model described by Rau and coworkers, who used two different modeling approaches [13]. This work attempts to improve on the models described above by [18] and [15]. First, they use a more sophisticated model, by modeling all five galaxies that are close to multiply lensed images and close to the cluster centre using individual mass profiles. This is crucial for reproducing the morphology of the lensed image of the main system. Secondly, they identify twice as many positional constraints as previously used. These include multiply-imaged clumps that are part of two Einstein rings formed by two cluster galaxies, as well as

details of the nonlinear configuration of the image covering the centre of the cluster. With this increased number of constraints, they can place tight constraints on the slope of the total mass density profile. Thirdly, they use a more sophisticated gravitational lens modeling method that was originally developed and applied on galaxy scales. In this method, they use the information provided by the positions of multiply-lensed images along with the full surface brightness distribution of the images.

Since this lens modeling technique makes use of both the positions of the lensed images and their surface brightness distribution, it is very important to minimize the light contamination from the lensing galaxies. This was an important part of the observational portion of this paper.

Following the ΛCDM paradigm, the parametric mass model considered in this paper includes a central dark matter halo for the cluster A, five central mass components for the BCG and the galaxies G1, G2, G3 and G4, one mass component for a massive galaxy at B, and one for a group of smaller galaxies at C. The choice for the positions of A, B and C closely followed the ones chosen in [15] (A, B and D respectively, in their paper). They also stress that [15] did not explicitly include the galaxies G1 and G2 that will prove to be important in the detailed mass reconstruction of this cluster.

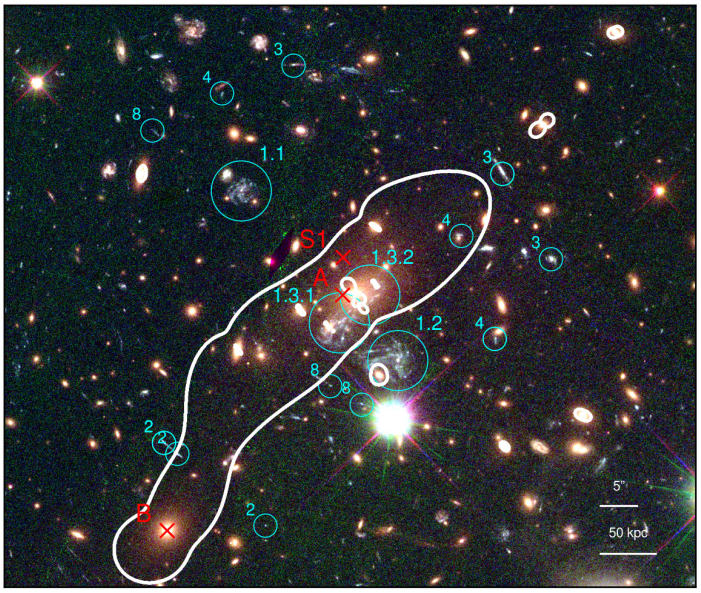

Figure 9.4: Model of MACSJ1149 by [13]. HST F814W/F606W/F555W RGB colour image from the Cluster Lensing And Supernova survey with Hubble (CLASH) observations of MACSJ1149 (north is up and east is left). Overlaid in white is the critical curve from the best model, for a source redshift of $z_s = 1.49$ and a cluster redshift of $z_l = 0.544$. The center of the reconstructed DM halo A is $\sim 1.5 arcsec$ left of the BCG. There are three separate main images labelled 1. The detailed morphology of the central image, 1.3, is more complicated, parts have a seven fold image configuration.

They model the mass distribution of MACS J1149.5+2223 with two different methods. They first build a model using the lensed image positions and constraints described, then, refine this model with a hybrid model that includes both the position constraints plus the full image surface brightness distribution.

The hybrid modeling technique includes all the positional constraints plus the full surface brightness distribution of image 1. First, they evaluate the quality of the results of this modeling in terms of the image positions. The rms distances of the separation of all, and central constraints are 0.94 and 0.063 arcsec, respectively, the means are 0.32 and 0.05 respectively.

Due to the increased number of constraints, the hybrid modeling technique puts more emphasis on the accurate reconstruction of the surface brightness distribution of the central image 1. Therefore, the respective rms is improved to a level comparable to the resolution limit of the CLASH data. Instead, the outer constraints are weighted less and consequently the image positions of the other images are reproduced less perfectly. As a consequence, the reconstruction of all multiple images is worse in terms of the total rms. However, the model based only on positions performs worse for the central image: the solution is usable as a starting point for the hybrid model, but it does not reproduce the image surface brightness distribution in detail.

These authors present a new and detailed model for the centre of the galaxy cluster MACS J1149.5+2223. In particular, they identified more than twice as many constraints as previously used. They also used a multiple lens plane algorithm in order to properly include the lensing contribution of the mass associated with the source S1. Finally, with a hybrid modeling approach, they performed the first detailed reconstruction of the surface brightness distribution of the system 1.

These results can be summarized as follows. These models recovered the surface brightness distribution of system 1 with a precision close to the noise level of the HST CLASH observations. Using a hybrid modeling approach, they have derived posterior probability density distributions of the main model parameters that are significantly tighter than those derived with the simpler position modeling. By using new constraints, they constrained three important details of the mass distribution: the individual mass distributions of the two cluster galaxies G1 and G2, and the total mass distribution of the cluster at the innermost radii. These results recovered the 2D logarithmic slopes for galaxies G1 and G2 measured at a distance corresponding to their respective Einstein radii in the cluster. The mass model suggests a large ($\sim$ 12 arcsec) core in the cluster DM distribution and that the total mass profile at the very centre of the cluster is dominated by the BCG.

Johnson Lens Model

The fourth paper describing a lens model for MACSJ1149.5+2223 is by Johnson and colleagues who describe the model used for the Hubble Frontier Fields project [7]. They constraints from the strongly lensed image lists in previous papers [15; 17; 18] supplemented by unpublished identifications. They then consolidate all lists of images. We

fix the redshifts of systems 1, 2, and 3 to the spectroscopic redshifts reported by [15]. Excluding a mis-identified image as a constraint, the model presented predicts a redshift of $z > 3$ for the two outer-most images of this image set, in stark contrast to the photometric estimate of $z \sim 1$. The nature of this system may be better understood with the full HFF depth and spectroscopic confirmation.

The lens model of MACS J1149.5+2223 at z=0.543 consists of two dark matter halos, one lying close to the BCG and the the other located near an overdensity of cluster galaxies 100 arctic north of the cluster center. We allow only the position, velocity dispersion, and cut radius of the second halo to vary in the model. We include the velocity dispersion and cut radii of the BCG and cluster member galaxy as free parameters.

They also include a galaxy-scale halo north of the cluster accounting for the lensing of image systems 9 and 10, due to the galaxy-galaxy lensing boosted by the mass from the dark matter halo of the cluster. Since neither of these two systems have spectroscopic redshifts, there are

insufficient constraints to attempt to model both the individual galaxy plus other substructure in that vicinity, which is essentially isolated from the rest of the cluster. Instead, they use a single halo with position priors matching a galaxy. The model requires an unrealistically high ellipticity, indicating that more substructure may be needed; we thus fix it to e=0.8 and leave the position angle, velocity dispersion, and cut radius as free parameters. The necessity of optimizing this halo in the model far away from the majority of modeling constraints suggests the presence of significant substructure in part of the lens plane. The critical curves, image constraints, mass distribution, and magnification map for this cluster are then shown in Figure 4 in the paper.

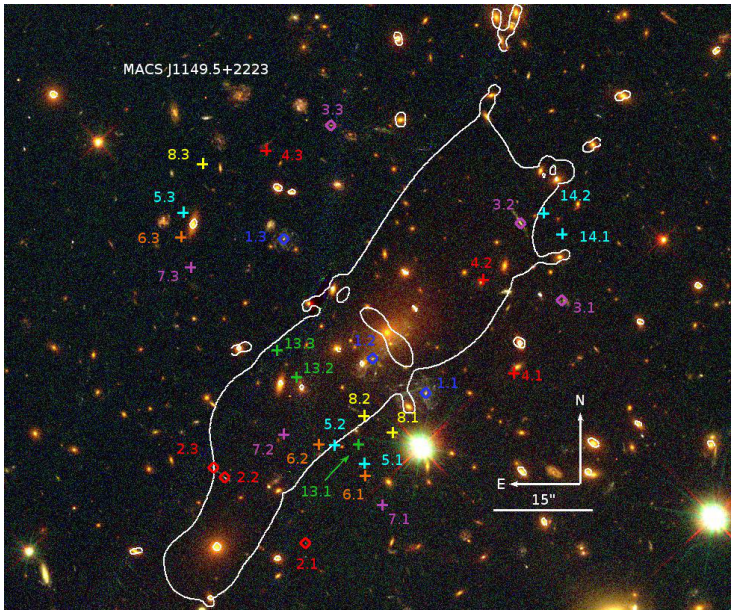

Figure 9.5: Top: False color image of MACSJ1149 from ACS imaging (red, F814W; green, F606W; blue, F435W). From [7].

The authors compute a cylindrical mass at the core of MACSJ1149 of $M(r < 500\text{kpc}) = 5.98^{+0.59}_{-0.25} \times 10^{14}$ $M_\odot$. They then directly compare this value with the model by [15], who found $M(r < 500\text{kpc}) = 6.7 \pm 0.4 \times 10^{14}$ $M_\odot$. In fact, the [15] model and the Johnson model were constructed independently with Lenstool and resulted in similar locations of cluster halo components in the lens plane. However, the previous model was built with fewer identified image systems. This model includes 35 images from 12 uniques sources, whereas [15] identified 19 images from 6 unique, multiply imaged sources. Johnson et al. found $M(< \text{crit}) = 1.12^{+0.01}_{-0.04} \times 10^{14}$ $M_\odot$ for the mass enclosed by the $z = 2$ critical curve ($0.40^{+0.01}_{-0.02}$ square arcmin), which does not agree with [19], who found that $M(< \text{crit}) = 1.71 \pm 0.20 \times 10^{14}$ $M_\odot$ (0.63 square arcmin). They also note that the [19] model does again not include any spectroscopic or photometric redshifts, have a different set of multiple image identifications, and do not treat their image redshift constraints as free parameters. The reader is referred to the discussion in [15], where they rule out the inner slope of the surface mass density profile of the [19] model by 7σ. This important result demonstrates how different modeling inputs can result in significantly different lens models.

MACSJ1149 as a Cosmic Telescope

Further understanding of this interesting lensing cluster is prompted for several reasons. Of greatest interest is that this cluster was used as a "cosmic telescope" to realize one of the great potentials of gravitational lensing. Gravitational lensing by galaxy clusters allows the detection of high-redshift galaxies fainter than what otherwise could be found in the deepest images of the sky. In a recent report, Zheng and colleagues reported imaging of a gravitationally magnified galaxy from the early Universe, at a redshift of $z = 9.6 \pm 0.2$ (that is, a cosmic age of 490 ± 15 million years, or 3.6 per cent of the age of the Universe) [17]. They estimate that it formed less than 200 million years after the Big Bang, implying a formation redshift of less than 14. Given the small sky area that their observations cover, faint galaxies seem to be abundant at such a young cosmic age, suggesting that they may be the dominant source for the early re-ionization of the intergalactic medium.

Constraining the Dark Energy Equation of State

The use of strong lensing by galaxy clusters to constrain the dark energy equation of state has been investigated [2]. The cores of massive clusters often contain several multiply imaged systems of background galaxies at different redshifts. The locations of lensed images can be used to constrain cosmological parameters due to their dependence on the ratio of angular diameter distances. These authors use a series of simulations, and conclude that cosmography with a set of well studied cluster lenses may provide a powerful complementary probe of the dark energy equation of state.

A full discussion of image locations and the dark energy equation of state is given in [2]. Part of that discussion is shown here. We consider a constant equation of state parameter w_X because that is how this is specified in the Lenstool and glafic codes. The lens equation is given by

$$\vec{\beta_i} = \vec{\theta_i} - \frac{2}{c^2}\frac{D_{ds}}{D_d D_s}\nabla\phi(\vec{\theta_i}), \tag{9.1}$$

where the angular coordinates of the source i and its corresponding image(s) are given by $\vec{\beta_i}$ and $\vec{\theta_i}$ respectively, and ϕ is the projected Newtonian potential of the lens. For the parametric models used in this work, the potential is typically normalized by the associated central velocity dispersion, σ_v. The subscripts d, and s correspond to the distances to the lens (deflector) and source. D_{ab} is defined as the angular diameter distance from z_a to z_b. In the case of a flat, two-component universe, D_{ab} is given by

$$D(z_a, z_b) = \frac{c/H_0}{1+z_b}\int_{z_a}^{z_b} \mathrm{d}z \ \left(\Omega_m(1+z)^3 + \Omega_X(z)\right)^{-1/2}, \tag{9.2}$$

where H_0 is the present day Hubble constant, c is the speed of light, and Ω_m is the present day matter density normalized by the critical density. The function $\Omega_X(z)$ is the contribution from dark energy and its form depends on the choice of parameterization. Here we consider a constant equation of state, w_x. However, it can also be parameterized as the widely used Chevallier, Polarski, and Linder (CPL) parameterization, $w_x(z) = w_0 + w_a z/(1+z)$ [2]. In this case, $\Omega_X(z)$ is given by

$$\Omega_X(z) = \Omega_X(1+z)^{3(1+w_0+w_a)}\exp\left[-\frac{3w_a z}{1+z}\right]. \tag{9.3}$$

.

These authors use a very innovative simulation method to show that CSL cosmography is not limited to a particular type of cluster mass profile. A sample result is shown in Figure 9.6, which shows that the results are similar for both NFW and PIEMD potentials.

Although they have used PIEMD lenses exclusively, the results are not dependent upon this choice of profile. To illustrate this point, they then use the Navarro-Frenk-White profile, which has a cusp with the density approaching r^{-1} in the inner regions, and transits to r^{-3} in the outer regions beyond the scale radius. This profile is significantly different from the PIEMD case.

For comparison, they then generate elliptical PIEMD and NFW lenses at a redshift of $z_l = 0.21$ with equal masses of 1.6×10^{15} $M_\odot$. The former has a velocity dispersion of 1300 km/s, core radius of 41 kpc and scale radius of 900 kpc. The latter has a concentration parameter $c = 4.5$ and a scale radius $r_s = 495\,\mathrm{kpc}$. Both have ellipticity parameters of 0.3. Since our purpose in this section is solely to compare different cluster-scale mass profiles, they neglect the role of sub-structure in what follows. They then lens a simulated source distribution for both cases and use the same number of images as constraints for parameter recovery, and run the MCMC sampler using the input models with flat priors. In the NFW case all parameters are free. In the PIEMD case, r_{core} is fixed to the input value so that the number of free parameters is the same in the two cases. Figure 9.6 compares the results from both cases. The solid and dashed contours show the PIEMD and NFW constraints respectively. Note the similarity of the results, indicating that a sample of NFW cluster lenses would generally yield similar constraints to those with the PIEMD cluster lenses.

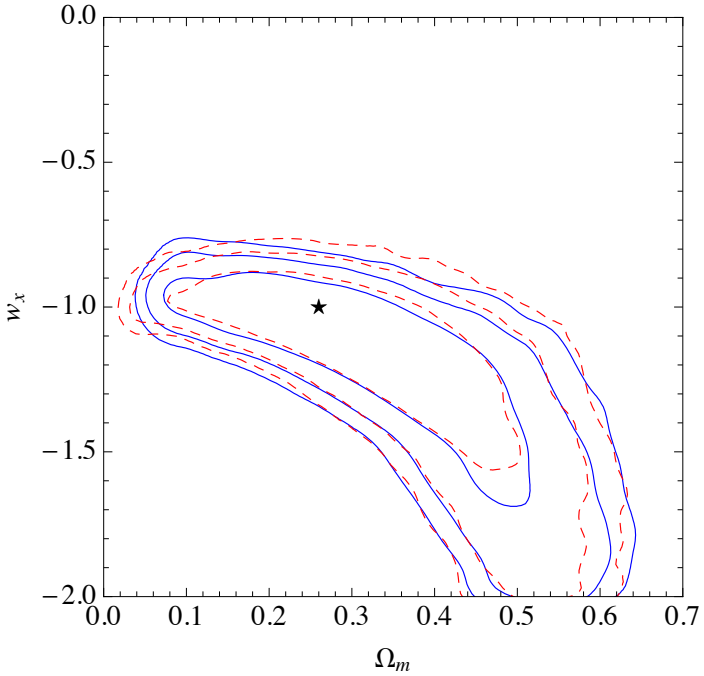

Figure 9.6: An illustration that similar dark energy constraints may be obtained from clusters with very different mass profiles. The solid and dashed contours correspond to PIEMD and NFW lenses respectively. For both cases the authors use mock catalogs of 21 images and assume only observational errors of $0.1''$ for each image. From [2]

9.3 Methods

The purpose of this study is to examine MACSJ1149.5+2223 as a way of constraining cosmological parameters. There is no attempt to repeat the work being done by the Frontier Fields project, which is focused on developing and comparing multiple lens models, including both LTM and non-LTM models. This study has four basic components. We will begin with validating lens models of MACSJ1149.5+2223 using both Lenstool and glafic. Second, these models will be investigated to see how well they can constrain cosmological parameters. Specifically, we will evaluate the Equation of State parameter, w_X in the plane of w_X vs. Ω_m. Third, after having robust models, the models will be modified to reflect the presence of a GRAMOR. Last, they will again be evaluated to see how well they constrain cosmological parameters. There are no previous studies looking at MACSJ1149.5 to constrain cosmologic parameters.

MACSJ1149.5+2223 Lens Models

The image catalog used in this model for MACSJ1149.5+2223 was obtained from the Hubble Frontier Fields Web Site [6]. The catalog of images was published by [10] as part of the CLASH program. The image catalog contains a total of 38 images in 13 families. The redshifts used are from [10]. Three of the images have published spectroscopic redshifts. Models in this chapter were developed using both Lenstool [8] and glafic [12]. Both of these codes are LTM (parametric) in their modeling methodology. All models in this study use a $\Omega_m = 0.3$, $\Omega_\Lambda = 0.7$, $H_0 = 70$ km s^{-1} cosmology.

Lenstool Model

The best-fit model for MACSJ1149 consists of two large-scale potentials (one with velocity dispersion in excess of 1000 km/s and another with velocity dispersion in excess of 600 km/s) and three potentials with velocity dispersions in excess of 300 km/s to model the central region. In addition it includes the potentials of 217 contributing cluster galaxies. All potentials are modeled with Pseudo Isothermal Elliptical Mass Distribution (PIEMD) profiles. This best-fit model for MACSJ1149 includes 13 families of multiple images of which three have published spectroscopic redshifts.

The lens model includes both cluster-scale halos and halos assigned to red-sequence cluster member galaxies, all represented by pseudo-isothermal elliptical mass distributions [8]. The PIEMD is parameterized by a two-dimensional location in the lens plane, a lens plane redshift, ellipticity and position angle, a fiducial velocity dispersion, core radius, and cut radius. The cut radius for these cluster-scale halos is much larger than the strong-lensing regime ($< 100''$ of fiducial center of cluster) and cannot be constrained in the model, so we fix the cut radius arbitrarily at 1500 kpc. Unless otherwise noted below, all of the other parameters of these cluster-scale halos are left as free parameters.

The model used with source-plane optimization is shown in Figure 9.7 with images, caustic and critical lines. This model is quite comparable to the four published lens models described above in the Introduction. This model was obtained from Limousine, and was then modified with the image positions from Merten [10].

MACSJ1149.5+2223 glafic Model

The glafic model used in this initial study uses a NFW potential, as well as a Jaffe potential. There is added external convergence / shear as well as a sum of Jaffe potentials used to represent the other galaxies. This was done in a manner similar to the model used by Oguri for SDSSJ1004 [12] as an initial guess for the model. Parameters were optimized and the model improved in an iterative manner.

The final glafic model is shown in Figure 9.8 with images and critical lines. This model is not quite as accurate as the Lenstool model used in this study, and does not compare as well to the four published models described in the Introduction. Improvements in this model will be necessary in the next phase of this project.

Evaluating the Equation of State Parameter

In order to evaluate constraints on the dark energy equation of state parameter, we perform a series of calculations with models using a range of values of w_X from -2.0 to 0.0 in steps of 0.1 (21 values) and at each of these values we also vary Ω_m from 0.0 to 1.0 in steps of 0.1 (11 values). The χ^2 values for these 231 results are then plotted on a contour plot and evaluated

at the 95% and 90% confidence levels. The values of w_X and Ω_m are set in the models for each run with both Lenstool and glafic.

Representation of the GRAMOR

Although GRAMORs were described some time ago [4], the first GRAMOR was observed in 2009 [18]. There have been no previous modeling studies to represent a GRAMOR with a strong lens model code, or to use it to constrain the values of cosmological parameters. There is no existing approach to this aspect of gravitational lens modeling.

Given the lack of an existing method, we will use two different methods in this study. In the Lenstool model, we will add additional images at the same location as the GRAMOR image (1.1) to represent a magnified image. In the glafic model, one can specify the flux for an image, so this will be varied to represent the magnified image.

9.4 Results

The result of this study will eventually include four parts including evaluation of the lens models with Lenstool (completed) and glafic (completed), constraining the equation of state with Lenstool (completed) and glafic (pending), representation of a GRAMOR in Lenstool (pending) and glafic (pending), and constraining the equation of state including a GRAMOR with Lenstool (pending) and glafic (pending).

Evaluation of Lens Models

The lens models are evaluated in comparison to the previously published models as discussed above in the Introduction. Other parameters include the χ^2 and the image rms value.

For each of the observed image systems with n images, we determine the goodness of fit for a particular set of model parameters using a source plane χ^2,

$$\chi^2 = \sum_{i=1}^{n} \frac{\left[M\left(\vec{\beta}_i - \left\langle \vec{\beta} \right\rangle\right)\right]^2}{\sigma_i^2}, \tag{9.4}$$

where $\vec{\beta}_i$ is the source plane position corresponding to image i, $\left\langle \vec{\beta} \right\rangle$ is the family barycenter, M is the magnification tensor, and σ_i is the total (observational and modeling) error. The total χ^2 was obtained by summing over families and was used in conjunction with a Markov Chain Monte Carlo (MCMC) sampler (Lenstool) to probe the posterior probability density function (PDF) as a function of all relevant model parameters [8] (SOM). The key degeneracies with cosmological parameters for this technique arise from the velocity dispersions, ellipticity and core radii of the large scale mass clumps in the model [9].

The fit is assessed by the RMS uncertainty in the image plane:

$$RMS^2_{images} = \sum_i ((x_i^{'} - x_i)^2 + (y_i^{'} - y_i)^2) \ / \ N_{images}, \tag{9.5}$$

where $x_i^{'}$ and $y_i^{'}$ are the locations given by the model, and x_i and y_i are the real images location, and the sum is over all N_{images} images. The best-fit solution is obtained by the minimum RMS, and the uncertainties are determined by the location of predicted images in the source plane [19].

MACSJ1149.5+2223 Lenstool Model

The images, critical lines and caustics are shown in Figure 9.7. This model is qualitatively similar to the four published models above, described in the Introduction. The χ^2 for the best model, with image-plane optimization, is 41.90 with an image rms of $0.48''$. Using source-plane optimization, the χ^2 value is 107.29, and the rms is $1.851''$.

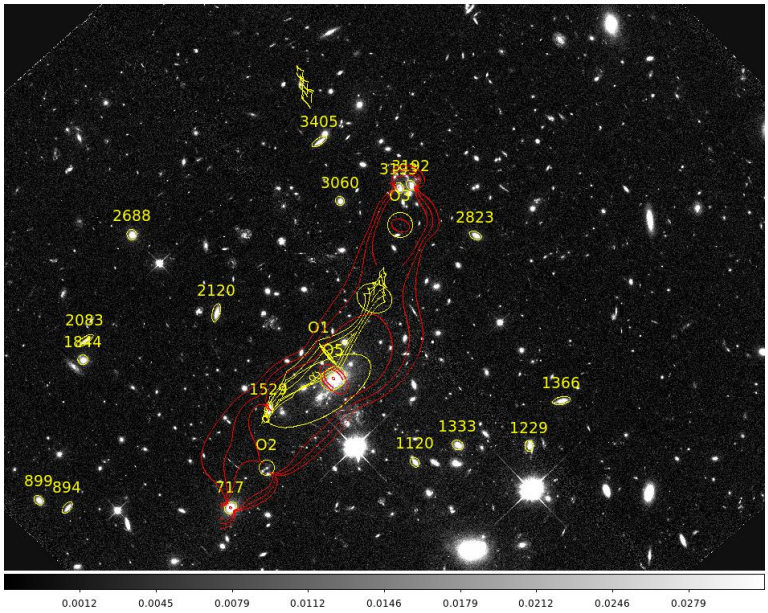

Figure 9.7: The Lenstool model of MACSJ1149.5+2223 with source plane optimization

The source-plane optimization model was used in this study to examine the equation of state parameter w_X. Th choice of this model was based on computational requirements, and has been used by many authors in this area. This is further discussed below in Section 9.5. We acknowledge the fact that the χ^2 value is higher for this model but based on a partial comparison of results, the contour curve for w_X vs. Ω_m will not be any different.

MACSJ1149.5+2223 glafic Model

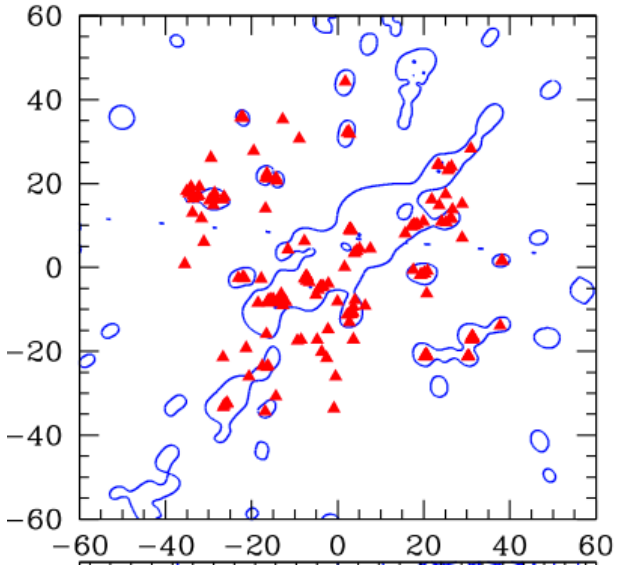

Figure 9.8: The glafic model of MACSJ1149.5+2223 with source plane optimization

Constraining the Equation of State

The method used to examine constraints on the Equation of State parameter is described above in 9.3. Briefly, we varied w_X and Ω_m and examined the contour plot of χ^2. The results for the Lenstool model are shown here. Results with the glafic model are pending future studies.

Lenstool: Constraining the Equation of State

The variation in χ^2 in the w_X - Ω_m plane is shown in Figure 9.9.

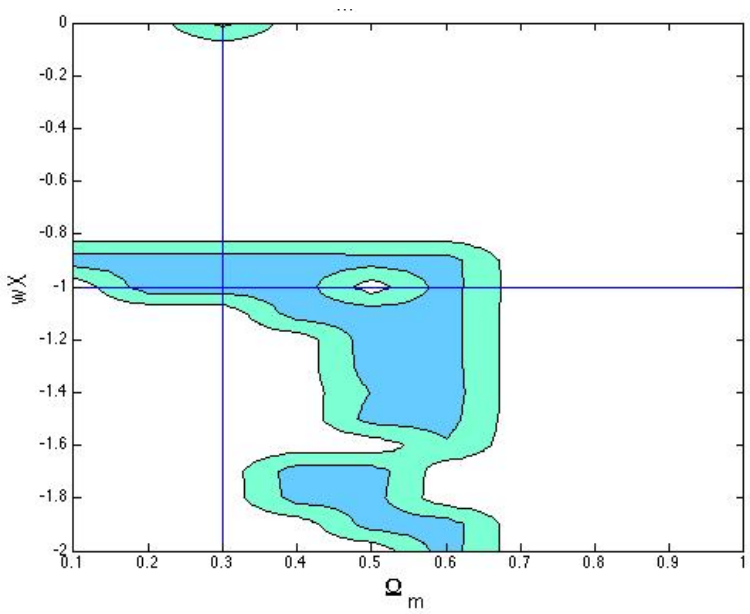

Figure 9.9: Lenstool: w_X varies with Ω_m

glafic: Constraining the Equation of State

Using the glafic model described above, we evaluated χ^2 throughout the w_X and Ω_m plane as described. However, there was no variation seen in the values of χ^2 at any point. This can only be interpreted to mean that the model as developed is inadequate and another model is necessary.

This result is pending future studies with a new lens model, and will be conducted in a manner similar to that used for Lenstool.

Representation of a GRAMOR in the Lens Model

This component of the project is still pending, and will proceed using bot the Lenstool and glafic models for MACSJ1149.5. The method to be used for this is described above in Section 9.3.

Constraining the Equation of State: GRAMOR

This component of the project is still pending, and will proceed using bot the Lenstool and glafic models for MACSJ1149.5. The method to be used for this is described above in Sections 9.3 and 9.3.

9.5 Discussion

Although it was recognized that distant clusters of galaxies are able to produce gravitationally lensed, highly magnified, yet morphologically regular images (GRAMORs) of distant galaxies [5; 16] some time ago, the first such image was observed in 2009 [18]. Since GRAMORs have a regular morphology, they are not easily identified, as in the case of giant arcs. [16] pointed out

that the predicted number of GRAMORs is expected to be comparable to that of giant arcs. They examined the statistical properties of GRAMORs by using two models of cluster mass profile, an isothermal sphere with a core and a universal dark matter halo profile and showed that a relative frequency of GRAMORs to giant arcs can be used to probe the density profile of clusters of galaxies. [5] show the use of GRAMORs in restricting the value of the cosmological constant.

Study of Abell1689 to Constrain Cosmologic Paramaters

There have been extensive studies of Abell1689 to constrain cosmological parameters [9]. The results of this are shown in Figure 9.10. In this study, the authors used a simplified model with a total of 21 free parameters, with two large scale potentials and a galaxy-scale potential for the central brightest cluster galaxy. These authors solved the lens equation in the source plane because it is computationally efficient to do so. Inverting in the lens plane provides additional information, but was felt to be computationally prohibitive.

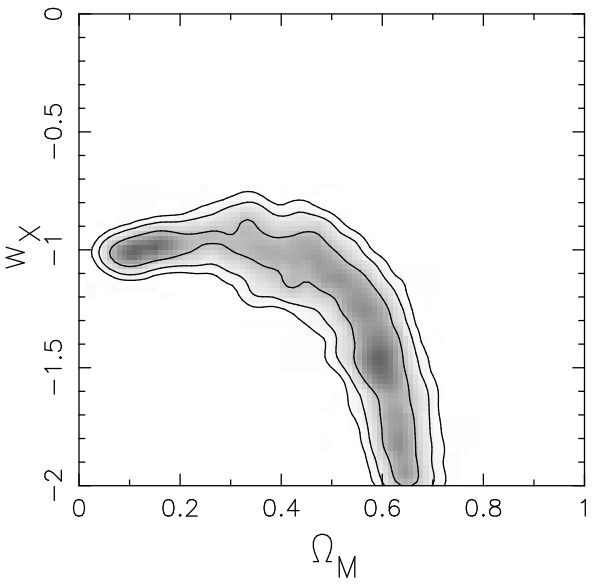

Figure 9.10: Constraint of w_X and Ω_m in A1689 in the study of [9]

Using GRAMORs to Constrain Cosmologic Parameters

A recent study from our own research group examined the lens statistics for GRAMORs [11]. They calculated the expected number distribution of GRAMORs as a function of source redshift changing several conditions. These results showed that a cluster with a flat core produces more GRAMORs which is consistent with previous studies. They also considered various values of lens redshift and found that the distribution has a sharp peak in most cases. In particular the peak becomes more sharp for clusters with a higher redshift. They then showed that the number of GRAMORs is expected to be ~ 2.1 per cluster in the most likely case, which means that a sufficient number of GRAMORs can be expected to be observed based on the statistics if we perform a systematic survey.

They also found that the number of GRAMORs depends strongly on the cosmological parameters, which is a unique property of GRAMORs. In the case of an arc, the PDF doesn't have such a big difference comparing two models. This is caused by the behavior of the parameter which represents the magnification of lensed images. The peak position in the PDF is at about $z = 1.6$ for the ΛCDM universe which is close to the observed value of$z_s = 1.4906$, while the PDF has a peak at about $z_s = 2$ in another model. It is rather surprising that only one system MACSJ1149.5+2223 and one image can give us a strong constraint on the existence of the cosmological constant [11].

Source Plane Optimization

It is acknowledged that optimization in the image plane may be superior is some instances. Despite this, optimization in the source plane is commonly used. In a study of SDSSJ1004+4112, Oguri used glafic to model that system. They employed a standard χ^2 minimization to find the best fit mass model. They used a downhill simplex method to find a minimum. To speed up the calculations, χ^2 was estimated in the source plane, which was found to be sufficiently accurate for their purposes [12].

Strong lens modeling with the standard χ^2 minimization is sometimes time-consuming, especially when many lens potential components and images are involved. One way to overcome this problem is to evaluate χ^2 in the source plane instead of the image plane. Although the source plane χ^2 involves approximations (given that observational measurements are always made in the image plane) and therefore is less accurate than the image plane χ^2, it allows one to estimate χ^2 without solving the nonlinear lens equation. This technique has been adopted by several authors, although the implementations were quite different for different papers. The technique used by Oguri is thoroughly described in Appendix B [12].

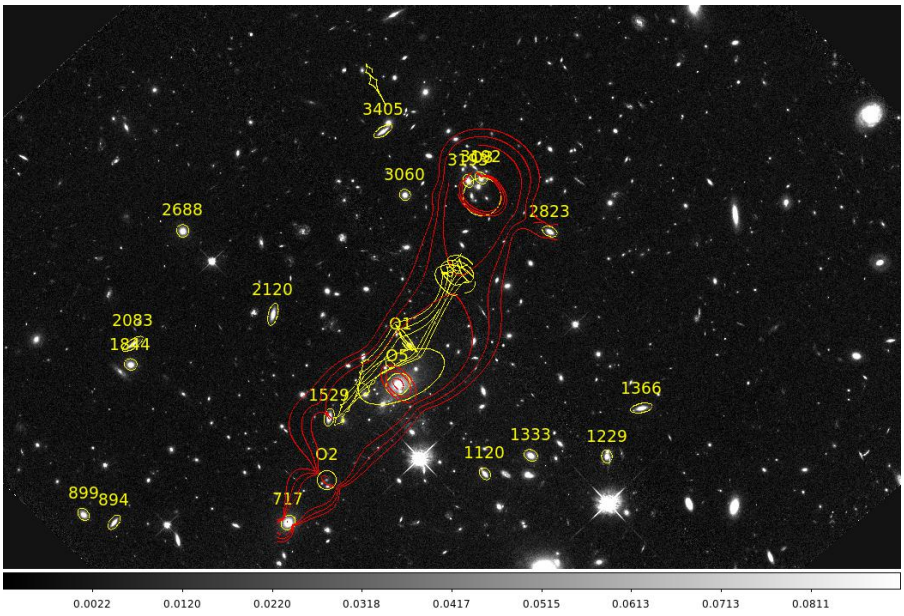

Figure 9.11: Original Lenstool model of MACSJ1149.5+2223 with image plane optimization

Source plane optimization was also used in the study of constraining cosmologic parameters

using a study of Abell1689 by [9]. They solved the lens equation in the source plane for Abell 1689 because it is computationally efficient. Inverting in the lens (image) plane provides additional information but is computationally prohibitive at present. Despite this, they had excellent results in constraining cosmological parameters in the $w_X - \Omega_m$ plane.

In another study, of COSMOS J095930+023427, by [1], they used optimization in the source plane. Optimization of the lens models was performed by means of Lenstool, adopting a Bayesian approach to strong lensing modeling. These investigators chose to use the source plane minimization algorithm for higher accuracy. In Lenstool, the positions of the images are the main input observational data to constrain the lens model parameters.

The Lenstool model with image plane optimization for the model in this study is shown in Figure 9.11, which can be compared to the models shown in Figure 9.7. Qualitatively, these two models appear quite similar. Quantitatively, they are somewhat different. The rms for the source plane optimized model is 1.783 arcsec. The minimum χ^2 with this model is 91.6. The rms for the image plane optimized model is 0.48 arcsec. The minimum χ^2 for this model is 41.9. Therefore, the model which is optimized in the image plane, is indeed somewhat better than the model optimized in the source plane, from a quantitative standpoint.

Lens Model Used in this Study

The Lenstool model adopted in this study is slightly different from the other models used, in that we use a LTM (parametric) model for all five galaxies as separate potentials, but we also use all 38 images in 13 families as described by Merten [10]. The initial model as obtained from Limousin with image plane optimization, has a χ^2 value of 41.9 and an rms of $0.48''$ which is an excellent model. The model we used was slightly different, in that we used source plane optimization and a slightly different image catalog. The chi^2 for this model is 91.6 and the rms is 1.783. This model is not quite as close as the original model. However, due to computing limitations, source plane optimization was necessary. In addition, based on a limited test evaluation, the overall shape of the Ω_m - w_X plane is the same, giving similar constraints on cosmological parameters. This supports the use of source plane optimization for this study. The Lenstool model seems acceptable for use in this study.

The glafic model developed so far is not quite as robust as the Lenstool model. The χ^2 value is 66.3, and the rms is $0.92''$. This model uses the same image catalog used in our Lenstool model, as described above. This was also done with source plane optimization. In the next phase of this project, we will use a different set of lens potentials to model J1149.5 with glafic.

Constraining the Equation of State

It is extremely interesting to compare the results of the simulation study performed by [2] in Figure 9.6 and the results from [9] for A1689, shown in Figure 9.10 with the results found here for J1149.5, in Figure 9.9. All three of these studies were conducted using Lenstool software.

The results of the study to evaluate constraint of cosmological parameters, specifically the dark energy equation of state parameter, w_X, is very interesting when the contour curve in this study for the Lenstool model of J1149.5 is compared to results of a simulation study and the study of A1689. These three studies all show quite similar results.

The glafic model did not constrain the equation of state parameter at all. That is, at all values of w_X, from -2.0 to 2.0 and all values of Ω_m, the χ^2 value did not change appreciably. There was some variation, but none of this was statistically significant and it was not possible to make a contour plot in the w_X - Ω_m plane. This may be due to a problem with the model which requires further refinement.

9.6 Conclusions and Future Work

This chapter reports a preliminary study of MACSJ1149.5+2223, using a basic lens model with both Lenstool and glafic. As of this writing, we have developed models with both Lenstool and glafic, and tested the constraint of the equation of state parameter using the Lenstool model. This model used five potentials and the complete image catalog used by Merten in the Frontier Fields project [10]. This preliminary study found that the Lenstool model was able to constrain w_X in the w_X - Ω_m plane with a shape very similar to that found with a simulation study [2]and when Lenstool was used to model A1689 [8]. In the studies to date, the glafic model did not constrain the values at all.

We also believe that a GRAMOR may be able to constrain the cosmological parameters. Future work with this project will be in several areas.

- We will refine the glafic model to see if this will provide some constraints in the w_X - Ω_m plane, which the current model does not.
- We will test the methods to represent a GRAMOR using Lenstool and glafic.
- We will alter the models (using both Lenstool and glafic) to represent image 1.1 as a GRAMOR, to see if this further constrains the cosmological parameters in the w_X - Ω_m plane.

Acknowledgments

The work in this chapter was very much dependent on the assistance of Prof Marceau Limousin, for providing the Lenstool model of MACSJ1149.5+2223 and the scientific contributions of Masayo Morioka. Their help is gratefully acknowledged.

References

[1] S. Cao, G. Covone, M. Paolillo, and Z.-H. Zhu. A multi-wavelength study of the gravitational lens COSMOS J095930+023427. *Research in Astronomy and Astrophysics*, **13**:15–27, January 2013. 315

[2] A. D'Aloisio and P. Natarajan. Cosmography with cluster strong lenses: the influence of substructure and line-of-sight haloes. *Mon Not Roy Astr Soc*, **411**:1628–1640, March 2011. xvi, 305, 307, 315, 316

[3] M. Fukugita, T. Futamase, and M. Kasai. A Possible Test for the Cosmological Constant with Gravitational Lenses. *Mon Not Roy Astr Soc*, **246**:24P, October 1990. 296

[4] T. Futamase, M. Hattori, and T. Hamana. Gravitationally Lensed yet Morphologically Regular Images in Clusters of Galaxies as Astronomical Tools. *ApJ Letters*, **508**:L47–L49, November 1998. 295, 296, 309

[5] T. Hamana, M. Hattori, H. Ebeling, J. P. Henry, T. Futamase, and Y. Shioya. Lensing Effects on the Protogalaxy Candidate cB58 and Their Implications for the Cosmological Constant. *Astrophys J*, **484**:574–580, July 1997. 296, 312, 313

[6] Hubble Frontier Fields Team. Hubble space telescope frontier fields data access pages. `http://archive.stsci.edu/prepds/frontier/lensmodels/`, November 2014. 296, 297, 308

[7] T. L. Johnson, K. Sharon, M. B. Bayliss, M. D. Gladders, D. Coe, and H. Ebeling. Lens models and magnification maps of the six Hubble Frontier Fields clusters. *ArXiv e-prints*, May 2014. 297, 303, 304

[8] E. Jullo, J.-P. Kneib, M. Limousin, Á. Elíasdóttir, P. J. Marshall, and T. Verdugo. A Bayesian approach to strong lensing modelling of galaxy clusters. *New Journal of Physics*, **9**:447, December 2007. 308, 309, 316

[9] E. Jullo, P. Natarajan, J.-P. Kneib, A. D'Aloisio, M. Limousin, J. Richard, and C. Schimd. Cosmological Constraints from Strong Gravitational Lensing in Clusters of Galaxies. *Science*, **329**:924–927, August 2010. xvi, 309, 313, 315

[10] J. Merten. Macsj1149.5+2223 image catalog. `http://archive.stsci.edu/pub/hlsp/frontier/macs1149/models/merten/v1/`, November 2014. 308, 315, 316

[11] M. Morioka and T. Futamase. Lens statistics with gravitationally lensed yet morphologically regular images. Manuscript in Preparation, November 2014. 313, 314

[12] M. Oguri. The Mass Distribution of SDSS J1004+4112 Revisited. *Proc Astr Soc Japan*, **62**:1017–, August 2010. 308, 314

[13] S. Rau, S. Vegetti, and S. D. M. White. Lensing model of MACS J1149.5+2223 - I. Cluster mass reconstruction. *Mon Not Roy Astr Soc*, **443**:957–968, September 2014. xvi, 298, 301, 302

[14] J. Richard, M. Jauzac, M. Limousin, E. Jullo, B. Clément, H. Ebeling, J.-P. Kneib, H. Atek, P. Natarajan, E. Egami, R. Livermore, and R. Bower. Mass and magnification maps for the Hubble Space Telescope Frontier Fields clusters: implications for high-redshift studies. *Mon Not Roy Astr Soc*, **444**:268–289, October 2014. 296

[15] G. P. Smith, H. Ebeling, M. Limousin, J.-P. Kneib, A. M. Swinbank, C.-J. Ma, M. Jauzac, J. Richard, E. Jullo, D. J. Sand, A. C. Edge, and I. Smail. Hubble Space Telescope Observations of a Spectacular New Strong-Lensing Galaxy Cluster: MACS J1149.5+2223 at z = 0.544. *ApJ Letters*, **707**:L163–L168, December 2009. xvi, 300, 301, 302, 303, 304

[16] L. L. R. Williams and G. F. Lewis. Undistorted lensed images in galaxy clusters. *Mon Not Roy Astr Soc*, **294**:299, February 1998. 296, 312

[17] W. Zheng, M. Postman, A. Zitrin, J. Moustakas, X. Shu, S. Jouvel, O. Høst, A. Molino, L. Bradley, D. Coe, L. A. Moustakas, M. Carrasco, H. Ford, N. Benítez, T. R. Lauer, S. Seitz, R. Bouwens, A. Koekemoer, E. Medezinski, M. Bartelmann, T. Broadhurst, M. Donahue, C. Grillo, L. Infante, S. W. Jha, D. D. Kelson, O. Lahav, D. Lemze, P. Melchior, M. Meneghetti, J. Merten, M. Nonino, S. Ogaz, P. Rosati, K. Umetsu, and A. van der Wel. A magnified young galaxy from about 500 million years after the Big Bang. *Nature*, **489**:406–408, September 2012. 303, 305

[18] A. Zitrin and T. Broadhurst. Discovery of the Largest Known Lensed Images Formed by a Critically Convergent Lensing Cluster. *ApJ Letters*, **703**:L132–L136, October 2009. xvi, 295, 296, 298, 299, 301, 303, 309, 312

[19] A. Zitrin, T. Broadhurst, R. Barkana, Y. Rephaeli, and N. Benítez. Strong-lensing analysis of a complete sample of 12 MACS clusters at z>0.5: mass models and Einstein radii. *Mon Not Roy Astr Soc*, **410**:1939–1956, January 2011. 300, 304, 309

[20] A. Zitrin, T. Broadhurst, K. Umetsu, D. Coe, N. Benítez, B. Ascaso, L. Bradley, H. Ford, J. Jee, E. Medezinski, Y. Rephaeli, and W. Zheng. New multiply-lensed galaxies identified in ACS/NIC3 observations of Cl0024+1654 using an improved mass model. *Mon Not Roy Astr Soc*, **396**:1985–2002, July 2009. 298

Chapter 10

Conclusions and Outlook

The modern science of gravitational lensing was born just 100 years ago with the advent of general relativity and then rapidly proceeded to sleep for another 64 years, awakening in 1979 with the observation of the first gravitational lens. Since that time, gravitational lensing has rapidly become one of the most important tools in modern cosmology. The value of strong gravitational lensing comes from our ability to analyze observational data.

In this dissertation, we have reviewed the state of strong gravitational lens model software, starting with a catalog of available software (Chapter 4), comparative lens model studies (Chapters 5 and 7), development of a program to translate lens model input files (Chapter 6) and then comparative studies of the results of lens model studies for time delays (Chapter 8) and the ability of lens models to constrain cosmologic parameters (Chapter 9). The extensive use of various strong gravitational lens model software codes in comparative studies has allowed us to make some conclusions about the overall state of the field, and raise some issues relevant to future studies.

10.1 Gravitational Lens Model Software

As we found in the study presented in Chapter 4, there are many different codes for strong gravitational lens models, including both LTM and non-LTM codes. Some of these codes have been in existence for many years (e.g. Lenstool) and are used around the world. Others are much more recent and used only by their authors.

There is great variability both in the ease-of-use of these codes as well as the volume of information that they produce. It seems that the more complex codes provide more data. All of the codes are subject to the old computer programming axiom of "garbage in - garbage out". The quality of the input model will determine the quality of the data produced.

10.2 Comparative Studies: Strong Gravitational Lens Models

There were two groups of studies conducted in this general area, including a study of time delays and mass calculations for two different systems by four lens model codes (Chapter 5) and a

comparison of lens model parameters calculated for four different systems by four different lens model codes (Chapter 7). In the study of two systems (a mock system and SDSSJ1004+4112), we compared time delay and mass calculations for four different codes and found a wide variation in results. The methodology was to look at the results using identical input models, rather than allowing each code to optimize the models. In Chapter 7, we did a similar analysis looking at the calculation of best fit lens parameters by four codes for four different systems. Again, we used models that were as identical as possible to see the differences in the results produced by each code. This methodology has a weakness in that due to differences in the codes, it is not always possible to use an identical model. Once again, as in Chapter 5, there were significant differences in the results produced by each code.

10.3 Gravitational Lens Model Translation

Creating lens model input files is extremely complex because there is a lot of information which must be entered in a specific format, and the format varies so much among the many software codes available. There does not seem to be a good solution to this problem. As a partial solution, the HydraLens program was written (Chapter 6 and Appendix A). This software is somewhat limited at present, as it only works for four different codes and cannot translate every feature. Despite this, the program could be very useful for beginners in the field, and should encourage the conduct of comparative lens models studies in the future.

10.4 Comparative Studies: Time Delay Calculations

Based on the observations of variability in Chapter 5, we performed a comparison of time delay calculations which was enhanced by this study of B1608+656 and RXJ1131−1231 which have been extremely well characterized in previous studies. The results of this study shown in Chapter 8 showed reasonable agreement with observational results, and variability among the results from several codes was less than that observed in Chapter 5. The best lens parameters were fairly close among the various codes tested. Further work is needed to refine the models used and to examine the effects of these differences on the calculation of H_0.

10.5 Comparative Studies: Constraining Cosmological Parameters

The study in Chapter 9 is a careful study of MACSJ1149.5+2223, with lens models using both Lenstool and glafic. We tested the ability of these models to constrain the equation of state parameter. The Lenstool model uses five PIEMD potentials and the complete image catalog used in the Hubble Frontier Fields project. This preliminary study found that the Lenstool model was able to constrain w_X in the w_X - Ω_m plane with a shape very similar to that found in other studies of A1689. In the studies performed to date, the glafic model did not constrain the values at all. We also believe that a GRAMOR may be able to further constrain the cosmological parameters. Future work with this project will be in several areas. We will refine the glafic model to see if this will provide some constraints in the w_X - Ω_m plane, which

the current glafic model does not. We will then test the methods to represent a GRAMOR using Lenstool and glafic. Finally, we will alter the models (using both Lenstool and glafic) to represent image 1.1 as a GRAMOR, to see if this further constrains the cosmological parameters in the w_X - Ω_m plane.

10.6 Outlook and Challenges for the Future of Lens Model Studies

Perhaps the most important result of the studies highlighted in this dissertation is that comparative studies are an important part of the future of gravitational lensing. Until the very recent past, this has rarely been a routine part of lens model studies, but it has been designed into the Hubble Frontier Fields lens study and hopefully will be an important part of major studies in the future.

There are two major barriers identified as a result of these studies, for the future conduct of comparative lens models studies. First, the input data used in each model code is highly dependent on the code used. There is absolutely no attempt to have a standard input format. Some of these differences are necessary because of the differences in the codes, and some of the differences are artificial. It would greatly benefit the future of lens model science if there were some standard core for data input which could then be augmented for each code. This would encourage and simplify future comparative studies. The HydraLens software was a basic attempt to accomplish this goal. There are surely other better ways that need implementation.

The other barrier to comparative studies is that it is often impossible to reproduce the data in a published study because the software has been made unavailable to anyone but the author of the software, and the study. Without the ability to reproduce a study, there can be little confidence in the voracity of the results. The lensing community must become more open with the tools it uses to obtain these important scientific results.

Overall, the future of comparative strong gravitational lens model studies is bright (pun intended)!

Appendix A HydraLens User Manual

.1 Introduction

HydraLens is software to aid in the generation of lens model files for supported lens model software. The HydraLens distribution includes 4 parts:

User's Manual .pdf file (This document)

Manuscript .pdf file

HydraLens source code Written in Visual Basic

HydraLens.exe Compiled program, runs under the Windows (Microsoft Corp, Redmond WA) operating system

At the present time the following strong gravitational lens model software is supported:

glafic

gravlens / lensmodel

Lenstool

PixeLens

There are a few caveats to using this software.

Purpose HydraLens has two purposes, lens model generation and lens model translation. However, this software is not magic. It cannot take the place of scientific insight into designing a model. The best way to view this software is as a first step toward making models for several lens modeling codes.

Model File Generation Model generation features are fully implemented for the four types of lens model software implemented. HydraLens greatly simplifies the task of preparing a lens model input file, by doing this through a GUI rather than a text editor.

Translation: Beta For model translation, this software should be considered as 'beta' software. It is not 'fully baked'.

Features I will implement more features over the next few months, and am happy to take suggestions from any users.

The purpose of this manual is to explain how to use HydraLens, not to explain how it works. Please refer to the manuscript for further information about the internal structure and function of HydraLens.

HydraLens has 4 modules plus a data module: Generate, Write, Translate and Parse. When the software is loaded, the user is presented with two choices, either to generate a new model or to read an existing model (for translation). This window is shown in Figure 1, and the main "actions" are easily shown with bright blue buttons in the GUI.

.2 Generate a Lens Model

This uses the Generate and Write Modules.

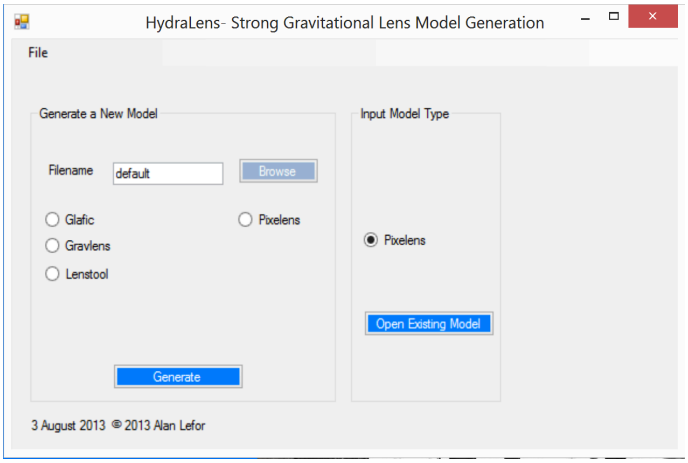

Figure 1: Initial window on program load allows generating a new model or reading an existing model. One of the two "action" buttons (enabled, in dark blue) is pressed after selecting the target software with the radio buttons.

Pixelens

glafic

Upon selecting glafic as the target software (Figure 1), the user is presented with a screen to decide which glafic file to generate (Figure 2).

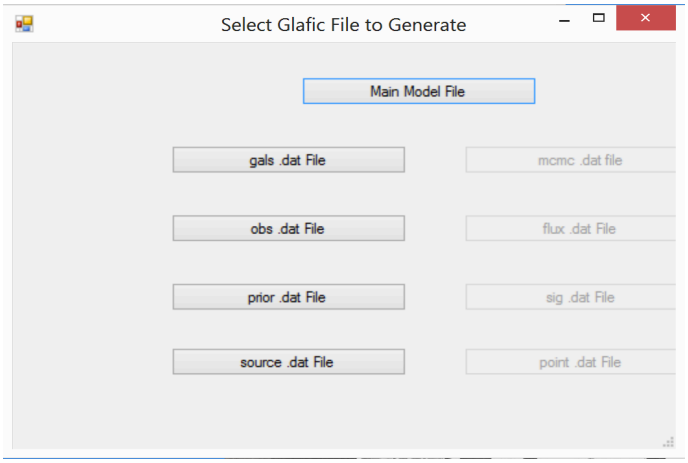

Figure 2: After selecting glafic as the output target, the user selects which of the glafic files will be generated. Usually, one starts with the 'Main Model File'

After selecting to generate the Main Model file, the user is presented with the glafic model generation screen (Figure 3) for further data entry.

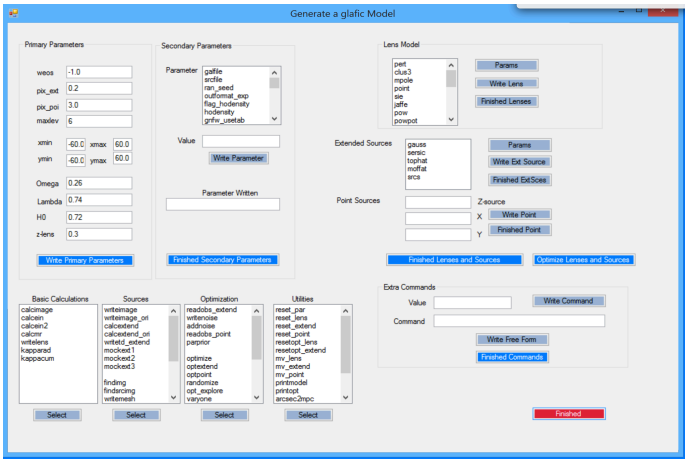

Figure 3: After selecting the Main Model File generation, the user is presented with this window to enter all of the data for a glafic model

gravlens / lensmodel

lensmodel Data File

The lensmodel data file cannot be generated until you add the data command (secondary). Once that command is added, a button appears to create the data file.

Lenstool

.3 Read an Existing Lens Model

This uses the Parse module only.

General Tips

- Be sure there are no blank lines in an existing model file

Pixelens

HydraLens can read any existing Pixelens input file, in preparation to translate it to any of the supported target model types. This includes double, quad and multi file types.

glafic

This feature is not yet implemented.

gravlens / lensmodel

This feature is not yet implemented

Lenstool

This feature is not yet implemented.

.4 Translate a Lens Model

This uses the translate and write modules.

General Tips

- Get the lens geometry, specifically the locations of the images
- Use PixeLens to rapidly prototype the system, check geometry and image position
- Translate PixeLens into Lenstool, lensmodel and glafic, which generates 2 files for each software including a model file and a data file. The models generates all have a single lens to make a "working model", but this will likely be changed.
- Models for lensmodel and lenstool (both model files and data files) need post processing to remove the seemingly empty last line (with gedit) and then use vi to get rid of all the ctrl-M characters on each line. This is not necessary for the glafic files.
- Add the correct potentials (lenses) to each model. Add optimization parameters if desired. Add fluxes to images in glafic and/or lensmodel.
- Add errors to glafic for flux and/or position
- You now have 4 functional models that can be easily refined, and edited with almost any text editor.

PixeLens

Limitations

Translations to and from Pixelens are somewhat limited because PixeLens is a non-LTM code, and therefore has no mass models. Translations from PixeLens do not provide a mass model. Translations from PixeLens basically provide the data files with coordinates for target model types.

Translations from Pixelens

Lenstool Lenstool models generated from pixelens have no potential, no lens model. The user must add parameters to the Primary Command 'Potential' and 'Limit.

Glafic Glafic models have a single SIS model. They start with 1 lenses and 0 extended sources. Point sources are added from the Pixlens model file. User must add lens models and optimizations.

gravlens / lensmodel gravlens /lensmodel models have a single SIS mass model. The user should modify the lens model and any desired optimization parameters.

Translations to Pixelens

Lenstool

Glafic

gravlens / lensmodel

What to do after a Translation to PixeLens

- You may want to adjust Pixrad
- Check the parity on the images. Parity is not carried over from glafic which does have that parameter but could have a different meaning. Parity in Pixelens files is important (see page 6, Sec 5.2.3)

glafic

Limitations

Translations to Glafic

Lenstool

Pixelens

gravlens / lensmodel

What to do after translation to Glafic

- From PixeLens you probably want to modify the initial mass model
- From PixeLens Set optimization flags, add fluxes to data file, add errors in flux and position to data file

Translations from Glafic

Lenstool

PixeLens

gravlens / lensmodel

gravlens / lensmodel

Limitations

Translations to gravlens / lensmodel

Lenstool

Glafic

PixeLens

What to do after translation to gravlens / lensmodel

- From PixeLens you probably want to modify the initial mass model
- From PixeLens Set optimization flags, add fluxes to data file, add errors in flux and position to data file

Translations from gravlens/lensmodel

Lenstool

Glafic

PixeLens

Lenstool

Limitations

- Spacing: No tab characters
- Potentials: Only one Potential

Translations to Lenstool

PixeLens

Glafic

gravlens / lensmodel

What to do after translation to Lenstool

- Translating from Pixelens, the software adds a simple SIE potential at (0,0) with vdisp=300. This is just to give a working model.
- Very important. Because of the vagaries of Windows and Linux interactions, you must edit the Lenstool model produced. Remove the last "line feed" so that "fini" is on its own line as the last line. Then, when you start Lenstool, you automatically enter the vi editor. Issue the command ":percents/ctrlVctrlM//g" to eliminate all the ctrlM control characters. This is essential to use the model file.
- The models generated all include "inverse 3" in the run mode section, which performs Bayesian optimization. If you don't want this, then comment out the line. If you leave it set to 3, there should be parameters to be optimized in the "limit" section (at baseline they are all set to 0)

Translations from Lenstool

Pixelens

Glafic

gravlens / lensmodel